Imperial College London

# Electrochemical behaviour of carbon steel in aqueous amine solvents for post combustion carbon capture

**Samara Aliyah Sadeek**

December 2021

Department of Chemical Engineering

Imperial College London

South Kensington Campus

London SW7 2AZ, UK

A thesis submitted to Imperial College London in partial fulfilment of the requirements of the degree of Doctor of Philosophy

## Declaration

I hereby declare that this thesis and the work reported herein was composed by and originated entirely from me. Information derived from the published and unpublished work of others has been acknowledged in the text and references are given in the list of sources.

Samara Aliyah Sadeek

## Copyright Notice

The copyright of this thesis rests with the author. Unless otherwise indicated, its contents are licensed under a Creative Commons Attribution-Non Commercial 4.0 International Licence (CC BY-NC). Under this licence, you may copy and redistribute the material in any medium or format. You may also create and distribute modified versions of the work. This is on the condition that: you credit the author and do not use it, or any derivative works, for a commercial purpose. When reusing or sharing this work, ensure you make the licence terms clear to others by naming the licence and linking to the licence text. Where a work has been adapted, you should indicate that the work has been changed and describe those changes. Please seek permission from the copyright holder for uses of this work that are not included in this licence or permitted under UK Copyright Law.'

*Dedicated to my parents,*
*Cheryl and Alim Sadeek*

# Acknowledgements

To my supervisor Anna Hankin, who has been truly instrumental in getting me to the end of my PhD, thank you for our many electrochemical discussions, for your feedback, your time, and your relentless support; words can't describe how grateful I am to you. To my co-supervisor Geoff Kelsall, who has been an endless source of electrochemical wisdom, brilliant ideas and guidance, thank you for your support, for all our lengthy, engaging discussions, and for patiently answering my many questions. To Franky Bedoya, who at times, acted as a third supervisor, I cannot thank you enough for the countless hours spent explaining electrochemical topics and for always being patient and willing to share useful advice. I'd also like to say thank you to Kyra Sedransk Campbell, who encouraged me to pursue a PhD and who supported me through my initial research years. Thank you to Paul Fennell who generously allowed me to run most of my experiments in his labs and to the Chemical Engineering Department for awarding me a PhD scholarship.

I am very grateful to Colin Hale for graciously spending many late nights and giving many hours of his limited time to make the pilot plant study possible. To the Mechanical Workshop, and in particular Jonathon Henton, for always kindly and ingeniously making every reactor or electrode design request possible. To other members of the Chemical Engineering department, especially Serafim Kalliadasis, Daryl Williams, Susi Underwood, Ben Kisnath, Patricia Carry, and of the Materials department, specifically Mary Ryan, Ecaterina Ware, Mahmoud Ardakani and Richard Sweeney, thank you all for supporting me throughout my PhD journey.

To Jose, thank you for being endlessly patient and the most helpful lab buddy even when we weren't sharing labs. And to Michael for filling my final months in the lab with laughter, fun, and in-depth academic and non-academic discussions; you've made it a truly enjoyable time even during a pandemic. Special thanks to the Campbell Group, Electrochemical Engineering Group, and the Electrochemical Systems Lab members – particularly Nadine, Minos, Efty, Franky, Sze, Xiaochu, Nahmkang for the helpful academic discussions and of course for all the fun and adventures.

I thank my mom, dad, and brother, Samir, heartily for the unwavering, limitless support and love. To Aunty San and Rissa, although we were far apart, you both were always available to provide words of encouragement and I am so grateful for that. To my friend, Lisa, thank you for our many conversations that were always filled with laughter and understanding, and for your triumphant effort in proofreading this thesis.

Lastly, I'd like to give my most heartfelt thank you to David Loughnane, without whom this PhD journey probably would neither have started, nor been completed.

# Abstract

Post combustion $CO_2$ capture (PCCC) through amine scrubbing is one of the few commercially deployed $CO_2$ emissions abatement technologies to date. Though essential for attaining global net zero anthropogenic $CO_2$ emissions, widescale deployment is being hampered by technical issues, one of which is the high costs due to corrosion in PCCC plants. Monoethanolamine (MEA), the benchmark amine solvent, has been demonstrated to become increasingly corrosive with elevated temperatures and $CO_2$ enrichment, so requiring plant construction with costly stainless steel (SS 316L), *ca.* 5 - 6 times the cost of carbon steel (CS). Methyldiethanolamine (MDEA), widely used in natural gas processing, has been reported to promote the formation of $FeCO_3$ on CS, which is thought to provide corrosion protection to the underlying substrate, particularly at high temperatures and when saturated with $CO_2$. Therefore, this project aimed to assess the use of pre-treated CS to eliminate the requirement for SS in areas of the PCCC plants particularly susceptible to corrosion, and explain the divergent behaviour exhibited by CS in $MEA_{(aq)}$ and $MDEA_{(aq)}$ solutions.

Voltammetry, chronoamperometry and electrochemical impedance spectroscopy, together with *ex-situ* surface characterisation by scanning electron microscopy, energy dispersive spectroscopy, and X-ray diffraction, were used to measure $FeCO_3$ film formation time, resistance to charge transfer, composition and morphology as a function of MDEA concentration at 80 °C. Protective crystalline $FeCO_3$ films were found to be formed optimally on CS (1018) within 72 h in 1 M $MDEA_{(aq)}$ solutions. Subsequent stability tests in $MEA_{(aq)}$ solutions demonstrated promising results, with pre-treated C1018 being 10 times more resistive to charge transfer than untreated C1018. Amine solutions were deaerated with $N_2$ and loaded with $CO_2$ prior to experiments and were purged with $CO_2$ during experiments. However, adventitious ingress of aerial $O_2$ caused iron oxide(s) to form on surface films in several experiments, accelerating localised attack, which has implications for implementing this strategy in PCCC plants, since feed gas streams typically contain $O_2$. Using these results, pre-treated C1018 coupons were tested in the PCCC pilot plant at Imperial College London. Though tested under non-ideal conditions, the surface film formed on coupons in the dilute 1 M $MDEA_{(aq)}$ pre-treatment solution remained intact and provided protection to the underlying substrate for up to 225 h in $MEA_{(aq)}$ solutions.

A diffusion reaction model was built to determine the effect of the concomitant $H^+$ release with $FeCO_3$ formation on the stability of surface films. A substantial local pH decrease was estimated from the model during the potentiostatic formation of $FeCO_3$, creating unfavourable conditions for its stability. Based on the observed presence of these films produced in $MDEA_{(aq)}$, a mechanism for local pH stabilisation was proposed, involving the effective protonation of MDEA and carbonate ions, thus providing an explanation for the divergent behaviour exhibited by CS in these two amines.

# Nomenclature

## Symbols

| | | |
|---|---|---|
| A | Surface Area | $m^2$ |
| $C_i$ | Concentration of species i | mol $dm^{-3}$ |
| C | Capacitance | F |
| D | Diffusion coefficient | $m^2$ $s^{-1}$ |
| E | Electrode potential | V |
| $E^o$ | Standard potential | V |
| $E_r$ | Reversible potential | V |
| f | Frequency | Hz |
| F | Faraday's constant | A s $mol^{-1}$ |
| $\Delta G$ | Gibbs energy of formation | J $mol^{-1}$ |
| $\Delta H$ | Enthalpy change | J $mol^{-1}$ |
| I | Current | A |
| $I_L$ | Mass transport limited current | A |
| j | Current density | A $m^{-2}$ |
| $j_L$ | Mass transport limited current density | A $m^{-2}$ |
| $j_o$ | Exchange current density | A $m^{-2}$ |
| k | Kinetic rate constant | Variable |
| $k_B$ | Boltzmann constant | J $K^{-1}$ |
| $k_m$ | Mass transport rate coefficient | m $s^{-1}$ |
| K | Equilibrium constant | 1 |
| $K_{sp}$ | Solubility limit | $mol^2$ $dm^{-6}$ |
| L | Length | m |
| m | Mass | kg |
| $m_i$ | Moles of species i | mol |
| M | Molecular weight | g $mol^{-1}$ |
| N | Molar flux | mol $m^{-2}$ $s^{-1}$ |
| p | Partial pressure of gas | Pa |
| q | Electric charge | A s |

| | | |
|---|---|---|
| $Q$ | Electric charge density | $A\ s\ m^{-2}$ |
| $Q_o$ | Constant phase element | $F\ s^{\alpha-1}\ m^{-2}$ |
| $r_o$ | Equivalent hydrodynamic radius | $m$ |
| $R$ | Ideal gas constant | $J\ mol^{-1}\ K^{-1}$ |
| $R$ | Electric resistance | $\Omega\ m^2$ |
| $s$ | Scan rate | $mV\ s^{-1}$ |
| $S$ | Saturation ratio | $1$ |
| $\Delta S$ | Entropy change | $J\ mol^{-1}$ |
| $t$ | Time | $s$ |
| $T$ | Temperature | $K$ |
| $u$ | Ionic mobility | $m^2\ V^{-1}\ s^{-1}$ |
| $V$ | Volume | $dm^3$ |
| $x$ | distance | $m$ |
| $Z$ | Impedance | $\Omega\ m^{-2}$ |
| $z_i$ | Charge of species i | $1$ |
| $\alpha$ | Transfer coefficient | $1$ |
| $\alpha$ | Constant phase element exponent | $1$ |
| $\beta$ | Tafel coefficient | $V^{-1}$ |
| $\beta$ | Tafel slope | $mV\ dec^{-1}$ |
| $\beta$ | Buffering capacity | $mol\ dm^{-3}$ |
| $\delta$ | Diffusion layer thickness | $m$ |
| $\epsilon_o$ | Vacuum permittivity | $F\ m^{-1}$ |
| $\epsilon_i$ | Relative permittivity | $1$ |
| $\gamma$ | Activity coefficient | $1$ |
| $\eta$ | Overpotential | $V$ |
| $\theta$ | Fractional surface coverage | $1$ |
| $\lambda$ | Wavelength | $nm$ |
| $\mu$ | Dynamic viscosity | $Pa\ s$ |
| $\nu$ | Kinematic viscosity | $m^2\ s^{-1}$ |
| $\varrho$ | Density | $kg\ m^{-3}$ |
| $\sigma$ | Supersaturation | $1$ |
| $\sigma_d$ | Warburg coefficient | $\Omega\ s^{-1/2}$ |
| $\tau$ | Time constant | $s$ |

| | | |
|---|---|---|
| $\tau$ | Shear stress | Pa |
| $\phi$ | Electric potential or Phase angle | V, ° |
| $\Phi$ | Faradaic efficiency | 1 or % |
| $\omega$ | Angular frequency | rad $s^{-1}$ |

## Subscripts and superscripts

| | |
|---|---|
| a | Anodic process |
| c | Cathodic process |
| ads | Adsorbed state |
| $\delta$ | Bulk value |
| s | Surface value |
| d | Diffusion process |

## Abbreviations

| | |
|---|---|
| O | Reducible species |
| R | Oxidisable species |
| $e^-$ | Electron |
| WE | Working electrode |
| CE | Counter electrode |
| RE | Reference electrode |
| SHE | Standard hydrogen electrode |
| OCP | Open circuit potential |
| CV | Cyclic voltammetry |
| RDE | Rotation disc electrode |
| RRDE | Rotating ring disc electrode |
| HER | Hydrogen evolution reaction |
| EIS | Electrochemical impedance spectroscopy |
| ICP | Inductively coupled plasma |

# Contents

**Acknowledgements** ..... **v**

**Abstract** ..... **vi**

**Nomenclature** ..... **vii**

**Contents** ..... **x**

**List of figures** ..... **xvi**

**List of tables** ..... **xxxii**

**1 Introduction** ..... **1**

**1.1 Project aims and objectives** ..... **2**

1.1.1 Project tasks ..... 3

**2 Literature Review** ..... **5**

**2.1 Electrochemistry fundamentals applied to corrosion** ..... **5**

2.1.1 Electrochemical thermodynamics ..... 7

2.1.2 Electrochemical kinetics ..... 12

**2.2 Carbon capture and storage** ..... **22**

**2.3 Corrosion in amine scrubbing plants** ..... **23**

**2.4 Steel dissolution and passivation in aqueous $CO_2$ solutions** ..... **27**

2.4.1 Solution speciation ..... 27

2.4.2 Active dissolution ..... 29

2.4.3 Passivation ..... 34

2.4.4 Electrochemical studies of Fe and carbon steel in aqueous $CO_2$ environments ..35

2.4.5 $FeCO_3$ formation ..... 39

**2.5 Corrosion in post combustion carbon capture plants** ..... **70**

2.5.1 Amine – $CO_2$ speciation ..... 70
2.5.2 Corrosion behaviour of steel in amine – $CO_2$ ..... 72
**3 Experimental Methods ..... 89**
**3.1 Preliminary immersion study ..... 92**
3.1.1 Experimental setup ..... 92
**3.2 Cyclic voltammetry study ..... 93**
3.2.1 Stationary disc electrode experimental method ..... 95
3.2.2 Rotating disc electrode experimental method ..... 96
3.2.3 Pt voltammetry experiments ..... 97
**3.3 Chronoamperometry study ..... 98**
3.3.1 Experimental setup ..... 98
3.3.2 Electrochemical measurements ..... 98
**3.4 Electrochemical impedance study ..... 99**
3.4.1 Open circuit film formation ..... 99
3.4.2 Open circuit film stability ..... 101
**3.5 Pilot plant study ..... 102**
3.5.1 Experimental matrix ..... 104
3.5.2 Electrodes used for pilot plant study ..... 107
3.5.3 Data acquisition ..... 109
3.5.4 Installation points and procedure ..... 112
3.5.5 Plant operation protocol ..... 115
3.5.6 Electrode pre-treatment and post pilot plant analysis ..... 117
**3.6 Surface characterisation and solution analytical techniques ..... 118**
3.6.1 Surface characterisation techniques ..... 118
3.6.2 Solution analytical techniques ..... 120
**4 Preliminary immersion study ..... 122**

**4.1 Introduction ..... 122**

**4.2 Results ..... 123**

4.2.1 Carbon steel immersion in aqueous monoethanolamine saturated with $CO_2$ ..... 123

4.2.2 Carbon steel immersion in aqueous methyldiethanolamine saturated with $CO_2$. ..... 127

**4.3 Conclusions ..... 131**

**5 Electrochemical behaviour of iron in amine solutions saturated with $CO_2$ ..... 132**

**5.1 Introduction ..... 132**

**5.2 Results ..... 133**

5.2.1 Electrochemical behaviour of iron in aqueous monoethanolamine (MEA) solutions saturated with $CO_2$ ..... 133

5.2.2 Electrochemical behaviour of iron in methyldiethanolamine (MDEA) aqueous solutions saturated with $CO_2$ ..... 161

**5.3 Comparison of electrochemical behaviour of iron in both aqueous amine solutions saturated with $CO_2$ ..... 177**

**5.4 Conclusions ..... 179**

**6 $FeCO_3$ formation on iron in amine solutions saturated with $CO_2$ ..... 180**

**6.1 Introduction ..... 180**

**6.2 Results ..... 180**

6.2.1 Current density transients of iron in aqueous monoethanolamine (MEA) saturated with $CO_2$ ..... 182

6.2.2 Current density transients of iron in aqueous methyldiethanolamine (MDEA) saturated with $CO_2$ ..... 188

6.2.3 Comparison of $FeCO_3$ formation on Fe in aqueous MEA and MDEA solutions saturated with $CO_2$ ..... 193

**6.3 Local solution chemistry changes during $FeCO_3$ formation on iron ..... 195**

**6.4 Conclusions ..... 206**

**7 Growth of resistive films on carbon steel in amine solutions saturated with $CO_2$ . 208**

**7.1 Introduction ..... 208**

7.1.1 Experimental considerations ..... 209

7.1.2 Data analysis considerations ..... 209

**7.2 Results and discussion ..... 214**

7.2.1 Impedance spectroscopy of carbon steel in MDEA and MEA ..... 214

7.2.2 Impedance spectroscopy of pre-treated carbon steel in aqueous MEA saturated with $CO_2$ ..... 231

7.2.3 Comparison of the performance of pre-treated electrodes ..... 244

7.2.4 Effect of adventitious dissolved $O_2$ ..... 252

**7.3 Conclusion ..... 256**

**8 Pilot plant study ..... 258**

**8.1 Introduction ..... 258**

**8.2 Experimental considerations ..... 259**

**8.3 Results ..... 263**

8.3.1 Pilot plant study results ..... 263

8.3.2 Electrochemical impedance spectroscopy results ..... 272

**8.4 Conclusions ..... 296**

**9 Conclusions ..... 299**

**10 Future work proposal ..... 305**

**11 References ..... 306**

**12 Appendices ..... 320**

**12.1 Chapter 2 appendix ..... 320**

12.1.1 Thermodynamic data ..... 320

12.1.2 Copyright permissions ..... 323

**12.2 Chapter 4 appendix ..... 324**

**12.3 Chapter 5 appendix ..... 325**

12.3.1 Cyclic voltammograms of iron and carbon steel in $MEA_{(aq)}$ solution saturated with $CO_2$ ....325
12.3.2 Effect of potential scan rate on PII current density....326
12.3.3 Dynamic viscosity....328
12.3.4 Cyclic voltammograms on Fe in $MEA_{(aq)}$ $CO_2$ as a function of temperature....329
12.3.5 Cyclic voltammograms on Fe in $MDEA_{(aq)}$ $CO_2$ as a function of temperature....330
12.3.6 Monolayer calculation....331
**12.4 Chapter 6 appendix....334**
12.4.1 Surface images....334
12.4.2 Diffusion coefficients....336
12.4.3 $FeCO_3$ saturation ratio....337
12.4.4 Dissolved $CO_2$ concentration....338
12.4.5 Solubility limit....340
12.4.6 Acid dissociation constants....343
12.4.7 In-situ spectro-electrochemistry cell....345
12.4.8 MATLAB Scripts....347
**12.5 Chapter 7 appendix....354**
12.5.1 Kramer-Kronig....354
12.5.2 Repeated experiments....355
12.5.3 Circuit fitting values....358
12.5.4 Surface characterisation....361
**12.6 Chapter 8 appendix....363**
12.6.1 Process conditions....363
12.6.2 Surface images....365
12.6.3 Potential-pH....365

12.6.4 Kramer-Kronig and EIS circuit fitting .....366
12.6.5 Material composition .....369

# List of figures

**Figure 2-1**: Schematic of a steel specimen dissolving in an aqueous electrolyte. .....5

**Figure 2-2:** Pourbaix diagram for Fe–$H_2O$ at 25 °C, 1 atm and total dissolved Fe concentration of $2 \times 10^{-4}$ mol $dm^{-3}$ showing potential-pH regions where the most stable form in which Fe exists is as dissolved species (labelled 'Corrosion'), insoluble species (labelled 'Passivation') and in the reduced form (labelled 'Immunity'). Calculations were based on the Gibbs energy of formation data in (Bard *et al*., 1985).....8

**Figure 2-3:** Potential-pH diagram for Fe–$H_2O$ at 25 °C, 1 atm and total dissolved Fe concentration of $2 \times 10^{-4}$ mol $dm^{-3}$. Calculations were based on the Gibbs energy of formation data in (Bard *et al*., 1985).....11

**Figure 2-4**: Anodic and cathodic half-cell reactions present simultaneously on a corroding metal in an aqueous acid solution. Diagram adapted from (Jones, 1996). .....12

**Figure 2-5:** Anodic and cathodic half-cell reactions and resulting mixed cell potential ($E_{CORR}$) and corrosion current density ($j_{CORR}$). Diagram adapted from (Fontana, 1986). .....13

**Figure 2-6:** Schematic of a typical current density-overpotential curve for anodic (oxidation) and cathodic (reduction) processes that may be modelled using the Butler-Volmer equation. .....15

**Figure 2-7**: Schematic of a typical Tafel plot showing anodic (oxidation) and cathodic (reduction) branches and corrosion current. .....16

**Figure 2-8:** Schematic of a typical current density-overpotential curve produced in linear polarisation resistance experiments used to determine corrosion current. .....17

**Figure 2-9:** Diffusion gradient between the electrode surface and the bulk solution induced by depletion of electroactive species O *via* a cathodic reaction. .....19

**Figure 2-10**: Schematic of a typical current density-overpotential curve for anodic (oxidation) and cathodic (reduction) processes that may be modelled using the Butler-Volmer equation, including limitations by mass transport. .....20

**Figure 2-11**: Speciation of $CO_2$ in $H_2O$ at 298 K, $pCO_2$ 1 atm and activity limited to unity. Calculations were based on Gibbs energy of formation data published in (Bard *et al*., 1985) . .....28

**Figure 2-12**: Potential-pH diagram for an Fe–$CO_2$–$H_2O$ system at 25 °C, and a total Fe concentration of $10^{-4}$ mol $dm^{-3}$, dissolved $C^{IV}$ activities limited to unity. Calculations were based on Gibbs energy of formation data published in (Bard *et al*., 1985) . The grey dotted vertical lines at pH 6.36 and 10.36 represent the boundaries at which $HCO_3^-$ and $CO_3^{2-}$ are the predominant dissolved $C^{IV}$ species.....29

**Figure 2-13**: Schematic of typical current-potential curve of metal undergoing active-passive transition in corrosive electrolyte. Diagram adapted from (Bockris, 2000). .....34

**Figure 2-14:** Cyclic voltammograms recorded with an Fe electrode in 0.75 mol $dm^{-3}$ $KHCO_3$ + 0.05 mol $dm^{-3}$ $K_2CO_3$ solutions with varying scan rates and temperatures (Valentini *et al*., 1985). Image reproduced with permission of the rights holder, Elsevier. .....37

**Figure 2-15:** Solution pH effect on solubility of $FeCO_3$ at 80 °C, $pCO_2$ 0.53 bar (Han, Brown & Nešić, 2010). Image reproduced with permission of the rights holder, AMPP GLOBAL CENTER, INC. .....44

**Figure 2-16**: (a) Habits of siderite and chukanovite; (b) Evolution of surface film with time formed on Fe in $CO_2$ saturated $NaHCO_{3(aq)}$ at 80 °C extracted from (Joshi *et al*., 2018). Image reproduced under the terms of the Creative Commons Attribution licence. .....50

**Figure 2-17:** Schematic of typical (a) initial and (b) complete current response due to application of a potential step. Plots were adapted from (Bockris, Reddy & Gamboa-Aldeco, 2002). .....52

**Figure 2-18:** Fe dissolution and electrocrystallisation current contributions to measured current density (Sk *et al*., 2017). Image reproduced with permission of the rights holder, Elsevier. .....54

**Figure 2-19:** Alternating voltage applied at a single frequency to an electrochemical system with reactive components and resulting current. The phase shift between the voltage and current ($\phi$) is shown. .....56

**Figure 2-20**: Phasor diagram of the impedance measured when a single frequency (f = ½ π ω) voltage perturbation is applied to an electrochemical system. The magnitude of the

impedance ($Z_o$) and the phase angle between the applied voltage and current response ($\phi$) are shown. .....57

**Figure 2-21:** Exemplary Nyquist plot of a steel electrode freely corroding in a neutral aqueous solution.....58

**Figure 2-22:** Exemplary Bode plots of **(a)** the phase angle and **(b)** modulus of the impedance data obtained with a steel electrode freely corroding a neutral aqueous solution. .....58

**Figure 2-23:** Combination of circuit components arranged in: (a) series, and (b) parallel.....62

**Figure 2-24:** Common equivalent circuit (the simplified Randles circuit) used to model a single electrode process and ohmic resistance.....62

**Figure 2-25:** Equivalent circuit used to a freely corroding steel with adsorbed species (Farelas *et al*., 2010). .....64

**Figure 2-26**: Equivalent circuits used to model carbon steel corrosion in $CO_{2(aq)}$ solutions...69

**Figure 2-27**: Chemical structure of MEA. .....70

**Figure 2-28:** Speciation of MEA and $CO_2$ in $H_2O$ at 298 K, $pCO_2$ 1 atm. Calculations were based on Gibbs energy of formation data published in (Bard *et al*., 1985). .....71

**Figure 2-29:** Chemical structure of MDEA. .....71

**Figure 2-30:** Speciation of MDEA and $CO_2$ in $H_2O$ at 298 K, $pCO_2$ 1 atm. Calculations were based on Gibbs energy of formation data published in (Bard *et al*., 1985) and the equilibrium constant for Equation **2-141** published in (Fernandes *et al*., 2012). .....72

**Figure 2-31:** Effect of solution velocity on corrosion of carbon steel in 5 M $MEA_{(aq)}$ - 0.2 $mol_{CO2}$ $mol_{MEA}^{-1}$ (Soosaiprakasam & Veawab, 2008). Image reproduced with permission of the rights holder, Elsevier. .....77

**Figure 2-32**: Effect of $CO_2$ loading on corrosion behaviour of 5 M $MEA_{(aq)}$ solution at 80 °C extracted from (Sun *et al*., 2011). Image reproduced with permission of the rights holder, Taylor & Francis. .....81

**Figure 3-1:** Pt flag counter electrode used in electrochemical experiments. .....90

**Figure 3-2**: C1018 Coupon used in immersion study. .....92

**Figure 3-3:** Schematic of **(a)** the rotating disc working electrode and **(b)** flow pattern induced by the rotation of the electrode. .....94

**Figure 3-4:** Schematic of electrochemical cell used for cyclic voltammetry and chronoamperometry experiments. Not shown: attachment to rotator.....96

**Figure 3-5:** Rotating disc electrode experimental setup. .....97

**Figure 3-6:** EIS experimental setup. .....100

**Figure 3-7**: ABB Carbon Dioxide Capture Plant at ICL (**a** - **b**) 1st floor and (**c**) control room. .....102

**Figure 3-8:** Flow sheet of ICL Carbon Dioxide Capture plant used to test pre-treated electrodes. .....103

**Figure 3-9:** Schematic of carbon capture plant operation and the originally intended electrode installation locations (red).....105

**Figure 3-10:** Schematic of the ICL Carbon Capture Pilot Plant with available tapping points for installation of electrodes (yellow) (does not show all heat exchangers present in the plant). .....106

**Figure 3-11:** Carbon steel coupon cut to be fitted into working electrode holder .....108

**Figure 3-12:** Final working electrode holder design.....108

**Figure 3-13:** Reference electrode holder .....109

**Figure 3-14:** Annotated flowsheet showing a section of the Carbon Capture Pilot Plant with locations of electrodes shown in red (reference electrode), blue (coated *i.e.* pre-treated coupon) and green (uncoated *i.e.* untreated coupon). Yellow boxes highlight all relevant valves and equipment this section of plant. .....110

**Figure 3-15:** Section of flowsheet of the Carbon Capture Pilot Plant showing the $CO_2$ absorption column. Yellow boxes highlight all relevant valves and equipment in this section of plant. .....111

**Figure 3-16**: Schematic of reference electrode and coupon tapping points on the pilot plant. .....112

**Figure 3-17**: Annotated photo of part of the ICL Carbon Capture Pilot Plant showing the location of the absorber and stripper (left) and close up photo of location of tapping points with installed reference electrode and uncoated and coated coupons.....114

**Figure 4-1:** SEM surface images of a pristine carbon steel (C1018) at **(a)** low magnification (150x) and **(b)** high magnification (1500x). .....123

**Figure 4-2**: Surface characterisation of a carbon steel coupon after immersion in 5 M $MEA_{(aq)}$ solution saturated with $CO_2$ ($pH_{80\ °C}$ 7.9) for one week at 80 °C. **(a)** Surface images taken with an SEM (200x magnification), inset (1500x magnification). **(b)** XRD pattern; grey circles (o) indicate peaks corresponding to ferrite (α-Fe).....124

**Figure 4-3:** Surface characterisation of a carbon steel coupon after immersion in 3 M $MEA_{(aq)}$ solution saturated with $CO_2$ ($pH_{80\ °C}$ 7.8) for one week at 80 °C. Surface images taken with an SEM **(a)** 200x, **(c)** 1500x, **(d)** 1000x magnifications. **(b)** XRD pattern; grey circles (o) indicate peaks corresponding to ferrite (α-Fe).....125

**Figure 4-4:** Surface characterisation of a carbon steel coupon after immersion in 1 M $MEA_{(aq)}$ solution saturated with $CO_2$ ($pH_{80\ °C}$ 7.7) for one week at 80 °C. Surface images taken with an SEM **(a)** 200x, **(c)** 1500x, **(d)** 2500x. **(b)** XRD pattern; grey circles (o) indicate peaks corresponding to ferrite (α-Fe) and black plus signs (+) indicate peaks corresponding to $FeCO_3$.....126

**Figure 4-5:** Surface characterisation of a carbon steel coupon after immersion in 5 M $MDEA_{(aq)}$ solution saturated with $CO_2$ ($pH_{80\ °C}$ 8.6) for one week at 80 °C. Surface images taken with an SEM **(a)** 200x, **(c)** 1500x, **(d)** 1500x. **(b)** XRD pattern; grey circles (o) indicate peaks corresponding to ferrite (Fe) and black plus signs (+) indicate peaks corresponding to $FeCO_3$.....128

**Figure 4-6:** Surface characterisation of carbon steel coupons after immersion in **(a** - **b)** 3 M $MDEA_{(aq)}$ solution saturated with $CO_2$ ($pH_{80\ °C}$ 8.3), **(a)** XRD pattern and, **(b)** SEM surface images at 200x magnification, inset 1500x magnification; and **(c** - **d)** 1 M $MDEA_{(aq)}$ solution saturated with $CO_2$ ($pH_{80\ °C}$ 7.9), **(c)** XRD pattern and **(d)** SEM surface images at 200x magnification, inset 1500x magnification, both for one week at 80 °C. .....130

**Figure 5-1:** Effect of MEA concentration, temperature and time on temperature-corrected average open circuit potentials of a stationary iron electrode in $MDEA_{(aq)}$ solutions saturated with $CO_2$.....133

**Figure 5-2**: Cyclic voltammograms on a Fe disc electrode in 5 M $MEA_{(aq)}$ saturated with $CO_2$ at 25 °C, pH *ca*. 7.9, at **(a)** scan rate of 20 mV $s^{-1}$ with (---) (1000 RPM) and without rotation

(-); **(b)** effect of potential scan rate on the voltammograms recorded in a quiescent solution. .....135

**Figure 5-3:** Potentials applied to Fe disc electrode during cyclic voltammetry with incrementally increased anodic potential limits; colours are coordinated by scan as a function of the total experimental time. .....137

**Figure 5-4**: Cyclic voltammograms of Fe disc electrode in quiescent 5 M $MEA_{(aq)}$, saturated with $CO_2$ at 25 °C, pH 7.9, at a scan rate of 20 mV $s^{-1}$ with increasingly positive potential limits. .....144

**Figure 5-5:** Effect of MEA concentration on cyclic voltammograms of **(a)** stationary and **(b)** rotating (1000 RPM) Fe disc electrode, in $solutions_{(aq)}$ saturated with $CO_2$ at 25 °C, at a scan rate of 20 mV $s^{-1}$.....145

**Figure 5-6**: Effect of potential scan rate on cyclic voltammograms obtained with Fe disc electrodes in quiescent **(a)** 1 M (pH 7.5) and **(b)** 3 M (pH 7.7). $MEA_{(aq),}$ saturated with $CO_2$ at 25 °C. .....151

**Figure 5-7:** Effect of temperature on cyclic voltammograms of Fe rotating (1000 RPM) disc electrode in 5 M $MEA_{(aq)}$ solutions saturated with $CO_2$; potential scan rate of 10 mV $s^{-1}$. ....152

**Figure 5-8:** Measured current density peaks associated with **(a - c)** $FeCO_3$ formation, extracted from voltammograms obtained on rotating (1000 RPM) disc Fe electrodes in 1, 3 and 5 M $MEA_{(aq)}$ saturated with $CO_2$ at 25 – 80 °C. **(d)** Dynamic viscosity as a function of MEA concentration (saturated with $CO_2$) and temperature derived from data taken from (Amundsen, Øi & Eimer, 2009).....154

**Figure 5-9:** Cyclic voltammograms recorded in 5 M $MEA_{(aq)}$ saturated with $CO_2$ at 25 °C on **(a)** stationary and rotating disc Pt disc electrodes and **(b)** stationary Fe and Pt disc electrodes. The Pt voltammograms were obtained after 15 cycles. .....157

**Figure 5-10:** Effect of MDEA concentration, temperature and time on temperature-corrected average open circuit potentials of a stationary iron electrode in $MDEA_{(aq)}$ solutions saturated with $CO_2$.....161

**Figure 5-11:** Cyclic voltammograms of Fe disc electrode in 5 M $MDEA_{(aq)}$ saturated with $CO_2$ at 25 °C, pH *ca*. 8.6, at a scan rate of 20 mV $s^{-1}$ with (---) (1000 RPM) and without rotation (-). .....163

**Figure 5-12:** Cyclic voltammograms obtained on an Fe disc electrode in quiescent 5 M $MDEA_{(aq)}$, saturated with $CO_2$ at 25 °C, pH *ca*. 8.6, at a scan rate of 20 mV $s^{-1}$ with varying potential limits. .....167

**Figure 5-13**: Effect of MDEA concentrations on cyclic voltammograms of **(a)** stationary and **(b)** rotating (1000 RPM) Fe disc electrodes, in $solutions_{(aq)}$ saturated with $CO_2$ at 25 °C, at a scan rate of 20 mV $s^{-1}$.....168

**Figure 5-14:** Effect of potential scan rate on cyclic voltammograms obtained with Fe disc electrodes in quiescent **(a)** 1 M (pH 7.6), **(b)** 3 M (pH 8.2), and **(c)** 5 M (pH 8.6), $MDEA_{(aq)}$ solutions saturated with $CO_2$. .....172

**Figure 5-15:** Effect of temperature on cyclic voltammograms of rotating (1000 RPM) disc Fe electrodes in 5 M $MDEA_{(aq)}$ saturated with $CO_2$ at a scan rate of 10 mV $s^{-1}$.....173

**Figure 5-16:** Current density peaks associated with $FeCO_3$ formation measured in **(a** - **b)** positive-going scan, and **(c)** negative-going scan; and **(d)** maximum $O_2$ evolution current density (at *ca*. +1.2 V), extracted from voltammograms obtained on rotating (1000 RPM) disc Fe electrodes in 1, 3 and 5 M $MDEA_{(aq)}$ solution saturated with $CO_2$ at 25 – 80 °C. .....175

**Figure 6-1:** Measured current transients and calculated bulk solution $FeCO_3$ saturation ratio ($S_{FeCO3}$) when $FeCO_3$ formation potentials were applied to rotating disc Fe electrodes (1000 RPM) in $MEA_{(aq)}$ saturated with $CO_2$ at 80 °C, for **(a)** 5400 s. Scaled plots of the current density transients for each solution are also presented, **(b)** 1 M $MEA_{(aq)}$ ($pH_{80°C}$ 7.7), **(c)** 3 M $MEA_{(aq)}$ ($pH_{80°C}$ 7.8), and **(d)** 5 M $MEA_{(aq)}$ ($pH_{80°C}$ 7.9). .....185

**Figure 6-2:** *Ex-situ* surface characterisation of Fe electrodes after chronoamperometry experiments in $MEA_{(aq)}$ using **(a** - **c)** SEM at 1000x showing surface features, with corresponding **(d** - **f)** surface composition detected using EDX and, **(g** - **i)** XRD with peaks corresponding to ferrite (α-Fe) highlighted. .....186

**Figure 6-3:** Total charge density passed during potentiostatic experiment with rotating disc (1000 RPM) Fe electrodes in $MEA_{(aq)}$ saturated with $CO_2$ at 80 °C. .....187

**Figure 6-4:** Measured current transients and calculated bulk solution $FeCO_3$ saturation ratio ($S_{FeCO3}$) when $FeCO_3$ formation potentials were applied to rotating disc Fe electrodes (1000 RPM) in $MDEA_{(aq)}$ saturated with $CO_2$ at 80 °C, for **(a)** 5400 s. Scaled plots of the current transients for each solution are also presented, **(b)** 1 M $MDEA_{(aq)}$ ($pH_{80°C}$ 7.9), **(c)** 3 M $MDEA_{(aq)}$ ($pH_{80°C}$ 8.3), and **(d)** 5 M $MDEA_{(aq)}$ ($pH_{80°C}$ 8.6) .....190

**Figure 6-5:** *Ex-situ* surface characterisation of Fe electrodes after chronoamperometry experiments in $MDEA_{(aq)}$ using **(a - c)** SEM at 1000x showing surface features, with corresponding **(d - f)** surface composition detected using EDX and, **(g - i)** XRD with peaks corresponding to Ferrite (α-Fe) highlighted. .....191

**Figure 6-6:** Total charge density passed during potentiostatic experiment with rotating disc (1000 RPM) Fe electrodes in $MDEA_{(aq)}$ saturated with $CO_2$ at 80 °C. .....193

**Figure 6-7:** $FeCO_3$ formation mechanism on an Fe electrode in aqueous $CO_2$ saturated system. .....195

**Figure 6-8:** Concentration profiles of **(a)** $Fe^{2+}$, and **(b)** $HCO_3^-$, and **(c)** local solution pH predicted from current density transient recorded with a rotating Fe disc electrode (1000 RPM) in 5 M $MEA_{(aq)}$ – $CO_2$, 80 °C **(d)** $FeCO_3$ saturation ratio (I = 2.48 M) calculated based on $Fe^{2+}$ concentration profile and $CO_3^{2-}$ from $H^+$ and $HCO_3^-$ for 1000 s. .....200

**Figure 6-9:** Diffusion coefficients of **(a)** $Fe^{2+}$, $HCO_3^-$ and **(b)** $H^+$ at 80 °C in aqueous amine solutions estimated using diffusion coefficients in water at 25 °C and corrected for temperature and viscosity. .....202

**Figure 7-1:** Equivalent circuit used for fitting the experimental impedance data of carbon steel electrodes after initial immersion in $MDEA_{(aq)}$ and $MEA_{(aq)}$ solutions saturated with $CO_2$ at 80 °C .....211

**Figure 7-2:** Equivalent circuits used for fitting the experimental impedance data of carbon steel electrodes at the end of immersion in $MDEA_{(aq)}$ and of (1 M $MDEA_{(aq)}$) pre-treated carbon steel in $MEA_{(aq)}$ solutions saturated with $CO_2$ at 80 °C. .....212

**Figure 7-3**: Experimental (o) and simulated (-) impedance data obtained at OCP with a CS electrode immersed in 1 M $MDEA_{(aq)}$, saturated with $CO_2$ (pH 7.9) 80 °C. OCP at 0 h = -0.590 V ,and at 72 h = -0.509 V. **(a - b)** Nyquist representations; Bode representations of **(c)** phase angle and **(d)** impedance magnitude. .....217

**Figure 7-4**: *Ex-situ* SEM images of CS electrode after immersion in 1 M $MDEA_{(aq)}$ saturated with $CO_2$ (pH 7.9) at 80 °C for *ca*. 72 h at magnifications of **(a)** 150x, **(b)** 500x and **(c)** 1000x .....218

**Figure 7-5:** Experimental (o) and simulated (-) data obtained at OCP with a CS electrode in 3 M $MDEA_{(aq)}$, saturated with $CO_2$ (pH 8.3) 80 °C. OCP at 0 h = -0.619 V , and at 96 h = -

0.425 V. **(a** - **b)** Nyquist representations; Bode representation of the **(c)** phase angle and **(d)** impedance magnitude. .....220

**Figure 7-6:** *Ex-situ* SEM images of the CS electrode after immersion in 3 M $MDEA_{(aq)}$ saturated with $CO_2$ (pH 8.3) at 80 °C for *ca*. 96 h at varying magnifications of **(a)** 150x, **(b)** 550x, **(c)** 1500x. .....221

**Figure 7-7**: *Ex-situ* SEM image (1500x magnification) of the CS electrode after immersion in 5 M $MDEA_{(aq)}$, saturated with $CO_2$ (pH 8.6) at 80 °C for *ca*. 156 h. .....223

**Figure 7-8:** Experimental (o) and simulated (-) impedance data obtained at OCP with a CS electrode in 5 M $MDEA_{(aq)}$ saturated with $CO_2$ (pH 8.6) at 80 °C. OCP at 0 h = -0.632 V and 156 h = -0.432 V. **(a** - **b)** Nyquist representations; Bode representation of the **(c)** phase angle and **(d)** magnitude of the impedance. .....223

**Figure 7-9**: Experimental (o) and simulated (-) impedance data obtained at OCP with CS electrodes in 1 (pH 7.9), 3 (pH 8.3) and 5 M (pH 8.6) $MDEA_{(aq)}$ saturated with $CO_2$ at 80 °C immediately after immersion: **(a)** Nyquist representation, Bode representation of the **(b)** phase angle and **(c)** ohmic resistance corrected impedance magnitude; and after film formation: **(d)** Nyquist representation and Bode representation of the **(e)** phase angle and **(f)** ohmic resistance corrected impedance magnitude.....225

**Figure 7-10:** OCP of electrode at the beginning (light) and end (dark) of pre-treatment in aqueous solutions of varying MDEA concentration saturated with $CO_2$ at 80 °C. .....226

**Figure 7-11: (a)** Immersion time for $FeCO_3$ film formation (• left y-axis) and dissolved $Fe^{2+}$ concentration (□ right y-axis); and **(b)** sum of charge transfer and coating resistance of electrodes at the beginning (light) and end (dark) of pre-treatment in solutions of varying MDEA concentrations saturated with $CO_2$ at 80 °C. .....227

**Figure 7-12**: Experimental (o) and simulated (-) impedance data obtained at OCP with a CS electrode in 5 M $MEA_{(aq)}$, saturated with $CO_2$ (pH 7.9) at 80 °C. OCP at 0 h = -0.653 V, 24 h = -0.655 V and 168 h = -0.660 V): **(a)** Nyquist representation; and Bode representation of the **(b)** phase angle and **(c)** impedance magnitude. **(d)** *Ex-situ* SEM images of CS electrode after immersion in 5 M $MEA_{(aq)}$ saturated with $CO_2$ (pH 7.9) at 80 °C for one week. .....230

**Figure 7-13**: *Ex-situ* XRD surface characterisation of CS electrode after immersion in 5 M $MEA_{(aq)}$ saturated with $CO_2$ (pH 7.9) at 80 °C for one week (o: Ferrite peaks). .....231

**Figure 7-14**: Experimental (o) and simulated (-) impedance data obtained at OCP with a pre-treated CS electrode in 5 M $MEA_{(aq)}$ solution saturated with $CO_2$ (pH 7.9) at 80 °C: **(a - c)** Nyquist representation and Bode representation of the **(d - e)** phase angle, and **(f)** the ohmic resistance corrected impedance magnitude. The impedance data of the CS electrode with the $FeCO_3$ film in the pre-treatment solution (1 M $MDEA_{(aq)}$ saturated with $CO_2$ at 80°C) is shown in grey.....235

**Figure 7-15**: *Ex-situ* surface characterisation of pre-treated CS electrode (1 M $MDEA_{(aq)}$-$CO_2$ 80°C) after immersion in 5 M $MEA_{(aq)}$, saturated with $CO_2$ (pH 7.9) at 80 °C for one week using **(a - c)** SEM, images taken at 550x and 1500x magnifications (above), and **(d)** XRD (below, left).....236

**Figure 7-16**: Experimental (o) and simulated (-) impedance data obtained at OCP with a pre-treated CS electrode in 5 M $MEA_{(aq)}$, saturated with $CO_2$ (pH 7.9) at 80 °C **(a - c)**: Nyquist representation; and Bode representation of the **(d - e)** phase angle, and **(f)** the ohmic resistance corrected magnitude of the impedance. The impedance data of the CS electrode with the $FeCO_3$ film in the pre-treatment solution (3 M $MDEA_{(aq)}$ solution saturated with $CO_2$ 80°C) is shown in grey.....239

**Figure 7-17**: *Ex-situ* surface characterisation of pre-treated CS electrode (3 M $MDEA_{(aq)}$-$CO_2$ 80°C) after immersion in 5 M $MEA_{(aq)}$ saturated with $CO_2$ (pH 7.9) at 80 °C for one week using **(a - c)** SEM, images taken at 550x and 1500x magnifications (above), and **(d)** XRD (below, left).....240

**Figure 7-18**: Experimental (o) and simulated (-) impedance data obtained at OCP with a pre-treated CS electrode in 5 M $MEA_{(aq)}$ saturated with $CO_2$ (pH 7.9) at 80 °C: **(a - c)** Nyquist representation; and Bode representation of the **(d - e)** phase angle, and **(f)** the ohmic resistance corrected magnitude of the impedance. The impedance data of the CS electrode with the $FeCO_3$ film in the pre-treatment solution (5 M $MDEA_{(aq)}$ solution saturated with $CO_2$ 80°C) is shown in grey.....242

**Figure 7-19**: *Ex-situ* surface characterisation of pre-treated CS electrode (3 M $MDEA_{(aq)}$-$CO_2$ 80°C) after immersion in 5 M $MEA_{(aq)}$ saturated with $CO_2$ (pH 7.9) at 80 °C for one week using **(a - c)** SEM, images taken at 1500x magnification (above), and **(d)** XRD (below, left). .....243

**Figure 7-20**: Experimental (o) and simulated (-) impedance data obtained when three pre-treated CS electrodes and one untreated electrode were immersed in 5 M $MEA_{(aq)}$, saturated

with $CO_2$ (pH 7.9) at 80 °C: **(a - b)** Nyquist representation and Bode representation of the **(c)** phase angle and **(d)** the magnitude of the impedance. .....245

**Figure 7-21**: Experimental (o) and simulated (-) impedance data obtained when three pre-treated CS electrodes and one untreated electrode were immersed in 5 M $MEA_{(aq)}$, saturated with $CO_2$ (pH 7.9) at 80 °C for one day: **(a - b)** Nyquist representation and Bode representation of the **(c)** phase angle and **(d)** the magnitude of the impedance. .....247

**Figure 7-22**: Experimental (o) and simulated (-) impedance data obtained at OCP when three pre-treated CS electrodes and one untreated electrode were immersed in 5 M $MEA_{(aq)}$, saturated with $CO_2$ (pH 7.9) at 80 °C for one week: **(a - b)** Nyquist representation and Bode representation of the **(c)** phase angle and **(d)** the magnitude of the impedance. .....250

**Figure 7-23**: Sum of charge transfer and coating resistances of 1, 3 and 5 M pre-treated and untreated CS electrodes in 5 M $MEA_{(aq)}$, saturated with $CO_2$ at 80 °C.....251

**Figure 7-24:** *Ex-situ* surface characterisation using XRD of $O_2$ contaminated pre-treated CS electrode in 1 M $MDEA_{(aq)}$-$CO_2$ 80°C, pH 7.9, which attained an OCP of *ca*. + 0.01 V. .....253

**Figure 7-25**: Experimental impedance data obtained with CS electrodes immersed in 1 M $MDEA_{(aq)}$, saturated with $CO_2$ (pH 7.9) at 80 °C for 72 h: **(a)** Nyquist representation and Bode representation of the **(b)** phase angle, and **(c)** the magnitude of the impedance; and when electrodes were initially transferred from the 1 M $MDEA_{(aq)}$-$CO_2$, 80 °C to 5 M $MEA_{(aq)}$, saturated with $CO_2$ (pH 7.9) at 80 °C: **(d)** Nyquist representation and Bode representation of the **(e)** phase angle, and **(f)** the magnitude of the impedance. The impedance data obtained with a bare CS electrode in 5 M $MEA_{(aq)}$, saturated with $CO_2$ (pH 7.9) at 80 °C is included in black in **d - f**. .....254

**Figure 7-26**: *Ex-situ* SEM images of pre-treated CS electrode with (**a - b**) OCP +0.006 V, and (**c - d**) OCP -0.509 V, (both in 1 M $MDEA_{(aq)}$-$CO_2$ 80°C) after immersion in 5 M $MEA_{(aq)}$, saturated with $CO_2$ (pH 7.9) at 80 °C. .....255

**Figure 8-1:** Plant operational period as a function of immersion period for pilot plant studies to test performance of C1018 coupon pre-treated using: **(a)** 1 M $MDEA_{(aq)}$ (Study 1) and **(b)** 3 M $MDEA_{(aq)}$ (Study 2). .....260

**Figure 8-2**: **(a)** Open circuit potential transients of uncoated CS coupons, recorded continuously whilst installed in pilot plant. **(b)** Open circuit potentials averaged over each non-operational period of uncoated CS coupons during the two pilot plant studies; error bars

shown in grey are barely visible as the OCP deviation was minimal for most of the averaged open circuit potentials. .....262

**Figure 8-3: (a)** Open circuit potential transients (*vs*. AgCl | Ag, not temperature corrected) of uncoated and 1 M $MDEA_{(aq)}$ pre-treated carbon steel. **(b)** Average open circuit potentials (*vs*. SHE, temperature corrected), calculated using potentials recorded over non-operational periods; error bars shown in black are barely visible as the OCP deviation was minimal for most averaged open circuit potentials. .....266

**Figure 8-4: (a)** Open circuit potential transients (*vs*. AgCl | Ag, not temperature corrected) of uncoated and 3 M $MDEA_{(aq)}$ pre-treated carbon steel. **(b)** Average open circuit potential (*vs*. SHE, temperature corrected) calculated using potentials over non-operational periods; error bars shown in black are barely visible as the OCP deviation was minimal for most averaged open circuit potentials. .....269

**Figure 8-5:** Average open circuit potential calculated using potentials over non-operational periods of pre-treated coupons in pilot plant. Error bars shown in grey (1 M) and black (3 M) are barely visible as the OCP deviation was minimal for most averaged open circuit potentials. .....271

**Figure 8-6**: Equivalent circuit used for fitting the experimental impedance data obtained with CS electrodes pre-treated in 3 M $MDEA_{(aq)}$ solution saturated with $CO_2$. .....273

**Figure 8-7**: Schematic of a CS electrode coated with an inner mixed phase layer and outer $FeCO_3$ layer, relevant to open circuit potentials *ca*. ≥ +0.3 V. .....275

**Figure 8-8:** Experimental (o) and simulated (-) impedance data at OCP during pre-treatment of a CS coupon in 1 M $MDEA_{(aq)}$ solution saturated with $CO_2$ (pH 7.9) 80 °C: **(a** - **b)** Nyquist representation and Bode representation of the **(c)** phase angle and **(d)** magnitude of the impedance; and in 3 M $MDEA_{(aq)}$ solution saturated with $CO_2$ (pH 8.3) 80 °C: **(e** - **f)** Nyquist representation and Bode representation of the **(g)** phase angle and **(h)** magnitude of the impedance. .....278

**Figure 8-9**: *Ex-situ* surface characterisation of CS coupon after pre-treatment in $MDEA_{(aq)}$. Pre-treatment solution: 1 M $MDEA_{(aq)}$ -$CO_2$ (pH 7.9) for *ca*. 116 h at 80 °C using **(a)** SEM, 1500x magnification and **(b)** XRD; 3 M $MDEA_{(aq)}$ - $CO_2$ (pH 8.3) for *ca*. 189 h at 80 °C using **(c)** SEM, 1500x magnification and **(d)** XRD.....280

**Figure 8-10**: Photos of **(a)** pristine CS coupon, and CS coupon pre-treated in **(b)** 1 M $MDEA_{(aq)}$ solution saturated with $CO_2$ (pH 7.9) for *ca*. 116 h, and **(c)** 3 M $MDEA_{(aq)}$ solution saturated with $CO_2$ (pH 8.3) for *ca*. 189 h, both at 80 °C. .....280

**Figure 8-11:** Pre-treated coupons after removal from pilot plant. **(a)** Pre-treated in 1 M $MDEA_{(aq)}$ and **(b)** Pre-treated in 3 M $MDEA_{(aq)}$.....283

**Figure 8-12:** Experimental (o) and simulated (-) impedance data at OCP obtained with CS coupons, after removal from the pilot plant, **(a** - **b**, **e** - **f)** Nyquist representation and Bode representation of the **(c**, **g)** phase angle and **(d**, **h)** magnitude of the impedance, in sample of pilot plant solution, 2.5 M $MEA_{(aq)}$, saturated with $CO_2$ (pH 7.7) at 60 °C.....287

**Figure 8-13:** *Ex-situ* SEM images (at 1500x magnification) of coupons pre-treated in **(a** - **c)** 1 M $MDEA_{(aq)}$ and **(d - f)** 3 M $MDEA_{(aq)}$ solutions, after removal from the pilot plant and laboratory EIS measurements in 2.5 M $MEA_{(aq)}$, saturated with $CO_2$ at 60 °C. .....289

**Figure 8-14:** *Ex-situ* surface characterisation with XRD of coupons pre-treated in **(a)**1 M $MDEA_{(aq)}$ and **(b)** 3 M $MDEA_{(aq)}$ solutions, after removal from the pilot plant and laboratory EIS measurements in 2.5 M $MEA_{(aq)}$, saturated with $CO_2$ at 60 °C. .....290

**Figure 8-15:** Untreated CS coupons **(a)** previously installed in pilot plant and **(b)** not exposed to pilot plant, both after EIS measurement in pilot plant solution sample 2.5 M $MEA_{(aq)}$, saturated with $CO_2$ (pH *ca*. 7.7) at 60 °C.....291

**Figure 8-16:** Experimental (o) and simulated (-) impedance data obtained with uncoated CS coupon after removal from pilot plant (pink) and with new CS coupon (black) in a sample of the pilot plant solution, 2.5 M $MEA_{(aq)}$, saturated with $CO_2$ (pH *ca*. 7.7) at 60 °C. **(a** - **b)** Nyquist representation and Bode representation of the **(c)** phase angle and **(d)** magnitude of impedance. .....292

**Figure 8-17:** Open circuit potential transients of CS coupon immediately after immersion in aqueous amine solution saturated with $CO_2$. .....293

**Figure 8-18:** Schematic of formation of pits through breakdown of an iron oxide film, solution ingress and reductive dissolution of the oxide film. .....294

**Figure 8-19:** *Ex-situ* surface characterisation using SEM imaging of uncoated coupons **(a** - **b)** after removal from the pilot plant, and **(d – e)** not installed in the pilot plant, and XRD **(c)** after removal from the pilot plant and **(f)** not installed in the pilot plant, all after EIS

measurement in sample of the pilot plant solution, 2.5 M $MEA_{(aq)}$, saturated with $CO_2$ (pH *ca*. 7.7) at 60 °C. .....295

**Figure 12-1:** Images of cross-section of coupons after immersion in $MDEA_{(aq)}$ solutions saturated with $CO_2$ at 80 °C. .....324

**Figure 12-2:** Cyclic voltammograms recorded on stationary Fe and carbon steel disc electrodes in 5 M $MEA_{(aq)}$ solution saturated with $CO_2$ at 25 °C.....325

**Figure 12-3:** Effect of potential scan rate on the magnitude of **(a** - **b)** PI, **(c** - **d)** PII, and **(d** - **e)** PIII on iron in 5 M $MEA_{(aq)}$ solution saturated with $CO_2$ (pH 7.9) at 25 °C.....326

**Figure 12-4:** Effect of potential scan rate on the magnitude of **(a** - **b)** PII, **(c** - **d)** $O_2$ evolution current on iron in 5 M $MDEA_{(aq)}$ solution saturated with $CO_2$ (pH 8.6) at 25 °C.....327

**Figure 12-5:** Dynamic viscosity as a function of **(a)** MEA concentration (saturated with $CO_2$) and temperature and **(b)** MDEA and MEA concentration at 80 °C. These were derived from data taken from (Amundsen, Øi & Eimer, 2009) for MEA and MDEA (Teng *et al*., 1994).328

**Figure 12-6:** Cyclic voltammograms recorded on rotating Fe disc electrodes in **(a)** 1 M $MEA_{(aq)}$ and **(b)** 3 M $MEA_{(aq)}$ solutions saturated with $CO_2$ at 25 – 80 °C. .....329

**Figure 12-7:** Cyclic voltammograms recorded on rotating Fe disc electrodes in **(a)** 1 M $MDEA_{(aq)}$ and **(b)** 3 M $MDEA_{(aq)}$ solution saturated with $CO_2$ at 25 – 80 °C. .....330

**Figure 12-8**: PII extracted from the voltammogram presented in Chapter 5 **Figure 5-4** with **(a)** current as a function time and **(b)** current as a function of total time elapsed from start of experiment.....331

**Figure 12-9:** *Ex-situ* surface image taken with a scanning electron microscope (1000x) of an Fe disc electrode surface after completion of chronoamperometry experiment in 3 M $MEA_{(aq)}$ solution saturated with $CO_2$ at 80 °C. Areas where $FeCO_3$ crystals may be present are highlighted. .....334

**Figure 12-10:** *Ex-situ* surface characterisation using scanning electron microscope of Fe electrode after completion of potentiostatic experiment (at $FeCO_3$ formation potential) in 5 M $MDEA_{(aq)}$ solution saturated with $CO_2$ at 80 °C, 1000 RPM. .....335

**Figure 12-11:** Dynamic viscosity as a function of amine concentration at 80 °C used to correct diffusion coefficients shown in Table **12 -6** . These were derived from data taken from (Amundsen, Øi & Eimer, 2009) for MEA and (Teng *et al*., 1994) for MDEA. .....336

**Figure 12-12:** $CO_2$–$H_2O$ speciation calculated using equilibrium concentrations predicted with Gibbs energy of formation data. .....338

**Figure 12-13:** Equilibrium concentrations of dissolved species in MEA–$CO_2$–$H_2O$ at 80 °C. .....341

**Figure 12-14:** Equilibrium concentrations of dissolved species in MDEA–$CO_2$–$H_2O$ at 80 °C. .....342

**Figure 12-15 :** Linear fit of ln $K_a$ data as a function of time reported in (Hamborg & Versteeg, 2009) .....344

**Figure 12-16**: **(a)** Photo of fabricated spectro-electrochemical flow cell, **(b)** cell dimensions. .....345

**Figure 12-17**: Schematic of proposed spectro-electrochemical experimental setup.....346

**Figure 12-18:** Experimental EIS data obtained for repeats of film formation on CS electrode immersed in 1 M $MDEA_{(aq)}$ saturated with $CO_2$ (pH 7.9) 80 °C. Pink corresponds to EIS data recorded after initial immersion of CS electrode in solution and dark red corresponds to EIS data recorded at the end of film formation: **(a – b)** Nyquist representation and **(c – d)** Bode representation of EIS data. .....355

**Figure 12-19**: Experimental EIS data obtained for repeats of film formation on CS electrode immersed in 3 M $MDEA_{(aq)}$ saturated with $CO_2$ (pH 8.3) 80 °C. Light blue corresponds to EIS data recorded after initial immersion of CS electrode in solution and dark blue corresponds to EIS data recorded at the end of film formation: **(a – b)** Nyquist representation and **(c – d)** Bode representation of EIS data. .....356

**Figure 12-20:** Experimental EIS data obtained for repeats of film formation on CS electrode immersed in 5 M $MDEA_{(aq)}$ saturated with $CO_2$ (pH 8.6) 80 °C. Light green corresponds to EIS data recorded after initial immersion of CS electrode in solution and dark green corresponds to EIS data recorded at the end of film formation: **(a – b)** Nyquist representation and **(c – d)** Bode representation of EIS data. .....357

**Figure 12-21:** SEM image of a polished CS electrode .....361

**Figure 12-22:** *Ex-situ* SEM images of CS electrode after immersion in 1 M $MDEA_{(aq)}$ saturated with $CO_2$ (pH 7.9) at 80 °C for *ca*. 72 hours and tabulated compositional analysis from point EDX. .....361

**Figure 12-23:** *Ex-situ* SEM images of the CS electrode after immersion in 3 M $MDEA_{(aq)}$ saturated with $CO_2$ (pH 8.2) at 80 °C for *ca*. 96 and tabulated compositional analysis from point EDX .....362

**Figure 12-24**: *Ex-situ* SEM image (1500x) of the CS electrode after immersion in 5 M $MDEA_{(aq)}$ saturated with $CO_2$ (pH 8.6) at 80 °C for *ca*. 156 hours tabulated compositional analysis from point EDX. .....362

**Figure 12-25:** Mass flow rate (black), temperature (red) and pH (green), of process fluid to which coupons were exposed after initial installation during pre-test in pilot plant. .....363

**Figure 12-26:** Mass flow rate (measured using FT103) of process fluid through pipelines in which coupons are installed for each operational period of both pilot plant studies. .....364

**Figure 12-27:** Process fluid temerpature (measured using TT210) to which coupons were exposed during each operational period of both pilot plant studies.....364

**Figure 12-28**: Process fluid pH (measured using AT100) indicative of conditions which coupons were likely exposed to during each operational period of both pilot plant studies. 364

**Figure 12-29:** SEM images of pristine carbon steel coupon at **(a)** 150x and **(b)** 1500x magnifications. .....365

**Figure 12-30:** Potential-pH diagram for Fe-$CO_2$-$H_2O$ system at 25 °C, dissolved Fe activity 257 mg $dm^{-3}$ (0.0047 mol $dm^{-3}$), $pCO_2$ = 0.1 MPa with dissolved activities of $C^{IV}$ species limited to unity at high pH. .....365

**Figure 12-31:** Material certification for carbon steel (C1018) used in experiments in this thesis. C1018 was sourced from Alabama Specialty Metals, USA. .....369

# List of tables

**Table 2-1:** Amount of $CO_2$ emitted normalised by energy produced from different fuels (Administration, 2021).....22

**Table 2-2:** Corrosion of stainless steel (SS) and carbon steel (CS) components in amine scrubbing plants documented in (DuPart, Bacon & Edwards, 1993b; Kittel & Gonzalez, 2014). .....26

**Table 2-3**: Kinetic constants ($A_r$ and $B$) derived to describe $FeCO_3$ precipitation kinetics. ....41

**Table 3-1:** Chemicals, gases and materials used in experiments. .....91

**Table 3-2**: Carbon steel (C1018) composition - the material certification is presented in the Appendix (Section 12.6). .....92

**Table 3-3:** Physical properties of carbon steel coupons used for preliminary immersion study including dimensions and surface area exposed to electrolyte. .....92

**Table 3-4:** Matrix of experiments intended for each pilot plant study.....105

**Table 3-5:** Physical properties of carbon steel coupons used for pilot plant studies including final dimensions and surface area exposed to electrolyte. .....107

**Table 4-1:** Average composition of different regions on the coupon after immersion in 3 M $MEA_{(aq)}$ solution saturated with $CO_2$ ($pH_{80\ °C}$ 7.8) for one week at 80 °C, detected using EDX. .....125

**Table 4-2:** Average composition of different regions on the coupon after immersion in 5 M $MDEA_{(aq)}$ solution saturated with $CO_2$ (pH 8.6) for one week at 80 °C detected using EDX. Region 1 corresponds to the area enclosed by the red circle and Region 2 by the white circle in **Figure 4-5c**. .....129

**Table 5-1**: Reversible potentials (*vs*. SHE) for redox reactions in Fe–$H_2O$–$CO_2$ at bulk solution pH at 25 °C (Fe concentration = $10^{-4}$ mol $dm^{-3}$).....150

**Table 5-2:** Temperature corrected reversible potentials (*vs*. SHE) for redox reactions on Fe-$CO_2$-$H_2O$ at 25 – 80 °C pH *ca*. 7.9 (Fe species concentration = $10^{-4}$ mol $dm^{-3}$). .....156

**Table 5-3:** Reversible potentials (*vs*. SHE) for redox reactions on Fe in $CO_{2(aq)}$ at bulk solution pH at 25 °C (Fe species concentration = $10^{-4}$ mol $dm^{-3}$). .....171

**Table 5-4:** Reversible potentials (*vs*. SHE) for redox reactions on Fe–$H_2O$–$CO_2$ at 25 – 80 °C pH *ca*. 8.6 (Fe species concentration = $10^{-4}$ mol $dm^{-3}$). .....176

**Table 7-1:** Normalised $EC_3$ component values for impedance data obtained when a CS electrode was immersed in 1 M $MDEA_{(aq)}$ saturated with $CO_2$ at 80 °C ($\alpha_{DL}$ values corresponding to $Q_{DL}$ are included in Appendix, Section 12.5, **Table 12-14**).....218

**Table 7-2:** Normalised $EC_3$ component values for impedance data obtained when a CS electrode was immersed in 3 M $MDEA_{(aq)}$ saturated with $CO_2$ at 80 °C. ($\alpha_{DL}$ values corresponding to $Q_{DL}$ are included in Appendix, Section 12.5, **Table 12-14**).....221

**Table 7-3**: Normalised $EC_3$ component values for impedance data obtained when a CS electrode was immersed in 5 M $MDEA_{(aq)}$ saturated with $CO_2$ at 80 °C. ($\alpha_{DL}$ values corresponding to $Q_{DL}$ are included in Appendix, Section 12.5, **Table 12-14**).....224

**Table 7-4**: Normalised $EC_1$ component values for impedance data obtained when a CS electrode was immersed in 5 M $MEA_{(aq)}$ saturated with $CO_2$ at 80 °C. .....231

**Table 7-5**: Normalised $EC_2$ component values for impedance data obtained when a pre-treated CS electrode (1 M $MDEA_{(aq)}$-$CO_2$ 80°C) was immersed in 5 M $MEA_{(aq)}$ saturated with $CO_2$ (pH 7.9) at 80 °C. .....236

**Table 7-6**: Normalised $EC_3$ component values for impedance data obtained when a pre-treated CS electrode (3 M $MDEA_{(aq)}$-$CO_2$ 80°C) was immersed in 5 M $MEA_{(aq)}$ saturated with $CO_2$ (pH 7.9) at 80 °C. .....240

**Table 7-7:** Normalised $EC_3$ component values for impedance data obtained when a pre-treated CS electrode (5 M $MDEA_{(aq)}$-$CO_2$ 80°C) was immersed in 5 M $MEA_{(aq)}$ saturated with $CO_2$ (pH 7.9) at 80 °C. .....243

**Table 7-8**: Comparison of ICP detected solution Fe concentration and XRD detected $FeCO_3$ : Fe predominant peak ratio on 1, 3, 5 M pre-treated electrodes and uncoated electrode, all after one week of immersion in 5 M $MEA_{(aq)}$, saturated with $CO_2$ at 80 °C.....251

**Table 8-1:** Temperature corrected open circuit potentials of CS coupons at the beginning and end of pre-treatment in $MDEA_{(aq)}$ saturated with $CO_2$ at 80 °C. .....279

**Table 8-2:** Normalised $EC_1$ component values for impedance data obtained when CS coupons were initially immersed in $MDEA_{(aq)}$ solutions saturated with $CO_2$ at 80 °C.....279

**Table 8-3:** Normalised $EC_3$ and $EC_4$ component values for impedance data obtained at end of pre-treatment of CS coupons in $MDEA_{(aq)}$ solutions saturated with $CO_2$ at 80 °C.....279

**Table 8-4:** Temperature corrected open circuit potential of pre-treated coupons in 2.5 M $MEA_{(aq)}$, saturated with $CO_2$ at 60 °C (pilot plant solution sample, pH *ca*. 7.7) after removal of coupons from the pilot plant.....288

**Table 8-5:** Normalised $EC_3$ and $EC_4$ component values used to model impedance data obtained with pre-treated CS coupons after removal from the pilot plant and immersed in sample of pilot plant solution 2.5 M $MEA_{(aq)}$, saturated with $CO_2$ (pH *ca*. 7.7) at 60 °C. .....288

**Table 8-6:** Normalised $EC_1$ component values for impedance data obtained when a CS electrode was immersed in 2.5 M $MEA_{(aq)}$ saturated with $CO_2$ at 60 °C. .....291

**Table 12-1:**Thermodynamic data used in the construction of E-pH diagrams (Bard *et al*., 1985) .....320

**Table 12-2:** Chemical reactions and corresponding equilibrium equations for the $CO_2$-$H_2O$ system. .....321

**Table 12-3:** Reactions considered in the construction of the E-pH diagram for the Fe-HO system with corresponding equations for reversible or equilibrium potentials or pH.....321

**Table 12-4:** Additional reactions considered in the construction of the E-pH diagram for the Fe–$H_2O$–$CO_2$ system, with corresponding equations for reversible or equilibrium potentials or pH.....322

**Table 12-5:** Copyright permissions.....323

**Table 12-6:** Diffusion coefficients of $Fe^{2+}$, $HCO_3^-$ and $H^+$ at 25 °C, in water (Newman & Thomas-Alyea, 2012), .....336

**Table 12-7:** $K_{sp}$, $CO_3^{2-}$ and $Fe^{2+}$ used in $S_{FeCO3}$ calculation. $K_{sp}$ used in bulk and local $S_{FeCO3}$ calculation. $CO_3^{2-}$ concentration used in bulk $S_{FeCO3}$ calculation. $Fe^{2+}$ concentration used for the final time bulk $S_{FeCO3}$ calculation. .....338

**Table 12-8**: $CO_3^{2-}$ mole fractions used to calculate $CO_3^{2-}$ dissolved concentrations in MEA–$CO_2$ solutions at 80 °C .....339

**Table 12-9:** $CO_3^{2-}$ mole fractions used to calculate $CO_3^{2-}$ dissolved concentrations in MDEA–$CO_2$ solutions at 80 °C .....340

**Table 12-10:** Ionic strength of MEA–$CO_2$ solutions at 80 °C based on equilibrium concentrations calculated using Gibbs energy of formation data (Bard *et al*., 1985).....341

**Table 12-11:** Ionic strength of MDEA–$CO_2$ solutions at 80 °C based on equilibrium concentrations calculated using Gibbs energy of formation data (Bard *et al*., 1985) and $CO_2$ loading data ($\alpha$) estimated from (Rho *et al*., 1997). .....343

**Table 12-12:** Validation of EIS data collected during film formation using Kramer-Kronig relations .....354

**Table 12-13**: Validation of EIS data collected during film dissolution using Kramer-Kronig relations .....354

**Table 12-14:** Circuit fitting values .....358

**Table 12-15**: Validation of EIS data collected during film formation using Kramer-Kronig relations .....366

**Table 12-16**: Circuit fitting values .....367

# 1 Introduction

Anthropogenic global warming, through continued emission of greenhouse gases, has been estimated to increase global temperatures by 1 °C since pre-industrial times. According to the Intergovernmental Panel on Climate Change (IPCC), if emission rates stay the same, a further 0.5 °C increase is expected by 2030. Continued rise in global temperatures at the current rate can have detrimental effects including rising sea levels, increased intensity and frequency of extreme weather events like droughts and flooding, all of which have the capacity to severely impact human life. $CO_2$ emissions represent 80 % of the total greenhouse gas emissions in the UK. Fossil fuel based power generation plants are a principal $CO_2$ emission source, accounting for *ca*. 16 % of the UK $CO_2$ emissions in 2019 (Strategy, 2021). Abatement strategies specifically for these point sources need to be implemented. Carbon capture and storage (CCS) is currently the most cost effective $CO_2$ emission mitigation strategy (Bui *et al*., 2018). This technology involves the capture of $CO_2$ from waste streams, for example from power generation plants, conversion of $CO_2$ to liquid state and transport to safe storage sites, thereby preventing release into the atmosphere. Extensive deployment of CCS on the scale needed to sufficiently reduce $CO_2$ emissions has not yet been achieved (Bui *et al*., 2018). Amine scrubbing is one of the most mature $CO_2$ capture technologies, and has been commercially used for decades in natural gas processing (NGP) (Bui *et al*., 2018). In addition to its maturity, this technology is particularly appealing since it can be retrofitted to existing power generation plants without requiring significant plant modification. Despite its long term use however, technical limitations still exists, which have hampered its implementation for post combustion $CO_2$ capture (PCCC). Corrosion is one of the primary technical issues (Kohl & Nielsen, 1997a), which needs to be addressed to accelerate deployment. Amines, the solvents used for $CO_2$ capture, are not inherently corrosive but become so upon absorption of $CO_2$. Monoethanolamine (MEA), the benchmark amine solvent for PCCC, has been reported to become increasingly corrosive when raised to high temperatures and, when enriched with

$CO_2$, thus requiring the use of costly stainless steel (SS 316L) in areas of the plants experiencing these conditions (Kohl & Nielsen, 1997a). Stainless steel however, is still vulnerable to corrosion in amine scrubbing plants and costs around 5 to 6 times that of carbon steel, currently $ 4.2k tonne$^{-1}$ (Ltd., 2021).

Methyldiethanolamine (MDEA), a popularly used amine for NGP, has been demonstrated to promote the formation of an $FeCO_3$ film on carbon steel (CS), thought to be protective to the underlying substrate, particularly at high temperatures and when saturated with $CO_2$. Corrosion rates as low as, *ca*. 0.1 mm y$^{-1}$ have been demonstrated for carbon steel in this amine (Xiang *et al*., 2015). Pre-treatment of carbon steel through the intermittent use of $MDEA_{(aq)}$ to induce the formation of an $FeCO_3$ film, prior to routine use of $MEA_{(aq)}$ for $CO_2$ capture, has been proposed as a corrosion mitigation strategy. Film regeneration, if needed, can then be achieved by reverting to use of $MDEA_{(aq)}$ as the $CO_2$ capture solvent. Since $MDEA_{(aq)}$ has been extensively used for $CO_2$ capture in NGP, the film formation and regeneration periods may minimise plant downtime since it may allow for continued $CO_2$ capture during these periods. Although preliminary studies (Campbell, Yu & Williams, 2017a, 2017b; Sadeek, Williams & Campbell, 2017) have demonstrated the formation of $FeCO_3$ films on CS in $MDEA_{(aq)}$, the protection afforded by this film, if any, has not been determined. A thorough investigation of this corrosion mitigation strategy must first be completed to determine if pre-treated carbon steel can be used in place of costly stainless steel (316 L), and in so doing increase the likelihood of widescale deployment of amine scrubbing for PCCC.

## 1.1 Project aims and objectives

The primary aim of this thesis was to assess the use of pre-treated carbon steel in highly corrosive sections of post combustion $CO_2$ capture plants to reduce the capital cost. A secondary aim was to elucidate the divergent behaviour exhibited by carbon steel in $CO_2$ saturated aqueous monoethanolamine and methyldiethanolamine solutions. The aims of this project could be achieved by accomplishing the following objectives:

- Establishing the effect of amine type on the electrochemical behaviour of carbon steel in $CO_2$ capture plants.
- Elucidating the surface reactions on iron (an appropriate surrogate for carbon steel) in $CO_2$ saturated aqueous monoethanolamine and methyldiethanolamine solutions and to

hypothesise a mechanism for $FeCO_3$ formation and dissolution in $CO_2$ saturated aqueous monoethanolamine and methyldiethanolamine solutions.

- Determining the optimal pre-treatment conditions of carbon steel in $CO_2$ saturated aqueous methyldiethanolamine solutions to produce electrically resistive films that are stable in $CO_2$ saturated monoethanolamine.

### 1.1.1 Project tasks

The following tasks were defined to meet the aims and objectives of this project:

1. Determination of solution speciation of $CO_2$ saturated aqueous monoethanolamine and methyldiethanolamine as a function of pH, based on thermodynamic data available in the literature.
2. Computation of an Fe–$CO_2$–$H_2O$ potential-pH diagram to enable interpretation of electrochemical experiments, including open circuit potential and cyclic voltammetry.
3. Determination of the effect of amine presence and type on the electrochemical response of iron in $CO_2$ saturated aqueous monoethanolamine and methyldiethanolamine solutions using cyclic voltammetry and comparing to data available in the literature; investigation of the impact of amine concentration and temperature on the electrochemical behaviour of iron in the aforementioned solutions.
4. Identification of the $FeCO_3$ formation potential and investigation of the $FeCO_3$ formation reaction(s) on iron in aqueous monoethanolamine and methyldiethanolamine at conditions conducive to $FeCO_3$ formation ($CO_2$ rich, 80 °C), using chronoamperometry and *ex-situ* surface characterisation techniques.
5. Formulation of a diffusion reaction model for the estimation of the local solution chemistry changes during the $FeCO_3$ formation reaction.
6. Determination of whether surface films formed on carbon steel in $CO_2$ saturated aqueous methyldiethanolamine are electrically resistive and explanation of the protection mechanism if any; investigation of the relationship between methyldiethanolamine concentration and surface film resistivity, both using electrochemical impedance spectroscopy and open circuit potential measurements.
7. Investigation of the stability of surface films formed on carbon steel *via* pre-treatment with $CO_2$ saturated aqueous methyldiethanolamine in $CO_2$ saturated aqueous monoethanolamine using electrochemical impedance spectroscopy.

8. Assessment of the feasibility of pre-treatment as a corrosion mitigation strategy through examination of pre-treated coupons after exposure to aqueous monoethanolamine in the $CO_2$ capture pilot plant using open circuit potential measurements and electrochemical impedance spectroscopy.

# 2 Literature Review

## 2.1 Electrochemistry fundamentals applied to corrosion

Corrosion is the deterioration of materials caused by spontaneous heterogenous chemical reactions with their environments. When a metal *e.g.* Fe is immersed in an aqueous electrolyte (*e.g.* acid), the metal may dissolve ($Fe^{2+}$) and result in liberation of $H_2$ bubbles at the surface. The overall reaction is given by Equation **2-1.**

$$Fe + 2H^+ \leftrightarrow Fe^{2+} + H_2 \qquad \textbf{2-1}$$

The points at which metal dissolution occurs are referred to as the anodic sites. Metal dissolution is accompanied by liberation of electrons to the bulk of the metal. The liberated electrons are scavenged by reduction processes at neighbouring cathodic sites, for example $H^+$ reduction, as depicted in **Figure 2-1**. Equation **2-1** can therefore be written as two separate electrochemical reactions in Equations **2-2** and **2-3**.

$$Fe_{(s)} \xrightarrow{\text{anodic}} Fe^{2+}_{(aq)} + 2e^- \qquad \textbf{2-2}$$

$$2\,H^+_{(aq)} + 2e^- \xrightarrow{\text{cathodic}} H_{2(g)} \qquad \textbf{2-3}$$

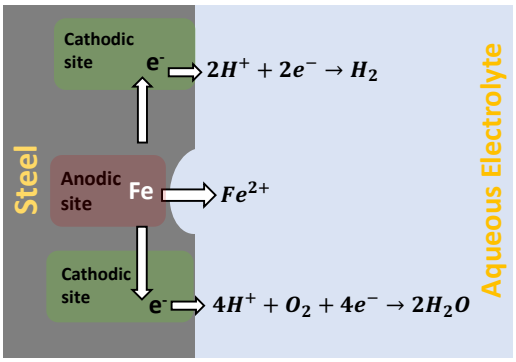



**Figure 2-1**: Schematic of a steel specimen dissolving in an aqueous electrolyte.

**Faraday's Law**

Since the corrosion of metals occurs *via* electron transfer, it is an electrochemical process and hence electrochemical principles are applied in the investigation of this process. The current, which is the conventional measure of electron flow, gives the rate of an electrochemical reaction. The current (*I)* is proportionally related to the reacted mass (*m*) by Faraday's law (Equation **2-4**), where *n* is the number of electrons transferred during the reaction (electron stoichiometry), *M* is the atomic weight, *F* is Faraday's constant (96 485 C $mol^{-1}$) and *t* is the time. Since one ampere of current is equivalent to one coulomb of charge per second, Faraday's law can also be written in terms of the charge (*q*) transferred during the reaction.

$$\mathrm{m} = \frac{\mathrm{ItM}}{\mathrm{nF}} = \frac{\mathrm{qM}}{\mathrm{nF}} \qquad \textbf{2-4}$$

The mass loss per unit area per unit time *i.e*. the corrosion rate, can then be determined by dividing Equation **2-4** by time and surface area (*A*).

$$\frac{\mathrm{m}}{\mathrm{t\,A}} = \frac{\mathrm{IM}}{\mathrm{A\,nF}} \qquad \textbf{2-5}$$

Since the transference of electrons results in a change in mass as described by Faraday's law, it can be inferred that the rate at which a metal corrodes can be evaluated by measuring the changes in mass. Immersion weight-loss tests are the most frequently conducted tests for assessing the corrosion of metals in aqueous environments. In these tests, a sample of the material of interest is submerged in the appropriate solution at representative conditions that may be encountered in practice, then retrieved, cleaned and weighed. The corrosion rate (*CR*) may be presented in different units and is calculated using Equation **2-6** where $\varrho$ is the density of the material, *t* is the time, *m* is the weight loss and *k* is a conversion constant, which depends on the units with which it is being reported (Jones, 1996).

$$\mathrm{CR} = \mathrm{k}\frac{\mathrm{m}}{\rho\,\mathrm{A\,t}} \qquad \textbf{2-6}$$

The ASTM Standard Guide for Laboratory Immersion Corrosion Testing of Metals (G31-21) outlines factors which may influence results of an immersion test (*e.g*. dissolved $O_2$, motion of environment relative to specimen, corrosion products), and recommends optimal operating methodologies and data interpretation protocol. Immersion weight-loss tests need to be sufficiently long to represent the conditions experienced in practice. These experiments do not provide insight to the complex surface mechanisms that may occur on a corroding substrate. Furthermore, these are not relevant to non-uniformly corroding metals.

Since corrosion of metal species are electrochemical by nature, electrochemical techniques may be applied to elucidate the surface mechanisms involved and may provide insight to guide surface treatment for improved corrosion resistance. An understanding of the electrochemical principles governing interfacial reactions is fundamental to investigating corrosion.

## 2.1.1 Electrochemical thermodynamics

Prior to making electrochemical measurements to determine the corrosion rate, one can first determine if the anodic and cathodic reactions, which constitute the corrosion process, will proceed spontaneously by considering the equilibrium thermodynamics at the electrode | electrolyte interface.

For a reaction (or pair of reactions) to occur spontaneously, the overall associated Gibbs free energy change ($\Delta G°$), for the given temperature and pressure, must be negative. The Gibbs free energy change for a reaction ($\Delta G°_{rxn}$) is obtained from Equation **2-7**, where $T$ is the temperature, $R$ is the ideal gas constant and $K_{eq}$ is the equilibrium constant for the reaction.

$$\Delta G^{o}{}_{rxn} = \sum_{i,products} \nu_i \, \Delta G_i^o - \sum_{j,reactants} \nu_j \, \Delta G_j^o = -R \, T \ln \, K_{eq} \qquad \textbf{2-7}$$

$\Delta G°$ is given by Equation **2-8** and $\Delta H°$ and $\Delta S°$ are the changes in the enthalpy and entropy respectively.

$$\Delta G_i^o = \Delta H_i^o - T \, \Delta S_i^o \qquad \textbf{2-8}$$

The interfacial potential difference ($E°$), referred to as the standard potential, that is required to invoke a reaction ($O + ne^- \rightarrow R$), with a positive Gibbs free energy change, may be computed using Equation **2-9**.

$$\Delta G^o = -nFE^o \qquad \textbf{2-9}$$

At the standard potential, $E°$, the concentration of oxidisable species ($R$) and reducible species ($O$) of the same couple are equal and zero net current flows. When the concentrations of these electroactive species are not equal, the reversible potential ($E_r$) can be determined from the Nernst Equation (Equation **2-10**), where $\gamma_O$ and $\gamma_R$ are the activity coefficients of $O$ and $R$ respectively.

$$E_r = E^o + \frac{RT}{nF} \ln \frac{\gamma_o [O]}{\gamma_R [R]} \qquad \textbf{2-10}$$

Since the activity coefficients for ions in different solutions are often unknown, they are assumed to be unity and Equation **2-10** is often re-written as Equation **2-11** .

$$E_r = E^o + \frac{RT}{nF} \ln \frac{[O]}{[R]} \qquad \textbf{2-11}$$

### 2.1.1.1 Potential-pH diagrams

Pourbaix diagrams, which represent reversible potentials as a function of pH, offer an efficient means of identifying if a metal will spontaneously corrode when exposed to an aqueous electrolyte. Three regions are often highlighted in the Pourbaix diagram (**Figure 2-2**); generally, at low (*i.e*. more negative) potentials, a metal will be thermodynamically stable and will exist in its reduced form and be 'immune' to corrosion. At potentials where soluble ions of the metal are stable, the metal will spontaneously dissolve *i.e*. 'corrosion' is likely to occur. The metal may be resistant to corrosion in potential-pH regions of 'passivity', where insoluble phases of the metal *e.g*. oxides are the most stable. For a given pH, the Pourbaix diagram may be consulted to determine the stability or likelihood of corrosion of the metal. A diagram which includes the identities of the soluble and insoluble species will provide far more information and will now be explained.

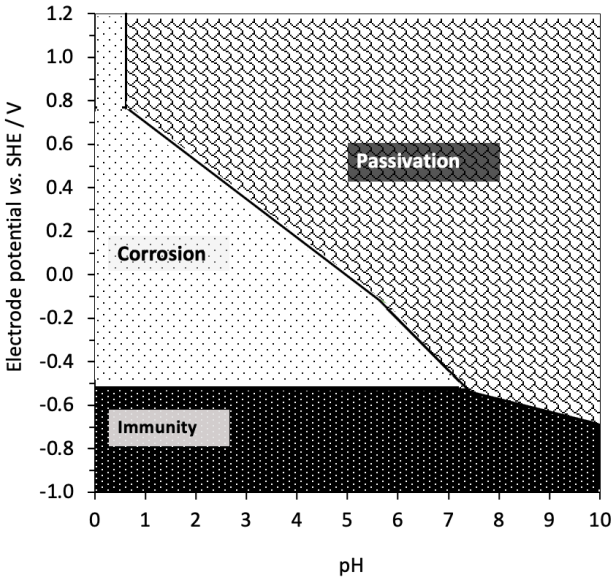



**Figure 2-2:** Pourbaix diagram for Fe–$H_2O$ at 25 °C, 1 atm and total dissolved Fe concentration of 2 × $10^{-4}$ mol $dm^{-3}$ showing potential-pH regions where the most stable form in which Fe exists is as dissolved species (labelled 'Corrosion'), insoluble species (labelled 'Passivation') and in the reduced form (labelled 'Immunity'). Calculations were based on the Gibbs energy of formation data in (Bard *et al*., 1985).

The Pourbaix diagram (**Figure 2-3**) for Fe in $H_2O$ is relevant since the corrosion of steel, the main component of which is Fe, in aqueous electrolytes is presented in this work. To construct E-pH diagrams, the Nernst equation (Equation **2-11**) is used to produce reversible potential equations for possible reactions. Reversible potentials are first formulated for:

1. Reactions involving electron ($e^-$) transfer but no proton ($H^+$) transfer, like that shown in Equation **2-12**. The reversible potential will not be a function of pH (Equation **2-13**) and will appear as a straight horizontal line, parallel to the pH axis for a specific dissolved species (here, $Fe^{2+}$) concentration. At higher concentrations of $Fe^{2+}$ in solution, the reversible potential will move upwards along the potential axis.

$$Fe^{2+}_{(aq)} + 2e^- \rightleftharpoons Fe_{(s)} \qquad \textbf{2-12}$$

$$E_{r,Fe/Fe^{2+}} = E^o_{Fe/Fe^{2+}} + \frac{RT}{2F}\ln[Fe^{2+}] \qquad \textbf{2-13}$$

2. Reactions involving both electron and proton transfer *e.g.* Equation **2-14**. The equilibrium potentials of such reactions will vary with pH and accordingly (**2-15**, **2-16**), will appear as straight lines with non-zero gradients in the E-pH plot.

   At potentials positive of the reversible potential the reverse reaction will proceed and conversely, at potentials below the reversible potential, the forward reaction will proceed.

$$2H_2O_{(l)} + 2e^- \rightleftharpoons H_{2_{(g)}} + 2OH^-_{(aq)} \text{ or } 2H^+_{(aq)} + 2e^- \rightleftharpoons H_{2_{(g)}} \qquad \textbf{2-14}$$

$$E_{r,H^+/H_2} = E^o_{H^+/H_2} + \frac{RT}{2F}\ln\left\{\frac{[H^+]^2}{pH_2}\right\} \qquad \textbf{2-15}$$

$$E_{r,H^+/H_2} = \frac{RT}{2F}\ln(10)\log\left\{\frac{[H^+]^2}{pH_2}\right\} = -0.0591pH - 0.0296\log(pH_2) \qquad \textbf{2-16}$$

3. Reactions involving no transference of electrons *i.e.* potential-independent, may also exist between dissolved species (*e.g.* $Fe^{2+}$) and soluble or insoluble (*e.g.* $Fe(OH)_2$) species. Such reactions are therefore illustrated as straight lines parallel to the potential (vertical) axis. The chemical equilibrium constant ($K$) for Equation **2-19** can be formulated as shown by Equation **2-17**. The value of $K$ can be calculated using Equation **2-7** and Gibbs energy of formation data (Bard *et al.*, 1985) to produce Equation **2-16**, where the concentration of $Fe(OH)_2$ is set to unity since it is a solid species. For a given $Fe^{2+}$ concentration, if the pH is above that computed from Equation **2-18**, $Fe^{2+}$ will react with water to form $Fe(OH)_2$ and below this pH, $Fe(OH)_2$ will dissociate to $Fe^{2+}$.

$$K_1{}^{1} = \frac{[Fe(OH)_2][H^+]^2}{Fe^{2+}} = 10^{-10.72} \quad \textbf{2-17}$$

$$\log[Fe^{2+}] = 10.72 - 2pH \quad \textbf{2-18}$$

| **Chemical reaction** | | |
|---|---|---|
| $\mathbf{K = 10^{-10.72}}$ | $Fe^{2+} + 2H_2O \rightleftharpoons Fe(OH)_{2(s)} + 2H^+$ | **2-19** |
| $\mathbf{K = 10^{3.76}}$ | $2Fe^{3+} + 3H_2O \rightleftharpoons Fe_2O_{3(s)} + 6H^+$ | **2-20** |

| **Electrochemical reactions** | | |
|---|---|---|
| $\mathbf{E^o = -0.409\ V}$ | $Fe^{2+} + 2e^- \rightleftharpoons Fe$ | **2-21** |
| $\mathbf{E^o = +0.770\ V}$ | $Fe^{3+} + e^- \rightleftharpoons Fe^{2+}$ | **2-22** |
| $\mathbf{E^o = -0.520\ V}$ | $Fe(OH)_2 + 2H^+ + 2e^- \rightleftharpoons Fe + 2H_2O$ | **2-23** |
| $\mathbf{E^o = -0.071\ V}$ | $Fe_3O_4 + 2H_2O + 2H^+ + 2e^- \rightleftharpoons 3Fe(OH)_2$ | **2-24** |
| $\mathbf{E^o = +0.213\ V}$ | $3Fe_2O_3 + 2H^+ + 2e^- \rightleftharpoons 2Fe_3O_4 + 1H_2O$ | **2-25** |
| $\mathbf{E^o = +0.881\ V}$ | $Fe_3O_4 + 8H^+ + 2e^- \rightleftharpoons 3Fe^{2+} + 4H_2O$ | **2-26** |
| $\mathbf{E^o = +0.659\ V}$ | $Fe_2O_3 + 6H^+ + 2e^- \rightleftharpoons 2Fe^{2+} + 3H_2O$ | **2-27** |

[1] The value of the equilibrium constant may vary depending on the Gibbs energy of formation data used to compute it.

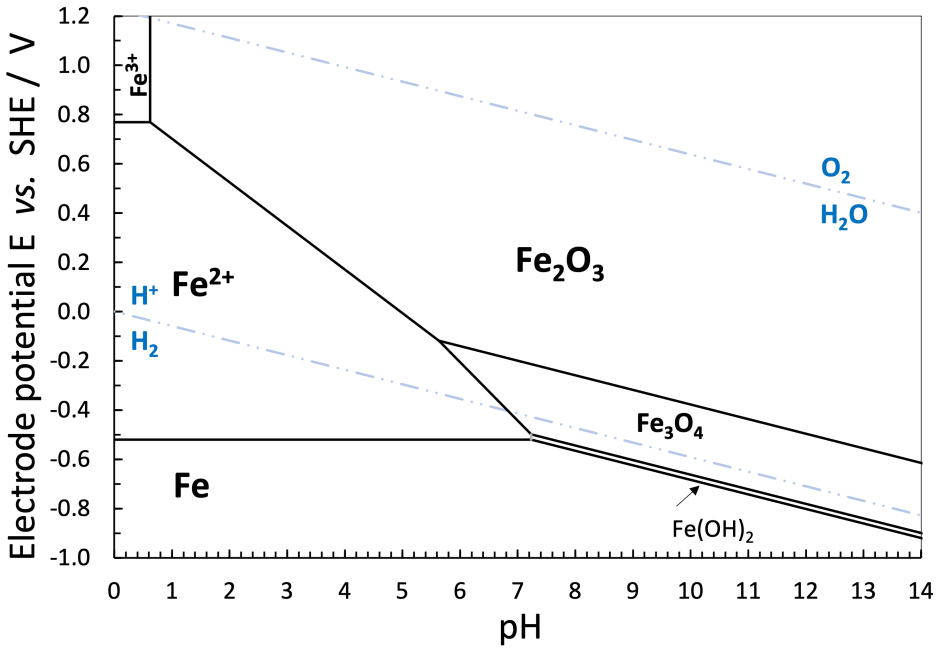



**Figure 2-3:** Potential-pH diagram for Fe–$H_2O$ at 25 °C, 1 atm and total dissolved Fe concentration of $2 \times 10^{-4}$ mol $dm^{-3}$. Calculations based on Gibbs energy of formation data in (Bard *et al.*, 1985).

Potential-pH diagrams therefore provide a compact summary of electron and proton transfer reactions, along with chemical reactions that are thermodynamically favourable when a metal is exposed to an aqueous electrolyte of interest. It should be noted that the relevant pH is that of the electrolyte in the vicinity of the metal. The local pH near an electrode may deviate from the bulk solution pH if the interfacial reactions involve the production or consumption of protons. It should also be noted that although some species may be predicted to be favourable when equilibrium is attained, the rate of formation of some phases may be kinetically slow, particularly at low temperatures. Generally, thermodynamic predictions may therefore be more useful at elevated temperature because of the faster kinetics expected at higher temperatures (Jones, 1996). To determine the rates at which the corrosion reactions proceed, the kinetics of the anodic and cathodic reactions must be investigated and are described in the subsequent sections.

## 2.1.2 Electrochemical kinetics

### 2.1.2.1 Mixed potential theory and open circuit potential

When a metal corrodes in an aqueous solution, both anodic (Equation **2-28**) and cathodic (Equation **2-29** or **2-30**) half cell reactions occur simultaneously on the surface.

$$M \rightarrow M^{n+} + ne^- \qquad \textbf{2-28}$$

*Acid* $$H^+ + 2e^- \rightarrow H_2 \qquad \textbf{2-29}$$

*Neutral / alkaline* $$2H_2O + 2e^- \rightarrow H_2 + 2OH^- \qquad \textbf{2-30}$$

Each of these reactions has its own half cell reversible potential and exchange current density ($j_o$). The exchange current ($I_o$) is equal to the magnitdue of the cathodic and anodic currents which flow at the reversible potential, and when it is normalised by the area over which it flows, it is termed the exchange current density ($j_o$). The reversible potentials and exchange current densities for each half cell reaction at different sites on the metal surface are shown in **Figure 2-4.**

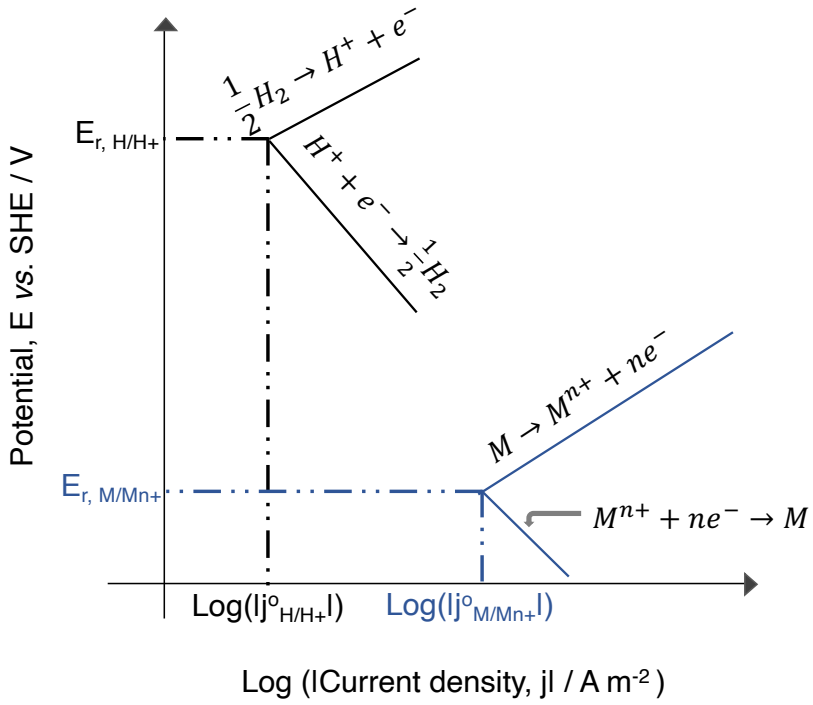



**Figure 2-4**: Anodic and cathodic half-cell reactions present simultaneously on a corroding metal in an aqueous acid solution. Diagram adapted from (Jones, 1996).

Since metals are electrically conductive, the two (or more) half-cell reversible potentials cannot co-exist separately on a metal substrate. Each of the half-cell reactions instead alter the interfacial potential to a common intermediate value (**Figure 2-5**) called the mixed potential or corrosion potential ($E_{CORR}$). The corresponding exchange current density is termed the corrosion current density ($j_{CORR}$, Equation **2-31**). At the corrosion potential, the rate of the anodic reaction (Equation **2-28**) will be equal to the rate of the cathodic reaction(s) (for example, Equation **2-9** or **2-10**).

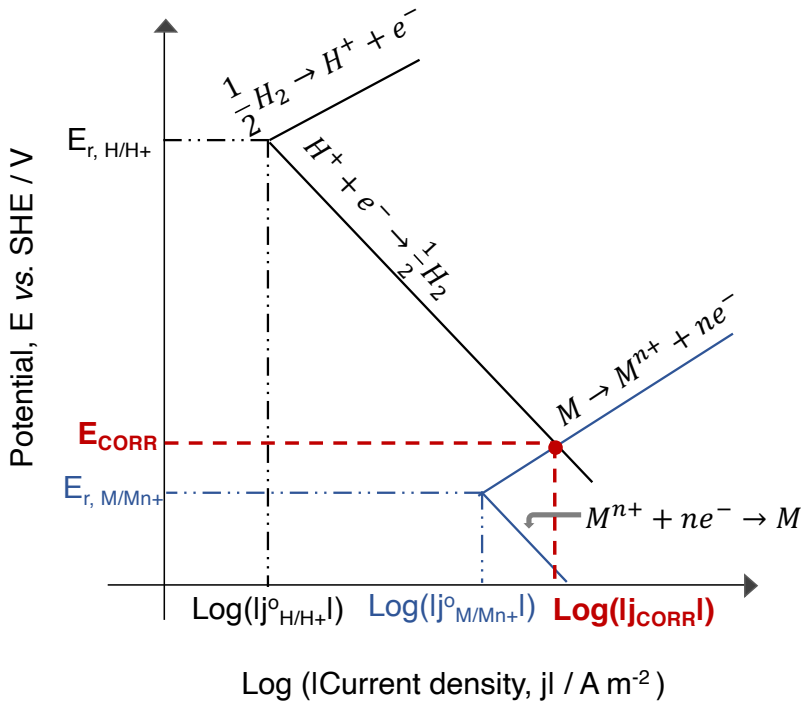



**Figure 2-5:** Anodic and cathodic half-cell reactions and resulting mixed cell potential ($E_{CORR}$) and corrosion current density ($j_{CORR}$). Diagram adapted from (Fontana, 1986).

$$I_{corr} = |I_c| = |I_a| \qquad \textbf{2-31}$$

It should be stated that the exact value of $E_{CORR}$ is dependent on the kinetics of each of the half-cell reactions involved. The electrode potential established across the interface of a metal and the electrolyte in which it is immersed, can be measured against a reference electrode of known potential relative to the standard hydrogen electrode (SHE). This open circuit potential may then be interpreted with the appropriate potential-pH diagram at the relevant electrolyte pH.

### 2.1.2.2 Polarisation

While electrochemical thermodynamics provide insight to the energetically feasible state of a metal when exposed to a specific electrolyte, kinetics describe the current densities which may arise from electrochemical reactions at an electrode-solution interface. An understanding of the fundamental laws governing the kinetics of electrochemical reactions is needed to conduct experiments, which may ultimately lead to improved methods of protection against corrosion.

As previoulsy explained, at the equlibrium potential of a given electrochemical reaction the forward and reverse reaction rates are equal (Equation **2-32**).

$$j_{net} = j_A + j_C = 0 \qquad \textbf{2-32}$$

Equation **2-21** has a standard potential of -0.409 V (under standard temperature and pressure, (Bard *et al*., 1985)); if a potential (+*E*) positve of -0.409 V is applied, any Fe species present will be oxidised, which will be accompanied by a flow of electrons into the metal, generating a positive current. If, however, a potential (-*E*), more negative than -0.409 V is applied, any $Fe^{2+}$ species will be reduced and electrons will flow out of the metal, generating a negative current. The driving force which causes the described departute from equilibrium is termed the overpotential ($\eta$).

$$\eta = E - E_r \qquad \textbf{2-33}$$

A mathematical description of the net current density ($j_{net}$) obtained due to the application of an overpotential ($\eta$) is given in Equation **2-34**, where $C_{R,S}$ and $C_{O,S}$ are the concentrations of the reduced and oxidised states at the electrode surface respectively, and $C_{R,\delta}$ and $C_{O,\delta}$ the bulk concentrations of the respective species, and $j_o$ is the exchange current density. The transfer coefficient ($\alpha$) is defined as the fraction of the applied overpotential ($\eta$) that is effective in altering the rate of the electrochemical reaction (Jones, 1996).

$$j_{net} = j_o \left[ \frac{C_{R,S}}{C_{R,\delta}} \exp\left\{ \frac{(1-\alpha)nF}{RT} \eta \right\} - \frac{C_{O,S}}{C_{O,\delta}} \exp\left\{ \frac{-\alpha nF}{RT} \eta \right\} \right] \qquad \textbf{2-34}$$

At low overpotentials, where the concentrations of electroactive species at the surface are approximately equal to that in the bulk, the current response can be simplifed to give the Butler-Volmer equation (Equation **2-35**). The current response is said to be kinetically controlled and is shown in **Figure 2-6**. The first term term within the square brackets

represents the oxidation or anodic current contribution to the net current $j$, and the second term, the reduction or cathodic current.

$$j_{net} = j_o \left[ \exp\left\{\frac{(1-\alpha)nF}{RT}\eta\right\} - \exp\left\{\frac{-\alpha nF}{RT}\eta\right\}\right] \quad \textbf{2-35}$$

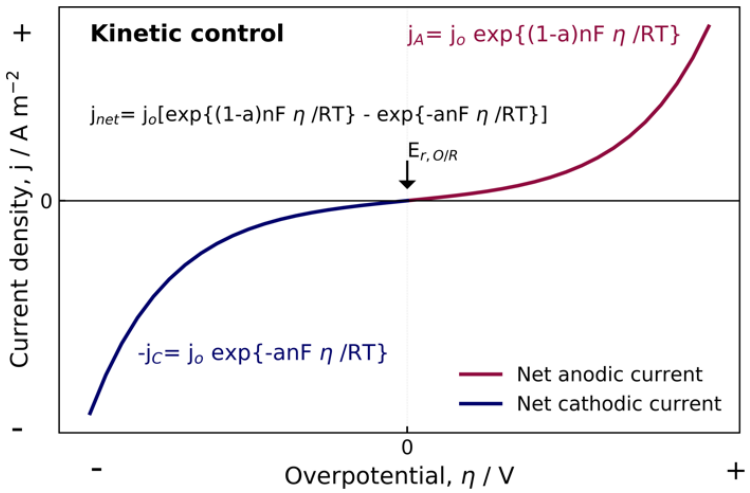



**Figure 2-6:** Schematic of a typical current density-overpotential curve for anodic (oxidation) and cathodic (reduction) processes that may be modelled using the Butler-Volmer equation.

When the overpotential is sufficiently high, one of the reactions dominates the current response and Equation **2-35** can be further simplifed. At $\eta \geq +0.1$ V, where the anodic reaction controls the measured current, the current response is given by Equation **2-36**.

$$j_{net} \cong j_A = j_o \exp\left\{\frac{(1-\alpha)nF}{RT}\eta\right\} \quad \textbf{2-36}$$

An analogous equation can be written when $\eta \leq -0.1$ such that the net current would be representative of the cathodic reaction.

$$j_{net} \cong -j_C = j_o \exp\left\{\frac{-\alpha nF}{RT}\eta\right\} \quad \textbf{2-37}$$

The Tafel equation (Equation **2-40**) can be obtained by linearising and rearranging Equation **2-36** using the steps shown in Equations **2-38** - **2-39**.

$$\ln j_A = \ln j_o + \left\{\frac{(1-\alpha)nF}{RT}\eta\right\} \quad \textbf{2-38}$$

$$2.303 \log j_A = 2.303 \log j_o + \left\{\frac{(1-\alpha)nF}{RT}\right\}\eta \quad \textbf{2-39}$$

$$\eta = \beta_A \log\left[\frac{j_A}{j_o}\right], \quad \text{where } \beta_A = \frac{2.303\ R\ T}{(1-\alpha)n\ F} \qquad \textbf{2-40}$$

Or for Equation **2-37**,

$$\eta = \beta_C \log\left[\frac{-j_C}{j_o}\right], \quad \text{where } \beta_C = \frac{2.303\ R\ T}{-\alpha n\ F} \qquad \textbf{2-41}$$

**Figure 2-7** is an exemplary Tafel plot and shows how the exchange current density ($j_o$) may be obtained. This is the current at the point of intersection of the extrapolated linear regions of the plot, which correspond to **2-39** and **2-40**, *i.e.* to zero overpotential. The gradients of these lines can be used to determine the transfer coefficeint ($\alpha$), if the current is activation controlled *i.e.* the electron transfer step is the rate determining step.

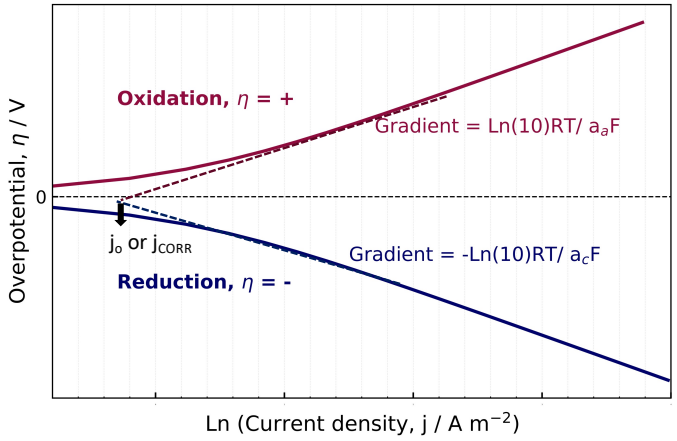



**Figure 2-7**: Schematic of a typical Tafel plot showing anodic (oxidation) and cathodic (reduction) branches and corrosion current.

In corrosion studies, Tafel plots are commonly used to determine the corrosion rate (*via* $j_{CORR}$) but require a single electrochemical reaction that is activation controlled. Experimentally, the Tafel plot is attained by first determining the open circuit potential ($E_{OCP}$ or $E_{CORR}$) of the metal-electrolyte pair of interest. The electrode (*i.e.* metal of interest) is then either anodically (positively) or cathodically (negatively) polarised with respect to the OCP, to *ca.* ±250 mV. The linear region of the anodic or cathodic branch is extrapolated to $E_{CORR}$ and the current at the point of intersection is $j_{CORR.}$ (Jones, 1996) explains that at least one decade of linearity in the semi-log plot is needed to attain a highly accurate value for $j_{CORR}$ .The corrosion current can then be coverted to corrosion rate using Equation **2-4**. This is only applicable to a uniformly corroding metal.

Another experiment, which was orginated by Stern and Geary, and now termed 'Linear Polarisation Resistance', may also be used to determine the corrosion current and rate. In such experiments, the potential is scanned from *ca*. -10 mV *vs*. $E_{OCP}$ to +10 mV *vs*. $E_{OCP}$. At such low overpotentials the current response is linear with respect to the applied overpotential (Equation **2-42**), *i.e*. it exhibits ohmic behaviour. The gradient of the curve (**Figure 2-8**) gives the resistance to charge transfer and can be used, along with the Tafel constants, to calculate the corrosion current (Equation **2-43**). This method can be done quickly and is simple to perform but the corrosion rate is representative only of short term, uniform corrosion and representative of a fresh electrode and electrolyte.

$$j = \frac{j_o nF}{RT}\eta \qquad \textbf{2-42}$$

$$j_{CORR} = \frac{\beta_A \beta_C}{2.303\,(R_p)(\beta_A + \beta_c)} \qquad \textbf{2-43}$$

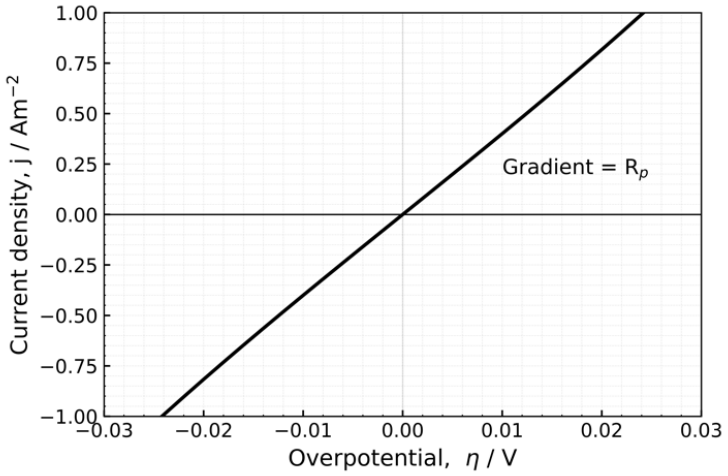



**Figure 2-8:** Schematic of a typical current density-overpotential curve produced in linear polarisation resistance experiments used to determine corrosion current.

The above discussion described the case where the current response, derived from application of a potential to an electrode exposed to electroactive species, is governed by the electron transfer process.

If larger overpotentials are to be investgiated or if the electron transfer reaction is fast, the mass transport of electroactive species towards or away from the electrode surface influences the current response. There are three fundmanental modes of mass transport: (1) migration, (2) diffusion, and (3) convection.

In electrochemistry, migration refers to the flux ($N_{migration}$) of charged species ($i$) induced by a potential gradient ($d\phi_i/ dx$) due to the presence of an electric field and is described by Equation **2-44** where $u_i$ is the ionic mobility, which is a function of the ionic charge and size.

$$N_{migration} = -u_i C_i \frac{d\phi}{dx} \qquad \textbf{2-44}$$

An electrostatic force may be exerted on the charged species moving toward or away from the electrode surface, which is induced by the potential drop ($d\phi_i/dx$) that exsists between the electode surface and electolyte (Fisher, 1996). This may in turn impact the driving force ($\eta$) for the heterogenous reaction, and hence the current response. If however excess chemically and electrochemically non-reacting species are added (≥ 0.1 M), the migration effect on the heterogenous reactions may by neglected (Fisher, 1996).

The second mode of transport, diffusion, arises when a concentration gradient ($dC_i/dx$) of species between the electrode surface and the bulk solution exists. The diffusional flux ($N_{diffusion}$) is described by Fick's first law (Equation **2-45**) and is proportional to the concentration gradient, with the proportionality factor being the diffusion coefficient ($D_i$) of the species $i$.

$$N_{diffusion} = -D_i \frac{dC_i}{dx} \qquad \textbf{2-45}$$

Concentration gradients develop when the electron transfer reaction rate is faster than the diffusion rate. Under non-steady state conditions, Fick's second law describes the rate of change of concentration of electroactive species with time (Equation **2-46**).

The concentration gradient results in the development of a diffusion layer, with a thickness $\delta$, which begins at the electrode surface and extends away from it as depicted in **Figure 2-9**.

$$\frac{dC_i}{dt} = D_i \frac{d^2 C_i}{dx^2} \qquad \textbf{2-46}$$

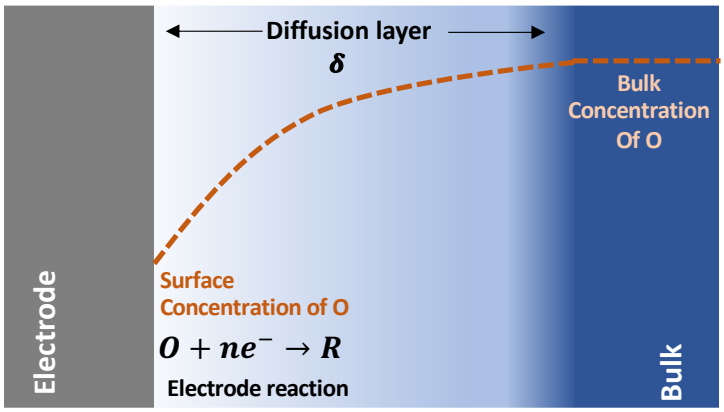



**Figure 2-9:** Diffusion gradient between the electrode surface and the bulk solution induced by depletion of electroactive species O *via* a cathodic reaction.

At high overpotentials, when the heterogenous electrode kinetic rate is much faster than the mass transport rate, the current response becomes limited by the mass transfer step and is independent of the potential. The current response under such conditions is described by Equation **2-47**. The mass transport rate coefficientt, $k_m$, is given by Equation **2-48**. The concentration of reacting species at the electrode ($C_{O,S}$ or $C_{R,S}$) would be zero since it is immediately consumed in the electrochemical reaction at the electrode surface. Therefore Equations **2-49** and **2-50** can be formulated where $j_L$ is the mass transport limited current density.

$$j = -n\,F\,D\frac{dC_{i,o}}{dx} = -n\,F\,D_{i,O}\left[\frac{C_{O,S} - C_{O,\delta}}{\delta}\right] \qquad \textbf{2-47}$$

$$k_{m_i} = \frac{D_i}{\delta} \qquad \textbf{2-48}$$

$$j_{L,O} = n\,F\,k_{m,O}C_{O,\delta} \qquad \textbf{2-49}$$

$$j_{L,R} = n\,F\,k_{m,R}C_{R,\delta} \qquad \textbf{2-50}$$

Under intermediate applied potentials, the charge transfer and mass transfer rates are comparable, so the current response is dependent on both processes, and was previously described by Equation **2-34**. Equations **2-34** and **2-47** to **2-50** can be used to derive equations for the ratio of the surface to bulk concentrations of the reducible and oxidative species (Equation **2-51**).

$$\frac{C_{O,S}}{C_{O,\delta}} = \frac{(j_{L,O} - j)}{j_{L,O}} \qquad \frac{C_{R,S}}{C_{R,\delta}} = \frac{(j_{L,R} - j)}{j_{L,R}} \qquad \textbf{2-51}$$

Substituion of the concentration ratios into Equation **2-34** and rearrangement yields Equation **2-52**, which describes the current density as a function of the applied overpotential under all conditions. **Figure 2-10** shows the current response attained under all conditions and is annotated to highlight sections where mass transport effects come into play.

$$j = \frac{j_o\left[\exp\left\{\frac{(1-\alpha)nF}{RT}\eta\right\} - \exp\left\{\frac{(-\alpha)nF}{RT}\eta\right\}\right]}{1 + \frac{j_o}{j_{L,R}}\exp\left\{\frac{(1-\alpha)nF}{RT}\eta\right\} + \frac{j_o}{j_{L,O}}\exp\left\{\frac{(-\alpha)nF}{RT}\eta\right\}} \qquad \textbf{2-52}$$

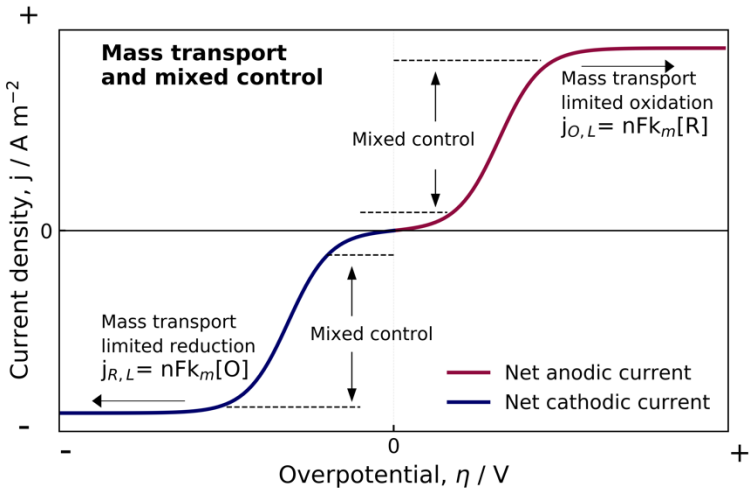



**Figure 2-10***:* Schematic of a typical current density-overpotential curve for anodic (oxidation) and cathodic (reduction) processes that may be modelled using the Butler-Volmer equation, including limitations by mass transport.

The final mode of transport of species to or away from the electrode surface is by convective diffusion. Convective diffusion may occur from 1) natural convection *e.g.* induced by density gradients within the solution or 2) forced convection *e.g.* due to use of pumps, or rotating disc electrodes. In a rotating disc electrode experiment, the movement of electroactive species toward the electrode surface is well controlled, which enables control of a precise diffusion layer thickness and allows estimation of concentration of limited reacting species or diffusion coefficients. The convective flux ($N_{\text{convective}}$) of the solution toward the electrode surface is described by Equation **2-53** where $v$ is the solution velocity.

$$N_{\text{convection}} = C_i v \qquad \textbf{2-53}$$

To summarise, the matematical descriptions of current responses derived from application of overpotentials were presented and included activation controlled, mixed control and mass transport controlled reponses. The application of the theoretical description of

electrochemical processes to determine the uniform corrosion rate, through polarisation experiments was also discussed.

Many commercially available alloys depend on passive surface films, which form upon exposure to air or to electrolyte, for their resistance to corrosion (Jones, 1996). Such surface films may be investigated using larger overpotentials than those previously described and are particularly relevant to work presented herein.

## 2.2 Carbon capture and storage

Widescale deployment of $CO_2$ emission mitigation technologies will be paramount to attaining the UK's goal of net zero $CO_2$ emissions by 2050. Carbon capture and storage (CCS), which involves the absorption, transport and safe storage of $CO_2$, is currently the most cost effective $CO_2$ emission mitigation strategy to prevent emissions from key sources like fossil fuel based power generation plants. The amount of $CO_2$ produced by a fuel when burnt is dependent on the carbon content of the fuel and is commonly compared on the basis of the energy produced (**Table 2-1**). Post combustion capture (PCCC) through amine scrubbing is one of the most mature $CO_2$ capture technologies to date since it has been commercially deployed and used for natural gas processing. Furthermore, it can be retrofitted to fossil fuel based power generations plants to remove $CO_2$ from waste gas streams before safely emitting it to the atmosphere.

**Table 2-1:** Amount of $CO_2$ emitted normalised by energy produced from different fuels (Administration, 2021).

| **Fuel sources** | **$CO_2$ emitted / lb $CO_2$ MMBTU$^{-1}$** | **$CO_2$ emitted × $10^{-8}$ / kg $CO_2$ J$^{-1}$** |
|---|---|---|
| Coal (anthracite) | 228.6 | 9.8 |
| Coal (bituminous) | 205.7 | 8.8 |
| Coal (lignite) | 215.4 | 9.2 |
| Coal (subbituminous) | 214.3 | 9.2 |
| Diesel fuel and heating oil | 161.3 | 6.9 |
| Gasoline | 157.2 | 6.7 |
| Natural gas | 117.0 | 5.0 |

Amine scrubbing plants are comprised of five major unit operations: absorber, stripper (or regenerator), heat exchanger, condenser and reboiler. The flue gas stream from the power plant contains $CO_2$[2], and up to 5 % $O_2$ (by volume) (Kittel & Gonzalez, 2014). It is first cooled to 40 to 55 °C at 1 atm before it enters the absorber where it is contacted with amine$_{(aq)}$

[2] The % composition of $CO_2$ present in the flue gas stream depends on the fuel source used in the power generation plant since the of the amount of $CO_2$ released (normalised by quantity of energy produced) varies with fuel source as shown in **Table 2-1**.

solvent flowing counter-currently. The solvent absorbs $CO_2$ from the flue gas stream forming a 'rich' amine solution in an exothermic reaction. The rich solution exits the bottom of the absorber and is pumped to a counter current heat exchanger where it is pre-heated by the hot incoming lean solution from the bottom of the stripper. The heated rich solution enters the top of the regenerator or stripper column at *ca*. 80 °C and 1 atm.

In the stripper, the rich amine is exposed to elevated temperatures *ca*. 120 °C, through the use of a steam reboiler, which results in $CO_2$ desorption from the amine, *i.e*. in the reverse reaction occurring in the absorber and in so doing, regenerates the solvent (termed the 'lean' solvent). The liberated gaseous $CO_2$ exits the top of the stripper and is dehydrated and compressed before being transported for utilisation or sequestration. The lean solvent exits the bottom of the stripper and is cooled by the counter current heat exchanger before being cycled back to the absorber for continued $CO_2$ capture.

Amine scrubbing has been used for decades in natural gas processing (NGP) for removal of $CO_2$ and $H_2S$ (DuPart, Bacon & Edwards, 1993a). There are some key differences between PCCC and NGP plants (Kittel *et al*., 2012). Firstly, the gases to be treated in NGP plants are typically pressurised up to 70 bar and consist predominantly of $CO_2$ and $H_2S$ (acid gases) and do not contain $O_2$. The primary objective of NGP is usually to recover NG with no traces of $H_2S$ and negligible amounts of $CO_2$. By contrast, in PCCC, the total pressure of the feed gas is 1 bar and it does not contain $H_2S$. Fast absorption is necessary to efficiently clean the high flow rates of incoming flue gas and the process energy consumption must be minimised since it is powered by the power generation plant to which it is attached. Since large amounts of energy are needed to remove $CO_2$ the regenerated or lean amines in PCCC plants typically contain 0.25 $mol_{CO2}$ $mol_{MEA}^{-1}$ (Kittel *et al*., 2012).

## 2.3 Corrosion in amine scrubbing plants

Despite long-term use, operational problems still exist in amine scrubbing plants. Corrosion is known to be one of the major operating problems encountered in amine scrubbing plants for NGP. Corrosion has been reported to occur in many parts of the plant including the bottom of the absorber, the stripper, reboiler, pumps and valves (DuPart, Bacon & Edwards, 1993a). Moreover, many different types of corrosion have been found to occur including uniform, galvanic, crevice, erosion, intergranular, stress corrosion cracking and de-alloying (DuPart, Bacon & Edwards, 1993a). **Table 2-2** includes some of the reported occurrences of corrosion reported in amine units. According to (Kohl & Nielsen, 1997a) stainless steel is

recommended for use in areas particularly prone to corrosion, these are the bottom of the absorber, heat exchanger, rich and lean lines between the heat exchanger and stripper, the majority of the stripper, overhead condenser and steam reboiler. However, based on the average world transaction prices for March 2021, stainless steel (316L) costs *ca*. 5.5 times that of carbon steel (Ltd., 2021) and, more importantly, has been demonstrated to be susceptible to corrosion as evident from **Table 2-2**. Furthermore, minimising costs is necessary to facilitate amine scrubbing for PCCC.

Numerous catastrophic industrial failures in amine scrubbing plants in the past, have been directly linked to corrosion (DuPart, Bacon & Edwards, 1993b). This has catalysed efforts to gain a fundamental understanding of the corrosion phenomena present in these systems. The corrosion mechanisms have been broadly divided into two categories: wet acid gas corrosion and $amine_{(aq)}$ corrosion (Kohl & Nielsen, 1997a). Wet acid gas corrosion, is caused by the dissolution of $CO_2$ (and in the case of NGP, $H_2S$) in the aqueous system. It is primarily found in areas of high acid gas concentration where water condensation may occur. This type of corrosion is particularly prevalent at the bottom of the absorber and top the stripper but has been reported to occur in all parts of the amine scrubbing process (Kittel *et al*., 2012).

$Amine_{(aq)}$ corrosion is defined as corrosion in the presence of $amine_{(aq)}$ and is typically found in the high temperature sections of the plant (Kohl & Nielsen, 1997a). Critically, amine type has been identified to significantly influence the corrosion observed: 1 ° are the most corrosive, 2 ° exhibit intermediate corrosivity, and 3 ° the least. (Kohl & Nielsen, 1997b) explain that a widely used solvent, monoethanolamine (MEA), is substantially more corrosive than most other amines, particularly at concentrations > 20 % at high acid gas loadings, requiring inhibitor addition for MEA concentration > 30 %. The impact of acid gas loading (*i.e*. the quantity of acid gas absorbed by a specific amount of solvent) has been established where increased gas loading has been reported to increase corrosivity of $amines_{(aq)}$.

Studies have also investigated the effect of temperature on corrosion behaviour in NGP plants. Electrochemical reactions (*i.e*. Fe oxidation) are thermally activated. Although $CO_2$ solubility decreases with temperature, the $CO_2$ enriched process fluid is heated prior to transfer to the stripper for desorption, which results in significant corrosion in these areas in the plant (Kohl & Nielsen, 1997a). The presence and concentration of degradation products

formed due to the interaction between $CO_2$ and $amines_{(aq)}$, particularly heat stable salts[3] , have also been demonstrated to create a more aggressive medium (Veawab, Tontiwachwuthikul & Chakma, 1999; Xiang *et al*., 2015). It has also been reported that solvent flow becomes an important factor when considering turbulent points *e.g*. gas flashing points, gas injection zones (DuPart, Bacon & Edwards, 1993b).

[3] Heat stable salts are formed from the neutralisation reaction between alkanolamines (*e.g*. MEA) and acids generated from either amine degradation especially when associated with $O_2$ or absorption of other species *e.g*. $SO_x$ and $NO_x$ (Aronu *et al*., 2014; Xiang *et al*.,2015).

**Table 2-2:** Corrosion of stainless steel (SS) and carbon steel (CS) components in amine scrubbing plants documented in (DuPart, Bacon & Edwards, 1993b; Kittel & Gonzalez, 2014).

| Plant | Acid gas | Solvent | Location | Corrosion type | Cause |
|---|---|---|---|---|---|
| **Treat synthesis gas at 348 psig** | 18 % $CO_2$ to <100 ppm $CO_2$ | 25 wt% MEA + Inhibitor | • Absorber tray (bottom) | • Uniform<br>• Galvanic | • Oxygen presence resulting in passive $FeCO_3$ film breakdown. Galvanic action between active and passive regions |
| **Ammonia plant ($CO_2$ removal)** | 17 % $CO_2$ to 100 ppm $CO_2$ | MDEA | • Absorber tray (bottom) | • Erosion | • Turbulent feed gas mixing with liquid prevent passivating film formation |
| **Ammonia plant ($CO_2$ removal)** | 1.5 % $CO_2$ to 100 ppm $CO_2$ | MDEA | • Stripper at tray (CS) and valve opening (SS)<br>• Heat exchanger<br>• Pumps | • Pitting<br>• Erosion<br>• Galvanic | • Acid gas flashing in heat exchanger due to pressure drop<br>• High lean loading<br>• Insufficient stripper steam<br>• Carbon solid circulation |
| **Treat 300 psig gas to produce fuel gas ( Newly commissioned)** | 45 % $CO_2$ to 20 ppm $H_2S$ | MDEA | • Circulating pump suction line (CS)<br>• Valves (CS)<br>• Absorber (bottom) (CS) | • Pitting<br>• Erosion | • Acid gas flashing<br>• Cavitation by bubble collapse<br>• High velocity impingement points |
| **Ammonia plant** | $CO_2$ | MDEA | • Heat exchanger (SS) | • Intergranular | • Depletion of Cr at grain boundaries during the material fabrication process (known as sentisation) |
| **Amine unit** | 6 % $CO_2$ & 2 -3 ppm $H_2S$ | DGA[4] | • Stripper trays and shell (SS) | • Uniform | • High $CO_2$ loading<br>• High temperature |
| **Amine unit** | $CO_2$ | DEA[5] | • Stripper (SS) | • Uniform | • High $CO_2$ loading<br>• High temperature |

[4] DGA: Diglycolamine ($C_4H_{11}NO_2$) has been used for natural gas treating, accounting for 2 % of the amine market share in 1990 (DuPart, Bacon & Edwards, 1993b).

[5] DEA: Diethanolamine ($NH(CH_2CH_2OH)_2$) has been extensively used for natural gas treating (DuPart, Bacon & Edwards, 1993b).

## 2.4 Steel dissolution and passivation in aqueous $CO_2$ solutions

Although steel corrosion in aqueous amine solutions has been investigated to some degree, far more research has been conducted on steel corrosion in $CO_2$ environments applicable to oil and gas pipelines. The relevant literature and fundamentals published in this field will therefore first be discussed in this section. This literature would be applicable to sections of PCCC plants undergoing wet acid gas corrosion. Literature on the corrosion of carbon steel in aqueous amine solutions for PCCC will then be presented in Section 2.5.

### 2.4.1 Solution speciation

Before discussing the surface reactions that are likely to occur on steel corroding in $CO_2$ environments, an understanding of the solution speciation is necessary for identification of the relevant surface reactions that may be present.

$CO_{2(g)}$ dissolves in water according to (Equation **2-54**). $CO_{2(aq)}$ is then hydrated to form carbonic acid ($H_2CO_3$) *via* Equation **2-55**. Carbonic acid may then dissociate to $HCO_3^-$ (Equation **2-56**) and subsequently $CO_3^{2-}$ (Equation **2-57**), depending on pH. $CO_2$ speciation in $H_2O$ is shown in **Figure 2-11**.

$$CO_{2(g)} \rightleftharpoons CO_{2(aq)} \quad \textbf{2-54}$$

$$CO_{2(aq)} + H_2O_{(l)} \rightleftharpoons H_2CO_{3(aq)} \quad \textbf{2-55}$$

$$H_2CO_{3(aq)} \rightleftharpoons HCO^-_{3(aq)} + H^+_{(aq)} \quad \textbf{2-56}$$

$$HCO^-_{3(aq)} \rightleftharpoons CO^{2-}_{3(aq)} + 2H^+_{(aq)} \quad \textbf{2-57}$$

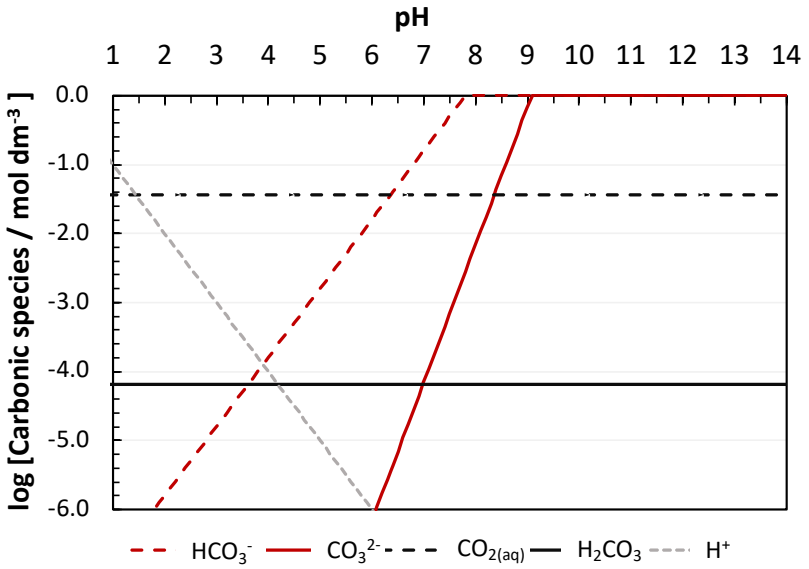



**Figure 2-11**: Speciation of $CO_2$ in $H_2O$ at 298 K, $pCO_2$ 1 atm and activity limited to unity. Calculations were based on Gibbs energy of formation data published in (Bard *et al*., 1985) .

The potential-pH diagram for Fe–$CO_2$–$H_2O$ is shown in **Figure 2-12** for a total [Fe] of $10^{-4}$ mol $dm^{-3}$ and includes only the most stable phases predicted thermodynamically. Amine species were not included in the potential-pH diagram since it was assumed that the amines are not directly involved in any chemical or electrochemical reactions and only affected the solution pH. The reversible potentials are calculated with reference to SHE. The chemical and electrochemical reactions used to produce **Figure 2-12** besides Equations **2-19** to **2-27** were:

| **Chemical reaction** | | |
|---|---|---|
| $\mathbf{K = 10^{+10.86}}$ | $Fe^{2+} + CO_{2(aq)} + H_2O \rightleftharpoons FeCO_{3(c)} + 2H^+$ | **2-58** |
| $\mathbf{K = 10^{+21.2}}$ | $FeCO_{3(c)} + 2H_2O \rightleftharpoons Fe(OH)_2 + CO_3^{2-} + 2H^+$ | **2-59** |
| **Electrochemical reactions** | | |
| $\mathbf{E^o = +0.328\ V}$ | $3CO_{2(aq)} + Fe_3O_4 + 2H^+ + 2e^- \rightleftharpoons 3FeCO_3 + H_2O$ | **2-60** |
| $\mathbf{E^o = -0.225\ V}$ | $FeCO_3 + 2H^+ + 2e^- \rightleftharpoons Fe + CO_{2(aq)} + H_2O$ | **2-61** |
| $\mathbf{E^o = -0.413\ V}$ | $FeCO_3 + H^+ + 2e^- + 4H_2O \rightleftharpoons Fe + HCO_3^-$ | **2-62** |
| $\mathbf{E^o = +0.893\ V}$ | $3HCO_3^- + Fe_3O_4 + 5H^+ + 2e^- \rightleftharpoons 3FeCO_3 + 4H_2O$ | **2-63** |
| $\mathbf{E^o = -0.719\ V}$ | $FeCO_3 + 2e^- \rightleftharpoons Fe + CO_3^{2-}$ | **2-64** |
| $\mathbf{E^o = +1.81\ V}$ | $3CO_3^{2-} + Fe_3O_4 + 8H^+ + 2e^- \rightleftharpoons 3FeCO_3 + 4H_2O$ | **2-65** |

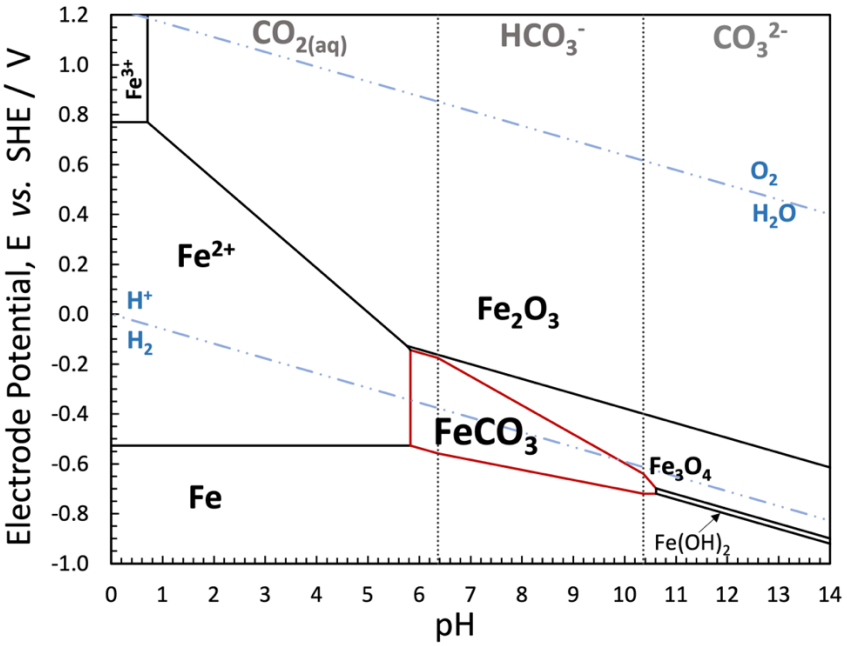



**Figure 2-12**: Potential-pH diagram for an Fe–$CO_2$–$H_2O$ system at 25 °C, and a total Fe concentration of $10^{-4}$ mol $dm^{-3}$, dissolved $C^{IV}$ activities limited to unity. Calculations were based on Gibbs energy of formation data published in (Bard *et al*., 1985) . The grey dotted vertical lines at pH 6.36 and 10.36 represent the boundaries at which $HCO_3^-$ and $CO_3^{2-}$ are the predominant dissolved $C^{IV}$ species.

## 2.4.2 Active dissolution

Two or more reactions will occur on a corroding metal in an aqueous electrolyte. The sources of the specific reacting species and the mechanisms by which each reaction proceeds will be considered. The reactions involved in $CO_2$ corrosion of steel are likely to be cathodic hydrogen evolution and anodic Fe dissolution.

**Cathodic hydrogen evolution**

There are two principal mechanisms, titled Volmer-Heyrovsky and Volmer-Tafel, by which cathodic hydrogen evolution reaction (HER) in acidic and neutral/alkaline solutions is thought to proceed. The Volmer step is the first step in both mechanisms. It involves the formation of an adsorbed H-atom *via* the discharge of an adsorbed proton (acidic) or water (neutral) molecule (Equation **2-66**) and occurs by a single electron transfer reaction. Subsequently H-atoms combine to form $H_2$ following different routes. In the Heyrovsky step, the $H_2$ formation involves the combination of the adsorbed H-atom with another H-atom *via* transference of a second electron (Equation **2-68**). The Tafel step, on the other hand, involves the chemical formation of $H_2$ by combination of two adsorbed H-atoms (Equation **2-69**).

| | | |
|---|---|---|
| *Volmer step* | $H_2O \rightarrow H^+_{ads} + OH^-$ | **2-66** |
| | $H^+_{ads} + e^- \rightarrow H_{ads}$ | **2-67** |
| *Heyrovsky reaction* | $H_{ads} + H_2O + e^- \rightarrow OH^- + H_2$ | **2-68** |
| *Tafel reaction* | $H_{ads} + H_{ads} \rightarrow H_2$ | **2-69** |

HER rate (by either mechanism) depends on the substrate upon which it proceeds. It is likely therefore that HER measured on one substrate will not provide a good kinetic prediction for HER on another substrate. This may occur since the rates at which the first (Equation **2-66** and **2-67**), and second steps (Equation **2-68** or Equation **2-69**), in either mechanism, proceed may be inherently different, and accordingly the rate determining step, which is responsible for the overall measured current density, will be different. Adsorption and desorption of H-atoms are competitive processes and the bond between the H-atoms and the metal substrate varies; a strong bond will facilitate proton-electron transfer and weak bonds will ensure that $H_2$ product will be quickly desorbed. The surface coverage ($\theta$) by adsorbed H-atoms or $H_2$ product will have an impact on the total measured current density. Experimental evaluation of the Tafel constant or slope ($\beta_c$), introduced in Section 2.1.2.2, which describes the change in current density response due to application of an overpotential (Equation **2-70**), may give insight to the reaction mechanism involved.

$$\beta = \frac{\partial \eta}{\partial \log j_{H^+}} = 2.303 \frac{RT}{\alpha n F} \qquad \textbf{2-70}$$

The transfer coefficient ($\alpha$) is often assumed to have a value 0.5, which results in a $\beta_c$ of 120 mV dec$^{-1}$ at 25 °C for a 2 electron transfer. There are three limiting cases. If the Volmer-Tafel mechanism is operative and the Tafel step is rate limiting, then a Tafel slope of 30 mV dec$^{-1}$ will be measured. If the Volmer-Heyrovsky step is operative, and the Heyrovsky step is rate determining, the Tafel slope will be 40 mV dec$^{-1}$. If the Volmer step is the rate determining step, regardless of the second step, the Tafel slope is 120 mV dec$^{-1}$. Theoretical predictions of the impact of surface coverage on the overall current density are available but will not be discussed here. The above does not consider the case of fast HER kinetics, where the measured current will be controlled by mass transport, and HER will be initiated at relatively low overpotentials. Fe and carbon steel (Fe = 98.68 %) were the two substrates used in this thesis. (Bockris & Drazic, 1962) investigated the impact of alloying impurities on HER (total impurity content of 0.2 %) using galvanostatic and potentiostatic measurements in a pH 3.1

0.5 M $FeSO_4$ + 0.5 mol $dm^{-3}$ $Na_2SO_4$ solution. The authors reported an order of magnitude difference on the exchange current density associated with the HER.

The $CO_2$ saturated $amine_{(aq)}$ solutions investigated in this thesis are of a neutral to mildly basic pH (*ca*. 7.5 – 8.6). Electrochemical reactions however, may yield or consume $H^+$, which may result in acidic or alkaline interfacial conditions respectively. Other $H^+$ donors (*e.g*. $HCO_3^-$) are present in solution.

One of the earliest studies that investigated the significance of $CO_2$ at pH 3.7 to 4.1, on corrosion of carbon steel (X52) was conducted by (deWaard & Milliams, 1975). The authors determined the corrosion current using LPR and the anodic Tafel constant $\beta_a$ (40 mV $dec^{-1}$) from polarisation curves. The cathodic Tafel constant ($\beta_c$) could not be measured since the current was mass transfer limited. The authors then formulated equations, which related the potential to the anodic current, anodic Tafel constant and pH, and an analogous cathodic equation was written. The equations were then used to formulate Equation **2-71**. The value of *A* was said to be dependent on the corrosion current and the pH (taken from elsewhere) and was measured experimentally to be 1.3 in this study. The authors proposed that since $\beta_c \rightarrow \infty$ would yield 1, the corrosion rate may be correlated with the concentration of undissociated $H_2CO_3$.

$$A = \frac{\beta_C - \beta_A}{(\beta_C + \beta_A)} \qquad \textbf{2-71}$$

The authors concluded that $H_2CO_3$ was the proton donor and the mechanism involved the slow direct reduction of $H_2CO_3$ *via* Equation **2-72**, and subsequent fast combination of absorbed H atoms *i.e*. Volmer-Tafel mechanism.

$$H_2CO_{3_{ads}} + e^- \rightarrow H_{ads} + HCO_3^- \qquad \textbf{2-72}$$

(Schmitt & Rothmann, 1977) proposed the involvement of $CO_{2(aq)}$ in HER, whereby $CO_2$ first adsorbs onto a surface (Equation **2-73**) and is then hydrated in the rate limiting step to form $H_2CO_3$ (Equation **2-74**) prior to the mechanism proposed by (deWaard & Milliams, 1975) as shown in Equation **2-72**.

$$CO_{2(aq)} \rightarrow CO_{2_{ads}} \qquad \textbf{2-73}$$

$$CO_{2_{ads}} + H_2O \rightarrow H_2CO_{3_{ads}} \qquad \textbf{2-74}$$

In a later study, (Więckowski *et al*., 1983) demonstrated the impact of dissolved $CO_2$ on the HER on Fe. The authors conducted cyclic voltammetry experiments on Fe in $NaCl_{(aq)}$

solutions containing HCl (pH to 3.85) and compared these to those recorded in $NaCl_{(aq)}$ solution saturated with $CO_2$ at the same pH. The HER current densities were higher in $CO_2$ containing solutions and the authors thus concluded that dissolved $CO_2$ species were involved in the reaction. Voltammograms were also recorded in 0.5 M $NaHCO_3$ to investigate the impact of $HCO_3^-$ but the pH was not reported. The authors concluded that both $H_2CO_3$ and $HCO_3^-$ were involved in HER on Fe.

(Gray *et al*., 1990) proposed that at pHs 6 – 10, direct reduction of $HCO_3^-$ *via* Equation **2-75**. Based on the solution speciation of $CO_2$ in $H_2O$ (**Figure 2-11**), $HCO_3^-$ is the predominant species within this pH range so its direct involvement in HER is reasonable.

$$2HCO_3^- + 2e^- \rightarrow H_2 + 2CO_3^{2-} \qquad \textbf{2-75}$$

In most of the aforementioned studies, the authors reported that stirring the solution increased the measured current densities, suggesting mass transport limited HER. The allocation of rate determining steps were hypothesised rather than demonstrated by Tafel slope evaluation.

(Nordsveen *et al*., 2003) postulated, but did not investigate experimentally, that $H_2CO_3$ at acidic pHs (exact pHs not stated) may act as a buffer, dissociating *via* Equation **2-56** to produce $H^+$ in the diffusion layer to replenish those consumed in the HER. In a later study, this theory was investigated by (Kahyarian & Nešić, 2019), where cathodic polarisation curves were obtained with carbon steel electrodes (X65) in 0.1 mol $dm^{-3}$ $NaCl_{(aq)}$ pH 4 and 5 at varying $pCO_2$ (0, 1, 5 bar) and at 25 °C. The authors reported that at pH 4, the cathodic currents were governed by charge transfer kinetics and were not significantly affected by $pCO_2$ changes since increased $pCO_2$ would increase the $[H_2CO_3]$ and hence the current. The authors demonstrated that at pH 5, the currents were completely under mass transport control therefore preventing determination of the HER mechanism. Simulated cathodic polarisation curves involving reduction of $H^+$ *via* Equation **2-29**, coupled with homogeneous reaction (Equation **2-56**), were demonstrated to agree closely with the experimental data. The authors thus concluded that $H_2CO_3$ was not directly involved in the electrochemical rection but rather acted as a source of $H^+$, corroborating the theory presented by (Nordsveen *et al*., 2003).

**Anodic Fe dissolution**

The anodic dissolution of Fe is the principal electro-dissolution reaction involved in carbon steel corrosion in $CO_{2(aq)}$ media. In acidic solutions, there are two fundamental mechanisms proposed for dissolution of Fe. The first mechanism was proposed by Heusler in 1958

(Dražić, 1989) and proceeds *via* Equations **2-76** (rate determining step) and **2-77** where the catalyst is FeOH. Heusler found that the Tafel slope for the Fe dissolution reaction was 30 mV $dec^{-1}$ and had a second order dependence on $OH^-$ .

$$Fe + OH^- + C \xrightarrow{\text{on FeOH}} FeOH^+ + C + 2e^- \quad \textbf{2-76}$$

$$FeOH^+ \rightarrow Fe^{2+} + OH^- \quad \textbf{2-77}$$

The second mechanism, now referred to as the BDD mechanism, was proposed by (Bockris, Drazic & Despic, 1961) and is given by Equations **2-78**- **2-80**, where Equation **2-79** is the rate determining step. This mechanism was formulated based on experimental studies of Fe dissolution in acidic solutions containing different anions including $ClO_4^-$, $SO_4^{2-}$, $Cl^-$, $Ac^-$, $NO_3^-$. Seven mechanisms for Fe dissolution were proposed and kinetic expressions for each were formulated and compared to Tafel slopes attained on Fe in each solution. A Tafel slope of 40 mV $dec^{-1}$ and a reaction order of *ca*. one with respect to $OH^-$ ions was obtained.

$$Fe + OH^- \rightarrow FeOH_{ads} + e^- \quad \textbf{2-78}$$

$$FeOH_{ads} \rightarrow FeOH^+ + e^- \quad \textbf{2-79}$$

$$FeOH^+ \rightarrow Fe^{2+} + OH^- \quad \textbf{2-80}$$

Subsequently, data published by other groups agreed with either of the mechanisms and it was later shown that the same sample of Fe resulted in different kinetic parameters so it was proposed that the internal and surface structure of Fe determined the operative mechanism (Dražić, 1989). Other researchers later proposed the 'branching' mechanism, where the rate-determining step in the BDD mechanism may change from Equation **2-79** to the desorption of adsorbed intermediate species shown by Equation **2-81** by changing the surface properties of the electrode.

$$FeOH^+_{ads} \rightarrow FeOH^+ \quad \textbf{2-81}$$

In neutral media, (Dražić & Hao, 1982) proposed an extension of the BDD reaction mechanism such that the surface coverage of $Fe(OH)_{ads} \rightarrow 1$, a reaction order of zero with respect to $OH^-$ ions and Tafel slope of 120 mV $dec^{-1}$.

The authors also proposed an Fe dissolution reaction mechanism for alkaline solutions based on anodic polarisation curves obtained in KOH in which $FeOH_{ads}$ and $Fe(OH)_{2,ads}$ were proposed to be intermediate species and $Fe(OH)_2$ the final product as described by Equations **2-82** to **2-85**; Equation **2-83** is the rate determining step and the surface coverage of $Fe(OH)_{ads}$ and $Fe(OH)_{2ads}$ between 0.2 and 0.8. The Tafel slope was reported to be 67 – 70

mV $dec^{-1}$, the reaction order was reported to be 1.1 with respect to $OH^-$ and -0.45 with respect to $HFeO_2^-$. These values were consistent with the theoretical values calculated for this mechanism.

$$Fe + H_2O \leftrightarrow FeOH_{ads} + H^+ + e^- \quad \textbf{2-82}$$

$$FeOH_{ads} + H_2O \rightarrow Fe(OH)_{2ads} + H^+ + e^- \quad \textbf{2-83}$$

$$Fe(OH)_{2ads} + OH^- \leftrightarrow HFeO_2^- + H_2O \quad \textbf{2-84}$$

$$HFeO_2^- + H_2O \leftrightarrow Fe(OH)_2 + OH^- \quad \textbf{2-85}$$

## 2.4.3 Passivation

In addition to the cathodic HER and anodic Fe dissolution occurring on metals in $CO_{2(aq)}$ media, surface film formation or passivation have been observed. (Jones, 1996) explains that passivity is a condition of corrosion resistance that occurs when protective surface films form on metals which may be as a result of large anodic polarisation. A characteristic current-potential curve is obtained when a passive film forms on an electrode as a result of anodically polarising the electrode and is shown in **Figure 2-13** (Bockris, 2000). As the potential is swept more positively, the current increases exponentially, as predicted by the Butler-Volmer equation (Equation **2-35**, **2-51**). The current response then no longer follows Butler-Volmer behaviour, and instead decays to a low value due to the formation of a passive film; the potential at which this occurs is referred to as the passivation potential. When the current stops falling and remains at a constant low value (*ca*. 0.2 A $m^{-2}$ at 25 °C for Fe in pH 8 electrolyte), the metal is said to be fully passivated (Bockris, 2000). The passive film may form by a direct electrochemical reaction between dissolved species and the metal substrate *e.g*. Equation **2-23**.

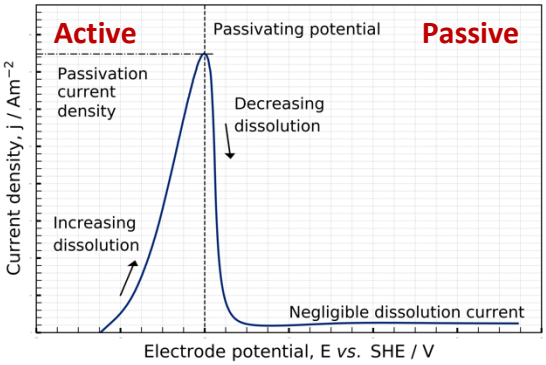



**Figure 2-13**: Schematic of typical current density-potential curve of metal undergoing active-passive transition in corrosive electrolyte. Diagram adapted from (Bockris, 2000).

From **Figure 2-12** it can be seen that at pH greater than *ca*. 5.8, multiple insoluble species are predicted to form as the potential is made increasingly positive. At *ca*. 5.8 < pH < 10.8, $FeCO_3$ is predicted to be the most thermodynamically stable phase at potentials between *ca*. -0.6 to -0.35 V (varies according to pH), whilst at pH > 10.8 $Fe(OH)_2$, is the most thermodynamically stable phase between *ca*. -0.8 to -0.75 V (depending on pH). At both pH ranges, the insoluble thermodynamically stable phases are $Fe_3O_4$ and $Fe_2O_3$. Accordingly, as the potential is swept more anodically, multiple oxidation reactions, involving phase transformations may occur, resulting in additional current density peaks rather than the single peak shown in **Figure 2-13.** Furthermore, although insoluble products may physically limit access to the electrode surface and provide protection by creating a diffusion barrier, the surface coverage, product conductivity, and film defects will likely control the degree of passivation achieved.

### 2.4.4 Electrochemical studies of Fe and carbon steel in aqueous $CO_2$ environments

In this work, Fe dissolution in $amine_{(aq)}$ solutions saturated with $CO_2$ of pH *ca*. 7.5 - 8.6 was investigated. Although most of the research on Fe dissolution in $CO_2$ containing environments has been in acidic solutions, some studies have been conducted in neutral and mildly alkaline solutions.

(Davies & Burstein, 1980) investigated the dissolution reactions occurring on stationary and rotating disc Fe electrode in 0.75 M $KHCO_3$, 0.05 M $K_2CO_3$ at pH 8.8, and also in borate solutions (pH 8.8) using anodic polarisation and open circuit potential measurements at 25 °C. The authors presented current density – potential plots as opposed to Tafel plots, which allowed for easier observation of different anodic reactions through the presence of observable current density peaks. The authors noted that the current densities measured in the solution containing $HCO_3^-$ were much higher than those in the borate solution. The authors demonstrated the presence of two anodic current density peaks in the $HCO_3^-$ solution, which they labelled A and B. The first peak, peak A, was stated to be lower in magnitude than peak B and was described as having a shoulder like appearance and was postulated to be due to $Fe(OH)_2$ formation (Equation **2-86**). At high sweep rates, the magnitude of peak A was demonstrated to increase and the authors proposed that it was due to $Fe(OH)_2$ reacting with $HCO_3^-$ to form $FeCO_3$ by Equation **2-87**. It was said that as the potential was swept to increasingly anodic values, the ratio of $FeCO_3$ to $Fe(OH)_2$ increased. The authors proposed

that peak B, shown to be mass transport limited, was due to the formation of $FeCO_3$ as an intermediate in the formation of $Fe(CO_3)_2^{2-}$ (*via* Equations **2-88** - **2-89**) and its slow diffusion through the surface film was responsible for the observed mass transport limitation. The postulation of $Fe(CO_3)_2^{2-}$ was based on a different set of anodic solubility experiments where the change in $[Fe^{II}]$ present in $FeSO_4$ solution due to addition of $HCO_3^-$ was measured. The continuous addition of $HCO_3^-$ was stated to initially result in $FeCO_3$ precipitation and subsequent dissolution to a pale green solution resulting in a measurable increase in $[Fe^{II}]$ in excess of that predicted by the solubility data of $FeCO_3$ and $Fe(OH)_2$. The authors interpreted this as indicative of a complex, proposed to be $Fe(CO_3)_2^{2-}$. The authors demonstrated that addition of $Fe^{II}$ to the electrolyte resulted in suppression of peak B, which was thought to be due to formation of excess $Fe(CO_3)_2^{2-}$. This study provided great insight to the anodic dissolution of Fe. However, the authors did not seem to consider the impact of local pH changes due to the release of $H^+$ or $OH^-$ on the stability of the product species formed, and hence the observed electrochemical behaviour. The possibility of oxidation and hence decomposition of $FeCO_3$ in the solubility experiments was also not considered. It is possible that $O_2$ ingress into the $FeSO_4$ – $HCO_3^-$ solution was responsible for the observed pale green discoloration in the solubility studies. Furthermore, it has been subsequently demonstrated that oxidation of $FeCO_3$ leads to the formation of hydroxycarbonate green rust ($GR(CO_3^{2-})$) (Reffass *et al*., 2006).

$$Fe + 2H_2O \rightarrow Fe(OH)_2 + 2H^+ + 2e^- \qquad \textbf{2-86}$$

$$Fe(OH)_2 + HCO_3^- \rightarrow FeCO_3 + H_2O + OH^- \qquad \textbf{2-87}$$

$$Fe + HCO_3^- \rightarrow FeCO_3 + H^+ + 2e^- \qquad \textbf{2-88}$$

$$FeCO_3 + HCO_3^- \rightarrow Fe(CO_3)_2^{2-} + H^+ \qquad \textbf{2-89}$$

(Valentini *et al*., 1985) investigated the impact of temperature (0 to 75 °C), ionic strength, rotation rate and scan rate on the anodic dissolution (and passivation) of polycrystalline iron in $KHCO_3$ and $K_2CO_3$ solutions of varied compositions with a $[HCO_3^-]$ : $[CO_3^{2-}]$ ratio of 15 and pH 8.9. The authors reported no change in electrochemical features observed as a function of temperature, though the current densities increased with increased temperature. Three anodic current density peaks were noted in the forward scan, and when the electrode was rotated, only two were observed, as shown in **Figure 2-14**. The authors also noted a reactivation peak (IV) on the reverse scan.

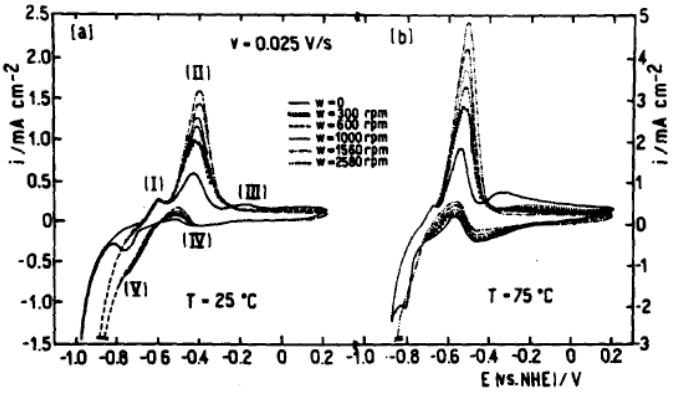



**Figure 2-14:** Cyclic voltammograms recorded with an Fe electrode in 0.75 mol $dm^{-3}$ $KHCO_3$ + 0.05 mol $dm^{-3}$ $K_2CO_3$ solutions with varying scan rates and temperatures (Valentini *et al.*, 1985). Image reproduced with permission of the rights holder, Elsevier.

The authors made similar observations as (Davies & Burstein, 1980) and provided the same interpretation for the first anodic reaction, attributing it to the formation of $Fe(OH)_2$. (Valentini *et al.*, 1985) however provided a more in depth discussion postulating its formation *via* the BDD mechanism and proposing a hydrous final state. The authors provided a different interpretation of the second anodic reaction stating that it likely involved three stages including thickening of the $Fe(OH)_2$ layer, continued dissolution of Fe through this layer and subsequent precipitation of $FeCO_3$ in an outer layer, and finally minimal chemical dissolution of $FeCO_3$. The authors reported that they were not able to differentiate between the influence of $HCO_3^-$ and $CO_3^{2-}$ on the second anodic peak, likely because the ratio of these two were kept constant in all experiments. This was therefore the aim of a subsequent study by the same group (Castro *et al.*, 1986). Most of the cyclic voltammetry experiments presented were conducted in solutions containing different concentrations of $KHCO_3$ (x) $K_2CO_3$ (y) ($0.075 \leq x \leq 2.5$, $0.015 \leq y \leq 1.5$) for pHs in the range 8.4 - 10.5. The authors showed that the magnitude of the first current peak (due to $Fe(OH)_2$ formation) increased with increased [$HCO_3^-$].

$$Fe(OH)_2 + HCO_3^- \rightarrow CO_3^{2-} + OH^- + Fe^{2+} + H_2O \qquad \textbf{2-90}$$

The authors proposed a more complicated process to be associated with the second anodic peak than earlier (Valentini *et al.*, 1985). This included the formation of a more complex passive layer consisting of an inner thin layer of oxide (chemical composition not suggested), then a hydrous layer, consistent with (Valentini *et al.*, 1985), and an outer $FeCO_3$ or $Fe(HCO_3)_2$ layer.

$$Fe^{2+} + 2HCO_3^- \rightleftharpoons Fe(HCO_3)_2 \quad \textbf{2-91}$$

$$Fe^{2+} + CO_3^{2-} \rightleftharpoons FeCO_3 \quad \textbf{2-92}$$

The authors ultimately deduced from a matrix of experiments where they tested the individual impact of pH, [$HCO_3^-$] and [$CO_3^{2-}$] that both [$HCO_3^-$] and [$CO_3^{2-}$] affected the magnitude of the second anodic peak and that the kinetic response was determined by [$HCO_3^-$]. The authors also stated that the local acidification, due to the consumption of $OH^-$ in the thickening of the $Fe(OH)_2$ layer (Equation **2-93**), would shift the $HCO_3^-$– $CO_3^{2-}$ equilibria in favour of $HCO_3^-$.

$$Fe^{2+} + 2OH^- \rightleftharpoons Fe(OH)_2 \quad \textbf{2-93}$$

The authors did not seem to however consider the formation of $FeCO_3$ through reaction between $Fe^{2+}$ or Fe and $HCO_3^-$, but rather $CO_3^{2-}$, which would have been consistent with the finding of $HCO_3^-$ being the controlling species involved in peak II.

A subsequent study by (Castro, Vilche & Arvia, 1991) employed the use of a rotating ring (Au) disc (Fe) electrode from which the authors could discriminate between anodic processes involving soluble and insoluble species in the same solutions as that used in (Castro *et al*., 1986). The first current density peak was demonstrated to involve not only the formation of $Fe(OH)_2$, but also the production of dissolved $Fe^{II}$[6]. The [$Fe^{II}$] at the second peak was said to vastly exceed the $[Fe(H_2O)_6^{2+}]_{eq}$ and $[Fe(OH)^+]_{eq}$ *i.e*. under saturated conditions with $Fe(OH)_2$ and $FeCO_3$. It was also stated that a linear relationship (slope *ca*. one) was observed between the disc current (log $i_D$) and log[$HCO_3^-$]. The authors therefore proposed that the detected $Fe^{II}$ must contain $HCO_3^-$ and suggested $FeHCO_3^+$ and $Fe(HCO_3)_2$. The authors proposed the presence of $FeHCO_3^+$ would likely favour the precipitation of $FeCO_3$ according to Equation **2-94** - **2-95**.

$$FeHCO_3^+ \rightleftharpoons Fe^{2+} + HCO_3^- \quad \textbf{2-94}$$

$$Fe^{2+} + HCO_3^- \rightleftharpoons FeCO_3 + H^+ \quad \textbf{2-95}$$

It is worth noting that the impact of local pH changes were neglected in the interpretation of the RRDE data. Given the strong dependence of [$HCO_3^-$] on pH (**Figure 2-11**), it is difficult to completely agree with the conclusions presented.

---

[6] Detected from the current measured on the Au ring held at a potential of +0.74 V, due to the oxidation of $Fe^{II}$ to $Fe_2O_3$, based on the potential - pH diagram shown in **Figure 2-12**.

## 2.4.5 $FeCO_3$ formation

### 2.4.5.1 $FeCO_3$ precipitation on carbon steel in aqueous $CO_2$ solutions

Crystallisation involves two steps, nucleation and growth, with each of these being described by distinct kinetics. (Garside, 1985) explains that primary nucleation involves the combination of solute atoms or molecules to produce ordered aggregates, called embryos. The overall free energy of these embryos will exceed a maximum value at a critical size, which is inversely related to the log of the saturation ratio. Embryos larger than the critical size will continue growing to form stable nuclei. The formation of new nuclei is therefore dependent on the rate at which the embryos can surmount the maximum free energy curve. Heterogeneous crystallisation, a category of primary nucleation, occurs in the presence of a solid interface. Nucleation on a surface is thought to require lower free energy change to induce nucleation (Garside, 1985). Heterogenous nucleation of $FeCO_3$ on carbon steel is therefore proposed to be a more likely mechanism.

According to (Karpinski & Bałdyga, 2019), precipitation is the rapid formation of a sparingly soluble crystalline (or amorphous) solid phase from a liquid phase. Nucleation is therefore an important stage in the precipitation process. The driving force for precipitation is the supersaturation ($\sigma$), which is defined by Equation **2-96**, where $\mu_{eq}$ is the chemical potential and may be rewritten in terms of the activity ($a$). A saturation ratio ($S$) can be determined from Equation **2-97** - **2-98** for small differences in activity or concentration ($c$).

$$\sigma = \frac{\mu - \mu_{eq}}{RT} = \ln\frac{a}{a_{eq}} \qquad \textbf{2-96}$$

$$\sigma \approx \frac{c - c_{eq}}{c_{eq}} = S - 1 \qquad \textbf{2-97}$$

$$S = \frac{c}{c_{eq}} \qquad \textbf{2-98}$$

(Nešić & Lee, 2003) proposed that the many imperfections present on the steel surface act as nucleation points and therefore the nucleation rate of $FeCO_3$ on carbon steel is very rapid. Most literature examining $FeCO_3$ precipitation and growth assumes that nucleation proceeds sufficiently rapidly so only crystal growth is considered in $FeCO_3$ film formation models.

Three crystal growth or precipitation rate ($PR$) kinetic models specific to $FeCO_3$ have been developed, all of which are based on a general semi-empirical crystal growth rate expression

(Equation **2-99**) where $k_r$ is the kinetic constant, $A/V$ is the surface area to volume ratio and ($\sigma_o$) is the driving force.

$$PR = k_r \frac{A}{V} \sigma_o^r \quad \textbf{2-99}$$

The earliest of the three *PR* models ($PR_I$) was developed by (Johnson & Tomson, 1991). The authors attempted to fit several empirical equations to experimental data that was obtained using a temperature-ramp approach with $FeCO_3$ seed crystals. Seed crystals were first grown in an anoxic environment and then used as the substrate for $FeCO_3$ precipitation, induced by linearly increasing the temperature (35 – 80 °C). The change in $[Fe^{2+}]$ with respect to both time and temperature was recorded. Equation **2-100** gave the best fit, where $K_{sp}$ is the solubility limit, which is the equilibrium concentration of solute species, in this case the product of $[Fe^{2+}]_{eq}$ and $[CO_3{}^{2-}]_{eq}$.

$$PR_I = k_r \frac{A}{V} K_{sp} [(S_{FeCO_3})^{0.5} - 1]^2 \quad \textbf{2-100}$$

(Hunnik, Hendriksen & Pots, 1996) attempted to develop a more accurate model (Equation **2-101**) considering a range of supersaturation levels (1 – 1000) and using a carbon steel pipe as the substrate for crystal nucleation and growth instead of seeded crystals. The authors stated that the precipitation rate ($PR_{II}$) was determined from the deviation from the linear increase of detected $[Fe^{2+}]$ with time. The *PR* equation determined by this group is given by Equation **2-101.**

$$PR_{II} = k_r \frac{A}{V} K_{sp} [S_{FeCO_3} - 1][1 - S_{FeCO_3}{}^{-1}] \quad \textbf{2-101}$$

The most recently developed relationship offered an alternative approach, where a gravimetric study was used (Sun & Nešić, 2008) to measure *PR* rather than changes in the $[Fe^{2+}]$. The investigation involved immersion of a low carbon steel substrate (X65, *C*: 0.05 %) in a solution (1 wt. % $NaCl_{(aq)}$) containing varied $[Fe^{2+}]$ (initial concentration: 50 ppm). The weight of the coupon with and without the product layer was determined to allow quantification of the scale mass. Results from this experiment found that a simpler relationship (Equation **2-102**) better described the *PR* ($PR_{III}$) and confirmed that the earlier models overestimate the *PR* by one or two orders of magnitude.

$$PR_{III} = k_r \frac{A}{V} K_{sp} [S_{FeCO_3} - 1] \quad \textbf{2-102}$$

In each of the above models, different expressions for the kinetic constant, $k_r$ were derived using the Arrhenius equation (Equation **2-103**), the constants are included in **Table 2-3**.

$$k_r = k_r^o e^{-\frac{\Delta H}{R}\left(\frac{1}{T}-\frac{1}{T_0}\right)} = e^{A_r - \frac{B}{RT}} \quad \textbf{2-103}$$

**Table 2-3**: Kinetic constants ($A_r$ and $B$) derived to describe $FeCO_3$ precipitation kinetics.

| $A_r$ | $B$ / J mol$^{-1}$ | Author |
|---|---|---|
| 56.3 | 127.3 | (Johnson & Tomson, 1991) |
| 52.4 | 119.18 | (Hunnik, Hendriksen & Pots, 1996) |
| 21.3 | 64.85 | (Sun & Nešić, 2008) |

In a more recent study (Barker *et al*., 2019), the performance of each model was used to predict the corrosion layer accumulation rate or *PR* of $FeCO_3$ on X65 carbon steel in 3.5 wt.% $NaCl_{(aq)}$, at 80 °C pH 6.3 and 6.8 on a pristine sample and a pre-filmed carbon steel sample. The authors reported that there was strong agreement between model derived by (Sun & Nešić, 2008) and their independently obtained experimental data at high saturation ratios.

**Effect of temperature:** The temperature dependence of the solubility limit ($K_{sp}$) of $FeCO_3$ has been studied widely both experimentally (Braun, 1991; Bénézeth, Dandurand & Harrichoury, 2009; Greenberg & Tomson, 1992) and theoretically through thermodynamic modelling (Helgeson, 1969; Preis & Gamsjäger, 2002; Marion, Catling & Kargel, 2003). These studies all agree that an inverse relationship exists between temperature and solubility limit. (Nordstrom *et al*., 1990) proposed that the relationship between $K_{sp}$ and $T$ (K) took the form of Equation **2-104**. Based on $FeCO_3$ solubility limit measurements over a temperature range of 25 to 94 °C, (Greenberg & Tomson, 1992) derived constants for Equation **2-104**; a= -50.3498, b= -0.041377, c= -2.1963 and d= 24.572.

$$\log K_{sp} = a + bT + \frac{c}{T} + d\log T \quad \textbf{2-104}$$

The ionic strength ($I$) of the solution in which precipitation of $FeCO_3$ occurred was found by (Silva, Liu & Millero, 2002) to also affect the solubility limit, where an increase in ionic strength resulted in an increase in $K_{sp}$ and hence created less favourable conditions for $FeCO_3$ precipitation. The most recent model improved the prediction of $K_{sp}$ by considering both temperature and ionic strength (Sun, Nešić & Woollam, 2009). This was formulated based on

two earlier models (Greenberg & Tomson, 1992) and (Silva, Liu & Millero, 2002) to give a final unified relationship with both temperature and ionic strength (0 – 2.5 mol $dm^{-3}$) (Equation **2-105**).

$$\log K_{sp} = -59.3498 - 0.041377T - \frac{2.1963}{T} + 24.5724\log(T) + 2.518\, I^{0.5} - 0.6571I \qquad \textbf{2-105}$$

The extent of protection (in terms of passivating the surface against corrosion) afforded by the film is highly dependent on its physical characteristics, specifically film porosity and thickness.

(Nazari, Allahkaram & Kermani, 2010) examined the impact of temperature (55-85 °C) on $FeCO_3$ film formation and thickness on CS (X70, C: 0.04 %) in 3 wt. % $NaCl_{(aq)}$ solution saturated with $CO_2$, pH 5.5 - 6.5. The authors reported that at 55 °C, no film formed, but at 65 °C a porous, 23 $\mu$m thick $FeCO_3$ film was observed with crystals of slightly rounded edges. The film thickness was said to increase with temperature to 32 $\mu$m at 75 °C, and 39 $\mu$m at 85 °C. The authors also reported that increasing the pH resulted in thicker films. The authors concluded that 85 °C and pH 6.5 were the optimum conditions for dense, thick film formation. It should be noted that the density was not measured, but instead deduced visually. Furthermore, the protectiveness of these films were not determined.

In another study, (Ingham *et al*., 2010) investigated the effect of temperature (40 – 90 °C) on the film formation kinetics of product layers on carbon steel at pH 6.3 using galvanostatic (*i.e*. constant current, +12.5 mA $cm^{-2}$) experiments coupled with *in-situ* XRD and subsequent surface imaging (SEM). The authors demonstrated that at 80 and 90 °C, the potential first became more negative but then climbed to increasingly positive values (> -0.5 V *vs*. AgCl | Ag, *ca*. -0.36 V *vs*. $SHE_{25\ ^{\circ}C}$), which coincided with the $FeCO_3$ detected signal becoming greater than that of the Fe signal; this occurred within 60 and 25 minutes of the start of the experiment respectively. At 40 and 60 °C, it was shown that $FeCO_3$ was detected but the Fe signal was far greater. Using SEM imaging of cross-sectioned samples, the thickness of the layer did indeed increase with increased temperature from 40 to 60 °C, but substantially decreased between 80 °C (20 μm) and 90 °C (8 μm). In another set of experiments, under potentiostatic control, the current was shown to decay more rapidly to low values as the temeprature increased and for a given time, the current density was increasingly lower with increased temperature. The authors therefore proposed that the thinner films formed more rapidly at higher temperartures, and films were composed of smaller crystals that enabled improved packing and hence provided more protection.

The impact of temperature on corrosion rate as a function of film morphology has been of interest with studies covering a wide temperature range 40 – 200 °C (Dugstad, 1998; Han *et al*., 2009; Tanupabrungsun, Brown & Nešić, 2013; Pessu, Barker & Neville, 2015).

(Tanupabrungsun, Brown & Nešić, 2013) examined the effect of elevated temperatures (80 – 200 °C) on corrosion rates of carbon steel (X65 and K03014) in 1 wt. % $NaCl_{(aq)}$ solution, pH 4 and 6, using LPR (and EIS). Since the solubility of $CO_2$ also varies as a function of temperature, the authors decided to fix the dissolved $CO_2$ concentration by using different partial pressures of $CO_2$ so that the individual effect of temperature on corrosion rate could be determined. The authors showed that after 20 hours of immersion at pH 6, the corrosion rate decreased with increasing temperture; the corrosion rate at 80 °C was up to one order of mangitude higher than those at all other tested temperatures from two hours onwards and decreased with time. The authors demonstrated that an apparently densely packed crystalline film, presumed to be $FeCO_3$, with variably sized, rounded crystals on the surface was formed and therefore concluded that its presence was reponsible for the decreased corrosion rate. The authors showed that the corrosion rate measured at 120 °C was lower than at 150 and 200 °C for the first 2 - 6 hours of immersion, but then slightly higher. A bed of cubic crystals (10 μm diameter), though with some observable pores, was demonstrated to have formed. The authors noted that at 150 °C, crystals appeared larger (*ca*. 25 μm) with defects, while at 200 °C smaller crystals with few defects were present. With the exception of 150 °C, as temperature increased, the grain size decreased. The authors concluded that at temperatures of 120 °C and above, corrosion rate decreased more rapidly due to $FeCO_3$ formation, consistent with the observations of film formation kinetics as a function of time made by (Ingham *et al*., 2010).

From the above discussion of hitherto published results it is apparent that all studies agree that increasing temperature promotes $FeCO_3$ formation. This is accomplished through the reducing effect of temperature on the solubility limit promoting $FeCO_3$ precipitation. Several authors have reported that below 60 °C, $FeCO_3$ film formation did not occur, however other studies (Videm, A.Dugstad & L.Lunde, 1994; Pessu, Barker & Neville, 2015) showed that protective film formation was in fact possible at a temperature of 50 °C under other conditions conducive to $FeCO_3$ growth (*i.e*. high pH = 7.8). It was observed that as temperature increased above 80 °C, film thickness decreased and density increased, producing compact and possibly more protective films. Nevertheless, further studies, which investigate the resistance provided by these films, are still needed.

**Effect of pH:** It has been shown both experimentally and computationally that pH is highly influential in $FeCO_3$ film formation (Kahyarian, Brown & Nešić, 2017). This dependence can be accounted for by considering the driving force ($S_{FeCO3}$) for precipitation. Saturation ratio is a function of $[CO_3^{2-}]$, which is highly dependent on pH (**Figure 2-11**); at 6.36 < pH < 10.36, the source of $CO_3^{2-}$, is likely to be the dissociation of $HCO_3^-$ since this is the predominant species in solution (**Figure 2-12**). The required $[Fe^{2+}]$ as a function of pH has been illustrated for 1 wt. % $NaCl_{(aq)}$ solution saturated with $CO_2$ at 80 °C (**Figure 2-15**) (Han, Brown & Nešić, 2010). According to (Han, Brown & Nešić, 2010), two general categories exist, which are divided by the saturation line $S_{FeCO3} = 1$, where $S_{FeCO3} < 1$ corresponds to under-saturated conditions where the $FeCO_3$ dissolution rate exceeds the PR; by contrast when $S_{FeCO3} > 1$, net $FeCO_3$ precipitation occurs. Additionally, the authors proposed the presence of a third segment, shown bounded by two dotted lines that is referred to as the "grey zone"; here, the authors stated unstable conditions for $FeCO_3$ formation exist where neither dissolution nor precipitation will dominate. Literature on the behaviour within each of the three regions exists.

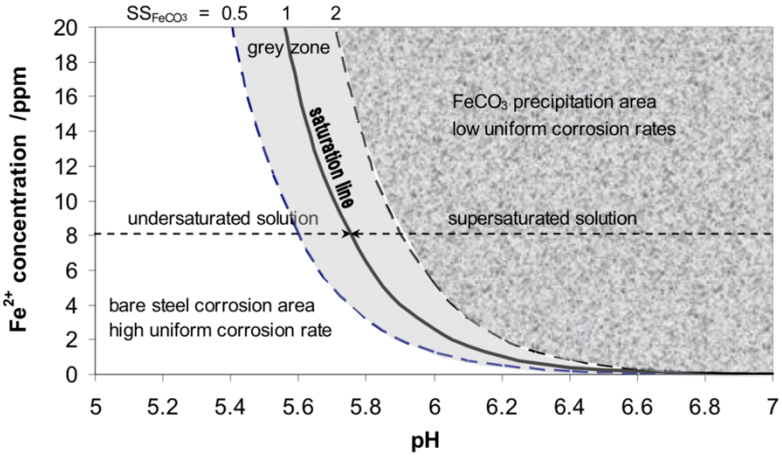



**Figure 2-15:** Solution pH effect on solubility of $FeCO_3$ at 80 °C, $pCO_2$ 0.53 bar (Han, Brown & Nešić, 2010). Image reproduced with permission of the rights holder, AMPP GLOBAL CENTER, INC.

Much of the research on the effect of pH was done at temperatures below 100 °C, however, (Tanupabrungsun, Brown & Nešić, 2013) attempted to elucidate pH effects (pH range 4 – 6) at elevated temperatures (80 – 200 °C) on $FeCO_3$ formation on carbon steel in a 1 wt.% $NaCl_{(aq)}$ solution, saturated with $CO_2$ (pH adjusted by addition of $NaHCO_3$). The corrosion rate was determined using LPR, and *ex-situ* surface analysis techniques (SEM, XRD) were used to analyse the film. The authors demonstrated that at pH 4, 80 °C, the corrosion rate

increased slightly and no product developed on the surface, but at 120 and 150 °C, the corrosion rate decreased after 20 hours by *ca*. 55 and 70 %, respectively, and the cubic crystalline product was $FeCO_3$. The authors also demonstrated that the corrosion rate decreased by two orders of magnitude (also after 20 hours) at 200 °C, but appeared to be damaged and dissolved in some areas, and $Fe_3O_4$ was also detected. Conversely at the higher pH (pH 6), the authors showed that the corrosion rates were consistently at least one order of magnitude lower than corrosion rates at the corresponding temperatures recorded in the pH 4 solutions. It was also shown that with the exception of 150 °C, crystals were smaller and the film more compact.

(Ieamsupapong *et al*., 2017) attempted to investigate $FeCO_3$ precipitation on carbon steel (UNS G10180) within the "grey zone" (**Figure 2-15**) at 80 °C (1 wt. % $NaCl_{(aq)}$ solution) over a nine day period, pH 5.4, 5.7, 6 and $[Fe^{2+}]$ of 40, 10, 3 ppm respectively. The corrosion rate (*via* LPR), OCP and surface analyses (SEM, EDX, XRD) were presented. The authors concluded from their investigation that $Fe_3C$ played a critical role in the formation of $FeCO_3$, creating stagnation areas where solution chemistry changed (increased $[Fe^{2+}]$ and higher pH). They also concluded that when the bulk $S_{FeCO3}$ is maintained at one, only partially protective product layer forms regardless of pH.

The pH dependence of $FeCO_3$ film formation in less acidic conditions and over a small pH range (6.3 – 6.6) on a carbon steel substrate (X65) in 1 wt. % $NaCl_{(aq)}$ with varied $S_{FeCO3}$ (7-150) and $[Fe^{2+}]$ between 5 and 50 ppm at 80 °C was investigated by (Chokshi, Sun & Nešić, 2005). The pH was modified by adding $NaHCO_3$ to a 1 wt. % $NaCl_{(aq)}$ solution previously saturated with $CO_2$ (1 bar) and the $[Fe^{2+}]$ was controlled by addition of $FeCl_2.H_2O$. The corrosion rate was determined using LPR and the experiments were repeated with metal coupons for surface analysis; however the surface area to volume ratios were not reported to be the same in the two sets of experiments. The authors stated that at pH 6.3 ($[Fe^{2+}]$ = 10 ppm, $S_{FeCO3}$ = 7) a very porous $FeCO_3$ film formed, with a corresponding corrosion rate at 45 hours of 0.65 mm $y^{-1}$. The authors then increased the pH to 6.6 ($[Fe^{2+}]$ = 10 ppm, $S_{FeCO3}$ = 30), and demonstrated that an observably compact film formed and reported a substantial drop in the corrosion rate to 0.2 mm $y^{-1}$ after 45 hours. The authors conducted another set of experiments but with $[Fe^{2+}]$ of 50 ppm and demonstrated that the $FeCO_3$ film consisted of smaller crystals, and was possibly more compact at pH 6.6 ($S_{FeCO3}$ = 150) than at pH 6.3 ($S_{FeCO3}$ = 37). The corrosion rate measured in the pH 6.6 ($[Fe^{2+}]$ = 50 ppm) was reported to decrease to *ca*. 0.2 mm $y^{-1}$ within 15 hours but was *ca*. 1.2 mm $y^{-1}$ in the pH 6.3 solution.

These results suggest that even slight pH increases substantially promote $FeCO_3$ formation, as was predicted from the $S_{FeCO3}$. It should be stated here that the authors did not consider the impact of $Fe^{2+}$ released from the surface when computing the $S_{FeCO3}$, so it is likely an underestimate of surface $S_{FeCO3.}$

The results of (Chokshi, Sun & Nešić, 2005) were supported by subsequent studies (Burkle *et al*., 2017; Ieamsupapong *et al*., 2017; Tanupabrungsun, Brown & Nešić, 2013). (Burkle *et al*., 2017) investigated the effect of pH (6.3 – 7) on the growth kinetics of $FeCO_3$ on X65 in 3.5 wt. % $NaCl_{(aq)}$ at 80 °C using *in-situ* XRD. The experiment was conducted for a 20 hour period, and the corrosion rate was determined by measuring the resistance to charge transfer using LPR (corrected for solution resistance) and anodic and cathodic Tafel constants obtained from potentiodynamic scans. The authors reported that the induction time (*i.e*. time taken to detect $FeCO_3$) and the corrosion rate decreased significantly with increased pH; at pH 6.3, the corrosion rate was said to stabilise after 120 minutes to 2.5 mm $y^{-1}$, whilst at pH 7.0, it rapidly decreased and stabilised to 0.2 mm $y^{-1}$. The authors reported a decrease in maximum crystal size from pH 6.6 to 7 from 11 μm to 6 μm and surface coverage increased from 20 % to almost 100 %. A MATLAB programme that identifies the presence of crystals from the resulting contrast in SEM images was said to be used to quantify surface coverage. The authors showed cross-sectional imaging obtained, through use of focused ion beam (FIB) and SEM, which revealed that the layer formed at pH 6.8 was on average 4 μm and porous, but layer formed at pH 7 was *ca*. 1.3 μm and far more compact. From this study, the authors concluded that the induction time for $FeCO_3$ formation decreases with increased pH, and compact more protective films form at higher pHs.

From the above it is clear that higher pHs promote $FeCO_3$ formation, as is expected from the increased $[HCO_3^-]$ and $[CO_3^{2-}]$ predicted as pH increases.

**Effect of flow:** The effect of solution flow on $FeCO_3$ film formation and growth is considered in two ways. First, the effect of flow velocity on $FeCO_3$ film formation has been studied. In stagnant systems, Fe dissolution occurs, resulting in a high concentration of Fe ions near the surface of the metal, creating an environment conducive to precipitation. By contrast, in the presence of flow, diffusion of Fe ions away from the surface and into the bulk is enhanced. This has been demonstrated in rotating disc experiments where high anodic Fe dissolution currents are noted in the presence of rotation (Valentini *et al*., 1985).

Second, after the $FeCO_3$ film has formed the effect of flow on the protectiveness of the film

has drawn interest. This is of particular concern as flow can introduce local film damage and if fluid velocity is sufficiently high, natural film repair can be hampered ultimately resulting in severe corrosion (Schmitt *et al*., 2000). Schmitt *et al*. 2000 investigated the effect of fluid velocity on the $FeCO_3$ surface film present on cylindrical steel (*C*: 0.39%) coupons (20 mm × 9 mm). The coupons were concentrically exposed to a controlled jet stream from a nozzle. The coupon and the jet nozzle were submerged in the test liquid, which was pumped to a 2 L autoclave filled with 1 wt. % $NaCl_{(aq)}$ solution at 80 °C, 5 bar $CO_2$ for 96 hours.

The authors reported that if pits were present on the surface of the steel, relatively low wall shear stresses of 0.2 Pa exacerbated the localised corrosion. The authors stated that the morphology of the $FeCO_3$ films present on pre-corroded samples were altered by flow intensity, which they defined to be a measure of the wall shear stress ($\tau$) given by Equation **2-106**, where $\varrho_f$ is the fluid intensity, $u$ is the flow velocity, Re is the Reynold's number, $x$ is the radial distance from the centre of the nozzle, $d$ is the inner diameter of the nozzle.

$$\tau = 0.0447\ \rho_f\ u^2 Re^{-0.182} \left(\frac{x}{d}\right)^{-2} \qquad \textbf{2-106}$$

The authors also reported that there was increased cracking tendency with increased flow intensity, which the authors proposed to be due to microturbulences in the near wall region.

These findings were corroborated by a later study (Nyborg & Dugstad, 2003) where a dense, $FeCO_3$ film formed on three different carbon steels (*C*: 0.15 to 0.2 %) at 80 °C, $pCO_2$ 1.8 bar and pH 5.8, failed locally with severe mesa[7] attack apparent (through imaging) when the fluid flow rate was set to 7 m $s^{-1}$. The authors reported that only a few samples underwent localised corrosion at 2.5 – 4 m $s^{-1}$, and no attack when flow rates were 0.1 – 0.5 m $s^{-1}$. The authors stated that if films were between 50 – 100 μm thick, localised corrosion did not occur.

Based on the above it is clear that increased flow velocity has the potential to impact $FeCO_3$ film formation, growth and stability. However the vast number of variables (temperature, pH, $pCO_2$) influencing the behaviour of the film make it exceedingly difficult to predict the effect of flow velocity in varied environments.

**Effect of corrosion products:** Corrosion product formation is directly dependent on the metal base. At carbon content (*C*) > 0.9 %, carbon steel consists of two phases, ferrite and

[7] The authors defined mesa attack to be localised break down of protective $FeCO_3$ films resulting in pitting. (Jones, 1996) explains that localised attack of otherwise resistant surfaces results in pit formation.

cementite, in an intermingled, finely laminated structure (Brandes & Brook, 1998). Generally, the Fe ions in the ferrite phase are more labile and as such cementite ($Fe_3C$) can be left behind due to preferential dissolution. (Crolet, Thevenot & Nešić, 1998) explain that $Fe_3C$ is electronically conductive, so when it is left undissolved, the steel (Fe) surface and exposed $Fe_3C$ are left on the surface, galvanic corrosion[8] may occur. (Farelas, Brown & Nešić, 2013) proposed that a cementite layer may also hinder diffusion of Fe ions away from the surface and creates stagnant pockets where increased supersaturation levels can be achieved more readily. The authors stated that the $Fe_3C$ layer had an anchoring effect making the $FeCO_3$ film increasingly adherent and stable.

Magnetite ($Fe_3O_4$) formation has also been reported as a common corrosion product present with or in place of $FeCO_3$ films at temperatures of 80 °C (Han *et al*., 2009; Motte *et al*., 2020) and 100 °C (Tanupabrungsun, Brown & Nešić, 2013).

In an early study (Han *et al*., 2009) postulated that $Fe_3O_4$ formed on carbon steel samples (C1018, X65) in 80 °C 1 wt. % $NaCl_{(aq)}$ solutions deaerated with $CO_2$ and pH adjusted through addition of $NaHCO_3$, acted as a thin passive layer. The authors interpreted the measured increase in OCP to *ca*. -0.2 V *vs*. AgCl | Ag (-0.06 V *vs*. $SHE_{25°C}$), which coincided with detected $Fe_3O_4$ using *ex-situ* grazing incidence XRD (GIXRD), to indicate that a protective layer had formed. Since $FeCO_3$ was detected on samples before the OCP increased, the authors concluded that $Fe_3O_4$ was responsible for protection of the substrate. No electrochemical measurements to quantify the film or charge transfer resistance (*i.e*. protection) were made; these postulations are therefore unsubstantiated. In another study by the group, (Tanupabrungsun, Brown & Nešić, 2013) investigated the impact of pH on the corrosion of mild steel (API 5L X65) at elevated temperatures in 1 wt. % $NaCl_{(aq)}$ using LPR and EIS, found that at pH 4, minimal $Fe_3O_4$ formed alongside $FeCO_3$ at 150 °C but more formed at 200 °C, based on the XRD data. Images of crystals presented under conditions where the coexistence was detected showed damaged crystals which may be due to partial dissolution of $FeCO_3$. By contrast, films containing only $FeCO_3$ were demonstrated to be closely packed with no apparent defects. In fact in an investigation of the electrical properties of corrosion layers formed in anoxic carbonated conditions using conductive atomic force microscopy (Mercier-Bion *et al*., 2018), regions of films consisting only of $FeCO_3$ and other ferrous

[8] Galvanic corrosion occurs when two dissimilar materials are in electrical contact and in the presence of a corrosive electrolyte, and one of the materials corrodes preferentially (Jones, 1996).

carbonates ($Fe_2OH_2CO_3$) on a steel nail (composition not stated) specimen were found to be insulating, whereas areas which consisted of $Fe_3O_4$ strips were electrically conductive. Although this study was conducted using archaeological nails, the specimen was extracted from anoxic carbonated sites, so are representative of Fe carbonate systems. The electronic conductivity of $Fe_3O_4$ may explain the observed disintegration of the $FeCO_3$ crystals shown by (Tanupabrungsun, Brown & Nešić, 2013).

Chukanovite ($Fe_2(OH)_2CO_3$) has been demonstrated to form alongside $FeCO_3$ (Mercier-Bion *et al*., 2018; Joshi *et al*., 2018; Li *et al*., 2019; Ingham *et al*., 2012; Sk *et al*., 2017), and its impact on $CO_2$ corrosion of steel is therefore of relevance. Although (Mercier-Bion *et al*., 2018) found that $Fe_2(OH)_2CO_3$ is insulating, findings from investigations by (Joshi *et al*., 2018) suggested that $Fe_2(OH)_2CO_3$ provided little protection to carbon steel undergoing $CO_{2(aq)}$ corrosion. In this study, $FeCO_3$ and $Fe_2(OH)_2CO_3$ formation and protection (quantified using LPR) were investigated on Fe in deionised $H_2O$ saturated with $CO_2$ at 80 °C pH 6.8 (pH adjusted using $NaHCO_3$) over 288 hours; experiments were conducted in a glove box to prevent $O_2$ contamination. The authors reported that after 24 hours of immersion, platy[9] crystals, detected to be chukanovite (*via ex-situ* Raman spectroscopy), and equant[10] habits, confirmed to be $FeCO_3$ (*ex-situ* Raman spectroscopy), were observed on the Fe surface (**Figure 2-16**). The authors described the $FeCO_3$ crystal habits as micro-facetted cylinders with trigonal-pyramidal caps and $Fe_2(OH)_2CO_3$ as plate like habits as shown in **Figure 2-16**. The ratio of $FeCO_3$ to $Fe_2(OH)_2CO_3$ was stated to increase as immersion time increased, and the corrosion rate was demonstrated to decrease concurrently. The authors proposed that the superior protection provided by $FeCO_3$ was related to its ability to pack together densely with time; close packing was less likely to be achieved by or in the presence of $Fe_2(OH)_2CO_3$ given the shape of the crystal habit. Images of the cross-section of samples, demonstrated the presence of observable gaps between the surface film layer and underlying substrate during early immersion periods where $Fe_2(OH)_2CO_3$ was present, whilst no gaps were shown to be present when the surface film consisted of only $FeCO_3$.

[9] Crystal habits of platy morphology are those with plate-like structures (Lee, Erdemir & Myerson, 2019).

[10] Crystal habits of equant morphology are those with low aspect ratios *e.g.* cubes and spheres (Lee, Erdemir & Myerson, 2019).

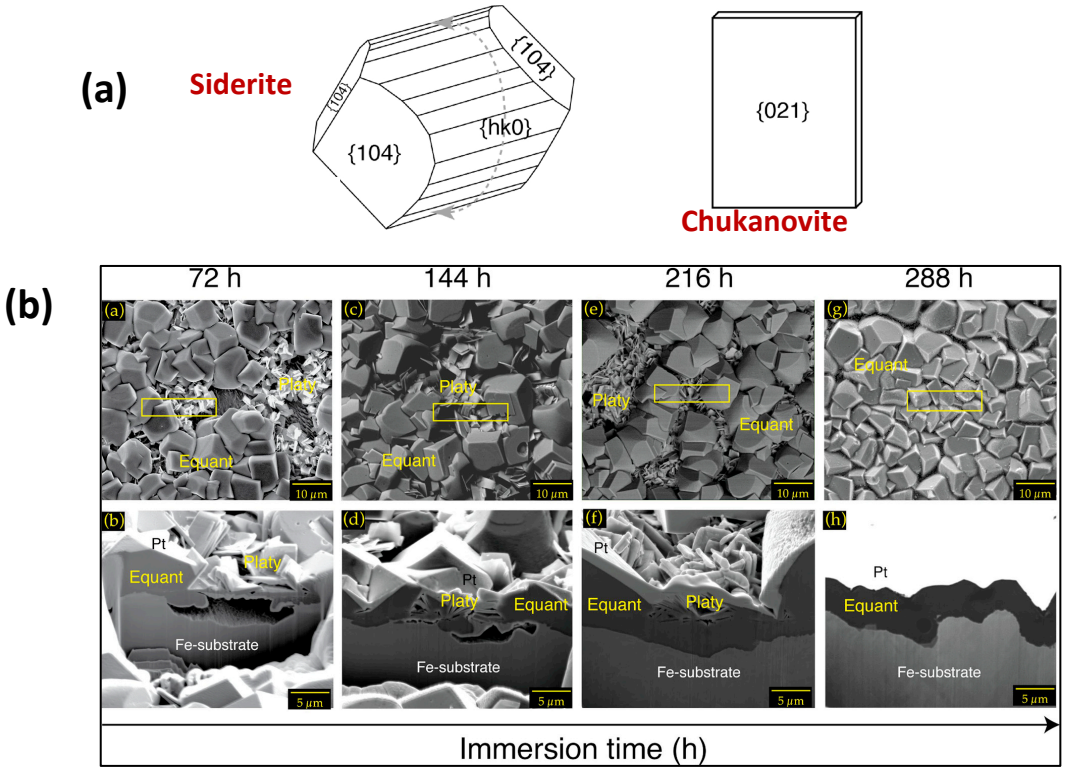



**Figure 2-16**: (a) Habits of siderite and chukanovite; (b) Evolution of surface film with time formed on Fe in $CO_2$ saturated $NaHCO_{3(aq)}$ at 80 °C extracted from (Joshi *et al*., 2018). Image reproduced under the terms of the Creative Commons Attribution licence.

The partial pressure of $CO_2$ is known to significantly affect corrosion of carbon steel and $FeCO_3$ film formation. A review of the corresponding literature however will not be included since the inlet feed gases to PCCC plants typically have a total pressure of 1 bar, therefore the impact of elevated $pCO_2$ is not extremely relevant to work presented in this thesis.

From the above discussion it is apparent that corrosion rate (obtained using LPR, potentiodynamic scans or weight loss measurements) was most commonly used to quantify the protectiveness of $FeCO_3$ films formed, if measured at all. Far more insight on the formation and resistance of these films can be determined using other techniques *e.g.* chronoamperometry and impedance spectroscopy. Moreover, since it has been demonstrated that non-uniform dissolution occurs in the corrosion of carbon steel in $CO_{2(aq)}$ systems and localised breakdown of $FeCO_3$ may occur in these environments, techniques that are not fundamentally developed to observe uniform corrosion will likely provide more useful insight to the resistance and stability of surface films. The literature corresponding to chronoamperometry and impedance spectroscopy are particularly relevant since these techniques were used in this thesis.

### 2.4.5.2 Potentiostatic experiments

#### Potentiostatic fundamentals

In potentiodynamic experiments (**Figure 2-13**), the passive film continues to form as the potential is swept more anodically beyond the passivation potential such that the film thickness increases with time (Jones, 1996), though other product species may also form. Using potentiostatic experiments (*e.g.* chronoamperometry), on the other hand, single species product formation may be investigated. Generally, in chronoamperometry experiments, the potential applied to the electrode is stepped from one value at which no electrochemical reaction occurs, to the value at which an electrochemical reaction of interest occurs. Typical current transients recorded as a result of potential application are shown in **Figure 2-17**. (Bockris, Reddy & Gamboa-Aldeco, 2002) explain that the initial response, from A to B, is a result of charging of the double layer up to the applied potential, at B to C the current decreases due to its use not only for double layer charging but also for interfacial electron transfer, and from C to D the double layer is almost charged so the current change slows. Following point D, the current response is a function of the diffusion of species toward or away from the electrode surface as shown in **Figure 2-17b**; the Cottrell equation[11] (Equation **2-107**) describes this response. Chronoamperometry can therefore be used to investigate diffusion controlled reactions at the electrode surface.

[11] The Cottrell equation was formulated for a single electrochemical reaction on a planar electrode involving species $i$, under diffusion control by solving for concentration of species $i$ ($C_i$) described by Fick's second law (Equation **2-46**) assuming the initial $C_i$ is equal to its bulk concentration ($C_\delta$), and boundary conditions of $C_i$ is zero at the electrode surface for $t > 0$, and at the end of the diffusion layer is equal to $C_\delta$ (Bard & Faulkner, 2001).

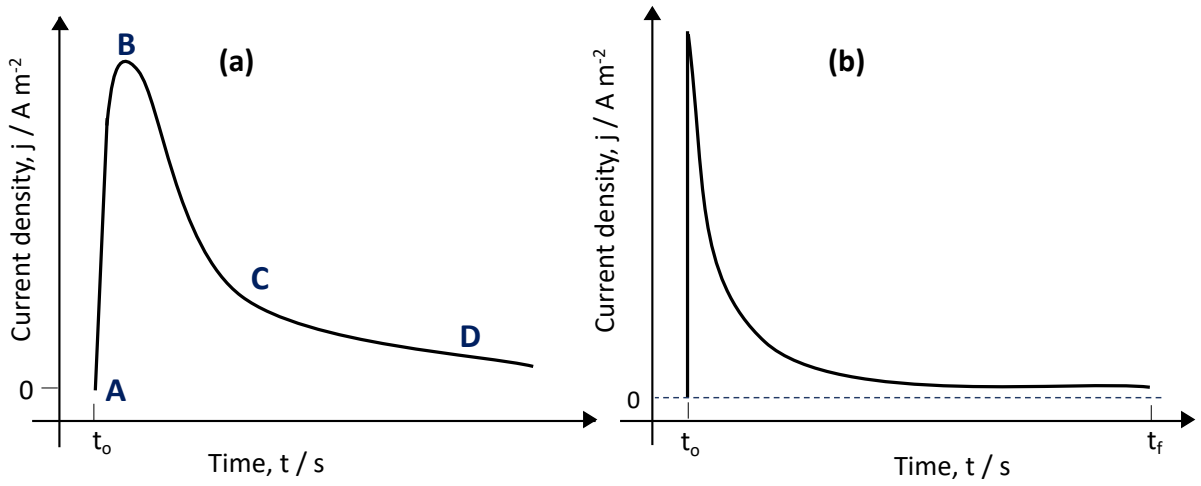



**Figure 2-17:** Schematic of typical (a) initial and (b) complete current density response due to application of a potential step. Plots were adapted from (Bockris, Reddy & Gamboa-Aldeco, 2002*)*.

$$j = \frac{nFD_i^{\frac{1}{2}}C_\delta}{\pi^{\frac{1}{2}}t^{\frac{1}{2}}} \qquad \textbf{2-107}$$

If however more complex processes are involved, for example homogeneous reaction and precipitation of species on the electrode surface, the current response will not be described by the Cottrell equation but will involve application of Fick's second law (Equation **2-46**) modified to include the different processes that will affect the surface concentrations of electroactive species.

Formation of crystalline species on the electrode may occur *via* direct electrochemical reaction with the electrode in a process termed electrocrystallisation. This phenomenon involves the diffusion of dissolved ions to the electrode surface, where they undergo an electron transfer reaction and adsorb on the surface, becoming 'ad-atoms'. Clustering of ad-atoms results in the formation of critical nuclei due to surface diffusion of individual ad-atoms. The clusters then grow to form deposits of crystalline material (Rodríguez-Amaro & Ruiz, 2001). The theoretical treatment of the electrocrystallisation response will not be included here as it was not applied to this work.

## Potentiostatic $FeCO_3$ formation literature

The impact of local solution chemistry on the formation and growth of surface films on different steels (AISI 1006, API J155, API 5CT L80) in $CO_2$ saturated 0.5 mol dm$^{-3}$ $NaCl_{(aq)}$ solutions, pH 4.2 – 7.3 (pH adjusted by addition of NaOH) was investigated by (Sk *et al.*, 2017) using chronoamperometry and *in-situ* synchrotron XRD. Firstly, the authors concluded

that $FeCO_3$ formation occurred by direct electrocrystallisation, in parallel with Fe dissolution, and the crystal growth kinetics varied quadratically with supersaturation at pH 6.8 and linearly at pH 7.3. It was proposed that the dissolution current, as well as the saturation ratio at the electrode surface, is controlled by the thickness of an initially precipitated amorphous surface layer, assumed to be $FeCO_3$. These conclusions were derived from the correlation of current transients and $FeCO_3$ detection using *in-situ* XRD. The authors observed that application of an anodic potential step from OCP resulted in a current transient that initially decreased to a plateau, after which it rose to a peak and subsequently decayed to a low value. This seemingly occurred at various rotation rates (0, 1000, 3000 RPM) and potentials (-0.68 to -0.6 V *vs*. SCE, -0.492 to -0.412 V *vs*. $SHE_{25\,°C}$), with a less exaggerated, lower magnitude, current density peak obtained with decreasing overpotential. The authors stated that the pre-peak plateau ($i_{plat}$), which was due to Fe dissolution, demonstrated an approximately Tafel relationship with change of electrode potential. The saturation ratio of $FeCO_3$, within the pre-peak plateau time period, was calculated using the surface $[Fe^{2+}]$ ($C_s$), estimated by extracting the slope ($k_m$) and intercept ($i_{diss,n}$) from a plot of $i_{plat}$ *vs*. $\omega^{-1/2}$ (Equation **2-109**) and using the Levich equation (Equation **2-108**) with an additional term ($i_{diss,n}$).

$$i_{plat} = k_m \omega^{\frac{1}{2}} + i_{diss,n} \qquad \textbf{2-108}$$

$$k_m = \frac{nFDc_s}{\delta \omega^{\frac{1}{2}}} \qquad \textbf{2-109}$$

The authors also demonstrated in previous works (Ingham *et al*., 2012, 2015) that the rise in current coincided with the *in-situ* detection of crystalline $FeCO_3$. The sum of the dissolution current and the electrocrystallisation current (Equation **2-110**) was demonstrated to closely reflect the measured current (**Figure 2-18**).

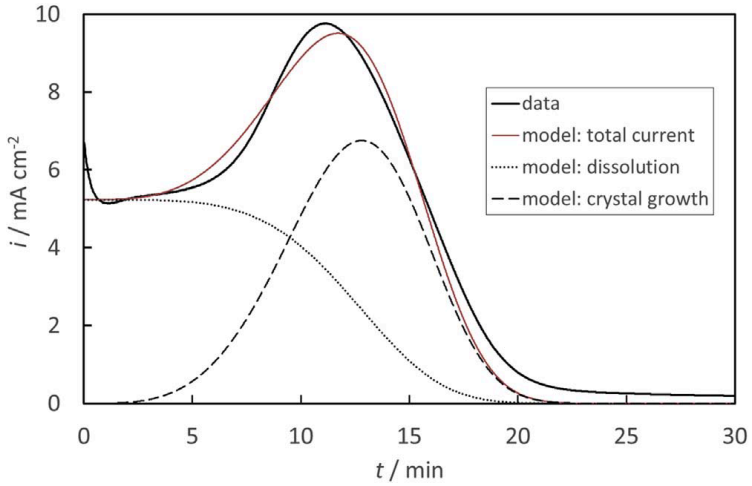



**Figure 2-18:** Fe dissolution and electrocrystallisation current contributions to measured current density (Sk *et al*., 2017*)*. Image reproduced with permission of the rights holder, Elsevier.

The rate constant for Equation **2-110** was derived by applying Avrami theory (Equation **2-111**), which relates the crystal volume ($V_{cryst}$) formed, determined by *in-situ* XRD, at a time ($t$), to the induction time ($t_d$) and total crystal volume ($V_m$). The exponent $n$ is dependent on the crystal shape and nucleation type (progressive or instantaneous).

$$i_{cryst} \propto \frac{dV_{cryst}}{dt} \qquad \textbf{2-110}$$

$$V_{cryst} = V_m\{1 - \exp\left[-(k_{Avrami}(t - t_d)^n\right]\} \qquad \textbf{2-111}$$

It was also demonstrated that the time to the peak current and time to decay, could be used to investigate the impact of different conditions (*e.g*. pH, rotation rate) on product layer formation.

It is worth mentioning that there was no evidence in the initial work (Ingham *et al*., 2015), where the theory of the formation of initial amorphous $FeCO_3$ originated, that it was in fact $FeCO_3$. Additionally (Sk *et al*., 2017) reported the formation of $Fe_2(OH)_2CO_3$ (chukanovite) after $FeCO_3$, so the crystal growth rate is representative of a mixed product layer. The presence of $Fe_2(OH)_2CO_3$ after $FeCO_3$ is peculiar since $Fe_2(OH)_2CO_3$ has been reported (Azoulay, Rémazeilles & Refait, 2012; Zheng *et al*., 2016b) to be metastable relative to $FeCO_3$, and is expected therefore to precede $FeCO_3$ formation. Lastly, in a subsequent *in-situ* synchrotron study of the anodic product formation by this group (Ingham *et al*., 2018), apparently using the same electrochemical set up as (Sk *et al*., 2017), inadvertent $O_2$ ingress through the silicone rubber that delivered the electrolyte to the electrochemical cell in which measurements were taken, was said to have occurred. This resulted in formation of other

species *e.g.* FeOOH and $Fe_3O_4$. Is it imaginable then that the unidentified amorphous layer could be $Fe_3O_4$ or $Fe_2O_3$. The authors stated that $FeCO_3$ formation had little or no dependence on the dissolved [$O_2$]. This conflicts with many studies that state $O_2$ free conditions are needed to prevent production of unwanted products when studying $FeCO_3$ formation (Fosbøl, Thomsen & Stenby, 2013). Accordingly, the growth kinetics of this study are likely indicative of multiple products. All in all, chronoamperometry, coupled with surface characterisation, has been demonstrated to provide useful insight to the formation rate of $FeCO_3$ under different conditions.

### 2.4.5.3 Electrochemical impedance spectroscopy

#### Electrochemical impedance spectroscopy fundamentals

##### Introduction

Measurement of the current response due to the application of a potential at a specific frequency to a corroding metal provides useful insight to the interfacial electrochemical processes. Alternating the frequency of the applied potential however, significantly increases the information that can be accessed. Electrochemical impedance spectroscopy (EIS) involves the application of current or potential perturbations (of varied frequencies) to an electrochemical system and the response instigated has contributions from both resistive and reactive (*i.e.* which store energy) components at the interface. EIS is particularly instrumental in examining corrosion processes involving product films since these films may possess reactive and resistive features. Both the added protection provided by coatings, as well as the protection mechanism involved, may be deduced through the measured response. Further, since the excitations are minimal, and alternating in nature, this technique is non-destructive, so the evolution of the electrode | electrolyte interface can be examined without modifying it.

##### Fundamentals

When a steady state electrochemical system is perturbed by applying an oscillating potential, as described by Equation **2-112**, where $E_o$ is the amplitude and $\omega$ the angular frequency (Equation **2-114**), it relaxes to a new steady state and in doing so, an oscillating current flows described by Equation **2-113**, where $I_o$ is the current amplitude (not the same as the exchange current density) and $\phi$ the phase shift between the applied potential and measured current. **Figure 2-19** illustrates the perturbation potential and current response. The time taken for this

relaxation is termed the time constant $\tau$ (s); fast processes are recorded at high frequencies and slow processes at low frequencies.

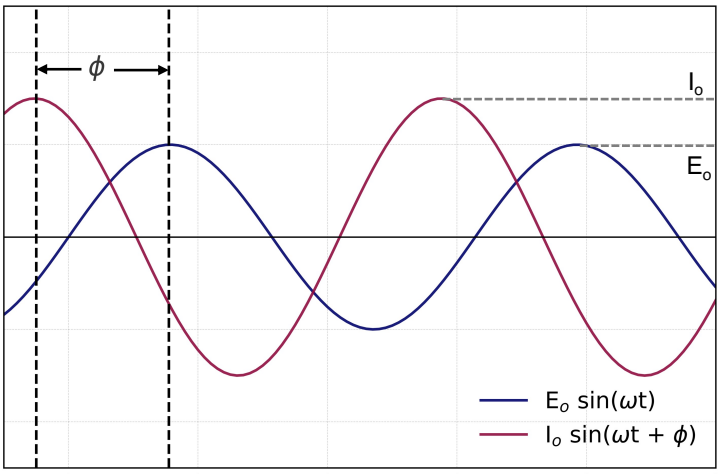



**Figure 2-19:** Alternating voltage applied at a single frequency to an electrochemical system with reactive components and resulting current. The phase shift between the voltage and current ($\phi$) is shown.

If the electrochemical system consists of purely resistive components, *i.e.* the current response is proportional to the applied voltage, $\phi = 0$ and the same current response would be measured regardless of the frequency of the alternating voltage. By contrast, if the electrochemical system has reactive components, the current response will not be proportional to the applied voltage, $\phi$ would not be equal to zero, and would be a function of the applied perturbation frequency.

$$E(t) = E_o \sin(\omega t) \quad \textbf{2-112}$$

$$I(t) = I_o \sin(\omega t + \phi) \quad \textbf{2-113}$$

$$\omega = 2\,\pi\,f \quad \textbf{2-114}$$

The ratio of the applied voltage to the measured current is called the impedance and is given by Equation **2-115** and is analogous to the resistance as described by Ohm's Law.

$$Z = \frac{E(t)}{I(t)} = \frac{E_o \sin(\omega t)}{I_o \sin(\omega t + \phi)} \quad \textbf{2-115}$$

Data representation

Using Euler's formula (Equation **2-116**), the impedance can be re-written in polar form and as a complex function (Equation **2-117**).

$$e^{j\phi} = \cos\phi + j\sin\phi \quad \textbf{2-116}$$

$$Z = Z_o e^{j\phi} = Z_o(\cos\phi + j\sin\phi) \quad \textbf{2-117}$$

$$Z_o = \frac{E_o}{I_o} \quad \textbf{2-118}$$

The impedance can be represented using a phasor diagram (**Figure 2-20**), which maps the impedance in polar co-ordinates. In this diagram, the magnitude of the impedance ($Z_o$) is represented by the length of the vector and the angle between the vector and the origin is the phase shift ($\phi$).

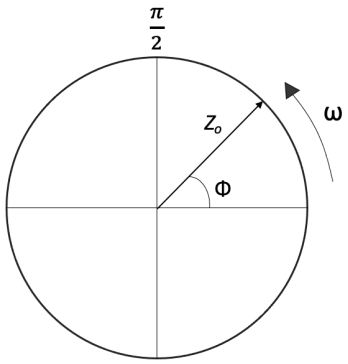



**Figure 2-20**: Phasor diagram of the impedance measured when a single frequency (f = ½ π ω) voltage perturbation is applied to an electrochemical system. The magnitude of the impedance ($Z_o$) and the phase angle between the applied voltage and current response ($\phi$) are shown.

The polar co-ordinates can also be resolved to cartesian co-ordinates using Equations **2-119** and **2-120**, and represented as a complex number by Equation **2-121**, where *Z'* is the real part of the impedance and *Z"* is the imaginary part of the impedance. Here *j* does not represent the current density, but instead it is equal to √-1. The magnitude of the impedance may be calculated using Equation **2-122**.

$$Z' = Z_o\cos(\phi) \quad \textbf{2-119}$$

$$Z'' = Z_o\sin(\phi) \quad \textbf{2-120}$$

$$Z = Z' + j\,Z'' \quad \textbf{2-121}$$

$$|Z| = \sqrt{(Z')^2 + (Z'')^2} \quad \textbf{2-122}$$

Using cartesian co-ordinates, the EIS data can be visualised using a Nyquist plot (**Figure 2-21**), which is a form of an Argand diagram. Each point on the Nyquist plot represents the impedance at a specific frequency. These plots often have characteristic shapes which may give an indication of the different electrode processes involved.

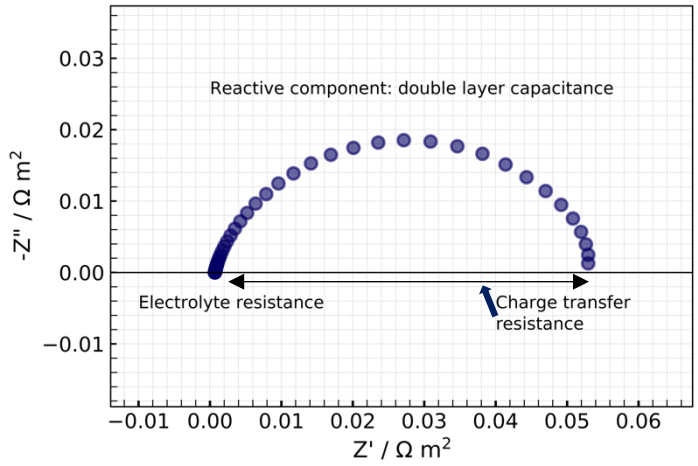



**Figure 2-21:** Exemplary Nyquist plot of a steel electrode freely corroding in a neutral aqueous solution.

It is also extremely useful to plot EIS data as a function of the frequency- such plots are referred to as Bode plots (**Figure 2-22**). The phase angle ($\phi$) and the magnitude of the impedance ($|Z|$), are plotted as a function of the frequency. All three plots must be visually inspected to gain an improved understanding of the different processes involved, as well as the magnitude of the individual contributions to the overall impedance.

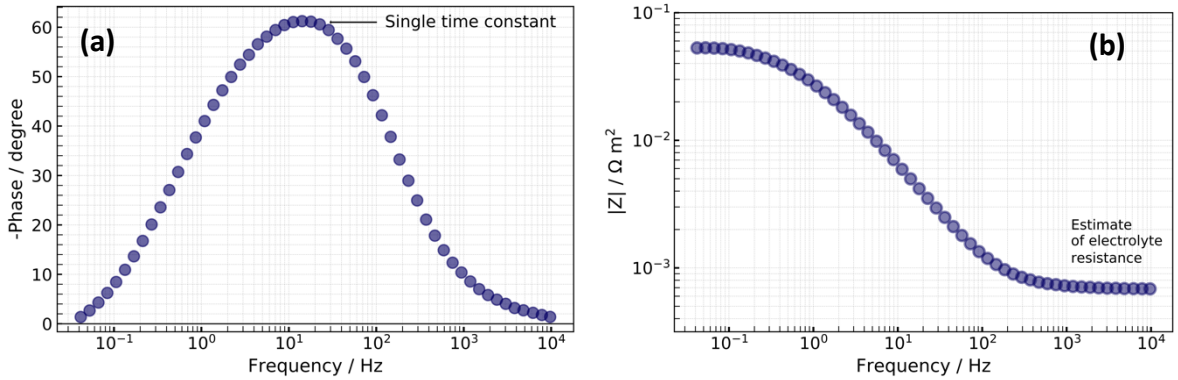



**Figure 2-22:** Exemplary Bode plots of **(a)** the phase angle and **(b)** modulus of the impedance data obtained with a steel electrode freely corroding a neutral aqueous solution.

Kramers-Kronig

The Kramers-Kronig transform is a method used to determine if collected impedance data can be modelled with an equivalent circuit. The Kramers-Kronig relations validate the collected impedance data by verifying if the data satisfies the following conditions:

1. Causal: The measured response is as a result of the applied perturbation potential.

2. Linear: The amplitude of the applied voltage waveform is sufficiently low such that the measured current varies linearly with the applied voltage.
3. Stable: The system does not continue to change after the external potential is no longer applied.

These relations calculate the imaginary part of the impedance from the real part of the impedance to confirm that the above conditions are satisfied.

**Data interpretation**

The impedance response measured when an electrochemical system is perturbed can be modelled using a combination of electrical components (*e.g.* resistors, capacitors) arranged in an equivalent electrical circuit. Applicable equivalent electrical circuits must meet two criteria: 1) selection or formulation must informed by knowledge of the possible processes involved, *e.g.* reactions, mass transfer effects; and 2) the overall error must be minimised. The error between the modelled circuit data and the measured data is calculated at every frequency in order to produce the overall deviation reported as a goodness of fit or $\chi^2$ value. Equivalent circuits provide a framework to quantitatively account for the different phenomena present and therefore enable enhanced data interpretation. Circuit components used or considered in this thesis are highlighted below.

Resistors

The current response due to the application of a potential to a resistor is described by Ohm's law (Equation **2-123**), which states that the current is proportional to the applied voltage. This means that the applied voltage and current are always in phase and so there is no imaginary component of the impedance (Equation **2-124**). The Nyquist plot for a resistor therefore consists of a single point on the real axis. This component is commonly used to model the charge transfer resistance of electrochemical reactions.

$$I = \frac{V}{R} \qquad \textbf{2-123}$$

$$Z_R = R \qquad \textbf{2-124}$$

Capacitors

A capacitor is a device which stores charge and is formed when two conducting plates are separated by a non-conducting media or dielectric. The current response of a capacitor due to the application of an alternating potential is described by Equation **2-125**, where *C* is the

capacitance. The phase angle between the measured current and the applied alternating voltage, of an ideal capacitor is –90 ° or -π/2. Since the applied voltage is an AC signal, Equation **2-125** is resolved in the frequency domain and the impedance is given by Equation **2-126** (in cartesian form), which indicates that there is no real part of the impedance. The Nyquist plot for a capacitor is therefore a vertical line at $Z' = 0$. Capacitors are often used to represent the double layer at the electrode-electrolyte interface, as well as to the capacitance of surface films or coatings formed on electrode surfaces in electrochemical systems. Coatings act like capacitors with the capacitance described by Equation **2-127** where $C_c$ is the coating capacitance, $\epsilon_c$ is the dielectric constant of coating material (*e.g.* $\epsilon_{Fe2O3}$ =7), $\epsilon_o$ is the permittivity of vacuum ($8.86 \times 10^{-12}$ F $m^{-1}$), and $d$ is the thickness of the coating (m). It should be noted that $\epsilon$ of water is 80 at 20 °C, so for porous coatings in aqueous electrolytes, the effective $\epsilon_c$ may be higher that of a non-porous coating.

$$I(t) = C\frac{dV(t)}{dt} \qquad \textbf{2-125}$$

$$Z_C = \frac{1}{j\,\omega\,C} \qquad \textbf{2-126}$$

$$C_C = \frac{\epsilon_c \epsilon_o A}{d} \qquad \textbf{2-127}$$

Diffusion element

As explained in Section 2.1.2.2, species need to diffuse toward or away from the electrode to undergo an electrochemical reaction (Equation **2-129**). The Warburg impedance element is used to model one dimensional semi-infinite unrestricted diffusion to a large planar electrode, and the impedance is described by Equation **2-128**. $\sigma_d$ is the Warburg coefficient ($\Omega\ s^{-1/2}$), and is given by Equation **2-130** where $C_O$ and $D_O$ are the bulk concentration and diffusion coefficient respectively of the reducible species and, $C_R$ and $D_R$ are the bulk concentration and diffusion coefficient of the oxidisable species (Equation **2-130**). The Nyquist plot produced from impedance data collected from a Warburg element consists of a straight line at a phase of 45 ° or π/4. The two other common diffusion responses are the finite space Warburg ($Z_{FSW}$) and the finite length Warburg ($Z_{FLW}$) and are described by Equations **2-131** and **2-132** respectively, where $\tau_d$ is the diffusion time constant and $R_d$ is the limiting diffusion resistance. Finite length Warburg impedance may appear in corrosion studies and it is typically used to model diffusion through a layer with a finite length (*e.g.* response recorded with a rotating

disc electrode or due to the presence of a finite stagnant porous film (Orazem & Tribollet, 2008).

$$Z_w = \frac{\sqrt{2}\,\sigma_d}{\sqrt{j\,\omega}} \quad \textbf{2-128}$$

$$O + ne^- \rightleftharpoons R \quad \textbf{2-129}$$

$$\sigma_d = \frac{R\,T}{n^2F^2A\,\sqrt{2}}\left(\frac{1}{C_O\sqrt{(D_O)}} + \frac{1}{C_R\sqrt{D_R}}\right) \quad \textbf{2-130}$$

$$Z_{FSW} = R_d \frac{\coth\left(\sqrt{j\,\omega\tau_d}\right)}{\sqrt{\tau_d j\,\omega}} \quad \textbf{2-131}$$

$$Z_{FLW} = R_d \frac{\tanh\left(\sqrt{\tau_d j\,\omega}\right)}{\sqrt{\tau_d j\,\omega}} \quad \textbf{2-132}$$

Constant phase elements

The constant phase element is one of the most commonly used circuit components in modelling impedance data. The mathematical description of the constant phase element resembles that of a capacitor and it is given by Equation **2-133**, where $Q_o$ (F $s^{\alpha-1}$) and $\alpha$ are the constant phase element parameters; $\alpha$ here is different from the transfer coefficient discussed in Section 2.1.2. Although a complete description of the physical nature of the constant phase element remains unknown, the versatility of its mathematical definition has made it capable of accurately modelling measured impedance data. The constant phase element can be used in place of different circuit components and depends on the value $\alpha$. When $\alpha = 1$, the unit of the constant phase element is F and it represents a capacitor. For $0.5 < \alpha < 1$, the constant phase element represent the non-ideal capacitive behaviour of coatings or double layers. Deviations from pure capacitive behaviour have been said to arise from a number of factors including surface heterogeneities (Lukács, 1999, 1997), reaction rate and current distributions (Kim, Pyun & Kim, 2003) and coating thickness variability (Schiller & Strunz, 2001). When $\alpha \leq 0.5$, the constant phase element represents the Warburg diffusion.

$$Z_Q = \frac{1}{Q_o(j\,\omega)^\alpha} \quad \textbf{2-133}$$

Equivalent circuits

These circuit components are combined in different configurations to describe different electrochemical systems. The mathematical description of the overall impedance of the entire

equivalent circuit is governed by the configuration of the components; when arranged in series (**Figure 2-23a**), the overall impedance is given by Equation **2-134**, and when arranged in parallel (**Figure 2-23b**) the overall impedance is given by Equation **2-135**.

$$Z_{series} = Z_A + Z_B \qquad \textbf{2-134}$$

$$\frac{1}{Z_{parallel}} = \frac{1}{Z_A} + \frac{1}{Z_B} \qquad \textbf{2-135}$$

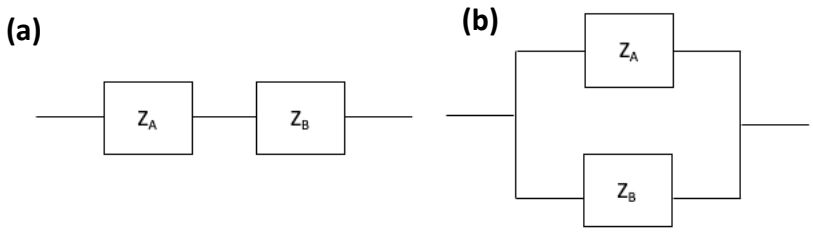



**Figure 2-23:** Combination of circuit components arranged in: (a) series, and (b) parallel.

Impedance spectra of a uniformly accessible electrode, like in the case of a freely corroding metal (Orazem & Tribollet, 2008), are often described by the equivalent circuit shown in **Figure 2-24**, known as the simplified Randles circuit, where $R_1$ is electrolyte resistance, $C_1$ is the double layer or interfacial capacitance and $R_2$ is the resistance to charge transfer of the electrochemical process.

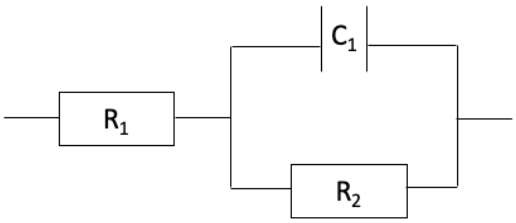



**Figure 2-24:** Common equivalent circuit (the simplified Randles circuit) used to model a single electrode process and ohmic resistance.

The mathematical description of the impedance of this circuit is given by Equation **2-136**, which was derived by combining the resistor impedance (Equation **2-124**) and the capacitor impedance (Equation **2-126**) following the rules provided by Equations **2-134** -**2-135**. The capacitor in the Randles circuit shown in **Figure 2-24** may be replaced with a constant phase element when the Nyquist plot of the EIS data appears as a depressed semicircle. This depression arises as a result of deviation from ideal behaviour of the capacitive components in the electrochemical cell. For the modified circuit, the impedance response (Equation

**2-136**) must be reformulated by replacing Equation **2-126** with **2-133**. The pseudo-capacitance can then be determined by equating the reformulated equation to Equation **2-136** and solving for the capacitance, which yields Equation **2-137**. Determination of the pseud-capacitance becomes increasingly complex as more circuit components are included.

$$Z = R_1 + \frac{R_1}{1 + \omega^2 R_1^2 C_1^2} - j\frac{\omega R_1^2 C_1}{(1 + \omega^2 R_1^2 C_1^2)} \quad \textbf{2-136}$$

$$C = Q^{\frac{1}{a}} R^{\frac{\alpha - 1}{\alpha}} \quad \textbf{2-137}$$

**Electrochemical impedance spectroscopy pitfalls**

Although EIS is a powerful technique and can be used to extract useful data corresponding to each feature / mechanism in an electrochemical system, there are some pitfalls which must be acknowledged. Countless circuits may be formulated to describe measured EIS data with many electrical components, which may result in a low overall error *i.e.* a better fit. However, such circuits may have little or no physical interpretation. Accordingly, only circuits which have a reasonable physical interpretation should be used to fit the measured data. Complementary techniques *e.g.* surface characterisation and measurements *e.g.* open circuit potentials, should be used to substantiate the choice of the equivalent circuit.

## Electrochemical impedance spectroscopy $FeCO_3$ formation literature

Compared to DC electrochemical techniques, EIS has not been as extensively used for investigation of active steel (or Fe) dissolution or $FeCO_3$ film formation in $CO_{2(aq)}$ solutions. Four EIS studies reporting surface film formation in carbon steel $CO_2$ corrosion are discussed below, and will be followed by a summary of the findings.

One of the early EIS studies (complemented by *ex-situ* XRD, SEM, FTIR) used to investigate steel undergoing $CO_{2(aq)}$ corrosion in conditions typical of oil wells was conducted by (Kinsella, Tan & Bailey, 1998). The main objective of this study was to determine the suitability of EIS. The impedance spectra of steel samples pre-treated in 3 wt. % $NaCl_{(aq)}$ solutions at 30 and 70 °C, $CO_2$ partial pressure of 101.325 and 689.5 kPa for varying times (up to 120 hours) was measured in another 3 wt. % $NaCl_{(aq)}$ solution, at the same temperature, but different $pCO_2$ of 101.1325 kPa. The authors reported a single, depressed semicircle based on the Nyquist plot and the Bode plot at the beginning of the immersion period indicative of a freely corroding surface. The authors seemingly interpreted the appearance of a second high frequency (*ca.* $10^{1.5}$ -$10^{3.5}$ Hz) time constant, which appeared after 24 hours to

be indicative of the presence of a protective film and extracted the resistance of the film and charge transfer by fitting the measured data with circuit **b** shown in **Figure 2-26**. The authors found that the electrode surface area to volume (*A*/*V*) ratio was the main factor determining the rate of film formation, and was favoured by high *A*/*V*. The authors demonstrated that films consisting of small crystals, which were formed at high temperature (70 °C) and pressure (689.5 kPa), were highly protective $FeCO_3$ based on *ex-situ* images correlated with the total extracted resistances. The authors concluded that EIS was particularly advantageous in studying $CO_2$ corrosion surface films given the speed of the technique and its ability to provide further insight to the mechanisms of film formation presumably as compared to common DC measurements which only enable corrosion rate determination. Despite the utility of this research, some deficiencies should be mentioned. Firstly, the simulated EIS data was not presented, nor were $\chi^2$ and Bode impedance modulus plots, all of which are crucial to validating the presented resistance values. Additionally, the OCP data and pH were not presented, which would have revealed further insight to the composition of the film.

Another EIS study (Farelas *et al*., 2010) investigated the evolution of dissolution processes exhibited by carbon steel (C1018) when exposed to $CO_2$ saturated 3 wt. % $NaCl_{(aq)}$ solution at 80 °C, pH 6 (adjusted through the introduction of $NaHCO_3$), under turbulent flow conditions. From this study, the authors concluded that surface film formation occurs *via* three stages. The impedance spectra (presumably measured at OCP, though not explicitly stated) were regularly recorded for 158 hours. The first stage (0 -15 hours) was proposed to involve the active dissolution of the ferrite phase, that was said to be enhanced by galvanic coupling with cementite upon which $H_2$ evolution was promoted, along with the adsorption of FeOH. The Nyquist plot, which took the shape of a single semicircle and included an inductive feature, was surprisingly interpreted by the authors to indicate the presence of two capacitive loops. The measured data was thus modelled using a fairly complicated circuit (**Figure 2-25**), and appeared to be a simplified Randles circuit augmented to include an inductive component (*L*) and an inductive resistance ($R_2$). The second stage (20 – 60 hours) was proposed to be the continued dissolution of ferrite, resulting in the revelation of a porous cementite layer and the EIS data was modelled using circuit **b** (**Figure 2-26**), where the outer RC loop represented

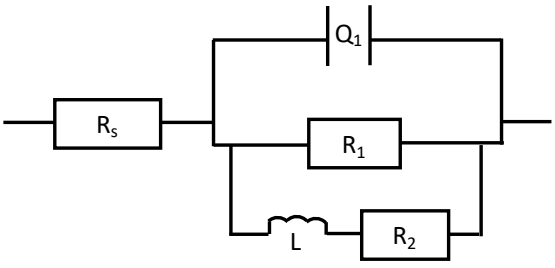



**Figure 2-25:** Equivalent circuit used to a freely corroding steel with adsorbed species (Farelas *et al*., 2010).

resistance ($R_1$) and the non-ideal capacitance ($Q_1$) of the cementite layer, and the inner RC loop of the charge transfer resistance ($R_2$) and the non-ideal double layer capacitance ($Q_2$). This model was more reasonable since two separate processes were observable in the Nyquist and Bode phase angle plots. In the third and final stage, continuous $FeCO_3$ precipitation within the porous cementite layer was said to have occurred, resulting in an observable increase in the presented impedance modulus Bode plots, and the data was again modelled using circuit **b** (**Figure 2-26**); for this model $Q_1$ and $R_1$ were representative of the non-ideal capacitance and resistance of mixed $Fe_3C$, $FeCO_3$ layer. Interestingly, the 'pore resistance', which was a measure of the hindered diffusion of species to and from the electrode due to the porous cementite layer, was the dominant resistance during stage one and two, but in the final stage, the charge transfer resistance was notably higher. The authors attributed the film protectiveness to the decrease in charge transfer area achieved through its presence. This is consistent with the presented resistances, where the charge transfer resistance was dominant when the film formed, but the authors did not explicitly comment on this. Although this study did provide some insight to the surface film formation process during $CO_2$ corrosion, some shortcomings need to be mentioned. Firstly, $\chi^2$ values were not presented in this study, so it is unclear if the chosen circuits modelled the measure spectra well, and also if the extracted resistance values were representative of the surface processes. The authors also did not conduct *ex-situ* characterisation to confirm the identity of the surface film, nor was the OCP data presented, which may have provided some insight to product phases at the electrode surface.

In a comparative study, (Burkle, 2017) investigated the growth and development of $FeCO_3$ films on carbon steel (UNS K03014) in 3.5 wt. % $NaCl_{(aq)}$ solutions at 80 °C, saturated with $CO_2$ for variable immersion periods. In this study two repetitions of each experiment were included and OCP data was presented along with the measured impedance spectra. However, EIS data was not fitted to any equivalent circuits to provide further qualitative or quantitative insight to the surface processes. In contrast to (Farelas *et al*., 2010), the initial impedance spectra consisted of a single depressed semicircle with no inductive loop, indicative of a freely corroding surface with negligible adsorption of species. The diameter of the semicircle decreased with time in the first four hours but then began increasing, indicating higher surface resistance and interpreted by the author to be onset of $FeCO_3$ formation; the OCP minimally increased during this time and was on average *ca*. -0.585 V (*vs*. $SHE_{25\ °C}$). *Ex-situ* imaging after 24 hours demonstrated the presence of a crystalline film, which was confirmed

to be $FeCO_3$ by XRD. After 60 hours, in one of the experimental runs, the OCP increased to *ca*. -0.330 V, but stayed relatively constant in the other run at *ca*. -0.526 V (*vs*. $SHE_{25\,°C}$). The change in OCP coincided with the appearance of a diffusion tail in the impedance spectra, whilst the spectra in the sample that did not undergo a significant change in OCP demonstrated a second capacitive loop, with an increasing diameter. Unfortunately, the authors did not present Bode plots, which may have revealed if other surface processes had developed and would have allowed comparison of the evolving overall magnitude of the impedance. *Ex-situ* imaging (SEM) revealed that the film on the electrode with the shift in OCP had sizeable gaps *ca*. 20 μm size, where the underlying substrate seemed visible and cracked, whilst the film on the electrode that did not undergo an OCP change had an apparently densely packed $FeCO_3$ film. The same observation was made for the 106 hour and 144 hour immersion times. Each time the OCP shift occurred and a diffusion tail emerged, the film appeared degraded, whereas in the repeats of the same experiment when the OCP stayed stable, the film was densely packed. The authors came to the surprising conclusion that the densely packed $FeCO_3$ film observed on some samples was not responsible for its protection, which was in direct contrast to (Farelas *et al*., 2010), but instead attributed to the cracked underlying layer and described it as 'an ultraprotective crystalline $FeCO_3$ bilayer'. To the authors point, when the OCP increased, the corrosion rate (determined *via* LPR) decreased more significantly (to 0.02 mm $yr^{-1}$ from 0.07 mm $yr^{-1}$) however, the sample appeared to have been undergoing non-uniform dissolution, in which case corrosion rate would not be an appropriate measure of protection. The authors decisively stated the protectiveness was correlated with the rise in OCP and said the shift in OCP was due to the hindered diffusion of $Fe^{2+}$ away from the surface resulting in suppression of the anodic dissolution reaction. The authors mentioned the possibility of $Fe_3O_4$ or $Fe_2(OH)_2CO_3$ formation but said there was no evidence (from XRD) of such phases and did not acknowledge the possibility of the other phases being amorphous, or too dispersed, and hence undetectable by XRD. In a later study, where (Burkle *et al*., 2017) utilised *in-situ* XRD to track the formation of $FeCO_3$, the bilayer was not observable, instead a packed $FeCO_3$ film was observed and the reported corrosion rate at pH 6.8 was 0.5 mm $yr^{-1}$. The corrosion rate appeared to be correlated with the surface coverage of $FeCO_3$. The OCP data was not reported in this study. Based on these observations, it is difficult to completely agree with the notion that the protectiveness of the $FeCO_3$ film in the earlier study (Burkle, 2017) was attributed to an underlying disrupted bilayer.

A more recent and comprehensive EIS study (Motte *et al*., 2020) examined the impact of small changes in pH (6 and 6.6) on the formation of a surface film on steel (C1018) in $CO_2$ corrosion at 80 °C over an 11 day (264 hour) period. The authors presented and interpreted OCP measurements with the aid of *ex-situ* characterisation including SEM, XRD and electron backscatter diffraction (EBSD) analysis, and thus provided further insight to the possible composition of the film. By contrast to the observations made by (Farelas *et al*., 2010) and consistent with (Burkle, 2017), the corrosion process in both solutions began as a single capacitive loop with no inductive feature and was therefore modelled with circuit **a** (**Figure 2-26**) for the first four days. In the pH 6.6 electrolyte, a second higher frequency time constant which overlapped with the first time constant, and a lower frequency (finite) diffusion tail both appeared after day five. A similar observation was made in the pH 6 solution. The authors believe that the presence of these additional features signalled the onset of a diffusion limited process, interpreted as indicative of the presence of a surface film. The EIS data was modelled with circuit **c** (**Figure 2-26**), which is a modified version of circuit **b**; finite length Warburg element ($W_d$) was used to simulate the diffusion process. The authors proposed that the presence of the diffusion feature in the pH 6.6 solution was related to the sharp increase of the OCP from *ca*. -0.576 V to -0.420 V (*vs*. $SHE_{25\,°C}$), but the OCP change occurred on day nine, three days after the diffusion feature appeared. Therefore it is difficult to agree with the proposition that the diffusion feature is linked to the increased OCP. The authors, like (Burkle, 2017) concluded that the OCP change observed at the higher pH, was indicative of the attainment of pseudo-passivation, and was as a result of a decrease in the anodic reaction rate relative to the cathodic reaction rate, due to a restriction of $Fe^{2+}$ away from the surface, but did not give an explanation for the sharp nature of the change, which may have been more gradual if the explanation provided for the OCP change was accurate. The authors also categorically stated that the rise in OCP was not as a result of the formation of other product species, therefore agreeing with (Burkle, 2017). However, *ex-situ* cross-section surface imaging showed the development of a different product species in very small regions, detected by EBSD to be $Fe_3O_4$ at the interface between the electrode surface and the predominant $FeCO_3$ product layer. Since this was detected on films produced in both electrolytes (pH 6 and 6.6), and the OCP change was only noted in the pH 6.6 solution, the authors concluded that the OCP change was not due the presence of this species. Given the minimal quantities, it is possible that there was slightly more $Fe_3O_4$ on the pH 6.6 sample, which resulted in the observable OCP change. The authors also stated that the resistance

provided by the surface film was not necessarily due to a specific product but instead stated that the resistance was due the physical barrier it provided between the electrolyte and the substrate.

It should also be noted that other EIS studies have proposed the presence of a duplex film structure, consisting of a mixed inner $Fe_3C$-$FeCO_3$ film and outer $FeCO_3$ film (Islam *et al*., 2021), a thicker inner film $FeCO_3$ layer and thinner outer $FeCO_3$ layer (Gao, Pang & Gao, 2011), an inner planar $FeCO_3$ layer and outer cubic $FeCO_3$ layer (Li *et al*., 2019), and have been modelled with circuit **d** (**Figure 2-26**).

To summarise, EIS was demonstrated to provide insight to possible mechanisms of surface film formation, as well as structure and composition on carbon steel in $CO_{2(aq)}$ environments. The onset of film formation generally seems to result in the presence of an additional high frequency time constant (Kinsella, Tan & Bailey, 1998; Motte *et al*., 2020) and a low frequency diffusion feature (Motte *et al*., 2020). Higher pH, temperature and pressure appear to improve product layer resistance. The film composition is not completely agreed upon nor is the exact species responsible for the protectiveness, and the relationship between OCP and onset of passivation or pseudo passivation remains debatable.

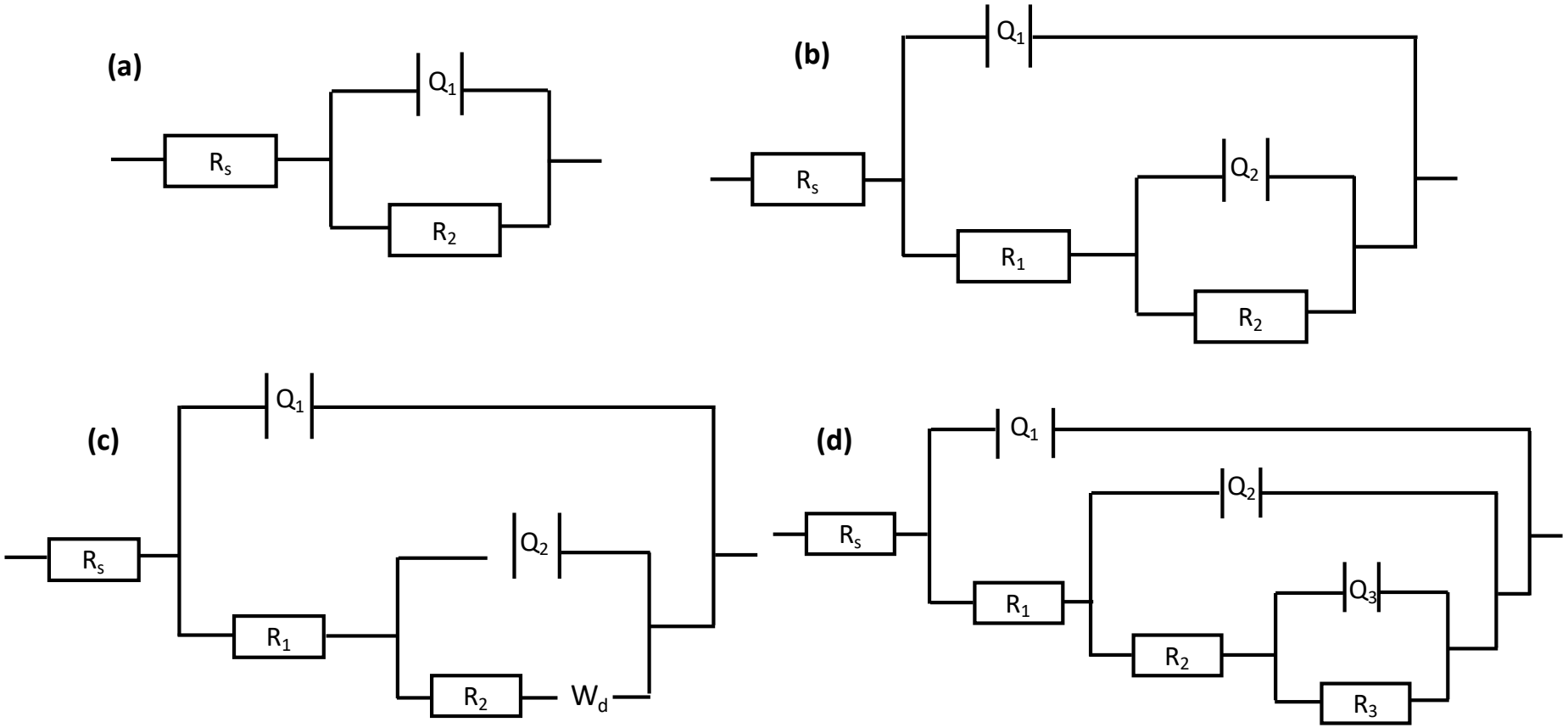



**Figure 2-26**: Equivalent circuits used to model carbon steel corrosion in $CO_{2(aq)}$ solutions.

## 2.5 Corrosion in post combustion carbon capture plants

Amines, as mentioned previously, are the solvents used in PCCC plants. These are organic compounds derived from ammonia ($NH_3$) by replacement of one or more H-atom(s) with organic substituents (Eller *et al*., 2000). Amines are then classified based on the number of H-atoms which are replaced by organic groups. Primary amines (1 °) are formed by the replacement of one H-atom. Secondary amines (2 °) are formed by the replacement of two H-atoms. Tertiary amines (3 °) are formed by the replacement of all three H-atoms. Studies investigating the corrosivity of several different amine types have been conducted. However, the work herein was primarily focused on two amines (monoethanolamine and methyldiethanolamine); as such, the literature pertaining to either of these amines will be discussed. Although amines are not intrinsically corrosive, absorption of $CO_2$ lowers the solution pH and increases the solution conductivity, which are thought to be responsible for the observed corrosivity of these solvents towards steel substrates. The mechanism by which amines capture $CO_2$ varies as a function of the amine structure. The speciation of $CO_2$ saturated amines will be discussed in Section 2.5.1.

### 2.5.1 Amine – $CO_2$ speciation

**Monoethanolamine**

Monoethanolamine (MEA, $OHC_2H_2NH_2$) (**Figure 2-27**) is considered the benchmark carbon capture solvent and is classed as a 1 ° amine. During $CO_2$ absorption, two moles of MEA react with one mole of $CO_2$, which results in the formation of one mole of carbamate ($OHC_2H_4NHCO_2^-$) and one mole of protonated amine ($OHC_2H_4NH_3^+$) as shown by Equations **2-138** - **2-139**. The maximum theoretical absorption ratio is therefore 0.5 $mol_{CO2}$ $mol_{MEA}^{-1}$. A single step and two step reaction mechanism have been proposed; the two step mechanism shown by Equations **2-138** - **2-139** is referred to as the zwitterion mechanism. It should be noted that the amine is in an aqueous solution so $CO_2$ absorption by $H_2O$ also occurs, as described by Equations **2-54** - **2-57**. MEA - $CO_2$ speciation in $H_2O$ is shown in **Figure 2-28.**

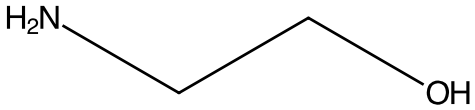



**Figure 2-27**: Chemical structure of MEA.

$$OHC_2H_4NH_{2(aq)} + CO_{2(aq)} \leftrightarrow OHC_2H_2NH_4^+COO^-_{(aq)} \quad \textbf{2-138}$$

$$OHC_2H_4NH_{2(aq)} + OHC_2H_4NH_2^+COO^-_{(aq)} \leftrightarrow OHC_2H_4NH_3^+{}_{(aq)} + OHC_2H_4NHCOO^-_{(aq)} \quad \textbf{2-139}$$

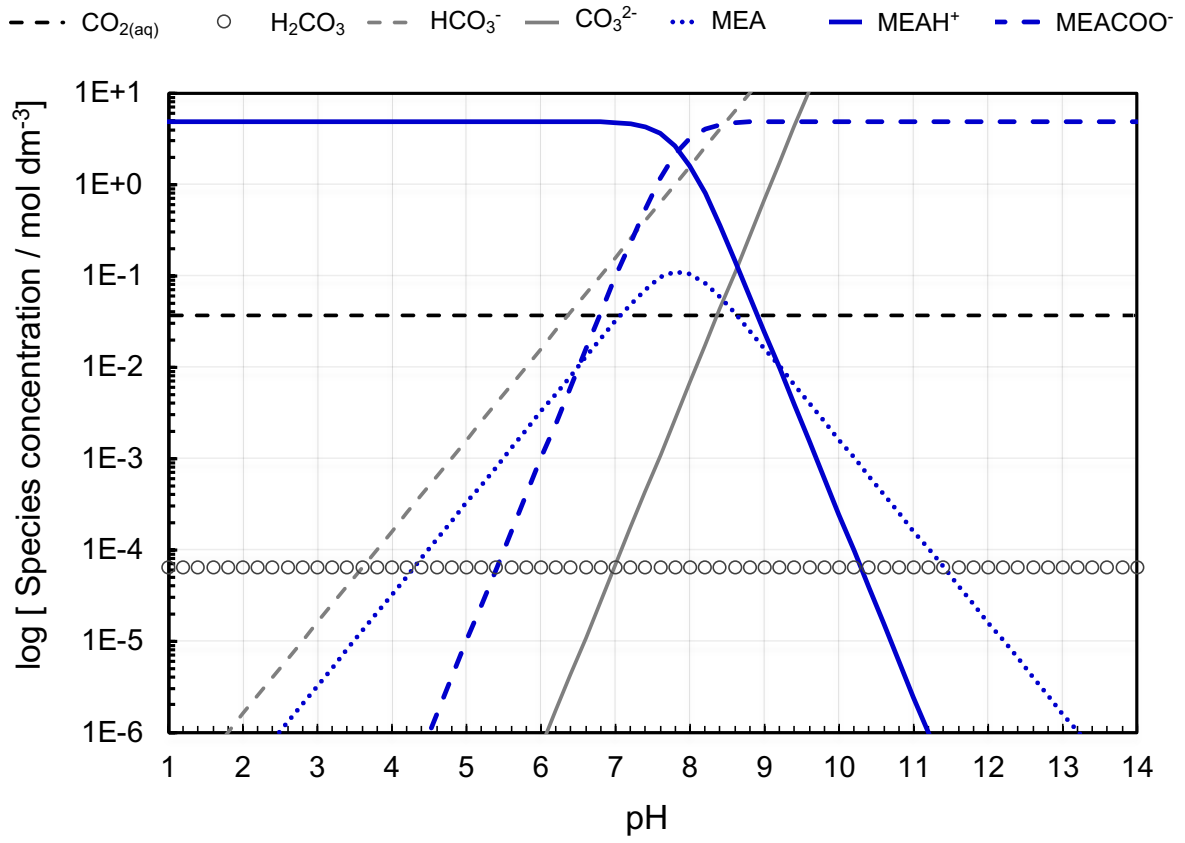



**Figure 2-28:** Speciation of MEA and $CO_2$ in $H_2O$ at 298 K, $pCO_2$ 1 atm. Calculations were based on Gibbs energy of formation data published in (Bard *et* al., 1985*)* and in (Fernandes *et al*., 2012).

**Methyldiethanolamine**

Methyldiethanolamine (MDEA, $CH_3N(C_2H_4OH)_2$) (**Figure 2-29**), a 3 ° amine, is an alternative to MEA (Zhang & Chen, 2011) and has been extensively used in NGP. By contrast to 1 ° (and 2 °) amines, $CO_2$ does not directly react with MDEA. Instead $CO_2$ hydrolysis must first occur (Equations **2-54** - **2-56**) before capture can be initiated. This is as a consequence of its chemical structure (**Figure 2-29**), since the N-atom in MDEA is not bonded to H-atoms. The overall reaction is shown by Equation **2-140**. Accordingly, the maximum theoretical $CO_2$ absorption ratio is 1 $mol_{CO2}$ $mol_{MDEA}^{-1}$. In addition to equilibrium reactions shown in **2-54** - **2-57**, the equilibrium reaction shown in Equation **2-141** is also present in solution. MDEA - $CO_2$ speciation in $H_2O$ is shown in **Figure 2-30.**

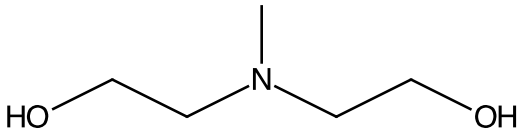



**Figure 2-29:** Chemical structure of MDEA.

$$CH_3N(C_2H_4OH)_{2(aq)} + H_2O_{(l)} + CO_{2(aq)} \leftrightarrow CH_3N(C_2H_4OH)_2H^+_{(aq)} + HCO^-_{3(aq)} \quad \textbf{2-140}$$

$$CH_3N(C_2H_4OH)_{2(aq)} + H^+_{(aq)} \leftrightarrow CH_3N(C_2H_4OH)_2H^+_{(aq)} \quad \textbf{2-141}$$

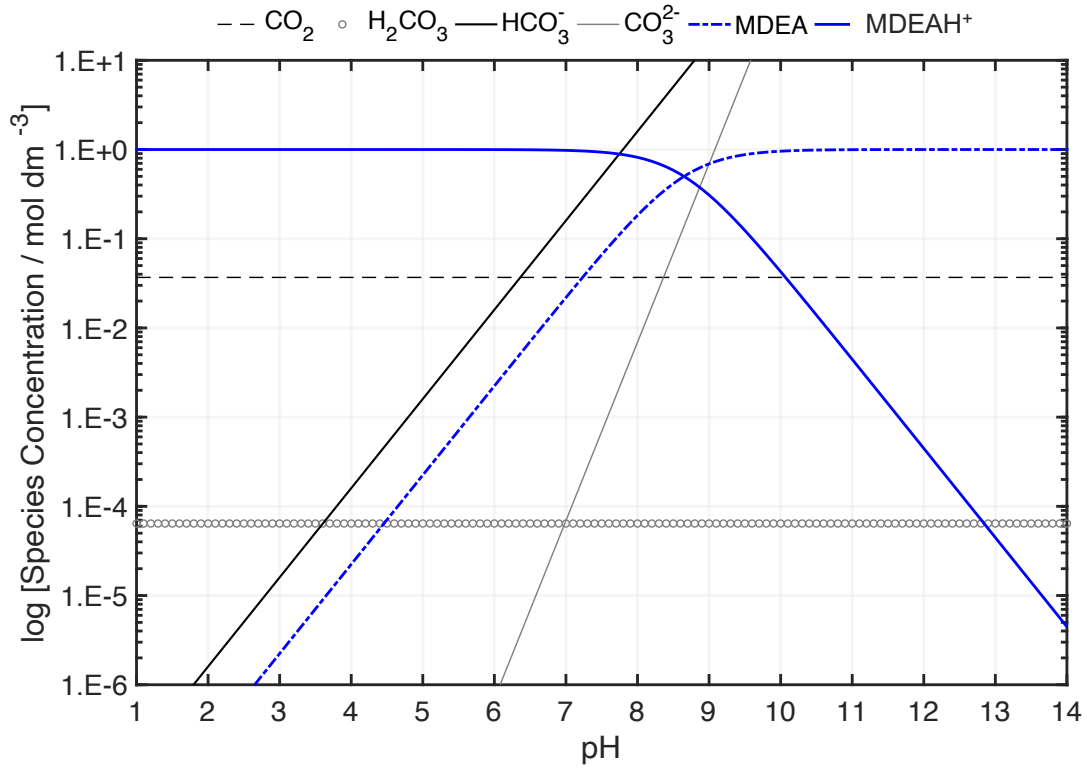



**Figure 2-30:** Speciation of MDEA and $CO_2$ in $H_2O$ at 298 K, $pCO_2$ 1 atm. Calculations were based on Gibbs energy of formation data published in (Bard *et al*., 1985) and the equilibrium constant for Equation **2-141** published in (Fernandes *et al*., 2012).

## 2.5.2 Corrosion behaviour of steel in amine – $CO_2$

One of the earliest corrosion studies on $CO_2$ loaded amine$_{(aq)}$ solvents conducted by (Tomoe, Shimizu & Kaneta, 1996) utilised a range experimental and analytical techniques, far more than is usually used, to provide some crucial insights to corrosion of carbon steel in $CO_2$ saturated amine$_{(aq)}$ solutions. The authors conducted both electrochemical (LPR) and weight loss experiments to determine the corrosion rate exhibited by carbon steel in different amine solutions (1 °: MEA and DGA; as well as 3 °: MDEA and TEA), *ex-situ* surface analyses (SEM, XRD) to identify surface films produced and investigated the solution composition ($^{13}$C NMR). Experiments were conducted at 135 °C. The authors reported that corrosion rates were suppressed by the formation of $FeCO_3$ in dilute amine$_{(aq)}$ solutions (0.01 – 2 M), regardless of amine type, similar to that observed in $CO_{2(aq)}$ solutions. At higher concentrations (3 – 6 M), divergent behaviour was said to have been exhibited by carbon

steel exposed to the 1 ° and 3 ° amines. In the 1 ° $amine_{(aq)}$ (MEA, DGA), corrosion rate was reported to increase with amine concentration and $Fe_2(OH)_2CO_3$ was detected, whilst in the 3 ° $amine_{(aq)}$ (TEA, MDEA), the corrosion rate was said to stay low and $FeCO_3$ was the only detected species. Additionally the authors detected dissolved $CO_2$ in the form of $HCO_3^-$ in the 1 ° (DGA) solution at low concentrations of 10 wt. %, which shifted predominantly to carbamate as concentration increased. The authors stated that at the same $amine_{(aq)}$ concentration that the dominant species became carbamate, there was an observed abrupt increase in corrosion rate and product morphology of carbon steel in DGA; this was said to be consistent with experiments conducted with MEA. The authors therefore concluded that the $CO_2$ absorption process and the dominant $CO_2$ species present in solution both play important roles in corrosion of carbon steel, as well as the composition, morphology and protectiveness of the surface film(s) formed.

#### 2.5.2.1 Corrosion behaviour of steel in MEA – $CO_2$

Soon after Tomoe's work was published, one particular group made corrosion behaviour of $MEA_{(aq)}$ (along with other amines) in PCCC its primary focus (Veawab *et al*. (1996 – 2017)). The following is a chronological account of the major findings of their work, with comparison to other literature. Literature on the influential factors affecting the corrosive nature of $MEA_{(aq)}$ will then follow and will include the significant contributions made by other groups.

Using weight loss tests (Veawab, Tontiwachwuthikul & Bhole, 1997) investigated the impact of MEA (and AMP) concentration (1, 2.5, 5, 7 M) and $O_2$ on the corrosion rate of 'plain' carbon steel (*C*: 0.15 %) saturated with 52 % $CO_2$ and 48 % air, and pure $CO_2$. The impact of $O_2$ will be discussed subsequently. Corrosion rate was reported to increase (by up to a factor of 5) with increased [MEA], consistent with findings reported by (Kittel *et al*., 2012), and were between 1.6 and 3 times higher than that measured in AMP solutions of the same concentration. The authors proposed that the higher corrosivity of MEA was a result of the higher expected $[HCO_3^-]$ but did not provide an estimate of the relative concentrations, nor was the pH reported, which would have provided some insight to the $[HCO_3^-]$. Subsequently, in another study (Veawab, Tontiwachwuthikul & Chakma, 1999) again determined the corrosion rate of carbon steel (*C*: 0.2 %) as a function of amine type (MEA, along with DEA, AMP, MDEA), concentration (1 – 5 M), temperature, $CO_2$ loading, $O_2$ content, but instead using potentiodynamic polarisation ($E_{CORR}$ ± *ca*. 250 mV, scan rate = 0.167 mV $s^{-1}$). The

effect of temperature, $CO_2$ loading and $O_2$ content will be considered in subsequent sections. At 80 °C and 0.2 $mol_{CO2}$ $mol_{amine}^{-1}$ loading, the authors reported increased corrosion rate with MEA concentration, which was consistent with the behaviour observed in saturated solutions (Veawab, Tontiwachwuthikul & Bhole, 1997). Interestingly, there appeared to be little difference in the cathodic current densities measured at different solution concentrations, but an observable change in anodic Fe dissolution currents with concentration, but the authors did not comment on this. The authors also reported higher anodic and cathodic currents in $MEA_{(aq)}$ than in other amine solutions. The authors concluded that amine type has a significant impact on corrosion of carbon steel and MEA was the most corrosive and MDEA the least. This trend was corroborated by later findings (Gunasekaran, Veawab & Aroonwilas, 2013; Yu, Campbell & Williams, 2016) and is also consistent with observations made in NGP (Kohl & Nielsen, 1997b).

Subsequent work attempted to identify the key reactions involved in the corrosion of carbon steel in MEA–$CO_{2(aq)}$ (Veawab & Aroonwilas, 2002) by comparing modelled polarisation curves to experimentally measured data. Three hydrogen evolution reactions involving either $H^+$, $H_2O$ and $HCO_3^-$ were considered. Seven chemical reactions including MEA protonation, $HCO_3^-$, $CO_3^{2-}$, $Fe(OH)_2$ and $FeCO_3$ formation were also included. Development of the model comprised of two fundamental steps; determination of solution speciation using a VLE – NRTL model and the chemical reactions, and then simulation of anodic Fe dissolution and cathodic hydrogen evolution polarisation curves using Equation **2-40** and **2-41** respectively. Seven current-potential curves were generated, of which three involved individual proton donors ($H^+$, $H_2O$, $HCO_3^-$), three involved combined pairs of the three proton donors, and the final scenario involved all three proton donors. The generated curves were then compared to previously obtained experimental data (carbon steel in 2 M, 0.4 $mol_{CO2}$ $mol_{MEA}^{-1}$ 80 °C) (Veawab, Tontiwachwuthikul & Chakma, 1999). The author reported that a very good match for both the anodic and cathodic branches was obtained with $H_2O$ but an even better one was observed with the combination $H_2O$ and $HCO_3^-$. Crucially, the experimental current-potential curves used in the selection of responsible proton donors may have been under mixed control, whilst in the modelled polarisation curves the currents were activation controlled, so it is possible that the oxidising agents were misassigned. More importantly, the simulated curves were for Fe whereas the experimental data was collected using a carbon steel electrode; the presence of impurities (*i.e.* as a result of alloying), like in the case of carbon steel, has been demonstrated to significantly alter HER kinetics (Bockris & Drazic, 1962). By contrast,

(Labiyi, 2016), considered only one scenario where the principal cathodic reactions proposed were HER involving $H^+$ and direct reduction of $H_2O$, as well as reduction of $O_2$ (Equation **2-142**).

$$2H_2O + O_2 + 4e^- \leftrightarrow 4OH^- \qquad \textbf{2-142}$$

Unlike (Veawab, Tontiwachwuthikul & Chakma, 1999), the simulated current-overpotential plots by (Labiyi, 2016) were formulated based on the extended Butler-Volmer equation (Equation **2-52**) with the mass transport limited current densities ($j_L$) experimentally determined by application of the Levich equation (Equation **2-143**, where *B* is a constant) to data collected from RDE experiments.

$$j_L = B\,\omega^{\frac{1}{2}} \qquad \textbf{2-143}$$

Labiyi's model was tested against data collected with an Fe electrode in $MEA_{(aq)}$ solutions at a range of electrode rotations (240 – 1500 RPM), $CO_2$ loading (0.2 - 0.6 $mol_{CO2}$ $mol_{MEA}^{-}$), amine concentrations (20 - 50 wt. %) and temperatures (25 – 80 °C) (Labiyi, 2016). Since the simulated polarisation curves appeared to closely match the experimentally obtained data, the author concluded that $H^+$, $H_2O$ and $O_2$ were responsible for the cathodic reactions and stated that $HCO_3^-$ did not undergo direct reduction but instead was a source of $H^+$ ions, similar to that reported by (Kahyarian & Nešić, 2019). The author did, however state that the corrosion rates predicted by the model were slightly higher than those measured under all conditions; it is possible that the inclusion of $O_2$ was responsible for this.

An extensive study conducted by (Soosaiprakasam & Veawab, 2008) investigated the impact of $CO_2$ loading (0.2 and 0.55 $mol_{CO2}$ $mol_{MEA}^{-1}$), solution velocity (0 − 2000 RPM), temperature (40 − 80 °C), $O_2$ content (0 – 0.1 bar) on the corrosivity of highly concentrated $MEA_{(aq)}$ solutions (5, 7 and 9 M) towards carbon steel (C1080). The objective of this study was also to provide a mechanism for corrosion of steel in $MEA_{(aq)}$. The corrosion rate was calculated from the corrosion current ($i_{CORR}$), which was determined from the intersection of the extrapolated linear regions of the anodic and cathodic branches (± 250 mV *vs.* $E_{CORR}$) recorded during cyclic polarisation experiments (0.166 mV $s^{-1}$). Agreeing with previous work, the corrosion rate was observed to increase with higher $CO_2$ loading, temperature (Veawab, Tontiwachwuthikul & Chakma, 1999) and $O_2$ content (Veawab, Tontiwachwuthikul & Bhole, 1997; Sun *et al.*, 2011); the impact of these factors on the corrosion of steel in $MEA_{(aq)}$ solutions will be discussed further in subsequent sections. The authors also reported increased corrosion rate with increased MEA concentration, as was

demonstrated for lower concentration ranges (Veawab, Tontiwachwuthikul & Chakma, 1999). Using a rotating disc electrode, the effect of solution velocity at 80 °C was examined by comparing generated polarisation plots using rotating disc electrodes of 2000 and 1000 RPM to results obtained using stationary electrodes. The authors reported as the rotation rate increased from 1000 to 2000 RPM, the corrosion rate increased by 18 % and stated that this was due to enhanced mass transport of species towards and away from the surface, which altered the Tafel slopes. The presented polarisation curve did in fact demonstrate increased cathodic current densities but little change was apparent on the anodic dissolution branch. The authors did not acknowledge that the cathodic reaction was under mass transport control rather than activation control. This provided evidence that Labiyi's model more accurately selected the species involved in the cathodic reactions; however, at these higher MEA concentrations, solution viscosities would be higher and hence mass transport limitations may be more pronounced. Interestingly, rotation (2000 RPM) significantly increased the anodic currents recorded in the passive region (**Figure 2-31**) where it increased the current density by an order of magnitude, as compared to that recorded at 0 RPM. These were contrary to observations made from voltammograms recorded on Fe in $HCO_3^-$/ $CO_3^{2-}$ (pH 8.9, 75 °C) (Valentini *et al*., 1985) (**Figure 2-14**) where the current density within the passive region was in fact lower with the rotating disc electrode. Furthermore, (Valentini *et al*., 1985) demonstrated that when the electrode was rotated the oxidative current at *ca*. -0.4 V *vs*. AgCl | Ag (-0.2 V *vs*. NHE) was not recorded, unlike that shown by (Soosaiprakasam & Veawab, 2008) (**Figure 2-31**). This possibly suggests a direct, though more likely indirect, effect of MEA on either the $FeCO_3$ formation or subsequent oxidation reactions. Another crucial factor, which was not previously investigated in corrosion studies was the effect of pre-corrosion; aiming to understand the corrosion of carbon steel equipment after a period of usage rather than fresh carbon steel samples, which would represent newly installed equipment. Carbon steel samples were pre-corroded for 7, 14 and 28 days in 5 M $MEA_{(aq)}$ at 80 °C 0.2 $mol_{CO2}$ $mol_{MEA}^{-1}$, 10.13 kPa (0.1 bar) $O_2$ and the corrosion rate was subsequently determined in the same solution. The corrosion rate of all pre-corroded samples were up to an order of magnitude higher than the fresh carbon steel samples with corrosion rate increasing with pre-corrosion duration.

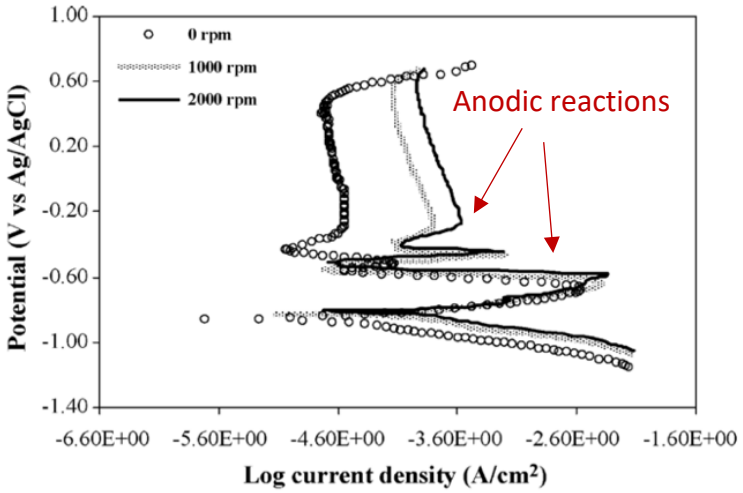



**Figure 2-31:** Effect of solution velocity on corrosion of carbon steel in 5 M $MEA_{(aq)}$ - 0.2 $mol_{CO2}$ $mol_{MEA}^{-1}$ (Soosaiprakasam & Veawab, 2008). Image reproduced with permission of the rights holder, Elsevier.

Although this study was extensive, there are some shortcomings that need to be mentioned, which also apply to the other work reported by this group. Firstly, the authors stated that solutions with loadings of 0.2 $mol_{CO2}$ $mol_{MEA}^{-1}$ were prepared by saturating a $MEA_{(aq)}$ solution with $CO_2$ then mixing this solution with an unsaturated one to achieve the required saturation. The authors then heated the solution to the appropriate temperature (40 or 80 °C); the $CO_2$ loading of a sample of the heated solutions was said to be verified through titration at the beginning and end of the experiment. The authors however did not confirm or comment on the solution pH nor $CO_2$ loading at the end of each experiment. It is known that $CO_2$ desorption occurs when $MEA_{(aq)}$ is heated 80 – 120 °C, and that $CO_2$ solubility decreases as temperature increases. It is thus difficult to believe that the solution remained at the reported loading for the duration of the experiment (estimated to be at least *ca*. 3.7 hours based on the scan window and scan rate). Secondly the initiation potential for the scan was not stated, nor was the scan stopped, electrode re-polished between the anodic and cathodic scans used for Tafel slope determination; it is likely that local pH changes (if HER was first recorded), or surface changes (due to product formation if anodic scan was first recorded), would alter the electrode reaction and/ or kinetics; the reported corrosion rates and Tafel slopes would likely not be representative of the intended conditions. Thirdly, the recorded cathodic currents were shown to increase when the electrode was rotated, indicating that the current was mass transfer limited; determining corrosion currents through Tafel analysis will therefore likely be misleading. The authors also did not provide a mechanism for anodic Fe dissolution, nor for the HER, likely because the Tafel slopes reported (*e.g.* $\beta_a$ = 73, 93, 88, 110, $\beta_c$ = 107, 102,

113) were quite different from slopes indicative of specific reaction mechanisms, which was the aim of this study.

## Effect of temperature

Most work investigating the impact of temperature on corrosion rate of carbon steel in $CO_2$ loaded $MEA_{(aq)}$ involved temperatures up to 80 °C (Veawab, Tontiwachwuthikul & Bhole, 1997; Veawab, Tontiwachwuthikul & Chakma, 1999; Veawab & Aroonwilas, 2002; Soosaiprakasam & Veawab, 2008; Sun *et al*., 2011; Kittel *et al*., 2012; Gunasekaran, Veawab & Aroonwilas, 2013); there is general agreement that the corrosion rate increases with temperature due to enhanced anodic Fe dissolution kinetics.

(Kittel *et al*., 2012) demonstrated that the uniform corrosion rate (*via* Tafel extrapolation of anodic and cathodic branches attained from potentiodynamic polarisation scan $\eta$ of -250 mV to 1000 mV, scan rate 0.167 mV $s^{-1}$ and weight loss) of carbon steel (*C*: 0.39 %) exhibited an Arrhenius relationship with temperature for each $CO_2$ loading (0, 0.25, 0.5 $mol_{CO2}$ $mol_{MEA}^{-1}$) for 30 – 80 °C. This was also reported in (Gunasekaran, Veawab & Aroonwilas, 2013). The authors (Kittel *et al*., 2012) hypothesised that this relationship can be extrapolated to predict the corrosion rate in the high temperature units found in the PCCC plant. They did not however consider the possibility of surface film formation, either creating a protective barrier and suppressing corrosion or the possibility of localised breakdown of the film, hence requiring other corrosion metrics. It is known that $FeCO_3$ precipitation is promoted by increased temperature. Conversely, concentration of dissolved $CO_2$ is thermodynamically predicted to be higher at lower temperatures, thus suggesting that higher temperatures would be less conducive to precipitation from the view of dissolved $CO_2$. Baring these factors in mind, the observed trend of corrosivity in the low temperature range (30 – 80 °C) should not be extrapolated to predict the corrosion behaviour of carbon steel in high temperature units (*i.e*. up to 120 °C). (Sun *et al*., 2011) conducted similar experiments to that described for (Kittel *et al*., 2012) but considered only 40 and 80 °C; importantly the authors presented scans that extended to $O_2$ evolution at *ca*. +1 V *vs*. SCE (*ca*. +1.2 V *vs*. $SHE_{25\,°C}$). The authors demonstrated that currents measured on a A106 carbon steel electrode for a $CO_2$ loading of 0.2 $mol_{CO2}$ $mol_{MEA}^{-1}$ within the entire scan were higher at 80 °C than at 40 °C. From the presented data it could also be observed that an additional anodic reaction, immediately following the highest anodic current density peak, had occurred. The authors stated that the current within the passive region, which they outlined to be -0.4 to -0.6 V *vs*. SCE, is a

measure of the resistance of a surface film formed on the electrode, and deduced that the film at 40 °C was more resistive. The authors did not however suggest an identity of the film, nor a formation mechanism. The authors also demonstrated that the current started rising at *ca*. +0.2 V *vs*. SCE (+0.39 V *vs*. $SHE_{25\,°C}$), before $O_2$ evolution is expected to occur, but did not comment on this. (Soosaiprakasam & Veawab, 2008) also investigated the impact of temperature on the electrochemical behaviour of carbon steel C1018 at the same temperatures, loadings, and similar scan window as (Sun *et al*., 2011). Interestingly, within the passive region the current recorded by (Soosaiprakasam & Veawab, 2008) at 80 °C was *ca*. one order of magnitude higher than that at 40 °C and an additional anodic reaction seemed to have occurred at *ca*. -0.2 V *vs*. SCE (-0.01 V *vs*. SHE). The authors proposed based on a potential-pH diagram of carbon steel–$CO_2$–$H_2O$ that within the passive region γ-$Fe_2O_3$ may have formed; this is also consistent with **Figure 2-12** . In direct contrast to (Sun *et al*., 2011), (Soosaiprakasam & Veawab, 2008) came to the conclusion that the film formed at 80 °C was more stable than that at 40 °C.

Only a few studies were conducted at elevated temperatures of up to 120 °C, representative of the stripper (Sadeek, Williams & Campbell, 2018; Yu *et al*., 2017; Yu, Campbell & Williams, 2016; Zheng *et al*., 2016b, 2016a).

The impact of product layers on the corrosion rate of carbon steel (A106) in $CO_2$ loaded 5 M $MEA_{(aq)}$ solutions at 80 and 120 °C was investigated by (Zheng *et al*., 2016b) using weight loss experiments *i.e*. assuming uniform corrosion. Using corrosion rate ($gm^{-2}\,d^{-1}$) as a metric, the authors reported that the corrosion rate at 120 °C was four times lower than that at 80 °C and a 61 % decrease was reported when the exposure time increased from 150 to 368 h (6.25 to 15.3 days). The authors demonstrated using SEM images and XRD that at 80 °C, no product formed but instead cementite was detected, while at 120 °C $FeCO_3$ was detected with increased intensity (measured using XRD) with time; the film appeared to be primarily composed of chukanovite based on the images presented. The authors concluded that the reduced corrosion rate was due to this product formation. It is worth mentioning that very little $FeCO_3$ was apparent from the presented images and the surface film appeared to be very porous but the authors did not comment on the possibility of localised attack. Contrary to (Zheng *et al*., 2016b), a study conducted by (Sadeek, Williams & Campbell, 2018) reported that a mixed surface film, composed of $FeCO_3$ and $Fe_2(OH)_2CO_3$ on C1018, formed after exposure to $CO_2$ saturated 5 M $MEA_{(aq)}$ solution at 80 °C but only cementite detected at 120 °C.

From the above discussion, a clear distinction should be made between the different sections of the plant, by temperature. For those working at < 80 °C (absorber and lean lines), increased corrosion rates with rising temperatures may be expected. By contrast, for ≥ 80 °C (the heat exchanger, stripper and rich high temperature lines) less consistent behaviours are likely to be observed due to product formation and changes in solution composition. The interplay of these solution components, particularly Fe dissolution and precipitation, affect the corrosion rate observed.

### Effect of $CO_2$ loading

The effect of $CO_2$ loading on corrosivity of $MEA_{(aq)}$ has been the primary focus of many studies. Lean $MEA_{(aq)}$ solvents typically contain 0.1 – 0.2 $mol_{CO2}$ $mol_{MEA}^{-1}$ while those described as rich contain 0.4 – 0.5 $mol_{CO2}$ $mol_{MEA}^{-1}$. Similar to the discussion on the impact of temperature, the $CO_2$ loading may affect the active corrosion reactions as well as the passive film formation.

A study conducted by (Sun *et al*., 2011) was one of the few that involved a large potential window (-1.2 to + 1 V *vs*. SCE) to investigate both the active and passive behaviour of carbon steel (A106) in 5 M $MEA_{(aq)}$ solutions; the impact of $CO_2$ loading (0.2 and 0.5 $mol_{CO2}$ $mol_{MEA}^{-1}$) at 40 and 80 °C was considered. The authors reported an order of magnitude increase in the corrosion rate (determined from Tafel analysis of cathodic and anodic Fe dissolution regions of polarisation curves) with increased $CO_2$ loading, agreeing with other published literature (Veawab, Tontiwachwuthikul & Chakma, 1999; Kittel *et al*., 2012; Zheng *et al*., 2016b). Both the anodic Fe dissolution and cathodic HER currents were reported to increase with increased $CO_2$ loading. The authors stated that this was a result of the increased [$HCO_3^-$], consistent with (Veawab & Aroonwilas, 2002) and with the concentration speciation shown in **Figure 2-28**. The authors did not consider changes in HER due to $H^+$ and $H_2O$, though this would be expected from the lower pH of the solution with the higher loading, which (Labiyi, 2016) demonstrated are involved in HER on Fe in $MEA_{(aq)}$ solutions loaded with $CO_2$ as discussed previously. The plots presented by the authors at both $CO_2$ loadings consisted of four anodic current density peaks prior to $O_2$ evolution (**Figure 2-32**), more than that reported by (Castro & Vilche, 1991; Castro, Vilche & Arvia, 1991; Castro *et al*., 1986) for Fe in $HCO_3^-$ / $CO_3^{2-}$ solutions. The authors did not propose specific reactions associated with the individual anodic current density peaks but instead stated that an oxide film likely formed following the first peak. The authors interpreted the lower

magnitude of the current following the first peak measured in 0.2 $mol_{CO2}$ $mol_{MEA}^{-1}$ to indicate that a more protective film had formed but did not comment on a formation mechanism. The authors also did not include any pH data, which would have informed the solution speciation, as shown in **Figure 2-28**, and hence the observed electrochemical behaviour.

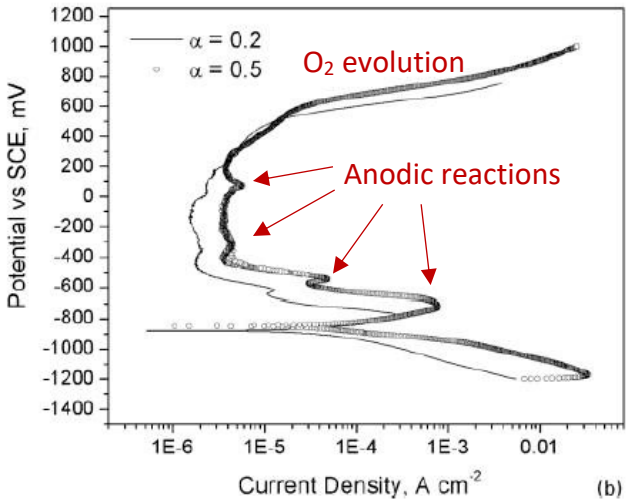



**Figure 2-32**: Effect of $CO_2$ loading on corrosion behaviour of 5 M $MEA_{(aq)}$ solution at 80 °C extracted from (Sun *et al*., 2011). Image reproduced with permission of the rights holder, Taylor & Francis.

The effects of $CO_2$ loading (0.2, 0.43 and 0.53 $mol_{CO2}$ $mol_{MEA}^{-1}$) on the corrosion rate of A106 carbon steel was also investigated by (Zheng *et al*., 2016b) in 5 M $MEA_{(aq)}$ solutions at 80 °C using weight loss measurements. The authors reported low initial corrosion rates at 0.2 $mol_{CO2}$ $mol_{MEA}^{-1}$ that increased by 20 % for the duration of the experiment with no surface film formation. The authors demonstrated that in the richly loaded systems (0.43 and 0.53 $mol_{CO2}$ $mol_{MEA}^{-1}$), although the rates were initially an order of magnitude higher than in the lean system, a substantial decrease in rate (50 % for the 0.43 $mol_{CO2}$ $mol_{MEA}^{-1}$ and 66.7 % for the 0.53 $mol_{CO2}$ $mol_{MEA}^{-1}$ relative to the initial values) occurred with increased immersion duration. In fact, the recorded rate in the 0.53 $mol_{CO2}$ $mol_{MEA}^{-1}$ solution, became lower than the 0.43 $mol_{CO2}$ $mol_{MEA}^{-1}$ when immersion times were beyond 260 hours and the rates recorded in 120 °C were even lower. The authors proposed that this was due to a more developed $FeCO_3$ film, though this was not apparent from surface images.

In summary, $CO_2$ loading seemingly increases uniform corrosion rates of carbon steel, however after long periods of immersion increased $CO_2$ loading appears to promote surface film formation, which may limit diffusion of electroactive species to or from the underlying surface.

## Effect of oxygen

The impact of $O_2$ on the electrochemical behaviour of carbon steel in $MEA_{(aq)}$ in both the active and passive regions has been reported. (Soosaiprakasam & Veawab, 2008; Kittel *et al*., 2012; Labiyi, 2016) all reported overlapping polarisation curves in the cathodic regions on carbon steel (or Fe in the case of Labiyi, 2016) in the absence and presence of $O_2$ at temperatures of 40 - 80 °C and variable loadings (0.2 - 0.5 $mol_{CO2}$ $mol_{MEA}^{-1}$). Labiyi noted, however higher Fe dissolutions currents. By contrast, (Sun *et al*., 2011) demonstrated that the presence of $O_2$ (6 % of purging gas) resulted in slightly lower cathodic currents and slightly higher anodic Fe dissolution currents in $CO_2$ saturated 5 M $MEA_{(aq)}$ at 80 °C. In fact, in an earlier study by (Veawab, Tontiwachwuthikul & Chakma, 1999), the corrosion rate (determined with Tafel analysis of potentiodynamic polarisation curves) of carbon steel in 0.2 $mol_{CO2}$ $mol_{MEA}^{-1}$, was shown to increase by 41 % when the % $O_2$ in the feed gas increased from 0 to 10 % at both 30 and 80 °C; however, the polarisation curves from which the corrosion current was extracted were not presented.

$O_2$ has been reported to more obviously alter the electrochemical behaviour at more positive potentials (Soosaiprakasam & Veawab, 2008; Kittel *et al*., 2012; Sun *et al*., 2011; Labiyi, 2016). (Sun *et al*., 2011) reported increase in the maximum current noted at the passivation potential with $O_2$, which the authors interpreted to mean that the material passivation was less likely to occur. (Kittel *et al*., 2012; Labiyi, 2016) both demonstrated that the currents more positive than the passivation potential were notably higher in the presence of $O_2$, suggesting that the passive film formed may be less protective.

## Summary of corrosion of carbon steel in MEA

To summarise, the corrosion behaviour of carbon steel has been extensively studied in MEA for PCCC. It has been found that $MEA_{(aq)}$ is more corrosive than most (or all) other amines used in PCCC. The corrosion rate of carbon steel has been demonstrated to increase with MEA concentration. The corrosivity was also demonstrated to increase with temperature (up to 80 °C), $CO_2$ loading, and the presence of $O_2$. $H_2O$ was agreed to be directly involved in cathodic HER, whilst $HCO_3^-$ was postulated to either be directly, or indirectly involved in HER. $O_2$ and $H^+$ were also reported to partake in cathodic reactions. Comparison of presented polarisation curves obtained for large potential windows (*i.e*. up to $O_2$ evolution onset), appeared different than those in Fe – $HCO_3^-$/ $CO_3^{2-}$ systems (without amines). Several anodic reactions were observed as the potential was swept more anodically, possibly suggesting

different electrochemical behaviour of Fe or steel in the presence of $MEA_{(aq)}$. Minimal interpretation of the observed behaviour within these regions were given. Closer examination of the electrochemical behaviour at more positive potentials, beyond anodic Fe dissolution may provide information for the divergent behaviour observed in $MEA_{(aq)}$ than in other amines, particularly 3 ° amines. It was also demonstrated that $FeCO_3$ formed only minimally or not at all, even at the high pHs (> 7) and temperatures 80 – 120 °C, known to be conducive to its formation in $MEA_{(aq)}$. Although it has been suggested that the presence of carbamate may be linked to the lack of protective surface film formation, the lack of $FeCO_3$ formation remains poorly understood.

#### 2.5.2.2 Corrosion behaviour of steel in MDEA – $CO_2$

Methyldiethanolamine has been reported to be one of the least corrosive amines in NGP (DuPart, Bacon & Edwards, 1993b). This has also been demonstrated by many PCCC corrosion studies of carbon steel in MDEA (Tomoe, Shimizu & Kaneta, 1996; Gunasekaran, Veawab & Aroonwilas, 2013; Veawab, Tontiwachwuthikul & Bhole, 1997; Sadeek, Williams & Campbell, 2018; Campbell, Yu & Williams, 2017b; Yu, Campbell & Williams, 2016; Campbell, Yu & Williams, 2017a).

Unlike most studies, which extract corrosion currents from the Tafel slopes estimated from potentiodynamic scans, (Gunasekaran, Veawab & Aroonwilas, 2013) also used EIS to extract the resistance to charge transfer of C1018 carbon steel in $CO_2$ saturated MDEA (along with MEA, DEA, AMP and PZ) at 80 °C. The authors reported that the charge transfer resistance value measured in MDEA was around four times that measured in MEA, but unfortunately did not give an explanation of this.

The corrosion rates of carbon steel in $MDEA_{(aq)}$ solutions (10, 27 and 37 wt. %) was tested at 50, 65, 80 °C using Tafel analysis of polarisation curves (Khorrami *et al*., 2008). The authors reported that the corrosion current increased with increased MDEA concentration particularly at 50 °C but less so at 65 and 80 °C. It was postulated that higher MDEA concentrations would result in higher $[HCO_3^-]$, which may result in accelerated Fe dissolution through $Fe(CO_3)^-_3$ as (Davies & Burstein, 1980) explained. Corrosion currents were demonstrated to decrease with increasing temperature and the authors proposed that this was due to the lower solubility of $CO_2$ at higher temperatures. The polarisation curves (up to +0.4 V *vs*. SCE) appeared to indicate two anodic reactions at *ca*. -0.6 V and -0.2 V *vs*. SCE. To investigate this further, the authors applied constant potentials of -0.4 V, -0.2 V and +0.1 V *vs*. SCE and

subsequently analysed the electrodes using XRD. $FeCO_3$ was shown to be detected at -0.4 V, both α-FeOOH and $FeCO_3$ at -0.2 V and predominantly $FeCO_3$ after +0.1 V. The authors stated that α-FeOOH formed inside the $FeCO_3$ film, which resulted in film instability and breakdown and then $FeCO_3$ formed again, explaining the order of detected products. Whilst this study was extensive and attempted to use a variety of techniques to elucidate the surface reactions, there are two crucial shortcomings that need to be mentioned. Firstly, the authors stated that the solution saturation procedure involved purging $MDEA_{(aq)}$ solutions with $CO_2$ for only 30 minutes, however it is known that MDEA absorbs $CO_2$ slowly, often requiring 24 hour periods to achieve full loading. Furthermore, at higher temperatures, before saturation has been achieved, the absorption kinetics would be faster, likely leading to higher $[HCO_3^-]$. The results presented and the interpretation provided are therefore probably not representative of the electrochemical behaviour of carbon steel in saturated $MDEA_{(aq)}$ solution and the impact of temperature was not investigated with convincing accuracy. The authors did not report pH values, but discussed relative $[HCO_3^-]$ and stated that $FeCO_3$ was not thermodynamically stable in $MDEA_{(aq)}$ but gave no explanation for this; this interpretation was likely based on a relatively high pH, at which $Fe(OH)_2$, $Fe_3O_4$ and $Fe_2O_3$ would be most thermodynamically favourable (**Figure 2-12**).

The long term corrosion behaviour of carbon steel (C1018) in $MDEA_{(aq)}$ has been given far more attention. $FeCO_3$ film formation in $MDEA–CO_{2(aq)}$ has been well documented as a key factor for reduced corrosion rates observed with this amine over longer time periods (≥ two days) (Tomoe, Shimizu & Kaneta, 1996; Xiang *et al*., 2015; Campbell *et al*., 2016; Yu, Campbell & Williams, 2016; Campbell, Yu & Williams, 2017a, 2017b; Sadeek, Williams & Campbell, 2017).

(Xiang *et al*., 2015) investigated the corrosion of carbon steel (UNS K02600) in 50 wt. % $MDEA_{(aq)}$ at 120 °C as a function of $CO_2$ loading (0.05 – 0.03 $mol_{CO2}$ $mol_{MDEA}^{-1}$) using LPR, OCP measurements, weight loss tests and *ex-situ* surface analyses (SEM-EDX). The impact of $O_2$ and a HSS was also investigated. Corrosion rates determined by weight loss were shown to be the lowest in $MDEA–CO_2$ (0.13 mm $y^{-1}$), then $MDEA–CO_2–HSS$ and highest in $MDEA–CO_2–HSS–O_2$ (0.75 mm $y^{-1}$); the trend was consistent with the corrosion rate trend determined using LPR, but corrosion rates were two orders of magnitude higher than that measured using LPR. Similarly, at lower loadings (0.05 $mol_{CO2}$ $mol_{MDEA}^{-1}$), the corrosion rate was shown to be the highest in $MDEA–CO_2–HSS–O_2$ (1.84 mm $y^{-1}$) but equal in $MDEA–CO_2–HSS$ and $MDEA–CO_2$ (0.14 mm $y^{-1}$); the rates measured with LPR were two orders of

magnitude lower. Presented surface images demonstrated the formation of seemingly compact $FeCO_3$ films at all conditions except in MDEA–$CO_2$–HSS–$O_2$ at low loading and mostly ferrite and cementite were detected. Polarisation curves recorded 48 hours after immersion were also presented (-1 to 0.8 V *vs*. AgCl | Ag, -0.9 to +0.9 V *vs*. $SHE_{25\ °C}$) in all six solutions (*i.e*. three combinations, two loadings each); at high loadings, without $O_2$ and HSS, two anodic current peaks were apparent but a stable passive film was not observed and the currents recorded with contaminants were slightly higher. At the lower loading, current densities were shown to be an order of magnitude higher in MDEA–$CO_2$–HSS–$O_2$, and four anodic peaks were visible. The authors did not suggest possible reactions. From this study, $FeCO_3$ was shown to be likely to form in $MDEA_{(aq)}$ solutions, even at low loadings. The low corrosion rates (except for MDEA–$CO_2$–HSS–$O_2$, at low loading) were proposed to be due to the formation of an $FeCO_3$ film, but the resistance to charge transfer provided by the is film was not quantified. Furthermore, neither an interpretation of OCP results, nor a thorough analysis of polarisation curves were presented.

(Yu, Campbell & Williams, 2016), investigated the effect of MDEA concentration (1 to 5 M, 120 °C) in $CO_2$ saturated solutions on carbon steel (C1018) through immersion testing accompanied by *ex-situ* surface analyses (SEM, EDX, XRD). It is important to note that the authors did not remove the product layer before determining the difference in weight before and after exposure to the amine solutions, so the rates presented in this study are of mass change rather than corrosion. The authors noted increased net mass loss with increased MDEA concentration for short exposure times (seven days) but showed decreased rates with increased concentration for extended durations (14 – 21 days). The authors demonstrated using SEM and XRD, that this was due to the formation of compact $FeCO_3$ films forming in the 3 M and in the 5 M solutions with enhanced coverage occurring with longer immersion duration; electrodes exposed to 1 M were not shown. (Campbell *et al*., 2016) corroborated the formation of $FeCO_3$ films under the same conditions as those reported by (Yu, Campbell & Williams, 2016) in a separate study, and quantified the film thickness to be 24.1± 5.7 $\mu$m on C1018 coupons after 48 days with a 75 % decrease in film growth rate after the first seven days. Similar behaviour was observed at 80 °C (Campbell, Yu & Williams, 2017a, 2017b; Sadeek, Williams & Campbell, 2017) but at 40 °C no surface film was apparent (Campbell, Yu & Williams, 2017b).

### 2.5.2.3 Pre-treatment studies

(Zheng *et al*., 2016a) first proposed pre-treating carbon steel to produce a protective $FeCO_3$ coating as a corrosion mitigation strategy for PCCC. The authors proposed first flushing the PCCC plant with 30 wt. % piperazine (PZ), another well investigated amine shown to enhance surface film formation, to produce an $FeCO_3$ coating. Then after the film has been formed, initiating plant operation with $MEA_{(aq)}$ and subsequently repeating the process during plant downtime. The authors pre-treated A106 in 30 wt. % PZ for two days, to form an $FeCO_3$ film. The pre-treated coupon was then immersed in 5 M $MEA_{(aq)}$ and the OCP measured; immediately after immersion, the potential decreased from -0.2 V *vs*. SCE to -0.8 V SCE and after 10 days the OCP began increasing to -0.5 V. The authors stated that this was a result of $Fe_3O_4$ formation and said, based on the surface images that the film, though compositionally different, was dense and hence would still protect the underlying steel - this is unconvincing without film or charge transfer resistance measurements. The authors attempted to pre-treat the coupon in different solution (10 wt. % $NaHCO_3$) and reported the resistance, determined by LPR, to be three orders of magnitude higher than initially measured within a one day period (at 80 °C). The authors therefore proposed the use of $NaHCO_3$ and 30 wt. % PZ; however, no results in this mixture were reported. The stability of the film produced in 10 wt. % $NaHCO_3$ was also not tested.

The potential of MDEA as a pre-treatment solution to produce and maintain $FeCO_3$ films on C1018 has been investigated by limited studies (Sadeek, Williams & Campbell, 2017; Campbell, Yu & Williams, 2017b, 2017a). (Campbell, Yu & Williams, 2017a) immersed carbon steel (C1018) coupons for seven days at 40 and 80 °C in MDEA, AMP (aminomethyl propanol[12]) (5 M) and $K_2CO_3$ aqueous solutions and measured the weight change (without product layer removal). The authors reported that $FeCO_3$ films were successfully formed at 80 °C but did not develop at 40 °C in the amine solutions. The authors demonstrated through surface imagining (SEM) that the films formed in MDEA and AMP at 80 °C remained intact after exposure to 2.5 M MEA for three weeks; the film formed in the $K_2CO_3$ pre-treatment solution was mostly dissolved after one week of exposure - disintegration of the crystals were apparent from the presented SEM images. The authors concluded from the weight change measurements, and the surface images that the films formed in MDEA and AMP were

[12] Aminomethyl propanol ($H_2NC(CH_3)_2CH_2OH$) is a sterically hindered amine that has been demonstrated to enhance $FeCO_3$ film formation (Sadeek, Williams & Campbell, 2018).

protective and resilient. A similar investigation was conducted in a related study (Sadeek, Williams & Campbell, 2017) where a seven day pre-treatment of C1018 was done with 5 M $MDEA_{(aq)}$ solution at an increased temperature of 120 °C and subsequent immersion in 5 M $MEA_{(aq)}$ solution saturated with $CO_2$ (also at 120 °C), to determine if pre-treatment could be considered as a mitigation strategy in the stripper. $FeCO_3$ film protection was compared to that provided by a selection of inhibitors added at 1000 ppm concentrations (CC: copper carbonate, STS: sodium thiosulphate, MBI: 2-mercaptobenzimidazole). The combined effect of pre-treatment (to form an $FeCO_3$ film) and inhibitor addition on the weight loss (without product removal) was also tested. Again, the relative performance was determined by % net mass change converted to rate of material size change (MSCR, mm $y^{-1}$) and deductions made from surface analyses (SEM, XRD). The authors demonstrated that compact $FeCO_3$ films formed on C1018 coupons at 120 °C after a seven day immersion in $CO_2$ saturated $MDEA_{(aq)}$ solution. The authors demonstrated that the $FeCO_3$ film remained relatively stable after one week of immersion in the $MEA_{(aq)}$ solution, though small pores appeared to have developed in the film possibly signalling localised attack. The authors found that the combination of both strategies resulted in film dissolution, and the CC addition appeared to protect the steel with the surface images of the tested coupon being nearly identical to a pristine sample. The authors reported a negative MSCR for the pre-treated sample, 0 mm $y^{-1}$ with CC and 0.41 mm $y^{-1}$ with MBI, concluding that pre-treatment with MDEA should be considered as a mitigation strategy.

Although the immersion studies conducted by (Zheng *et al*., 2016a; Campbell, Yu & Williams, 2017a; Sadeek, Williams & Campbell, 2017) demonstrated that compact $FeCO_3$ films can be formed in PZ, MDEA and AMP, and in the case of MDEA and AMP, seemingly remained intact on exposure to MEA, the corrosion resistance provided by these films during pre-treatment and in $MEA_{(aq)}$ solutions was not investigated. The film compositions in the aforementioned amines, have been determined by XRD, to be $FeCO_3$ when pre-treated. However OCP and EIS studies in non-amine containing $CO_{2(aq)}$ (pH 6 – 8), suggested that the protection afforded by surface films in $CO_2$ containing solutions was due to an oxide layer (Han *et al*., 2009) at the interface or a $FeCO_3$ thin bilayer (Burkle, 2017) composed of smaller films rather than the films containing larger $FeCO_3$ crystals.

A thorough investigation using, for example, OCP and EIS needs to be conducted to investigate the evolving composition of the surface films, and crucially, to determine if the films increase the electrical resistance of the steel interface with solution. The species

responsible for the protection, if any, need to be elucidated. This will not only be useful for understanding corrosion in PCCC plants but also in oil and gas pipelines. The changing film stability in $MEA_{(aq)}$ solutions, in terms of protection, needs to be quantified. A closer investigation of $FeCO_3$ formation / stability in the presence of MEA needs to be examined since its absence on carbon steel in $MEA_{(aq)}$ solutions is yet to be completely understood (Section 2.5.2.1). It is also of utmost importance that the time required for complete film formation, as well as the amine concentrations conducive to film formation to be determined, before pre-treatment can be confirmed to be a reliable corrosion mitigation strategy. Furthermore, the impact of $O_2$ should also be considered since its presence has been demonstrated to hinder stable $FeCO_3$ formation (Reffass *et al*., 2006).

# 3 Experimental Methods

The electrochemical measurements in this thesis were carried out using a BioLogic potentiostat (SP-300) (BioLogic Science Instruments, France) and EC-Lab software. The electrochemical reagents were purchased from Sigma-Aldrich (Merck Life Science, Dorset UK). The iron and carbon steel working electrode materials were purchased from Sigma-Aldrich and Imotron (Imotron Instruments B.V. Netherlands) and manufactured by Alabama Specialty Products, USA. **Table 3-1** includes a summary of the chemicals and materials used. Different working electrode designs and dimensions were used for each study and are described in each of the following experimental sections. Most working electrodes were made by embedding either Fe or C1018 in a PTFE sheath.

Working electrodes were prepared by wet grinding using P600, P800, P1200, P2400, P4000 grinding papers sequentially on a Buehler Alpha 2 speed grinder-polisher, and then polished by hand with 0.03 μm alumina polishing suspension on a polishing cloth until a mirror finish was achieved. All polishing materials were purchased from Buehler (ITW Test & Measurement GmbH, Germany). The electrodes were rinsed thoroughly with deionised water after polishing.

Pt flag (surface area: $2 \times 10^{-4}$ $m^2$) (**Figure 3-1**) or mesh counter electrodes were used for all electrochemical measurements, except open circuit potential measurements, the Pt was purchased from Goodfellow (Goodfellow Cambridge Ltd, Huntingdon, UK) and assembled into flags by Cambridge Glassblowing (Cambridge Glassblowing Ltd, Cambridge, UK).

A Cole-Parmer (Cole-Parmer Instrument Company Ltd, UK) AgCl | Ag (saturated KCl) reference electrode, which has a potential of +0.199 V *vs*. SHE (standard hydrogen electrode), was used in most electrochemical experiments. Most potentials were temperature corrected and converted to *vs*. SHE using Equation **3-1**. Unless specified otherwise, all

potentials are given relative to SHE henceforth. The reference electrode tip was properly submerged in a saturated KCl solution when stored and the potential was measured against another unused Cole-Parmer AgCl | Ag reference electrode before each experiment using a voltmeter.

$$E_{SHE} = E_{(AgCl\,|\,Ag)_{sat}} + \left[0.199 - 0.00101\left(T_{electrolyte} - 25\,°C\right)\right] \quad \textbf{3-1}$$

De-ionised water, typically with a conductivity of $5 \times 10^{-6}$ S m$^{-1}$, was used for wet grinding electrodes and preparing aqueous electrolytes. After each aqueous amine solution was prepared and transferred to the electrochemical cell, it was thoroughly purged with $N_2$ for at least 2 hours and then saturated with $CO_2$ for at least 24 hours. $CO_2$ bubbling was continued for the duration of each experiment to maintain saturated conditions. All gases were obtained from BOC (BOC Ltd, Imperial College London, UK). Experiments were conducted with two amines: monoethanolamine (MEA) and methyldiethanolamine (MDEA) at three concentrations, 1, 3 and 5 M and at 25, 40 and 80 °C. Before commencing electrochemical or immersion experiments, the pH and electrolyte temperature were checked using a Hanna Instruments HI5552 pH meter (Hanna Instruments Ltd UK). The recorded pH was used to determine the $CO_3^{2-}$ concentration based on the total dissolved '$CO_2$' calculated from solubility correlations of $CO_2$ in $H_2O$ published in (Green & Perry, 2008) at $pCO_2$ of 1 atm. The temperature of the water bath or hot plate was altered if needed and it was ensured that the pH was stable. The pH probe was calibrated on a regular basis and before most electrochemical experiments using a three point calibration with three buffer solutions: pH 4.0, 7.0 and 10.0.

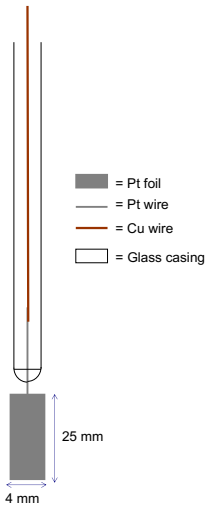



**Figure 3-1:** Pt flag counter electrode used in electrochemical experiments.

**Table 3-1:** Chemicals, gases and materials used in experiments.

| Item | State | Source | Purity |
|---|---|---|---|
| **Monoethanolamine** | Liquid | Sigma Aldrich | ≥ 98 % |
| **Methyldiethanolamine** | Liquid | Sigma Aldrich | ≥ 99% |
| **$CO_2$** | Gas | BOC | 99.8 % |
| **$N_2$** | Gas | BOC | 99.998 % |
| **Fe (rod)** | Solid | Sigma Aldrich | 99.98 % |
| **C1018 (rod)** | Solid | Imotron | N/A |
| **Pt (foil and wire)** | Solid | Goodfellow | 99.95 % |
| **Cu (wire)** | Solid | Goodfellow | ≥ 99.9 % |

## 3.1 Preliminary immersion study

A preliminary study involving the immersion of carbon steel coupons in $MEA_{(aq)}$ and $MDEA_{(aq)}$ solutions saturated with $CO_2$ at 80 °C for one week was conducted to confirm the presence or absence of surface films reported in literature.

### 3.1.1 Experimental setup

Carbon steel (C1018 ) coupons used for the preliminary immersion study were obtained from Imotron and manufactured by Alabama Specialty Products, USA. The coupons had a glass bead finish. The composition (supplied by manufacturer) and dimensions of the coupons are given in **Table 3-2** and **Table 3-3**, respectively. An image of the coupon is shown in **Figure 3-2**. Coupons were prepared for immersion studies by washing with DI water and drying with a tissue. A strip of PTFE tape *ca*. 15 cm in length was threaded through the hole at the top of the coupon and knotted – this was done to enable suspension of the coupons in the solution.

**Table 3-2**: Carbon steel (C1018) composition - the material certification is presented in the Appendix (Section 12.6).

| Fe | Mn | C | Cu | P, S, Si, Ni, Cr, Mo, Al | Other trace elements |
|---|---|---|---|---|---|
| 98.682 | 0.8 | 0.18 | 0.14 | 0.1-0.012 | 0.001 - 0.0066 |

**Table 3-3:** Physical properties of carbon steel coupons used for preliminary immersion study including dimensions and surface area exposed to electrolyte.

| Density / kg $dm^{-3}$ | Original dimensions (W ×L ×T) / × $10^{-3}$ m | Final surface area × $10^{-4}$ $m^2$ |
|---|---|---|
| 7.87 | 9.46 × 76.2 × 1.46 | 17.03 |




**Figure 3-2**: C1018 Coupon used in immersion study.

250 mL of electrolyte ($MDEA_{(aq)}$ or $MEA_{(aq)}$) was prepared and added to a 250 mL round bottom three neck flask. The round bottom flask was seated in a Dry-Syn block (Asynt, UK) on an aluminium heat transfer plate fabricated in-house by the Mechanical Workshop, positioned on top of a hot plate (IKA England Ltd, UK) (**Figure 3-6**). The centre neck was sealed with a silicone septum. A condenser, sealed with a rubber septum and fitted with a syringe vent[13] (**Figure 3-6**), was inserted into one side neck and a rubber septum was added to the other side neck. A syringe needle attached to a silicone tubing carrying $N_2$ gas pierced the rubber septum to purge the solution. After purging, the $N_2$ gas line was switched to $CO_2$ to saturate the solution. The hot plate was switched on and set to 80 °C. When the electrolyte was saturated, the centre silicone septum was lifted and the prepared coupon was lowered into the flask using the PTFE tape. The silicone septum was then reinserted and it held the PTFE tape in place so the coupon was suspended in a fixed position in the solution. After one week of immersion, the coupon was removed from the solution and rinsed thoroughly with DI water, dried and stored. Coupons were subsequently analysed using XRD, SEM-EDX (Section 3.6.1).

## 3.2 Cyclic voltammetry study

Cyclic voltammetry was used as an exploratory technique to probe interfacial reactions occurring on an Fe electrode in $MEA_{(aq)}$ and $MDEA_{(aq)}$ solutions saturated with $CO_2$ to gain insight to the varied behaviour exhibited by carbon steel in these two amines.

In cyclic voltammetry, potentiodynamic conditions are imposed on a working electrode using a potentiostat whereby the potential of the material is altered in a predefined manner as a function of time as described by Equation **3-2**.

$$\mathrm{E_{WE}}(\mathrm{t}) = \mathrm{E_1} \pm \mathrm{st} \qquad \textbf{3-2}$$

Where *s* is the rate at which the potential is scanned and *t* is the time. The electrode potential, $E_{WE}$ (V), was swept in one direction from a starting value, $E_1$ (V), to another and then reversed to the initial limit. This process can be repeated continuously. The current response to the imposed potential can indicate the number, type and nature of reactions taking place. However, even with a E-pH diagram to help with the interpretation, it can be difficult to

[13] The vent exhaust should have been fed to a Dreschel bottle containing DI water to prevent significant $O_2$ ingress through the vent. Since the vent was left open to the atmosphere some $O_2$ ingress would have occurred.

determine if observed reactions are due to precipitation or dissolution or are a result of local pH changes due to for example $H_2$ or $O_2$ evolution reactions.

A diffusion layer is developed at the interface of the electrode with the solution due to initiated concentration gradients of species. In such cases, it is preferable to impose conditions of well-defined hydrodynamics in the vicinity of the electrode. This is accomplished through continuous stirring or, more reproducibly, through the use of a rotating disc electrode; the latter was utilised in this thesis.

The rotating disc electrode is commonly used as the working electrode since it generates well defined, stable hydrodynamic conditions, which are described by the Levich equation. The rotating disc electrode is constructed by embedding a cylindrical rod in an insulating sheath such that the disc is left exposed. The top of the fabricated electrode is attached to a rotator (**Figure 3-3a**) while the bottom of the electrode is immersed in the solution of interest, such that the surface area of the disk faces downwards. The rotational motion of the electrode creates a solution flow pattern (**Figure 3-3b**). The rotating electrode essentially acts as a pump, drawing fresh electrolyte towards the disc surface and then spinning it radially outward from the axis of rotation.

Due to friction between the electrolyte and the disc, a thin stagnant film of electrolyte is created at the surface of the disc where the thickness ($\delta$) is uniform over the surface. This layer creates a region through which the electroactive species must diffuse to participate in heterogenous reactions (*i.e.* at the electrode surface). The diffusion layer thickness is given by Equation **3-3** where $D$ is diffusion coefficient of the electroactive species, $\nu$ is the kinematic viscosity, and $f$ the electrode rotation frequency. Accordingly, the diffusion layer thickness ($\delta$) decreases with increasing rotational rate.

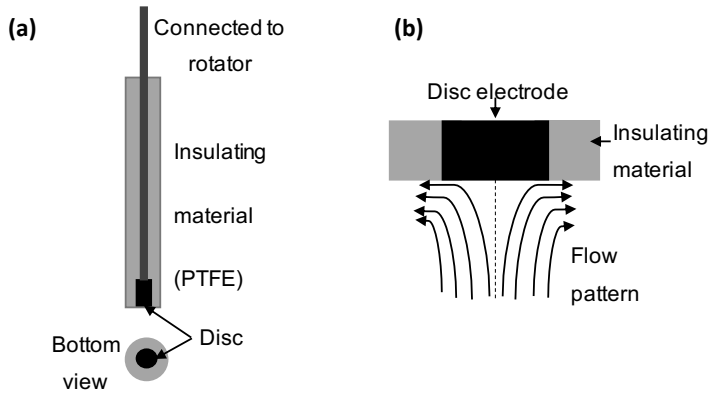



**Figure 3-3:** Schematic of **(a)** the rotating disc working electrode and **(b)** flow pattern induced by the rotation of the electrode.

The Levich equation (Equation **3-4**) describes the mass transport limited current at a rotating disc electrode, where *F* is Faraday's constant, *n* is the number of electrons transferred in the reaction, *A* is the electrode surface area, *D* the diffusion coefficient of the electroactive species with a bulk solution concentration *C* and *f* is the electrode rotation rate with units Hz.

$$\delta = \frac{1}{1.554}\, D^{\frac{1}{3}} \nu^{\frac{1}{6}} f^{-\frac{1}{2}} \qquad \textbf{3-3}$$

$$I_L = 1.554\, n\, F\, A\, D^{\frac{2}{3}} \nu^{-\frac{1}{6}} f^{\frac{1}{2}} C \qquad \textbf{3-4}$$

It should be stated that frequent polishing of the electrode between experiments, could result in the face of the electrode surface and insulating material being unlevelled, therefore no longer being completely perpendicular to the solution flow path, which may affect the hydrodynamics of the solution at the electrode surface.

## 3.2.1 Stationary disc electrode experimental method

Experiments were conducted in a jacketed glass electrochemical cell (EuroCell, Gamry Instruments, USA) connected to a recirculating water bath (Optima TX150, Grant Instruments Ltd, UK) to control the electrolyte temperature. The reference and counter electrodes were described previously and a 6.3 mm diameter Fe disc working electrode with a surface area of $3.1 \times 10^{-5}$ $m^2$ was used. Electrolyte and working electrode were prepared as previously described and $CO_2$ was continuously bubbled through the solution for the duration of the experiment. All three electrodes, along with a condenser (for 40 and 80 °C experiments) were added to the electrochemical cell, which housed the prepared electrolyte as depicted in **Figure 3-4**. The working electrode was electrochemically pre-treated by applying a potential of -0.810 V (*vs*. SHE) for *ca*. 1 - 2 minutes to remove any oxides formed on the electrode surface in the short time between completion of polishing and immersion in electrolyte.

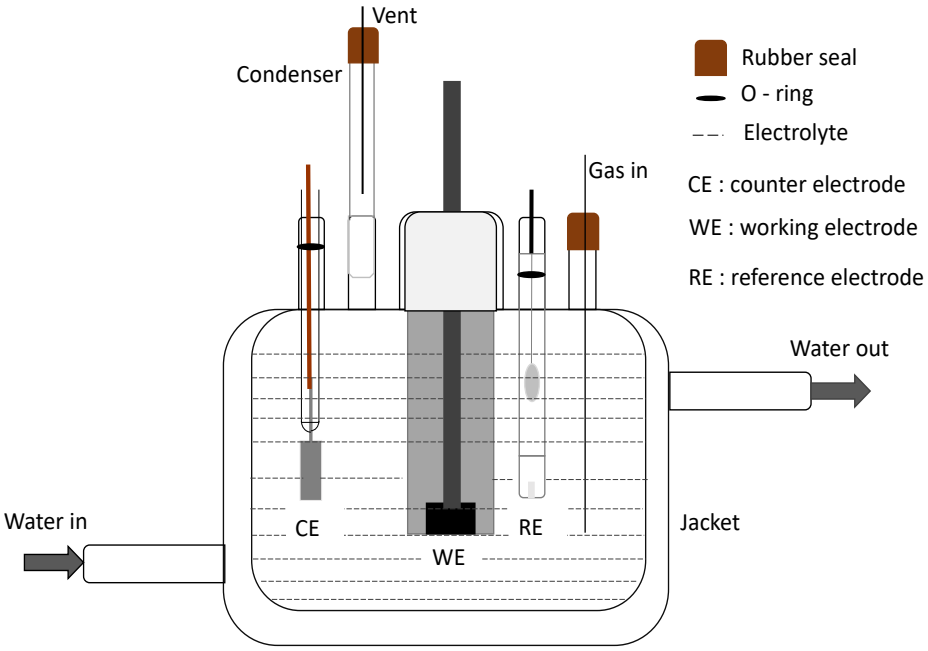



**Figure 3-4:** Schematic of electrochemical cell used for cyclic voltammetry and chronoamperometry experiments. Not shown: attachment to rotator.

After electrochemically pre-treating the electrode, the open circuit potential (OCP) was measured until the $|\Delta E_{WE}| \leq 1$ mV $h^{-1}$ (at most). This was done since the local pH would have decreased due to $H_2$ evolution during the electrochemical pre-treatment process. After sufficient time, indicated by the time at which the OCP stabilised, the local pH would have returned to the bulk pH.

A potential scan was then initiated, typically starting from -0.8 V, and swept to +1.2 V, then reversed to -0.8 V. This was repeated using scan rates of 10, 20, 40, 80 and 100 mV $s^{-1}$. The working electrode was electrochemically pre-treated between each scan and the OCP was measured and compared to the initial OCP to ensure that the electrode surface was sufficiently similar at the beginning of each scan. In two instances, the potential scan was initiated at the OCP to determine the impact, if any, of initial $H_2$ evolution on the observed anodic reactions. This is described in more detail in the Results section (Chapter 5).

## 3.2.2 Rotating disc electrode experimental method

Rotating disc electrode experiments were used for the potentiodynamic and potentiostatic investigations of iron in aqueous amine solutions saturated with $CO_2$. The experimental setup was similar to that described for the stationary disc electrode experiments (Section 3.2.1) with the same reference, working and counter electrodes. The top of the working electrode

was inserted into a Pine Research shaft (Pine Research Instrumentation, USA) (**Figure 3-5**) and controlled using a Pine Research MSR rotator. Scan rates of 10 or 20 mV $s^{-1}$ were used and the working electrode was rotated at 1000, 1250, 1500, 1750, 2000, 2250 RPM. The same experimental procedure as that used for the stationary disc electrode experiments was used for rotating disc electrode experiments. The obtained experimental results could not be used to extract limiting currents involved in $FeCO_3$ formation due to the complex nature of this reaction, which involved a change in the limiting species from $Fe^{2+}$ to $HCO_3^-$.

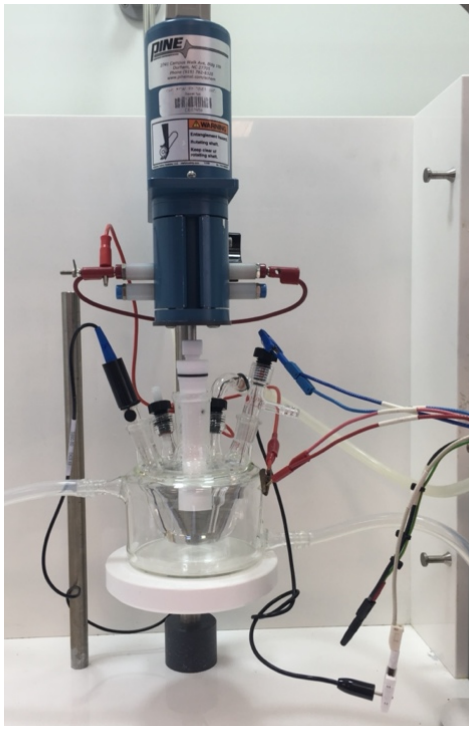



**Figure 3-5:** Rotating disc electrode experimental setup.

## 3.2.3 Pt voltammetry experiments

In order to determine if $MEA_{(aq)}$ was directly involved in electrochemical reactions, voltammograms were also recorded on Pt. A Pt-Pt rotating ring disc electrode tip from Pine Research was fitted in a PTFE shaft with a protruding stainless steel rod fabricated in-house by the Mechanical Workshop. Only the Pt disc was electrically connected to the stainless steel rod using a stainless steel spring. The same electrode and electrolyte preparation protocol described previously were followed and the experimental setup described in Section 3.2.1 was used. Both stationary and rotating disc electrode experiments were conducted.

## 3.3 Chronoamperometry study

Chronoamperometry was used to investigate the $FeCO_3$ formation reaction on rotating disc Fe electrodes in $MEA_{(aq)}$ and $MDEA_{(aq)}$ solutions saturated with $CO_2$ at 80 °C.

### 3.3.1 Experimental setup

The experimental setup described in Section 3.2.1 and shown in **Figure 3-4** and **Figure 3-5** was used for these experiments. A removable head Fe disc electrode (surface area: $1.9 \times 10^{-5}$ $m^2$) was used as the working electrode. The Fe disc inserts were cut in-house by the Mechanical Workshop from an Fe rod and were polished using a PTFE holder and cap. The Fe disc was then removed from the PTFE cap and inserted into a PEEK (Polyether ether ketone) cap and screwed into the PTFE holder. A PEEK cap was used instead of a PTFE cap because it has a higher glass transition temperature, so it did not soften and was able to maintain a tight seal on the disc insert for the duration of the high temperature experiments. The electrolyte was prepared as described previously.

### 3.3.2 Electrochemical measurements

1. The electrode was inserted into the Pine rotator and lowered into the electrochemical cell. The rotator was switched on and set to 1000 RPM and the OCP was measured.
2. A cyclic voltammogram was recorded starting at the OCP to +1.2 V, then reversed to -0.8 V and ended at the OCP. The scan rate used was 20 mV $s^{-1}$. The potential corresponding to the peak current associated with $FeCO_3$ formation ($E_{FeCO3}$) was recorded.
3. A potential of -0.8 V was applied to reduce any product species formed during the cyclic voltammetry scan from the electrode surface. The OCP was again recorded to confirm that it matched the original OCP.
4. The $FeCO_3$ formation potential ($E_{FeCO3}$) was then applied and the current measured for 5400 seconds (90 minutes).
5. The electrode was removed from solution, washed with DI water, removed from the sample holder and stored until it was subsequently characterised using XRD and SEM-EDX (Section 3.6.1).

## 3.4 Electrochemical impedance study

Electrochemical impedance spectroscopy (EIS) was used to determine if the $FeCO_3$ films formed on carbon steel (CS) in methyldiethanolamine (MDEA) solutions saturated with $CO_2$ at 80 °C were sufficiently electrically resistive for use as protective films to limit corrosion in 5 M $MEA_{(aq)}$ solutions saturated with $CO_2$ at 80 °C. The collected EIS data were fitted with equivalent circuits using the EC-Lab software to extract different parameters *e.g.* electrical resistance to charge transfer to enable quantitative comparison of the surface films.

### 3.4.1 Open circuit film formation

#### 3.4.1.1 Experimental setup

Round bottom 250 mL three neck flasks were used as the reaction vessels for EIS experiments. These were preferred over the electrochemical cell used for potentiostatic and potentiodynamic experiments because they could be better sealed, which was found to be essential for long-duration experiments. Furthermore, the height of the cell allowed the electrode to be submerged at a greater distance away from the electrolyte surface where $O_2$ concentration would be highest, if $O_2$ ingress were to occur inadvertently.

Solutions were prepared as described at the beginning of this chapter. When the electrolyte was saturated, C1018 pre-cut disc inserts (surface area: $1.9 \times 10^{-5}$ $m^2$) (**Table 3-2**) were polished as described previously. The disc inserts were then fitted to the electrode holder and the stainless steel rod at the top of the electrode holder was threaded through a *ca.* 3 mm hole bored in a silicone septum stopper and the electrode was immersed in the solution through the centre neck, as shown in **Figure 3-6**. To take electrochemical measurements, the condenser was quickly removed and the reference electrode was inserted into the neck in which the condenser was situated. The rubber septum through which the gas was delivered was quickly replaced by another rubber septum, which had both a syringe needle to deliver $CO_2$ gas and the counter electrode (threaded through the septum). This ensured that $CO_2$ was continuously bubbling through the electrolyte to keep the solution saturated and limit $O_2$ ingress[14]. Every effort was made to limit $O_2$ ingress into the solution, however some small amount is expected

[14] Some $O_2$ ingress would have occurred since the vent was open to the atmosphere and since the cell was opened to take the electrochemical measurements.

to have entered the solution. After electrochemical measurements were completed, the condenser and rubber septum were re-installed.

This procedure was followed for:

i. 1, 3 and 5 M $MDEA_{(aq)}$ solutions: to investigate the effect of MDEA concentration on the time required for film formation and electrical resistivity of films.

ii. 5 M $MEA_{(aq)}$ solutions: to compare to EIS results obtained in $MEA_{(aq)}$ solutions.

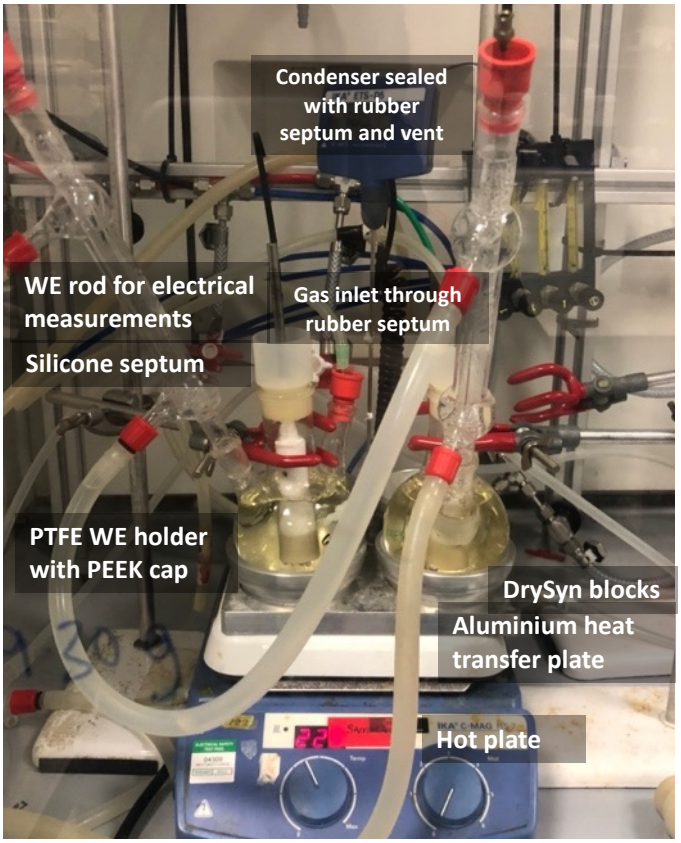



**Figure 3-6:** EIS experimental setup.

### 3.4.1.2 Electrochemical impedance measurements

When the electrode was initially immersed, a potential of -0.8 V was applied for 1 minute to reduce any species formed on the electrode surface due to aerial oxidation. After the electrode attained a stable open circuit potential (OCP) (at most $|\Delta E_{WE}| \leq 1$ mV $h^{-1}$), the impedance measurement was made at the attained OCP with an AC-signal amplitude of ±10 mV, for a frequency range of $10^5 - 10^{-2}$ Hz with 10 points per frequency decade. In the first set of EIS experiments, EIS data was recorded every 24 hours. When there was little or no observable change between consecutive datasets, the electrode was removed from solution, rinsed with DI water and stored until it was characterised using XRD, SEM–EDX.

## 3.4.2 Open circuit film stability

To investigate the stability and electrical resistance of the $FeCO_3$ films formed in each $MDEA_{(aq)}$ solution in 5 M $MEA_{(aq)}$ saturated with $CO_2$ at 80 °C:

1. The CS electrode was removed from the $MDEA_{(aq)}$ solution at the end of the film formation process and immediately immersed in a prepared 250 mL 5 M $MEA_{(aq)}$ saturated with $CO_2$ at 80 °C.
2. The electrode potential was measured until a stable OCP (at most $|\Delta E_{WE}| < 1$ mV $h^{-1}$) was attained.
3. The EIS data was then measured at the OCP using the settings described in Section 3.4.1.2 (excluding the electrochemical pre-treatment).
4. The EIS data was measured at most every 24 hours until either the response was the same as the initial impedance measured before the film was produced in the pre-treatment solution, or until the response remained relatively unchanged for 48 hours. The data recorded after initial immersion, one day and one week are presented in Chapter 7.
5. *Ex-situ* XRD was used to confirm the primary phase present in the films and *ex-situ* imaging and chemical composition determination were done using a scanning electron microscope (SEM ) fitted with an electron dispersive X-ray (EDX) analyser.

## 3.5 Pilot plant study

One of the aims of this thesis was to investigate the feasibility of inducing the formation of a corrosion-inhibiting $FeCO_3$ film on carbon steel (CS) in the $CO_2$ rich, high temperature components of a carbon capture plant. In a plant, this would be accomplished through intermittent use of methyldiethanolamine (MDEA) as the carbon capture solvent between routine operating periods, where monoethanolamine (MEA) is used as the primary solvent. This strategy could minimise plant shut-down periods for corrosion maintenance, since the plant can continue to operate, albeit at a lower production rate, during maintenance periods.

CS coupons, which were pre-treated with two MDEA (1 and 3 M) solutions to produce an $FeCO_3$ film in the laboratory, were installed in the pipelines preceding the absorption column in the ABB Carbon Dioxide Capture Pilot Plant[15] at the Chemical Engineering Department at Imperial College London. Images of the plant are shown in **Figure 3-7** and a flowsheet of the plant in **Figure 3-8**. Continuous *in-situ* open circuit potential measurements were recorded to enable monitoring of changes at the electrode surface; furthermore, after retrieval from the pilot plant, the remaining protection provided by the $FeCO_3$ film was examined in an aliquot of the pilot plant solution *via* impedance spectroscopy in the lab.




**Figure 3-7**: ABB Carbon Dioxide Capture Plant at ICL (**a** - **b**) 1st floor and (**c**) control room.

[15] https://360-visit.imperial.ac.uk/areas-of-interest/campus-highlights/chemical-engineering-carbon-capture-pilot-plant/carbon-capture-pilot-plant

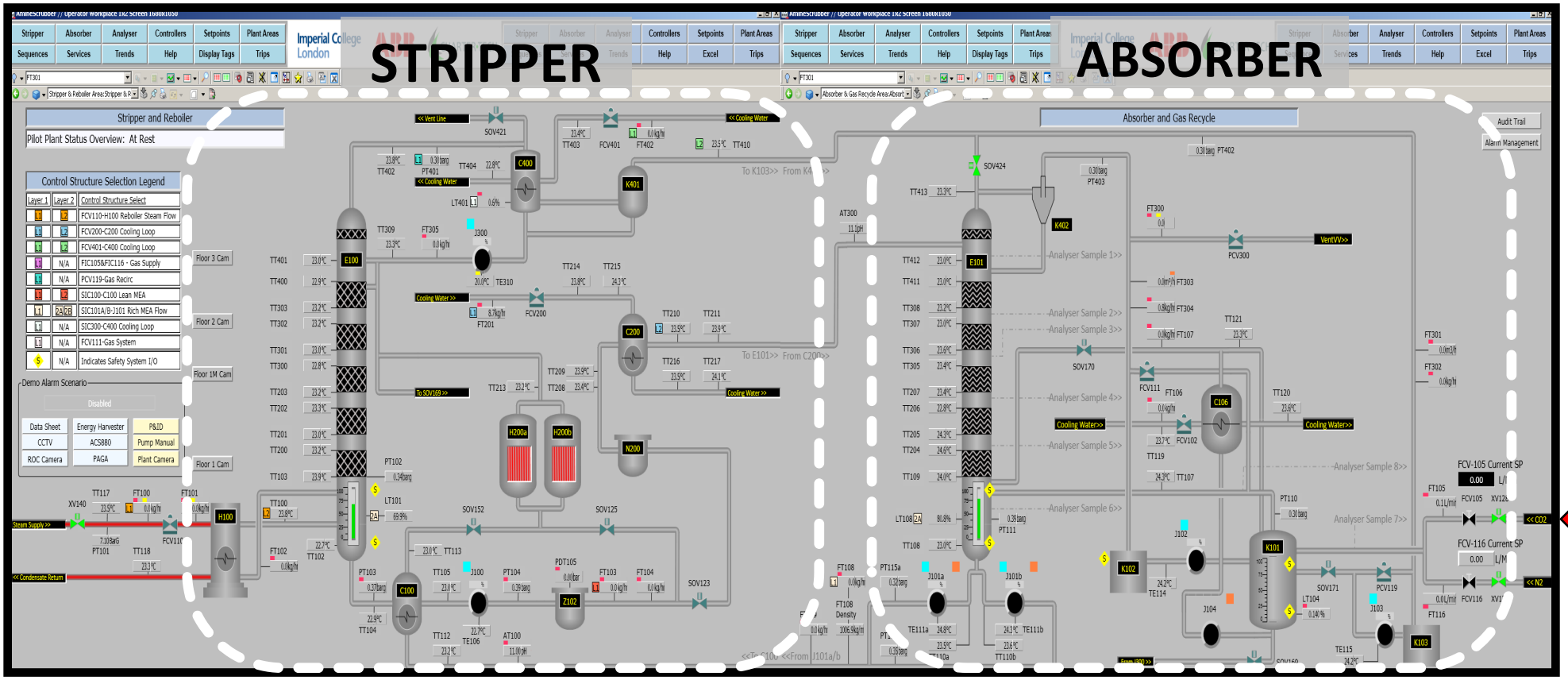



**Figure 3-8:** Flow sheet of ICL Carbon Dioxide Capture plant used to test pre-treated electrodes.

## 3.5.1 Experimental matrix

### 3.5.1.1 Optimal experimental matrix (original intention of this work)

$FeCO_3$ precipitation is favoured by high temperatures > 60 °C (Nazari, Allahkaram & Kermani, 2010) and under $CO_2$-saturated conditions. Amine-induced $FeCO_3$ film formation on CS as a reliable corrosion mitigation strategy is therefore only applicable to high temperature, $CO_2$-rich sections of the plant. It will be shown in Chapter 7 that protective $FeCO_3$ films can be produced in 80 °C, $CO_2$-saturated $MDEA_{(aq)}$ solutions. These conditions are present in the pipelines between the exit of the heat exchanger and the inlet of the stripper (**Figure 3-9**).

The originally planned investigation, outlined here, was more extensive and ambitious relative to what was ultimately possible in the pandemic-induced circumstances. The intention in this feasibility study was to install the electrodes between the pipelines at the outlet of the pre-heater and inside the stripper for at least two weeks of continuous plant operation. The intended experimental matrix for each campaign is included in **Table 3-4**. A total of 18 coupons were to be installed in the plant under three conditions: two coupons were needed per condition per material so that one could be used for immediate *ex-situ* surface characterisation using SEM-EDX and XRD, and the other could be investigated using impedance spectroscopy in the laboratory and subsequently characterised using the aforementioned surface analysis techniques. This experimental matrix would have been useful for investigating the impact of flow regimes, temperature and film stability under realistic operating conditions. More importantly, comparison of the pre-treated CS with untreated CS and the current industry standard SS and would have enabled a critical assessment of the practicality of this corrosion mitigation strategy.

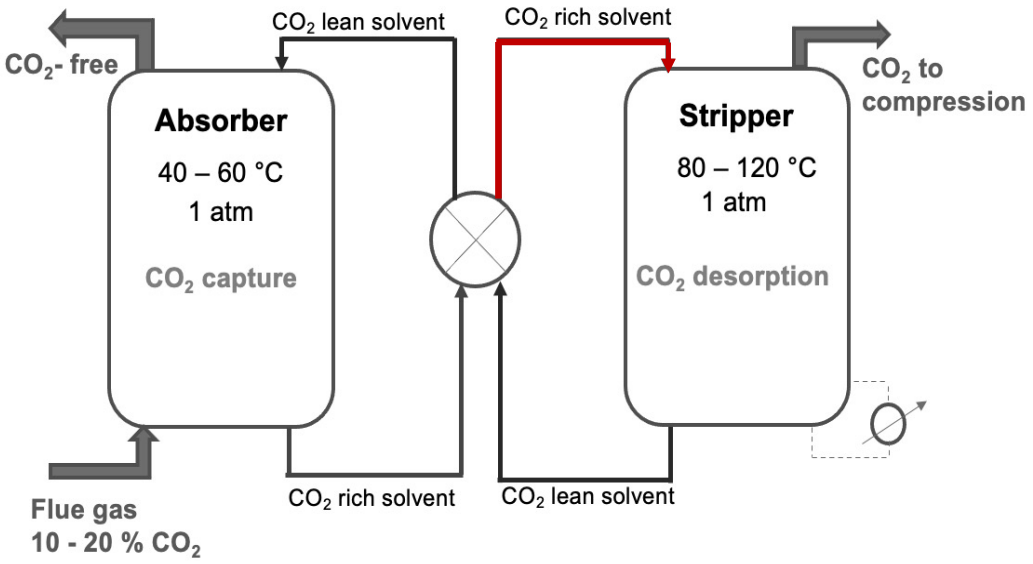



**Figure 3-9:** Schematic of carbon capture plant operation and the originally intended electrode installation locations (red).

**Table 3-4:** Matrix of experiments intended for each pilot plant study.

| Electrode | Conditions | Purpose |
|---|---|---|
| Pre-treated C1018<br>× two per condition | • Rich pipeline after absorber<br>• Rich pipeline before stripper<br>• Stripper inlet | To test stability of films on pre-treated coupons and quantify film protection<br>• Coupon 1: *Ex-situ SEM and XRD*<br>• Coupon 2*: EIS measurement and Ex-situ SEM and XRD* |
| Un-treated C1018 × two per condition | • Rich pipeline after absorber<br>• Rich pipeline before stripper<br>• Stripper inlet | To quantify added protection provided by coating<br>• Coupon 1: *Ex-situ SEM and XRD*<br>• Coupon 2*: EIS measurement and Ex-situ SEM and XRD* |
| Un-treated SS316L<br>× two per condition | • Rich pipeline after absorber<br>• Rich pipeline before stripper<br>• Stripper inlet | To compare coating protection to current standard<br>• Coupon 1: *Ex-situ SEM and XRD*<br>• Coupon 2*: EIS measurement and Ex-situ SEM and XRD* |

### 3.5.1.2 Executed experimental matrix

Unfortunately, only three tapping points were available in the pilot plant at the time this research was carried out. These points were located along the pipelines before the inlet of the absorber through which lean (*i.e.* $CO_2$-free) solvent flows (**Figure 3-10**).

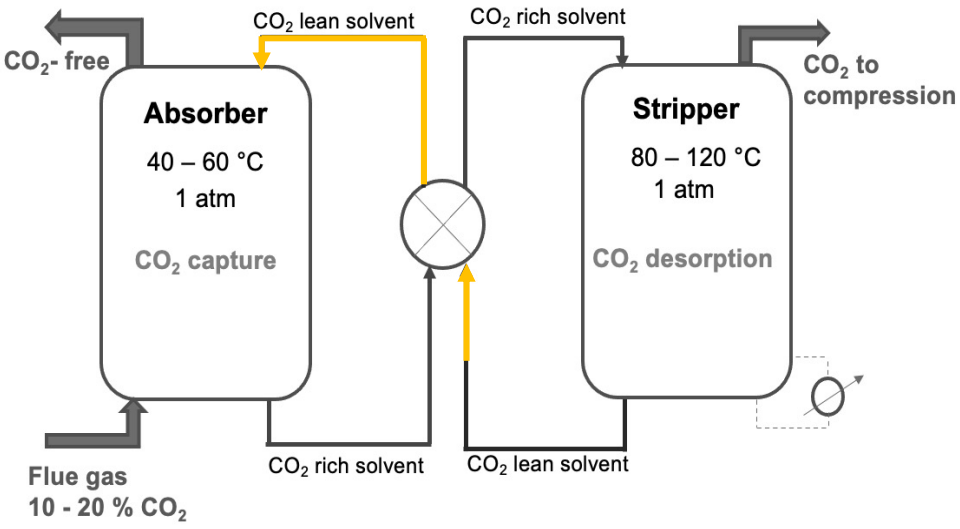



**Figure 3-10:** Schematic of the ICL Carbon Capture Pilot Plant with available tapping points for installation of electrodes (yellow) (does not show all heat exchangers present in the plant).

In an attempt to test the coupons under the relevant conditions, the plant was operated in manual mode, and the bottom of the stripper was heated only to sufficiently low temperatures *i.e.* < 80 °C to prevent desorption of $CO_2$. Theoretically, this should result in the solution exiting the bottom of the stripper being saturated with $CO_2$. The heat exchangers, which used cooling water as the coolant, were not supplied with cooling water to maintain the temperature. This operating protocol would allow the solvent flowing past the electrodes to be as hot and rich as possible. Although the plant could only be operated under relatively representative conditions, in addition to there being only three tapping points available, the plant was only available for *ca.* one month to conduct the studies reported in this thesis. This reduced availability was due to COVID-19:

i. The steam supply to the plant was not activated for at least 10 months and XV-140, which opens the steam supply to the plant, could not be opened. After weeks of troubleshooting, this problem was fixed.
ii. Remote undergraduate teaching was being conducted in the plant, which took substantially longer than in-person teaching. This decreased the availability of the plant for academic research experiments.
iii. Electrode fabrication and tests took longer due to reduced workshop operating hours.

Hence, only two studies were ultimately conducted in the available time. It was therefore decided that the three tapping points should be used to house one pre-treated CS electrode, one untreated CS electrode, to allow comparison between data collected from the two studies,

and one reference electrode for open circuit potential measurements. An image of the section of the pilot plant in which the coupons were installed is shown in **Figure 3-17**.

Lastly, the plant could only be operated when the plant operator was on campus and was fully available. The plant operation hours for the two tests were therefore dictated by the operator's availability. The electrodes were embedded in the plant for *ca*. 9.4 days (~ 225 hours). The plant was operational during five of these days and for five hours each day, giving a cumulative operational time of *ca*. 25 hours.

## 3.5.2 Electrodes used for pilot plant study

### 3.5.2.1 Working electrode

Carbon steel (C1018 ) coupons used in the pilot plant study were obtained from Imotron and manufactured by Alabama Specialty Products, USA. The dimensions and composition (supplied by manufacturer) of the coupons are given in **Table 3-5** and **Table 3-2.** An image of the coupon is shown in **Figure 3-2**.

**Table 3-5:** Physical properties of carbon steel coupons used for pilot plant studies including final dimensions and surface area exposed to electrolyte.

| **Density / kg dm$^{-3}$** | **Original dimensions (W × L ×T) / × 10$^{-3}$ m** | **Final dimensions (W × L × T) / × 10$^{-3}$ m** | **Final surface area × 10$^{-4}$ m$^2$** |
|---|---|---|---|
| 7.87 | 9.46 × 76.2 ×1.46 | 9.46 × 43.2 × 1.46 | 9.86 |

Electrode holders were designed and fabricated in-house by the Mechanical Workshop to house the carbon steel coupons and mount the coupons in the tapping points available in the pilot plant. The holders needed to be appropriately sized to (i) facilitate coupon insertion into the pipeline, enabling the coupon to be fixed in a particular orientation relative to the solution flow (length and thickness both perpendicular to the flow, width parallel to the flow), (ii) prevent leaking of the process fluid and (iii) allow for electrical measurements to be made. Two electrode holder prototypes were fabricated and installed in the selected tapping points in the plant and tested for leaks by increasing the pressure in the plant through $N_2$ injection and circulation of aqueous amine.

The final design required the coupons to be cut as shown in **Figure 3-11**, so that each could be slotted into a PEEK cap through a rectangular incision. The PEEK cap screwed into the main body of the holder, which was made out of glass-filled PTFE. Inside the PEEK cap, the

rectangular narrow edge of the coupon was inserted through a silicone wafer, sandwiched between two PEEK wafers, each with rectangular incisions. These three wafers sealed the opening, through which the coupon extended, to prevent electrolyte ingress to the body of the electrode holder. A stainless steel spring was used to electrically connect the top of coupon to a stainless steel rod, which protruded from the back of the electrode holder. A narrow groove was made at the end of the stainless steel rod to enable easy attachment of the crocodile clips, *via* which electrical connections were made. A 10.5 mm (0.41 ") hole was bored in a ½" hexagonal NPT plug, through which the electrode holder was inserted and screwed into the tapping points on the plant. Two silicone O-rings, fitted into two incisions made along outer body of the PTFE holder, were used to prevent process fluid from leaking between the holder and the NPT plug (**Figure 3-12**).

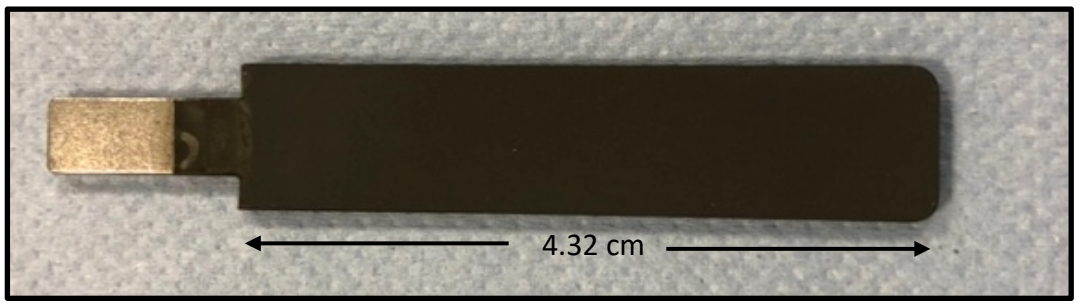



**Figure 3-11:** Carbon steel coupon cut to be fitted into working electrode holder

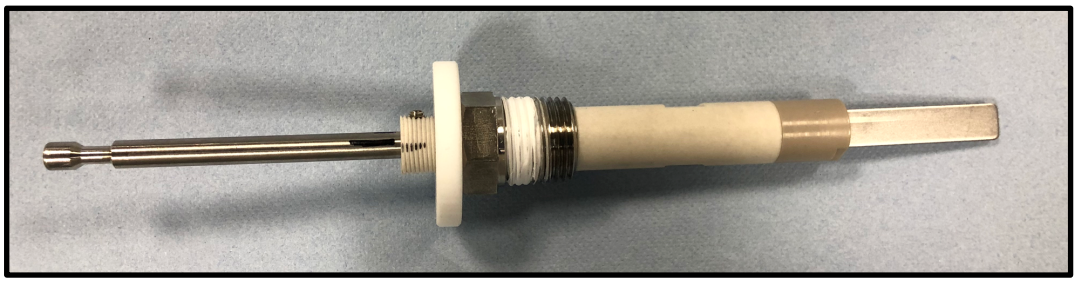


**Figure 3-12:** Final working electrode holder design

### 3.5.2.2 Reference electrode

A leak-free AgCl | Ag reference electrode with a PEEK outer body and a non-porous junction produced by Innovative Instruments, USA, was used for the pilot plant study. Since this electrode was leak-free, it was appropriate for long immersion periods. The PEEK outer body was also particularly suitable, as it could easily withstand the elevated pressures it was exposed to in the pilot plant and was chemically compatible with the amine solvent.

Another holder also needed to be fabricated to house the reference electrode. A similar design was used but, since the reference electrode was cylindrical, silicone O-rings could be used to prevent solution ingress through the reference electrode opening. The holder acted as a sleeve such that the top of the reference electrode protruded through the back of the holder, as shown in **Figure 3-13**.

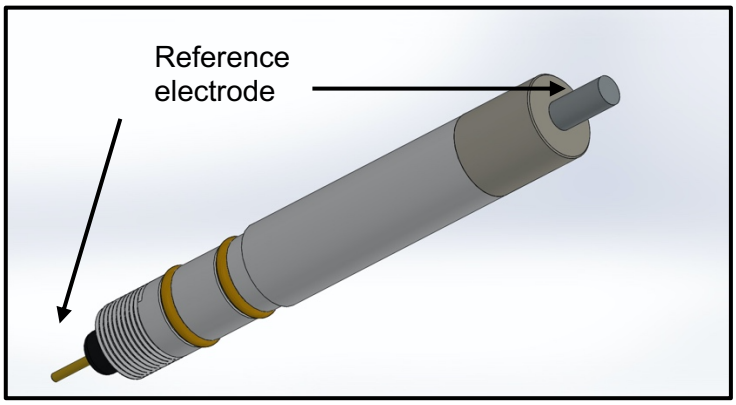



**Figure 3-13:** Reference electrode holder

## 3.5.3 Data acquisition

### 3.5.3.1 Open circuit potential data

A National Instruments Data Acquisition (NI DAQ) device, USB-6210, was used to acquire open circuit potential data of the two working electrodes against one common reference electrode. Two analogue differential input signals were measured using three input screened cables, which were attached to each of the three electrodes. NI DAQ Express software was used to record the data using two differential input channels. The sample collection was set to continuous mode with a sampling rate of 10 Hz (1 measurement per 0.1 seconds).

### 3.5.3.2 Pilot plant data

The ABB process control system continuously collects data from pH, temperature, pressure and flow detectors fitted throughout the plant. The solution pH, measured using detector AT100 located at the exit pipelines from the absorber (E101), fluid temperature near the electrodes, measured using TT210, and the fluid flow rate, measured using FT103, were relevant to this project. The detectors and major operating equipment are highlighted in the flowsheets shown in (**Figure 3-14** and **Figure 3-15**)

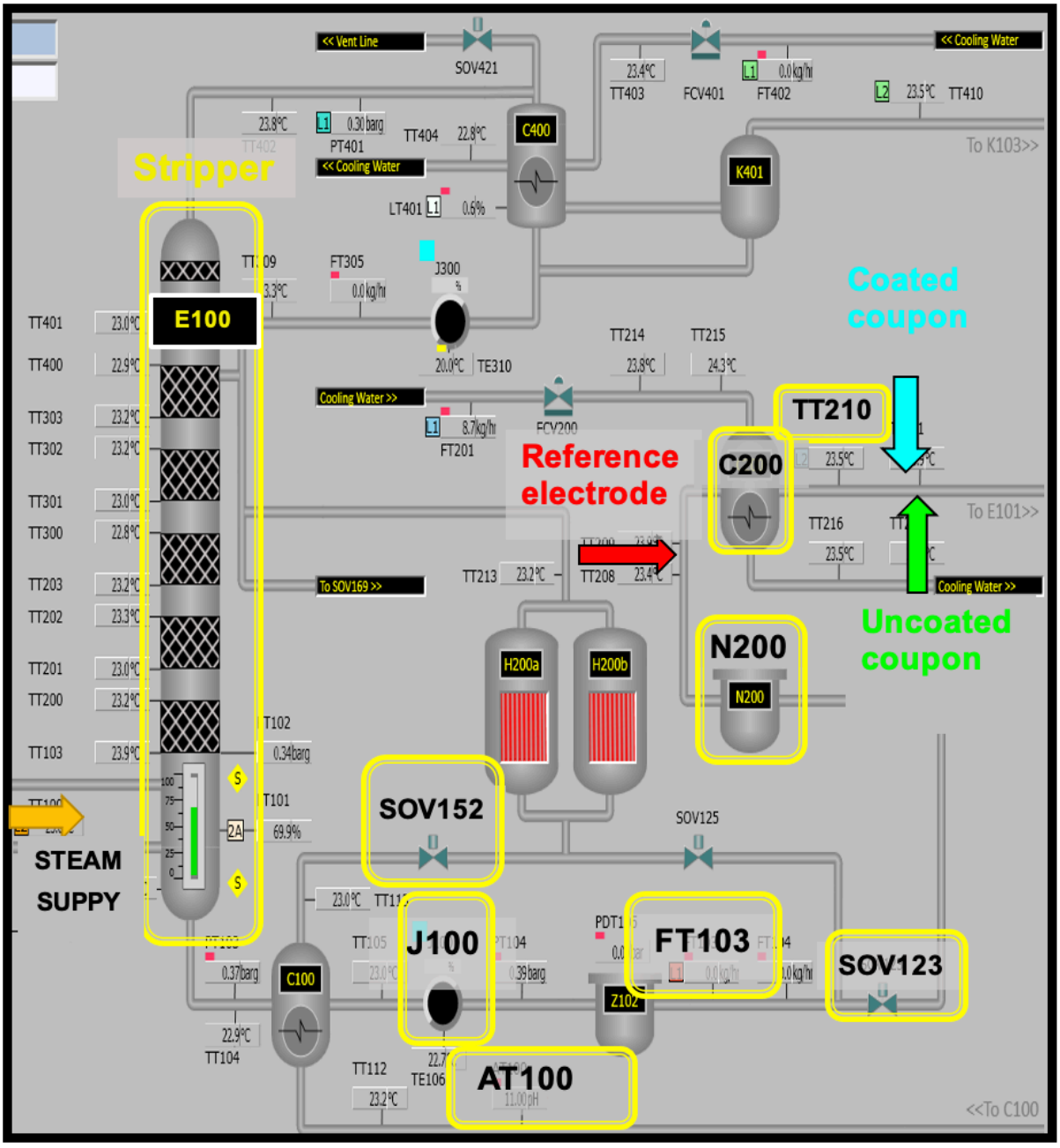



**Figure 3-14:** Annotated flowsheet showing a section of the Carbon Capture Pilot Plant with locations of electrodes shown in red (reference electrode), blue (coated *i.e.* pre-treated coupon) and green (uncoated *i.e.* untreated coupon). Yellow boxes highlight all relevant valves and equipment this section of plant.

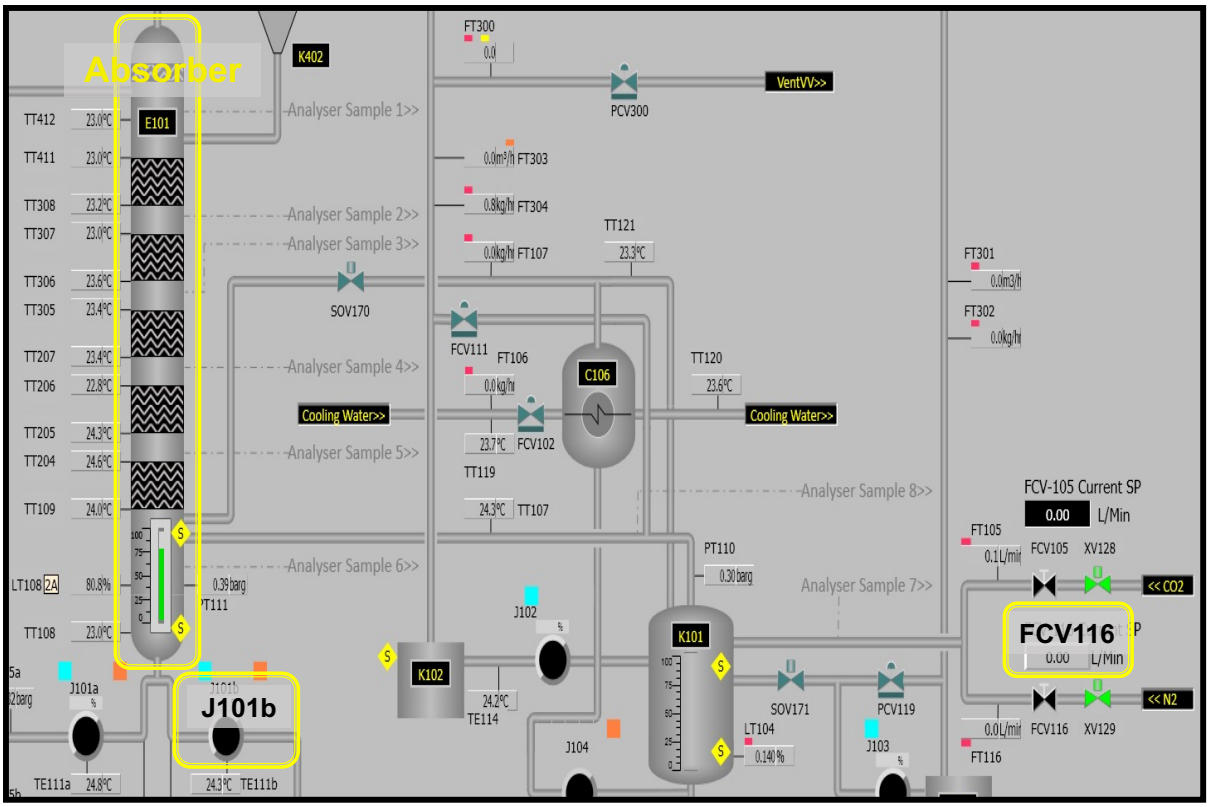



**Figure 3-15:** Section of flowsheet of the Carbon Capture Pilot Plant showing the $CO_2$ absorption column. Yellow boxes highlight all relevant valves and equipment in this section of plant.

## 3.5.4 Installation points and procedure

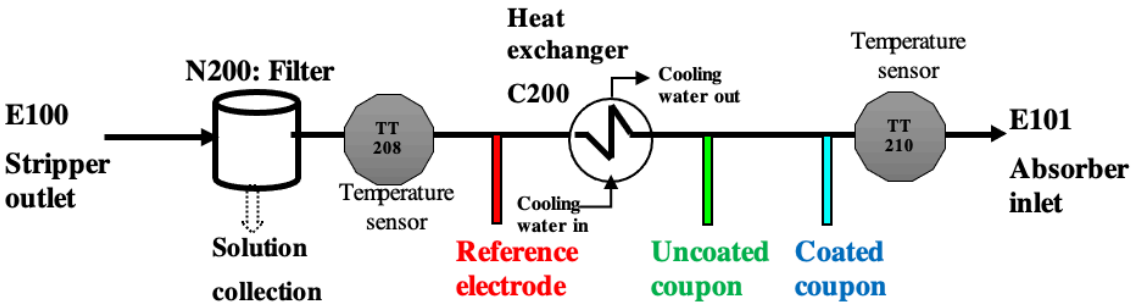



**Figure 3-16**: Schematic of reference electrode and coupon tapping points on the pilot plant.

Three tapping points were available on the plant. This allowed installation of three electrodes, one of which was a coated carbon steel coupon and the other an uncoated carbon steel coupon, and one reference electrode. The procedure for installing the electrodes was as follows:

1. The pipes, which the electrodes were installed in, were drained through filter N200 using the manual valve below the filter (**Figure 3-16**). The amine solution was collected to be fed back into the system after the installation. The valve was then closed, plug refitted with PTFE tape and inserted back into the line.
2. The reference electrode tapping point was then carefully opened and any remaining amine solution collected. The reference electrode was inserted into the line and the NPT plug tightened.
3. The white threading on the working electrodes (**Figure 3-12**) were marked to ensure that the coupon was oriented such that the thinnest edge of the coupon would be in line with the fluid flow direction. The NPT plug threads were then carefully wrapped in PTFE tape (> 6 turns) to prevent any leaks. The NPT fitting at the first working electrode tapping point was carefully removed and any remaining amine solution collected. The uncoated electrode was inserted into the pipeline and the NPT fitting tightened. The electrode was then rotated until the marking faced upward. The white disc was then tightened to fix the electrode orientation.
4. Temperature probe TT-211, which is the back-up temperature sensor to TT210, was then carefully removed so that its port could be used as a tapping point for the second working

electrode (**Figure 3-17**). The coated electrode was then inserted into the port following the same steps described in step 3.

5. The collected amine solution was then fed back into the stripper *via* a sampling point. The amine solution was poured into a funnel, the end of which was fitted with flexible PVC tubing, which was inserted into the sampling point near stage 2 of the stripper E100 (**Figure 3-16**).
6. The $N_2$ flow to the plant was then initiated through FCV116 to increase the pressure in the plant (**Figure 3-15**).
7. The electrodes were then checked for any signs of leaking.
8. The DAQ cables were then connected to the two working electrodes and the reference electrode. The DAQ express measurement was then started.
9. The amine solution was circulated around the plant in a figure eight loop by:
    i. Opening SOV152 and SOV123 to create a flow path between the bottom of the stripper E100 and the top of the absorber E101.
    ii. Pumps J100 at the bottom of E100 and J101b at the bottom of E101 were then set to a low flow rate of 5%.
10. The plant was left running in this mode for *ca*. 10 minutes until liquid flowing through the absorber was observed through the viewing window.
11. The electrodes were then checked again for any signs of leaking.
12. The DAQ measurements were compared to the voltage measurement between each working electrode and the reference electrode on an independent voltameter.
13. The plant was left running in this mode for *ca*. 1 hour.
14. Approximately 24 hours later, the electrodes were checked one more time for any signs of leaking.




**Figure 3-17**: Annotated photo of part of the ICL Carbon Capture Pilot Plant showing the location of the absorber and stripper (left) and close up photo of location of tapping points with installed reference electrode and uncoated and coated coupons.

## 3.5.5 Plant operation protocol

The procedure outlined below describes the general protocol followed, however, there were minor differences between each daily run.

1. The $N_2$ flow to the plant was started through FICV116 (**Figure 3-15**) to increase the pressure in the plant.
2. The amine solution was circulated around the plant in a figure 8 loop until the liquid level in the absorber and the stripper stabilised by:
    i. Opening SOV152 and SOV123 to create a flow path between the bottom of the stripper E100 and the top of the absorber E101.
    ii. Initiating pump J100 at the bottom of stripper and J101b at the bottom of the absorber and setting to a low flow rate of *ca*. 5 %. If the stripper level dropped too low (< 20 %) or if the deviation between the absorber and stripper was too large, pump J100 and J101b flow rates were altered to prevent further decrease or deviation respectively.
3. FCV105, which allows $CO_2$ to enter the plant, was then opened to allow a flow rate of 3.4 L $min^{-1}$ (0.4 kg $h^{-1}$) to 5 L $min^{-1}$ (0.59 kg $h^{-1}$).
4. The steam supply (*ca*. 150 °C, 5.4 bar(g)) to the plant was opened using XV140 (not shown). FCV110 was then opened to 1 % to begin heating the bottom of the stripper (**Figure 3-15**).
5. The plant was left running in this mode to heat the process solution. The temperature at the electrode eventually increased to *ca*. 60 °C but could not get to a higher temperature for a long period of time since the liquid levels in the stripper began to surge due to a phenomenon termed 'Ledinegg instability'. The pressure at the top of the absorber also began increasing due to vaporization of the amine solvent and the build-up of $CO_2$ at the top of the absorber because of (1) the lower residence time of the solvent in the absorber and (2) the amine being fed from the stripper being in rich form rather than lean. This increased pressure at the top of the absorber then impeded the flow of steam into the plant. The $CO_2$ and $N_2$ supplies were stopped intermittently throughout the operating period to prevent the pressure from increasing substantially.
6. When the pressure at the top of the absorber became > 0.45 bar(g), the pressure relief valve, PCV300 (not shown), was opened to varying degrees to vent the gas.

7. After the electrodes were exposed to a temperature of *ca*. 52 °C ± 2 °C (with the exception of Tuesday 12th January), for at least 1 hour, FCV110 was closed (**Figure 3-15**).
8. $CO_2$ (3.4 to 5 L $min^{-1}$) and $N_2$ (9 L $min^{-1}$) supplied to the plant were then re-started, unless already open, to ensure that the pressure at the top of the absorber did not drop substantially during the cooldown period.
9. The pumps J100 (**Figure 3-14**) and J101b (**Figure 3-15**) at the bottom of the stripper and absorber, respectively, were then increased from 5 % to 6 % and then to 8 %. This was done to remove the hot liquid in the stripper at a faster rate and consequently decrease the time for the plant to cool down sufficiently.
10. In two instances, the cooling water was pumped through heat exchanger C200 (**Figure 3-14**, **Figure 3-17**), located between reference and working electrodes, *via* FCV200, to reduce the temperature of C200 along with its inlet and outlet lines and in so doing, aid in decreasing the process fluid temperature throughout the system. This meant that the solutions to which the electrodes were exposed would have undergone a rapid temperature change. This step was only done during the first high temperature operational day (for both tests). It was not repeated on subsequent days since rapid cooling of the process fluid is not representative of the normal plant operation.
11. When the temperature transmitter readings (TT102-3, TT200-3, TT300-3, TT400-1) on the stripper column (**Figure 3-14**) decreased to < 65 °C, the manual valves on the steam line were shut.

It is worth mentioning that in both studies when the electrodes were initially installed, process fluid was circulated through the plant for *ca*. 1 hour at room temperature and then left for *ca*. 24 hours before the first operational period, where the plant was run at higher temperatures as described in 3.5.5. Since the process fluid was circulated for a short duration and at room temperature, it was not counted as a period.

## 3.5.6 Electrode pre-treatment and post pilot plant analysis

Two pre-treatment solutions were used in this study: 1 M $MDEA_{(aq)}$ – $CO_2$ and 3 M $MDEA_{(aq)}$ – $CO_2$, 80 °C. 250 mL of 1 M and 3 M $MDEA_{(aq)}$ solutions were prepared, heated to 80 °C, and saturated with $CO_2$. Pre-cut carbon steel coupons were inserted into electrode holders, designed similarly to that shown in **Figure 3-12**, and the stainless steel rod was threaded through a hole bored in a silicone septum stopper. A mounted coupon was immersed in each pre-treatment solution. The OCP was measured until it stabilised (at most $|\Delta E| < 1$ mV $h^{-1}$) the electrochemical impedance was recorded at the OCP with an AC-signal amplitude of ±10 mV, for a frequency range of $10^6$ – $10^{-2}$ Hz with 10 points per frequency decade. When there was no longer any change in the EIS data for more than 24 hours, the CS electrode was removed from the solution. After removing from the solution, the coupons were wiped to remove any residual solution, removed from the sample holder and mounted into the electrode holders fabricated for the pilot plant.

At the end of the immersion period in the pilot plant, an aliquot of pilot plant solution was collected from the tap located below the filter. The samples of the pilot plant solution were heated to the maximum temperature of the process fluid in the pilot plant, and saturated with $CO_2$. The coupons, which were previously installed in the pilot plant, were detached from the electrode holders and mounted into the lab sample holders. The coupons were then immersed in the prepared sample of the pilot plant solution and the OCP and EIS at OCP measured using the same specifications as those described in the pre-treatment process.

Two extra coupons were pre-treated in the 1 and 3 M $MDEA_{(aq)}$ solutions to allow for surface characterisation using SEM-EDX and XRD. The coupons which were installed in the pilot plant were similarly characterised after conducting the OCP and EIS tests in the laboratory.

## 3.6 Surface characterisation and solution analytical techniques

### 3.6.1 Surface characterisation techniques

#### 3.6.1.1 Scanning electron microscopy and electron dispersive X-ray spectroscopy

The surface morphology and topography of electrodes and coupons were investigated using a JEOL JSM 6010 LA scanning electron microscope (SEM) which has an integrated electron dispersive X-ray (EDX) spectrometer. In a SEM an electron gun produces electrons which are accelerated towards an anode and focused through lenses. The focused electron beam scans the sample and, on contact with the sample, triggers the displacement and release of electrons from within a few nanometres of the sample's surface. These electrons are detected and an image is built-up, which gives a topographical description of the sample. The accelerating voltage and spot size of electron beam, along with the magnification, focus, astigmatism, brightness and contrast of the image are controlled to improve image quality. An accelerating voltage of 20 kV and a beam spot size 50 – 60 was used to capture surface images presented in the Chapters 4 to 8 of this thesis.

The EDX spectrometer was used to attain an elemental analysis of electrodes and coupons, which were imaged using the SEM. In this technique, the sample is irradiated with a high energy beam of electrons or protons. On contact, the high energy particles knock electrons out from the higher binding electron level of atoms on the sample. This leaves a vacancy in the energy level of the atom, which results in an X-ray of a specific wavelength being emitted. This detected X-ray is characteristic of the atomic structure of the element and therefore gives the elemental composition of the sample. Both the chemical elements and relative abundance within a point or area on the sample can be attained. It is important to note that there are different types of characteristic X-rays, which are categorised based on the shells in which the initial vacancy is created and the shell from which the electron comes from to fill that vacancy. X-rays classed as K-series are the most effective, yielding the highest intensity and so detection is most accurate. As the atomic number of the element increases, the effectiveness of the X-ray generated increases *i.e.* higher intensity radiation is emitted, which results in a more accurate elemental analysis. Accordingly, detection of lower

atomic number elements (*i.e.* C and O) is less accurate. This is particularly relevant in this thesis since the primary elements observed throughout this study are Fe, C, O.

**Sample preparation**

Iron disc electrodes used for chronoamperometry experiments, carbon steel disc electrodes used for EIS experiments and coupons from the preliminary immersion tests and the two pilot plant studies were characterised using SEM-EDX. Images of the cross-section of coupons from the preliminary immersion test were also obtained using the SEM.

All samples were rinsed with DI water and dried before analysing with SEM-EDX. Coupon samples of size 5 mm × 5 mm were cut using a vice and hacksaw. The coupon samples or disc electrodes were mounted on Agar Scientific 100 mm stubs using adhesive carbon discs. The coupons used for cross-section imaging were placed upright in a mounting cup using support clips and then embedded in an epoxy mounting resin. The resin was left to dry overnight then detached from the mounting cups. The samples were then wet ground using P600, P800, P1200, P2400 grinding papers sequentially on a Buehler Alpha 2 speed grinder-polisher, and then polishing by hand with 0.03 μm alumina polishing suspension on a polishing cloth until a mirror finish was achieved, and thoroughly rinsed. This method ensured that the top layer of resin was removed to reveal a uniform cross-section. The mounting resin, cups and support clips were purchased from Buehler (ITW Test & Measurement GmbH, Germany).

Dust and metal filing residue were removed from the surface using compressed air just before coating the sample. Silver paint was applied to one corner of the sample to the stub or from the metal sample to the bottom of the mould to ensure good electrical conductivity and subsequently coated with gold using EMITECH k550 Golder target coater at 20 mA for 30s.

### 3.6.1.2 X-ray diffractometry

The PAnalytical X-Pert X-Ray Diffractometer was used for *ex-situ* detection of crystalline phases (*e.g.* Fe, $FeCO_3$, $Fe_2O_3$, $Fe_3O_4$) on coupons after immersion in $amine_{(aq)}$ solutions, and on electrodes after chronoamperometry and EIS experiments.

In this technique, a beam of electrons is produced by heating a filament in a cathode ray tube, which is then filtered to produce monochromatic radiation and accelerated towards the sample by application of a voltage. When the monochromatic beam of X-rays is incident on

the crystalline material, X-ray beams are re-emitted by the electrons in the atoms present in the highly ordered crystalline lattice in the sample through a process termed elastic scattering.

At very specific incident angles, the elastically scattered waves constructively interfere, which results in strong amplification of the waves. The diffracted waves are detected and the signal intensity is converted to a count rate. The angle between the sample, the detector and the source X-ray are rotated, which allows development of a spectrum of signals with peaks appearing at points of constructive interference. Using Bragg's law (Equation **3-5**), which relates the spacing between planes of atoms (*d*) in the crystal lattice to the angle between the incident and scattered X-rays ($2\theta$) and the wavelength of the incident X-ray ($\lambda$), the recorded intensity at each angle is converted to a *d*-spacing which reveals the phase identity through comparison to standard reference patterns; ***n*** is the diffraction order.

$$\mathbf{n}\,\lambda = 2\mathrm{d}\sin(\theta) \qquad \textbf{3-5}$$

**Sample preparation**

Iron disc electrodes from chronoamperometry experiments, carbon steel disc electrodes from EIS experiments and coupons from the preliminary immersion tests and pilot plant studies were prepared for XRD by first washing the sample with DI water and, in the case of the coupons, cutting a 10 mm × 10 mm square using a vice and hacksaw. Each sample was mounted on a sample holder using plasticine if necessary. All samples were analysed for $2\theta$ = 10 ° to 100 ° with a step size of 0.0334 s and scan time of 40 s. X-ray diffraction pattern were analysed using X'Pert High Score Plus software.

## 3.6.2 Solution analytical techniques

### 3.6.2.1 Inductively coupled plasma mass spectrometry

The elemental Fe concentration of solutions used in electrochemical experiments and aliquots of the pilot plant solution were detected using an Agilent 7900 inductively coupled plasma mass spectrometry (ICP-MS).

In this instrument, the liquid samples are pumped into the system *via* a peristaltic pump to a nebuliser where it is converted to an aerosol. The aerosolised sample droplets are then transported to a plasma torch. The plasma is produced by partially ionising either He for detection of Mn or Cr and $H_2$ for detection of Fe. The plasma ionises the sample droplets and the ions are extracted through a quadrupole which separates the ions based on their mass to

charge ratio. The separated ions are then transported to an electron multiplier detector where the emission spectra is detected from the excited sample ions. The emission spectra enables determination of the elemental species present and the species concentration is determined by comparison to the emission intensity using standard solutions of known concentrations. The ICP-MS was calibrated for Fe, Cr and Mn using 0, 5, 50, 100, 500 ppb standard solutions.

**Sample preparation:**

An ICP matrix solution was made by diluting 69 % nitric acid AnalaR NORMAPUR analytical grade to 2 %. 10 mL samples were then prepared by diluting the samples by a factor of 1000 in the ICP matrix solution to ensure that Fe sample concentration was < 500 ppb. The 10 mL samples were then filtered using a syringe filter (0.22 μm). Three sets of each sample were prepared and the mean and standard deviation was determined and presented. The ion concentration of blank solutions (ICP matrix solutions) were measured at the beginning of each run and at intervals between samples to verify that there was no sample carryover between samples.

# 4 Preliminary immersion study

## 4.1 Introduction

The corrosion of carbon steel in amine scrubbing plants has been reported to be enhanced in monoethanolamine (MEA) relative to other amines, specifically methyldiethanolamine (MDEA), both in natural gas processing (NGP) (Kohl & Nielsen, 1997b, 1997a; DuPart, Bacon & Edwards, 1993a) and post combustion carbon capture (PCCC) (Tomoe, Shimizu & Kaneta, 1996; Kittel *et al*., 2009; Gunasekaran, Veawab & Aroonwilas, 2013) plants. The hot (80 °C), $CO_2$ saturated $MEA_{(aq)}$ and $MDEA_{(aq)}$ solutions have a pH of *ca*. 7.7 – 8.6, at concentrations of 1 – 5 M, and according to the potential-pH diagram (**Figure 2-12**), $FeCO_3$ is the most thermodynamically stable phase within the potential range of *ca*. -0.55 to -0.40 V in both solvents. Based on the literature however, compact $FeCO_3$ films have not been observed on carbon steel in 5 M $MEA_{(aq)}$ solutions. Preliminary studies (Campbell, Yu & Williams, 2017a, 2017b; Sadeek, Williams & Campbell, 2017) have proposed the pre-treatment of carbon steel with $MDEA_{(aq)}$ to induce the formation of an $FeCO_3$ film but have only demonstrated the formation of films in 5 M $MDEA_{(aq)}$ solutions. This brief chapter therefore serves to confirm the observation of $FeCO_3$ film formation made in previous studies, and to determine if consistent behaviour is exhibited over a range of MDEA concentrations (1 – 5 M). The surface films, if any, formed on carbon steel in $MEA_{(aq)}$ will also be verified and it will be determined if similar behaviour is observed over a range of concentrations (1 – 5 M). No electrochemical experiments were conducted in this chapter, only an elementary analysis based solely on surface characterisation. A description of the procedure can be found in Chapter 3, Section 3.1.

## 4.2 Results

Carbon steel coupons were immersed in $CO_2$ saturated $MEA_{(aq)}$ and $MDEA_{(aq)}$ solutions for a one week period at 80 °C, conditions representative of the heat exchanger and pipelines between the heat exchanger and inlet to the stripper. The surface area to volume ratio (*A*/*V*) was relatively high at *ca*. 3.9 $m^{-1}$, which has been observed to be conducive to $FeCO_3$ formation. The coupons were then retrieved from the solution, washed and analysed using SEM and XRD. Whilst immersed, the carbon steel coupons would have undergone corrosion, which would have resulted in release of Fe ions from the coupon into the solution. A sample of each solution was taken after retrieval of the coupons at the end of the immersion period and analysed using ICP to determine the Fe concentration.

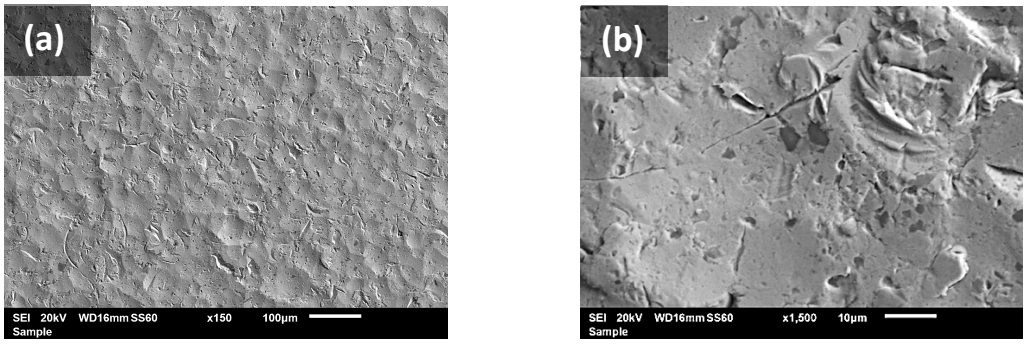



**Figure 4-1:** SEM surface images of a pristine carbon steel (C1018) at **(a)** low magnification (150x) and **(b)** high magnification (1500x).

### 4.2.1 Carbon steel immersion in aqueous monoethanolamine saturated with $CO_2$

**Figure 4-2 - Figure 4-4** show the surface analyses of the coupons exposed to 5, 3 and 1 M $MEA_{(aq)}$ solutions. At the end of the one week immersion period, the 5 M solution had an Fe ion concentration of 218 mg $dm^{-3}$, indicating significant Fe dissolution had occurred. The coupons exposed to this solution appeared cracked and roughened with no obvious signs of surface film formation. This appeared to be consistent across the surface as can be seen from the low magnification (200x) image. This was confirmed by EDX (not shown) and XRD (**Figure 4-2b**), which detected only ferrite. These observations are consistent with those reported by (Xiang *et al*., 2014; Yu, Campbell & Williams, 2016; Yu *et al*., 2017; Sadeek, Williams & Campbell, 2018).

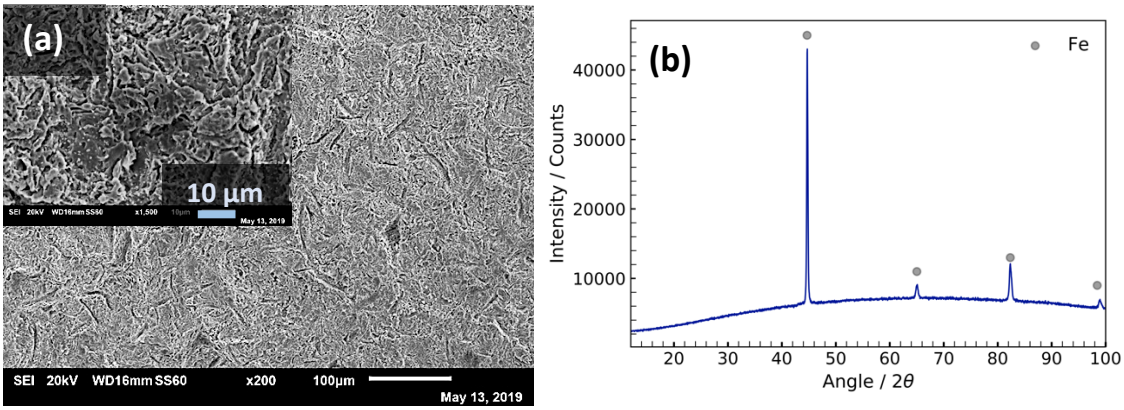



**Figure 4-2**: Surface characterisation of a carbon steel coupon after immersion in 5 M $MEA_{(aq)}$ solution saturated with $CO_2$ ($pH_{80\ °C}$ 7.9) for one week at 80 °C. **(a)** Surface images taken with an SEM (200x magnification), inset (1500x magnification). **(b)** XRD pattern; grey circles (o) indicate peaks corresponding to ferrite (α-Fe).

The dissolved Fe concentration of the 3 M solution at the end of the immersion period was detected to be 83.2 mg $dm^{-3}$, less than 40 % of that detected in the 5 M solution. Surface images showed that the coupon exposed to the 3 M solution (**Figure 4-3**) was less cracked and roughened than that exposed to the 5 M solution and from closer inspection some product was deposited on the surface. The visibly uncovered areas were detected to have an Fe composition of 75.6 % by mass and a C content of 20 % by mass, with minimal O detected, whilst the areas with product were detected to have a lower relative Fe composition of 50 % and C and O composition of *ca*. 25 % by mass. The composition expected for $FeCO_3$ is Fe: 48 %, C: 10 % and O: 41 % by mass. $Fe_2O_3$ has a composition of Fe: 52 % and O: 17 % and $Fe_3O_4$ a composition of Fe: 78 % and O: 22 %. No crystalline products were, however, detected with XRD (**Figure 4-3b**). The product identity is therefore unclear but based on the detected composition it could be an amorphous Fe-oxide species on an Fe–$Fe_3C$ substrate. Therefore, it can be deduced that crystalline $FeCO_3$ was not present on the surface.

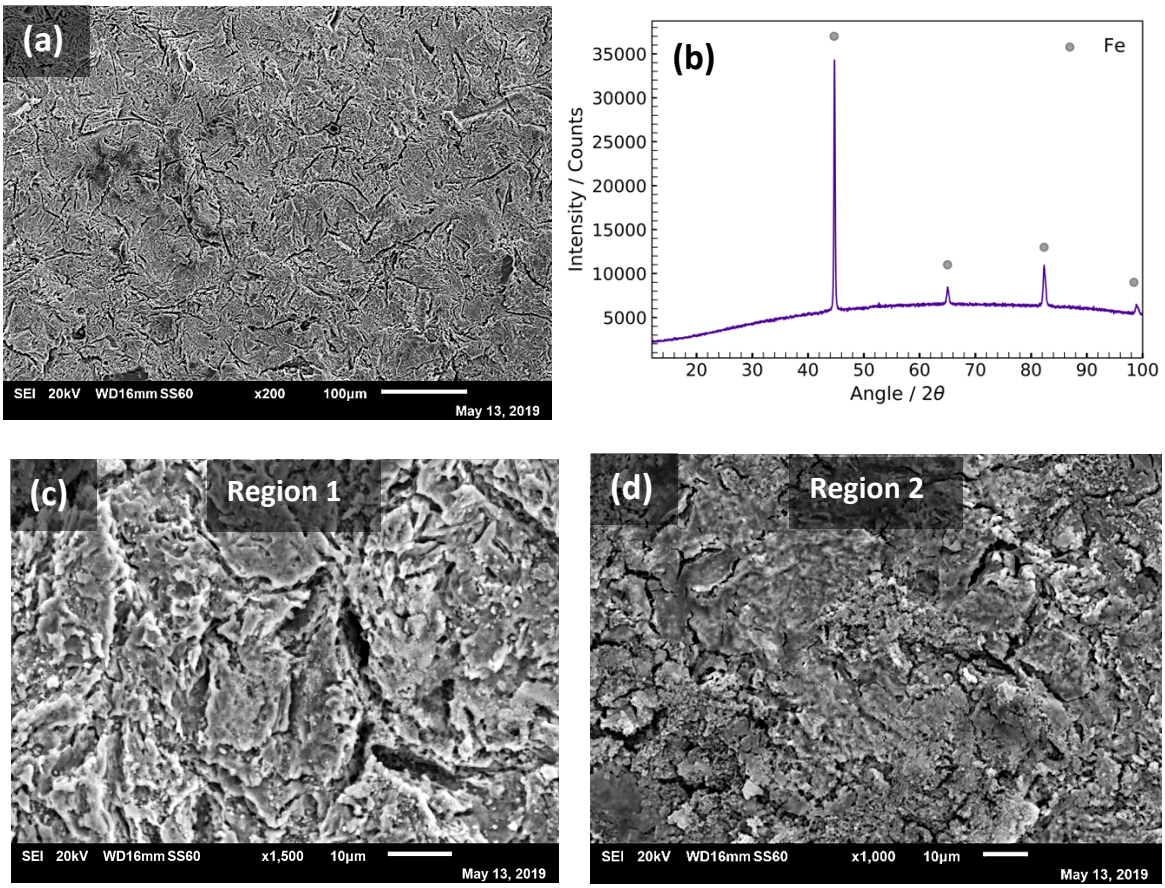



**Figure 4-3:** Surface characterisation of a carbon steel coupon after immersion in 3 M $MEA_{(aq)}$ solution saturated with $CO_2$ ($pH_{80\,°C}$ 7.8) for one week at 80 °C. Surface images taken with an SEM **(a)** 200x, **(c)** 1500x, **(d)** 1000x magnifications. **(b)** XRD pattern; grey circles (o) indicate peaks corresponding to ferrite (α-Fe).

**Table 4-1:** Average composition of different regions on the coupon after immersion in 3 M $MEA_{(aq)}$ solution saturated with $CO_2$ ($pH_{80\,°C}$ 7.8) for one week at 80 °C, detected using EDX.

| Component | Region 1 (% by mass) | Region 2 (% by mass) |
|---|---|---|
| **Fe** | 75.61 ± 3.2 | 50 ± 2.1 |
| **C** | 19.9 ± 0.1 | 25.31 ± 0.2 |
| **O** | 4.79 ± 1.1 | 24.48 ± 1.3 |

The 1 M solution had an exceedingly low Fe concentration of 0.4 mg $dm^{-3}$ at the end of the immersion period and the surface images (**Figure 4-4**) revealed very different behaviour than that noted in the 3 and 5 M solutions. The coupon appeared to be covered by a surface film

(**Figure 4-4a**) composed of some *ca*. 1 μm crystals (**Figure 4-4c**). These were detected by XRD to be $FeCO_3$ (**Figure 4-4b**). The crystalline product was not however densely packed and small areas (*ca*. 6 μm) of uncovered substrate were apparent (**Figure 4-4c**).

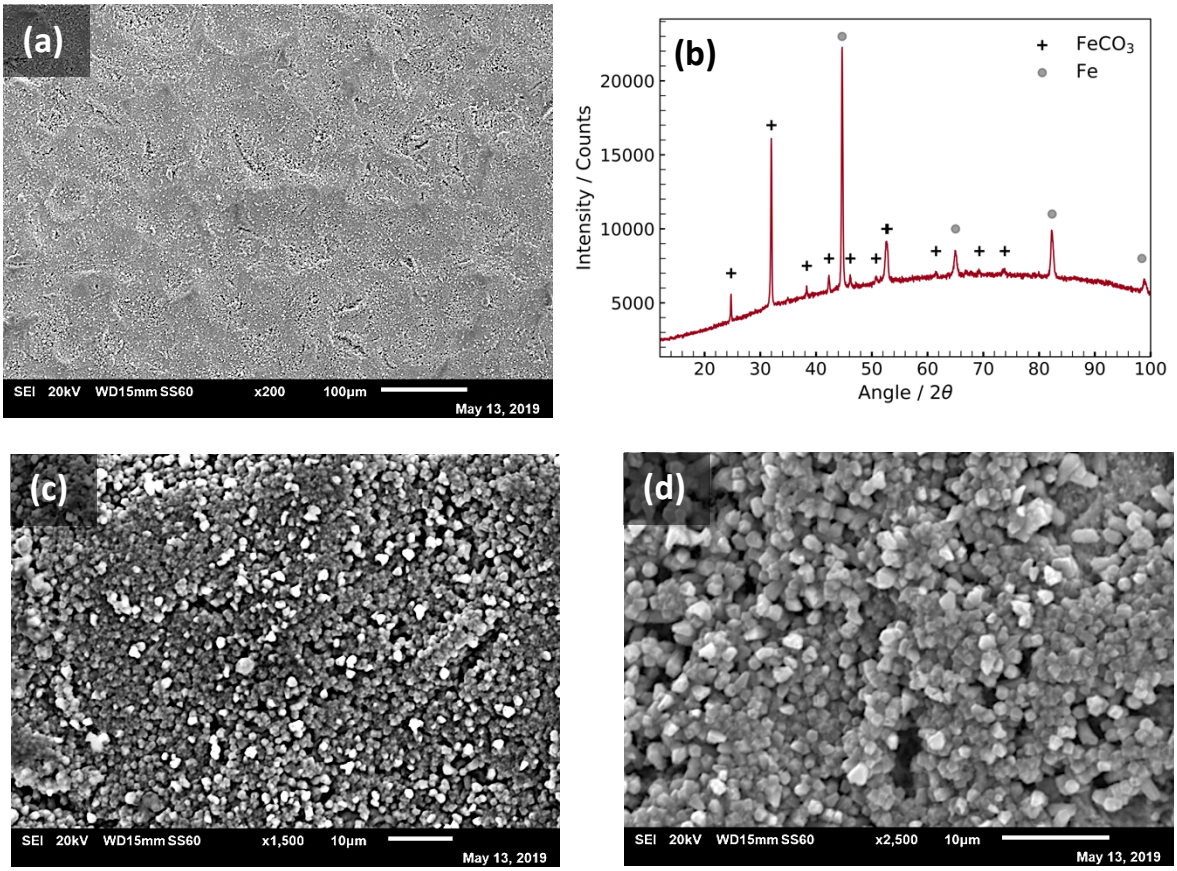



**Figure 4-4:** Surface characterisation of a carbon steel coupon after immersion in 1 M $MEA_{(aq)}$ solution saturated with $CO_2$ ($pH_{80\,°C}$ 7.7) for one week at 80 °C. Surface images taken with an SEM **(a)** 200x, **(c)** 1500x, **(d)** 2500x. **(b)** XRD pattern; grey circles (o) indicate peaks corresponding to ferrite (α-Fe) and black plus signs (+) indicate peaks corresponding to $FeCO_3$.

Based on these results, it can be confirmed that $FeCO_3$ is less likely to form at higher MEA concentrations, even when the dissolved Fe concentration in solution is relatively significant. In the most dilute $MEA_{(aq)}$ solution of 1 M however, $FeCO_3$ did in fact form. This is consistent with findings presented in a study by (Tomoe, Shimizu & Kaneta, 1996) where it was reported that $FeCO_3$ films were detected on carbon steel (STPG 38) after immersion in $10^{-2}$ to 2 M $MEA_{(aq)}$ solutions, but not at higher concentrations.

### 4.2.2 Carbon steel immersion in aqueous methyldiethanolamine saturated with $CO_2$

**Figure 4-5** and **Figure 4-6** show the surface analyses of the coupons exposed to 5, 3 and 1 M $MDEA_{(aq)}$ solutions and the dissolved Fe concentration present in the solutions at the end of the one week immersion period were 99.6, 64.1 and 9.9 mg $dm^{-3}$ respectively. The coupon exposed to the 5 M solution was covered in a surface film, though gaps (*ca*. 10 μm) were apparent even from the low magnification (200x) images (**Figure 4-5a**)**.** The surface film appeared, from the surface images, to be composed of trigonal-capped habits, diameter *ca*. 4 μm, (**Figure 4-5c**) similar to that described by (Joshi *et al*., 2018) for $FeCO_3$. XRD confirmed the presence of $FeCO_3$ with the signal intensity of the predominant $FeCO_3$ peak ($2\theta$ = 32 °) *ca*. 2.6 times that of the predominant ferrite peak ($2\theta$ = 45 °) (**Figure 4-5d**), suggesting a relatively thick film. Imaging of the cross-section (Appendix, Section 12.2) indicated a surface film of *ca*. 6.7 μm. The surface exposed by the minor gap was detected by EDX to have a composition of *ca*. Fe: 9 %, C: 29 % , O: 36 %, Si: 26 % (by mass) (**Table 4-2**). The low Fe content suggests that the exposed area may not be the substrate, but the high Si composition suggests that it was. In fact, the darkened spots observable on the pristine carbon steel sample shown in **Figure 4-1b** were detected by EDX (not shown) to have a relatively higher composition of the other alloying elements (*e.g*. Si, Mn).

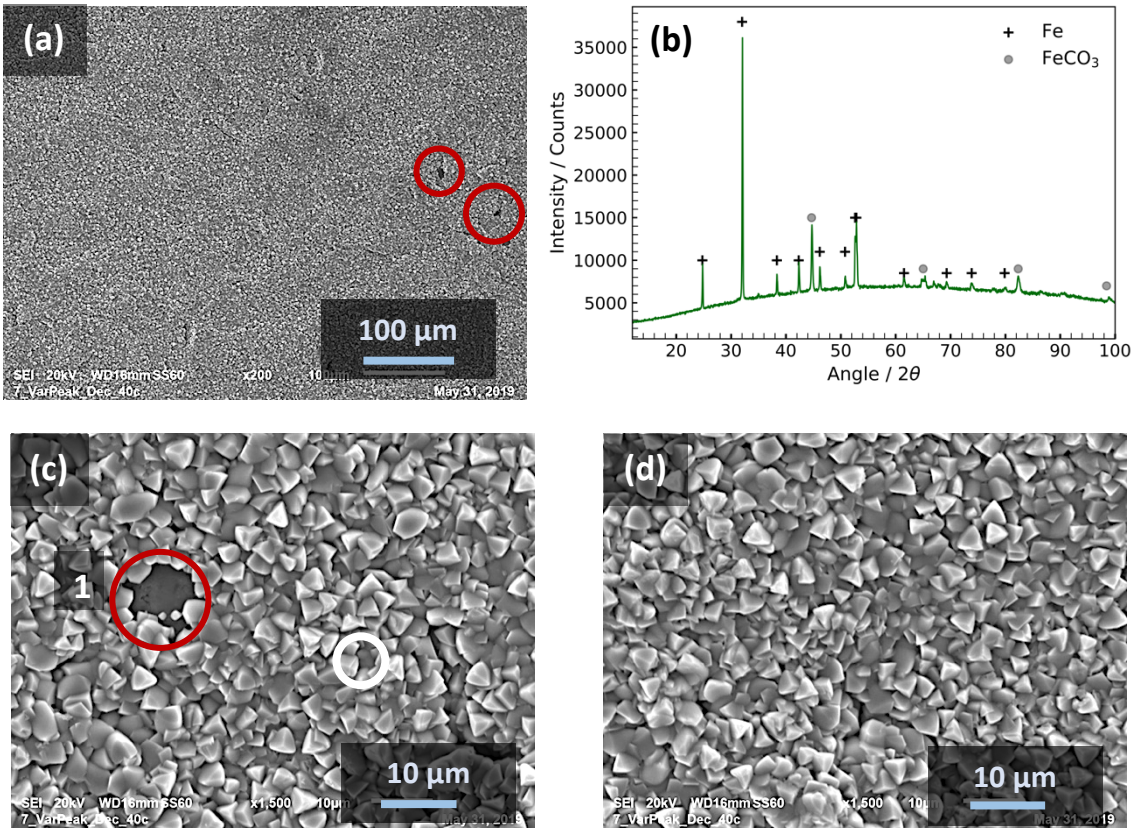



**Figure 4-5:** Surface characterisation of a carbon steel coupon after immersion in 5 M $MDEA_{(aq)}$ solution saturated with $CO_2$ ($pH_{80\,°C}$ 8.6) for one week at 80 °C. Surface images taken with an SEM **(a)** 200x, **(c)** 1500x, **(d)** 1500x. **(b)** XRD pattern; grey circles (o) indicate peaks corresponding to ferrite (Fe) and black plus signs (+) indicate peaks corresponding to $FeCO_3$.

**Table 4-2:** Average composition of different regions on the coupon after immersion in 5 M $MDEA_{(aq)}$ solution saturated with $CO_2$ (pH 8.6) for one week at 80 °C detected using EDX. Region 1 corresponds to the area enclosed by the red circle and Region 2 by the white circle in **Figure 4-5c**.

| Component | Region 1 (% by mass) | Region 2 (% by mass) |
|---|---|---|
| **Fe** | 8.80 ± 6.54 | 56.22 ± 11.46 |
| **C** | 29.38 ± 0.97 | 17.67 ± 1.34 |
| **O** | 35.52 ± 6.13 | 26.11 ± 10.11 |
| **Si** | 26.32 ± 0.56 | N/A |

The coupon exposed to the 3 M solution also appeared to have developed a complete film, similar to that observed for the coupon exposed to the 5 M solution, but with no observable gaps (**Figure 4-6b**). The crystalline product appeared to have the same shape as that developed in the 5 M solution and crystallites were of a similar size of *ca*. 3 – 4 μm. XRD confirmed the surface film was composed purely of $FeCO_3$ (**Figure 4-6a**), with the predominant $FeCO_3$ peak ($2\theta$ = 32 °) *ca*. two times that of the predominant ferrite peak ($2\theta$ = 45 °), suggesting a slightly less thick film than that formed in the 5 M solution. It was confirmed by imaging of the cross-section that the surface film was *ca*. 5.1 μm (Appendix, Section 12.2).

Similar behaviour was observed for the coupon immersed in the 1 M solution as that demonstrated in the higher concentration solutions, but a few distinctions should be mentioned. From the low magnification (200x) image (**Figure 4-6c**), the film appeared to be thin, as it resembled the slightly undulating topography observable on a pristine coupon (**Figure 4-1a**). The XRD pattern also suggested this with the predominant $FeCO_3$ peak being only *ca*. 1.4 more intense than the major ferrite peak. It should be noted that the comparison of the relative peaks between the three XRD patterns or even within each pattern is not necessarily accurate since the background signal exhibited by the bending of the spectra were not even. The inference of the comparative thicknesses of the films were however corroborated with imagining of the cross-section, from which a thickness of *ca*. 4 μm was determined (Appendix, Section 12.2). The surface film also appeared to be more densely packed, than those produced in the more concentrated solutions, with the majority of the crystals being relatively small *ca*. 1 -2 μm.

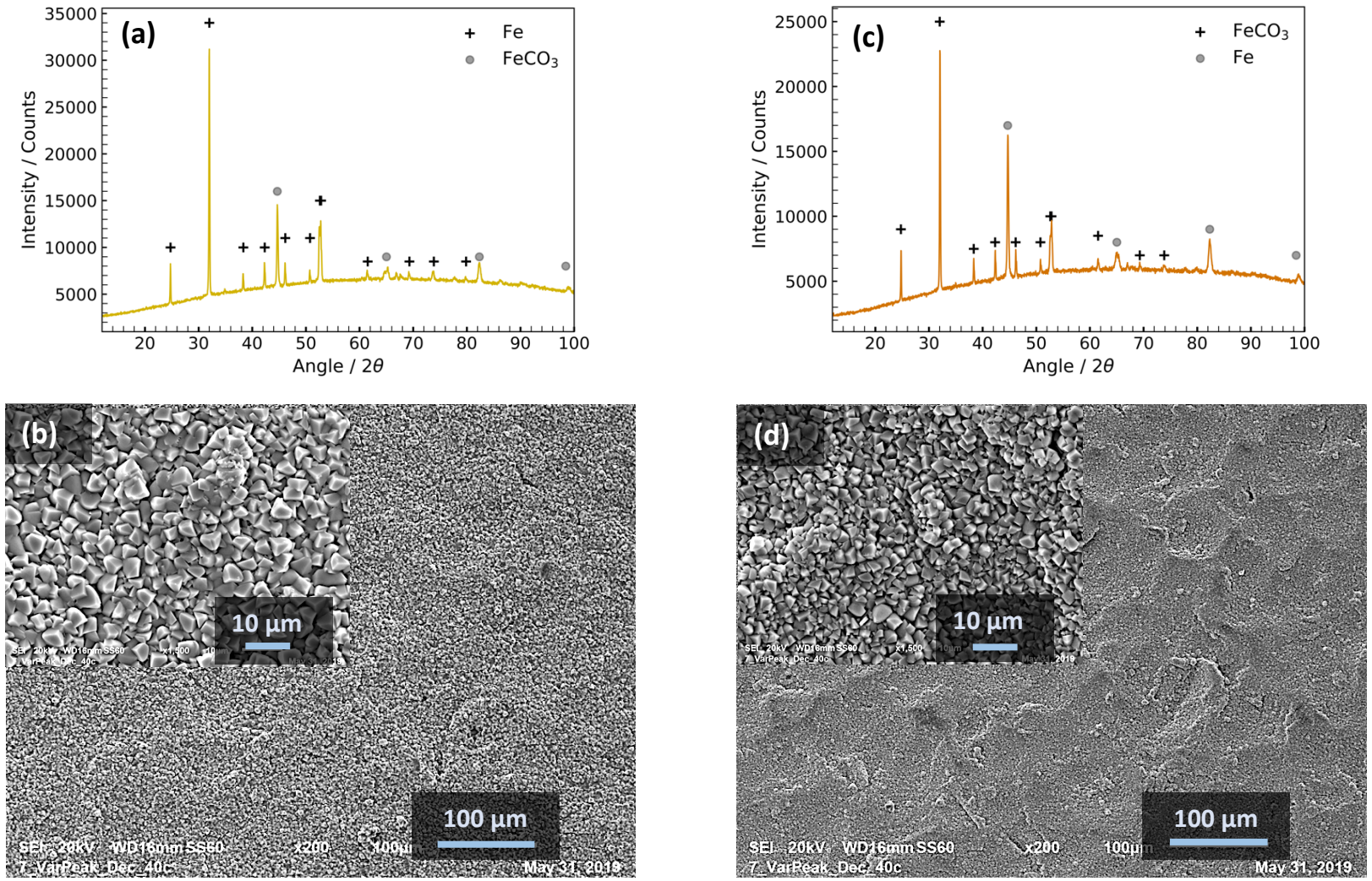



**Figure 4-6:** Surface characterisation of carbon steel coupons after immersion in **(a - b)** 3 M $MDEA_{(aq)}$ solution saturated with $CO_2$ ($pH_{80\,°C}$ 8.3), **(a)** XRD pattern and, **(b)** SEM surface images at 200x magnification, inset 1500x magnification; and **(c - d)** 1 M $MDEA_{(aq)}$ solution saturated with $CO_2$ ($pH_{80\,°C}$ 7.9), **(c)** XRD pattern and **(d)** SEM surface images at 200x magnification, inset 1500x magnification, both for one week at 80 °C.

## 4.3 Conclusions

The behaviour of carbon steel, when exposed to $MEA_{(aq)}$ and $MDEA_{(aq)}$ under hot (80 °C), $CO_2$ saturated conditions, has been observed. It was confirmed that $FeCO_3$ did not form on coupons exposed to concentrated $MEA_{(aq)}$ solutions (5 and 3 M), even though the solution Fe concentration was higher than all other solutions and the solutions were saturated with $CO_2$. No surface film formed on the coupon exposed to 5 M $MEA_{(aq)}$, whilst some amorphous product, thought to be oxide-based, was observed after immersion in 3 M $MEA_{(aq)}$. In the lowest tested concentration (1 M), a surface film of $FeCO_3$ was detected to have formed, but it was not densely packed and covered the surface incompletely. By contrast to the behaviour observed in $MEA_{(aq)}$, coupons immersed in $MDEA_{(aq)}$, regardless of concentration, all developed relatively packed $FeCO_3$ surface films. The film formed in the most concentrated solution was the thickest at *ca*. 6 μm, but had gaps. As concentration decreased, the thickness of the film also decreased, with a *ca*. 4 μm film forming in the 1 M $MDEA_{(aq)}$ solution. The results presented within this chapter broadly agreed with the literature and demonstrated that all three concentrations of MDEA can be considered for pre-treatment, from a corrosion mitigation standpoint.

# 5 Electrochemical behaviour of iron in amine solutions saturated with $CO_2$

## 5.1 Introduction

It has been shown in Chapters 2 and 4 that carbon steel exhibits different behaviour in monoethanolamine (MEA) and methyldiethanolamine (MDEA) aqueous solutions saturated with $CO_2$. Open circuit potential measurements and cyclic voltammetry were used as exploratory techniques to begin to probe these differences. Iron was used as a surrogate for carbon steel to decrease the complexity of the analysis[16]. The potential-pH diagram presented in Chapter 2 (**Figure 2-12**), will be used to support the interpretation of the recorded open circuit potentials and cyclic voltammograms.

[16]To verify that the electrochemical behaviour exhibited by carbon steel was accurately represented by iron, voltammograms were recorded with both iron and carbon steel in 5 M $MEA_{(aq)}$, saturated with $CO_2$ at 25 °C and compared. The voltammograms measured on both electrodes were nearly identical and are included in Appendix (Section 12.3.1).

## 5.2 Results

### 5.2.1 Electrochemical behaviour of iron in aqueous monoethanolamine (MEA) solutions saturated with $CO_2$

#### 5.2.1.1 Open circuit potential of Fe in aqueous MEA saturated with $CO_2$

The temperature-corrected open circuit potential (OCP) measurements of a stationary iron electrode in 1 (pH 7.5 ± 0.08 ), 3 (pH 7.7 ± 0.09) and 5 (pH 7.9 ± 0.001) M $MEA_{(aq)}$ solutions saturated with $CO_2$ at 25 and 80 °C are shown in **Figure 5-1**.

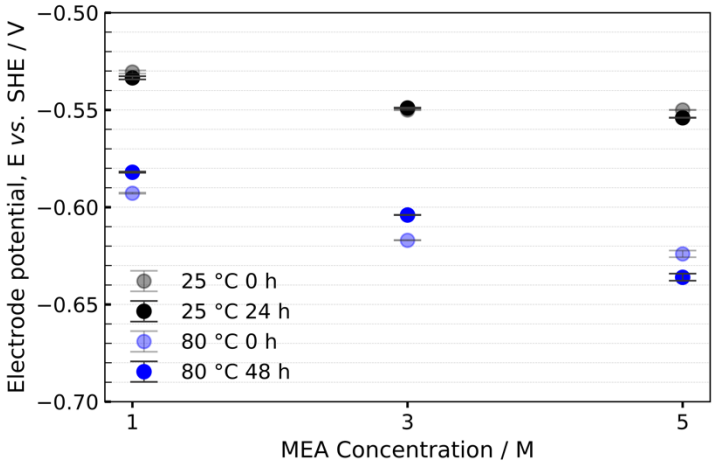



**Figure 5-1:** Effect of MEA concentration, temperature and time on temperature-corrected average open circuit potentials of a stationary iron electrode in $MEA_{(aq)}$ solutions saturated with $CO_2$.

From **Figure 5-1** it can be seen that the average OCPs attained after initial immersion in the electrolytes at 25 °C were almost equal to those measured after *ca*. 24 hours of immersion. The OCPs became increasingly negative with higher MEA concentration, with the Fe electrode in the 1 M solution attaining an average OCP of -0.535 V and -0.555 V in the 5 M solution. Based on **Figure 2-12**, $FeCO_3$ is predicted to be the most thermodynamically stable phase under these conditions. However, it has been demonstrated in the literature that $FeCO_3$ formation is unfavourable at temperatures < 60 °C (Nazari, Allahkaram & Kermani, 2010). It is likely that at 25 °C, $Fe^{2+}$ dissolution (*via* **5-1**) occurred and was balanced by $H_2$ evolution (*via* **5-2**). The presence of these two reactions leads to the increasingly negative OCP with increased MEA concentration due to the higher pH, as predicted by Equation **5-4**, which was derived from the Nernst equation, assuming a dissolved $Fe^{2+}$ concentration of $10^{-4}$ mol $dm^{-3}$.

$$Fe^{2+}{}_{(aq)} + 2e^- \rightleftharpoons Fe_{(s)} \quad \textbf{5-1}$$

$$2H^+{}_{(aq)} + 2e^- \rightleftharpoons H_2 \qquad 2H_2O + 2e^- \rightleftharpoons H_2 + 2OH^-_{(aq)} \quad \textbf{5-2}$$

$$Fe_{(s)} + 2H^+_{(aq)} \overset{K_{eq}}{\longleftrightarrow} Fe^{2+}_{(aq)} + H_{2_{(g)}} \quad \textbf{5-3}$$

$$E_{OCP} = E^o_{1-2} - \frac{RT}{nF}\ln\left(\frac{[Fe^{2+}]}{[H^+]^2}\right) \quad \textbf{5-4}$$

When the Fe electrodes were initially immersed in the $MEA_{(aq)}$ solutions saturated with $CO_2$ at 80 °C, the OCPs followed the same trend of decreasing electrode potentials with increasing MEA concentration as was observed at 25 °C. The electrodes in the 1, 3 and 5 M solutions attained average OCPs of *ca*. -0.593, -0.617 and -0.624 V respectively, all of which were more negative than those measured at 25 °C and agree with thermodynamic predictions given by Equation **5-4**. At these potentials and the corresponding solution pHs ($pH_{80\ °C}$ 7.7 – 7.9), $FeCO_3$ is predicted to be the most thermodynamically stable phase. Furthermore, the solution temperature of 80 °C is favourable for $FeCO_3$ precipitation (Nazari, Allahkaram & Kermani, 2010). After 48 hours of immersion, the OCPs of the Fe electrodes in the 1 and 3 M $MEA_{(aq)}$ solutions became more positive at *ca*. -0.582 V and *ca*. -0.604, respectively. By contrast, the electrode in the 5 M solution attained a more negative potential of *ca*. -0.636 V.

### 5.2.1.2 Cyclic voltammetry of Fe in aqueous MEA saturated with $CO_2$

**Figure 5-2a** shows cyclic voltammograms of both a stationary and a rotating Fe disc electrode in 5 M $MEA_{(aq)}$ saturated with $CO_2$ at pH 7.9. These were measured by cycling the electrode potential from an initial potential of -0.80 V to +1.2 V at a scan rate of 20 mV $s^{-1}$. Although the OCPs of iron in $MEA_{(aq)}$ solutions were within the range of -0.64 to -0.593 V, a wide potential scan window, far beyond measured OCPs, was used in cyclic voltammetry experiments to enable a more complete investigation of possible surface reactions on iron in both amines.

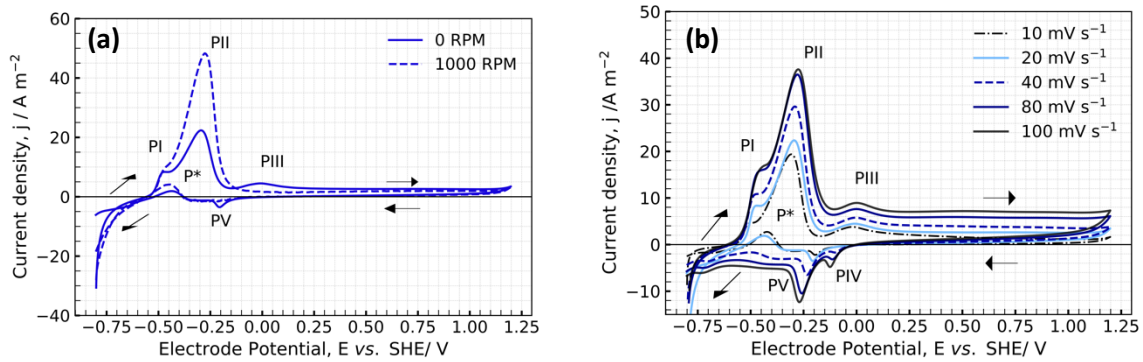



**Figure 5-2**: Cyclic voltammograms on a Fe disc electrode in 5 M $MEA_{(aq)}$ saturated with $CO_2$ at 25 °C, pH *ca*. 7.9, at **(a)** scan rate of 20 mV $s^{-1}$ with (---) (1000 RPM) and without rotation (-); **(b)** effect of potential scan rate on the voltammograms recorded in a quiescent solution.

Initially, negative currents were recorded between -0.8 and -0.55 V. Three oxidation current density peaks were then evident on the positive-going potential scan in the quiescent solution for (**Figure 5-2a**) applied potentials between -0.55 V and +1.2 V:

1. -0.55 V ≤ PI ≤ -0.45 V
2. -0.45 V ≤ PII ≤ -0.15 V
3. -0.01 V ≤ PIII ≤ +0.15 V

In the negative-going potential scan, a net oxidation current density peak (P*) occurred at -0.48 V ≤ P* ≤ -0.35 V. The presence of this anodic peak in the negative-going scan has been previously reported for Fe in $HCO_3^-$/ $CO_3^{2-}$ electrolytes pH 8.4 – 10.5 (Davies & Burstein, 1980; Valentini *et al*., 1985; Castro *et al*., 1986).

One reduction current density peak (PV) was evident in the region -0.35 V ≤ PV ≤ -0.15 V. At scan rates ≥ 40 mV $s^{-1}$, an additional reduction peak (PIV), preceding PV, was measured at potentials at -0.15 V ≤ PIV ≤ -0.05 (**Figure 5-2b**).

When the electrode was rotated, the shape of peak PI was less distinct, the second oxidation current density peak (PII) increased from *ca*. 22.5 A $m^{-2}$ to *ca*. 47.5 A $m^{-2}$ and the third oxidation peak (PIII), as well as the reduction peak (PV), no longer appeared. Furthermore, the current density associated with the anodic reaction (P*) increased.

**Figure 5-2b** shows corresponding voltammograms as a function of potential scan rate for a stationary Fe disc electrode. The relationship between peak current density and scan rate can provide mechanistic insight to the associated electrochemical reaction, such that a linear increase in peak current density with potential scan rate would be expected for electrochemical reactions involving adsorption or surface transformation processes (*e.g.* oxide formation) (Bard & Faulkner, 2001), whilst for transport controlled electrochemical reactions, associated peak current densities ($j_p$) would be expected to increase linearly with the square root of the scan rate ($s$), as described by the Randles-Sevcik equation (Equation **5-5**).

$$j_p = 0.446\ n\ F\ C_\delta \left(\frac{nFD_i\ s}{RT}\right)^{\frac{1}{2}} \qquad \textbf{5-5}$$

Although the peak current densities associated with the first and second oxidation reactions (PI and PII) increased with increased potential scan rate, a linear dependence of the magnitude of PI or PII on scan rate was not observed, nor on the square root of the potential scan rate (Appendix, Section 12.3.2). By contrast, the peak current density associated with the third oxidation reaction appeared to be linearly dependent ($R^2$ = 0.998) on the scan rate (Appendix, Section 12.3.2).

To further investigate the electrochemical reactions in **Figure 5-2**, the applied potential was swept at the same scan rate of 20 mV $s^{-1}$, but starting at the open circuit potential (-0.550 V). This was done to remove the effect of initial net $H^+$ production on local pH. Furthermore, the upper potential limit was increased incrementally by at least 0.07 V between scans, such that an increasingly wider potential range (**Figure 5-3**) was applied. This approach was designed to enable the allocation of anodic and cathodic current density peaks to redox pairs.

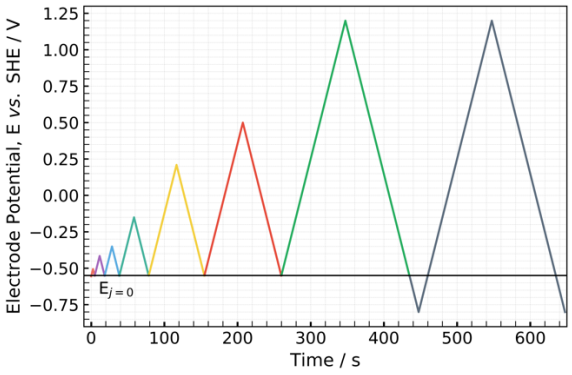



**Figure 5-3:** Potentials applied to Fe disc electrode during cyclic voltammetry with incrementally increased anodic potential limits; colours are coordinated by scan as a function of the total experimental time.

From **Figure 5-4a**, the first oxidation reaction appeared in the range of -0.550 to -0.45 V, which is consistent with **Figure 5-2** and corresponds to PI. However, this peak did not reappear during the second potential scan (blue, **Figure 5-4b**). Eventually, PI reappeared after *ca*. 150 s (**Figure 5-4f**). It is possible that the reaction associated with PI involved solution-based species, which were depleted in the first scan. Therefore PI is proposed to be due to $Fe(OH)_2$ formation *via* **5-6**, which has a reversible potential of -0.557 V at the solution pH *ca*. 7.9 (**Table 5-1**). However, based on the potential-pH diagram (**Figure 2-12**), at a pH of 7.9, $FeCO_3$ is predicted to be the most thermodynamically stable phase. To resolve this inconsistency, the local pH, rather than the bulk pH was considered. The associated local pH due to $H_2$ evolution (*via* **5-2**) at potentials of -0.8 to -0.55 V (**Figure 5-2**), was estimated to be *ca*. 11.1[17], at which $Fe(OH)_2$ formation is predicted to be the most thermodynamically stable phase (**Figure 2-12**). It is evident from **Figure 5-2**, that PI was followed by a plateau, which probably was due to passivation of the electrode by an adsorbed $Fe(OH)_2$ layer, though this is not consistent with the non-linear dependence between the magnitude of PI and scan rate. The subsequent rise in current following the plateau was likely a consequence of dissolution

[17] It was assumed that all of the charge passed between -0.8 and -0.55 V, was used for $OH^-$ formation, formed *via* **5-2**, using Faraday's law of electrolysis (Equation **2-4**). The moles of $OH^-$ produced was then converted to an average concentration within the diffusion layer by dividing by the volume of the diffusion layer. The volume of the diffusion layer was estimated using the thickness ($\delta$) of the diffusion layer from $\delta = 2\sqrt{D_{OH^-}\, t}$, where $t$ was the time elapsed between scanning from -0.8 to -0.55 V and an estimate of $D_{OH^-}$ obtained from (Newman & Thomas-Alyea, 2012). An example of this calculation is included in Appendix, Chapter 12.3 (Section 12.3.6).

of $Fe(OH)_2$ due to a local pH decrease as a result of the accompanying $H^+$ formation (*via* **5-6**). Unlike the current density response shown in **Figure 5-2**, in **Figure 5-4a**, PI was not followed by a distinct plateau, so the $Fe(OH)_2$ formed in **Figure 5-4a** was probably by a dissolution-precipitation mechanism, rather than a surface transformation, whereby minimal surface coverage occurred.

$$Fe(OH)_{2(c)} + 2H^+_{(aq)} + 2e^- \rightleftharpoons Fe_{(s)} + H_2O \qquad \textbf{5-6}$$

In the third potential scan (green, **Figure 5-4b**), a second oxidation reaction, which corresponds to PII in **Figure 5-2**, began to occur at *ca*. -0.50 V; this was apparent from the increased current density, which rose to a peak at *ca*. -0.30 V. This reaction produced the highest current density of *ca*. 25 A $m^{-2}$ and is thought to be due to $FeCO_3$ formation *via* **5-8**, which has a reversible potential of -0.647 V[18] (**Table 5-1**). It is unclear whether this reaction occurred *via* Fe dissolution (**5-1**) and subsequent precipitation (*via* **5-7**), with $FeCO_3$ precipitation occurring when the saturation ratio ($S_{FeCO3}$), given by Equation **5-10** exceeded unity, or by surface transformation (*via* **5-8**). If $FeCO_3$ formed *via* a dissolution-precipitation mechanism, then the formation reaction would likely be limited initially[19] by $Fe^{2+}$. If the reaction followed a surface transformation mechanism then it would likely be limited by $HCO_3^-$. It should be noted that $FeCO_3$ has been reported to be electrically insulating (Mercier-Bion *et al*., 2018), so $FeCO_3$ formation is expected to have a passivating effect and result in a decrease in the current density following its formation, as was indeed observed in **Figure 5-2** and **Figure 5-4b**. The voltammetry results can be interpreted in two ways. First, in the view of a dissolution-precipitation mechanism, the increase in recorded current density with rotation could be interpreted as the electrode rotation resulting in higher transport rates of $Fe^{II}$ away from the electrode surface than in the quiescent solution. Therefore, $FeCO_3$ precipitation on a rotating electrode required a higher current density for sufficient accumulation of $Fe^{II}$ to occur. The second interpretation is that the $FeCO_3$ formation occurred *via* surface transformation and the reaction is limited by $HCO_3^-$. As the electrode is rotated, more $HCO_3^-$ is drawn toward the surface and the recorded current increases due to surface transformation *via* **5-8**. If the second interpretation holds true, then it can be assumed that the

[18] Calculated using a $HCO_3^-$ based on solution pH of 7.9.

[19] As $FeCO_3$ forms, the local pH is expected to decrease and so too will the $HCO_3^-$ concentration, which may in fact fall below the $Fe^{2+}$ concentration and hence $HCO_3^-$ may become the limiting species.

measured current density can be directly converted to the quantity of $FeCO_3$ formed, which was calculated to be at most *ca*. 56 monolayers[20] (Appendix, Section 12.3.6). Since it is unclear which mechanism is responsible, **5-8** will be used throughout this thesis as it accurately represents the global reaction for both mechanisms. As mentioned previously, the relationship between the magnitude of PII and potential scan rate was not linear ($R^2 = 0.96$) suggesting that $FeCO_3$ formation did not occur *via* a surface transformation mechanism (Appendix, Section 12.3.2).

Regardless of the mechanism, $H^+$ is produced concomitantly with $FeCO_3$, and by Le Chatelier's principle the equilibrium shown in **5-9** will shift to the left and result in a decrease in the local $HCO_3^-$ concentration[21]. Therefore, this reaction is self-limiting since the decreased $HCO_3^-$ concentration would result in the $FeCO_3$ saturation ratio (Equation **5-10**) decreasing, thus possibly creating unfavourable conditions for $FeCO_3$ precipitation and causing its dissolution. Hence, the production of $H^+$ ions resulted in either partial or complete dissolution of the $FeCO_3$ formed, and the Fe electrode was likely to have been left bare for the negative-going potential scan. The oxidation current density recorded in the negative-going scan in **Figure 5-4b**, is proposed to be due to the reactivation of **5-8**. This is consistent with the results obtained in **Figure 5-2**, and is estimated to be equivalent to the formation of 21 monolayers of $FeCO_3$.

$$Fe^{2+}{}_{(aq)} + HCO_3^-{}_{(aq)} \rightleftharpoons + FeCO_{3(c)} + H^+{}_{(aq)} \qquad \textbf{5-7}$$

$$FeCO_{3(c)} + H^+{}_{(aq)} + 2e^- \rightleftharpoons Fe_{(s)} + HCO_3^-{}_{(aq)} \qquad \textbf{5-8}$$

$$CO_{2(aq)} + H_2O \rightleftharpoons H^+{}_{(aq)} + HCO_3^-{}_{(aq)} \qquad \textbf{5-9}$$

$$S_{FeCO_3} = \frac{[Fe^{2+}][CO_3^{2-}]}{K_{sp}} \qquad \textbf{5-10}$$

In the fourth scan (yellow, **Figure 5-4c**), a third oxidative reaction followed PII, beginning at *ca*. -0.14 V, resulting in a broad, but substantially smaller current density peak (PIII) of *ca*. 7

---

[20] Surface roughness was not accounted for.

[21] If it is assumed that all of the charge passed was used for $FeCO_3$ formation, and one mole of $H^+$ formed for each mole of $FeCO_3$, then the local pH would decrease to 1.7, if $H^+$ diffusion away from the electrode is ignored, at which the $HCO_3^-$ concentration would be $8 \times 10^{-7}$ mol $dm^{-3}$. This is however an overestimation of the local pH decrease. The calculation is included in Appendix (Section 12.3.6).

A $m^{-2}$ at *ca*. +0.02 V, consistent with that observed in **Figure 5-2**. The broad nature of the oxidation peak suggests the occurrence of multiple oxidation reactions, which are likely to include the oxidation of $FeCO_3$ to $Fe_3O_4$ *via* **5-11** ($E_{r,\ Fe3O4/FeCO3}$ = -0.266 V, **Table 5-1**) and $Fe_3O_4$ to $Fe_2O_3$ *via* **5-13** ($E_{r,\ Fe2O3/Fe3O4}$ = -0.253 V, **Table 5-1**). However, if the $FeCO_3$ formed previously underwent partial or complete dissolution due to the expected decrease in the local pH, the bare electrode surface may have been oxidised from Fe to $Fe_3O_4$ *via* **5-12** ($E_{r,\ Fe3O4/Fe}$ = -0.554 V, **Table 5-1**) and subsequently to $Fe_2O_3$ *via* **5-13**. The cyclic voltammogram measured during rotation supports the latter reaction assignment. PIII did not appear in **Figure 5-2a**, indicating the absence of the third oxidation reaction. Rotating the electrode, probably prevented a significant decrease in local pH since the majority of the $H^+$ ions produced by **5-8** would be more efficiently transported away from the electrode surface. In this case, PIII was not observed since at the mildly basic solution pH, the $FeCO_3$ on the electrode surface was stable and perhaps non-porous, so it, and Fe, both do not undergo further oxidation. It is also apparent from **Figure 5-4d**, and more obviously from **Figure 5-4e**, that as the PII current density increased, PIII current density decreased. This may be because a greater fraction of the surface was covered with $FeCO_3$, leaving less of the surface available for Fe oxide formation *via* **5-12** and **5-13**. This may suggest that both $FeCO_3$ and Fe oxidation contributed to PIII.

$$Fe_3O_{4(c)} + 3HCO_{3\,(aq)}^{-} + 5H^+_{(aq)} + 2e^- \rightleftharpoons 3FeCO_{3(c)} + 4H_2O \qquad \textbf{5-11}$$

$$Fe_3O_{4(c)} + 8H^+_{(aq)} + 8e^- \rightleftharpoons 3Fe_{(s)} + 4H_2O \qquad \textbf{5-12}$$

$$3Fe_2O_{3(c)} + 2H^+_{(aq)} + 2e^- \rightleftharpoons 2Fe_3O_{4(c)} + H_2O \qquad \textbf{5-13}$$

On the negative-going scan from the fourth potential sweep (yellow, **Figure 5-4c**), a small reduction current density peak of *ca*. -1 A $m^{-2}$ at -0.078 V was recorded and corresponds to PIV in **Figure 5-2b**. Based on the reversible potentials calculated at the bulk solution pH *ca*. of 7.9, $Fe_2O_3$ reduction should not have occurred at potentials more positive than -0.251 V. However, on the positive-going scan, $FeCO_3$ (*via* **5-8**), $Fe_3O_4$ (*via* **5-12**) and $Fe_2O_3$ (*via* **5-13**) formation, all would have resulted in $H^+$ production, which would have caused a decrease in

the local pH to less than *ca*. 2.34[22] and thus have resulted in a positive shift of the reversible potential. Additionally, this peak was evident only at scan rates ≥ 40 mV $s^{-1}$ (**Figure 5-2b**) and not at a scan rate of 20 mV $s^{-1}$ in **Figure 5-2a**, for which the potential was reversed *ca*. 53 s after it was in the scans shown in **Figure 5-4c** (yellow). In the wider potential window scan at a scan rate of 20 mV $s^{-1}$ (**Figure 5-2a**), the $H^+$ ions produced on the positive-going scan would have had sufficient time to diffuse away from the electrode surface and hence the local pH may have returned to the bulk pH. Therefore, the small reduction peak (PIV) was believed to be associated with reduction of the oxide formed at PIII, and given the magnitude of the current density, suggests only partial reduction. The small magnitude of PIV could also have been a result of both oxide reduction, and reactivation of oxidative Fe dissolution and $FeCO_3$ precipitation.

Following the minimal reduction peak noted on the negative-going scan from the fourth sweep, the magnitude of the reduction current density began increasing at *ca*. -0.1 V and continued to do so until *ca*. -0.26 V. Subsequently, the magnitude of the cathodic current density began decreasing and at *ca*. -0.28 V, a net anodic current density peak (P*) was again measured. The presence of the third oxidation reaction appeared to impact the magnitude of P* (**Figure 5-4d**). It is likely that the $Fe_2O_3$ formed on the positive-going scan at PIII and was reduced in the negative-going scan and the magnitude of P* decreased due to the effect of the reduction current on the net recorded current density.

In the absence of PIII, P* was *ca*. 17.5 A $m^{-2}$, which was estimated to be equivalent to the formation of 21 monolayers of $FeCO_3$, but when PIII was recorded, P* was *ca*. 10.5 A $m^{-2}$, which corresponds to 12 monolayers of $FeCO_3$. Further, in scans six and seven (**Figure 5-4e**), the potential was swept to increasingly positive values and then the negative-going scans were recorded; with increasing positive potential limit, the anodic reactivation peak (P*) became increasingly smaller. This suggested that the oxidative reaction associated with PIII continued to occur as potentials progressively more positive than +0.02 V were applied to the electrode, resulting in the $FeCO_3$ formed at PII, and subsequently $Fe_3O_4$, or both being oxidised (*via* **5-11** and **5-13**). Therefore, the $Fe_2O_3$ seemingly hindered the anodic reactivation of **5-8**. However, greater oxidation currents association with $Fe_2O_3$ formation in the positive-

[22] The local pH was estimated to decrease to pH 1.7 due to the formation of $FeCO_3$ *via* **5-8**. If PIII is considered to be due only to $Fe_3O_4$ formation *via* **5-11**, then the local pH due only to **5-11** is estimated to be 2.34 calculated following the procedure outlined in the Appendix (Section 12.3.6).

going scan, would have subsequently resulted in greater reduction current densities in the negative-going scan, and so apparently smaller oxidative $FeCO_3$ formation which is associated with P*.

Another key observation, which was not addressed previously, is that PV appeared only when the potential was swept to +1.2 V (**Figure 5-2** and **Figure 5-4f**). As the potential was swept to more positive potential limits, it is probable that $Fe_3O_4$ was oxidised completely to $Fe_2O_3$ at potentials greater than the reversible potential of -0.251 V (**Table 5-1**), and $H^+$ ions were produced concomitantly with $Fe_2O_3$ formation (*via* **5-13**). It is possible that $Fe_2O_3$ reduced directly to $FeCO_3$ (*via* **5-14**), or *via* $Fe_3O_4$ as an intermediate phase (*via* **5-13** and **5-11**). When the scan rate was sufficiently high ≥ 40 mV $s^{-1}$ (**Figure 5-2b**), the local pH decrease resulted in separation of the two reduction current density peaks (associated with **5-13** and **5-11**).

$$Fe_2O_{3(c)} + 2HCO_{3\,(aq)}^{-} + 4H_{(aq)}^{+} + 2e^{-} \rightleftharpoons 2FeCO_{3(c)} + 3H_2O \qquad \textbf{5-14}$$

The presence of the two reduction peaks (**Figure 5-2b**), substantiates the previous suggestion that the broad nature of PIII was due to the presence of multiple oxidation reactions. The subsequent increase in reduction current densities at applied potentials < -0.60 V was due to $H_2$ evolution.

The positive-going part of the voltammograms recorded in 5 M $MEA_{(aq)}$ saturated with $CO_2$ shown in **Figure 5-2** and **Figure 5-4** closely resemble those presented by (Valentini *et al*., 1985), which were obtained with an Fe electrode in 0.75 mol $dm^{-3}$ $KHCO_3$ + 0.05 mol $dm^{-3}$ $K_2CO_3$ solutions pH 8.9 at 25 - 75 °C (**Figure 2-14**) within a potential scan window of -1 to +0.2 V at a scan rate 25 mV $s^{-1}$. The authors reported three anodic current density peaks corresponding to PI, PII and PIII reported here, in the positive-going scan in quiescent solutions, and only two anodic peaks when a rotating Fe disc electrode was used. On the negative-going potential scan however, reduction peaks PIV and PV were not reported by the authors, but instead an increase in the magnitude of the cathodic current density at a. -0.2 V, and subsequently an anodic reactivation peak at *ca*. -0.7 to -0.4 V. Since PIV (at *ca*. -0.1 V in **Figure 5-2** and *ca*.-0.01 V **Figure 5-4**) is thought to be due to $Fe_2O_3$ reduction as a result of a local pH decrease, it is reasonable that it was absent in the voltammograms measured in $KHCO_3$ + $K_2CO_3$ (Valentini *et al*., 1985) because the bulk solution pH of the solution used in that study was higher (8.9) and the $CO_3^{2-}$, present in high concentrations, would have acted to prevent local pH decreases by reacting with $H^+$ to produce $HCO_3^-$. Additionally, the voltammogram recorded here with a rotating Fe disc electrode (**Figure 5-2**), *i.e*. where local

pH changes would be minimised, was identical to that presented by (Valentini *et al*., 1985), possibly suggesting that MEA, $MEAH^+$ and $MEACOO^-$ are not electro-active.

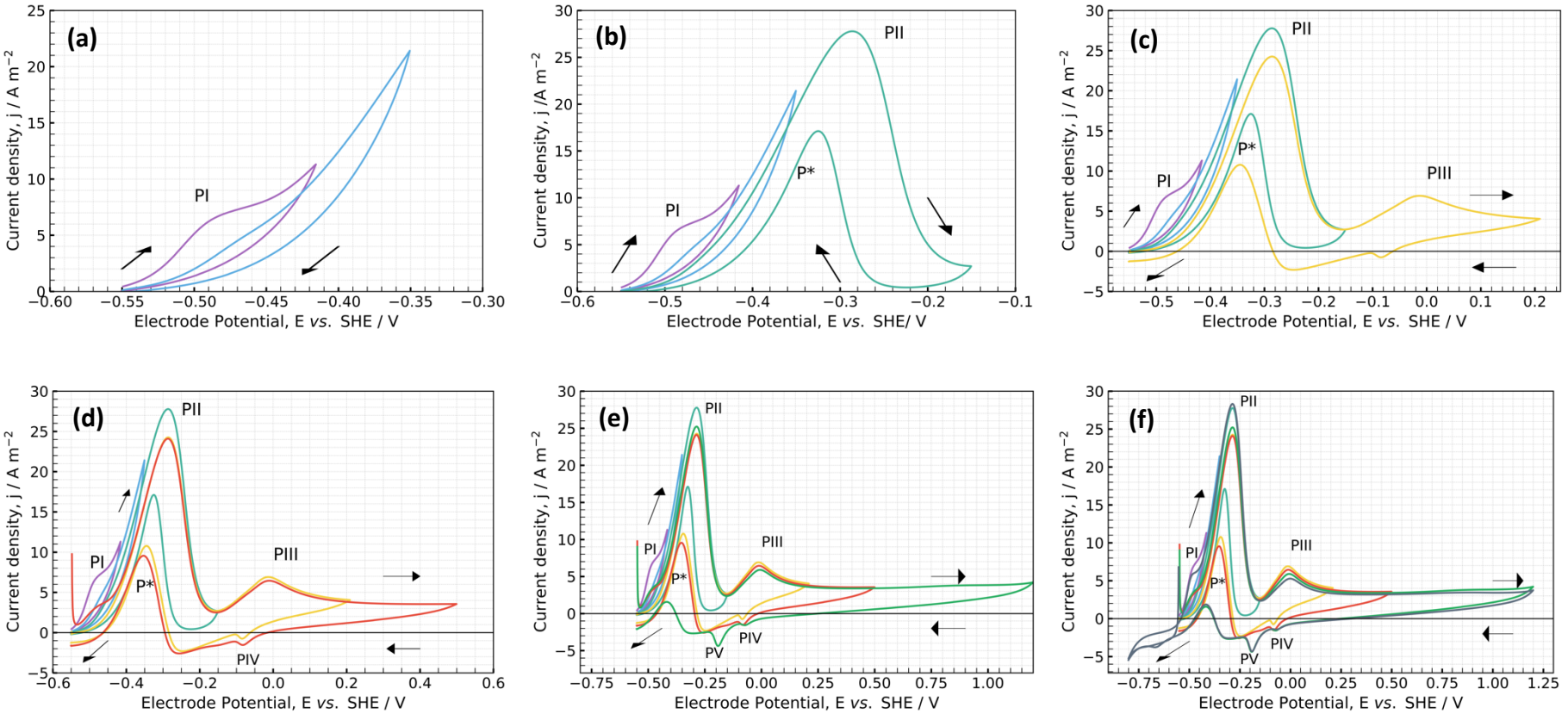



**Figure 5-4***:* Cyclic voltammograms of Fe disc electrode in quiescent 5 M $MEA_{(aq)}$, saturated with $CO_2$ at 25 °C, pH 7.9, at a scan rate of 20 mV $s^{-1}$ with increasingly positive potential limits.

### 5.2.1.3 Effect of MEA concentration on the cyclic voltammetry of Fe in aqueous MEA solutions saturated with $CO_2$

The effect of MEA concentration was investigated on the electrochemical behaviour of iron in $CO_{2(aq)}$ solutions, the solution pH of which varied with MEA concentration; 5, 3 and 1 M $MEA_{(aq)}$ solutions had pHs of *ca*. 7.9, 7.7 and 7.5, respectively at 25 °C. Hence, the voltametric results reflect the coupled effect of pH and MEA concentration. Cyclic voltammograms for stationary and rotating Fe disc electrodes in each of the aforementioned $MEA_{(aq)}$ solutions at 25 °C are presented in **Figure 5-5a** and **Figure 5-5b**, respectively.

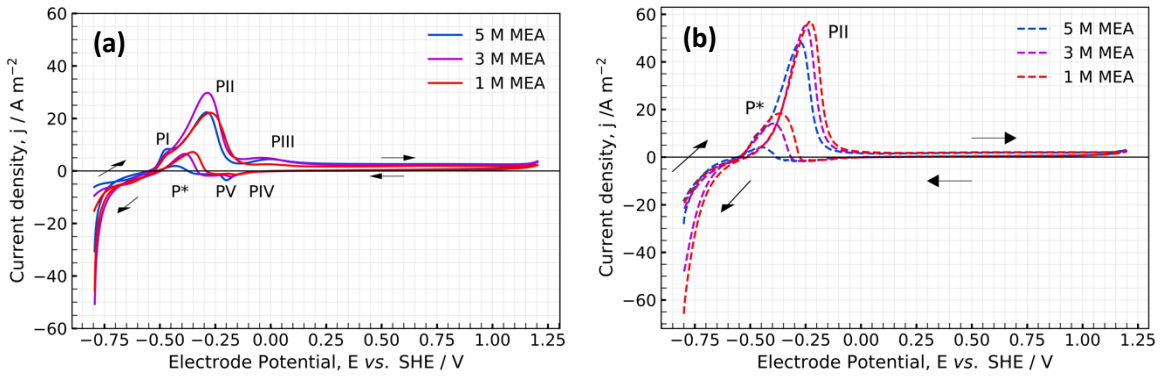



**Figure 5-5:** Effect of MEA concentration on cyclic voltammograms of **(a)** stationary and **(b)** rotating (1000 RPM) Fe disc electrode, in solutions$_{(aq)}$ saturated with $CO_2$ at 25 °C, at a scan rate of 20 mV s$^{-1}$.

Cathodic current densities were recorded for applied potentials ≤ -0.53 V, due to $H_2$ evolution *via* **5-2** which, in quiescent solutions, likely resulted in significant increases in local $OH^-$ concentrations[23]. Since the reversible potentials for $H_2$ evolution for all three solutions are between -0.467 and -0.442 V (**Table 5-1**), it is reasonable to assume that this was the predominant reaction occurring at potentials ≤ -0.53 V. Based on the measured current densities, $H_2$ and $OH^-$ ions were produced at the highest rate in the 3 M, and the least in the 5 M $MEA_{(aq)}$ solutions (**Figure 5-5a**).

Subsequently, in the quiescent solutions, the first oxidation reaction, apparent from PI, occurred in the range of -0.525 V to -0.450 V (**Figure 5-5a**). This current density peak (PI) was followed by a shoulder or plateau in the 5 M $MEA_{(aq)}$ solution, suggesting a

[23]pH 11.1, which was estimated to be the local pH due to $H_2$ evolution from the voltammogram shown in Figure 5-2, corresponds to a $OH^-$ concentration of *ca*. 1.3 × 10$^{-3}$ mol dm$^{-3}$, substantially higher than 7.9 ×10$^{-7}$ mol dm$^{-3}$ at the bulk solution pH of 7.9 (5 M $MEA_{(aq)}$ saturated with $CO_2$).

concentration limited or passivating reaction, whereas PI measured in the 1 and 3 M solutions were not followed by a plateau. Additionally, net current densities began rising into the anodic region at a slightly more negative potential of *ca*. -0.55 V in the 5 M solution. These possibly indicate that the nature of the first oxidation reaction was different in the 1 and 3 M solutions. In the 5 M solution, this peak was previously attributed to $Fe(OH)_2$ formation. Although more $OH^-$ ions were likely produced in the 1 and 3 M $MEA_{(aq)}$ solutions, the 5 M electrolyte was more viscous (**Figure 5-8d**) so $OH^-$ ion diffusion away from the electrode surface was likely to have been faster in the 1 and 3 M $MEA_{(aq)}$ solutions. Given the absence of the current plateau, it is thought that PI may be associated instead with $Fe^{II}$ dissolution (*via* **5-1**) or a combination of $Fe^{II}$ dissolution and $Fe(OH)_2$ formation (*via* **5-6**); the reversible potentials at each solution pH are given in **Table 5-1**. In fact, (Castro, Vilche & Arvia, 1991) demonstrated, using a rotating ring (Au) disc (Fe) electrode that this oxidation peak was due to the formation of both dissolved ($Fe^{II}$) and insoluble ($Fe(OH)_2$) species on an Fe electrode in $HCO_3^-$/ $CO_3^{2-}$ pH 9.5. When the electrode was rotated, PI did not appear in the 1 and 3 M solutions (**Figure 5-5b**), since the $OH^-$ ions produced by $H_2$ evolution would have had a much smaller effect on the local $OH^-$ concentration due to the accelerated transport rates. By contrast, PI still appeared in the 5 M $MEA_{(aq)}$ solution, but did not exhibit a shoulder-like appearance, so under these conditions PI may be due predominantly to Fe dissolution.

The second oxidation reaction, due to $FeCO_3$ precipitation *via* **5-8**, produced the highest peak current density of *ca*. 35 A $m^{-2}$ in the 3 M $MEA_{(aq)}$ solution, whereas current densities of PII were *ca*. 25 A $m^{-2}$ in both the 5 and 1 M $MEA_{(aq)}$ solutions. Theoretically, $FeCO_3$ precipitates when the saturation ratio, given by Equation **5-10**, exceeds unity. The flux of $Fe^{II}$ ($N_{Fe^{II}}$) from the electrode surface is a function of the concentration gradient $\left(\frac{dC_{Fe}}{dx}\right)$ and diffusion coefficient ($D_{Fe^{II}}$), as described by Equation **5-15**. The diffusion coefficient is a function of the viscosity as described by the Stokes-Einstein equation (Equation **5-16**), where $k_B$ is the Boltzmann's constant, $T$ is the temperature, $r_o$ is the equivalent hydrodynamic radius of the diffusing species, and $\mu$ is the dynamic viscosity, which increases with increased MEA concentration (**Figure 5-8**).

$$N_{Fe^{II}|\,x=0} = -D_{Fe^{II}} \frac{dC_{Fe}}{dx} \qquad \textbf{5-15}$$

$$D_{Fe^{II}} = \frac{k_B T}{6\,\pi\, r_{o_{Fe^{II}}} \mu} \qquad \textbf{5-16}$$

Based on the diffusion rate, the accumulation of $Fe^{II}$ in the diffusion layer would be fastest in the 5 M solution and slowest in the 1 M solution and as a result, a lower oxidative dissolution current density would have been required for $FeCO_3$ precipitation in the 5 M $MEA_{(aq)}$ solution.

Further, it appeared that more $Fe(OH)_2$ had formed on the electrode surface in the 5 M solution; this would probably have impeded $Fe^{2+}$ diffusion away from the electrode surface. On the other hand, diffusion rates of $H^+$ ions away from the electrode surface would have decreased as MEA concentrations were increased, resulting in the local pH decrease being sustained for a longer period of time, so decreasing the $HCO_3^-$ concentration, resulting in higher Fe dissolution current densities needed for $S_{FeCO3}$ to exceed unity. Lastly, the higher bulk pH with increased MEA concentration would have produced greater $HCO_3^-$ concentrations in solution, favouring $FeCO_3$ precipitation.

The interplay of these factors is likely responsible for the parabolic correlation between PII and MEA concentration shown in **Figure 5-6c**. The processes affecting $FeCO_3$ formation will be explored in more detail in Chapter 6.

In contrast to the quiescent solutions, when the electrode was rotated, the current density associated with $FeCO_3$ precipitation increased with decreasing MEA concentration (**Figure 5-6**). In the presence of rotation, $Fe^{II}$ ions as well as $H^+$ ions would have been transported away from the electrode surface more rapidly accordingly to the Levich equation (Equation **3-4**). This may suggest that the effect of solution viscosity, and hence relative transport rates, would have been less important when the electrode was rotated. Given the higher $HCO_3^-$ concentrations in more concentrated $MEA_{(aq)}$ solutions, the increased Fe dissolution current densities (**Figure 5-5b** and **Figure 5-6**) required for $S_{FeCO3}$ to exceed unity at lower MEA concentrations, seems reasonable.

The broad third current density peak (PIII), believed to be due to two oxidation reactions either involving Fe and/or $FeCO_3$ oxidation *via* **5-11** to **5-13**, was recorded in the 3 and 5 M quiescent solutions, but it was not discernible in the 1 M $MEA_{(aq)}$ solution. However, it was expected that the $FeCO_3$ formed in the 1 M solution would be the least stable given its lower bulk pH. The absence of PIII in the voltammogram measured in the 1 M $MEA_{(aq)}$ solution suggested that the $FeCO_3$ formed in this solution was the most stable. When the electrode was rotated, the third oxidation peak did not appear in any of the three solutions. The absence of

PIII for the rotating electrode in all three solutions and in the quiescent 1 M $MEA_{(aq)}$ solution was probably due to the rotation-induced accelerated removal of $H^+$ produced with the $FeCO_3$ by reaction **5-8**, or as a result of the relatively lower solution viscosity in the case of the 1 M $MEA_{(aq)}$ quiescent solution. This ensured that the $FeCO_3$ film remained intact and provided a barrier to limit oxidation rates.

A reduction peak (PV), thought to be due to reduction of $Fe_2O_3$ either directly to $FeCO_3$ or *via* $Fe_3O_4$, was recorded at applied potentials between +0.05 V and -0.25 V in each of the solutions on a stationary Fe disc electrode (**Figure 5-5a**). It was most discernible at *ca*. -0.2 V in the 5 M solution. PV was much less distinct in the 3 M $MEA_{(aq)}$ solution, in which it was recorded between *ca*. -0.15 V and -0.2 V, and even less so in the 1 M solution between *ca*. -0.12 V and -0.18 V. The reversible potentials for $Fe_2O_3$ and $Fe_3O_4$ reduction are given as a function of solution pH in **Table 5-1**; all are more negative than the potentials at which the current densities began increasing in **Figure 5-5a**. This suggests that $Fe_2O_3$ and $Fe_3O_4$ reduction should not have occurred. However, as explained previously, the local pH is likely to be lower since $H^+$ would have been produced in $FeCO_3$ and $Fe_2O_3$ formation, and $H^+$ diffusion may have been impeded by any porous product ($FeCO_3$ or $Fe_2O_3$) left on the surface. Development of pores may have occurred due to mechanical stresses at the electrode surface induced by the increased molar volumes of $FeCO_3$ or $Fe_2O_3$, which are $2.9 \times 10^{-5}$ and $3.1 \times 10^{-5}$ mol $m^{-3}$, respectively, relative to Fe ($7 \times 10^{-6}$ mol $m^{-3}$). The reversible potentials at the local pH would be more positive than those given in **Table 5-1**. The relative magnitudes of PV in the three solutions were reasonable since they followed the same trend as PIII and were associated with the reduction of the product formed during the positive-going potential scan following PII. The lack of $O_2$ evolution at potentials $\geq$ +0.764 V, which is expected at the bulk solution pH (**Table 5-1**), also suggested that the local pH did decrease significantly on the positive-going potential scan. At the lower local pH of 2.34 estimated previously (Section 5.2.1.2), the reversible potential for $O_2$ evolution is +1.1 V. However, $O_2$ evolution kinetics on $Fe_2O_3$ or $FeCO_3$ may be very slow given their low electronic conductivities.

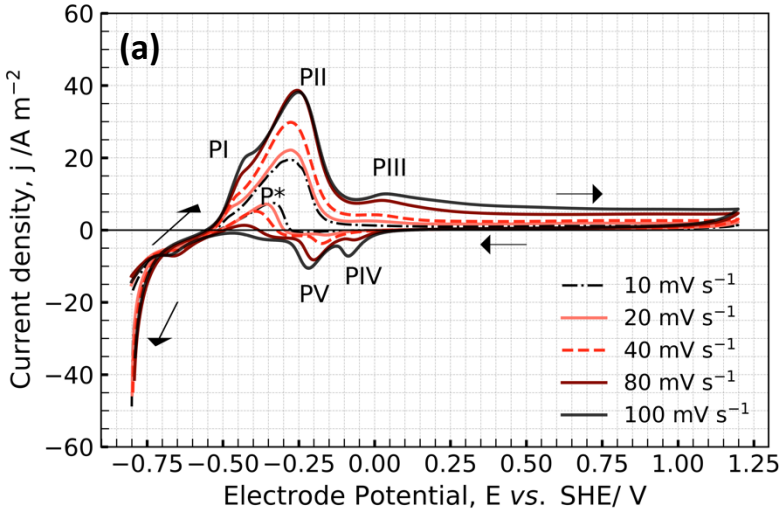
When the electrodes were rotated in all three solutions, PV was not evident (**Figure 5-5b**) but minimal reduction current densities were produced at potentials $\leq$ -0.1 V. The absence of a distinct reduction peak was expected since it is believed to be associated with the products formed on the previous positive-going potential scan at PIII, which was not discernible when the electrode was rotated.

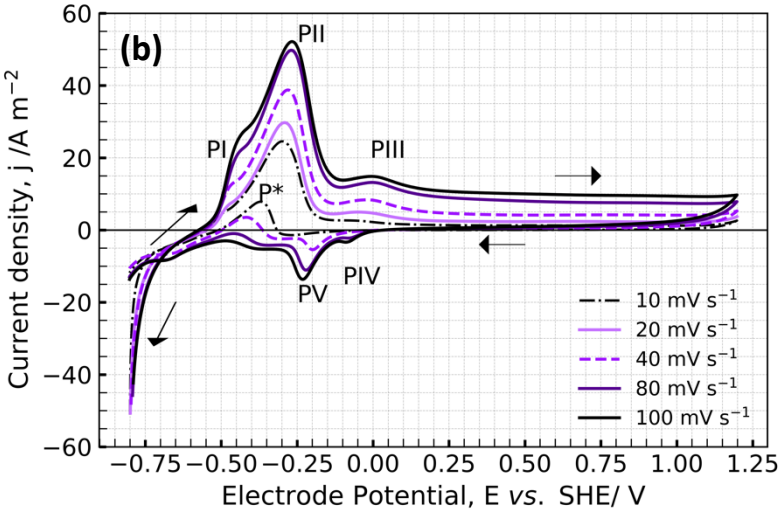
The first reduction peak, PIV was measurable only in quiescent solutions at scan rates ≥ 40 mV $s^{-1}$ in all three solutions (**Figure 5-2b**, **Figure 5-6**) and was believed to be associated with formation of $Fe_2O_3$ *via* **5-11** to **5-13**.

Following PIV and PV, the anodic reactivation peak (P*) appeared in the voltammograms measured in all three electrolytes (**Figure 5-5a**) with both the stationary and rotating electrodes at applied potentials of -0.5 V ≤ P* ≤ -0.3 V, and -0.55 V ≤ P* ≤ -0.25 V. The peak current density associated with this reaction decreased with increasing MEA concentration both with and without electrode rotation (**Figure 5-5a** and **Figure 5-6**). Based on the potential sweep experiments presented in **Figure 5-4**, this reaction was assigned to reactivation of the $FeCO_3$ formation reaction. In the rotating disc experimental results shown in **Figure 5-5b**, it seemed that the $FeCO_3$ film produced on the positive-going scan was relatively stable since it apparently did not undergo further oxidation. Based on the reversible potentials presented in **Table 5-1**, at potentials more positive than -0.623 V, -0.640 V and -0.647 V in the 1, 3 and 5 M solutions respectively, $FeCO_3$ formation is predicted to be thermodynamically feasible. It should be mentioned that in the quiescent solutions, P* became less prevalent as the potential scan rate increased in all three solutions (**Figure 5-6**). This is thought to have occurred because, at higher scan rates, $Fe_2O_3$ appeared to have been produced (*via* $Fe_3O_4$) on the positive-going potential scan, so was reduced in the subsequent negative-going scan. The coupled effect of $Fe_2O_3$ reduction and possible $FeCO_3$ formation in the negative-going scan, resulted in the observed net negative current densities at potentials ≤-0.35 V, at which P* was observed at lower scan rates.

**Table 5-1**: Reversible potentials (*vs*. SHE) for redox reactions in Fe–$H_2O$–$CO_2$ at bulk solution pH at 25 °C (Fe concentration = $10^{-4}$ mol $dm^{-3}$).

| **Reactions** | **pH 7.47** | **pH 7.74** | **pH 7.86** |
|---|---|---|---|
| $2H^+_{(aq)} + 2e^- \rightleftharpoons H_2 \qquad 2H_2O + 2e^- \rightleftharpoons H_2 + 2OH^-_{(aq)}$ | -0.442 | -0.450 | -0.464 |
| $Fe(OH)_{2(c)} + 2e^- + 2H^+_{(aq)} \rightleftharpoons Fe_{(s)} + 2H_2O$ | -0.533 | -0.550 | -0.557 |
| $Fe^{2+}_{(aq)} + 2e^- \rightleftharpoons Fe_{(s)}$ | -0.549 | | |
| $FeCO_{3(c)} + H^+_{(aq)} + 2e^- \rightleftharpoons Fe_{(s)} + HCO^-_{3\,(aq)}$ | -0.623 | -0.640 | -0.647 |
| $Fe_3O_{4(c)} + 3HCO^-_{3\,(aq)} + 5H^+_{(aq)} + 2e^- \rightleftharpoons 3FeCO_{3(c)} + 4H_2O$ | -0.241 | -0.257 | -0.264 |
| $Fe_3O_{4(c)} + 8H^+_{(aq)} + 8e^- \rightleftharpoons 3Fe_{(s)} + 4H_2O$ | -0.528 | -0.545 | -0.551 |
| $3Fe_2O_{3(c)} + 2H^+_{(aq)} + 2e^- \rightleftharpoons 2Fe_3O_{4(c)} + H_2O$ | -0.228 | -0.244 | -0.251 |
| $O_2 + 4H^+ + 4e^- \rightleftharpoons 2H_2O$ | +0.787 | +0.771 | +0.764 |



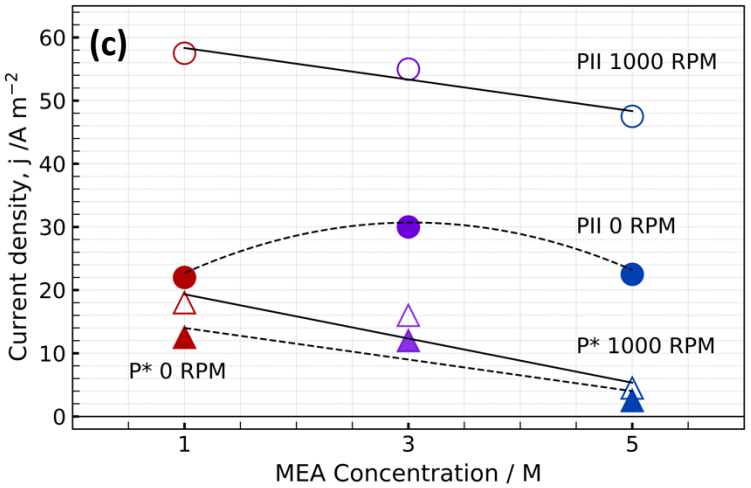




**Figure 5-6**: Effect of potential scan rate on cyclic voltammograms obtained with Fe disc electrodes in quiescent **(a)** 1 M (pH 7.5) and **(b)** 3 M (pH 7.7). $MEA_{(aq)}$, saturated with $CO_2$ at 25 °C.

**(c)** Peak current densities measured in voltammograms obtained with Fe disc electrode in 1, 3 and 5 M $MEA_{(aq)}$ solutions saturated with $CO_2$ at 25 °C; scan rate 20 mV $s^{-1}$ ; PII: o without rotation, ● with rotation; P*: ∆ without rotation, ▲ with rotation; rotation rate = 1000 RPM.

### 5.2.1.4 Effect of temperature on the cyclic voltammetry of Fe in aqueous MEA solutions saturated with $CO_2$

The effect of temperature on the electrochemical behaviour of iron in 1, 3 and 5 M $MEA_{(aq)}$ saturated with $CO_2$ was investigated using cyclic voltammetry. The voltammograms obtained on an Fe rotating disc electrode in 5 M $MEA_{(aq)}$ saturated with $CO_2$ as a function of temperature are shown in **Figure 5-7**. Current density peaks associated with oxidative reactions as a function of both temperature and MEA concentration are also presented in **Figure 5-8**. To avoid $CO_2$ bubble adhesion, and hence noisy data at 80 °C, voltammograms collected for the purpose of examining the impact of temperature were obtained using rotating disc electrodes.

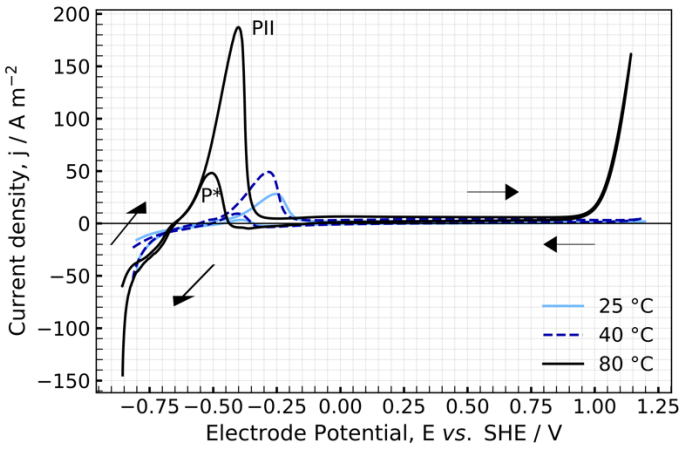



**Figure 5-7:** Effect of temperature on cyclic voltammograms of Fe rotating (1000 RPM) disc electrode in 5 M $MEA_{(aq)}$ solutions saturated with $CO_2$; potential scan rate of 10 mV $s^{-1}$.

The potential was cycled from -0.8 V to *ca*. +1.2 V, at a scan rate of 10 mV $s^{-1}$. At potentials ≤ -0.6 V, negative current densities due to $H_2$ evolution were recorded at all three temperatures, with $H_2$ evolution current densities increasing with increasing temperature. The potentials at which the crossover from cathodic to anodic current densities occurred shifted to more negative values as the solution temperature was increased; this is consistent with thermodynamic predictions of reversible potentials using Nernst equations and the OCP measurements (**Figure 5-1**). As discussed previously, during a positive-going potential scan, the first oxidation reaction at a rotating Fe electrode was assumed to be Fe dissolution and $Fe(OH)_2$ formation; peak current densities associated with these reactions (PI) was *ca*. 4.2 A $m^{-2}$ at -0.45 V and 25 °C (**Figure 5-2b**), *ca*. 3.5 A $m^{-2}$ at-0.525 V and 40 °C (**Figure 5-7**), but was not discernible at 80 °C. At these potentials $Fe(OH)_2$ formation is feasible based on the

pH and reversible potentials, which have been calculated as a function of temperature (**Table 5-2**). $Fe(OH)_2$ was formed in part, due to the $OH^-$ ions produced during $H_2$ evolution. As the temperature was increased, the diffusion rates of $OH^-$ ions in the aqueous solution would have increased, as approximated from Equation **5-17**; this was derived from the Stokes-Einstein equation and where $T_1$ is temperature 1 (*e.g.* 25 °C), $T_2$ temperature 2 (*e.g.* 80 °C), $D_{T1}$ and $D_{T2}$ are the diffusion coefficients at each temperature and $\mu_{T1}$ and $\mu_{T2}$ are the dynamic viscosities at each temperature that have been shown to decrease with increasing temperature (Amundsen, Øi & Eimer, 2009) (**Figure 5-8d**). Therefore, it is possible that less $Fe(OH)_2$ formed as the electrolyte temperature increased. The current density associated with $Fe(OH)_2$ formation in the 1 and 3 M solutions (Appendix, Section 12.3) were both nearly equal and were higher than that measured in the 5 M solution at 25 °C as was discussed previously.

$$D_{T_2} = D_{T_1}\frac{T_2}{T_1}\frac{\mu_{T_1}}{\mu_{T_2}} \text{ and } T_2 > T_1\,, \mu_{T_1} > \mu_{T_2} \;\therefore D_{T_2} > D_{T_1} \qquad \textbf{5-17}$$

Following $Fe(OH)_2$ formation, the current density began (or continued) increasing at all temperatures (**Figure 5-7**), which was likely caused by the formation of $FeCO_3$ (*via* **5-8**) with the peak current density of *ca.* 50 A $m^{-2}$ at 40 °C and 180 A $m^{-2}$ at 80 °C. In fact, the increase in current density with increased temperature followed an Arrhenius relationship as shown in **Figure 5-8b**. This was somewhat unexpected since PII was believed to be due to anodic Fe dissolution, until the local $Fe^{2+}$ concentration was sufficiently high to result in $FeCO_3$ precipitation. Further, the solubility product ($K_{sp}$) of $FeCO_3$ decreases with increased temperature, as was discussed in Chapter 2 (Section 2.4.5.1), so $FeCO_3$ precipitation is favoured at increased temperatures. The onset of $FeCO_3$ formation was found to occur at progressively negative potentials as the temperature increased, which was in agreement with the thermodynamic predictions shown in **Table 5-2**.

At 25 °C, the peak current density associated with $FeCO_3$ formation was slightly higher in the 3 M solution than the 1 and 5 M solutions (**Figure 5-8a**). At 40 °C (**Figure 5-8a**) PII current densities were approximately equal in the 3 and 5 M solutions at *ca.* 50 A $m^{-2}$, and were both higher than those recorded at 25 °C. By contrast, the magnitude of PII measured in the 1 M solution was nearly equal to that measured at 25 °C (**Figure 5-8**). At 80 °C, PII current density was the highest in the 5 M solution, *ca.* 1.3 times that measured in the 3 M solution (151 A $m^{-2}$), and *ca.* 3.4 times that recorded in the 1 M solution (83 A $m^{-2}$).

Unlike that shown in the 5 M solution, the relationship between peak current densities associated with $FeCO_3$ formation and temperature recorded in the 1 and 3 M solutions did not

follow an Arrhenius relationship (**Figure 5-8b**), which was expected given that this reaction is associated with both dissolution and precipitation of a passivating phase ($FeCO_3$). **Figure 5-8d** shows that the effect of temperature on $MEA_{(aq)}$ solution viscosities is more exaggerated as MEA concentration increases. The effect of temperature on the magnitude of PII therefore varies with concentration, which is likely responsible for the changing trend of the magnitude of PII with MEA concentration for each of the examined temperatures shown in **Figure 5-8a**.

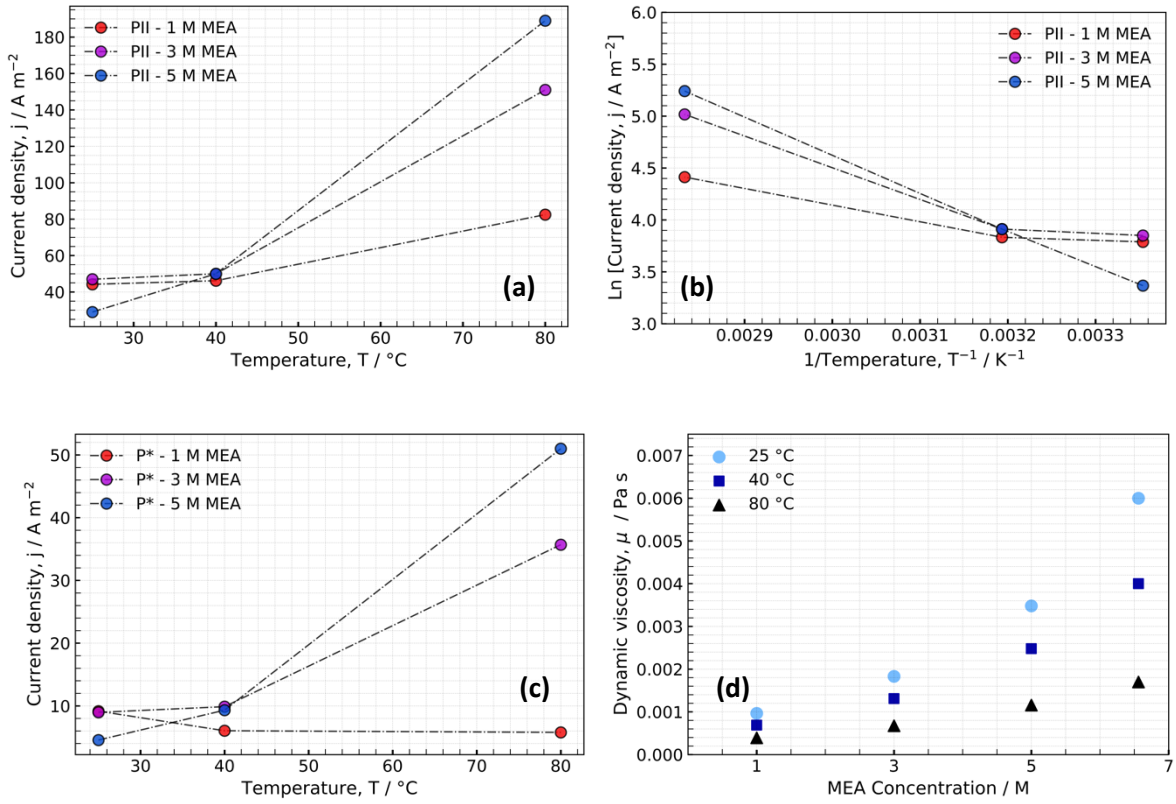



**Figure 5-8:** Measured current density peaks associated with **(a - c)** $FeCO_3$ formation, extracted from voltammograms obtained on rotating (1000 RPM) disc Fe electrodes in 1, 3 and 5 M $MEA_{(aq)}$ saturated with $CO_2$ at 25 – 80 °C. **(d)** Dynamic viscosity as a function of MEA concentration (saturated with $CO_2$) and temperature derived from data taken from (Amundsen, Øi & Eimer, 2009).

The third oxidation peak, related to Fe and/ or $FeCO_3$ and $Fe_3O_4$ oxidation (*via* **5-11** - **5-13**), was not discernible at 25 or 40 °C but a small increase in current density from *ca*. 3 A $m^{-2}$ to 5 A $m^{-2}$, which began at *ca*. -0.15 V, was observed at 80 °C (**Figure 5-7**). Similar behaviour was recorded in the 1 and 3 M solutions (Appendix, Section 12.3.4). The reversible potentials of $FeCO_3$ (*via* **5-11**) and Fe oxidation (*via* **5-12**) are more negative at -0.688 and -0.640 V, respectively, at 80 °C (**Table 5-2**). Therefore, the driving force for $FeCO_3$ formation or Fe oxidation, is higher as compared to those at 25 and 40 °C, so it is reasonable that the two aforementioned reactions occurred.

The current density measured at 80 °C was shown to increase significantly at potentials > + 1 V. At this potential $O_2$ evolution *via* **5-18** is feasible. A minimal increase in current density at potentials ≥ + 1 V was noted at 40 °C and even less so at 25 °C for all three $MEA_{(aq)}$ solutions. In the negative-going scan, no reduction peaks (PIV and PV) were evident at 25 and 40 °C, but at 80 °C the cathodic current densities began increasing at *ca*. -0.2 V and a reduction peak (PV) was apparent at -0.35 V. The occurrence of PV is expected given the presence of PIII on the positive-going scan at 80 °C. PV is thought to be due to the reduction of $Fe_2O_3$ and / or $Fe_3O_4$ to $FeCO_3$; the latter has a reversible potential of -0.352 V at 80 °C (**Table 5-2**). The early onset of $Fe_2O_3$ reduction, *i.e*. at potentials more positive than the reversible potential (at the solution pH) was possibly due to the decreased local pH expected from the significant $H^+$ production accompanying $O_2$ evolution (*via* **5-18**) noted on the positive-going scan. This early onset of $Fe_2O_3$ reduction was also observed in Section 5.2.1.3.

The anodic reactivation reaction, giving rise to P*, was evident at all three temperatures, and was lowest at 25 °C of *ca*. 5 A $m^{-2}$ and the highest at 80 °C of *ca*. 51 A $m^{-2}$ (**Figure 5-7**). As explained previously, this peak is thought to be due (in part) to reactivation of $FeCO_3$ formation and was observed in all three $MEA_{(aq)}$ solutions following similar trends as those described for PII (**Figure 5-8c**).

$$O_2 + 4H^+ + 4e^- \rightleftharpoons 2H_2O \qquad \textbf{5-18}$$

**Table 5-2:** Temperature corrected reversible potentials (*vs*. SHE) for redox reactions on Fe–$CO_2$–$H_2O$ at 25 – 80 °C pH *ca*. 7.9 (Fe species concentration = $10^{-4}$ mol $dm^{-3}$).

| Reaction | 25 °C | 40 °C | 80 °C |
|---|---|---|---|
| $2H^+_{(aq)} + 2e^- \rightleftharpoons H_2 \qquad 2H_2O + 2e^- \rightleftharpoons H_2 + 2OH^-_{(aq)}$ | -0.464 | -0.490 | -0.553 |
| $Fe(OH)_{2(c)} + 2e^- + 2H^+_{(aq)} \rightleftharpoons Fe_{(s)} + H_2O$ | -0.557 | -0.582 | -0.645 |
| $Fe^{2+}_{(aq)} + 2e^- \rightleftharpoons Fe_{(s)}$ | -0.520 | -0.525 | -0.540 |
| $FeCO_{3(c)} + H^+_{(aq)} + 2e^- \rightleftharpoons Fe_{(s)} + HCO^-_{3\,(aq)}$ | -0.647 | -0.658 | -0.688 |
| $Fe_3O_{4(c)} + 3HCO^-_{3\,(aq)} + 5H^+_{(aq)} + 2e^- \rightleftharpoons 3FeCO_{3(c)} + 4H_2O$ | -0.264 | -0.290 | -0.352 |
| $Fe_3O_{4(c)} + 8H^+_{(aq)} + 8e^- \rightleftharpoons 3Fe_{(s)} + 4H_2O$ | -0.551 | -0.577 | -0.640 |
| $3Fe_2O_{3(c)} + 2H^+_{(aq)} + 2e^- \rightleftharpoons 2Fe_3O_{4(c)} + H_2O$ | -0.251 | -0.277 | -0.340 |
| $O_2 + 4H^+ + 4e^- \rightleftharpoons 2H_2O$ | +0.764 | +0.738 | +0.676 |

### 5.2.1.5 Cyclic voltammetry of Pt in aqueous MEA saturated with $CO_2$

The electrochemical processes observed in the voltammograms recorded on Fe electrodes in $MEA_{(aq)}$ solutions saturated with $CO_2$ (**Figure 5-2**, **Figure 5-4** - **Figure 5-7**) were interpretable without needing to consider the direct electrochemical involvement of MEA or MEA based species (*e.g*. $MEAH^+$ or $MEACOO^-$, **Figure 2-28**). To ensure that this was reasonable, cyclic voltammograms of Pt in 5 M $MEA_{(aq)}$, saturated with $CO_2$ were measured, since Pt exhibits distinctive pH-dependent voltametric behaviour in aqueous systems. **Figure 5-9a** shows the electrochemical response of Pt in 5 M $MEA_{(aq)}$ saturated with $CO_2$ and in **Figure 5-9b**, the voltammogram was superimposed on the voltammogram recorded with Fe for easy comparison. The characteristic shape expected of a Pt voltammogram, though not well developed, was recorded in the amine solution, indicating that MEA, $MEAH^+$ and $MEACOO^-$ were not involved directly in electrochemical reactions.

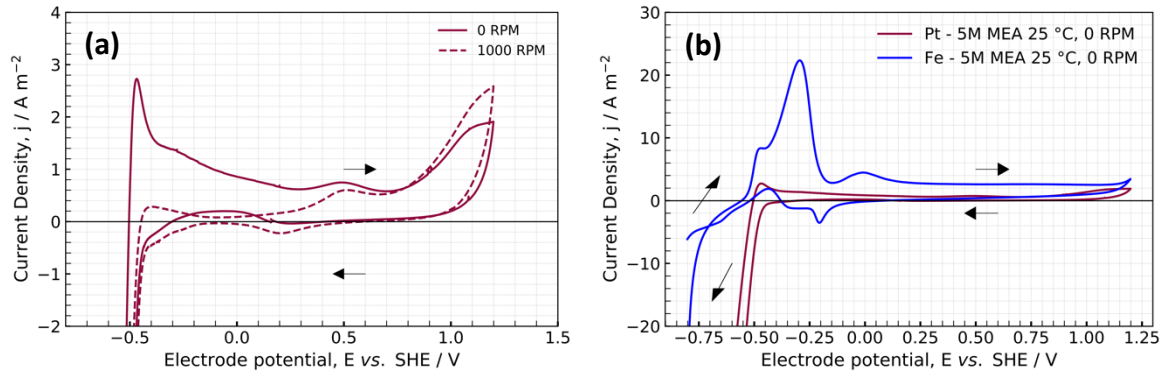



**Figure 5-9:** Cyclic voltammograms recorded in 5 M $MEA_{(aq)}$ saturated with $CO_2$ at 25 °C on **(a)** stationary and rotating disc Pt disc electrodes and **(b)** stationary Fe and Pt disc electrodes. The Pt voltammograms were obtained after 15 cycles.

### 5.2.1.6 Summary of electrochemical behaviour of Fe in aqueous MEA saturated with $CO_2$

Open circuit potential and voltametric behaviour of Fe in $MEA_{(aq)}$ saturated with $CO_2$, including effects of temperature and MEA concentration, were reported in Sections 5.2.1 and 5.2.1.2, respectively. It was found that the OCP of Fe ranged from -0.555 to -0.535 V at 25 °C, becoming increasingly negative in more concentrated $MEA_{(aq)}$ solutions, and from -0.640 to -0.582 V at 80 °C (**Figure 5-1**). Based on the E-pH predictions (**Figure 2-12**), $FeCO_3$ was expected to be the most thermodynamically favourable phase over the range of relevant conditions (pH 7.5 – 7.9). The OCP values agreed broadly with the potentials corresponding to zero current in cyclic voltammetry experiments.

Pt voltametric experiments confirmed that MEA (as well as $MEAH^+$ and $MEACOO^-$) could be treated as electro-inactive. Furthermore, voltammograms recorded on Fe electrodes in MEA–$CO_2$–$H_2O$ closely resembled those obtained in non-MEA containing solutions (Castro *et al*., 1986; Valentini *et al*., 1985), though these involved a smaller potential scan window of *ca*. -1 to +0.2 V.

Voltametric experiments conducted on Fe seemed to indicate that $Fe(OH)_2$ was in fact the first insoluble product to form, either *via* surface transformation or dissolution of $Fe^{II}$ and precipitation, at potentials of *ca*. -0.425 in close proximity to the OCP in the 5 M solution and is thought to have a slightly passivating effect (**Figure 5-2**). This peak was labelled PI and was evident even without preceding $OH^-$ formation due to $H_2$ evolution (**Figure 5-4a**). Less $Fe(OH)_2$ appeared to have formed in the more dilute solutions (1 and 3 M), interpreted by the

absence of a well-defined plateau following PI (**Figure 5-5a**). As temperature was increased, PI became increasingly less discernible (**Figure 5-7**).

With increasing electrode potential, the second oxidation reaction, giving rise to PII, was interpreted as $FeCO_3$ formation by a dissolution-precipitation mechanism; Fe dissolution as $Fe^{2+}$ is believed to have occurred until a sufficient concentration accumulated at the electrode for the saturation ratio (Equation **5-10**) to exceed unity. PII was evident at *ca.* ≥ -0.35 V, substantially more positive than the OCP (**Figure 5-2**). In quiescent solutions at 25 °C, at which the effect of viscosity may have had a significant effect on PII, the maximum current density was detected in the 3 M $MEA_{(aq)}$ solution (**Figure 5-5a**, **Figure 5-6c**). This trend was proposed to be due to the balance of the intermediate accumulation rate of $Fe^{2+}$ and $H^+$ escape. By contrast, when the electrode was rotated, the magnitude of PII decreased with increasing MEA concentration, interpreted as indicative of the surface concentration of $Fe^{2+}$ required for $FeCO_3$ precipitation to passivate the electrode. The decreased $Fe^{2+}$ dissolution current with increased MEA concentration, may have indicated that $FeCO_3$ precipitation is more likely in the 5 M solution. This is reasonable since the bulk pH increases with MEA concentration; as $H^+$ is produced with $FeCO_3$, the local pH would have been relatively higher in the 5 M as compared to the less concentrated solutions, so passivation of the electrode was possibly more facile. The enhanced $Fe(OH)_2$ formation in the 5 M solution also possibly skewed the trends and resulted in faster $FeCO_3$ precipitation. Increasing the electrolyte temperature to 80 °C, which is known to be conducive to $FeCO_3$ precipitation, resulted in PII being the highest in the 5 M and decreasing with decreasing MEA concentration (**Figure 5-6c**). Although increased temperatures are favourable for $FeCO_3$ precipitation, the decreased solution viscosity would have resulted in faster transport of $Fe^{2+}$ away from the electrode surface. PII followed an Arrhenius type relationship with temperature only in the 5 M solution (**Figure 5-8b**), suggesting that Fe dissolution had a more substantial effect on PII than $FeCO_3$ precipitation. At 40 and 80 °C, as MEA concentration decreased, $FeCO_3$ precipitation became more favourable.

The third oxidation reaction, labelled PIII, was postulated to be Fe and $FeCO_3$ oxidation to $Fe_3O_4$ and $Fe_2O_3$. In quiescent, concentrated (3 and 5 M) solutions at 25 °C, PIII was discernible (**Figure 5-5a**), but not when the electrode was rotated (**Figure 5-5b**). The absence of PIII when the electrode was rotated suggested that a local pH decrease facilitated either the partial or complete dissolution of $FeCO_3$ and hence oxidation in the quiescent solutions. However, this oxidation reaction was not evident in the 1 M $MEA_{(aq)}$ solution (**Figure 5-5a**),

possibly suggesting that the $FeCO_3$ formed in this less concentrated solution was more stable at 25 °C. At 80 °C, with electrode rotation, the PIII was in fact present, which likely occurred due to faster Fe oxidation kinetics with increased temperature (**Figure 5-7**).

$O_2$ evolution did not occur in any of the three solutions at 25 °C even at potentials of *ca*. +1.2 V, significantly more positive than the reversible potentials (**Table 5-1**) and was explained to be likely as a result of local pH decrease, which accompanied $FeCO_3$, and/or $Fe_2O_3$ formation. It is also proposed that $O_2$ evolution may not have occurred due to the low electronic conductivities of $Fe_2O_3$ and $FeCO_3$, which were likely present on the electrode surface. However, increased $O_2$ evolution was evident at 40 °C and far more at 80 °C, due to faster $O_2$ evolution kinetics with increased temperature.

At most, two cathodic peaks were noted on the negative-going potential scans in all $MEA_{(aq)}$ solutions at 25 – 80 °C. PIV, which was attributed to $Fe_2O_3$ reduction, appeared only in the quiescent solutions at 25 °C and at high scan rates ≥ 40 mV $s^{-1}$ at *ca*. -0.08 V in the 1 and 3 M solutions (**Figure 5-6a** - **b**), or when the scan was reversed immediately following $Fe_2O_3$ formation in the 5 M solution (**Figure 5-4c**), and at -0.125 V; always more positive than its reversible potential (**Table 5-1**) due to the decreased local pH, which was exaggerated at faster scan rates (**Figure 5-2b**, **Figure 5-6a** - **b**). PIV was not evident under any other conditions. By contrast PV, assigned to both $Fe_2O_3$ and $Fe_3O_4$ reduction, was apparent at most scan rates, but only if the potential was swept sufficiently positive to +1.2 V on the positive-going scan. Sweeping the potential to +1.2 V may have resulted in either complete oxidation to $Fe_2O_3$ or, if the scan rate is sufficiently low, allow the local pH to return to the bulk pH and so only one reduction peak is observed.

On negative-going potential scans and at more negative potentials than those corresponding to PV, an anodic peak, P*, occurred, and is believed to be due to the net current process of oxide reduction and reactivation of oxidative $FeCO_3$ formation. P* was evident in all three solutions at relatively low scan rates (**Figure 5-2b**, **Figure 5-6a** - **b**), and when the electrode was rotated, and followed the same trend as PII with MEA concentration at all temperatures (**Figure 5-6c**). At higher scan rates, P* was not detected, probably due to the high reduction current densities, resulting in a net negative current density.

To conclude this section, it was found that $Fe(OH)_2$ formation is more likely with increased MEA concentration. A specific MEA concentration as optimal for passivation by $FeCO_3$

formation, which held true for all temperatures and conditions (*i.e.* with and without convective transport), was not identified. Instead it was found that variable amounts of $Fe^{2+}$ dissolution were required for $FeCO_3$ formation, depending on the operating conditions. At lower temperatures, $FeCO_3$ formation did not follow a clear trend with MEA concentration due to the interplay of varied solution viscosity and solution pH. At 80 °C, $FeCO_3$ formation may be more likely in dilute (1 M) $MEA_{(aq)}$ solutions, as was reported for carbon steel in Chapter 4. $H^+$ ion production seemed to have had a significant effect on the local pH, which resulted in the absence of expected reactions or onset of reduction reactions at more positive potentials than expected at the bulk pH.

### 5.2.2 Electrochemical behaviour of iron in methyldiethanolamine (MDEA) aqueous solutions saturated with $CO_2$

The open circuit potential (OCP) and cyclic voltammetry experiments presented in the $MEA_{(aq)}$ study (Section 5.2.1) were also conducted in $MDEA_{(aq)}$ solutions saturated with $CO_2$. The results of these experiments will be presented in the subsequent sections (Section 5.2.2.1 - 5.2.2.4) and will be followed by a discussion on the comparative electrochemical response of Fe in $MEA_{(aq)}$ and $MDEA_{(aq)}$ solutions (Section 5.3).

#### 5.2.2.1 Open circuit potential in aqueous MDEA saturated with $CO_2$

The temperature-corrected open circuit potential (OCP) measurements of a stationary iron electrode in 1 (pH 7.6 ± 0.13 ), 3 (pH 8.2 ± 0.07) and 5 (pH 8.6 ± 0.04) M $MDEA_{(aq)}$ solutions saturated with $CO_2$ at 25 and 80 °C are shown in **Figure 5-10**.

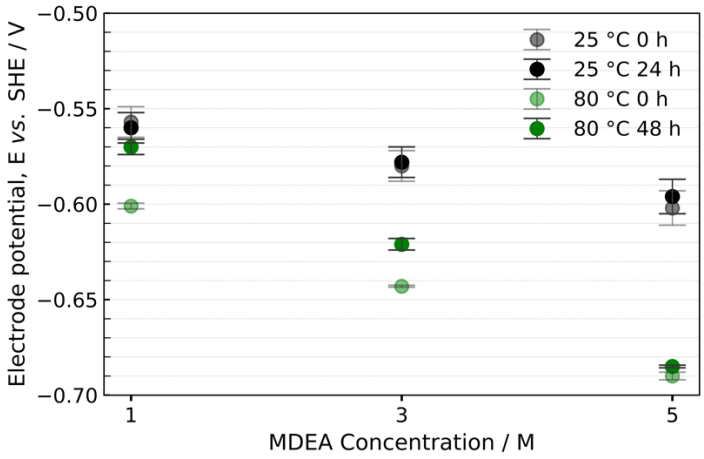



**Figure 5-10:** Effect of MDEA concentration, temperature and time on temperature-corrected average open circuit potentials of a stationary iron electrode in $MDEA_{(aq)}$ solutions saturated with $CO_2$.

From **Figure 5-10**, it can be seen that the average OCPs attained after initial immersion in the 25 °C electrolytes were almost equal to those measured after *ca*. 24 hours of immersion. The OCPs became increasingly negative with higher MDEA concentrations, with the Fe electrode in the 1 M solution attaining an average OCP of -0.557 V and that in the 5 M, -0.602 V. Based on **Figure 2-12**, $FeCO_3$ is predicted to be the most thermodynamically stable phase at the measured potentials and electrolyte pHs.

As was discussed in Section 5.2.1, it is likely that the reactions at the electrode surface were $Fe^{2+}$ dissolution (*via* **5-1**), accompanied by $H_2$ evolution (*via* **5-2**) .The presence of these two reactions leads to increasingly negative OCPs with increased MDEA concentration since the more concentrated solutions had higher pHs; the relationship between OCP and MDEA concentration is thus consistent with that predicted by Equation **5-4**.

When the Fe electrodes were immersed initially in the 80 °C $MDEA_{(aq)}$ solutions saturated with $CO_2$, the OCPs followed the same trend of decreasing electrode potential with increasing MDEA concentration, as was observed at 25 °C. The electrodes in the 1, 3 and 5 M solutions attained average OCPs of *ca*. -0.601, -0.643 and -0.690 V, respectively, all of which were more negative than those measured at 25 °C. After 48 hours of immersion, the average OCPs of the Fe electrodes in all three solutions were higher than those measured after initial immersion, with the deviations between potentials decreasing as MDEA concentration increased, possibly suggesting that surface changes (*e.g*. product formation) occurred more quickly in the 1 M solution and the least in the 5 M solution. At the potentials obtained after 48 hours of immersion (-0.68 to -0.57 V) and the corresponding solution pHs ($pH_{80\ °C}$: 7.9 – 8.6), $FeCO_3$ is predicted to be the most thermodynamically stable phase. Furthermore, at 80 °C, $FeCO_3$ precipitation has been reported to be more feasible than at lower temperatures (Braun, 1991; Bénézeth, Dandurand & Harrichoury, 2009; Greenberg & Tomson, 1992).

### 5.2.2.2 Cyclic voltammetry in aqueous MDEA saturated with $CO_2$

**Figure 5-11** shows cyclic voltammograms of both stationary and rotating Fe disc electrodes in 5 M $MDEA_{(aq)}$ saturated with $CO_2$ at pH *ca*. 8.6. These were measured by cycling the electrode potential from an initial potential of -0.80 V to +1.2 V at a scan rate of 20 mV $s^{-1}$. **Figure 5-12** shows the cyclic voltammograms measured at increasingly positive potentials to aid interpretation of **Figure 5-11**.

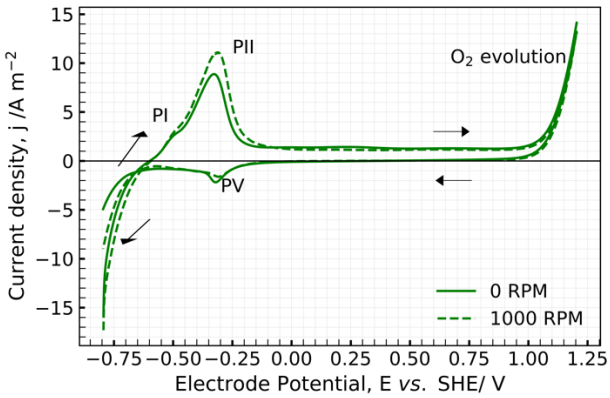



**Figure 5-11:** Cyclic voltammograms of Fe disc electrode in 5 M $MDEA_{(aq)}$ saturated with $CO_2$ at 25 °C, pH *ca*. 8.6, at a scan rate of 20 mV $s^{-1}$ with (---) (1000 RPM) and without rotation (-).

From **Figure 5-11**, cathodic current densities were recorded on the positive-going potential scan between -0.8 and -0.64 V. Subsequently, one clearly discernible positive current density peak was evident between-0.45 and -0.15 V, labelled PII (**Figure 5-11**). A less obvious peak, labelled PI, which preceded PII, was also evident at potentials between -0.55 and -0.45 V, (**Figure 5-11**).

The initial negative current densities recorded between -0.8 and -0.64 V were associated with $H_2$ evolution (*via* **5-2**), with a maximum current density of -15 A $m^{-2}$, increasing to -17.5 A $m^{-2}$ when the electrode was rotated.

On the positive-going scan, the first oxidation peak was much less distinct than that recorded in the 5 M $MEA_{(aq)}$ solution, and was not evident if the potential scan was started at the OCP (**Figure 5-12**). However, when the potential was scanned from an initial value of -0.8 V, $OH^-$ ions produced by $H_2$ evolution likely resulted in a local pH increase, and a higher $OH^-$ concentration. Only then was PI, evident, and is thought to have been due to $Fe(OH)_2$ formation *via* **5-6**, which has a reversible potential of -0.599 V at pH 8.6 (**Table 5-3**).

From **Figure 5-11**, it is evident that the second current density peak, PII, was the only clearly observable oxidative peak, with a magnitude of 9.5 A $m^{-2}$ at -0.340 V. The associated global reaction is described by **5-8**, and is hypothesised to follow a dissolution-precipitation mechanism, with an accompanying release of $H^+$ ions, as discussed in Section 5.2.1.2 for $MEA_{(aq)}$ solutions. The reversible potential at the solution pH of 8.6 is -0.648 V (**Table 5-3**). Increasing the potential scan rate (**Figure 5-14c**) resulted in increased magnitudes of PII, but the dependence was not linear with the square root of the scan rate (Appendix, **Figure 12-4**). Similarly, rotating the electrode resulted in the magnitude of PII increasing to 12.5 A $m^{-2}$, likely due to the enhanced transport of $Fe^{II}$ away from the electrode surface, thus requiring further Fe dissolution to $Fe^{2+}$ for $FeCO_3$ precipitation. From the third potential sweep (**Figure 5-12**) it is estimated that *ca*. 18 monolayers of $FeCO_3$ formed on the positive-going scan, whilst only 3 monolayers are estimated to have formed in the negative-going potential scan at *ca*. -0.4 V.

PIII, associated with Fe, $FeCO_3$ and $Fe_3O_4$ oxidation (*via* **5-11** to **5-13**), was not evident at 20 mV $s^{-1}$, both in **Figure 5-11** and **Figure 5-12**, suggesting that there was little or no conversion of $FeCO_3$ (*via* dissolution and / or oxidation). Rotation had minimal effect on the recorded current densities, which were at most *ca*. 0.5 A $m^{-2}$ and were lower than those recorded in the absence of rotation for potentials +0.125 V to +0.5 V. PIII became apparent only at scan rates ≥ 80 mV $s^{-1}$ (**Figure 5-14c**), with current densities beginning to increase at *ca*. +0.06 V and reaching a maximum of *ca*. 4.5 A $m^{-2}$ at *ca*.+ 0.375 V for a scan rate of 80 mV $s^{-1}$. $FeCO_3$ or Fe oxidation to $Fe_2O_3$ is therefore thought to occur only when $FeCO_3$ dissolution rates were adequate. At higher scan rates, the $H^+$ produced concomitantly with $FeCO_3$ would have had less time to diffuse away from the electrode surface and the local pH would have been sufficiently low to allow for its dissolution and Fe oxidation. This is also consistent with the potential scans presented in **Figure 5-12**. In the third scan (**Figure 5-12c**), in which the negative-going potential scan was applied immediately following the production of $FeCO_3$, P* was recorded since the time elapsed (*ca*. 8 s) was insufficient for $H^+$ diffusion away from the electrode surface, estimated to require *ca*. 13 s[24]. However, in the fourth scan

[24] The time ($t$) required for $H^+$ diffusion away from the electrode was estimated using $\delta = 2\sqrt{D_{H^+}\, t}$, where $D_{H+}$ was taken to be 9.3 × $10^{-9}$ $m^2$ $s^{-1}$ (Newman & Thomas-Alyea, 2012), and the diffusion layer thickness ($\delta$) was estimated from Equation **3-3**, with the kinematic viscosity of 5 M $MDEA_{(aq)}$ calculated with data from (Teng *et al*., 1994).

(**Figure 5-12d**), the potential was swept to +0.5 V, before applying the negative-going scan, giving the $H^+$ adequate time to diffuse away from the electrode surface, and so no net positive current density was recorded in the negative-going potential scan. A minimal reduction peak was observable at *ca*. -0.25 V, *i.e*. at a potential more positive than the reduction peak evident in **Figure 5-11**; this can be seen more clearly in **Figure 5-12e**. This reduction peak, is believed to be consistent with PV (*i.e*. due to $Fe_3O_4$ reduction) observed in the $MEA_{(aq)}$ solutions (**Figure 5-2**, **Figure 5-6**), indicating that some Fe or $FeCO_3$ oxidation did in fact occur on the positive-going scan. The cathodic current density would have resulted in a smaller net current and may have been responsible for the absence of P*in **Figure 5-12d**.

At potentials ≥ + 1 V, the current density began increasing and at the highest applied potential of +1.2 V, attained a maximum value of *ca*. 14 A $m^{-2}$, which was assumed to be caused by $O_2$ evolution *via* **5-18** (**Figure 5-11**). This behaviour was observed at all recorded scan rates with the maximum current density increasing with increasing scan rate (**Figure 5-14c**), though not linearly, nor with the square root of the scan rate (Appendix, Section 12.3). Rotating the electrode resulted in a slightly lower maximum current density of *ca*. 13 A $m^{-2}$. The production of $O_2$ at the electrode surface may have resulted in the formation of $Fe_3O_4$ (*via* **5-19**) or $Fe(OH)_3$ (*via* **5-20**).

$$4FeCO_3 + O_2 \rightleftharpoons 2Fe_2O_3 + 4CO_2 \qquad \textbf{5-19}$$

$$4FeCO_3 + 6H_2O + O_2 \rightleftharpoons 4Fe(OH)_3 + 4CO_2 \qquad \textbf{5-20}$$

On the negative-going scan (**Figure 5-11**) the current densities slowly shifted from positive to negative until a reduction peak (PV) of *ca*. -2.5 A $m^{-2}$ appeared at *ca*. -0.325 V. The voltammograms recorded at higher scan rates exhibited increasingly negative current density peaks (**Figure 5-14c**), with the lowest magnitude current density of -1 A $m^{-2}$ recorded at a scan rate of 10 mV $s^{-1}$, and the most negative of *ca*. -7 A $m^{-2}$ recorded at 100 mV $s^{-1}$, in the range of -0.250 to -0.50 V. In $MEA_{(aq)}$ solutions and in **Figure 5-12d**, PV is thought to be due to the reduction to $Fe_3O_4$, of $Fe_2O_3$ *via* **5-13** at > +1 V. However in **Figure 5-12e** (yellow), the reduction peak (PV) appeared to be at a slightly more negative-potential than that observed in the fourth (green scan), and from **Figure 5-12e** appears to be different from PV. It is also only observable if $O_2$ was evolved on the positive-going scan. Therefore, it is possible that this peak was due both to $Fe_2O_3$ and $O_2$ reduction (*via* **5-13** and **5-18**), both of which are feasible at -0.325 V (**Table 5-3**).

Rotation appeared to have minimal effect on the magnitude of PV, which was measured to be -1.5 A $m^{-2}$, slightly smaller than that measured in the absence of rotation. This result is consistent with the smaller $O_2$ evolution current densities evident on the positive-going scan at *ca*. +1.2 V. The data presented in **Figure 5-12** further substantiates this claim, where a reduction peak is only clearly discernible when the potential was first swept to +1.2 V. Therefore, PV is associated with the reduction of species formed in the positive-going scan at +1.2 V.

Finally, a minor reduction peak is observed in **Figure 5-12e** at *ca*. -0.725 V and is thought to be due to the reduction of the remaining $Fe(OH)_2$ formed *via* **5-6** on the positive going scan. The reversible potential of this reaction is -0.6 V at pH *ca*. 8.6 (**Table 5-3**), so $Fe(OH)_2$ reduction is feasible at -0.725 V. Increasingly negative current densities due to $H_2$ evolution were observed following the $Fe(OH)_2$ reduction peak.

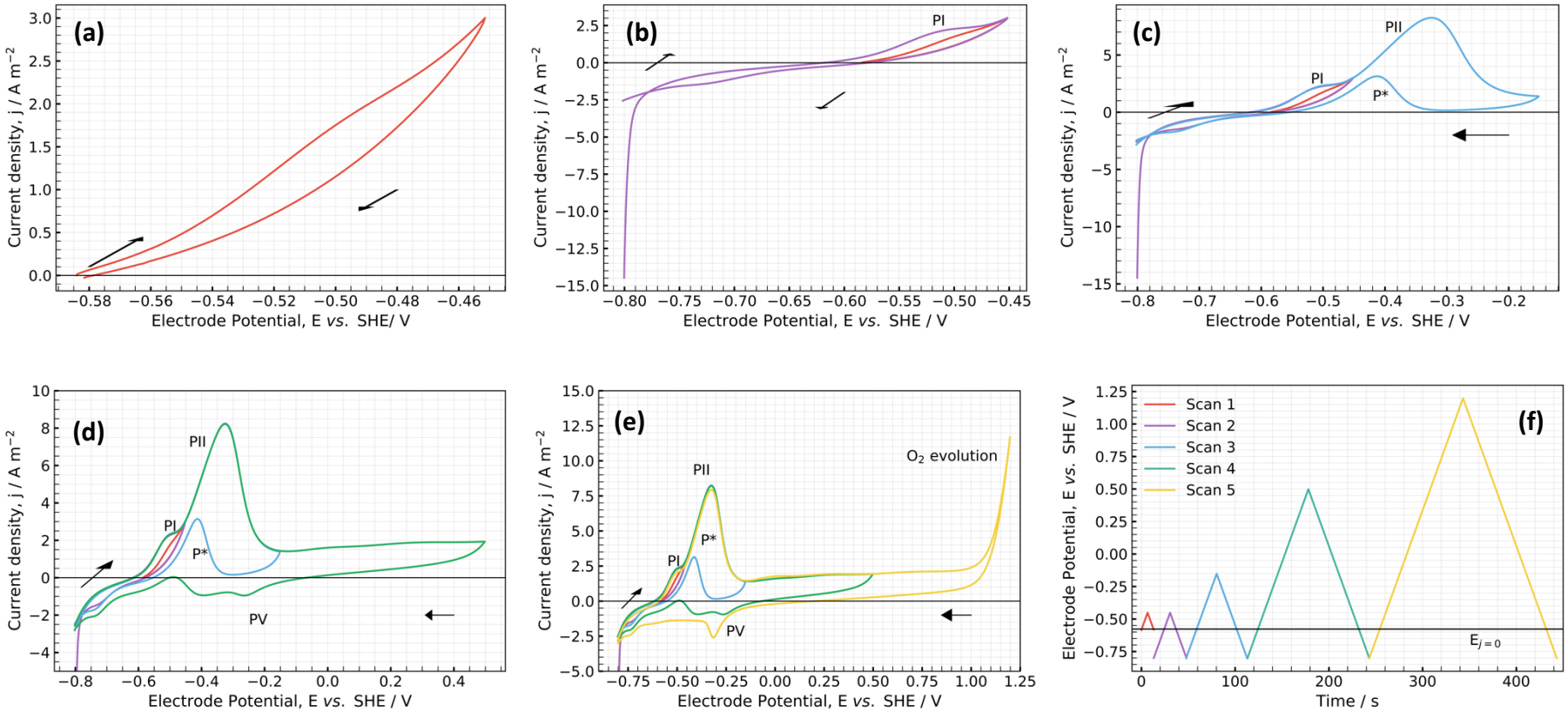



**Figure 5-12:** Cyclic voltammograms obtained on an Fe disc electrode in quiescent 5 M $MDEA_{(aq)}$, saturated with $CO_2$ at 25 °C, pH *ca*. 8.6, at a scan rate of 20 mV $s^{-1}$ with varying potential limits.

### 5.2.2.3 Effect of MDEA concentration on the cyclic voltammetry of Fe in aqueous MDEA solutions saturated with $CO_2$

The solution pHs attained under $CO_2$ saturated conditions varied with MDEA concentration, from pH *ca*. 8.6, to *ca*. 8.2, to *ca*. 7.6 as the MDEA concentration decreased from 5 M, to 3 M to 1 M. Hence, the voltametric results reflect the coupled effects of MDEA concentration and pH. **Figure 5-13** shows the voltammograms recorded at a scan rate of 20 mV $s^{-1}$ cycled from -0.8 to +1.2 V on an Fe disc electrode in 1, 3 and 5 M $MDEA_{(aq)}$ solutions saturated with $CO_2$ at 25 °C. The effects of potential scan rates are presented in **Figure 5-14**.

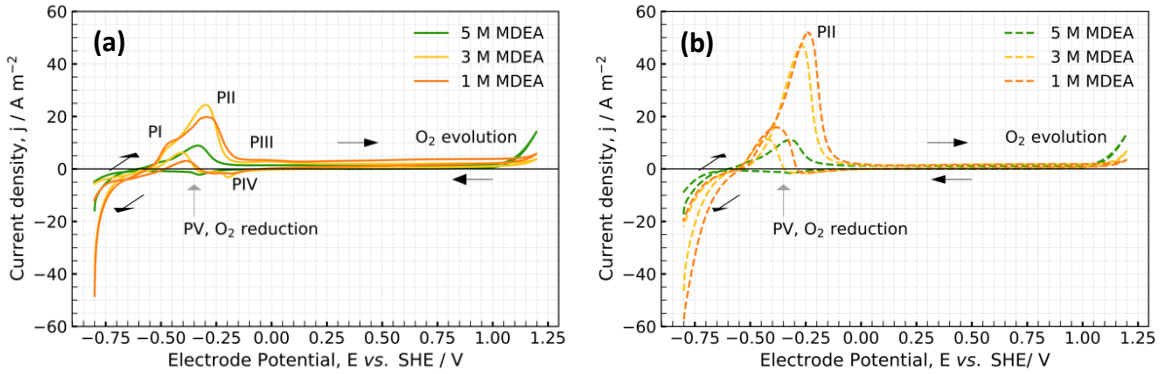



**Figure 5-13**: Effect of MDEA concentrations on cyclic voltammograms of **(a)** stationary and **(b)** rotating (1000 RPM) Fe disc electrodes, in $solutions_{(aq)}$ saturated with $CO_2$ at 25 °C, at a scan rate of 20 mV $s^{-1}$.

From **Figure 5-13**, it can be seen that negative current densities were recorded initially when the potentials applied to the Fe disc electrodes were < -0.55 V, with the magnitude of the current density decreasing with increasing MDEA concentration. As discussed previously in Section 5.2.1.2, these negative current densities were due to $H_2$ evolution, *via* **5-2**, and the reversible potentials at each $MDEA_{(aq)}$ solution pH are included in **Table 5-3**. The reversible potential in the 1 M solution of pH *ca*. 7.6 is the least negative of the three, indicating that the driving force for $H_2$ evolution would be greatest in the 1 M solution, thus resulting in the largest $H_2$ evolution current densities. Rotation at 1000 RPM increased the maximum $H_2$ evolution current densities in the lower concentration solutions, with that recorded in the 1 M solution increasing from *ca*. 50 A $m^{-2}$ to 57 A $m^{-2}$ and that recorded in the 3 M from *ca*. 40 A $m^{-2}$ to 45 A $m^{-2}$, but had little effect on $H_2$ evolution in the 5 M solution. The effect of rotation may have been to decrease concentrations of $H_2$ bubbles adhering to the electrode surface, thereby increasing the active surface area and so current densities.

At potentials ≥ -0.55 V, positive current densities were recorded in all three solutions on the positive-going scan (**Figure 5-13**). PI was recorded in all three solutions between -0.525 V and -0.42 V, and is most defined in the 1 M solution. As noted previously (Section 5.2.2.2), this peak is likely due to $Fe(OH)_2$ formation (*via* **5-6**), with the computed reversible potentials given in **Table 5-3**, due to the excess $OH^-$ formed by $H_2$ evolution. Based on the stepped potential experimental results presented in **Figure 5-12** and discussed in Section 5.2.2.2, it is probable that if the potential scans were initiated at the OCP in each solution, $Fe(OH)_2$ formation would not have occurred. Further, the magnitude of PI was the highest in the 1 M solution possibly because the most $OH^-$ was produced in that solution. In the rotating disc electrode experiments, PI was not apparent in any of the three solutions since the $OH^-$ ions produced by $H_2$ evolution would have been transported efficiently away from the electrode surface, thereby preventing $Fe(OH)_2$ formation.

As in the case of the 5 M solution, a second oxidative reaction, apparent from current density peak PII, was evident in all three solutions within the potential range of -0.4 to -0.35 V (**Figure 5-13**). This peak was assigned to the formation of $FeCO_3$ (*via* **5-8**). As explained previously, the mechanism of $FeCO_3$ formation involves $Fe^{2+}$ release from the electrode surface, and subsequent accumulation, until the saturation ratio (Equation **5-10**) exceeds unity. This results in precipitation of $FeCO_3$, which has a passivating effect on the electrode, which is apparent from the subsequent decay in current densities with time. This passivation reaction appeared to occur with the least Fe dissolution in the 5 M solution, and required the most Fe dissolution in the 3 M solution, with the 1 M requiring slightly less than the 3 M. The 5 M solution was the most viscous of the three, which would have resulted in slower diffusion of $Fe^{II}$ species away from the electrode and hence a higher accumulation rate of $Fe^{2+}$ at the electrode surface. It should be noted that diffusion of $H^+$ ions away from the surface would have also been slower in the 5 M electrolyte, but at the bulk solution pH of 8.6, the impact of the $H^+$ release on local pH may have been less detrimental to $FeCO_3$ stability relative to the 1 and 3 M solutions. When the electrodes were rotated (**Figure 5-13b**), the peak current density associated with $FeCO_3$ formation exhibited an inverse relationship with MDEA concentration. This is likely because the bulk solution pH and thus $HCO_3^-$ concentration was higher as MDEA concentration increased and the $FeCO_3$ saturation ratio would have therefore exceeded unity faster in the more concentrated $MDEA_{(aq)}$ solutions.

Following PII, the current densities recorded in all three solutions decreased to an average of *ca*. 2.7 A $m^{-2}$ (**Figure 5-13a**). There was a subsequent very minimal increase in the current

density to *ca*. 2.9 A $m^{-2}$ recorded in the 1 M as well as in the 3 M solutions as the electrode was swept to potentials ≥ + 0.1 V, but not in the 5 M solution. It is possible that the $Fe(OH)_2$ formed at PI in the 1 and 3 M solutions hindered diffusion of $H^+$ ions formed *via* **5-8** at PII, away from the electrode surface, so causing some dissolution of $FeCO_3$ resulting in subsequent oxidation *via* **5-11** and possibly **5-12**. However, when the electrodes were rotated (**Figure 5-13b**), there was no increase in current density immediately following PII, suggesting that the $FeCO_3$ was not oxidised, due to the efficient removal of $H^+$ by electrode rotation and absence of $Fe(OH)_2$.

At potentials ≥ + 1 V, the current densities began increasing and were the highest in the 5 M solution at *ca*. 15 A $m^{-2}$, then the 1 M at 7 A $m^{-2}$ and lastly *ca*. 3.5 A $m^{-2}$ in the 3 M solution both with and without rotation (**Figure 5-13**). At this potential, $O_2$ evolution, *via* **5-18**, is thought to have occurred, the calculated reversible potentials for this reaction are at most + 0.78 V for all three solutions (**Table 5-3**). Although **Figure 5-13** showed that there was some degree of $O_2$ evolution in the 1 and 3 M solutions, **Figure 5-14** showed that there was far more $O_2$ evolution in the 5 M solution at all scan rates.

On the negative-going scan (**Figure 5-13a**) at 20 mV $s^{-1}$, current densities became negative at *ca*. -0.1 V in the 1 and 3 M solutions with current density peaks appearing at *ca*. -0.17 V in the 1 M solution and at *ca*. -0.19 V in the 3 M solution. At scan rates ≥ 40 mV $s^{-1}$ (**Figure 5-14**), another reduction reaction occurred in both the 1 and 3 M solutions with current density peaks evident at *ca*. -0.23 V and *ca*. 0.25 V, respectively. By contrast, only one reduction reaction was apparent in the 5 M solution (**Figure 5-11**) at a more negative potential of *ca*. -0.325 V. In fact, as the concentration of MDEA decreased from 5 to 1 M, PIV became more distinct (**Figure 5-14**). In the 1 and 3 M quiescent solutions at high scan rates, the two reduction reactions are thought to be $Fe_2O_3$ to $Fe_3O_4$ (*via* **5-13**) and $Fe_3O_4$ to $FeCO_3$ (*via* **5-11**), since PIII, which is associated with $FeCO_3$ to $Fe_2O_3$, *via* $Fe_3O_4$, were evident under these conditions. However, in the 5 M solution, only one reduction peak was discernible at all scan rates, and is proposed to be due to reduction of $O_2$ (and probably $Fe_2O_3$). **Figure 5-14** substantiates this proposition since the reduction peak was observed only if significant $O_2$ evolution occurred in the positive-going scan.

P* was not recorded in any of the voltammograms measured in the 5 M solution, but did appear at lower scan rate voltammograms (≤ 40 mV $s^{-1}$) in the 1 and 3 M solutions (**Figure 5-14a**, **b**). In the absence of rotation, P* was measured in the 1 and 3 M solutions between -0.3 and -0.5 V (**Figure 5-13a**), with a current density peak of *ca*. 4 A $m^{-2}$ at *ca*. -0.38 V in the

1 M solution and a higher current density peak of *ca*. 7 A $m^{-2}$ at *ca*. -0.4 V in the 3 M solution. When the rotating Fe disc electrode was used, the magnitude of P* decreased with increasing MDEA concentration. It was evident that the relationship between the magnitude of PII and MDEA concentration was also exhibited by P* with both stationary and rotating Fe disc electrodes (**Figure 5-13**).

**Table 5-3:** Reversible potentials (*vs*. SHE) for redox reactions on Fe in $CO_{2(aq)}$ at bulk solution pH at 25 °C (Fe species concentration = $10^{-4}$ mol $dm^{-3}$).

| **Electrochemical Reactions** | **pH 7.61** | **pH 8.19** | **pH 8.58** |
|---|---|---|---|
| $2H^+_{(aq)} + 2e^- \rightleftharpoons H_2 \qquad 2H_2O + 2e^- \rightleftharpoons H_2 + 2OH^-_{(aq)}$ | -0.450 | -0.486 | -0.508 |
| $Fe(OH)_{2(c)} + 2e^- + 2H^+_{(aq)} \rightleftharpoons Fe_{(s)} + H_2O$ | -0.542 | -0.576 | -0.599 |
| $Fe^{2+}_{(aq)} + 2e^- \rightleftharpoons Fe_{(s)}$ | -0.549 | | |
| $FeCO_{3(c)} + H^+_{(aq)} + 2e^- \rightleftharpoons Fe_{(s)} + HCO^-_{3\,(aq)}$ | -0.623 | -0.629 | -0.648 |
| $Fe_3O_{4(c)} + 3HCO^-_{3\,(aq)} + 5H^+_{(aq)} + 2e^- \rightleftharpoons 3FeCO_{3(c)} + 4H_2O$ | -0.363 | -0.449 | -0.507 |
| $Fe_3O_{4(c)} + 8H^+_{(aq)} + 8e^- \rightleftharpoons 3Fe_{(s)} + 4H_2O$ | -0.537 | -0.571 | -0.594 |
| $3Fe_2O_{3(c)} + 2H^+_{(aq)} + 2e^- \rightleftharpoons 2Fe_3O_{4(c)} + H_2O$ | -0.236 | -0.271 | -0.294 |
| $O_2 + 4H^+ + 4e^- \rightleftharpoons 2H_2O$ | +0.779 | +0.745 | +0.722 |

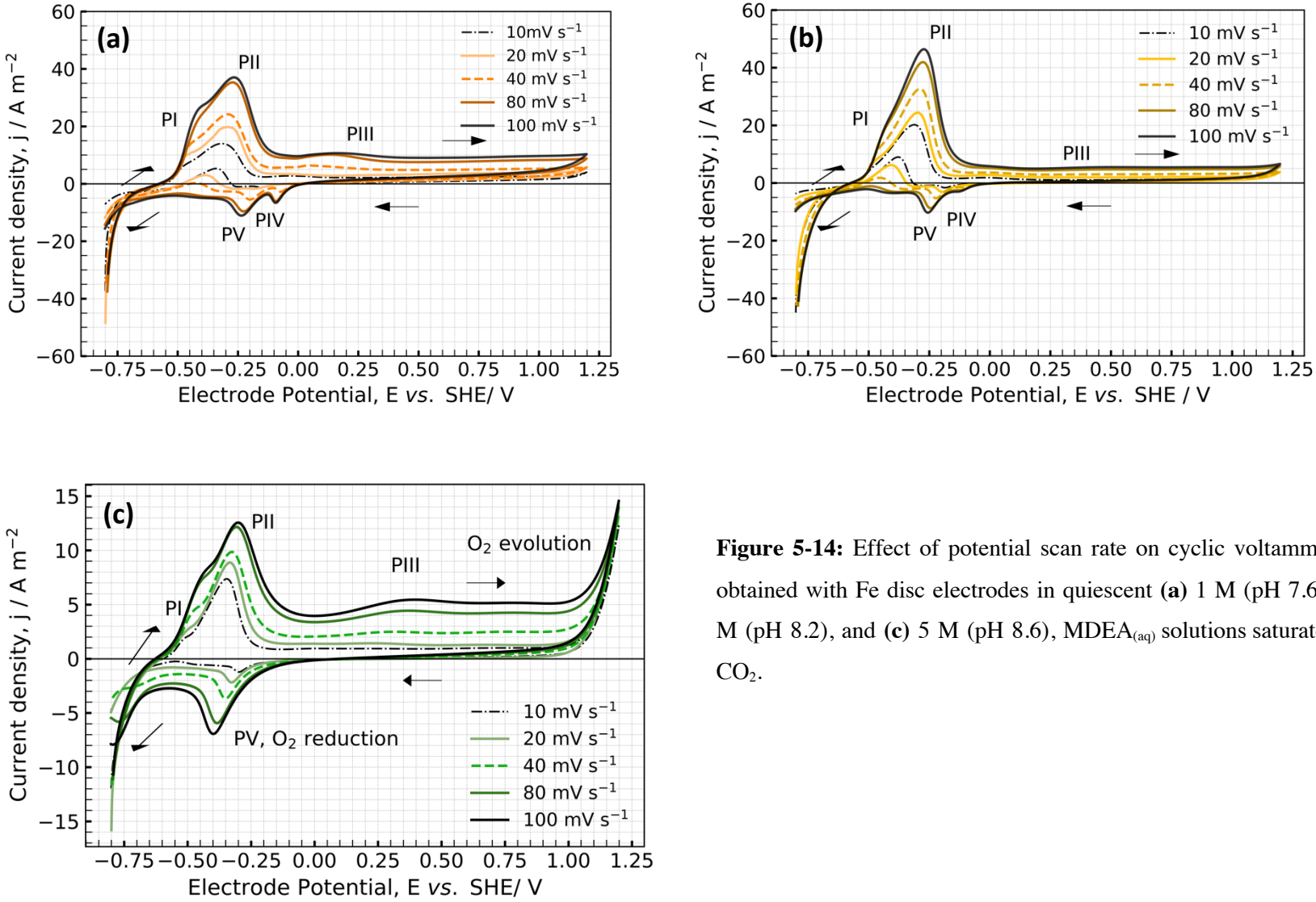



**Figure 5-14:** Effect of potential scan rate on cyclic voltammograms obtained with Fe disc electrodes in quiescent **(a)** 1 M (pH 7.6), **(b)** 3 M (pH 8.2), and **(c)** 5 M (pH 8.6), $MDEA_{(aq)}$ solutions saturated with $CO_2$.

### 5.2.2.4 Effect of temperature on the cyclic voltammetry of Fe in aqueous MDEA solutions saturated with $CO_2$

The effect of temperature on the electrochemical behaviour of Fe in 1, 3 and 5 M $MDEA_{(aq)}$ saturated with $CO_2$ was investigated using cyclic voltammetry. The voltammograms obtained on an Fe rotating disc electrode in 5 M $MDEA_{(aq)}$ saturated with $CO_2$ as a function of temperature are shown in **Figure 5-15**. Current density peaks associated with oxidative reactions as a function of both temperature and MDEA concentration are presented in **Figure 5-16**, and the voltammograms from which peak current densities were taken in addition to **Figure 5-15** are included in the Appendix (Section, 12.3.5). As in the $MEA_{(aq)}$ solutions, the presence of $CO_2$ and possibly $H_2$ bubbles on stationary electrodes at 80 °C resulted in noisy data, so voltammograms collected for the purpose of examining the effect of temperature were obtained using only rotating disc electrodes.

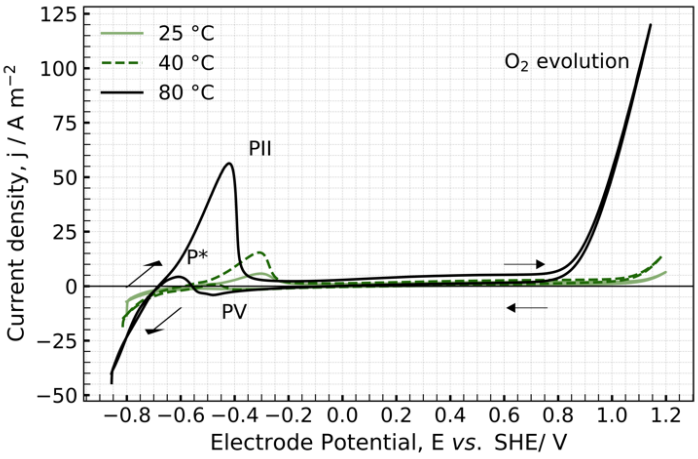



**Figure 5-15:** Effect of temperature on cyclic voltammograms of rotating (1000 RPM) disc Fe electrodes in 5 M $MDEA_{(aq)}$ saturated with $CO_2$ at a scan rate of 10 mV $s^{-1}$.

At all three temperatures, on scanning the potential from a start potential of -0.8 V (**Figure 5-15**), $H_2$ evolution occurred with the highest current density measured at 80 °C and the lowest at 25 °C, as expected. Current densities became positive at *ca*. -0.50 V at 25 °C, -0.550 V at 40 °C, and -0.625 V at 80 °C.

With increasing potentials, $Fe(OH)_2$ formation was believed to have occurred, giving rise to PI at 25 – 40 °C, but apparently not at 80 °C. The onset of $FeCO_3$ formation, resulting in PII, began at increasingly negative potentials with higher temperatures. PII did not exhibit an Arrhenius type relationship with temperature, as indicated by the non-linear correlation between the natural log of the peak current densities against the inverse temperature (**Figure**

**5-16b**); at 80 °C, the maximum current density was *ca*. 55 A $m^{-2}$, which was 3.6 times that at 40 °C and *ca*. 8 times that measured at 25 °C. At 25 °C, PII current densities decreased with increasing MDEA concentration (**Figure 5-16a**), whilst at 40 and 80 °C, the magnitude of PII recorded in the 3 M solution was the highest, followed by that recorded in the 1 M, and that measured in the 5 M solution was the lowest. PII measured in the 1 and 3 M solutions also did not show an Arrhenius relationship with temperature (**Figure 5-16b**).

It was unclear if any $FeCO_3$ oxidation occurred at 25 – 80 °C as evidenced by the absence of PIII in the 10 mV $s^{-1}$ scans shown in **Figure 5-15**. There may have been minimal oxidation at potentials > +0.1 V from the very small increase in current density.

In **Figure 5-15**, $O_2$ evolution occurred at potentials ≥ +0.9 V in the 5 M $MDEA_{(aq)}$ solution, with onset potentials decreasing as the temperature was increased; hence, $O_2$ evolution current densities were expectedly greatest at 80 °C and smallest at 25 °C, as in both the 1 and 3 M $MDEA_{(aq)}$ solutions. At 25 °C, the $O_2$ evolution current density was highest in the 5 M solution and decreased with decreased MDEA concentration (**Figure 5-16d**). This was consistent with the voltametric results as a function of scan rate in quiescent solutions (**Figure 5-14**). However, at 80 °C, the $O_2$ evolution current densities were the smallest in the 1 M, intermediate in the 5 M and greatest in the 3 M solution (**Figure 5-16d**).

On the negative-going potential scan at a rate of 10 mV $s^{-1}$, from *ca*. +1.2 V to -0.8 V at the rotating disc Fe electrode in 5 M $MDEA_{(aq)}$ solution, PV, related to $O_2$ (and $Fe_2O_3$) reduction was evident at -0.25 V at 25 °C, -0.3 V at 40 °C and -0.425 V at 80 °C. The voltammograms recorded in the 1 and 3 M solutions at 25 and 40 °C did not show a distinct reduction peak (Appendix Section 12.3.5) but negative current densities were recorded at potentials ≤ -0.25 V indicating that a reduction process, probably of $Fe_2O_3$ and / or $Fe_3O_4$, did occur. At 80 °C, the voltammogram measured in the 1 M solution exhibited similar behaviour to that observed in the 5 M solution (**Figure 5-15**), with current densities becoming negative at ≤ -0.40 V, with no obvious peak (Appendix, Section 12.3.5). By contrast, in the 3 M solution very small negative current densities were recorded, as was expected from the minimal $FeCO_3$ oxidation current densities observed on the positive-going scan (Appendix, Section 12.3.5).

On scanning the Fe potential to more negative potentials in the 5 M $MDEA_{(aq)}$ solution, shown in **Figure 5-15**, P* appeared at 40 and 80 °C with peak current densities of *ca*. 2 A $m^{-2}$ at -0.450 V and *ca*. 5 A $m^{-2}$ at -0.650 V respectively. However, no $FeCO_3$ reactivation reaction was evident at 25 °C, as discussed previously in Section 5.2.2.2. At all temperatures,

in the 1 and 3 M solutions, P* appeared and followed the same trend with MDEA concentration as for PII (**Figure 5-16c**); at 25 °C, the magnitude of P* was greatest in the 1 M solution, smallest in the 5 M, and at 40 and 80 °C, the greatest in the 3 M solution, and the smallest in the 5 M solution (**Figure 5-16c**).

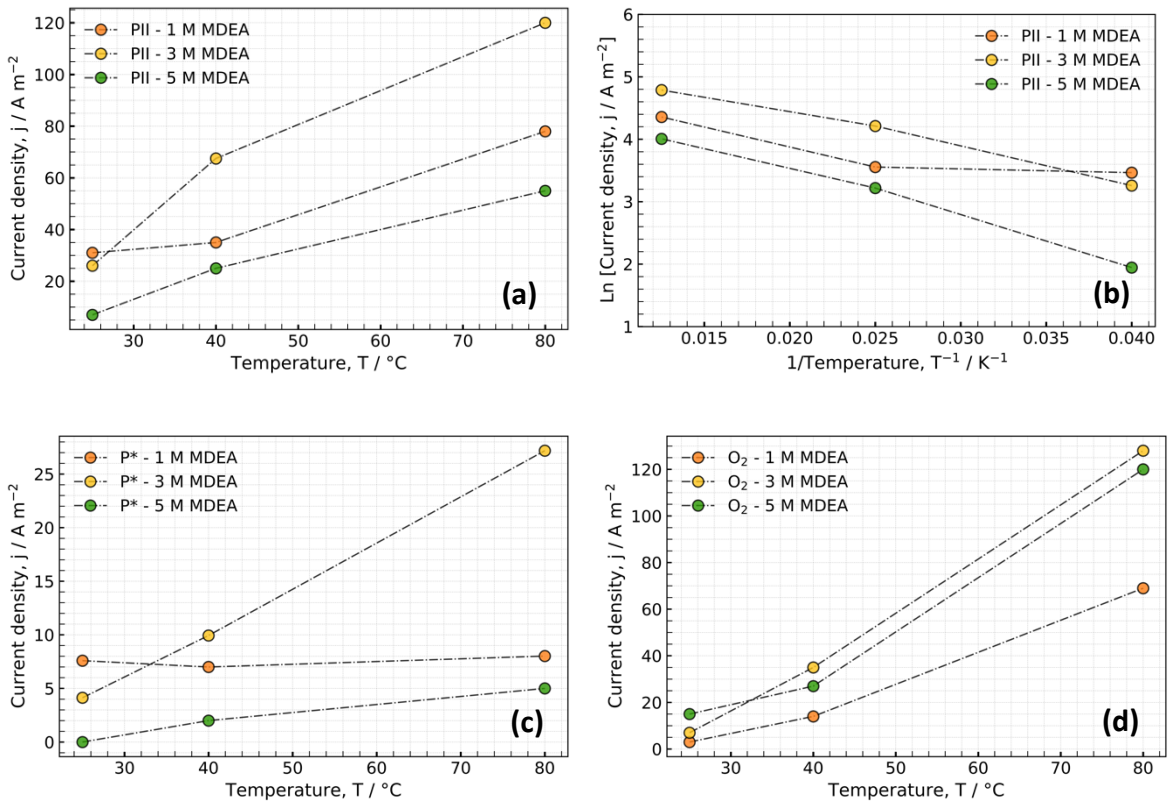



**Figure 5-16:** Current density peaks associated with $FeCO_3$ formation measured in **(a - b)** positive-going scan, and **(c)** negative-going scan; and **(d)** maximum $O_2$ evolution current density (at *ca*. +1.2 V), extracted from voltammograms obtained on rotating (1000 RPM) disc Fe electrodes in 1, 3 and 5 M $MDEA_{(aq)}$ solution saturated with $CO_2$ at 25 – 80 °C.

**Table 5-4:** Reversible potentials (*vs*. SHE) for redox reactions on Fe–$H_2O$–$CO_2$ at 25 – 80 °C pH *ca*. 8.6 (Fe species concentration = $10^{-4}$ mol $dm^{-3}$).

| Reaction | 25 °C | 40 °C | 80 °C |
|---|---|---|---|
| $2H^+_{(aq)} + 2e^- \rightleftharpoons H_2 \qquad 2H_2O + 2e^- \rightleftharpoons H_2 + 2OH^-_{(aq)}$ | -0.508 | -0.534 | -0.603 |
| $Fe(OH)_{2(c)} + 2e^- + 2H^+_{(aq)} \rightleftharpoons Fe_{(s)} + H_2O$ | -0.599 | -0.626 | -0.694 |
| $Fe^{2+}_{(aq)} + 2e^- \rightleftharpoons Fe_{(s)}$ | -0.520 | -0.525 | -0.540 |
| $FeCO_{3(c)} + H^+_{(aq)} + 2e^- \rightleftharpoons Fe_{(s)} + HCO^-_{3\,(aq)}$ | -0.623 | -0.629 | -0.648 |
| $Fe_3O_{4(c)} + 3HCO^-_{3\,(aq)} + 5H^+_{(aq)} + 2e^- \rightleftharpoons 3FeCO_{3(c)} + 4H_2O$ | -0509 | -0.595 | -0.812 |
| $Fe_3O_{4(c)} + 8H^+_{(aq)} + 8e^- \rightleftharpoons 3Fe_{(s)} + 4H_2O$ | -0.595 | -0.621 | -0.689 |
| $3Fe_2O_{3(c)} + 2H^+_{(aq)} + 2e^- \rightleftharpoons 2Fe_3O_{4(c)} + H_2O$ | -0.205 | -0.320 | -0.389 |
| $O_2 + 4H^+ + 4e^- \rightleftharpoons 2H_2O$ | +0.720 | +0.695 | +0.626 |

## 5.3 Comparison of electrochemical behaviour of iron in both aqueous amine solutions saturated with $CO_2$

Open circuit potential measurements and cyclic voltammetry were used to investigate the electrochemical behaviour of Fe in MEA and MDEA aqueous solutions saturated with $CO_2$ to provide insight into the mechanisms of corrosion behaviour of steel immersed to the two $CO_2$ capture solvents.

OCPs became increasingly negative with increasing amine concentration for both amines at 25 °C, and showed little change in a 24 hour period. The OCPs recorded at 80 °C were all more negative than the corresponding values at 25 °C. After 48 hours of immersion at 80 °C, the OCPs became less negative relative to their initial values, except those in 5 M $MEA_{(aq)}$. The OCPs attained in $MDEA_{(aq)}$ solutions of the same concentration as the $MEA_{(aq)}$ solutions were consistently more negative at both temperatures. $FeCO_3$ was determined to be the most thermodynamically stable phase at all temperatures, concentrations and amine types from the measured OCPs of *ca*. -0.68 to -0.53 V based on the potential-pH diagram (**Figure 2-12**).

From the data presented in Sections 5.2.1.2 - 5.2.1.4, and 5.2.2.2 - 5.2.2.4, there were some similarities and differences exhibited by Fe in the aqueous amine solutions saturated with $CO_2$. The voltammograms in all electrolytes which were initiated at -0.8 V, started with $H_2$ evolution and formation of $OH^-$ ions. This resulted in $Fe(OH)_2$ formation in $MDEA_{(aq)}$ solutions as the potential was swept more positively, and enhanced its formation in $MEA_{(aq)}$ solutions.

From the voltametric behaviour, $FeCO_3$ was inferred to form in both $MEA_{(aq)}$ and $MDEA_{(aq)}$ solutions at all concentrations, temperatures and under stationary and rotating conditions. In quiescent solutions at 25 °C, a parabolic relationship (**Figure 5-6c**, **Figure 5-13a**) was observed between the magnitude of PII, corresponding to $FeCO_3$ formation, and amine concentration in both amines, for which the 3 M solution produced the highest current density. By contrast, when voltammograms were recorded with rotating disc electrodes at 25 °C, the associated current densities exhibited an inverse relationship with concentration in both amines (MEA: **Figure 5-6c** , MDEA: **Figure 5-13b**). At 40 and 80 °C, the magnitude of PII in the two amines exhibited different trends with concentration, where a parabolic relationship was observed with MDEA concentration (**Figure 5-16**), consistent with that observed in quiescent solutions at 25 °C. Conversely, the magnitude of PII exhibited a more

complex relationship with MEA concentration as the electrolyte temperature was increased from 25 – 80 °C (**Figure 5-8a**); at 25 °C the magnitude of PII was the smallest in the 5 M solution, whilst at 40 °C, the value of PII in all three solutions were approximately equal, and then at 80 °C, PII was the greatest in the 5 M solution and the smallest in the 1 M solution. An Arrhenius relationship was demonstrated to exist between the magnitude of PII and temperature in the 5 M $MEA_{(aq)}$ solution only, suggesting that Fe dissolution dominated the current response.

With rotating disc electrodes, $FeCO_3$ oxidation did not occur in either of the amine solutions at any concentration with a scan rate of 20 mV $s^{-1}$ at 25 °C, but was apparent at 80 °C in 1 M solutions of both amines (Appendix, Section 12.3.4 - 12.3.5). Divergent behaviour was evident in the absence of rotation; peak (PIII), proposed to be associated with $Fe_3O_4$ and $Fe_2O_3$ formation, was not observed at any MDEA concentration at scan rates ≤ 40 mV $s^{-1}$, but PIII was observed in 3 and 5 M $MEA_{(aq)}$ solutions at the same scan rates.

Contrasting $O_2$ evolution kinetics were exhibited in the two amines at most temperatures and concentrations. Generally, the kinetics of $O_2$ evolution at potentials ≥ 1 V were considerably faster in $MDEA_{(aq)}$ solutions; this was most notable from comparison of voltammograms collected in 5 M 25 °C solutions (**Figure 5-2**, **Figure 5-11**), on both rotating and stationary Fe disc electrodes. $O_2$ evolution currents were noted in all solutions at 80 °C, likely as a result of accelerated kinetics because of the elevated temperature (**Figure 5-7**, **Figure 5-15**).

In both amines, an additional reduction peak, preceding PV, was evident as each amine concentration was decreased from 5 to 1 M. Reduction peaks were thought to be associated with $Fe_2O_3$ reduction to $FeCO_3$, with intermediate formation of $Fe_3O_4$. In 5 M $MDEA_{(aq)}$, this peak was thought to be predominantly due to $O_2$ reduction; the $O_2$ was formed in the positive-going scan. Dissimilar behaviour between amines was also evident in the anodic reactivation of $FeCO_3$ formation (P*) at amine concentrations of 5 M; P* occurred in 5 M $MEA_{(aq)}$ solutions at scan rates ≤ 20 mV $s^{-1}$, but not in 5 M $MDEA_{(aq)}$ solutions. As the concentrations of both amines was decreased, P* became increasingly discernible.

## 5.4 Conclusions

Open circuit potential measurements and cyclic voltammetry were used to investigate and compare the electrochemical behaviour exhibited by iron, as a surrogate for carbon steel, in $MEA_{(aq)}$ and $MDEA_{(aq)}$ solutions saturated with $CO_2$ as a function of amine concentration and solution temperature. A potential-pH diagram of Fe–$CO_2$–$H_2O$ was used for interpretation of OCP measurements and cyclic voltammograms.

Iron electrodes attained OCPs of *ca*. -0.69 to -0.53 V, indicative of $FeCO_3$ in all $MEA_{(aq)}$ and $MDEA_{(aq)}$ solutions saturated with $CO_2$ at 25 and 80 °C. However, voltammograms suggested that $Fe(OH)_2$ was likely to have formed at *ca*. -0.5 V *i.e*. near OCPs in 5 M $MEA_{(aq)}$ solution. With few exceptions, voltammograms were initiated at -0.8 V, which seemed to have resulted in an additional oxidative reaction, proposed to be $Fe(OH)_2$ formation, at *ca*. -0.5 V in $MDEA_{(aq)}$, and appeared to enhance its formation in $MEA_{(aq)}$ solutions. All voltammograms should have been initiated at OCP to ensure that subsequently measured oxidation and reduction current densities were not obscured by initial $H_2$ evolution.

In addition to $Fe(OH)_2$, $FeCO_3$ and $Fe_2O_3$ anodic formation was observed on stationary Fe disc electrodes in $MEA_{(aq)}$ solutions at potentials of -0.5 to -0.45 V, -0.4 to -0.2 V, and -0.1 to +0.1 V, respectively at 25 °C. Both Pt and Fe voltametric experiments in $MEA_{(aq)}$ confirmed that MEA, $MEAH^+$ and $MEACOO^-$ were electro-inactive as voltammograms closely resembled those recorded in mildly alkaline, or in the case of Fe, alkaline-carbonate solutions not containing MEA. In the absence of $H_2$ evolution, $FeCO_3$ formation appeared to be the only clearly discernible oxidation reaction in $MDEA_{(aq)}$ over the potential range of -0.6 to +1 V at low scan rates. Accordingly, it was deduced that $FeCO_3$ was less likely to undergo oxidation in $MDEA_{(aq)}$ than in $MEA_{(aq)}$ solutions, evident from the absence of an anodic peak immediately following $FeCO_3$ formation. This suggests that $FeCO_3$ may in fact form on Fe in both amines, but dissolves or oxidises more readily in $MEA_{(aq)}$. A further investigation of the relative stability of $FeCO_3$ on Fe will be reported in Chapter 6.

# 6 $FeCO_3$ formation on iron in amine solutions saturated with $CO_2$

## 6.1 Introduction

In Chapter 4 it was demonstrated that $FeCO_3$ formed on carbon steel when exposed to $MDEA_{(aq)}$ solutions saturated with $CO_2$ at 80 °C, regardless of concentration, but only formed on carbon steel in dilute $MEA_{(aq)}$ (1 M) solutions under the same conditions. Chronoamperometry, in which a fixed potential is applied to a working electrode and the resulting current densities measured as a function of time, can be used to investigate electrode surface processes. A description of this technique is given in Chapter 2, Section 2.4.5.2. In this chapter, results of chronoamperometric experiments are reported to monitor the formation of $FeCO_3$ on iron, as a surrogate for carbon steel, in $MEA_{(aq)}$ and $MDEA_{(aq)}$ $CO_2$ saturated solutions, to provide insight to any mechanistic differences. The experimental procedure followed is outlined in Chapter 3, Section 3.3. The experimental results will also be interpreted with the aid of predictions of local solution chemistry changes and will be included in Section 6.3.

## 6.2 Results

The $FeCO_3$ formation potentials on Fe electrodes in $MEA_{(aq)}$ and $MDEA_{(aq)}$ solutions saturated with $CO_2$ at 80 °C were determined firstly by measuring the cyclic voltammogram on a rotating (at 1000 RPM) Fe disc electrode in each solution. The potential, typically in the

range -0.40 to -0.350 V[25], at which the maximum positive current density was recorded on the positive-going sweep, was assumed to correspond to $FeCO_3$ formation. After electrochemically pre-treating the Fe electrode to remove any species formed in the voltammetry experiment, the $FeCO_3$ formation potential was applied continuously to the rotating disc Fe electrode. The current transients obtained in $MEA_{(aq)}$ and $MDEA_{(aq)}$ solutions saturated with $CO_2$ are presented in **Figure 6-1** and **Figure 6-4** respectively. The total charges passed during potentiostatic experiments were also calculated and are presented in **Figure 6-3** and **Figure 6-6**. Results obtained from electrochemical experiments were supplemented by *ex-situ* images, obtained using scanning electron microscopy (SEM), together with corresponding surface chemistry detected using electron dispersive spectroscopy (EDX) and X-ray diffraction (XRD), and are reported in **Figure 6-2** and **Figure 6-5**.

To support further analysis of the current density transients, the cumulative charge densities passed were calculated and assumed to be related only to oxidative Fe dissolution as $Fe^{2+}$ ions. The charge was converted to the moles ($m$) of $Fe^{2+}$ ions produced, using Faraday's law of electrolysis (Equation **6-1**) and assuming 2 F ($n$) are transferred per mole of $Fe^{2+}$ produced with a charge yield or Faradaic efficiency ($\Phi$) of 1. Since a rotating disc electrode was used, the moles of $Fe^{2+}$ produced, calculated using Equation **6-1**, were assumed to be transferred to the bulk and converted to bulk $Fe^{2+}$ concentration using the electrolyte volume of 0.16 $dm^3$. The saturation ratio ($S_{FeCO3}$) was then estimated using Equation **5-10** with the $CO_3^{2-}$ concentration estimated to be between $1.0 \times 10^{-3}$ and $5.3 \times 10^{-3}$ mol $dm^{-3}$ calculated using the mole fraction of $CO_3^{2-}$ based on the solution pH, and a total dissolved $CO_2$ concentration of 0.0129 mol $dm^{-3}$ (Appendix, Section 12.4.4). The solubility limit, $K_{sp}$ (mol$^2$ $dm^{-6}$), in each solution was calculated using Equation **6-2** (Sun, Nešić & Woollam, 2009), in which $T$ (K) is the solution temperature and $I$ (mol $dm^{-3}$) the ionic strength calculated from Equation **6-3** ($C_i$ and $z_i$ are the concentration and charge of species $i$) based on equilibrium concentrations (Appendix, Section 12.4, **Figure 12-13** - **Figure 12-14**). The calculated bulk solution $FeCO_3$ saturation ($S_{FeCO3}$) ratio was plotted as a function of time in **Figure 6-1** and **Figure 6-4**.

$$\Phi Q = m\ n\ F \qquad \textbf{6-1}$$

[25] These potentials were, in some cases, slightly different (± 20 mV) from the voltammograms presented in Chapter 5, since the reference electrode potential drifted with frequent exposure to high temperatures.

$$\log K_{sp} = -59.3498 - 0.041377\,T - \frac{2.1963}{T} + 24.5724\log(T) + 2.518\,I^{0.5} - 0.657\,I \qquad \textbf{6-2}$$

$$I = \frac{1}{2}\sum C_i\,z_i^2 \qquad \textbf{6-3}$$

### 6.2.1 Current density transients of iron in aqueous monoethanolamine (MEA) saturated with $CO_2$

**Transient in 1 M $MEA_{(aq)}$:** When the potential of the rotating Fe disc electrode was stepped from OCP to the $FeCO_3$ formation potential in the 1 M $MEA_{(aq)}$ solution saturated with $CO_2$ at 80 °C, the current density, shown in red in **Figure 6-1a**, **b**, immediately increased to a peak value of 110 A $m^{-2}$, due to double layer charging (Bockris, Reddy & Gamboa-Aldeco, 2002), before decreasing quickly and steadily. At *ca*. 10 s (**Figure 6-1b**), the rate of change of the current density slowed and eventually at *ca*. 90 s the current density began to increase again, reaching a peak of *ca*. 45 A $m^{-2}$ at 150 s, suggesting the onset of an electrode process, and subsequently declined rapidly to *ca*. 0.4 A $m^{-2}$. The current density did not reach 0 A $m^{-2}$ within the duration of the experiment. The increase in the current densities to a peak at 150 s is thought to have been due to $FeCO_3$ precipitation. (Ingham *et al*., 2012) also observed this increase in current density to a peak when an overpotential was applied to a carbon steel electrode in a $CO_{2(aq)}$ solution and confirmed that it coincided with the formation of $FeCO_3$ using *in-situ* XRD. Based on the charge passed, the estimated bulk $FeCO_3$ saturation ratio, $S_{FeCO3}$ at $t$ = 150 s was *ca*. 50, indicating that $FeCO_3$ precipitation was feasible. Further, the subsequent rapid decrease following the current density peak suggested that (partial) passivation of the electrode occurred. The surface images (**Figure 6-2a**) showed a roughened underlying substrate, substantiated by EDX, which detected predominantly Fe (**Figure 6-2d**), with several dispersed circular patches of crystals, which were found to have a composition of Fe: 65.4 %, C: 12.1 % and O:22.5 % by mass. Since the mass % of Fe, C and O in $FeCO_3$ are 49, 11 and 40, respectively and given the dispersed nature of the product clusters, these results were interpreted to be the detection of $FeCO_3$ as well as the Fe substrate. Furthermore, $FeCO_3$ formation was observed on carbon steel electrodes after immersion in 1 M $MEA_{(aq)}$ saturated with $CO_2$ at 80 °C for one week (Chapter 4). Although the substrate is of course different, the predominant component is Fe, so this does suggest that $FeCO_3$ formation on Fe in 1 M $MEA_{(aq)}$ is reasonable. No crystalline product phases were detected using XRD (**Figure 6-2g**), which is reasonable since the clusters of product, thought to be $FeCO_3$, only sparsely covered the electrode surface and the cluster depth appeared to be thin.

**Transient in 3 M $MEA_{(aq)}$:** The current density transient measured when the $FeCO_3$ formation potential was applied to a rotating Fe disc electrode in 3 M $MEA_{(aq)}$ solution saturated with $CO_2$ at 80 °C is shown in purple in **Figure 6-1a, c**. Similar to the current density transient measured in the 1 M solution, the current density initially rose rapidly, to *ca*. 350 A $m^{-2}$ and then immediately decreased. At *ca*. 210 s, the gradient of the current density transient changed abruptly and the current density decreased, gradually asymptoting to 0 A $m^{-2}$. At the end of the experiment, the current density averaged *ca*. 5.5 A $m^{-2}$, an order of magnitude higher than that measured in the 1 M solution. The decrease in the current density following the notable change in the gradient was possibly indicative of product formation on the electrode surface. The bulk $S_{FeCO3}$ corresponding to the point of gradient inflection was estimated to be *ca*. 80. Subsequent surface characterisation with SEM showed that the surface was partially covered with seemingly amorphous product; the chemical composition was detected by EDX to be Fe: 83.4 %, C: 6.4 % and O: 10.1 % (by mass), whilst the underlying substrate was detected to be Fe (92 % by mass) (**Figure 6-2e**). Since this product layer was less dispersed, it was thought that if $FeCO_3$ was present, the detected composition would be closer to that expected for $FeCO_3$. The measured XRD pattern (**Figure 6-2h**) also indicated the presence of ferrite. On balance, it was difficult to draw concrete conclusions from the EDX and XRD data. However, it should be stated that minimal areas on the electrode surface, which were not analysed using EDX, resembled the electrode tested in the 1 M electrolyte (Appendix, Section 12.4, **Figure 12-9**), possibly suggesting that $FeCO_3$ was present but in much lower quantities. Amorphous product, thought to be oxide-based was observed on carbon steel coupons after immersion in 3 M $MEA_{(aq)}$ at 80 °C for one week (Chapter 4). However, the O composition detected by EDX was *ca*. 25 % (by mass), much higher than that detected here.

**Transient in 5 M $MEA_{(aq)}$:** The current density transient measured when the $FeCO_3$ formation potential was applied to a rotating Fe disc electrode in 5 M $MEA_{(aq)}$ saturated with $CO_2$ at 80 °C is shown in blue in **Figure 6-1a, d**. When the electrode was stepped to the $FeCO_3$ formation potential, the current density increased to just under 500 A $m^{-2}$ and then decreased. At *ca*. 30 s, the rate of decrease of the current density slowed and at *ca*. 200 s, the current density began minimally increasing to *ca*. 160 A $m^{-2}$. Unlike the current density transients measured in the 1 and 3 M solutions, the minor current density peak was not followed by a dramatic decrease and appeared instead to reach a steady state value, suggesting a diffusion limited process. The bulk $S_{FeCO3}$ corresponding to the point at which the

gradient changed was *ca*. 200, but as mentioned previously, since the current density did not decrease substantially, if $FeCO_3$ formed on the surface it was either minimal or subsequently dissolved, and did not have a passivating effect on the electrode. *Ex-situ* surface images (**Figure 6-2c**) showed a bare, but apparently roughened surface, which was confirmed by EDX with only Fe detected at 97 % (by mass) (**Figure 6-2f**).

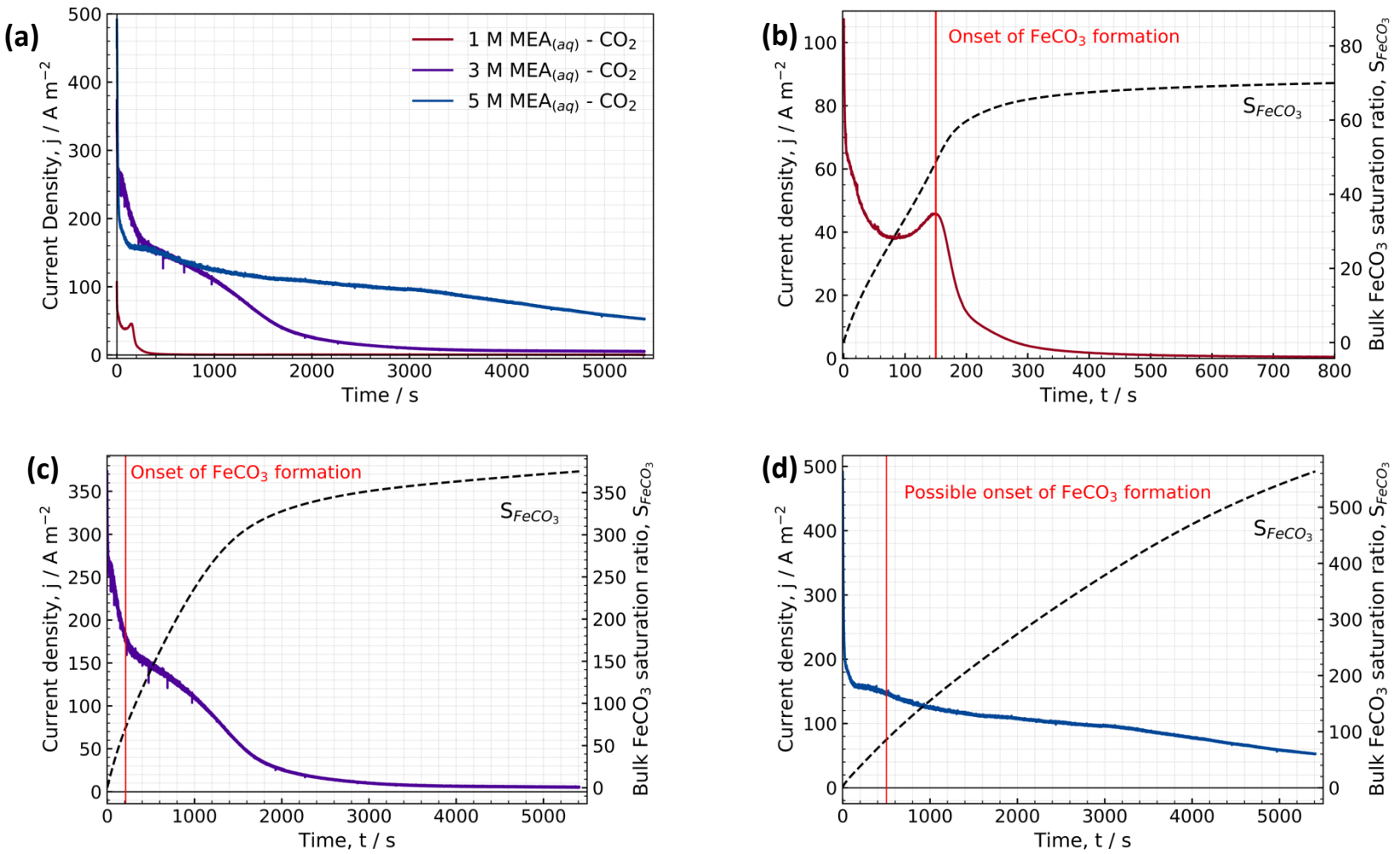
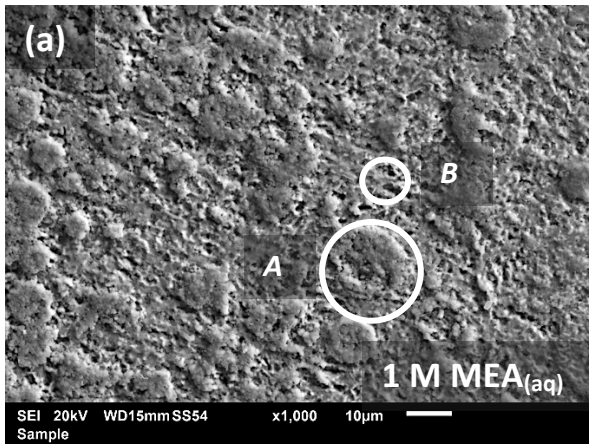
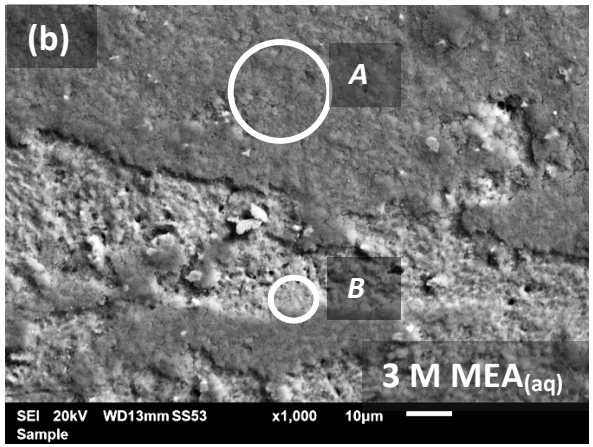
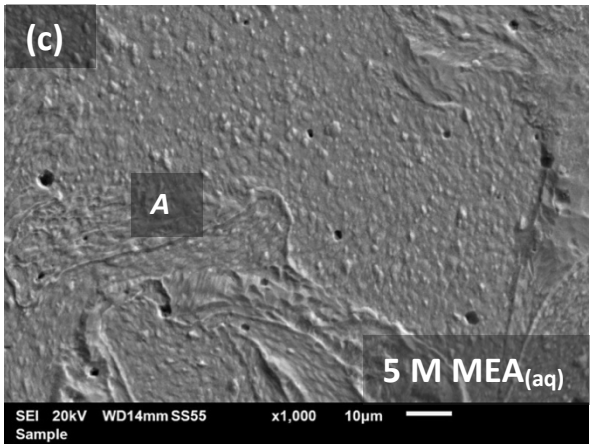



**Figure 6-1:** Measured current densities transients and calculated bulk solution $FeCO_3$ saturation ratio ($S_{FeCO3}$) when $FeCO_3$ formation potentials were applied to rotating disc Fe electrodes (1000 RPM) in $MEA_{(aq)}$ saturated with $CO_2$ at 80 °C, for **(a)** 5400 s. Scaled plots of the current density transients for each solution are also presented, **(b)** 1 M $MEA_{(aq)}$ ($pH_{80°C}$ 7.7), **(c)** 3 M $MEA_{(aq)}$ ($pH_{80°C}$ 7.8), and **(d)** 5 M $MEA_{(aq)}$ ($pH_{80°C}$ 7.9).




**(d)** Point EDX of A and B on Fe electrode after experiment in 1 M $MEA_{(aq)}$ (% mass)

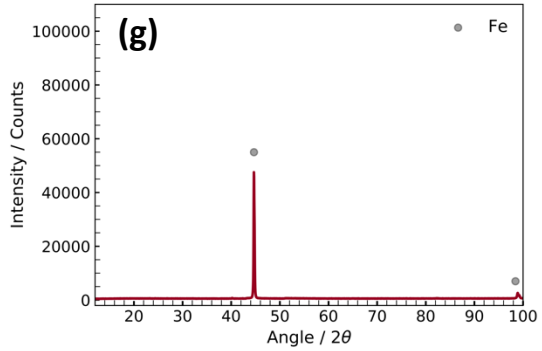
| Point | Fe | C | O |
|---|---|---|---|
| A | 65.38 | 12.13 | 22.49 |
| B | 85.24 | 7.07 | 7.69 |

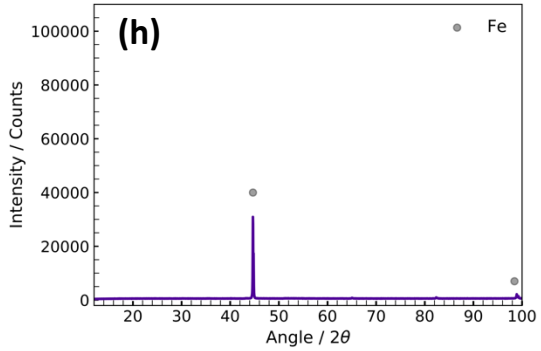
**(e)** Point EDX of A and B on Fe electrode after experiment in 3 M $MEA_{(aq)}$ (% mass)

| Point | Fe | C | O |
|---|---|---|---|
| A | 83.44 | 6.43 | 10.13 |
| B | 91.99 | 4.49 | 3.52 |

**(f)** Point EDX of A on Fe electrode after experiment in 5 M $MEA_{(aq)}$ (% mass)

| Point | Fe | C | O |
|---|---|---|---|
| A | 97.11 | 2.89 | 0.00 |



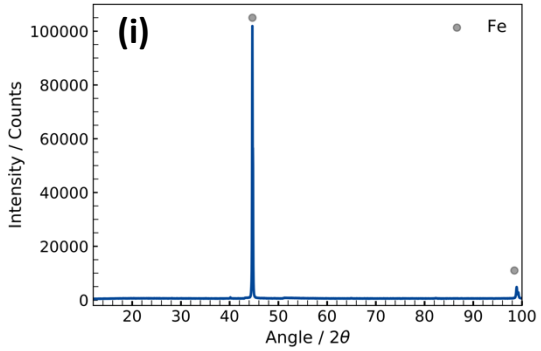




**Figure 6-2:** *Ex-situ* surface characterisation of Fe electrodes after chronoamperometry experiments in $MEA_{(aq)}$ using **(a - c)** SEM at 1000x showing surface features, with corresponding **(d - f)** surface composition detected using EDX and, **(g - i)** XRD with peaks corresponding to ferrite (α-Fe) highlighted.

**Comparison of $FeCO_3$ formation on Fe in aqueous MEA solutions saturated with $CO_2$**

The current density transients measured in $MEA_{(aq)}$ solutions of 1, 3 and 5 M concentrations, had varying shapes, but similarly consisted of a current density peak within the first *ca*. 500 s of the experiment, with the peak in the 1 M electrolyte being the most well defined and the transient in 5 M having the least defined peak. The current density peak observed within the first 500 s of the experiment is thought to have been due to the onset of $FeCO_3$ formation. The saturation ratio ($S_{FeCO3}$) in all three solutions were >> 1 at the peak current density and was followed by a decrease, though to varying degrees, which supports the $FeCO_3$ precipitation hypothesis.

Total charge densities passed at the Fe disc electrodes increased linearly with MEA concentration (**Figure 6-3**). This was expected since the initial current density measured in the 5 M solution was the highest and was *ca*. five times greater than the smallest initial current density measured in the 1 M electrolyte. From 300 s onwards, the current remained the greatest in the 5 M solution, followed by the 3 M and then the 1 M solutions. Further, the current density transient recorded in the 1 M solution decreased to less than 1 A $m^{-2}$ within the first 600 s of the experiment, the 3 M decreased to less than 10 A $m^{-2}$ within the first 2000 s, and in both cases current densities were ≤ 6 A $m^{-2}$ by the end of the experiment. By contrast, the current density transient recorded in the 5 M $MEA_{(aq)}$ solution did not decrease below 60 A $m^{-2}$. Comparison of the surface images did not necessarily indicate a trend in product type or the extent of surface coverage, but it clearly showed deposition of some material on electrodes exposed to the 1 and 3 M solutions but nothing on the electrode immersed in the 5 M $MEA_{(aq)}$ solution.

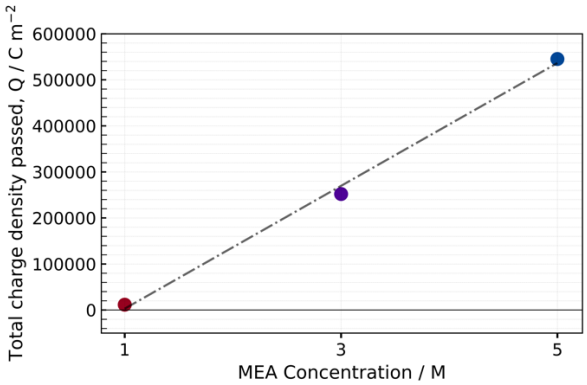



**Figure 6-3:** Total charge density passed during potentiostatic experiment with rotating disc (1000 RPM) Fe electrodes in $MEA_{(aq)}$ saturated with $CO_2$ at 80 °C.

### 6.2.2 Current density transients of iron in aqueous methyldiethanolamine (MDEA) saturated with $CO_2$

The current density transients measured when the potentials of rotating disc Fe electrodes were stepped to $FeCO_3$ formation potentials in $MDEA_{(aq)}$ solutions saturated with $CO_2$ at 80 °C of varying concentrations are shown in **Figure 6-4**.

**Transient in 1 M $MDEA_{(aq)}$:** The orange current density transient (**Figure 6-4a**, **b**) corresponds to that measured in the most dilute solution, 1 M $MDEA_{(aq)}$. When the potential was applied, the current densities increased to *ca*. 140 A $m^{-2}$ then decreased rapidly. After *ca*. 100 s, the current began decreasing at a noticeably lower rate (**Figure 6-4b**), and then at *ca*. 400 s the current densities decreased substantially from *ca*. 34 to 10 A $m^{-2}$ by 1000 s. The corresponding calculated bulk $S_{FeCO3}$ at 400 s was *ca*. 25, indicating that $FeCO_3$ precipitation was possible. Subsequently, the current densities continued decreasing and were 0.6 A $m^{-2}$ by the end of the experiment. Surface images clearly showed crystals scattered over the visible underlying substrate (**Figure 6-5a**), which were detected by EDX to have a composition of Fe: 60.9 %, C: 10.85 % and O: 28.3 % (by mass) (**Figure 6-5d**). These crystals were large and their shape was sufficiently discernible for them to be identified as botryoidal. The habit (Saunders & Swann, 1992) and composition (by EDX), both suggest that the product on the surface was $FeCO_3$. However, there was insufficient product to be detected by XRD (**Figure 6-5g**).

**Transient in 3 M $MDEA_{(aq)}$:** The current density transient measured when the $FeCO_3$ formation potential was applied to a rotating Fe disc electrode in 3 M $MDEA_{(aq)}$ saturated with $CO_2$ at 80 °C is shown in yellow in **Figure 6-4a**, **c**. When the electrode potential was stepped to the $FeCO_3$ formation potential, the current densities quickly rose to *ca*. 140 A $m^{-2}$, then decreased and increased again through a peak of *ca*. 132 A $m^{-2}$ and subsequently gradually decreased (**Figure 6-4c**). At *ca*. 120 s, the rate of current density change began decreasing more noticeably, and at *ca*. 240 seconds, the current densities started to decrease more rapidly and dropped from *ca*. 60 A $m^{-2}$ at 240 s to *ca*. 20 A $m^{-2}$ at 500 s. The bulk $S_{FeCO3}$ was *ca*. 40 and this increased rate of change of current density was thought to be indicative of $FeCO_3$ formation. The current densities then decreased slowly to almost 0.9 A $m^{-2}$ by the end of the experiment (**Figure 6-4a**), also suggesting that a passivating process had occurred. Surface images showed that the electrode was covered, though not completely, in crystalline product and EDX detected the surface composition to be Fe: 52.5 %, C: 16.2 % and O: 31.3

% (**Figure 6-5e**). Although there was apparent coverage of the surface with crystalline product, the layer was incomplete and seemingly too thin to be detected by XRD (**Figure 6-5h**).

**Transient in 5 M MDEA$_{(aq)}$:** The current density transient measured when the potential of $FeCO_3$ formation was applied to a rotating Fe disc electrode in 5 M MDEA$_{(aq)}$ saturated with $CO_2$ at 80 °C is shown in green in **Figure 6-4a, d**. As for the current density transients in 1 and 3 M MDEA$_{(aq)}$, the current density increased initially to *ca*. 65 A m$^{-2}$, decreased, then rose through a very minimal peak at *ca*. 25 s and then began decreasing at a near constant rate until *ca*. 200 s, when it began decreasing at a slower rate (**Figure 6-4d**) . At *ca*. 950 s, the current density decreased substantially from 34 A m$^{-2}$ to *ca*. 6 A m$^{-2}$ at 1000 s, and continued decreasing thereafter. The bulk $S_{FeCO3}$ was estimated to be 97, so as in the case of the current density transients in the 1 and 3 M MDEA$_{(aq)}$ solutions, it was believed that the transient was indicative of $FeCO_3$ formation. At *ca*. 3000 s (**Figure 6-4a**), the current density became negative and by the end of the experiment was *ca*. -2.7 A m$^{-2}$, the negative sign indicating that a net reduction reaction was occurring at the electrode surface. This was unexpected and it is unclear why this happened and it occurred even in repetitions of this experiment.

Surface images collected (**Figure 6-5c**) showed a seemingly smooth surface with a clearly discernible product layer (labelled 'A' in **Figure 6-5c**), with surface composition of Fe: 75.3 %, C: 9.4 % and O: 15.3 % (by mass), according to EDX analysis, suggesting detection of the Fe substrate with some contribution from the product layer. From these findings it was difficult to deduce if $FeCO_3$ was present. Since the current density decreased by an order of magnitude within a 100 s period and decreased to 0 A m$^{-2}$ within *ca*. 3000 s, it is likely that a passivating product layer formed on the surface. Given the smooth appearance, rather than a roughened surface commonly formed due to Fe dissolution, it was possible that a film with small crystals was present but not visible using the low resolution SEM. Due to COVID19, the higher resolution SEM was unavailable and so a further examination of this surface was not possible. However, this experiment was conducted previously, but for a shorter time period, and the current density transient had the same form. High resolution SEM images of the electrode used in the previous experiment (Appendix, Section 12.4, **Figure 12-9**) show a compact film of crystals on the electrode surface believed to be $FeCO_3$. The formation of a compact, insulating film is consistent with the measured current density transient, and so was believed to be present on the electrode in the 5 M MDEA$_{(aq)}$ solution (**Figure 6-4a**, **d**).

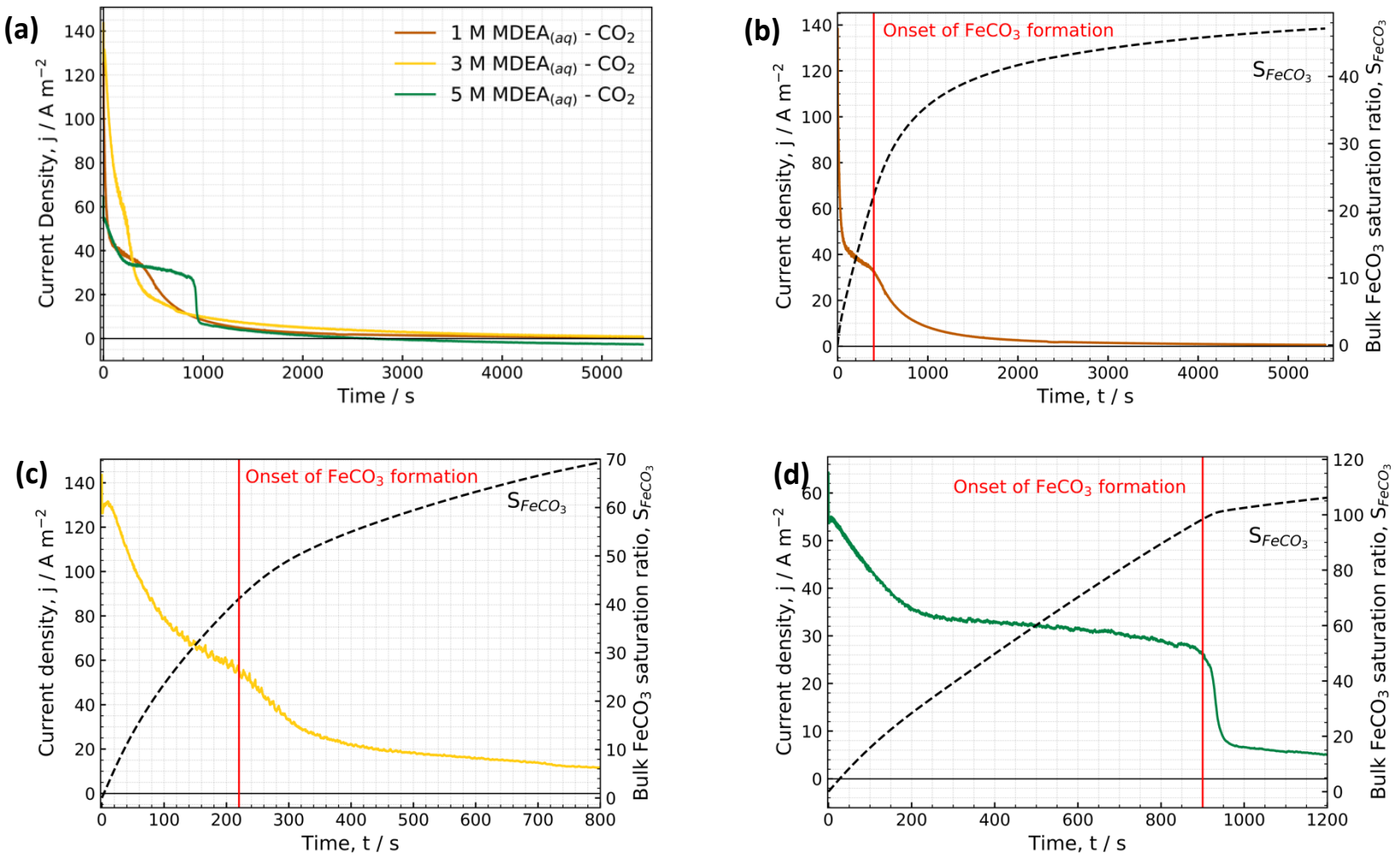
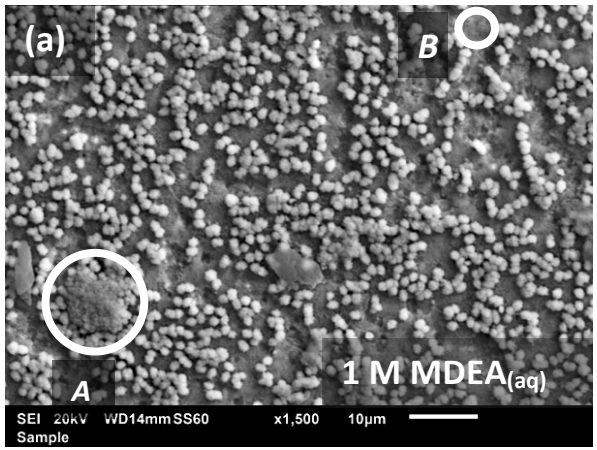
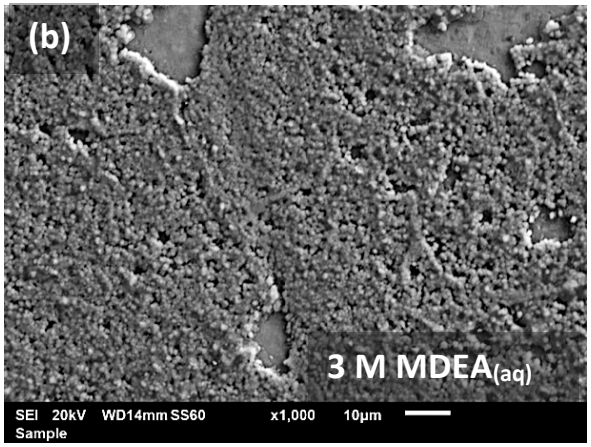
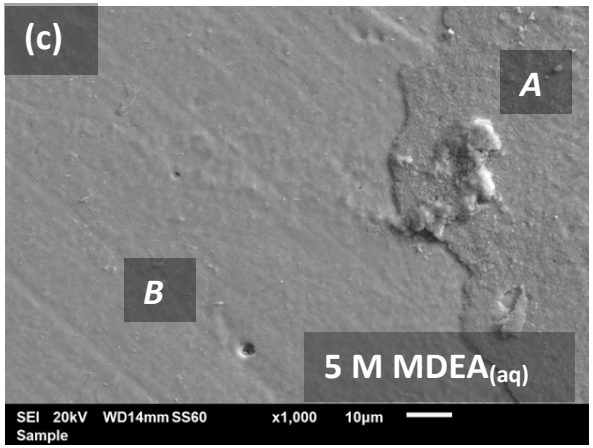



**Figure 6-4:** Measured current density transients and calculated bulk solution $FeCO_3$ saturation ratio ($S_{FeCO3}$) when $FeCO_3$ formation potentials were applied to rotating disc Fe electrodes (1000 RPM) in $MDEA_{(aq)}$ saturated with $CO_2$ at 80 °C, for **(a)** 5400 s. Scaled plots of the current transients for each solution are also presented, **(b)** 1 M $MDEA_{(aq)}$ ($pH_{80°C}$ 7.9), **(c)** 3 M $MDEA_{(aq)}$ ($pH_{80°C}$ 8.3), and **(d)** 5 M $MDEA_{(aq)}$ ($pH_{80°C}$ 8.6)




**(d)** Point EDX of A and B on Fe electrode after experiment in 1 M MDEA (% mass)

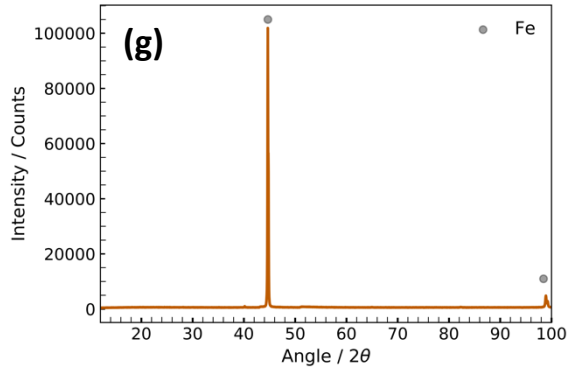
| Point | Fe | C | O |
|---|---|---|---|
| A | 60.9 | 10.85 | 28.26 |
| B | 82.39 | 6.65 | 10.96 |

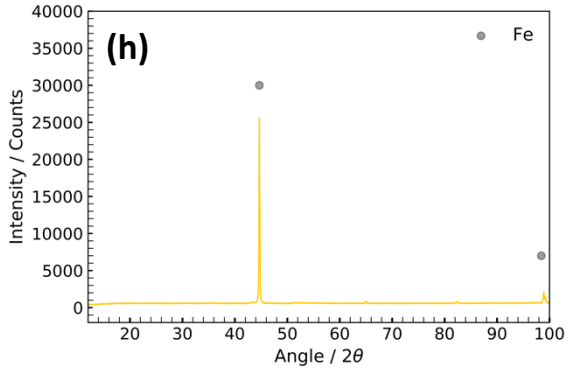
**(e)** EDX of Fe electrode after experiment in 3 M MDEA (% mass)

| Point | Fe | C | O |
|---|---|---|---|
| A | 52.52 | 16.18 | 31.31 |

**(f)** Point EDX of A and B on Fe electrode after experiment in 5 M MDEA (% mass)

| Point | Fe | C | O |
|---|---|---|---|
| A | 75.26 | 9.44 | 15.29 |
| B | 83.45 | 7.12 | 9.43 |



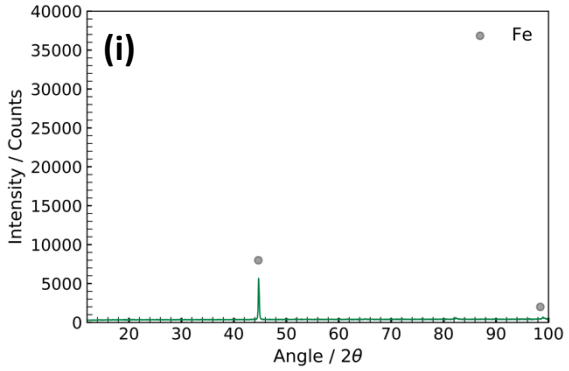




**Figure 6-5:** *Ex-situ* surface characterisation of Fe electrodes after chronoamperometry experiments in $MDEA_{(aq)}$ using **(a - c)** SEM at 1000x showing surface features, with corresponding (**d - f**) surface composition detected using EDX and, **(g - i)** XRD with peaks corresponding to Ferrite (α-Fe) highlighted.

**Comparison of $FeCO_3$ formation on Fe in aqueous MDEA solutions saturated with $CO_2$**

The current density transients recorded in the three $MDEA_{(aq)}$ solutions exhibited similar forms and trends, with each undergoing an initial significant increase in current density in response to the applied potential, then a gradual decrease in current density followed by a steeper decrease; for the electrode in the 1 M solution, this change occurred within 700 s, whilst that in the 3 M electrolyte occurred within 300 s and in the 5 M electrolyte, within 1000 s. Following their sharp decreases, current densities decreased gradually and tended to 0 A $m^{-2}$ in all three solutions. The initial high current densities and subsequent immediate decrease are thought to be due to charging of the double layer as was described in Chapter 2 (Section 2.4.5.2). The current densities recorded subsequently are thought to be due to continued Fe dissolution, during which $Fe^{2+}$ ions would be continuously dispersed from the surface. As proposed previously, the decrease in current densities is thought to be a consequence of passivation. Prior to the passivation process, the $Fe^{2+}$ concentration within the diffusion layer would increase with time, ultimately leading to $FeCO_3$ saturation ratios >>1 and precipitation on the electrode surface. The calculated bulk solution $FeCO_3$ saturation ratio at the inferred onset of precipitation (**Figure 6-4b**), followed a linear relationship with MDEA concentration, with the greatest saturation ratio estimated in the 5 M solution (97) and the lowest in the 1 M (25) solution.

By the end of the chronoamperometric experiments (5400 s), the current density in the 3 M solution was *ca*. 0.9 A $m^{-2}$, slightly higher than 0.6 A $m^{-2}$ measured in the 1 M electrolyte and -2.7 A $m^{-2}$ in the 5 M solution. Given these final current density values, the total charge density passed as a function of MDEA concentration presented in **Figure 6-6**, is reasonable; charge density passed in the 3 M was the highest, followed by the 1 M and subsequently the 5 M. These results seem to contradict the surface images from which it may be deduced that the surface coverage was the highest in the 3 M, and lowest in the 5 M. However, there was substantial variability across the surface and it was explained previously that there was likely high surface coverage with crystals < 1 μm in size on the electrode exposed to the 5 M solution that could not be imaged with the low resolution SEM.

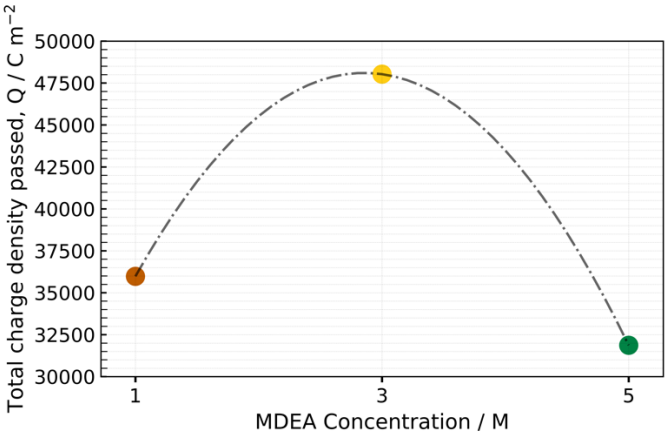



**Figure 6-6:** Total charge density passed during potentiostatic experiment with rotating disc (1000 RPM) Fe electrodes in $MDEA_{(aq)}$ saturated with $CO_2$ at 80 °C.

### 6.2.3 Comparison of $FeCO_3$ formation on Fe in aqueous MEA and MDEA solutions saturated with $CO_2$

The current density transients, total charge density passed and *ex-situ* characterisation of Fe electrodes in $MEA_{(aq)}$ and $MDEA_{(aq)}$ solutions were presented and discussed in Sections 6.2.1 and 6.2.2 respectively.

Generally, the current density transients recorded in $MEA_{(aq)}$ seem to consist of a current density peak, though minimal in the 3 and 5 M solutions, which was thought to be associated with $FeCO_3$ formation (**Figure 6-1**). By contrast, the current density transients measured in $MDEA_{(aq)}$ appeared to consist of a shoulder, probably due to steady Fe dissolution, followed by a steep decrease, the steepness depending on MDEA concentration (**Figure 6-4**).

The total charge density passed in $MEA_{(aq)}$ solutions was consistently higher than passed in $MDEA_{(aq)}$. This was particularly notable from comparison of the charge passed in the 5 M solutions where that passed in $MEA_{(aq)}$ was *ca*. 17 times that passed in $MDEA_{(aq)}$. The charge density passed was correlated with MEA concentration such that the cumulative charge density in the 1 M was the smallest (**Figure 6-3**), and greatest in 5 M solution. Similarly, the $S_{FeCO3}$ (**Figure 6-1**), and the presence of $FeCO_3$ (**Figure 6-2**) seem to be correlated with MEA concentration; the maximum $S_{FeCO3}$ in 1 M was *ca*. 80 and clusters of $FeCO_3$ crystals were observable, the maximum $S_{FeCO3}$ in 3 M was *ca*. 375 and minimal $FeCO_3$, if any, was discernible on the sample, whereas in the 5 M, the maximum $S_{FeCO3}$ exceeded 500 with no observable precipitation. Conversely, the total charge density passed in $MDEA_{(aq)}$ solutions exhibited a parabolic relationship with concentration; the total charge density passed in the 1

and 5 M solutions were similar at *ca*. $3.6 \times 10^4$ C m$^{-2}$ and $3.2 \times 10^4$ C m$^{-2}$ respectively, and that passed in the 3 M solution was the highest at *ca*. $4.8 \times 10^4$ C m$^{-2}$. The maximum $S_{FeCO3}$ increased with concentration from *ca*. 50 in the 1 M to 115 in the 5 M, but there was no obvious variation in surface coverage (**Figure 6-5**) with MDEA concentration. It is worth noting that if the charge passed is consumed only for $FeCO_3$ formation *via* **5-8**, *i.e*. assuming a charge yield ($\Phi$) of unity and ignoring the effect of surface roughness, the charge density required per monolayer of $FeCO_3$ formed would be 4 C m$^{-2}$. Based on the cumulative charge density passed in the chronoamperometric experiments on both amines, up to *ca*. $10^5$ monolayers of $FeCO_3$ would be expected to have formed on the Fe electrodes in both solutions. The charge yield for $FeCO_3$ formation on Fe in either amine saturated with $CO_2$ is therefore likely to have been substantially lower than unity.

The behaviour in the 1 M $MEA_{(aq)}$ solution resembled that in the $MDEA_{(aq)}$ solutions most closely, and possibly suggested that MEA did in fact have an effect on the $FeCO_3$ precipitation process. Additionally, the Fe electrode in 1 M $MEA_{(aq)}$ was the only electrode on which $FeCO_3$ crystals were imaged definitively and the total charge densities passed were comparable to those recorded in all three $MDEA_{(aq)}$ solutions. This is consistent with the behaviour observed by carbon steel in the preliminary immersion tests presented in Chapter 4, Section 4.2.1, where $FeCO_3$ was only observed in 1 M $MEA_{(aq)}$ solution.

## 6.3 Local solution chemistry changes during $FeCO_3$ formation on iron

In the preceding sections (Sections 6.2.1 - 6.2.2), $FeCO_3$ formation was investigated using current density transients measured when previously determined $FeCO_3$ formation potentials were applied to rotating disc Fe electrodes in $MEA_{(aq)}$ and $MDEA_{(aq)}$ solutions saturated with $CO_2$ at 80 °C. The results were discussed and interpreted by calculating the bulk $Fe^{2+}$ concentration using the charge density passed during the experiment. It was deduced from the current density transients and electrode surface characterisation that $FeCO_3$ precipitation was less likely in $MEA_{(aq)}$ solutions as the MEA concentration increased, despite exceedingly high bulk saturation ratios. The variation in the general form of the current density transients in the two amines may suggest the possibility of different surface mechanisms involved in the precipitation reaction. However, these results did not provide sufficient evidence to draw meaningful explanations for the increased likelihood of $FeCO_3$ formation in $MDEA_{(aq)}$ relative to $MEA_{(aq)}$.

It is possible that the estimated saturation ratios calculated using the charge densities passed were misleading. Changes in the local solution chemistry, specifically due to $FeCO_3$ formation, and diffusion and / or accumulation rate of $Fe^{2+}$ need to be considered. $FeCO_3$ formation on an Fe electrode is thought to occur *via* a dissolution (**5-1**) precipitation (**5-7**) mechanism with $Fe^{2+}$ and dissolved $CO_2$ as precursors for the reaction. At the $CO_2$-saturated-amine pHs of 7.7 – 8.6, $CO_2$ is predicted to exist predominantly as $HCO_3^-$ (**Figure 2-11**). Therefore, $FeCO_3$ formation is likely to occur predominantly *via* **5-7**, resulting in the release of $H^+$ as depicted in **Figure 6-7**.

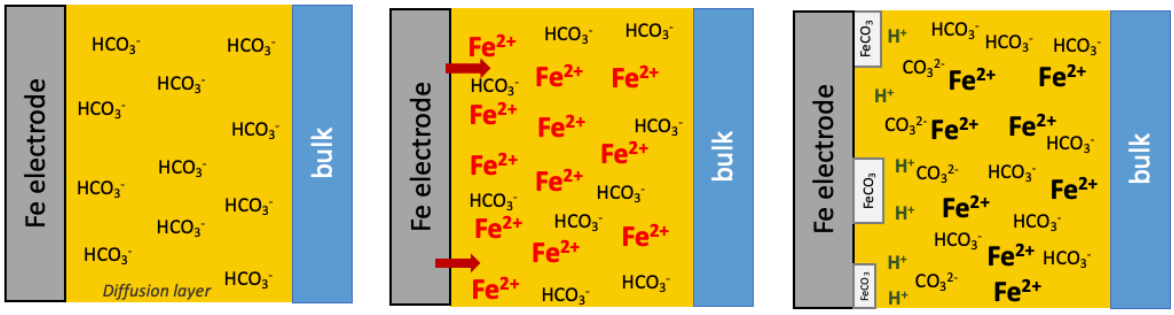



**Figure 6-7:** $FeCO_3$ formation mechanism on an Fe electrode in aqueous $CO_2$ saturated system.

The Nernst-Planck equation (Equation **6-4**) was used to produce a simple one-dimensional[26] diffusion-reaction model to further predict the effect of local solution chemistry on the precipitation and stability of $FeCO_3$. $C_i$ (mol $dm^{-3}$) and $z_i$ represent the concentration and charge of species *i* with diffusion coefficient $D_i$ ($m^2$ $s^{-1}$); the latter were estimated assuming the electrolyte solution was water at 25 °C (Newman & Thomas-Alyea, 2012) and subsequently temperature and viscosity ($\nu$) correcting using the Stokes-Einstein equation (Equation **5-17**) (Appendix, Section 12.4, **Figure 12-11**). $\Phi_i$ is the electrostatic potential, *F* is Faraday's constant (96 485.34 C $mol^{-1}$), $v_x$ (m $s^{-1}$) is the convective velocity computed using Equation **6-5**, where $\omega$ (rad $s^{-1}$) is the angular velocity of the electrode and $R_i$ is the reaction rate.

$$\frac{\partial C_i}{\partial t} - D_i \frac{\partial^2 C_i}{\partial x^2} - \frac{z_i F}{RT} D_i C_i \frac{\partial^2 \phi}{\partial x^2} + v_x \frac{\partial C_i}{\partial x} = R_i \qquad \textbf{6-4}$$

$$v_x = 0.51023\, \omega^{\frac{3}{2}} \nu^{-\frac{1}{2}} x^2 \qquad \textbf{6-5}$$

$Fe^{2+}$, $HCO_3^-$, $H^+$ and $FeCO_3$ were the only species considered and $FeCO_3$ formation (*via* **5-7**), the only reaction included in the model. Assuming negligible electromigration effects, Equations **6-6** to **6-9** were formulated to predict the prevailing concentration profiles of the aforementioned species in the 5 M $MEA_{(aq)}$ $CO_2$ saturated solution due to application of the $FeCO_3$ formation potential. Since the concentration of non-reacting amine electrolyte is estimated to be *ca*. 5 M at pH 7.9, the assumption of negligible electromigration effects is thought to be valid. In the system of partial differential equations, $k_r$ ($m^3$ $kmol^{-1}s^{-1}$ ) is the $FeCO_3$ formation kinetic constant calculated using Equation **6-10** (Sun & Nešić, 2008) where *A*/*V*[27] is the surface area to volume ratio and was taken to be equivalent to the inverse of the diffusion layer thickness calculated from the Equation **6-11**, derived from the Levich equation and $K_e$ is the equilibrium constant for reaction **5-7** calculated using Gibbs energy of formation data (Bard *et al*., 1985).

---

[26] Considering only diffusion in the x-direction, perpendicular to the electrode surface.

[27] The tests conducted by (Sun & Nešić, 2008) in deriving $k_r$ involved adding $Fe^{2+}$ to a $NaCl_{(aq)}$ solution which contained carbon steel electrodes. Therefore, the added $Fe^{2+}$ needed to diffuse to the electrode surface for $FeCO_3$ precipitation and *A*/*V* was defined as the electrode surface area to total electrolyte volume. Since the source of $Fe^{2+}$ in the experiments conducted in this chapter was the electrode, the volume of electrolyte was taken as that within the diffusion layer, so the *A*/*V* ratio was taken as the diffusion layer thickness.

$$\frac{\partial C_{Fe^{2+}}}{\partial t} = D_{Fe^{2+}} \frac{\partial^2 C_{Fe^{2+}}}{\partial x^2} - v_x \frac{\partial C_{Fe^{2+}}}{\partial x} - k_r C_{Fe^{2+}} C_{HCO_3^-} + \frac{k_r}{K_e} C_{H^+} C_{FeCO_3} \quad \textbf{6-6}$$

$$\frac{\partial C_{HCO_3^-}}{\partial t} = D_{HCO_3^-} \frac{\partial^2 C_{HCO_3^-}}{\partial x^2} - v_x \frac{\partial C_{HCO_3^-}}{\partial x} - k_r C_{Fe^{2+}} C_{HCO_3^-} + \frac{k_r}{K_e} C_{H^+} C_{FeCO_3} \quad \textbf{6-7}$$

$$\frac{\partial C_{H^+}}{\partial t} = D_{H^+} \frac{\partial^2 C_{H^+}}{\partial x^2} - v_x \frac{\partial C_{H^+}}{\partial x} + k_r C_{Fe^{2+}} C_{HCO_3^-} - \frac{k_r}{K_e} C_{H^+} C_{FeCO_3} \quad \textbf{6-8}$$

$$\frac{\partial C_{FeCO_3}}{\partial t} = D_{FeCO_3} \frac{\partial^2 C_{FeCO_3}}{\partial x^2} - v_x \frac{\partial C_{H^+}}{\partial x} + k_r C_{Fe^{2+}} C_{HCO_3^-} - \frac{k_r}{K_e} C_{H^+} C_{FeCO_3} \quad \textbf{6-9}$$

$$k_r = \frac{A}{V} \exp\left(21.3 - \frac{64851.4}{RT}\right) \quad \textbf{6-10}$$

$$\delta = 1.61\, D^{\frac{1}{3}} \omega^{-\frac{1}{2}} \nu^{\frac{1}{6}} \quad \textbf{6-11}$$

Neumann boundary conditions were used at the electrode surface for all species. The flux of $Fe^{2+}$ at the electrode surface was calculated by fitting a line to the current density transient (**Figure 6-1d**) within 280 and 1000 s, since the gradient of the transient was relatively constant during this period. This flux was used to define the boundary condition for Equation **6-6** at the electrode surface (Equation **6-12**). The concentration gradients of $HCO_3^-$, $H^+$ and $FeCO_3$ at the electrode surface were equated to 0 mol $m^{-2}$.

$$-D_{Fe^{2+}} \frac{dC_{Fe^{2+}{}_{x=0}}}{dx} = \frac{j_{measured}}{n\,F}, \qquad j_{measured} = 104 - 0.02t \quad \textbf{6-12}$$

Dirichlet boundary conditions[28] were used at the end of the diffusion layer where the concentrations were equated to bulk concentrations; $C_{Fe2+}$ was arbitrarily set to $10^{-9}$ mol $dm^{-3}$, $C_{HCO3-}$ to 0.0114 mol $dm^{-3}$ (Appendix, Section 12.4.4), $C_{H+}$ was calculated from the bulk solution pH of 7.9, and $C_{FeCO3}$ to 0 mol $dm^{-3}$. The initial conditions were equal to the boundary conditions at the diffusion layer interface with the bulk solution.

The *pdepe* solver in MATLAB was used to evaluate the system of equations for 50 equally spaced points for a time interval of 1000 s and spatial interval 0 to $\delta$. A larger mesh size of 200 did not noticeably affect the obtained concentrations at the electrode surface.

---

[28] A Neumann boundary condition should ideally be used at the end of the diffusion layer for $Fe^{2+}$ to allow for accumulation of $Fe^{2+}$ in the bulk solution. However, setting the $Fe^{2+}$ concentration gradient to 0 mol $m^{-2}$ at x = $\delta$ resulted in negative concentration values near $\delta$. Since the purpose of this model was to predict the local solution chemistry (at the electrode surface), the $Fe^{2+}$ concentration at $\delta$ was arbitrarily set to $10^{-9}$ mol $dm^{-3}$. The impact of this change in boundary conditions on the concentrations of $Fe^{2+}$, $HCO_3^-$ and $H^+$ was ≤ 18 %.

$FeCO_3$ saturation ratios were then calculated using Equation **5-10**. It should be started that homogenous chemical reactions, specifically $CO_2$–$H_2O$ chemical equilibrium reactions, were not incorporated in the system of partial differential equations (Equations **6-6** - **6-10**) since their inclusion resulted in unstable solutions, in the form of oscillating concentration profiles. Instead, the $CO_3^{2-}$ solution concentrations were calculated subsequently using the computed $H^+$ and $HCO_3^-$ concentration profiles predicted by the *pdepe* function to solve Equations **6-13** - **6-15**, and the solubility limit ($K_{sp}$) was calculated using Equation **6-2** with an ionic strength ($I$) of 2.48, estimated based on equilibrium concentrations in 5 M MEA–$CO_2$–$H_2O$ and is described in the Appendix (Section 12.4.5).

$$HCO_{3(aq)}^{-} \overset{K_{e,bi}}{\longleftrightarrow} CO_{3(aq)}^{2-} + H_{(aq)}^{+} \qquad \textbf{6-13}$$

$$K_{e,b} = 10^{-\left(10.61 - 4.97\times10^{-3}\,T(F) + 1.331\times10^{-5}\,T(F)^2 - 2.624\times10^{-5}\,p - 1.166\cdot I^{0.5} + 0.3466\,I\right)} \qquad \textbf{6-14}$$

$$C_{CO_3^{2-}} = \frac{C_{HCO_3^-}\,K_{e,b}}{10^{-pH}} \qquad \textbf{6-15}$$

**Figure 6-8a** - **b** show the concentration profiles for $Fe^{2+}$, $HCO_3^-$ and the solution pH calculated from the $H^+$ concentration within the diffusion layer. The concentration of $Fe^{2+}$ at the electrode was predicted to increase due to a constant $Fe^{2+}$ flux from the electrode surface. The $HCO_3^-$ concentration at the electrode surface was estimated to decrease from 0.0114 M to 0.006 M due to consumption in $FeCO_3$ formation reaction. It should be re-emphasised here that the homogenous reactions between dissolved '$CO_2$' species ($CO_{2(aq)}$, $H_2CO_3$, $HCO_3^-$, $CO_3^{2-}$) were not included in the system on partial differential equations as explained previously, and so the $HCO_3^-$ concentration computed from the *pdepe* solver is an overestimate. The local pH was predicted to decrease sharply within the first 200 s and continued to decrease gradually for the simulated 1000 s from 7.9 to *ca*. 3.7. This decrease was expected since the high $Fe^{2+}$ and $HCO_3^-$ concentrations would result in $FeCO_3$ formation, and for each mole of $FeCO_3$ produced, one mole of $H^+$ would also form (*via* **5-7**). The corresponding saturation ratio profile is given in **Figure 6-8d**. The highest predicted saturation ratio was 0.015, substantially lower than unity, which is required for $FeCO_3$ precipitation. When the local pH decrease is accounted for, the saturation ratio is more than four orders of magnitude lower than that estimated in **Figure 6-1d**. To attain a saturation ratio of unity, at a solution pH of 3.7 ($[CO_3^{2-}] = 1.2 \times 10^{-7}$ mol dm$^{-3}$), and $K_{sp}$ of $9.5 \times 10^{-10}$ mol$^2$ dm$^{-6}$, the $Fe^{2+}$ concentration would need to be $8.2 \times 10^{-3}$ mol dm$^{-3}$,

*ca*. two orders of magnitude greater than that predicted in **Figure 6-8a**. Therefore, $FeCO_3$ precipitation was not predicted to be feasible in the 5 M $MEA_{(aq)}$ solution when the local pH decrease is accounted for. Similar local pH results were obtained for the 1 and 3 M solutions as well as the $MDEA_{(aq)}$ solutions. However, surface imaging revealed $FeCO_3$ precipitation did in fact occur on electrodes tested in $MDEA_{(aq)}$ solutions and in the 1 M $MEA_{(aq)}$ solution (**Figure 6-2**, **Figure 6-5**). This strongly suggests that other homogeneous reaction(s), which were not incorporated in the model, may be present and act to impede local pH changes and are discussed in the subsequent section.

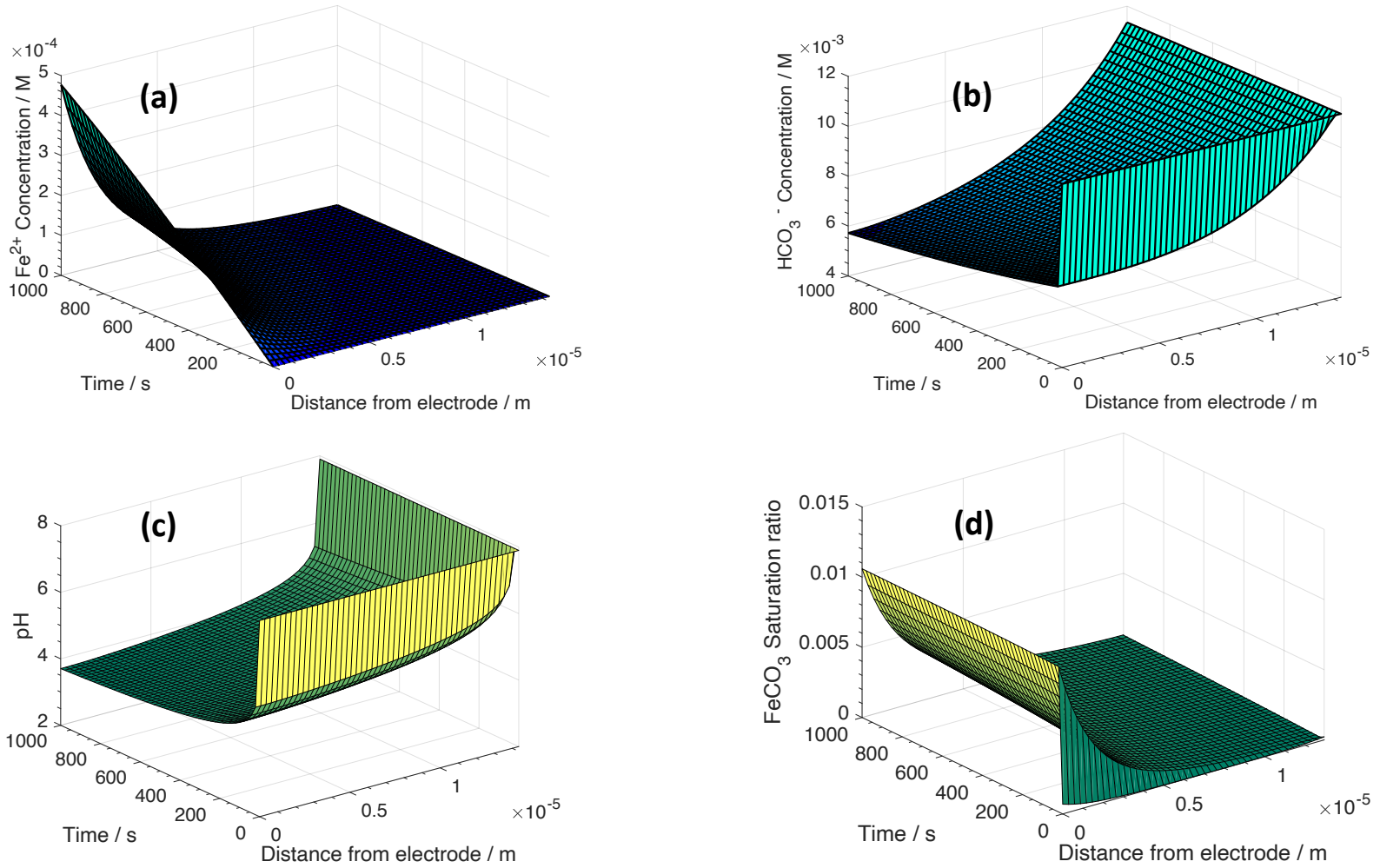



**Figure 6-8:** Concentration profiles of **(a)** $Fe^{2+}$, **(b)** $HCO_3^-$, and **(c)** local solution pH predicted from current density transient recorded with a rotating Fe disc electrode (1000 RPM) in 5 M $MEA_{(aq)}$ – $CO_2$, 80 °C **(d)** $FeCO_3$ saturation ratio (I = 2.48 M) calculated based on $Fe^{2+}$ concentration profile and $CO_3^{2-}$ from $H^+$ and $HCO_3^-$ concentration profiles.

**Buffering capacity**: Buffer solutions act to resist pH changes by either absorbing $H^+$ or realising $OH^-$ ions. The buffer capacity, given by Equation **6-16** (Stumm & Morgan, 1995), where $dC_A$ is the quantity of acid added and $d$pH is the change in solution pH due to acid addition, is a measure of the resistance to change of solution pH for a solution containing a buffering agent. The overall buffer capacity is given by the summation of the buffer capacity of each buffering component ($\beta_i$) as shown in Equation **6-17**, $\beta_w$ is the buffering capacity of water (Urbansky & Schock, 2000). (Urbansky & Schock, 2000) also showed that when pH = $pK_a$, the buffer capacity is maximised.

Both MEA and MDEA may act to resist pH change by accepting excess $H^+$ *via* **6-18** and **6-19** respectively. At 80 °C, the $pK_a$ of **6-18** is calculated to be 8.05, which is above the solution pH, whilst the $pK_a$ of **6-19** is 7.65, which is below the solution pH. Dissociation constants were calculated using data from (Kamps & Maurer, 1996) and (Hamborg & Versteeg, 2009) are included in the Appendix (Section 12.4.6). Accordingly when $H^+$ are released *via* **5-7**, MDEA is likely to more effectively regulate pH changes in $CO_2$ saturated solutions at 80 °C relative to MEA.

$$\beta = -\frac{dC_A}{dpH} \qquad \textbf{6-16}$$

$$\beta = \beta_w + \sum\beta_i \qquad \textbf{6-17}$$

$$MEA + H^+ \leftrightarrow MEAH^+, \qquad pK_{a,80°C} = 8.05 \qquad \textbf{6-18}$$

$$MDEA + H^+ \leftrightarrow MDEAH^+, \qquad pK_{a,80°C} = 7.65 \qquad \textbf{6-19}$$

Another crucial factor is the quantity of buffering agent present in solution, since these agents would not be able to regulate solution pH once depleted. The mass balances for MEA and MDEA involved in $CO_2$ capture is given by Equation **6-20** and **6-21** respectively (**Figure 2-28**, **Figure 2-30**). For a given amine concentration, more MDEA will be present in the solution and theoretically would be capable of consuming more $H^+$ ions.

$$\text{Total amine concentration} = [MEACOO^-] + [MEA] + [MEAH^+] \qquad \textbf{6-20}$$

$$\text{Total amine concentration} = [MDEA] + [MDEAH^+] \qquad \textbf{6-21}$$

In addition to the free amines, $CO_3^{2-}$, present in $CO_2$ saturated amine solutions, may also serve to impede pH change *via* **6-13**. For each tested concentration, $MDEA_{(aq)}$ solution pHs were higher than the corresponding $MEA_{(aq)}$ solution, and from **Figure 2-11**, the $CO_3^{2-}$ concentration would also be higher. The influence of variable buffering capacity of MEA and

MDEA on $FeCO_3$ stability has not been proposed previously or discussed in the literature. The overall charge density passed during the chronoamperometry experiments shown in **Figure 6-3** and **Figure 6-6** was as a result of the net effect of oxidative Fe dissolution and $FeCO_3$ precipitation. The higher buffering capability of MDEA could, in part, explain the substantially higher overall charge densities passed in $MEA_{(aq)}$ solutions relative to $MDEA_{(aq)}$ (**Figure 6-3**, **Figure 6-6**) since $FeCO_3$ precipitated on the electrode surface would result in a lower net oxidative current.

**Diffusion coefficients**: The saturation ratio may also be affected by the solution viscosity. The diffusion coefficient of a species, *i*, is inversely related to the solution viscosity. Different species have different ionic radii, so different diffusion coefficients, which were estimated for $Fe^{2+}$, $HCO_3^-$ and $H^+$ in $MEA_{(aq)}$ and $MDEA_{(aq)}$ solutions of 1, 3 and 5 M at 80 °C, and are presented in **Figure 6-9**. Comparing firstly the viscosity of amine solutions, for a given concentration, the viscosity of $MDEA_{(aq)}$ is greater than that of $MEA_{(aq)}$, and as the concentration of each amine increases, so too does the viscosity (Appendix, Section 12.4.2). Accordingly, the diffusion coefficient of all three species decrease with increasing amine concentration and the diffusion coefficient of each species is higher in $MEA_{(aq)}$ than $MDEA_{(aq)}$, indicating that species diffuse more slowly towards and away from the electrode surface in $MDEA_{(aq)}$ solutions.

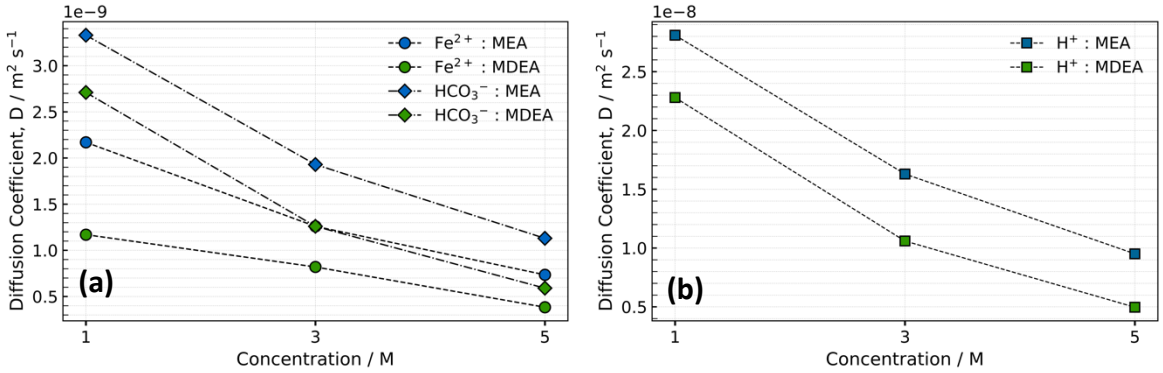



**Figure 6-9:** Diffusion coefficients of **(a)** $Fe^{2+}$, $HCO_3^-$ and **(b)** $H^+$ at 80 °C in aqueous amine solutions estimated using diffusion coefficients in water at 25 °C and corrected for temperature and viscosity.

$Fe^{2+}$ ions, which diffused away from the electrode, have the smallest diffusion coefficient (**Figure 6-9**), meaning that they would diffuse at the slowest rate away from the electrode surface for a given concentration gradient and electrode rotation rate. If the electrode was freely releasing $Fe^{2+}$ ions, *i.e.* at open circuit, the $Fe^{2+}$ accumulation rate would increase with amine concentration and would in fact be greater in $MDEA_{(aq)}$ than $MEA_{(aq)}$ solutions,

resulting in a greater expected precipitation rate in MDEA. This is consistent with the total charge densities passed presented in **Figure 6-3** and **Figure 6-6**.

Since $HCO_3^-$ ions would have diffused from the bulk to the electrode surface, the decreasing diffusion coefficient of $HCO_3^-$ with amine concentration had the opposite effect on saturation ratio to that of $Fe^{2+}$ ions. Considering only the $HCO_3^-$ diffusion coefficient, the $FeCO_3$ saturation ratio is expected to be greater with lower amine concentration. The interplay of these diffusion coefficients possibly explains the parabolic relationship observed between total charge densities passed and MDEA concentration (**Figure 6-6**).

The diffusion coefficient of $H^+$ ions is also greater in $MEA_{(aq)}$ than $MDEA_{(aq)}$ solutions, and decreases with increasing concentration in both amines. The saturation ratio is sensitive to pH changes, due to the exponential dependence of $HCO_3^-$ on pH. Based on the $H^+$ diffusion coefficients, for a specific time period *dt*, the $FeCO_3$ saturation ratio is therefore expected to decrease with increasing amine concentration, which contradicts the trend observed with MEA (**Figure 6-3**). Further, this suggests that $FeCO_3$ precipitation is more likely in $MEA_{(aq)}$ than $MDEA_{(aq)}$ solutions, which conflicts with the observations made from the experimental results. The varying diffusion rates of the dissolved species to and from the electrode surface, was therefore neither the sole, nor the most influential factor affecting $FeCO_3$ formation and stability.

**Complexation:** It has been proposed in the literature that MEA (or $MEAH^+$ / $MEACOO^-$) may complex with $Fe^{2+}$ (Shimizu, Hirano & Tomoe, 2016), but there is no known published evidence for the detection of such species[29]. However, this proposition is thought to be reasonable, since it is well-known that ammonia complexes with metal ions and it has also been demonstrated that MEA complexes with $Co^{II}$, $Cu^{II}$, $Ni^{II}$, and $Zn^{II}$ (Amjad *et al*., 2016). Complexation between $Fe^{2+}$ and MEA would decrease the local $Fe^{2+}$ concentration and excess $Fe^{2+}$ would be required for $FeCO_3$ precipitation. Also, it has been demonstrated that tertiary amines are less likely to complex with metal ions due to the steric hindrance provided by the

[29] UV-vis spectroscopy was used in an attempt to detect such species in $Fe^{2+}$ - $CO_2$ saturated $MEA_{(aq)}$ solutions in this study, but rapid $Fe^{2+}$oxidation prevented collection of meaningful results and so are not presented. *In-situ* spectro-electrochemical techniques *e.g*. chronoamperometry accompanied by Raman or UV-vis spectroscopy is needed to provide evidence for complexation. A flow cell was fabricated to conduct spectro-electrochemical experiments but these experiments could not be carried out since access to required equipment was terminated due to COVID19. The reactor design is included in the Appendix (Section 12.4.7).

additional alkyl groups (Kandegedara & Rorabacher, 1999). At lower MEA concentrations, there would be less amine available for complexation, and so $FeCO_3$ precipitation would be more likely for more dilute $MEA_{(aq)}$ solution, agreeing with *ex-situ* surface analysis (**Figure 6-2**) and current density transients (**Figure 6-1**).

**Dissolved '$CO_2$' concentration:** Given the higher solution pH of $MDEA_{(aq)}$ solutions, at a given concentration than MEA, a fraction of formation of $FeCO_3$ *via* **6-22** is more likely with MDEA, though it would not be the predominant $FeCO_3$ formation reaction since the concentration of $HCO_3^-$ is at least 14 times that of $CO_3^{2-}$ at pH 8.6 (**Figure 2-11**). Unlike **5-7**, this reaction mechanism does not involve the formation of $H^+$ so $FeCO_3$ precipitation requires less $Fe^{2+}$.

$$Fe^{2+}_{(aq)} + CO^{2-}_{3(aq)} \leftrightarrow FeCO_{3(c)} \qquad \textbf{6-22}$$

**Summary of local solution chemistry:**

$FeCO_3$ precipitation in aqueous $CO_2$ environments is a function of $Fe^{2+}$, $CO_3^{2-}$ concentrations (and $K_{sp}$), both of which are influenced by amine type and concentration. $FeCO_3$ formation, with $HCO_3^-$ as a precursor, results in a release of $H^+$s, which decreases the local solution pH. The relative buffering capacity, due to MEA / MDEA, and $CO_3^2$, in aqueous amine solutions saturated with $CO_2$ is likely to affect the required $Fe^{2+}$ needed for $FeCO_3$ precipitation and its subsequent stability. $MDEA_{(aq)}$ solution saturated with $CO_2$ was proposed to have a higher buffering capability due to its 1) higher concentration relative to $MEA_{(aq)}$ $CO_2$ saturated solutions as a result of MEA carbamate ($MEACOO^-$) formation (Equation **6-20** - **6-21**), its lower $pK_a$ relative to amine solution pH indicating that it will more optimally absorb $H^+$ as the solution pH decreases, and 3) its higher $CO_3^{2-}$concentration. The lower $[HCO_3^-]$ : $[CO_3^{2-}]$ ratio in $MDEA_{(aq)}$ saturated with $CO_2$ also suggests that a fraction of the $FeCO_3$ will be formed directly from $CO_3^{2-}$ and thus have no effect on local pH. The diffusion coefficients of all species were smaller in all $MDEA_{(aq)}$ solutions than in $MEA_{(aq)}$ solutions and decreased with increasing amine concentration. This means that for a given quantity of $H^+$ released due to $FeCO_3$ formation, the local pH would decrease at a faster rate in MDEA. The diffusion coefficients of $Fe^{2+}$ and $HCO_3^-$ are estimated to be smaller in $MDEA_{(aq)}$ solutions and to decrease with increased concentration. The effect of these two would have opposing effects on the rate at which the $FeCO_3$ saturation ratio increases and possibly explains the highest total charge density passed in 3 M $MDEA_{(aq)}$ solution. Finally, complexation of $Fe^{2+}$ with an

MEA species, if present, would decrease the local $Fe^{2+}$ concentration, and make $FeCO_3$ formation less likely.

The proposed superior buffering capability of $MDEA_{(aq)}$ solutions saturated with $CO_2$, together with the higher $CO_3^{2-}$ concentration and predicted faster $Fe^{2+}$ accumulation rate due to higher solution viscosity, are thought to be responsible for the observed enhanced $FeCO_3$ precipitation and stability in $MDEA_{(aq)}$ solutions saturated with $CO_2$ at 80 °C.

## 6.4 Conclusions

$FeCO_3$ formation on an Fe RDE in $MEA_{(aq)}$ and $MDEA_{(aq)}$ solutions saturated with $CO_2$ at 80 °C was investigated by identifying and applying $FeCO_3$ formation potentials and measuring resultant current densities. Chronoamperometry experiments were complemented with *ex-situ* surface characterisation techniques including SEM-EDX and XRD. No trace of $FeCO_3$ precipitation was observed on the Fe electrode in the highest concentration $MEA_{(aq)}$ solution despite large oxidation current densities and substantial estimated bulk saturation ratio of > 500. As concentrations of MEA were decreased, current density transients, and in the case of 1 M, *ex-situ* analysis, suggested the presence of $FeCO_3$. By contrast to behaviour observed in $MEA_{(aq)}$ solutions, crystalline product was demonstrated to have formed on Fe in all $MDEA_{(aq)}$ solutions. The total charge densities passed at *ca.* -0.4 V were found to exhibit a linear relationship with MEA concentration and a parabolic relationship with MDEA concentration.

Interpretation of the experimental results was aided by modelling the diffusion of $Fe^{2+}$, $HCO_3^-$ and $H^+$ and $FeCO_3$ formation, which predicted a substantial local pH decrease to *ca.* 4 due to $FeCO_3$ formation from $HCO_3^-$. Such low pHs would require $Fe^{2+}$ concentrations in excess of $10^{-3}$ mol $dm^{-3}$ for $FeCO_3$ precipitation, making $FeCO_3$ formation unfeasible at the calculated $Fe^{2+}$ concentrations. It was proposed that MDEA and $CO_3^{2-}$ in $MDEA_{(aq)}$ $CO_2$ saturated solutions possibly serve as effective buffers through MDEA protonation and $HCO_3^-$ formation, thus preventing the released $H^+$ from decreasing the local pH. This has not been postulated previously to explain the favourable $FeCO_3$ formation on carbon steel in $MDEA_{(aq)}$ solutions relative to $MEA_{(aq)}$.

The diffusion coefficients of $H^+$, $HCO_3^-$ and $Fe^{2+}$ were obtained from the literature and corrected for solution viscosity and temperature. The diffusion coefficients of all three species were estimated to be higher in $MEA_{(aq)}$ than in $MDEA_{(aq)}$ solutions and to decrease with increasing amine concentration. It was noted that the diffusion coefficients of different species have opposing effects on the saturation ratios of $FeCO_3$. Higher $Fe^{2+}$ diffusion coefficients would result in slower $Fe^{2+}$ accumulation rates and increased saturation ratios. Higher $H^+$ and $HCO_3^-$ diffusion coefficients would have the opposite effect of enhancing saturation ratios. The inverse relationship between $H^+$ diffusion coefficient and MEA concentration is likely to be partially responsible for the positive correlation between amine concentration and total charge density passed.

The competing processes of $H^+$ release, proposed absorption by amine and $CO_3^{2-}$, and varying diffusion rates of reacting species to and from the electrode surface, are thought to be responsible for the parabolic relationship between the total charge density passed with MDEA concentration.

Although the products formed on Fe electrodes were inferred by EDX to be $FeCO_3$, crystalline habits were not clearly discernible, particularly with 1 – 3 M $MEA_{(aq)}$ and 5 M $MDEA_{(aq)}$. Small amounts of products were also dispersed so could not be detected by XRD. A combination of *in-situ* spectro-electrochemical techniques would allow for meaningful conclusions of the products formed. It would also enable determination of the time corresponding to the onset of $FeCO_3$ formation and subsequently changes in the corresponding local solution chemistry, including dissolution of $FeCO_3$ due to local pH decreases, and the possibly complexation between $Fe^{2+}$ and MEA species.

# 7 Growth of resistive films on carbon steel in amine solutions saturated with $CO_2$

## 7.1 Introduction

Electrochemical impedance spectroscopy (EIS) is a non-destructive, *in-situ* technique, which can be used to monitor the evolution of electrode resistance and changes in interfacial phases with time. The theoretical background of this technique can be found in Chapter 2, Section 2.4.5.3. The technique specifications used to measure the data presented in this chapter are outlined in Chapter 3, Section 3.4.

In this chapter, EIS was used to:

i. Determine if the $FeCO_3$ films formed on carbon steel (CS) in aqueous methyldiethanolamine ($MDEA_{(aq)}$) solutions saturated with $CO_2$ at 80 °C are sufficiently electrically resistive for use as protective films to limit corrosion.
ii. Compare the electrical resistance of the films formed in varying concentrations of MDEA (1, 3 and 5 M) to determine the optimum solution concentration for $FeCO_3$ film growth.
iii. Determine if the $FeCO_3$ film on pre-treated CS electrodes remain stable in aqueous monoethanolamine ($MEA_{(aq)}$) solutions saturated with $CO_2$.

### 7.1.1 Experimental considerations

In the first set of EIS experiments in $MDEA_{(aq)}$, the resistive film formation process was monitored by recording the impedance spectra on a daily basis until there was no noticeable change between the spectra measured on consecutive days. During these measurements, the cell was opened to enable the immersion of the reference and counter electrodes; this procedure was subsequently shown to have inadvertently allowed $O_2$ ingress into the solutions, despite continued $CO_2$ bubbling. Due to the effect of amine concentration on electrolyte viscosity as was explained in Chapter 5 and Chapter 6 (Section 6.3), $O_2$ affected the electrodes in the different solutions to varying degrees, where the electrode in the 1 M $MDEA_{(aq)}$ solution was the most 'contaminated' and that in the 5 M solution the least. It was found that $O_2$ contamination resulted in the formation of an oxide (or carbonate-oxide) film, as evidenced from changes in the OCP, which were less resistive and inhibited the development of a more protective pure $FeCO_3$ film. From these results, it could be incorrectly inferred that the film resistivity increased with MDEA concentration, but the composition of these films were not identical. Therefore, preventing $O_2$ ingress was found to be critical to comparing the formation, resistivity and stability of $FeCO_3$ films in different $MDEA_{(aq)}$ solutions. However, from the first set of experiments, the approximate time for complete $FeCO_3$ film formation was determined. This duration varied with MDEA concentration. In subsequent experiments, which are presented in Section 7.2.1, OCP and EIS measurements were made only twice on each electrode: (1) when the electrode was immersed initially in the electrolyte and (2) at the end, when the film was expected to have formed. Film formation experiments were repeated at least twice and results are included in the Appendix (Section 12.5, **Figure 12-18** - **Figure 12-20**). A comparison of the EIS data obtained for an $O_2$ contaminated film and a non-contaminated film, as well as film stability in $MEA_{(aq)}$ are included at the end of this chapter (Section 7.2.4).

### 7.1.2 Data analysis considerations

#### 7.1.2.1 Equivalent circuit fitting

The measured impedance spectra were modelled using equivalent circuits to (1) compare quantitatively the electrical resistance of the $FeCO_3$ films formed in each $MDEA_{(aq)}$ solution and (2) corroborate the presence of different surface features deduced from visual inspection of data.

To select an appropriate equivalent circuit (*EC*) to model the measured data, the Nyquist and Bode representation of the impedance data were first inspected visually to infer the number and type(s) of processes present.

'Initial guess' values for resistor and capacitor components were attained by selecting the subset of corresponding EIS data points and applying a circle fit analysis using the 'Electrochemical Circle Fit' feature included in the EC-Lab software. To calculate an initial guess for the diffusion parameter ($\sigma_d$), the impedance ($Z_w$) and frequency ($f$) corresponding to a data point within what was deduced visually to be the diffusion part of the Nyquist plot, was selected and applied to Equation **7-1.** This equation was presented and explained in Chapter 2, Section 2.4.5.3, but is repeated here for easy reference.

$$Z_w = \frac{\sqrt{2}\,\sigma_d}{\sqrt{j\,2\,\pi\,f}} \qquad \textbf{7-1}$$

*EC*s used to represent the predetermined processes in the context of electrode dissolution and film formation were then found in the literature. The circuit which gave the best fit, as confirmed from the goodness of fit, *i.e.* weighted $\chi^2$ value, and was found to be reasonable from comparison with 'initial guess' values as well as the measured impedance modulus, was selected. Iterative modelling was then conducted to improve the circuit fit until the weighted $\chi^2$ was $\leq 0.09$[30].

$EC_1$ (**Figure 7-1**) describes a single time constant process and was used to model EIS data collected when pristine CS electrodes were immersed initially in $MDEA_{(aq)}$ and $MEA_{(aq)}$ solutions. $R_S$ represents the ohmic or electrolyte resistance, $R_{CT}$ the interfacial resistance to charge transfer and $C_{DL}$ is the double layer capacitance. $C_{DL}$ was replaced with a constant phase element ($Q$), which better modelled non-ideal capacitive behaviour of the double layer. The constant phase element value was then converted to the (pseudo) double layer capacitance ($C_{DL}$) using Equation **7-2**.

$$C_{DL} = Q^{\frac{1}{\alpha}} R_{CT}^{\frac{1-\alpha}{\alpha}} \qquad \textbf{7-2}$$

[30]The $\chi^2$ value obtained for a an equivalent circuit fitting should be minimised as much as reasonably possible since it indicates the deviation between the fitting and measured values. In this thesis, EIS was used to measure the uncontrolled formation of non-homogenous $FeCO_3$ films formed *via* a dissolution-precipitation mechanism, which resulted in relatively high $\chi^2$ values; hence, the choice of a relatively large weighted $\chi^2$ criterion.

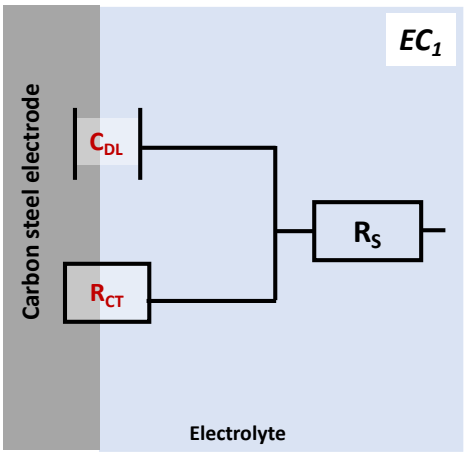



**Figure 7-1:** Equivalent circuit used for fitting the experimental impedance data of carbon steel electrodes after initial immersion in $MDEA_{(aq)}$ and $MEA_{(aq)}$ solutions saturated with $CO_2$ at 80 °C

$EC_2$ (**Figure 7-2**) is a two time constant hierarchical circuit often used to model electrodes covered by surface films (Amirudin & Thierry, 1995; Orazem & Tribollet, 2008:chap.9; Farelas *et al.*, 2010). $R_S$ represents the ohmic or electrolyte resistance, $C_C$ and $R_C$ the coating capacitance and resistance respectively, and $C_{DL}$ and $R_{CT}$ the double layer capacitance and resistance to charge transfer. Constant phase elements ($Q$) were again used in place of the capacitors to represent their non-ideal behaviour. For $EC_2$, the constant phase element used to describe the double layer capacitance ($C_{DL}$) could be converted to the effective double layer capacitance ($C_{eff}$) using Equation **7-3**, which assumes a normal time constant distribution through the surface layers (Hirschorn *et al.*, 2010).

$$C_{eff} = Q_{DL}^{\frac{1}{\alpha}} R_C^{\frac{(1-\alpha)}{\alpha}} \qquad \textbf{7-3}$$

$EC_3$ (**Figure 7-2**) is similar to $EC_2$ with the only difference being the inclusion of a diffusion element ($W$). This circuit has been proposed to model the impedance data collected for a surface film formed on carbon steel in $CO_{2(aq)}$ solutions at 80 °C (Motte *et al.*, 2020). The Warburg element ($W$) is used to represent semi-infinite diffusion. A constant phase element ($Q$) ($\alpha \leq 0.5$) was used in place of the Warburg component to model non-ideal diffusion.

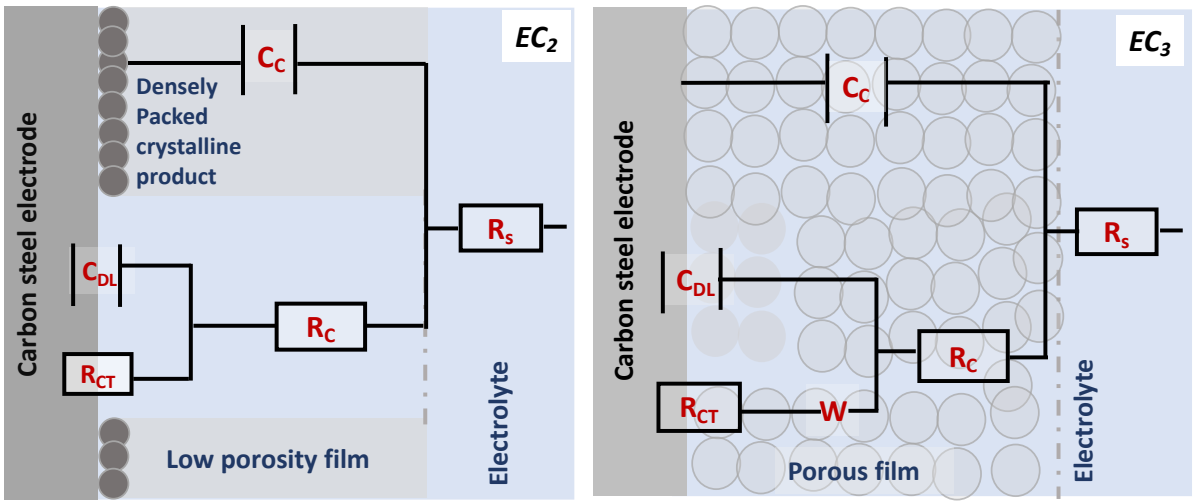



**Figure 7-2:** Equivalent circuits used for fitting the experimental impedance data of carbon steel electrodes at the end of immersion in $MDEA_{(aq)}$ and of (1 M $MDEA_{(aq)}$) pre-treated carbon steel in $MEA_{(aq)}$ solutions saturated with $CO_2$ at 80 °C.

### 7.1.2.2 Ohmic resistance correction

The electrolyte resistance of $MDEA_{(aq)}$ solutions increased with increased MDEA concentration and the electrolyte resistance of $MEA_{(aq)}$ is not equal to that of $MDEA_{(aq)}$ at the same concentration. Therefore, the impedance modulus (|Z|) needed to be corrected for varying ohmic resistances in all solutions, to enable accurate comparisons between impedance spectra. When EIS data were measured with electrodes in solutions of the same amine and amine concentration, the impedance modulus was not corrected for ohmic resistance. Equation **7-4** was used for the correction (Orazem, Pébère & Tribollet, 2006) where *Z'* represents the real part of the impedance, $R_{e,est}$ the estimation of the ohmic resistance and *Z"* the imaginary part of the impedance. (Orazem, Pébère & Tribollet, 2006) recommend estimating $R_{e,est}$ independently where possible, but also explain that as the frequency tends to infinity, the impedance becomes equal to the electrolyte resistance. In this chapter, $R_{e,est}$ was estimated from circuit fitting. To determine that this estimation was valid, it was compared to the *Z'* corresponding to the highest frequency ($10^5$ Hz) collected. The difference between *Z'* at $10^5$ Hz and $R_{e,est}$ was less than 5 Ω, so was thought to be adequate for the ohmic resistance correction.

$$|Z|_{adj} = \sqrt{(Z' - R_{e,est})^2 + (Z'')^2} \qquad \textbf{7-4}$$

#### 7.1.2.3 Kramers-Kronig

The Kramers-Kronig analysis, explained previously in Chapter 2, Section 2.4.5.3, was conducted using the *Kramers-Kronig* feature included in the EC-lab software and was used to calculate the percentage error – results are included in the Appendix (Section 12.5, **Table 12-12** - **Table 12-13**). Most of the presented data gave an error of ≤ 15 %.

## 7.2 Results and discussion

### 7.2.1 Impedance spectroscopy of carbon steel in MDEA and MEA

Typical impedance data for CS immersed in 1, 3 and 5 M $MDEA_{(aq)}$ solutions saturated with $CO_2$ at 80 °C are shown in **Figure 7-3**, **Figure 7-5** and **Figure 7-8** respectively, and are supplemented by images obtained subsequently *ex-situ* by scanning electron microscopy (SEM), shown in **Figure 7-4**, **Figure 7-6** and **Figure 7-7**. Impedance data were collected until the effect of time no longer became evident; this point was assumed to mark the completion of the protective $FeCO_3$ film formation, though $O_2$ ingress during the measurement is assumed to have affected film growth.

For the improved set of experiments, a comparison of the Nyquist and Bode representations of the impedance data (both measured and simulated) at initial immersion and after film formation as a function of amine concentration is presented in **Figure 7-9**. The CS impedance behaviour in each $MDEA_{(aq)}$ solution will be discussed first and the observed trends will be discussed thereafter.

**Immersion in 1 M $MDEA_{(aq)}$:** Upon immersion of the CS electrode in the 1 M electrolyte, an OCP of -0.590 V was obtained, confirming that the electrode had not undergone substantial aerial oxidation before immersion in the solution. From the Bode representation of the phase angle (**Figure 7-3c**), one definitive time constant can be seen at *ca*. $10^2$ Hz. This is thought to be related to a charge transfer process of Fe dissolution from the electrode surface when exposed to the electrolyte. It seems that there is another time constant at *ca*. $10^{-1}$ Hz, which was thought initially to be due to the adsorption of amine-based species on the electrode surface but this was not evident when the electrode was immersed in more concentrated solutions. Further, $CO_2$ bubble adhesion to the electrode surface introduced noise into the data collected at low frequencies (< $10^0$ Hz), so these data were excluded from the subsequent analysis and circuit fitting. It should be mentioned that the bubbles are thought to be $CO_2$ rather than $H_2$ given the mildly alkaline pH (7.9) at which $H_2$ evolution kinetics would be slow. $EC_1$ fitted the initial EIS data well and indicated that the charge transfer resistance was quite low at $9 \times 10^{-3}$ Ω $m^2$.

After *ca*. 72 h (three days) of immersion in the 1 M solution, the OCP increased to -0.509 V and the detected bulk solution Fe concentration was 42.9 ± 3 mg $dm^{-3}$; under these conditions

$FeCO_3$ is predicted to be the most thermodynamically favourable phase. When the electrode was immersed in the 1 M electrolyte, it is likely that the CS surface underwent non-uniform dissolution, as was proposed for CS when exposed to $CO_{2(aq)}$ electrolytes, whereby ferrite dissolved preferentially, leaving a porous cementite ($Fe_3C$) layer (Crolet, Thevenot & Nešić, 1998). Based on the detected bulk solution Fe concentration of $7.8 \times 10^{-4}$ mol $dm^{-3}$ (42.9 mg $dm^{-3}$), the calculated $CO_3^{2-}$ concentration[31] of $1.5 \times 10^{-3}$ mol $dm^{-3}$, and the solubility product ($K_{sp}$) of $7.2 \times 10^{-10}$ $mol^2$ $dm^{-6}$ (Equation **6-2**), the bulk solution $FeCO_3$ saturation ratio (Equation **5-10**) was $1.7 \times 10^3$ . Within the porous cementite layer, the $FeCO_3$ saturation ratio would be even greater, making it highly conducive to $FeCO_3$ precipitation .

Continuous dissolution of Fe and $FeCO_3$ precipitation would allow for further development of the $FeCO_3$ film. The low magnification SEM image (**Figure 7-4a**) shows that the surface was covered completely in a layer of densely packed small crystals (*ca*. 1 μm) (**Figure 7-4c**) with protruding larger crystals (*ca*. 10 μm) (**Figure 7-4b**). Energy-dispersive X-ray spectroscopy (EDX) detected the presence of Fe, C and O at 60, 10, 30 mass % respectively, (Appendix, Section 12.5, **Figure 12-22**), substantiating the presence of $FeCO_3$ (with an expected mass % of Fe: 48.2, C: 10.4, O: 41.3). **Figure 7-3d** shows that the impedance modulus increased significantly for all applied frequencies at the end of the three day immersion, indicating that the observed $FeCO_3$ film provided protection to the underlying steel substrate. The Nyquist plot (**Figure 7-3a**) appears to consist of at least two convoluted semicircles and possibly a 45 ° line suggesting a diffusion process. The Bode representation of the phase angle confirmed the presence of two time constants, one between $10^{3.5}$ and $10^{4.5}$ Hz, and another at *ca*. $10^2$ Hz due to the charge transfer process at the electrode surface. It has been demonstrated in the literature (Motte *et al*., 2020; Kinsella, Tan & Bailey, 1998) that a high frequency time constant (*ca*. $10^3$ to $10^4$ Hz) appeared when a surface film formed on CS in $CO_{2(aq)}$ environments; whilst charge transfer processes were captured at intermediate frequencies (*ca*. $10^{-1}$ to $10^2$ Hz (Farelas *et al*., 2010)). Therefore, the time constant measured

[31]The $CO_3^{2-}$ concentrations in all three solutions were estimated based on a total dissolved $CO_2$ concentration of 0.0129 mol $dm^{-3}$ (based on a temperature of 80 °C) and a $CO_3^{2-}$ mole fraction determined from the estimated mole fractions of $CO_3^{2-}$ at the solution pH and assuming $HCO_3^-$ and $CO_3^{2-}$ are the only dissolved $CO_2$ species. The methods for calculating the concentration of $CO_3^{2-}$ and the $K_{sp}$ are outlined in the Appendix (Section 12.4.4 - 12.4.5).

at *ca*. $10^4$ Hz is thought to be due to the coating and the other (at $10^2$ Hz) is associated with the charge transfer process.

It should be stated that two time constants are discernible from **Figure 7-3c** but are not well defined since both occur at similar frequencies. In repetitions of this experiment, the time constants were even closer together (Appendix, Section 12.5, **Figure 12-18**) and were visually indifferentiable.

From **Figure 7-4a**, the coating appeared to be an interlinked bed of multiple sized crystals; surface images demonstrating islands of very compact small crystals (*ca*. 1 μm) surrounded by less compacted, larger crystals (*ca*. 4.5 μm) closely resembled those presented by (Barker *et al*., 2019), which were confirmed in that study with XRD to be $FeCO_3$. $EC_2$ and $EC_3$ (**Figure 7-2**) were then used to fit the EIS data; $EC_3$ gave a better fit, indicating that two time constants as well as a diffusion feature were indeed present. The presence of the diffusion process is as a result of the porous nature of the coating. From the circuit fitting, the coating resistance was found to be *ca*. $10^{-2}$ Ω $m^2$ (**Table 7-1**). According to (Amirudin & Thierry, 1995) a coating resistance of $10^3$ Ω $m^2$ is recommended for polymer coatings to provide good corrosion protection for steel substrates, but the authors also explained that required coating resistances should be specific to the electrolyte conductivity. However, the charge transfer resistance was substantially higher than the coating resistance. This revealed an important finding that, although $FeCO_3$ has been found to be insulating (Mercier-Bion *et al*., 2018:p.108), the porous nature of the film disables it from acting as a fully electrically insulating protective film. Instead, it creates a physical barrier that decreases the electroactive surface area (*i.e*. the area which is exposed to the electrolyte), so increasing the charge transfer resistance substantially from $9 \times 10^{-3}$ Ω $m^2$ to $7 \times 10^{-1}$ Ω $m^2$ (**Table 7-1**). From **Figure 7-3** and **Figure 7-4**, it can be concluded that the $FeCO_3$ film produced within 72 h (three days) of immersion in the 1 M $MDEA_{(aq)}$ solution was electrically resistive.

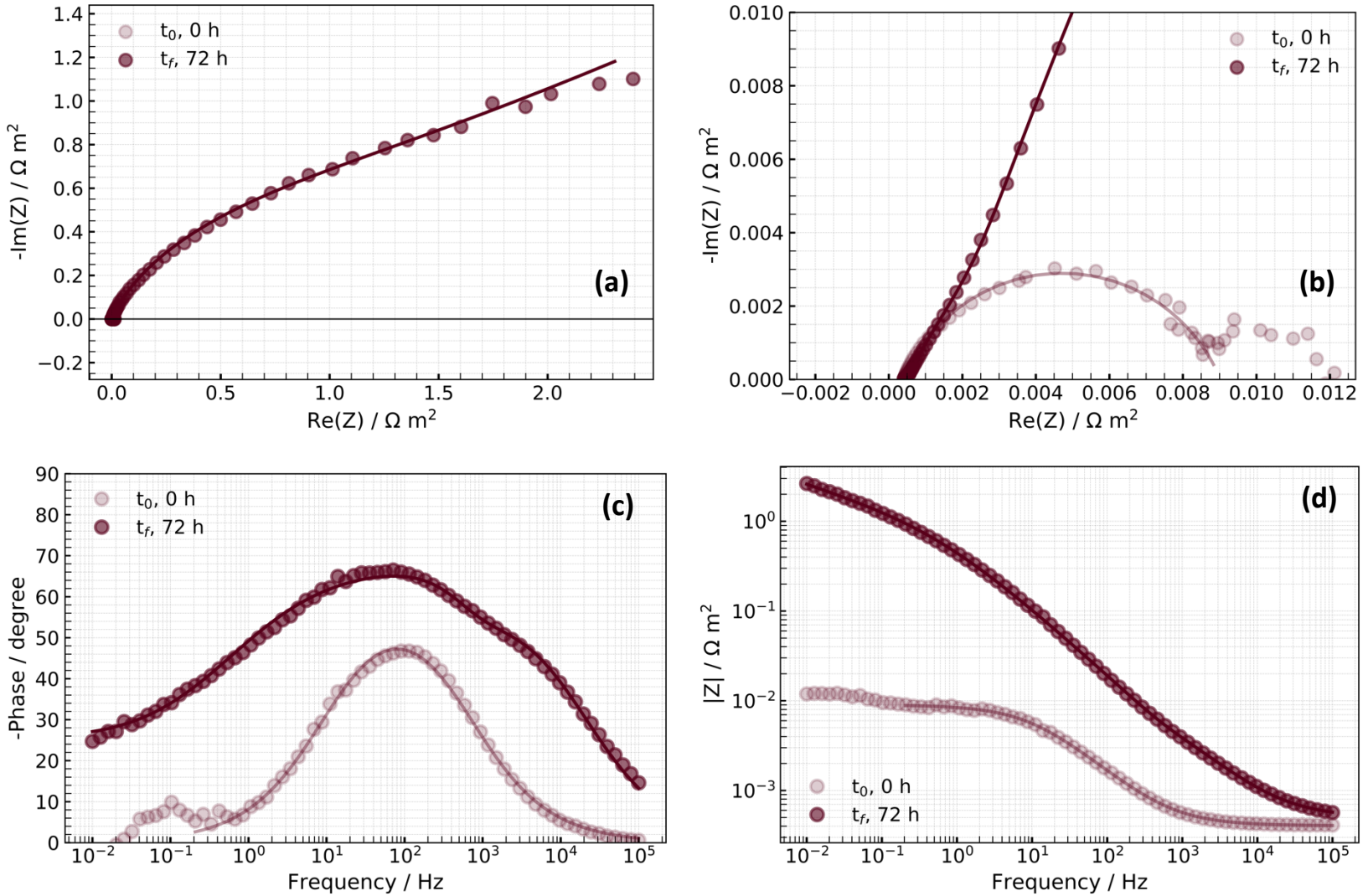



**Figure 7-3**: Experimental (o) and simulated (-) impedance data obtained at OCP with a CS electrode immersed in 1 M $MDEA_{(aq)}$, saturated with $CO_2$ (pH 7.9) 80 °C. OCP at 0 h = -0.590 V, and at 72 h = -0.509 V. **(a - b)** Nyquist representations; Bode representations of **(c)** phase angle and **(d)** impedance magnitude.

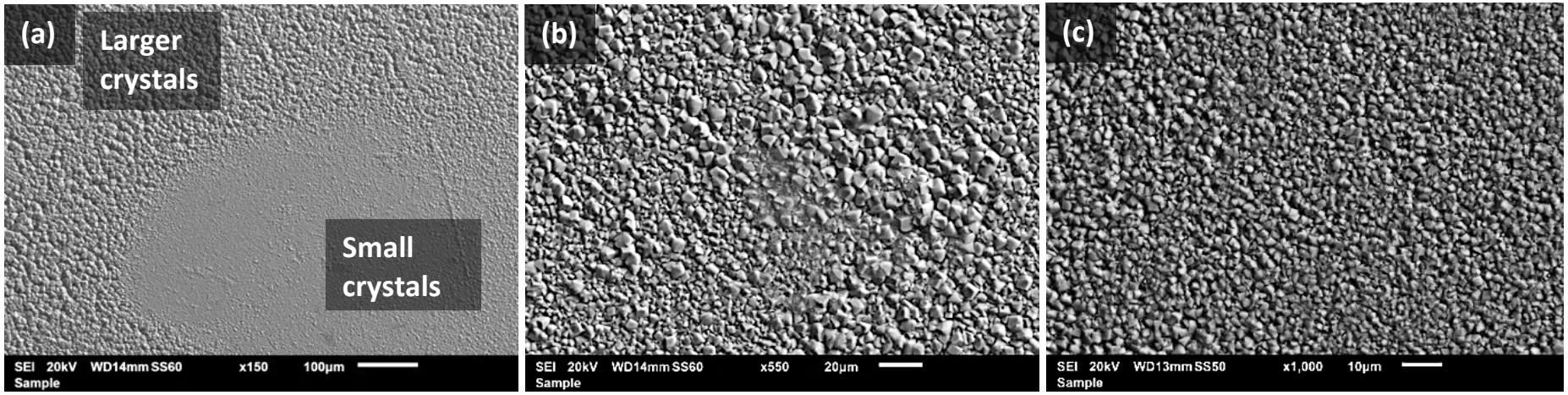



**Figure 7-4**: *Ex-situ* SEM images of CS electrode after immersion in 1 M $MDEA_{(aq)}$ saturated with $CO_2$ (pH 7.9) at 80 °C for *ca*. 72 h at magnifications of **(a)** 150x, **(b)** 500x and **(c)** 1000x.

**Table 7-1:** Normalised $EC_3$ component values for impedance data obtained when a CS electrode was immersed in 1 M $MDEA_{(aq)}$ saturated with $CO_2$ at 80 °C ($\alpha_{DL}$ values corresponding to $Q_{DL}$ are included in Appendix, Section 12.5, **Table 12-14**).

| **Time** | $R_C$ / Ω m² | $Q_C$ / F $s^{\alpha-1}$ $m^{-2}$ | $R_{CT}$ / Ω m² | $Q_{DL}$ / F $s^{\alpha-1}$ $m^{-2}$ [$C_{DL}$ / F $m^{-2}$] | $\frac{\chi^2}{\lvert Z \rvert}$ |
|---|---|---|---|---|---|
| $t_0$ **: 0 h** | N/A | N/A | $9 \times 10^{-3}$ | [2.8] | 0.03 |
| $t_f$ **: 72 h** | $2 \times 10^{-2}$ | $4 \times 10^{-1}$ | $7 \times 10^{-1}$ | $1 \times 10^{-2}$ | 0.05 |

**Immersion in 3 M $MDEA_{(aq)}$:** The 96 h (four day) evolution of the CS electrode impedance when immersed in 3 M $MDEA_{(aq)}$ solution saturated with $CO_2$ at 80 °C is reported in **Figure 7-5**. When immersed initially in the 3 M electrolyte, the electrode stabilised at an OCP of -0.619 V, indicating that the electrode did not undergo significant (aerial) oxidation before exposure to the electrolyte. As in the 1 M electrolyte, the EIS data recorded at frequencies < $10^{-1}$ Hz were noisy due to $CO_2$ bubble adhesion on the electrode surface and so was excluded from the analysis. The Nyquist plot (**Figure 7-5a**) showed one semicircle suggesting a single time constant process. **Figure 7-5c** substantiated the presence of just one time constant at *ca*. $3 \times 10^{1}$ Hz. $EC_1$ fitted the measured data well and confirmed that there was a single RC process at the surface. The resistance to charge transfer was low at $2 \times 10^{-2}$ Ω $m^2$, as expected.

After *ca*. 96 h (four days), the OCP increased to -0.425 V and the measured dissolved Fe concentration in solution was 25 mg $dm^{-3}$, which suggested a degree of corrosion and hence the accompanying presence of $FeCO_3$ was expected. At this $Fe^{2+}$ concentration, an estimated $CO_3^{2-}$ concentration of $3.4 \times 10^{-3}$ mol $dm^{-3}$, a $K_{sp}$ of $9.1 \times 10^{-10}$ $mol^2$ $dm^{-6}$ (Appendix, Section 12.4.4 - 12.4.5.1) the solution $FeCO_3$ saturation ratio (Equation **5-10**) is estimated to be $2.8 \times 10^{3}$, further implying that an $FeCO_3$ film would be present on the electrode surface. This was substantiated by the SEM images presented in **Figure 7-6**, which showed a bed of crystals (*ca*. 5 μm) of similar trigonal-capped habit to that found in the experiments in the 1 M $MDEA_{(aq)}$ solution. EDX confirmed that these were $FeCO_3$ crystals (Fe: 45 %, C: 14 %, O: 40 %, by mass). The increase in the impedance modulus (at all frequencies) from the initial immersion data to 96 h post-immersion confirmed that the $FeCO_3$ coating was electrically resistive of the order of $10^{-1}$ to $10^{0}$ Ω $m^2$ (**Figure 7-5d**). The number of time constants was not discernible from visual inspection of the Nyquist plot (**Figure 7-5a**), but the lower frequency data (< 0.53 Hz) indicated the presence of a diffusion process. It was also difficult to distinguish the number of processes involved at the electrode surface from **Figure 7-5c**.

$EC_3$ was found to model the measured impedance data well, thereby demonstrating that there were two time constants present, one related to the charge transfer process at lower frequencies, and the other related to the coating at higher frequencies, as well as a diffusion feature. From the circuit fitting, the coating resistance was *ca*. $3 \times 10^{-2}$ Ω $m^2$ (**Table 7-2**), similar to that of the initial charge transfer resistance, whilst the new charge transfer resistance was an order of magnitude greater at $3 \times 10^{-1}$ Ω $m^2$.

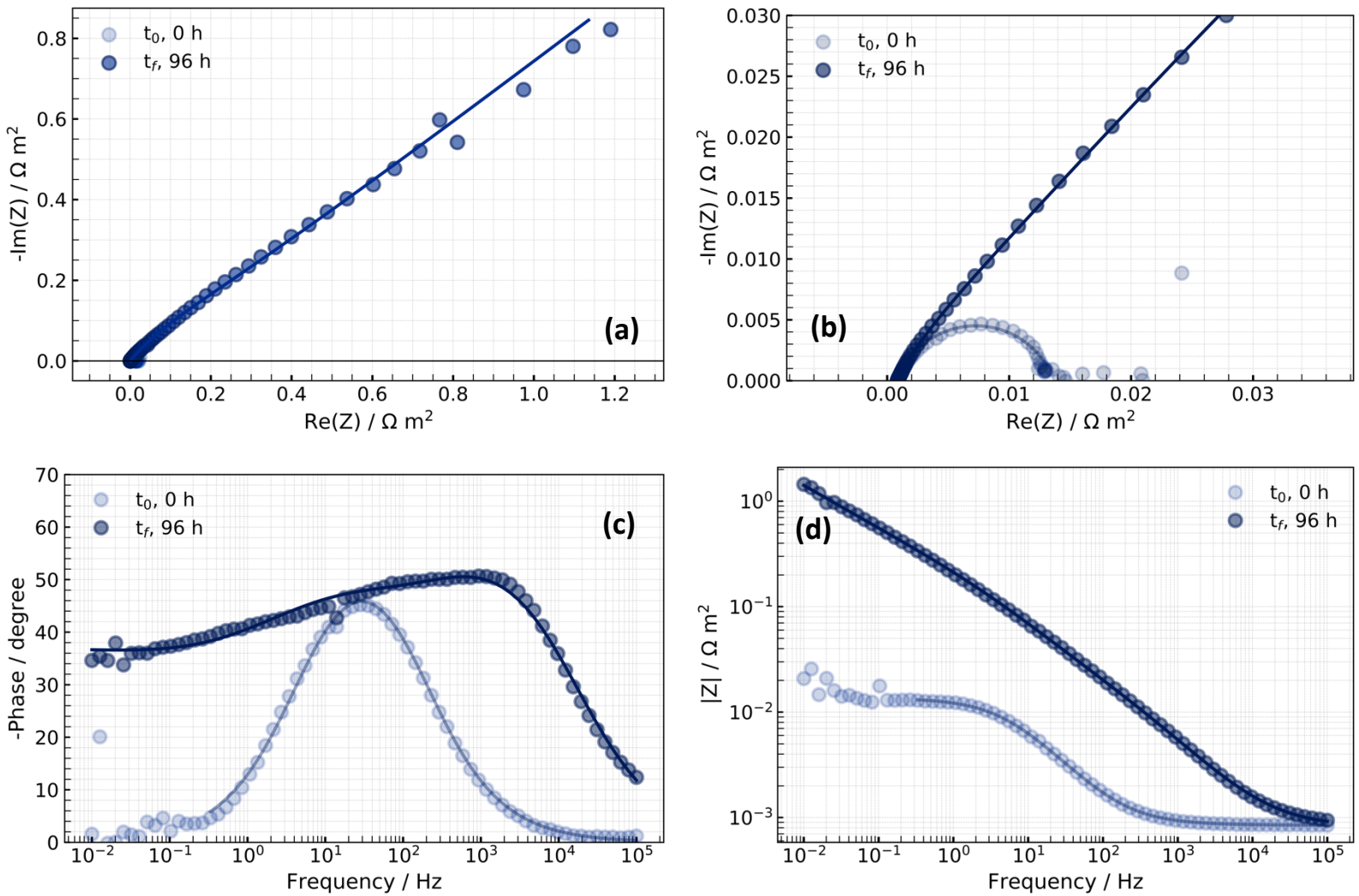



**Figure 7-5:** Experimental (o) and simulated (-) data obtained at OCP with a CS electrode in 3 M $MDEA_{(aq)}$, saturated with $CO_2$ (pH 8.3) 80 °C. OCP at 0 h = -0.619 V, and at 96 h = -0.425 V. **(a - b)** Nyquist representations; Bode representation of the **(c)** phase angle and **(d)** impedance magnitude.

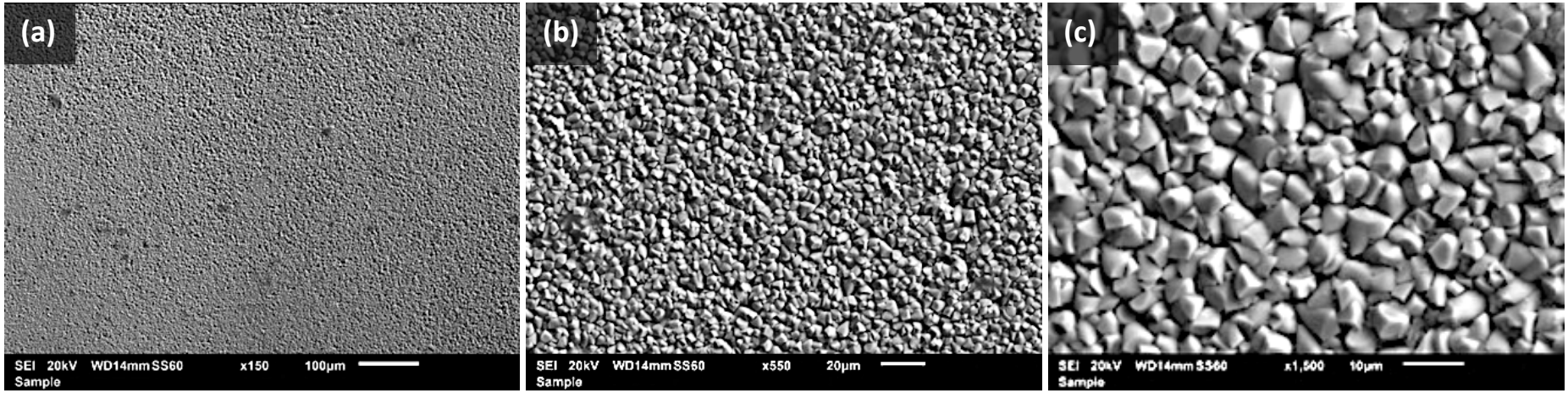



**Figure 7-6:** *Ex-situ* SEM images of the CS electrode after immersion in 3 M $MDEA_{(aq)}$ saturated with $CO_2$ (pH 8.3) at 80 °C for *ca*. 96 h at varying magnifications of **(a)** 150x, **(b)** 550x, **(c)** 1500x.

**Table 7-2:** Normalised $EC_3$ component values for impedance data obtained when a CS electrode was immersed in 3 M $MDEA_{(aq)}$ saturated with $CO_2$ at 80 °C. ($\alpha_{DL}$ values corresponding to $Q_{DL}$ are included in Appendix, Section 12.5, **Table 12-14**).

| **Time** | $R_C$ / Ω m² | $Q_C$ / F $s^{\alpha-1}$ $m^{-2}$ | $R_{CT}$ / Ω m² | $Q_{DL}$ / F $s^{\alpha-1}$ $m^{-2}$ [$C_{DL}$ / F $m^{-2}$] | $\frac{\chi^2}{\lvert Z \rvert}$ |
|---|---|---|---|---|---|
| $t_0$ **: 0 h** | N/A | N/A | $9 \times 10^{-3}$ | [2.6] | 0.01 |
| $t_f$ **: 96 h** | $3 \times 10^{-2}$ | $4 \times 10^{-1}$ | $3 \times 10^{-1}$ | $8 \times 10^{-1}$ | 0.05 |

**Immersion in 5 M $MDEA_{(aq)}$:** The behaviour exhibited by the CS electrode in 5 M $MDEA_{(aq)}$ solution saturated with $CO_2$ at 80 °C was consistent with that observed in the 1 and 3 M solutions. An OCP of -0.633 V was obtained initially when the electrode was immersed in the solution. EIS data obtained at frequencies < $10^{-1}$ Hz were obscured by $CO_2$ bubbles adhering to the electrode surface and were excluded from subsequent analysis. Both the Nyquist plot and the Bode representation of the phase angle (**Figure 7-8a** - **c**) showed one time constant at *ca*. $10^{1}$ Hz, indicating a single charge transfer process. Circuit fitting with $EC_1$ gave the resistance to charge transfer of $2 \times 10^{-2}$ Ω $m^2$.

It should be pointed out that the time required for the $FeCO_3$ film formation was the least predictable in the 5 M electrolyte. Given the stochastic nature of the nucleation and growth process, which depends on the number of surface defects present, as well as the slow release of $Fe^{2+}$ ions from the CS electrode, the time required for film formation in the 5 M $MDEA_{(aq)}$ solution varied substantially (6.5 ± 1 days).

After on average 156 h (6.5 days), the OCP increased to -0.432 V and the detected Fe concentration in solution was 42.5 ± 4.6 mg $dm^{-3}$, which equates to a saturation ratio of $4 \times 10^{3}$ (Equation **5-10**) for a $CO_3^{2-}$ concentration of $5.3 \times 10^{-3}$ mol $dm^{-3}$ and a $K_{sp}$ of $1.02 \times 10^{-9}$ $mol^2$ $dm^{-6}$ (Appendix, Section 12.4.4 - 12.4.5.1), implying of the presence of $FeCO_3$. Surface imaging (**Figure 7-7**) confirmed that a surface film was present on the electrode and EDX detected Fe, C and O (44, 17, 40 % mass, respectively), confirming $FeCO_3$. The electrode impedance modulus was up to two orders of magnitude greater than that of the initially immersed electrode (**Figure 7-8d**) at all perturbation frequencies. As for data from the 3 M solution, the number of time constants present at the end of the immersion period was not clearly discernible but, after iterative circuit fitting, $EC_3$ gave the better fit. Therefore, it was confirmed that two time constants were present (due to coating at higher frequencies and charge transfer at lower), together with a diffusion process. The coating resistance was found to be $1 \times 10^{-2}$ Ω $m^2$ (**Table 7-3**), slightly smaller than that of the initial charge transfer process, whilst the final charge transfer resistance was $2 \times 10^{-1}$ Ω $m^2$, an order of magnitude higher than when initially immersed.

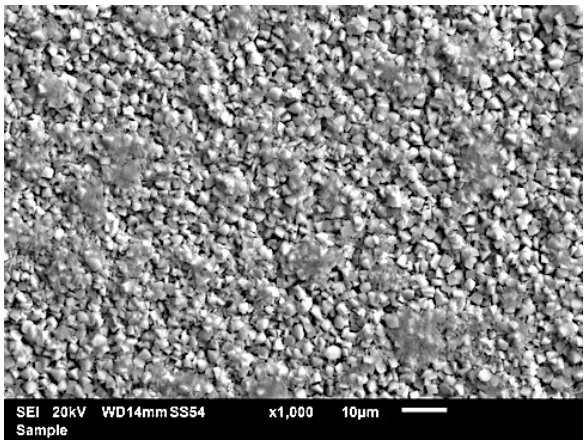



**Figure 7-7**: *Ex-situ* SEM image (1500x magnification) of the CS electrode after immersion in 5 M $MDEA_{(aq)}$, saturated with $CO_2$ (pH 8.6) at 80 °C for *ca*. 156 h.

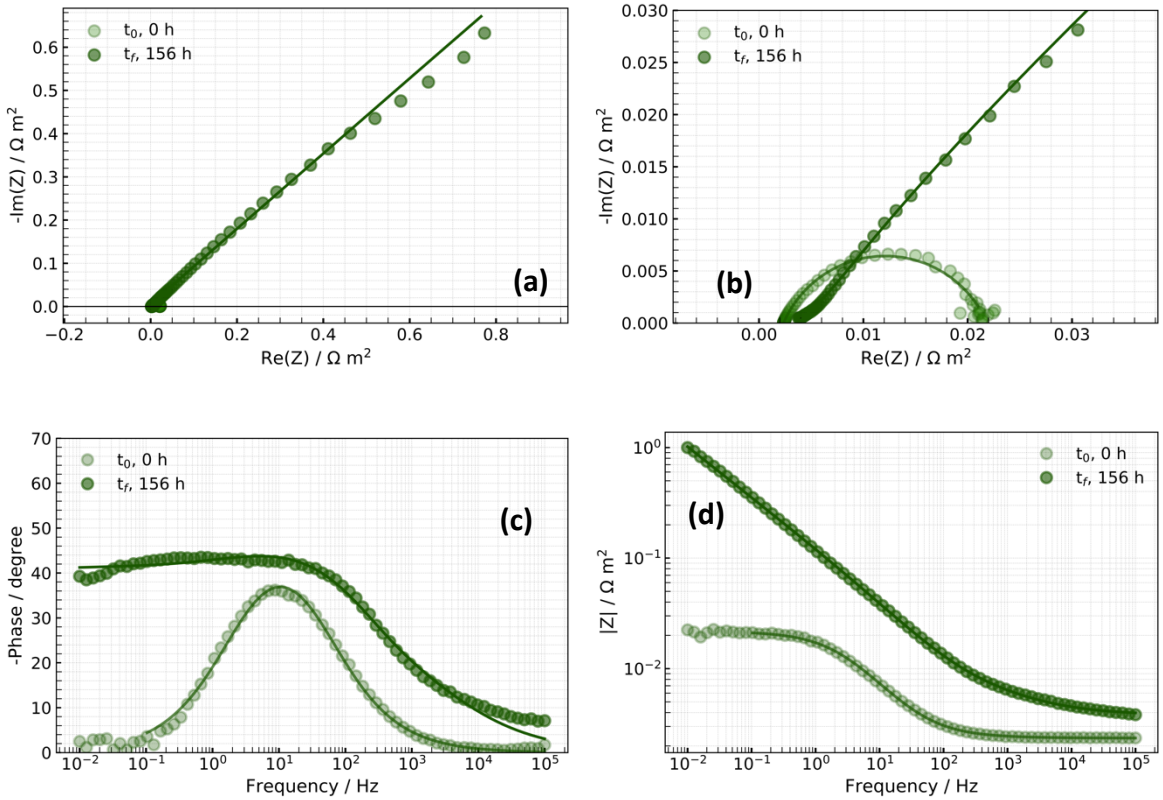



**Figure 7-8:** Experimental (o) and simulated (-) impedance data obtained at OCP with a CS electrode in 5 M $MDEA_{(aq)}$ saturated with $CO_2$ (pH 8.6) at 80 °C. OCP at 0 h = -0.632 V and 156 h = -0.432 V. **(a** - **b)** Nyquist representations; Bode representation of the **(c)** phase angle and **(d)** magnitude of the impedance.

**Table 7-3**: Normalised $EC_3$ component values for impedance data obtained when a CS electrode was immersed in 5 M $MDEA_{(aq)}$ saturated with $CO_2$ at 80 °C. ($\alpha_{DL}$ values corresponding to $Q_{DL}$ are included in Appendix, Section 12.5, **Table 12-14**).

| Time | $R_C$ / Ω m² | $Q_C$ / F $s^{\alpha-1}$ $m^{-2}$ | $R_{CT}$ / Ω m² | $Q_{DL}$ / F $s^{\alpha-1}$ $m^{-2}$ [$C_{DL}$ / F $m^{-2}$] | $\frac{\chi^2}{\lvert Z \rvert}$ |
|---|---|---|---|---|---|
| $t_0$ : 0 h | N/A | N/A | $9 \times 10^{-3}$ | [2.9] | 0.02 |
| $t_f$ : 156 h | $1 \times 10^{-2}$ | $2 \times 10^{0}$ | $2 \times 10^{-1}$ | $3 \times 10^{-1}$ | 0.06 |

**Comparison between results obtained in $MDEA_{(aq)}$ solutions:** Comparative EIS data collected when each CS electrode was immersed initially in 1, 3 and 5 M $MDEA_{(aq)}$ solutions saturated with $CO_2$ at 80 °C is given in (**Figure 7-9a** - **c**). All three EIS data sets were fitted with $EC_1$ as discussed previously, indicating that Fe dissolution was the only electrode process present initially. The Nyquist plots (**Figure 7-9a**) show that as the concentration of MDEA increased, so too did the diameter of the semicircle, suggesting an increase in initial charge transfer resistance with MDEA concentration. This was corroborated by the Bode representation of the phase angle (**Figure 7-9b**), which showed a shift in the time constant to lower frequencies as MDEA concentration was increased, likely due to increased charge transfer resistance. This was confirmed by the impedance modulus (corrected for ohmic resistance) plot (**Figure 7-9c**), which demonstrated that the overall electrode resistance (*i.e.* at low frequencies) was the greatest in the 5 M solution and smallest in the 1 M solution.

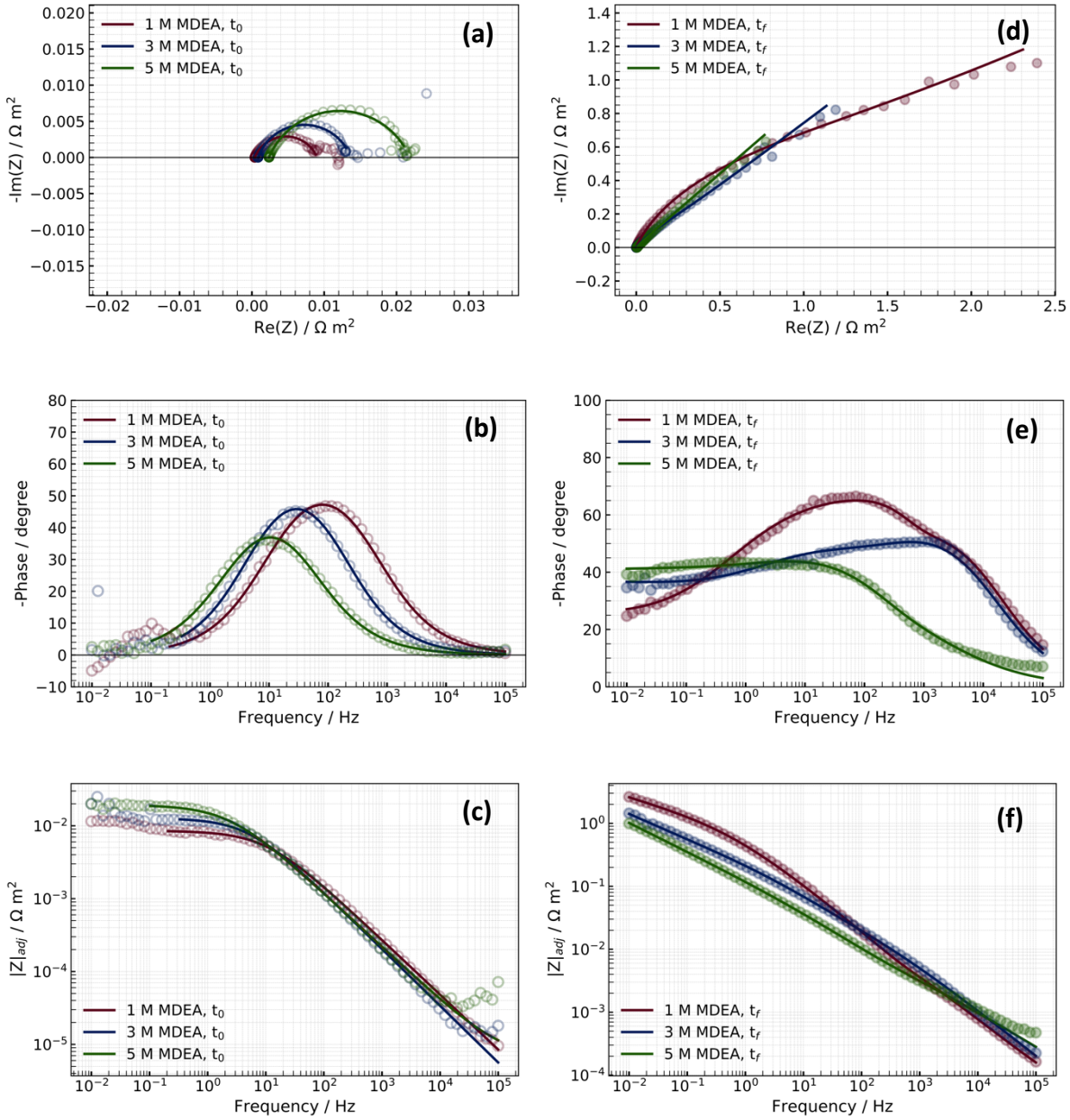



**Figure 7-9**: Experimental (o) and simulated (-) impedance data obtained at OCP with CS electrodes in 1 (pH 7.9), 3 (pH 8.3) and 5 M (pH 8.6) $MDEA_{(aq)}$ saturated with $CO_2$ at 80 °C immediately after immersion: **(a)** Nyquist representation, Bode representation of the **(b)** phase angle and **(c)** ohmic resistance corrected impedance magnitude; and after film formation: **(d)** Nyquist representation and Bode representation of the **(e)** phase angle and **(f)** ohmic resistance corrected impedance magnitude.

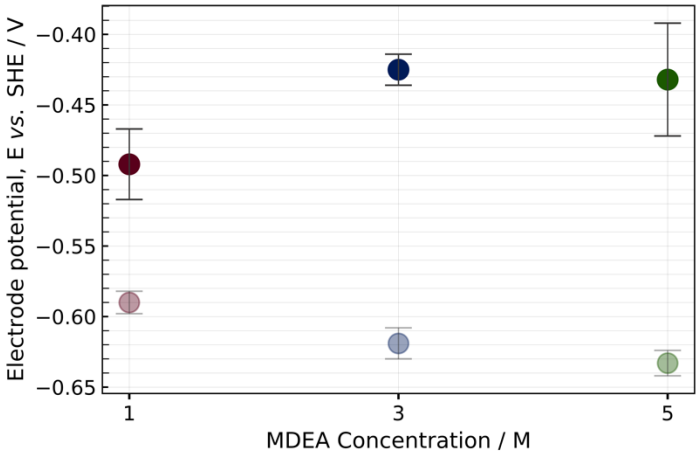



**Figure 7-10:** OCP of electrode at the beginning (light) and end (dark) of pre-treatment in aqueous solutions of varying MDEA concentration saturated with $CO_2$ at 80 °C.

**Figure 7-10** shows that the OCP was also correlated with MDEA concentration, as the OCP shifted to increasingly negative values as the MDEA concentration increased. Since pH increased with increased MDEA concentration, this decrease in OCP is expected (Equation **5-4**).

From Equations **7-5** - **7-6**, it can be concluded that at higher pHs, Fe dissolution will occur less readily.

$$Fe_{(s)} + 2H^{+}_{(aq)} \overset{K_{eq}}{\longleftrightarrow} Fe^{2+}_{(aq)} + H_{2(g)} \qquad \textbf{7-5}$$

$$[Fe^{2+}] = K_{eq}10^{-2pH} \qquad \textbf{7-6}$$

Since the dissolution of $Fe^{2+}$ ions from the CS electrode took progressively longer with increasing MDEA concentration, both the development of the porous cementite layer due to the preferential dissolution of ferrite, and the attainment of supersaturated conditions occurred at a slower rate with greater MDEA concentration. Therefore, it is reasonable that as MDEA concentration was increased, so too did film formation times, as shown in **Figure 7-11a**. The solution $Fe^{2+}$ concentration may be expected to be the lowest in the 5 M solution due to its pH, but **Figure 7-11a** shows that $Fe^{2+}$ concentration was greater in the 5 M solution than that detected in the 3 M solution and comparable to that present in the 1 M solution. This was reasonable since the electrode was immersed for the longest period of time in the 5 M solution, so there was more time for the bulk solution Fe concentration to increase. Although the electrode was immersed in the 1 M solution for the shortest period of time, the higher $H^{+}$ concentration in the 1 M solution would have driven the dissolution of Fe, and due to its

lower viscosity, the $Fe^{2+}$ ions would have diffused readily to the bulk solution, resulting in the dissolved Fe concentration being equivalent to that detected in the 5 M solution.

The EIS data of the electrodes after film formation are given in **Figure 7-9d** - **f**. As was discussed previously, it is difficult to determine the number of processes from the Nyquist and phase angle plots, but circuit fitting confirmed that all three sets of EIS data were best described by $EC_3$, indicating the presence of two time constants, due to the coating and charge transfer processes, and a diffusion element. From **Figure 7-9f**, it can be seen that the impedance moduli (corrected for ohmic resistance) of all three electrodes were similar at higher frequencies (between 200 Hz and 5000 Hz), with the modulus in the 3 M solution being the highest, and are likely representative of the coatings. The circuit fitting substantiated this, as the coating resistance in 3 M solution was slightly greater than those of the coatings in the 1 and 5 M solutions.

The impedance modulus of the electrode exposed to the 1 M was the greatest at all frequencies < $10^2$ Hz, at which contributions from both the charge transfer resistance and diffusion processes would be present. The sum of the coating and charge transfer resistances derived from circuit fitting was demonstrated to decrease with increasing MDEA concentration (**Figure 7-11b**). The charge transfer resistances were all at least one order of magnitude higher than that of the corresponding coating resistance. This indicates that the $FeCO_3$ film formed on all three electrodes exhibited the same physical protection mechanism of decreasing the electroactive surface area of the underlying substrate.

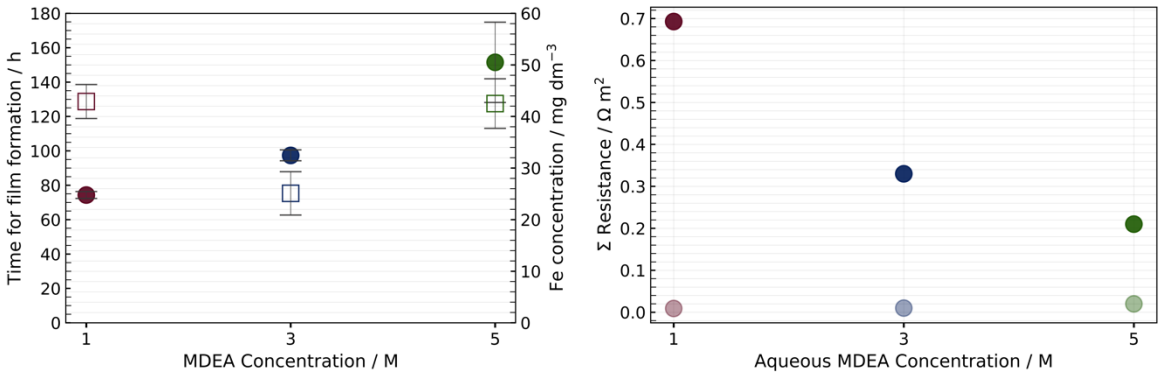



**Figure 7-11: (a)** Immersion time for $FeCO_3$ film formation (• left y-axis) and dissolved $Fe^{2+}$ concentration (□ right y-axis); and **(b)** sum of charge transfer and coating resistance of electrodes at the beginning (light) and end (dark) of pre-treatment in solutions of varying MDEA concentrations saturated with $CO_2$ at 80 °C.

The impedance data collected when a pristine CS electrode was immersed in 5 M $MEA_{(aq)}$ solution saturated with $CO_2$ at 80 °C for a one week period is shown in **Figure 7-12**. It should be stated that due to the time-scale of low frequency measurements, the adhesion of $CO_2$ bubbles on the electrode surface obscured the signal, resulting in erroneous data at frequencies < 0.08 Hz. Therefore, these data points were excluded from subsequent analysis and fittings.

When the CS electrode was immersed initially in the $MEA_{(aq)}$ solution, an OCP of -0.653 V was attained. The Nyquist representation of the impedance data (**Figure 7-12a**), obtained after initial immersion took the form of a single semicircle circle, indicating the presence of one interfacial process. The Bode representation of the phase angle also was that expected for a single process with a RC time constant at *ca*. $10^2$ Hz (**Figure 7-12b**). This was further confirmed by circuit fitting where $EC_1$ (**Figure 7-1**) fitted the impedance data well and was caused by Fe dissolution from the electrode surface. The overall resistance (*i.e*. at low frequencies) was of the order of $10^{-2}$ Ω $m^2$, as can be seen from the Bode representation of the impedance modulus (**Figure 7-12c**). After one day of immersion, the Nyquist plot showed a minimal increase in the diameter of the semicircle, corresponding to a small increase in the electrode resistance. The Bode representation of the phase angle showed a substantial shift in the time constant to a lower frequency of *ca*. 4 Hz. Circuit fitting with $EC_1$ confirmed a small increase in the electrode resistance to charge transfer but, more importantly, it showed a significant increase in the interfacial capacitance, suggesting an increase in the electroactive area.

Subsequently, the OCP shifted minimally, becoming increasingly negative at *ca*. -0.655 V after one day and -0.660 V after one week of immersion. The Nyquist plots also showed little change between one day and one week of immersion. A minimal shift in the charge transfer time constant to a lower frequency of *ca*. 1 Hz is observed in **Figure 7-12c**. The time constant for $EC_1$, which represents these EIS data, is given by the Equation **7-7**. A shift in the time constant to lower frequencies indicates that either the resistance or the effective double layer capacitance has increased. The charge transfer resistance could increase if corrosion products were to form on the electrode, which would limit contact between the electrode and the electrolyte. Since no corrosion product was detected by XRD (**Figure 7-13**), nor observed by surface imaging (**Figure 7-12d**), it can be assumed that this shift in time constant was due to an increase in the capacitance. This was confirmed by circuit fitting (**Table 7-4**).

$$\tau = \frac{1}{2\,\pi f} = R_1 C_{DL} \qquad \textbf{7-7}$$

Since capacitance is an indirect measure of electroactive area, an increase suggests non-uniform Fe dissolution, since it would increase the electrode surface area in contact with the electrolyte. This was supported by the SEM images showing the initially smooth electrode surface (Appendix, Section 12.5, **Figure 12-21**) became roughened, likely due to the preferential dissolution of the uppermost ferrite layer as evidenced by the exposed cementite (**Figure 7-12d**), thereby increasing sites for charge transfer. The solution Fe concentration increased by 61 mg $dm^{-3}$ after one week of electrode immersion. Hence, it can be concluded that when the CS electrode was exposed to 5 M $MEA_{(aq)}$ saturated with $CO_2$ at 80 °C, it began to dissolve and continued to do so with no apparent precipitation of $FeCO_3$ or oxide formation to provide any form of substantial or superficial protection. This is consistent with the results presented in Chapter 4 (Section 4.2.1), and also in Chapter 6 (Section 6.2.1), where no evidence was found for $FeCO_3$ precipitation on a CS coupon or an Fe electrode even when the potential was applied at which $FeCO_3$ formation was thought to have occurred.

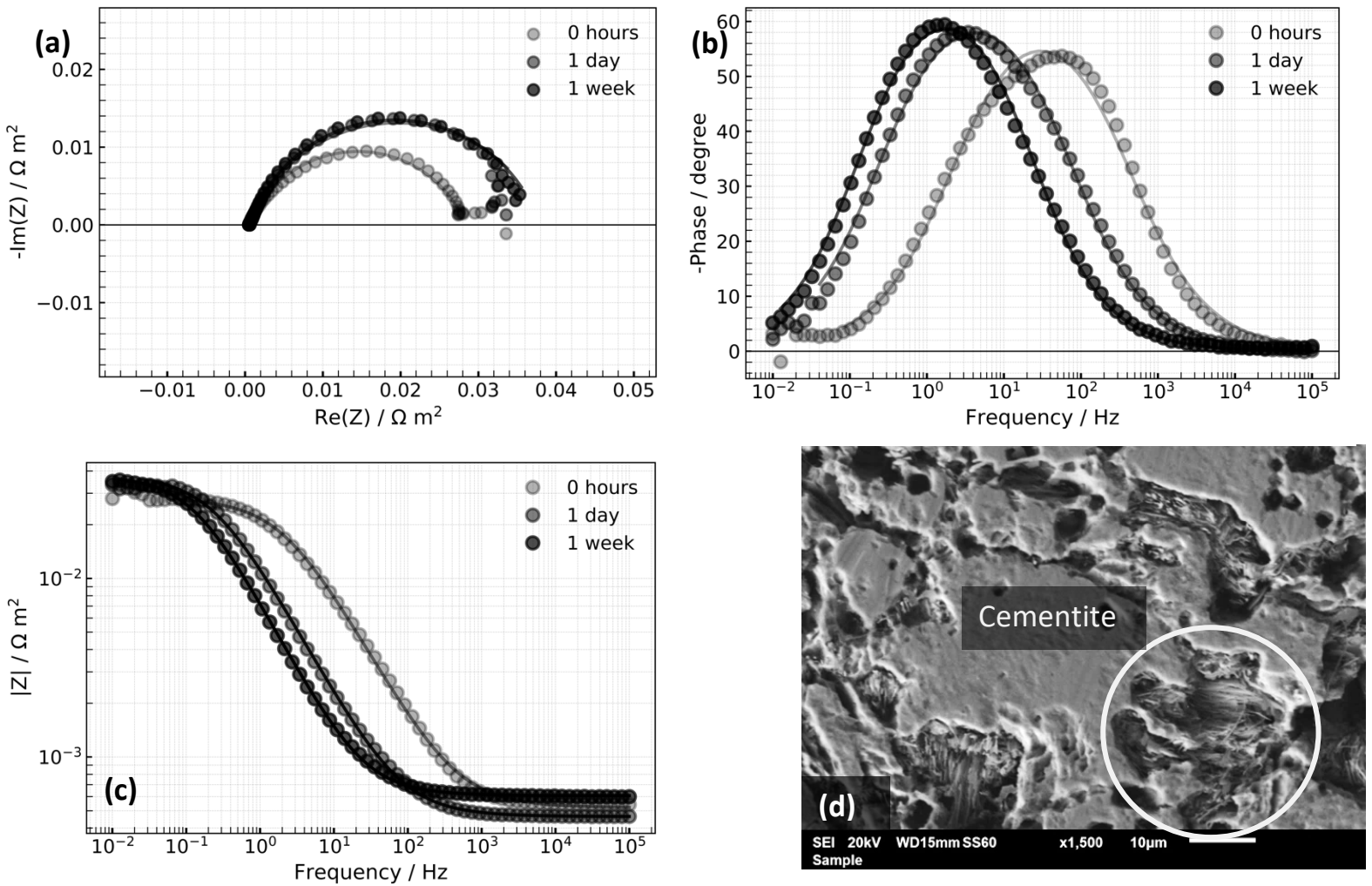



**Figure 7-12**: Experimental (o) and simulated (-) impedance data obtained at OCP with a CS electrode in 5 M $MEA_{(aq)}$, saturated with $CO_2$ (pH 7.9) at 80 °C. OCP at 0 h = -0.653 V, 24 h = -0.655 V and 168 h = -0.660 V): **(a)** Nyquist representation; and Bode representation of the **(b)** phase angle and **(c)** impedance magnitude. **(d)** *Ex-situ* SEM images of CS electrode after immersion in 5 M $MEA_{(aq)}$ saturated with $CO_2$ (pH 7.9) at 80 °C for one week.

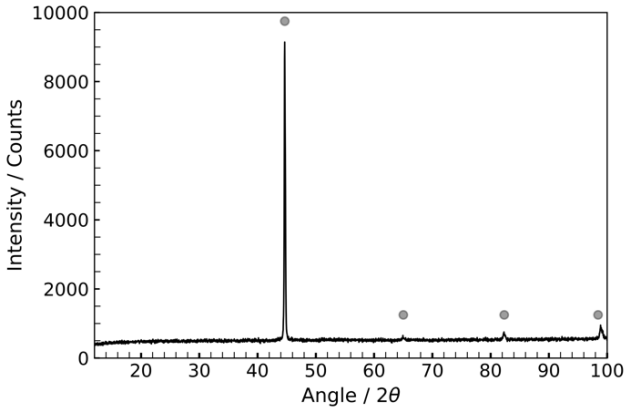



**Figure 7-13**: *Ex-situ* XRD surface characterisation of CS electrode after immersion in 5 M $MEA_{(aq)}$ saturated with $CO_2$ (pH 7.9) at 80 °C for one week (o: Ferrite peaks).

**Table 7-4**: Normalised $EC_1$ component values for impedance data obtained when a CS electrode was immersed in 5 M $MEA_{(aq)}$ saturated with $CO_2$ at 80 °C.

| Component | 0 hour | 1 day | 1 week |
|---|---|---|---|
| $R_{CT}$ / Ω m² | $3 \times 10^{-2}$ | $4 \times 10^{-2}$ | $4 \times 10^{-2}$ |
| $C_{DL}$ / F m$^{-2}$ | 2.7 | 17.5 | 32.2 |
| $\frac{\chi^2}{\lvert Z \rvert}$ | 0.10 | 0.05 | 0.03 |

## 7.2.2 Impedance spectroscopy of pre-treated carbon steel in aqueous MEA saturated with $CO_2$

Firstly, CS electrodes were pre-treated to form an electrically resistive $FeCO_3$ film in 1, 3 and 5 M $MDEA_{(aq)}$ solutions saturated with $CO_2$ at 80 °C and results were presented in Section 7.2.1. To test the stability and electrical resistivity of the $FeCO_3$ coating in 5 M $MEA_{(aq)}$, each pre-treated electrode was transferred directly from the pre-treatment solution to the 5 M $MEA_{(aq)}$ solution saturated with $CO_2$ at 80 °C. The OCP was then measured until it became steady ($\Delta E_{OCP}$ < 1 mV h$^{-1}$), when the EIS data was recorded. Impedance data were measured at the OCP after: 1) initial immersion, 2) *ca*. one day and 3) *ca*. one week for the electrodes pre-treated in the 1, 3 and 5 M $MDEA_{(aq)}$ solution saturated with $CO_2$; data are presented in **Figure 7-14**, **Figure 7-16** and **Figure 7-18**, respectively.

**Stability of the 1 M $MDEA_{(aq)}$-generated coating:** When the CS electrode was initially removed from the 1 M pre-treatment solution and immersed in 5 M $MEA_{(aq)}$ solution, the OCP decreased from -0.509 V (in the pre-treatment solution) to -0.596 V, though still more positive than an uncoated electrode (-0.653 V) in the $MEA_{(aq)}$ solution. The impedance data obtained after initial immersion was noisy, particularly for the high frequency points (> 39,287 Hz) and the low frequency points (< 0.05 Hz). The presence of noise was expected given the initially inhomogeneous aqueous environment, whereby residual MDEA would be diffusing away from the electrode and MEA diffusing into the pores of the film. Hence, data points were analysed and fitted only at frequencies > 0.05 Hz and < 39,287 Hz. From **Figure 7-14a** - **b**, it appeared that the electrode impedance decreased substantially upon immersion in the test solution. One or two convoluted semicircles were still apparent from the Nyquist plot, but there was no perceptible diffusion feature. The Bode representation of the impedance modulus confirmed that, when compared to the electrode before transfer from the pre-treatment solution, there was an order of magnitude decrease in electrode impedance at all frequencies (**Figure 7-14f**). The coating time constant was not clearly discernible from the phase angle plot (**Figure 7-14d** - **e**), but as was reported previously, the apparent lack of time constant does not indicate that a coating was not present, as the charge transfer and coating time constants may be similar and so are not differentiable from **Figure 7-14d** - **e.**

After *ca*. one day of immersion in 5 M $MEA_{(aq)}$, from the Nyquist plot, the electrode impedance appeared to have increased. This was confirmed by **Figure 7-14f** in which the overall electrode resistance (*i.e*. measured at 0.01 Hz) was *ca*. $4 \times 10^{-1}\ \Omega\ m^2$, slightly higher than that measured when the electrode was immersed initially (*ca*. $2 \times 10^{-1}\ \Omega\ m^2$). The Bode representation of the phase angle showed a small separation in the two time constants, with the charge transfer time constant corresponding to *ca*. $10^1$ Hz and the coating to *ca*. $10^{3.5}$ Hz. After one week, the Nyquist plot showed little change had occurred. The Bode representation of the phase angle again showed a further separation between the charge transfer process and the coating process.

Since it was unclear from the EIS data if the Nyquist plots consisted of two convoluted semicircles or one very depressed semicircle, it was first attempted to fit the data using $EC_1$ (**Figure 7-1**), but this did not yield an acceptable fit, so $EC_2$ and $EC_3$ were then attempted. $EC_2$ gave a good fit and was also used to model impedance data after one day and one week of electrode immersion and gave good fits as confirmed from the weighted $\chi^2$ values reported in **Table 7-5**. Therefore, this confirmed that two time constants were present in the EIS data

measured on all three days. From the fitting results (**Table 7-5**), it can be seen that upon initial immersion, the coating resistance decreased from $2 \times 10^{-2}\ \Omega\ m^2$ before immersion in 5 M $MEA_{(aq)}$ solution to $6 \times 10^{-3}\ \Omega\ m^2$, whilst the charge transfer resistance decreased minimally from $4 \times 10^{-2}\ \Omega\ m^2$ to $2 \times 10^{-2}\ \Omega\ m^2$.

The effective interfacial or double layer capacitance ($C_{eff}$) increased by almost two orders of magnitude, suggesting that there was an increase in the electroactive area. It is likely that upon immersion, there was initial dissolution of $FeCO_3$ from the outer layer of the coating, which possibly created pores, providing limited pathways between the electrolyte and electrode. The limited nature of these pathways was substantiated by the absence of a diffusion feature since the diffusion was too slow to be measured in the timescale of the experiment (*ca*. 0.28 h). Since the coating was so densely packed beneath areas of protruding crystals (**Figure 7-4**), the majority of the underlying substrate was protected. It is probable that within these limited pathways there was then re-precipitation of $FeCO_3$, as evidenced by the increase in the electrode resistance after one day of immersion to $4 \times 10^{-1}\ \Omega\ m^2$, and a 50 % decrease in effective interfacial capacitance ($C_{eff}$) (**Table 7-5**). The increase in coating capacitance from $6 \times 10^{-1}$ to $2 \times 10^{0}\ F\ s^{\alpha-1}\ m^{-2}$, as suggested by the constant phase element values ($Q_c$, **Table 7-5**), was likely due to the uptake of solution in the porous film. The capacitance is given by the Equation **7-8** (Orazem & Tribollet, 2008), where $\epsilon$[32] represents the permittivity of the coating, $\epsilon_o$ is the permittivity of vacuum and $\delta_f$ is the film thickness. When the electrode was immersed initially in the test solution, aqueous electrolyte would have diffused into the pores of the coating. Since the relative permittivity of water is *ca*. 61 at 80 °C (Malmberg & Maryott, 1956), solution present in the pores of the coating would have increased the coating permittivity, so increasing the coating capacitance.

$$C = \frac{\epsilon \epsilon_o}{\delta_f} \qquad \textbf{7-8}$$

The use of the change in the constant phase element values as indicative of the change in coating capacitance is not strictly accurate as the coating resistance and $\alpha$ parameters would affect the conversion. Since the coating resistances were similar on both days, and the $\alpha$ parameters were 0.84 and 0.74 (Appendix, Section 12.5, **Table 12-14**), and the change in constant phase element was much larger, it was thought that there was likely an increase in

[32] The permittivity of $FeCO_3$ is reported to between 3.8 and 6.78. (Liu *et al*., 2019; Rosenholtz & Smit, 1936).

coating capacitance between the two days, but not necessarily by the same amount as the increase in value of the constant phase element. The fitting values after one week of electrode immersion showed that coating and charge transfer resistances were equivalent to the values after one day of immersion. The effective interfacial capacitance increased slightly between the one day and one week of immersion, suggesting that there was an increase in electroactive area. This is consistent with the surface images presented in **Figure 7-15**, from which it is apparent that, although the $FeCO_3$ film was still present, some areas were covered incompletely by larger crystals where the electrolyte could have come into contact with the underlying CS electrode and facilitate its dissolution as $Fe^{2+}$ ions.

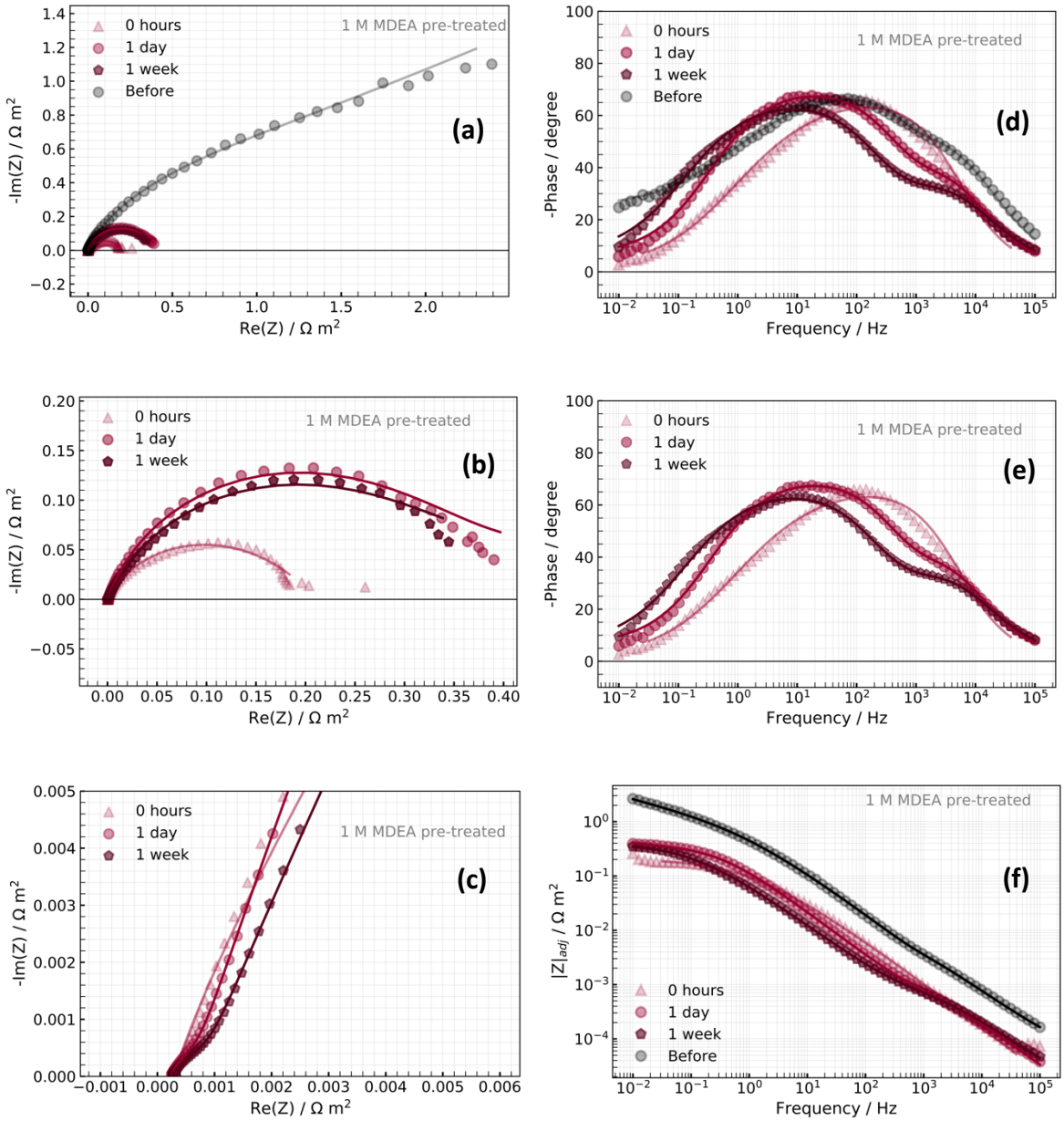



**Figure 7-14**: Experimental (o) and simulated (-) impedance data obtained at OCP with a pre-treated CS electrode in 5 M $MEA_{(aq)}$ solution saturated with $CO_2$ (pH 7.9) at 80 °C: **(a - c)** Nyquist representation and Bode representation of the **(d - e)** phase angle, and **(f)** the ohmic resistance corrected impedance magnitude. The impedance data of the CS electrode with the $FeCO_3$ film in the pre-treatment solution (1 M $MDEA_{(aq)}$ saturated with $CO_2$ at 80°C) is shown in grey.

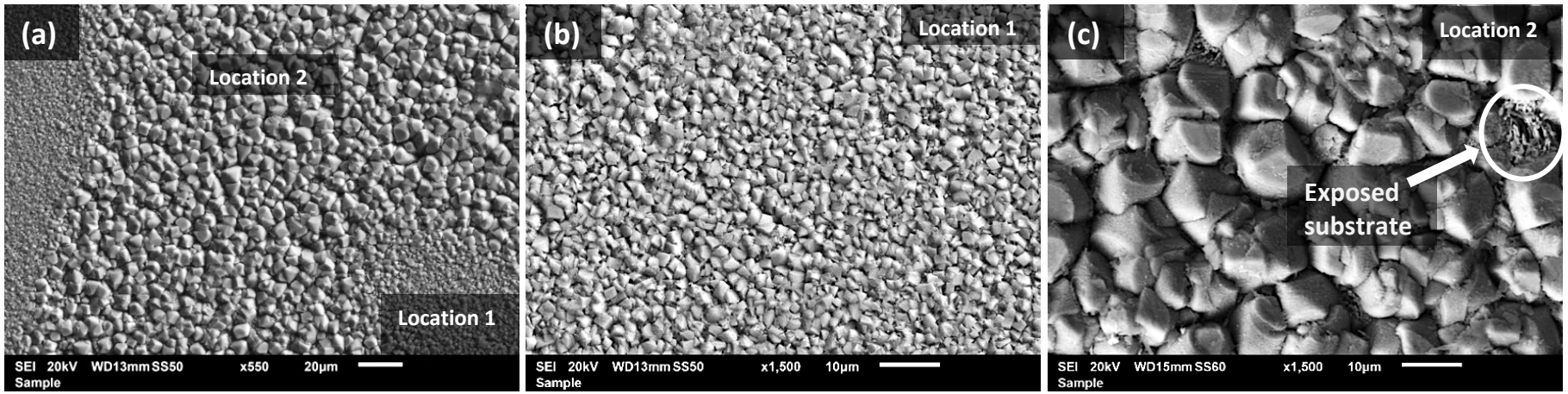



**Figure 7-15**: *Ex-situ* surface characterisation of pre-treated CS electrode (1 M $MDEA_{(aq)}$-$CO_2$ 80°C) after immersion in 5 M $MEA_{(aq)}$, saturated with $CO_2$ (pH 7.9) at 80 °C for one week using **(a - c)** SEM, images taken at 550x and 1500x magnifications (above), and **(d)** XRD (below, left).

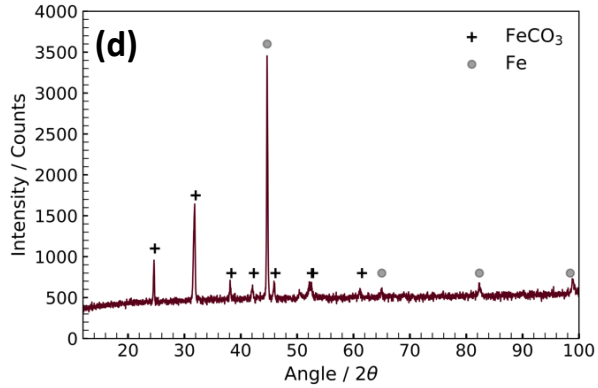



**Table 7-5**: Normalised $EC_2$ component values for impedance data obtained when a pre-treated CS electrode (1 M $MDEA_{(aq)}$-$CO_2$ 80°C) was immersed in 5 M $MEA_{(aq)}$ saturated with $CO_2$ (pH 7.9) at 80 °C.

| Time | $R_C$ / Ω m² | $Q_C$ / F $s^{\alpha-1}$ $m^{-2}$ | $R_{CT}$ / Ω m² | $C_{eff}$ / F $m^{-2}$ * | $\frac{\chi^2}{\lvert Z\rvert}$ |
|---|---|---|---|---|---|
| **Before** | $2 \times 10^{-2}$ | $4 \times 10^{-1}$ | $4 \times 10^{-1}$ | $1 \times 10^{-2}$ | 0.04 |
| **0 hours** | $4 \times 10^{-3}$ | $6 \times 10^{-1}$ | $2 \times 10^{-1}$ | $7 \times 10^{-1}$ | 0.18 |
| **1day** | $2 \times 10^{-3}$ | $2 \times 10^{0}$ | $4 \times 10^{-1}$ | $3 \times 10^{-1}$ | 0.01 |
| **1 week** | $2 \times 10^{-3}$ | $4 \times 10^{0}$ | $4 \times 10^{-1}$ | $6 \times 10^{-1}$ | 0.05 |

*Converted from constant phase element ($Q$) to effective charge transfer capacitance ($C_{eff}$) by assuming a normal distribution of time constants through a surface layer using Equation **7-3** (Hirschorn *et al*., 2010).

**Stability of the 3 M $MDEA_{(aq)}$-generated coating:** At the end of pre-treatment in the 3 M $MDEA_{(aq)}$ solution saturated with $CO_2$ solution at 80 °C, a protective $FeCO_3$ film formed and an analysis of the corresponding impedance data was given in Section 7.2.1. Upon immersion of the pre-treated electrode in 5 M $MEA_{(aq)}$ solution saturated with $CO_2$ 80 °C, the OCP decreased from -0.425 V (in the pre-treatment solution) to -0.570 V. As for the initial EIS data obtained with a 1 M $MDEA_{(aq)}$ pre-treated CS electrode in 5 M $MEA_{(aq)}$, the initial EIS data (**Figure 7-16**) obtained with the 3 M $MDEA_{(aq)}$ pre-treated electrode at low frequencies (< 0.05 Hz) was very noisy, likely due to the inhomogeneous aqueous environment, so these were not included in subsequent analysis or circuit fitting.

The Nyquist plot (**Figure 7-16a**) showed one or two convoluted semicircles, though apparently smaller than the one(s) observed for the pre-treated electrode before transferring to 5 M $MEA_{(aq)}$, and possibly exhibiting a diffusion feature. The Bode phase angle plot (**Figure 7-16e**) appeared to include two time constants, at *ca*. $10^{3.5}$ - $10^5$ Hz (coating) and another at *ca*. $10^2$ Hz (charge transfer), thus confirming the presence of two convoluted semicircles in **Figure 7-16a**. The decrease in magnitude of the semicircles was likely due to decreased protection provided by the coating. This was corroborated by the results in **Figure 7-16f**, which showed that the impedance modulus was smaller at all measured frequencies than that obtained on the pre-treated electrode before being transferred to the test solution. It was not obvious if the diffusion through the film was captured sufficiently in the initial EIS data. Therefore, both $EC_2$ and $EC_3$ were used to fit the data. After iterative fitting, only $EC_3$ gave an acceptable fit (**Table 7-6**), which included coating, charge transfer and diffusion processes. The fitting results indicated that the coating resistance decreased by an order of magnitude to $5 \times 10^{-3}$ Ω $m^2$ after initial immersion and so too did the charge transfer resistance to $2 \times 10^{-1}$ Ω $m^2$ (**Table 7-6**).

After *ca*. one day of immersion in 5 M $MEA_{(aq)}$ solution, it was difficult to determine from the Nyquist plot if there was an increase in electrode resistance or if the diffusion rate through the coating was faster and so measured at higher frequencies. **Figure 7-16d** - **e** show that the time constant related to charge transfer had also shifted to a lower frequency, indicating that either the interfacial capacitance or charge transfer resistance increased. **Figure 7-16f** confirmed that the impedance modulus for 0.2 Hz < $f$ < 2 kHz was less than or equal to that measured when that electrode was immersed initially. Small decreases in charge transfer and coating resistances were derived from circuit fitting. As represented by the constant phase element, the coating capacitance increased, probably due to aqueous solution

uptake in the film, and the interfacial capacitance also increased suggesting an increase in the electroactive area.

The Nyquist representation of the EIS data measured at one week of immersion showed a very small semicircle recorded at high frequencies (**Figure 7-16c**) and was thought to be due to the coating. However, the coating time constant was not discernible from **Figure 7-16e**. Although there was no apparent coating time constant, $EC_3$, which includes two time constant processes, gave the best fitting of the EIS data. XRD confirmed that $FeCO_3$ was indeed present, but from the surface images (**Figure 7-17**) it can be seen that large regions (>10 μ m) were left completely uncoated, thereby rendering the film ineffective. The lack of protection provided by the film was verified by the impedance modulus (**Figure 7-16f**). The circuit fitting showed that the coating resistance decreased to $7 \times 10^{-4}$ Ω $m^2$ and so too did the charge transfer resistance to $4 \times 10^{-2}$ Ω $m^2$ (**Table 7-6**). The constant phase element representing the interfacial capacitance also tripled, for which the surface images provided supporting evidence.

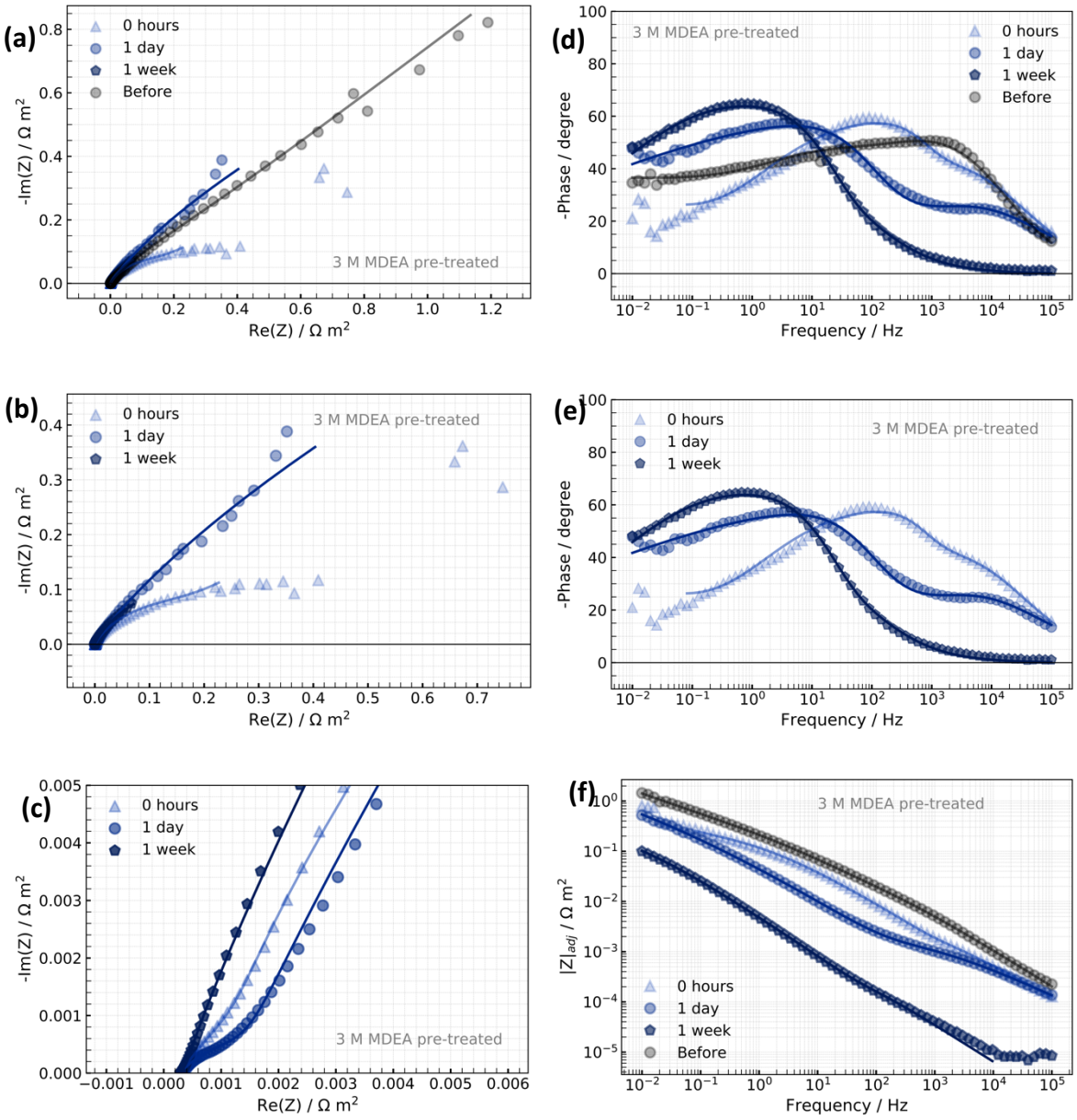



**Figure 7-16**: Experimental (o) and simulated (-) impedance data obtained at OCP with a pre-treated CS electrode in 5 M $MEA_{(aq)}$, saturated with $CO_2$ (pH 7.9) at 80 °C **(a - c)**: Nyquist representation; and Bode representation of the **(d - e)** phase angle, and **(f)** the ohmic resistance corrected magnitude of the impedance. The impedance data of the CS electrode with the $FeCO_3$ film in the pre-treatment solution (3 M $MDEA_{(aq)}$ solution saturated with $CO_2$ 80°C) is shown in grey.

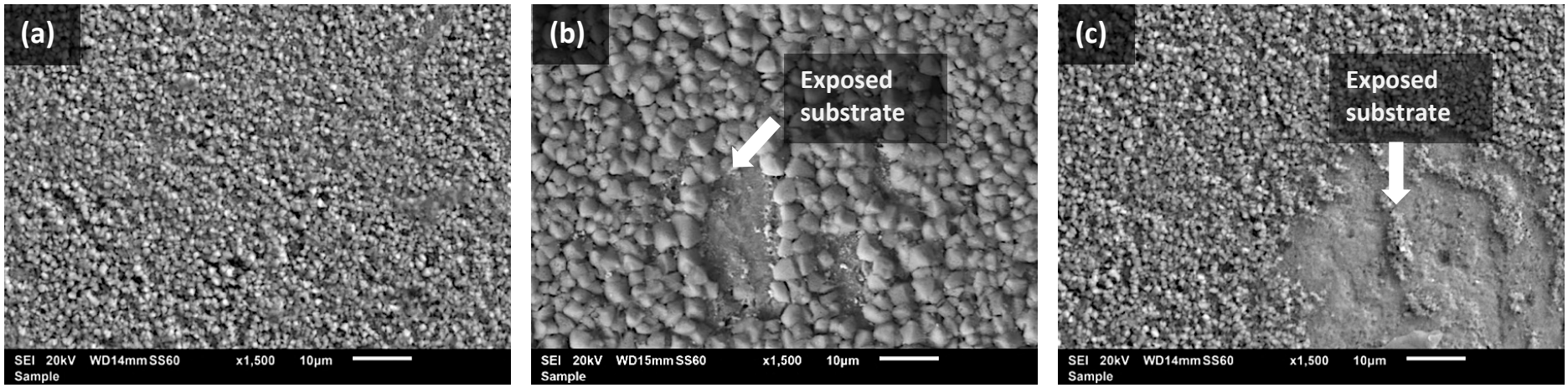



**Figure 7-17**: *Ex-situ* surface characterisation of pre-treated CS electrode (3 M $MDEA_{(aq)}$-$CO_2$ 80°C) after immersion in 5 M $MEA_{(aq)}$ saturated with $CO_2$ (pH 7.9) at 80 °C for one week using **(a - c)** SEM, images taken at 550x and 1500x magnifications (above), and **(d)** XRD (below, left).

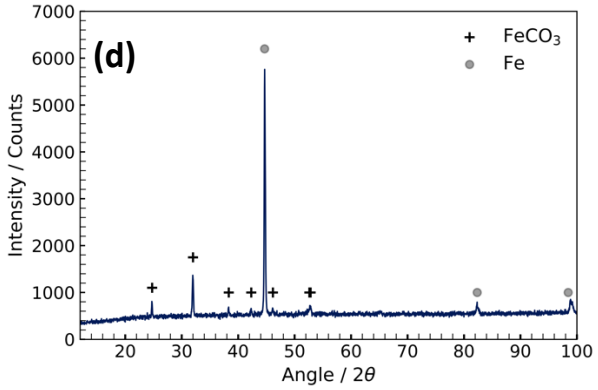



**Table 7-6**: Normalised $EC_3$ component values for impedance data obtained when a pre-treated CS electrode (3 M $MDEA_{(aq)}$-$CO_2$ 80°C) was immersed in 5 M $MEA_{(aq)}$ saturated with $CO_2$ (pH 7.9) at 80 °C.

| Time | $R_C$ / Ω m² | $Q_C$ / F $s^{\alpha-1}$ $m^{-2}$ | $R_{CT}$ / Ω m² | $Q_{DL}$ / F $s^{\alpha-1}$ $m^{-2}$ | $\frac{\chi^2}{\lvert Z \rvert}$ |
|---|---|---|---|---|---|
| **Before** | $3 \times 10^{-2}$ | $4 \times 10^{-1}$ | $3 \times 10^{-1}$ | $8 \times 10^{-1}$ | 0.04 |
| **0 hours** | $5 \times 10^{-3}$ | $1 \times 10^{0}$ | $2 \times 10^{-1}$ | $5 \times 10^{-2}$ | 0.07 |
| **1day** | $2 \times 10^{-3}$ | $5 \times 10^{0}$ | $1 \times 10^{-1}$ | $2 \times 10^{0}$ | 0.08 |
| **1 week** | $7 \times 10^{-4}$ | $5 \times 10^{1}$ | $4 \times 10^{-2}$ | $6 \times 10^{0}$ | 0.03 |

**Stability of the 5 M $MDEA_{(aq)}$-generated coating:** After pre-treatment in 5 M $MDEA_{(aq)}$ solution saturated with $CO_2$ at 80 °C, the CS electrode was transferred to 5 M $MEA_{(aq)}$ solution saturated with $CO_2$ at 80 °C; the OCP decreased from -0.432 V (in the pre-treatment solution) to -0.572 V. The impedance data obtained after immersion is shown in **Figure 7-18**. From the Nyquist plot (**Figure 7-18a** - **c**), it appears that there were two convoluted semicircles with a diffusion feature. The Bode representation of the phase angle (**Figure 7-18d** - **e**) substantiated this, where the coating time constant appears to be present at *ca*. $10^4$ Hz and the charge transfer time constant at *ca*. $10^0$ Hz, which at lower frequencies is followed by a plateau, assumed to be indicative of a diffusion process. Iterative circuit fitting indicated that $EC_3$ gave the best fit, thereby confirming the existence of the three aforementioned processes. **Figure 7-18f** shows that the impedance modulus was lower for all frequencies after transferring the pre-treated electrode indicating that the film was less protective. This was confirmed by the circuit fitting values, as both the coating and charge transfer resistance values decreased by an order of magnitude (**Table 7-7**). After one day of immersion of the pre-treated CS electrode, the Nyquist plot suggested that the impedance increased, though minimal change was apparent from the Bode representation of the impedance modulus and phase angle. Circuit fitting confirmed the observations made from the Nyquist plot, where the charge transfer and coating resistances increased slightly. After one week, the Nyquist plot showed that the high frequency semicircle, thought to be associated with the coating, no longer overlapped with the charge transfer process (**Figure 7-18c**). This was also evident in **Figure 7-18d** - **e**, in which the coating time constant appeared to correspond to a higher frequency (*ca*. $2 \times 10^4$ Hz). Although $FeCO_3$ was still present after the one week period, as confirmed by XRD (**Figure 7-19a**), the surface images showed areas of bare substrate (**Figure 7-19b**), and what appeared to be partially dissolved crystals (**Figure 7-19c** - **d**). Further, the circuit fitting values confirmed a decrease in coating and charge transfer resistances (**Table 7-7**).

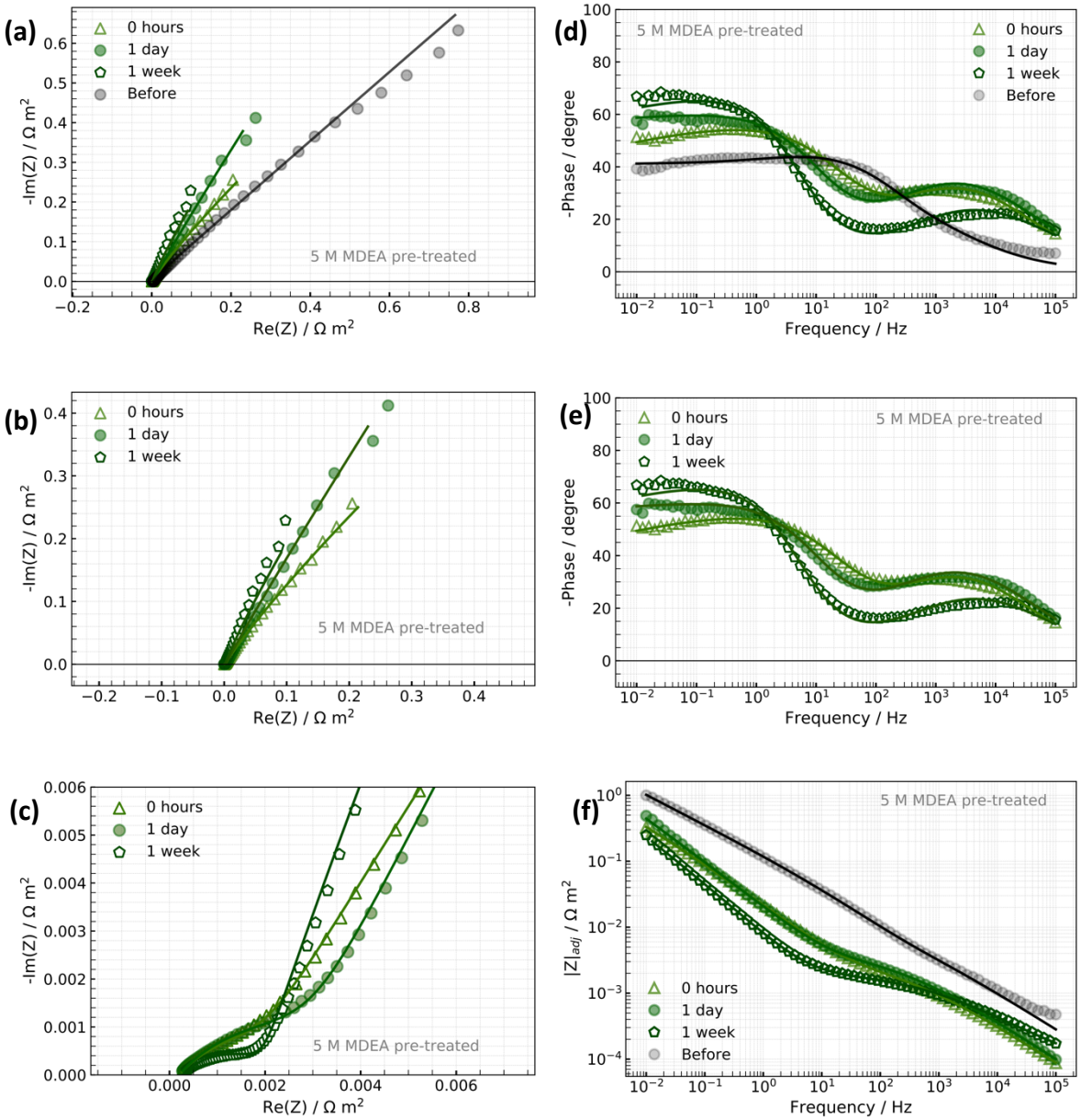



**Figure 7-18**: Experimental (o) and simulated (-) impedance data obtained at OCP with a pre-treated CS electrode in 5 M $MEA_{(aq)}$ saturated with $CO_2$ (pH 7.9) at 80 °C: **(a - c)** Nyquist representation; and Bode representation of the **(d - e)** phase angle, and **(f)** the ohmic resistance corrected magnitude of the impedance. The impedance data of the CS electrode with the $FeCO_3$ film in the pre-treatment solution (5 M $MDEA_{(aq)}$ solution saturated with $CO_2$ 80°C) is shown in grey.

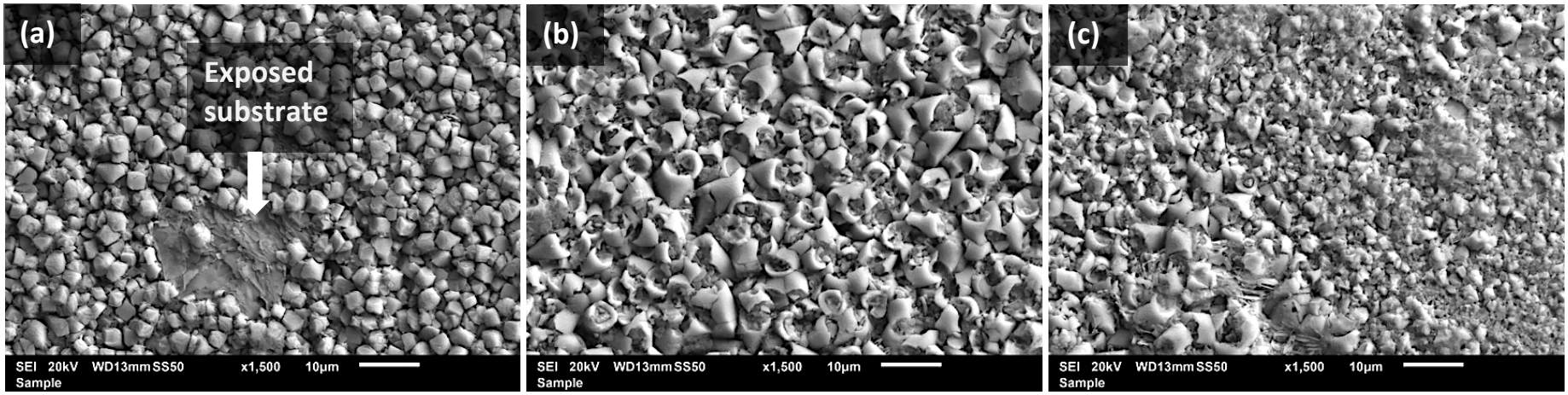



**Figure 7-19**: *Ex-situ* surface characterisation of pre-treated CS electrode (3 M $MDEA_{(aq)}$-$CO_2$ 80°C) after immersion in 5 M $MEA_{(aq)}$ saturated with $CO_2$ (pH 7.9) at 80 °C for one week using **(a - c)** SEM, images taken at 1500x magnification (above), and **(d)** XRD (below, left).

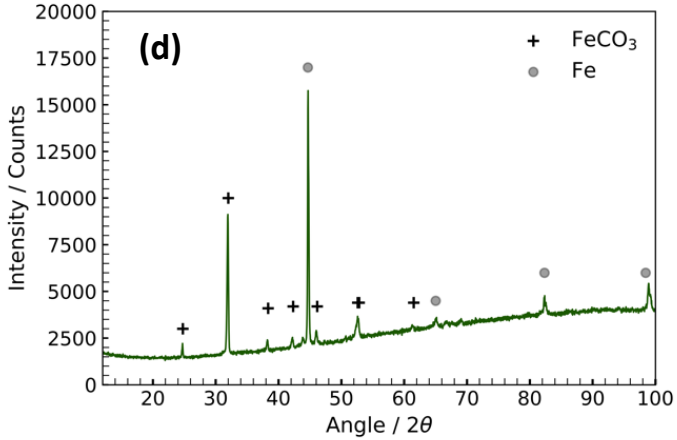



**Table 7-7:** Normalised $EC_3$ component values for impedance data obtained when a pre-treated CS electrode (5 M $MDEA_{(aq)}$-$CO_2$ 80°C) was immersed in 5 M $MEA_{(aq)}$ saturated with $CO_2$ (pH 7.9) at 80 °C.

| Time | $R_C$ / Ω m² | $Q_C$ / F $s^{\alpha-1}$ $m^{-2}$ | $R_{CT}$ / Ω m² | $Q_{DL}$ / F $s^{\alpha-1}$ $m^{-2}$ | $\frac{\chi^2}{\lvert Z\rvert}$ |
|---|---|---|---|---|---|
| **Before** | $2 \times 10^{-2}$ | $2 \times 10^{0}$ | $4 \times 10^{-1}$ | $3 \times 10^{-1}$ | 0.04 |
| **0 hours** | $3 \times 10^{-3}$ | $6 \times 10^{0}$ | $8 \times 10^{-2}$ | $8 \times 10^{0}$ | 0.03 |
| **1day** | $4 \times 10^{-3}$ | $6 \times 10^{0}$ | $1 \times 10^{-1}$ | $9 \times 10^{0}$ | 0.09 |
| **1 week** | $2 \times 10^{-3}$ | $7 \times 10^{0}$ | $6 \times 10^{-2}$ | $3 \times 10^{1}$ | 0.09 |

### 7.2.3 Comparison of the performance of pre-treated electrodes

To enable easy comparison between data collected in different pre-treatment solutions, as well as on a pristine electrode, the impedance data obtained after initial, one day and one week immersion of the three pre-treated and untreated electrodes in 5 M $MEA_{(aq)}$ solution saturated with $CO_2$ at 80 °C are presented in **Figure 7-20**, **Figure 7-21** and **Figure 7-22** respectively. A plot of the sum of the coating and charge transfer resistances obtained from circuit fittings is given in **Figure 7-23**.

From the comparative Nyquist plot (**Figure 7-20d**), it appears that the resistance of the uncoated electrode was smaller than each of the coated electrodes. **Figure 7-20d** confirms this for the 1 and 3 M coatings, for which the impedance modulus was greater than that of the uncoated electrode for all frequencies < $10^{3.5}$ Hz. It is difficult to deduce from **Figure 7-20d** if the electrode pre-treated in the 5 M solution was more resistive than the untreated steel. However, **Figure 7-23** confirms that the total resistance of the 5 M pre-treated electrode was $9 \times 10^{-2}$ Ω $m^2$, which is higher than the untreated electrode with a resistance of $2.7 \times 10^{-2}$ Ω $m^2$.

Another important observation from **Figure 7-20a** is the apparent varying surface processes exhibited by the four electrodes. The impedance behaviour of the uncoated electrode was shown previously (Section 7.2.2) to be best described by $EC_1$ (**Figure 7-1**), which models a single time constant process. The electrode pre-treated in the 1 M solution was demonstrated in Section 7.2.2 to be characterised by a two time constant process, with no diffusion feature, whilst the Nyquist plots for the electrodes pe-treated in the 3 and 5 M solutions included two convoluted semicircles and a diffusion tail. Therefore, this indicates that the diffusion of the solute species to and from the substrate was severely limited by the 1 M generated coating. By contrast, the diffusion through the 3 and 5 M generated coatings was sufficiently fast to be captured in the timescale of the EIS measurement, indicating that they were likely less protective.

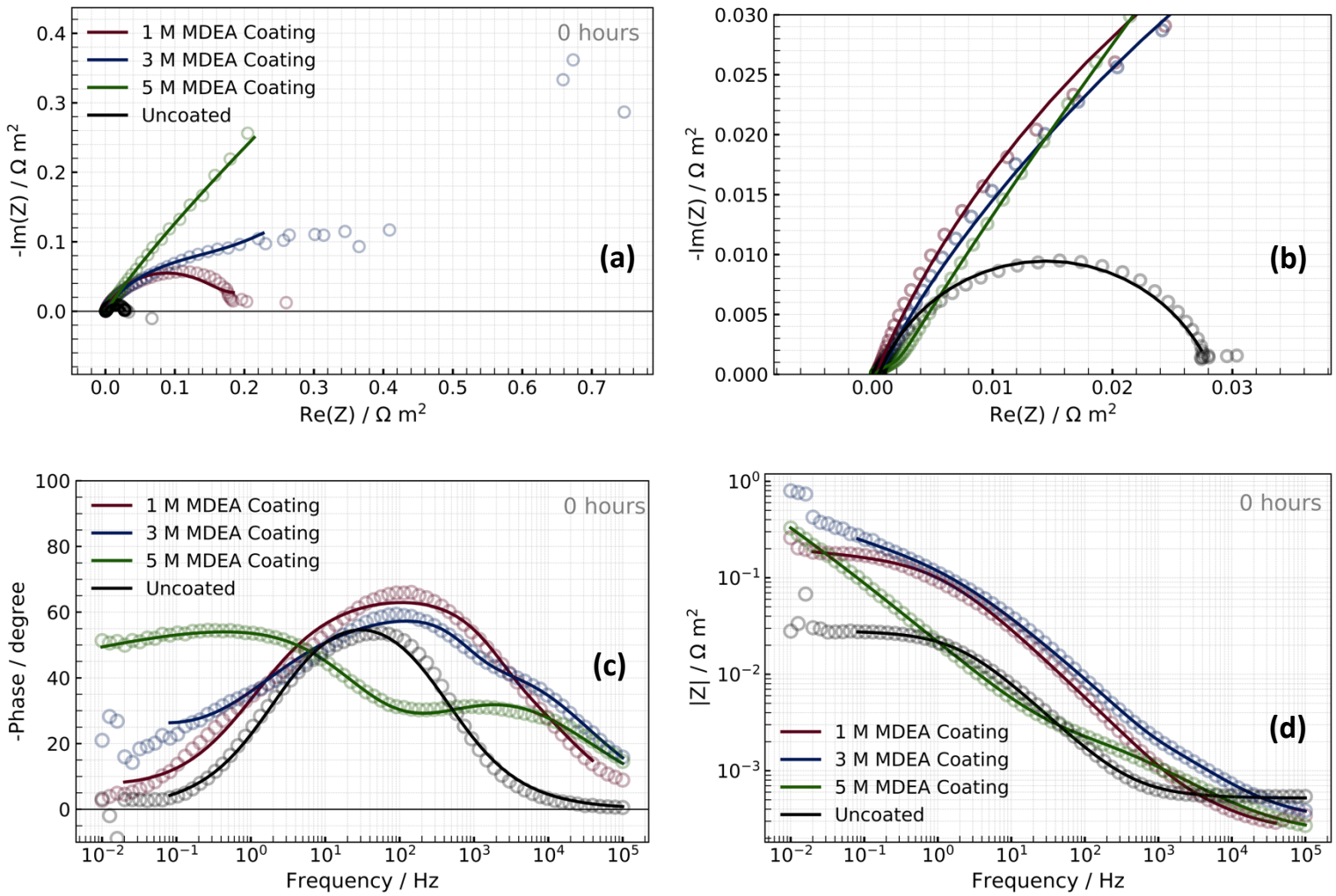



**Figure 7-20**: Experimental (o) and simulated (-) impedance data obtained when three pre-treated CS electrodes and one untreated electrode were immersed in 5 M $MEA_{(aq)}$, saturated with $CO_2$ (pH 7.9) at 80 °C: **(a - b)** Nyquist representation and Bode representation of the **(c)** phase angle and **(d)** the magnitude of the impedance.

The Nyquist plot of the EIS data (**Figure 7-21a**) of the four electrodes after one day of immersion suggested that the same mechanisms persisted for all four electrodes, as was confirmed by circuit fitting (Section 7.2.2). Unlike the impedance modulus data recorded after initial immersion, the impedance modulus (**Figure 7-21d**) for all coated electrodes were undoubtedly greater than that of the uncoated electrode for frequencies < 60 kHz, and the 1 M coated electrode gave the largest impedance modulus for frequencies < 150 Hz, followed by the electrodes coated in the 3 M and then the 5 M solutions. It should be stated here that since the diffusion rates through the 3 and 5 M coatings were not the same, it was difficult to visually determine from **Figure 7-21d**, which electrode resistance was higher. The sum of the coating and charge transfer resistances (**Figure 7-23**) demonstrated that all three coated electrodes were more resistive than the uncoated electrode and that samples coated in the 3 and 5 M solutions were equally resistive. **Figure 7-23** also shows that the electrode resistance of the CS pre-treated in the 1 M solution increased substantially after one day of immersion, the untreated and 5 M pre-treated electrode resistances increased minimally and the 3 M decreased by almost 50 %.

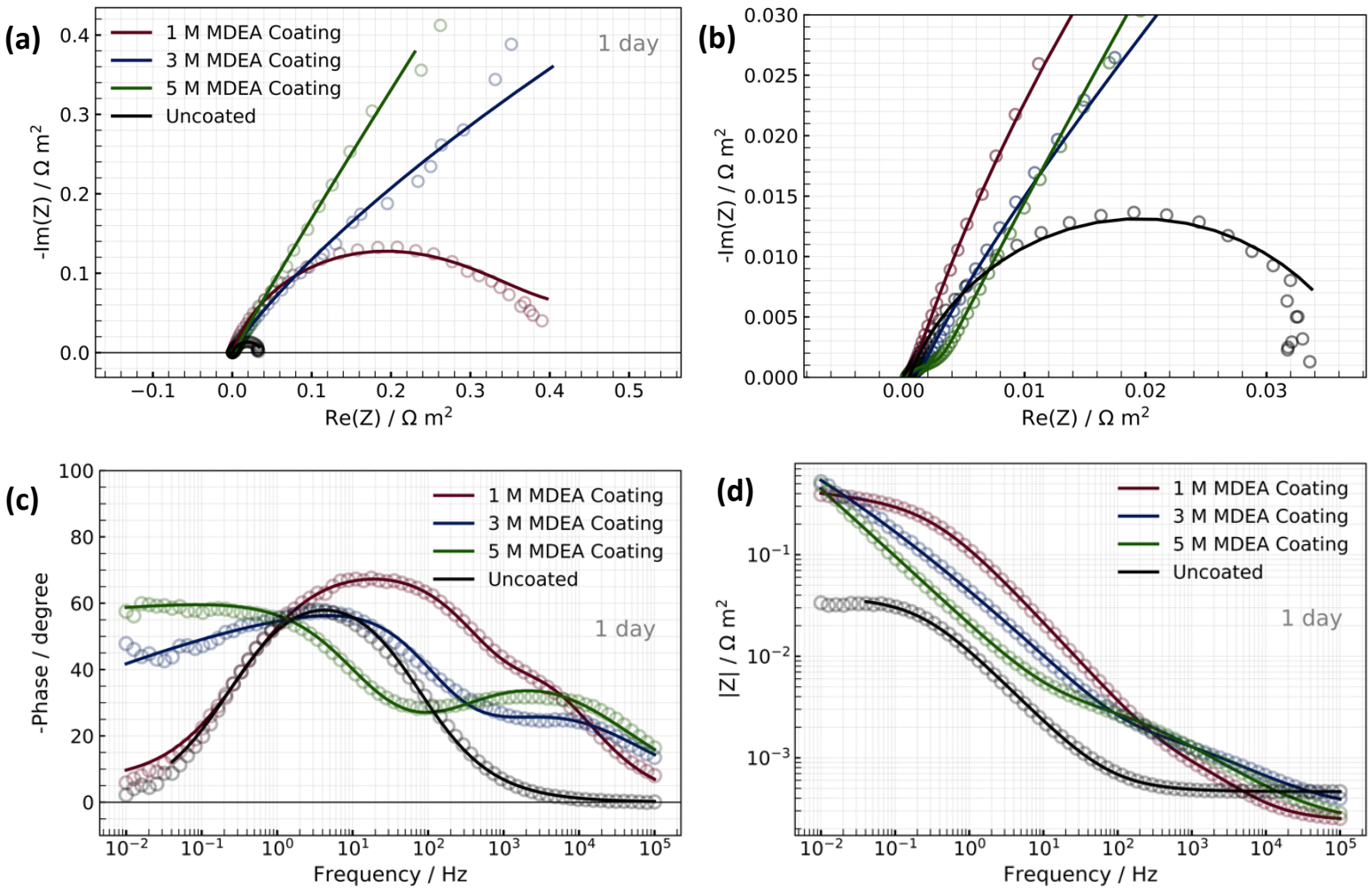



**Figure 7-21**: Experimental (o) and simulated (-) impedance data obtained when three pre-treated CS electrodes and one untreated electrode were immersed in 5 M $MEA_{(aq)}$, saturated with $CO_2$ (pH 7.9) at 80 °C for one day: **(a** - **b)** Nyquist representation and Bode representation of the **(c)** phase angle and **(d)** the magnitude of the impedance.

From the Nyquist plot (**Figure 7-22a** - **b**) of the EIS data collected at *ca*. one week of immersion in 5 M $MEA_{(aq)}$ solutions, it appeared that the three pre-treated electrodes were still more resistive than the untreated electrode. However from visual inspection of **Figure 7-22d**, it seemed probable that the resistance of the 3 and 5 M pre-treated and the untreated electrodes may have been equal. It was confirmed, from the sum of charge transfer and coating resistances, that the electrode pre-treated in the 1 M solution was the most resistive and was equal to that reported for one day of immersion (**Figure 7-23**). The electrode pre-treated in the 5 M solution was the second most resistive, but its resistance was noticeably smaller than that obtained after one day of immersion. Interestingly, from post processing of the XRD data, the $FeCO_3$ : Fe ratio of the 1 M treated electrode was smaller than that of the 5 M pre-treated sample (**Table 7-8**). It is possible that the $FeCO_3$ film left on the 5 M pre-treated sample was thicker, though less dense, than the film on the 1 M pre-treated electrode. This is substantiated by the fact that the underlying substrate, *i.e*. below the film, was also detected by XRD. Although the $FeCO_3$ may have been thicker, presumably due to crystal size (*ca*. 3 μm, **Figure 7-19b**), it was not densely packed and was shown to offer incomplete surface coverage (**Figure 7-19b**). Therefore, it can be deduced that $FeCO_3$ film resistance was not necessarily correlated with film thickness. By contrast with the 1 and 5 M pre-treated electrodes, the 3 M coating, which was still present, as apparent from **Figure 7-17a** with an $FeCO_3$ : Fe ratio of 0.24 (**Table 7-8**), no longer provided enhanced protection, as the electrode resistance was shown to be equivalent to that of the uncoated sample (**Figure 7-23**). This is an extremely important finding since the passivation afforded by surface films (*e.g*. $Al_2O_3$) are often positively correlated with film thickness. However, with $FeCO_3$ films in $amine_{(aq)}$ solutions, film density appears to be the more crucial factor. It is possible that film formation *via* a dissolution-precipitation mechanism will produce less dense films as compared to those formed by surface transformation. Furthermore, these high density films are likely to be thinner since they are composed of smaller crystals that can pack more closely together, and in so doing, provide enhanced protection. (Burkle *et al*., 2017) has also shown this for $FeCO_3$ films in $NaCl_{(aq)} – CO_2$ solutions, though at lower solution pHs (6.8).

The $Fe^{II}$ concentration of the 5 M $MEA_{(aq)}$ solutions used to test the performance of the pre-treated and uncoated electrodes at the end of the one week test period are given in **Table 7-8**. The solution in which the uncoated electrode was immersed had by far the greatest Fe concentration, up to 80 % greater than that detected in the solutions used to test the pre-treated electrodes. The solution used to test the 1 M coating had the second highest detected

dissolved Fe concentration. This is in agreement with the EIS data, since the 1 M pre-treated electrode showed the largest initial decrease in electrode resistance, which indicated that upon immersion there was partial dissolution of the $FeCO_3$ film, and hence an increase in dissolved Fe concentration. The Fe concentration in the solutions used to evaluate the efficacy of the 3 and 5 M pre-treatment were almost equal, with the 3 M being slightly lower.

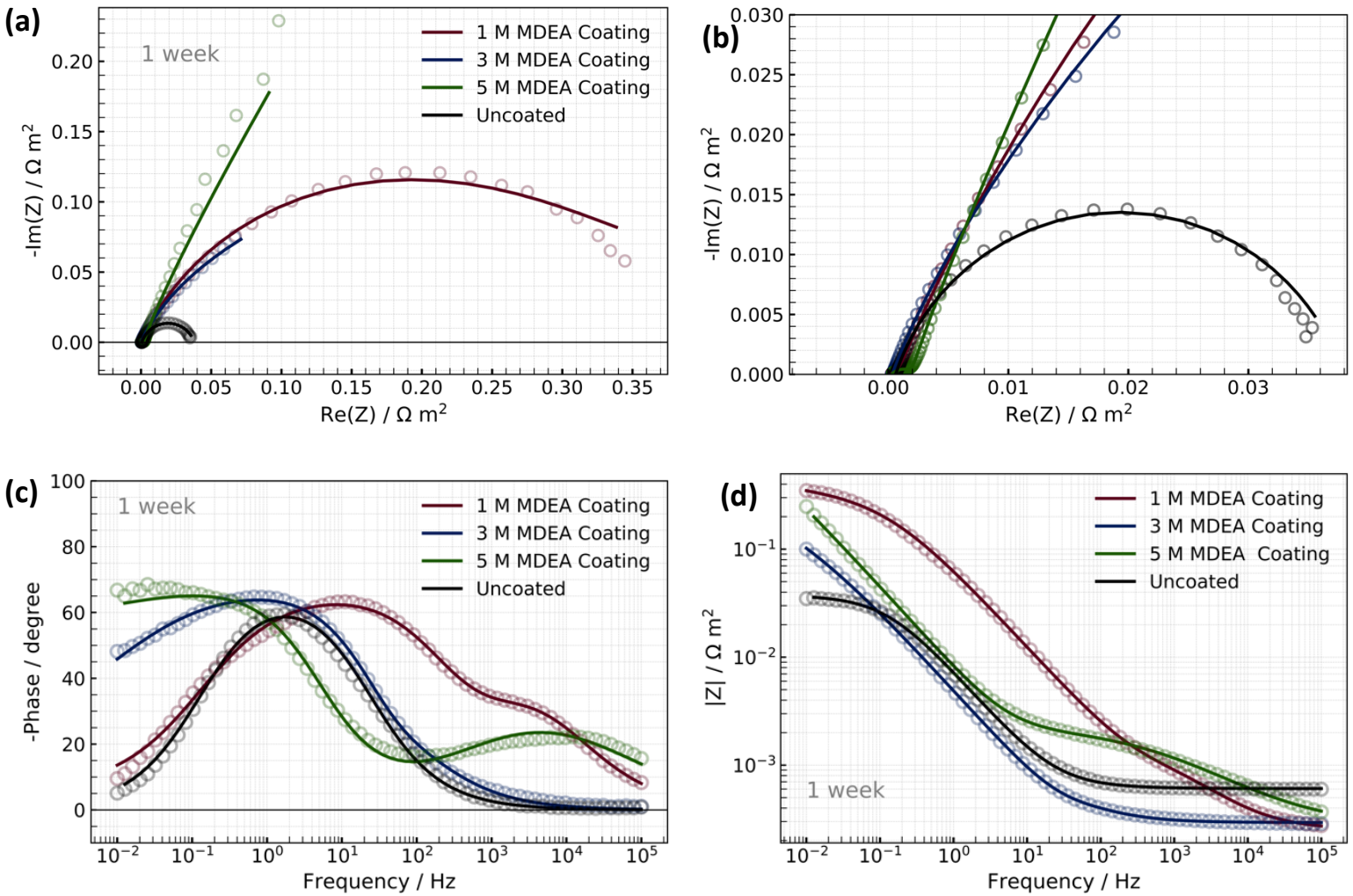



**Figure 7-22**: Experimental (o) and simulated (-) impedance data obtained at OCP when three pre-treated CS electrodes and one untreated electrode were immersed in 5 M $MEA_{(aq)}$, saturated with $CO_2$ (pH 7.9) at 80 °C for one week: **(a** - **b)** Nyquist representation and Bode representation of the **(c)** phase angle and **(d)** the magnitude of the impedance.

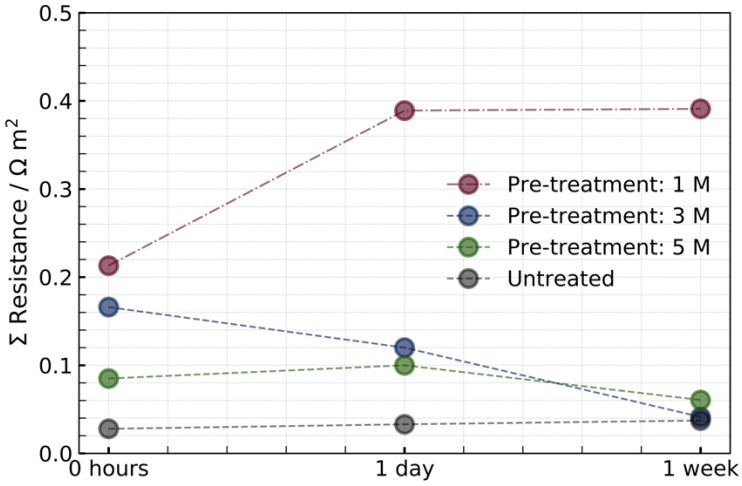



**Figure 7-23**: Sum of charge transfer and coating resistances of 1, 3 and 5 M pre-treated and untreated CS electrodes in 5 M $MEA_{(aq)}$, saturated with $CO_2$ at 80 °C.

**Table 7-8**: Comparison of ICP detected solution Fe concentration and XRD detected $FeCO_3$ : Fe predominant peak ratio on 1, 3, 5 M pre-treated electrodes and uncoated electrode, all after one week of immersion in 5 M $MEA_{(aq)}$, saturated with $CO_2$ at 80 °C.

| **Pre-treatment** | **Fe concentration / mol dm$^{-3}$** | **$FeCO_3$ : Fe*** |
|---|---|---|
| 1 M $MDEA_{(aq)}$ | 33.5 ± 1.3 | 0.48 |
| 3 M $MDEA_{(aq)}$ | 26.9 ± 1.1 | 0.24 |
| 5 M $MDEA_{(aq)}$ | 28.3 ± 1.1 | 0.56 |
| Untreated | 60.6 ± 1.2 | 0 |

* To enable comparison of the relative abundance of $FeCO_3$ and Fe on the surface of the electrodes, the ratio of the intensities corresponding to the highest intensity 2θ for $FeCO_3$ (2θ =31.937 °) and Fe (2θ = 44.674 °) was calculated. If the background response was uneven (*e.g* **Figure 7-19**), it was subtracted using X'Pert HighScore before retrieving the intensities.

### 7.2.4 Effect of adventitious dissolved $O_2$

As explained in Section 7.1.1, in the initial experiments, EIS measurements were taken daily to track the development of the $FeCO_3$ coating. This inadvertently allowed $O_2$ ingress into the electrolyte, which was shown to affect the electrode surfaces to varying degrees in different amine concentrations. **Figure 7-25a** - **c** shows a comparison of the EIS data of a CS electrode after being immersed in 1 M $MDEA_{(aq)}$ saturated with $CO_2$ at 80 °C for *ca*. 72 h (three days). The CS electrode in the cell, which was opened for daily measurements, attained an OCP of *ca*. + 0.01 V within one day of immersion. At a solution pH of 7.9, this OCP is indicative of the presence of iron oxide phases such as $Fe_3O_4$ or $Fe_2O_3$ at the electrode surface (**Figure 2-12**), although only $FeCO_3$ was detected with XRD (**Figure 7-24**). It is likely that when the cell was opened, aerial $O_2$ dissolved into the solution, diffused through the porous $FeCO_3$ film (if any) to the electrode surface and resulted in the formation of iron oxide on the electrode. Unlike $FeCO_3$, $Fe_3O_4$ is not electrically insulating (Mercier-Bion *et al*., 2018; Vella & Emerson, 2012), so iron oxide films containing $Fe_3O_4$ provide only superficial protection to the underlying substrate. The Nyquist plot (**Figure 7-25a**) and the Bode representation of the impedance modulus (**Figure 7-25c**), confirm that the electrode with the pure $FeCO_3$ film (*i.e*. OCP: -0.509 V) was more resistive than the film grown in the presence of adventitious dissolved $O_2$, causing increased electrode potential and (hydr-) oxide formation.

The protection provided and the stability of the mixed oxide-carbonate and $FeCO_3$ films were investigated in 5 M $MEA_{(aq)}$ saturated with $CO_2$ at 80 °C. Upon immersion, the $O_2$ contaminated electrode OCP immediately adopted a potential of -0.649 V and the EIS data (**Figure 7-25d** - **f**) confirmed that the oxide surface film provided no additional protection to the underlying substrate. The Nyquist plot (**Figure 7-25d**) showed a single semicircle, suggesting the absence of a coating, for which an additional RC loop would have been expected. This was confirmed by the Bode representation of the phase angle (**Figure 7-25e**) where a single time constant was present. The impedance modulus plot indicated that the electrode exposed to dissolved $O_2$ had a lower impedance modulus than both the uncoated and the $FeCO_3$ coated electrode at all measured frequencies (**Figure 7-25f**). Surface imaging (**Figure 7-26**) of the electrodes after removal from the 5 M $MEA_{(aq)}$ solution revealed that $FeCO_3$ was still present on the electrode exposed to dissolved $O_2$ but there were large areas of exposed corroded CS substrate. Therefore, this suggests that areas previously covered by iron oxide suffered from preferential attack, leading to enhanced corrosion of the underlying

substrate. Increases in molar volume from Fe ($7 \times 10^{-6}$ mol $m^{-3}$) to $Fe_3O_4$ ($4.5 \times 10^{-5}$ mol $m^{-3}$) or $Fe_2O_3$ ($3 \times 10^{-5}$ mol $m^{-3}$) could have caused fractures induced by mechanical stresses and hence continued oxidation of the substrate through the developed pores. Furthermore, it is imaginable that since $Fe_3O_4$ is conductive, oxidative dissolution of the Fe substrate may also have been accelerated. By contrast, the $FeCO_3$ film on the electrode, which was not contaminated by $O_2$, was left intact and provided additional protection against corrosion, as was apparent from the EIS data and the surface images. This is a crucial finding since most studies of surface film formation in $CO_{2(aq)}$ media fail to report OCP data or, in the case of (Han *et al.*, 2009; Burkle, 2017), interpret the significant rise in OCP as indicative of protective surface film formation. The OCP was demonstrated here to be an instrumental indicator of the phases present at the electrode surface, which ultimately determine the susceptibility of the film to breakdown. It is important to highlight that it may have been concluded from the EIS data, that the mixed oxide-carbonate film was protective, but comparison to a pure $FeCO_3$ film reveals its superiority over a mixed iron oxide-carbonate film. More crucially, the film stability tests conducted in $MEA_{(aq)}$ proved that a pure $FeCO_3$ film is not only more protective but its purity is the source of its stability. Under the conditions tested within this chapter, the presence of iron oxide appears to have created conditions that accelerate non-uniform, localised attack.

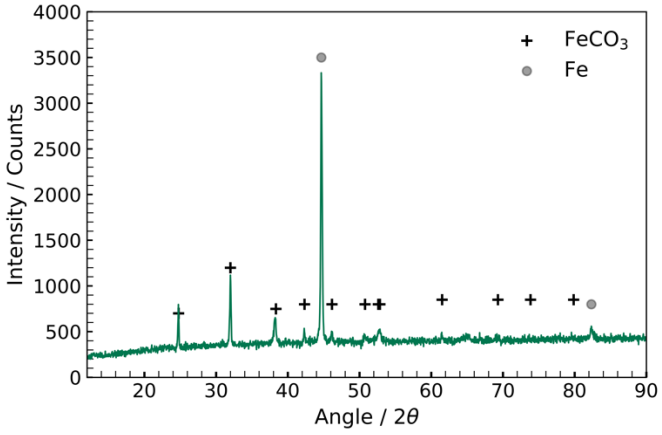



**Figure 7-24:** *Ex-situ* surface characterisation using XRD of $O_2$ contaminated pre-treated CS electrode in 1 M $MDEA_{(aq)}$-$CO_2$ 80°C, pH 7.9, which attained an OCP of *ca.* + 0.01 V.

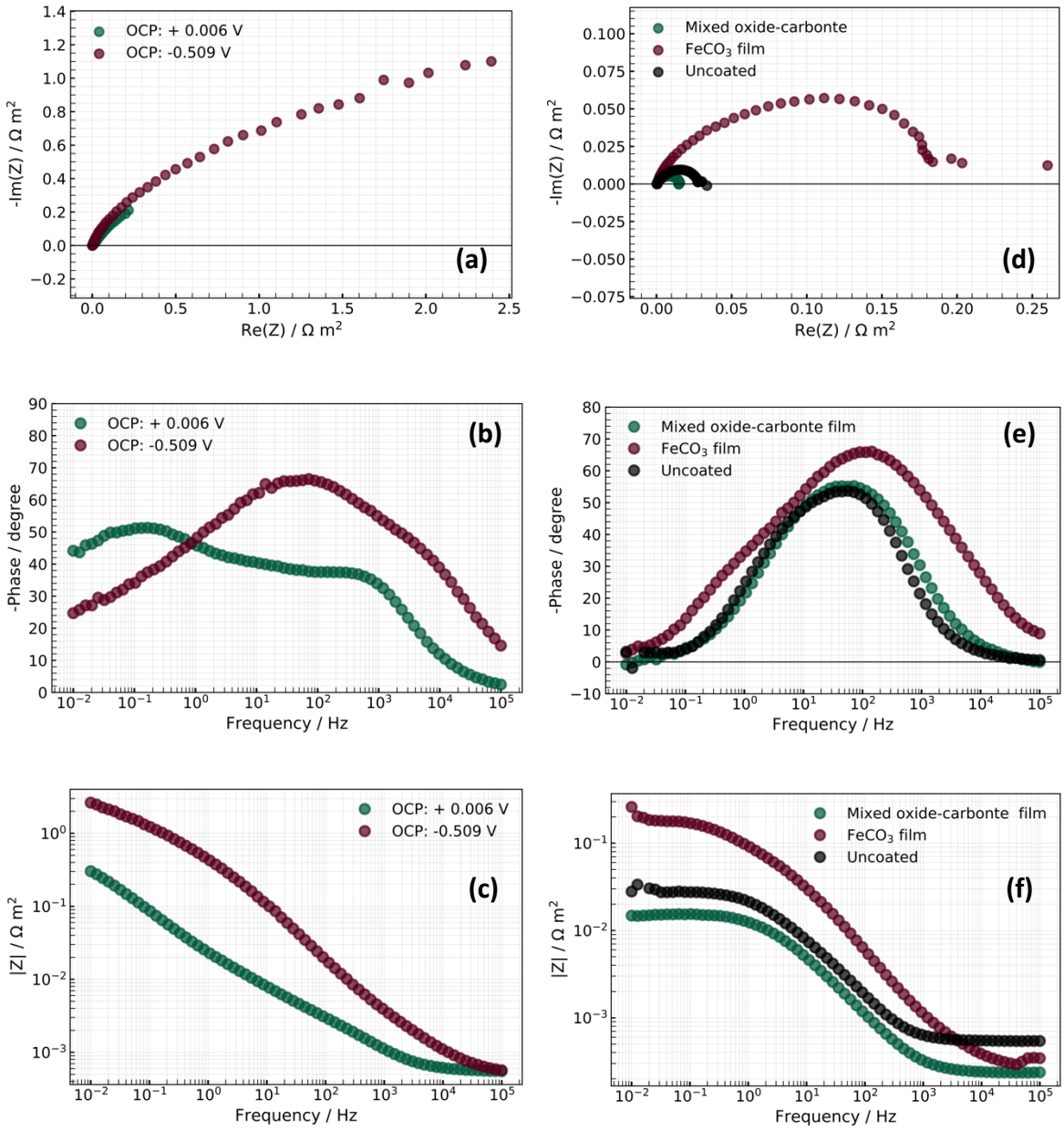



**Figure 7-25**: Experimental impedance data obtained with CS electrodes immersed in 1 M $MDEA_{(aq)}$, saturated with $CO_2$ (pH 7.9) at 80 °C for 72 h: **(a)** Nyquist representation and Bode representation of the **(b)** phase angle, and **(c)** the magnitude of the impedance; and when electrodes were initially transferred from the 1 M $MDEA_{(aq)}$-$CO_2$, 80 °C to 5 M $MEA_{(aq)}$, saturated with $CO_2$ (pH 7.9) at 80 °C: **(d)** Nyquist representation and Bode representation of the **(e)** phase angle, and **(f)** the magnitude of the impedance. The impedance data obtained with a bare CS electrode in 5 M $MEA_{(aq)}$, saturated with $CO_2$ (pH 7.9) at 80 °C is included in black in **d** - **f**.

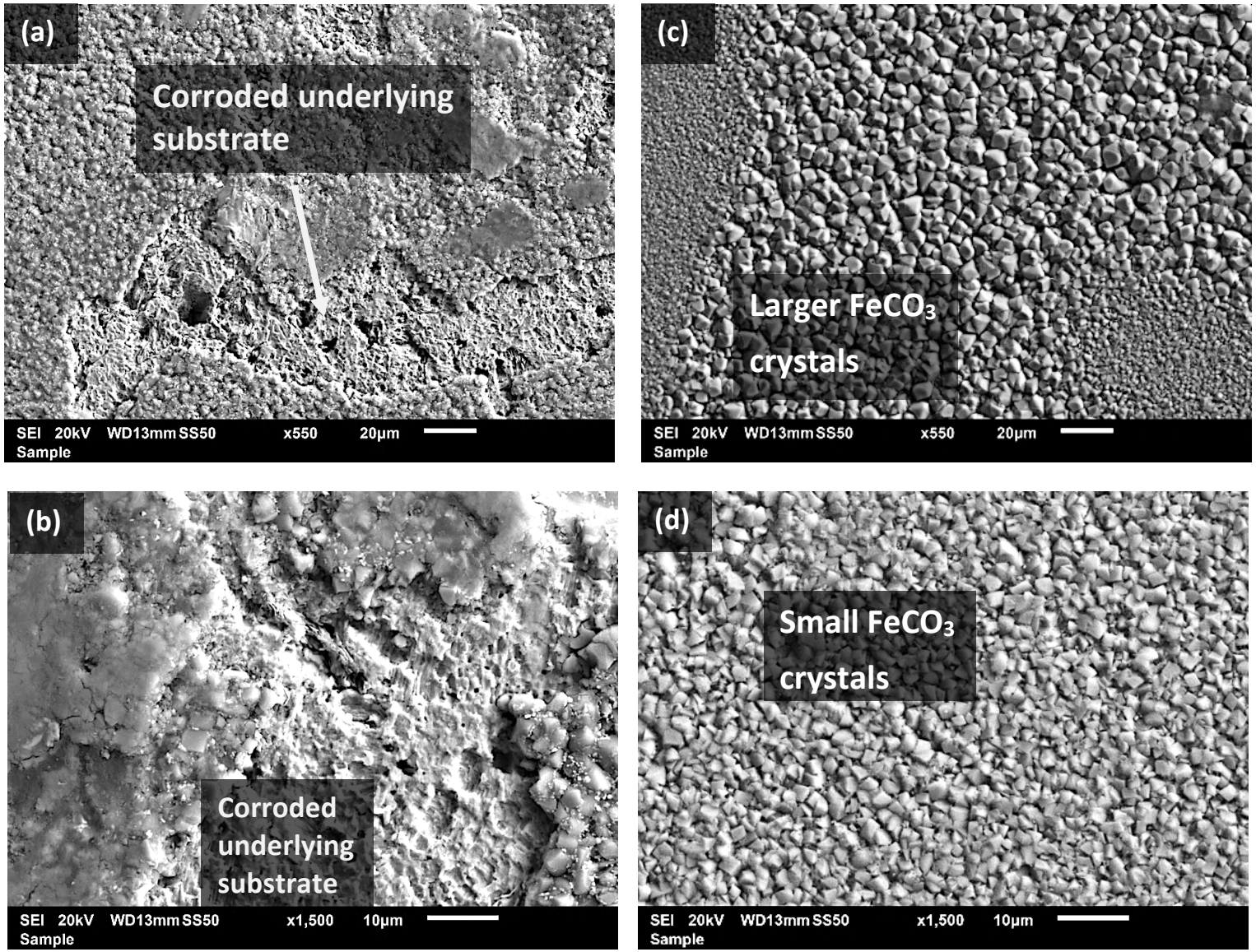



**Figure 7-26**: *Ex-situ* SEM images of pre-treated CS electrode with (**a** - **b**) OCP +0.006 V, and (**c** - **d**) OCP -0.509 V, (both in 1 M $MDEA_{(aq)}$-$CO_2$ 80°C) after immersion in 5 M $MEA_{(aq)}$, saturated with $CO_2$ (pH 7.9) at 80 °C.

## 7.3 Conclusion

The open circuit behaviour of carbon steel in $MDEA_{(aq)}$ and $MEA_{(aq)}$ solutions saturated with $CO_2$ at 80 °C was investigated. Several conclusions can be made from this study. Firstly, all carbon steel electrodes exposed to $MDEA_{(aq)}$ formed protective $FeCO_3$ films when $O_2$ ingress was prevented. The $FeCO_3$ film formation rate was the highest in the 1 M $MDEA_{(aq)}$ solution and was also the most resistive. The film formation time increased with MDEA concentration where the film formed in *ca*. three days in the 1 M solution and took on average six to seven days to form in the 5 M solution. Carbon steel dissolution is thought have occurred in a non-uniform manner where the ferrite phase dissolved preferentially due to galvanic coupling between the ferrite and cementite phases, when in contact with the solution. This left a porous cementite layer in which $FeCO_3$ supersaturation was readily attained. The $FeCO_3$ film took the shortest period of time to form in the 1 M solution because it had the smallest pH of the three tested solutions which drove Fe dissolution at the highest rate of the three solutions. The $FeCO_3$ film formed in the 1 M electrolyte was of mixed crystal sizes and appeared to have a densely packed underlying (inner) layer with areas of larger protruding crystals. The films formed in the 3 and 5 M solutions were more uniform in crystal size with apparently larger crystals that, from visual inspection, were less densely packed. The EIS data collected with the three $FeCO_3$ films included a diffusion feature, which confirmed that the films were porous in nature and, although $FeCO_3$ has been reported to be insulating, the porosity of the film prevented the films from being electrically insulating. Therefore, the resistances of the coatings were found to be minimal but more importantly, this revealed that films physically protected the underlying substrate by serving as barriers, which limited the electroactive area. The $FeCO_3$ film formed in the 1 M solution was also the most resistive of the three and was found to be at least twice as resistive as the films formed in the 3 and 5 M solutions. The film formed in the 5 M solution was found to be the least resistive and the time for film formation varied the most by up to one day. This was expected since its greater pH resulted in slow release of $Fe^{2+}$ ions and so slow development of a cementite layer and $FeCO_3$ film.

Secondly, by contrast to the electrodes immersed in $MDEA_{(aq)}$ solutions, no surface film formed on the carbon steel electrode after one week of immersion in 5 M $MEA_{(aq)}$ solution saturated with $CO_2$ at 80 °C. Instead, non-uniform dissolution occurred.

The performance of the electrodes after pre-treatment in 1, 3 and 5 M $MDEA_{(aq)}$ solutions were tested in 5 M $MEA_{(aq)}$ solution saturated with $CO_2$ at 80 °C. Varied levels of protection

were provided by films pre-treated in the three $MDEA_{(aq)}$ solutions. The resistance of all films decreased upon immersion in the test solution. The EIS data after CS pre-treatment in the 3 and 5 M solutions showed that there was a diffusion process present, which indicated that electrolyte propagated through the film to the electrode surface at a sufficiently fast rate to be captured by the EIS measurement. No diffusion process was apparent in the EIS data from the 1 M pre-treated electrode, indicating that the film was sufficiently dense to slow the diffusion of the electrolyte through it. All three films protected the CS substrate up to one day after immersion in the test solution where the total electrode resistance was up to one order of magnitude higher than that of the bare CS electrode. However, the films formed in the 3 and 5 M solutions began dissolving as time progressed and at the end of the one week period, the film formed in the 3 M solution provided no additional protection. The film formed in the 5 M solution was still protective relative to the untreated CS, but was unlikely to have been so beyond the one week period. Although the resistivity of the 1 M generated film decreased upon initial immersion, the film appeared to stabilise after one day of immersion and remained consistently protective after the one week period.

Lastly, $O_2$ contaminated films were found to provide little or no protection to the underlying substrate. The effect of inadvertent $O_2$ ingress into the electrolyte during an initial set of experiments varied in severity depending on the MDEA concentration; iron oxide formation occurred readily in the least concentrated $MDEA_{(aq)}$ solution due to its relatively lower viscosity. The presence of $O_2$ hindered continued $FeCO_3$ formation and instead resulted in the formation of a non-protective mixed oxide-carbonate layer, which was evident from the OCP and surface imaging. An OCP > -0.3 V was indicative of the presence of oxide phases on the electrode surface. The OCP was found to be an exceedingly good predictor of overall film resistance and susceptibility to breakdown in $MEA_{(aq)}$ as it is able to indicate the presence of minimal traces of iron oxide that are otherwise imperceptible. OCP measurements are therefore crucial in the investigation of surface film composition.

# 8 Pilot plant study

## 8.1 Introduction

One of the aims of this thesis was to investigate the feasibility of inducing the formation of protective $FeCO_3$ films on carbon steel as a corrosion mitigation strategy in amine scrubbing plants for post combustion $CO_2$ capture. Lab-scale experiments were conducted in Chapter 7 and promising results of enhanced corrosion resistance were reported. In this chapter, pre-treatment was tested again, but in the ABB Carbon Dioxide Capture Pilot Plant[33] at the Department of Chemical Engineering, Imperial College London. Two pilot plant studies were conducted to test and compare the performances of $FeCO_3$ coatings produced on carbon steel coupons in two pre-treatment solutions:

- Study 1: Carbon steel coupon in 1 M $MDEA_{(aq)}$ saturated with $CO_2$ at 80 °C, pH 7.9
- Study 2: Carbon steel coupon in 3 M $MDEA_{(aq)}$ saturated with $CO_2$ at 80 °C, pH 8.3

Carbon steel (CS) coupons were pre-treated in the laboratory. The pre-treatment process was monitored using electrochemical impedance spectroscopy and open circuit potential (OCP) measurements. The open circuit potential was shown in Chapter 7 to be a sensitive indicator of the development of a surface film on CS electrodes. To investigate the stability and evolution of the coatings in the pilot plant, the OCP was measured continuously during

[33] https://360-visit.imperial.ac.uk/areas-of-interest/campus-highlights/chemical-engineering-carbon-capture-pilot-plant/carbon-capture-pilot-plant

electrode immersion. An uncoated CS electrode accompanied the pre-treated electrode in each pilot plant study to determine the impact of the coating (if any), and to serve as a control to assess if electrodes in the two studies were exposed to comparable conditions. After removal from the pilot plant, the resistance of the film coatings were re-assessed in the laboratory using EIS, and characterised using SEM-EDX and XRD.

## 8.2 Experimental considerations

A complete description of the experimental matrix, electrode specifications, holder design, coupon installation, plant operation and data acquisition protocols are included in Chapter 3, Section 3.5. **Figure 8-1** shows the active plant operation periods as a function of the total immersion period for the two pilot plant studies.

A concerted effort was made to run the plant using the same protocol for both studies to ensure that the electrodes were exposed to the same conditions and hence allow for fair comparison between the studies. However, there were some unavoidable sources of possible inconsistency:

i. The intervals between plant operating periods were not the same between the two studies, as shown in **Figure 8-1**; this was because the operation of the pilot plant is not fully automated and depends on the intervention of the pilot plant operator.
ii. The total immersion period of the studies varied by *ca*. one hour
iii. Two separate leak-free AgCl | Ag reference electrodes (RE) were used in the two studies. The two REs were sourced from the same manufacturer and displayed no potential difference relative to each other prior to initiation of the pilot plant experiments; the equilibrium potential of this type of RE is known and stable at 25 °C. However, the equilibrium potential is a function of temperature, so as the temperature of the electrolyte in which it is immersed changes, so too does the equilibrium potential. The temperature also affects the solubility of KCl, which in turn affects the equilibrium potential. Although the AgCl | Ag (saturated KCl) RE is considered one of the most robust to temperature change, after exposure to high temperatures for a long period of time (*i.e*. hours), the potential drifts in the order of mV. Since the interval between the two studies was short, there was insufficient time to revive the RE (if needed), so instead two different REs were used. To ensure that

the OCPs were comparable, each RE was tested against an independent, unused RE immediately before insertion in the pilot plant. Both REs showed an offset ≤ 1.5 mV, which is much smaller than the changes in electrode potentials recorded during the two studies. Hence any difference between recorded OCP measurements in studies 1 and 2 were not considered to be a consequence poor RE stabilities.

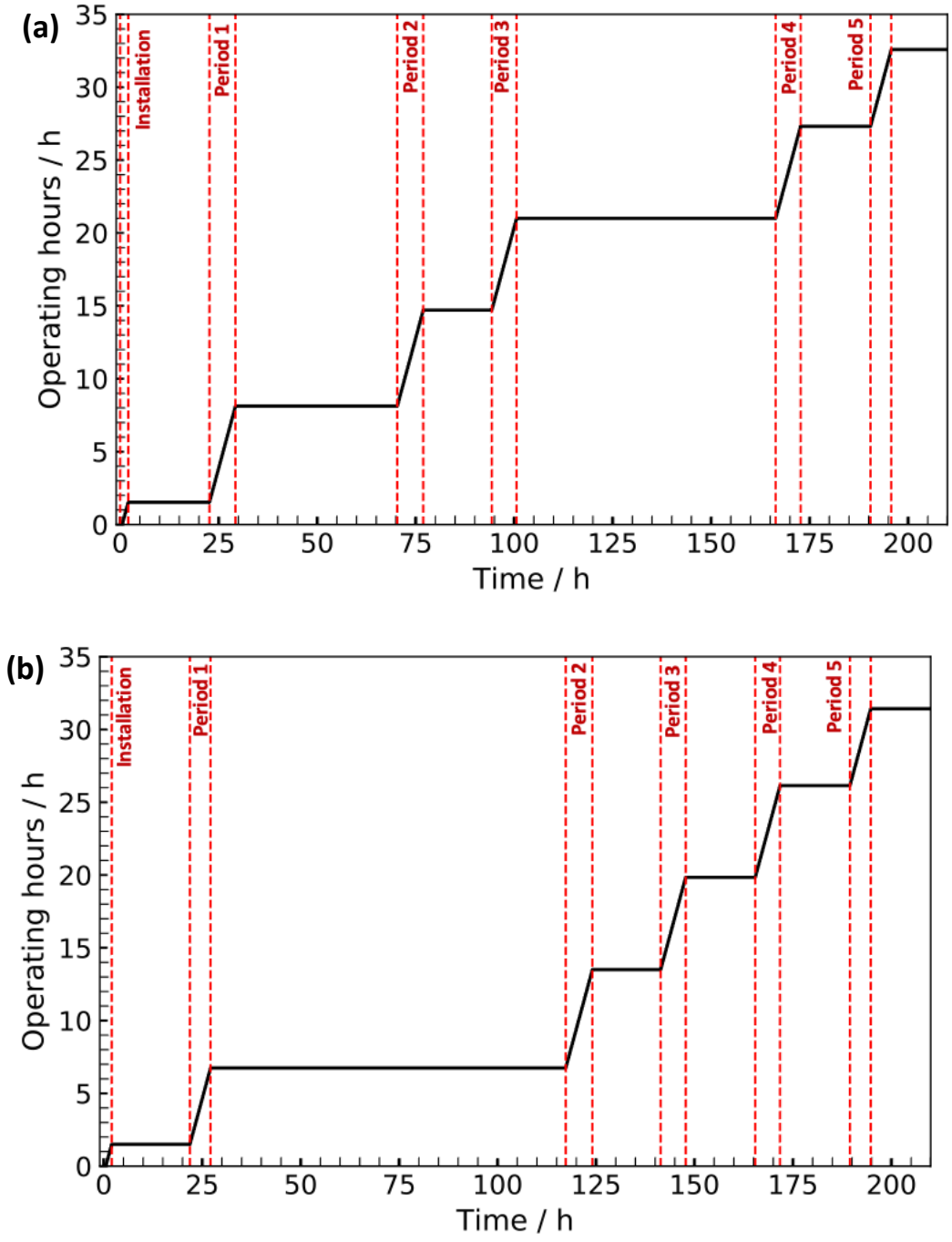



**Figure 8-1:** Plant operational period as a function of immersion period for pilot plant studies to test performance of C1018 coupon pre-treated using: **(a)** 1 M $MDEA_{(aq)}$ (Study 1) and **(b)** 3 M $MDEA_{(aq)}$ (Study 2).

The impact of the inconsistencies shown in **Figure 8-1** was assessed by comparing the open circuit potential transients of the uncoated samples used in the two studies (**Figure 8-2**); **Figure 8-2a** shows the raw, *in-situ*, continuous, open circuit potential data and **Figure 8-2b** shows the averaged, temperature-corrected OCP (*vs*. SHE). The data shown in **Figure 8-2b** was calculated by averaging the potential measurements collected during non-operational periods and temperature using an average of the temperatures recorded at the end of the preceding period and the beginning of the subsequent period. Averaging the OCPs in the non-operational periods was thought to be most useful since the plant was operated in a transient manner such that the solution speciation and temperature were continuously changing. However, during non-operational periods the electrodes were exposed to a stable electrolyte and were able to achieve a steady state potential.

Operational periods 1, 4 and 5 (**Figure 8-1**, **Figure 8-2a**) were conducted at the same total immersion times, so the potential transients of the uncoated electrodes recorded within those periods can be used to compare the conditions (**Figure 8-2b**) to which the electrodes were exposed. The potential transients during these periods were nearly identical, indicating that the coated electrodes in both studies were exposed to comparable conditions. The pH, recorded using AT100 (located at the absorber exit), temperature, monitored using TT210 (located in close proximity to the coupons), and the electrolyte flow rate, collected using FT103 (located before filter N200), for each operational period of the two studies were plotted together in the Appendix (Section 12.6**, Figure 12-25** - **Figure 12-28**) to enable comparison of the process fluid conditions for both studies.

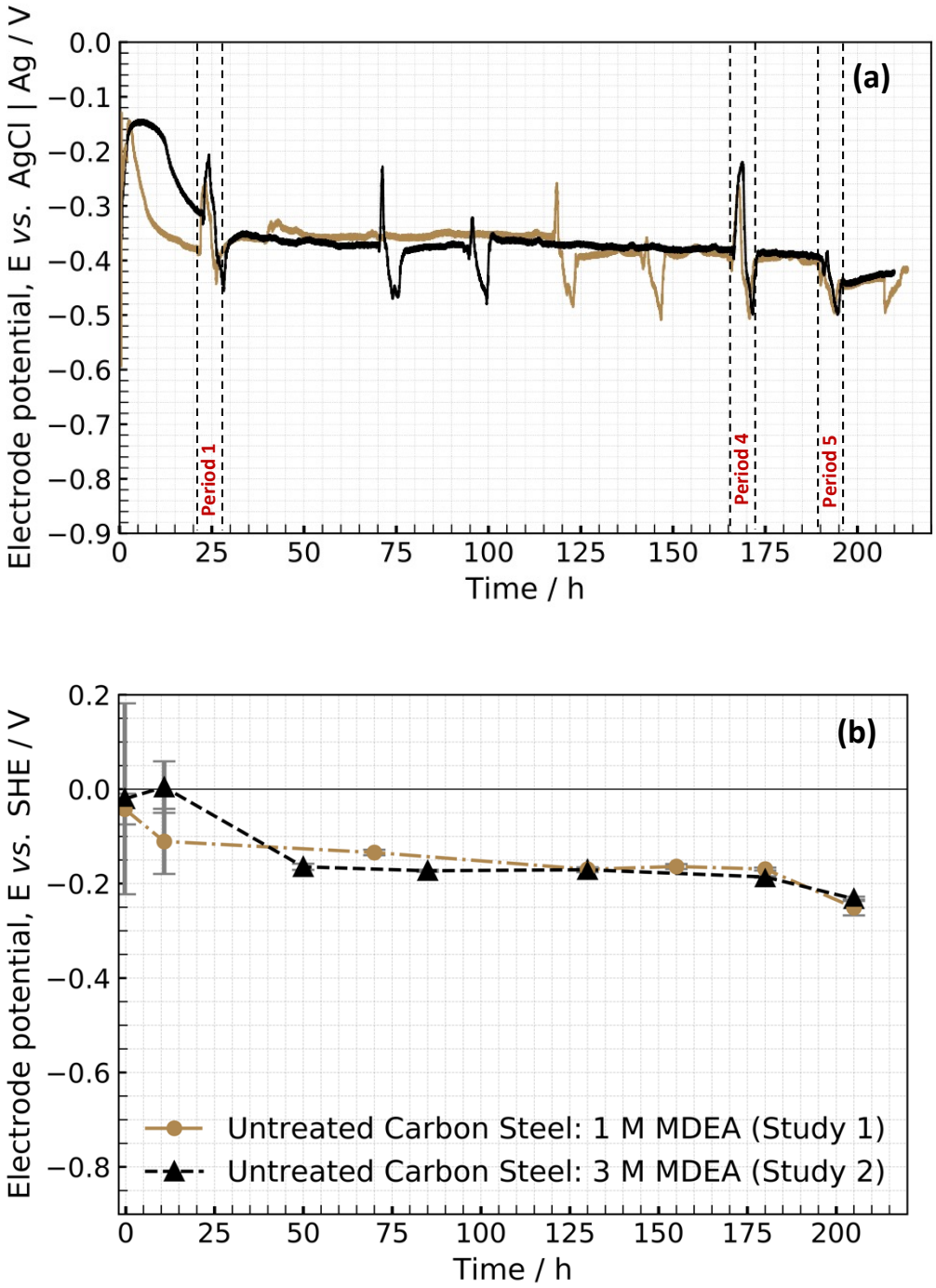



**Figure 8-2**: **(a)** Open circuit potential transients of uncoated CS coupons, recorded continuously whilst installed in pilot plant. **(b)** Open circuit potentials averaged over each non-operational period of uncoated CS coupons during the two pilot plant studies; error bars shown in grey are barely visible as the OCP deviation was minimal for most of the averaged open circuit potentials.

## 8.3 Results

The *in-situ* continuous OCP data collected during each pilot plant study, together with a comparison of the two studies, will first be presented (Section 8.3.1). The OCP and EIS data collected during the pre-treatment process and after coupon retrieval from the pilot plant, supplemented by *ex-situ* surface characterisation, will then be discussed (Section 8.3.2).

### 8.3.1 Pilot plant study results

#### 8.3.1.1 Stability of 1 M $MDEA_{(aq)}$ generated film

The *in-situ,* continuous potential transients of the CS coupon pre-treated in the 1 M $MDEA_{(aq)}$ solution saturated with $CO_2$ at 80 °C and an untreated CS coupon are shown in **Figure 8-3a**. The average, temperature-corrected OCPs (*vs*. SHE) are given in **Figure 8-3b**. During the pre-test, when both the pre-treated and untreated electrodes were installed in the tapping points and the plant was live, the electrode potentials began decreasing immediately (*i.e*. became more negative) but then increased sharply as shown by the potential transients (**Figure 8-3a**). This sudden electrode potential change occurred as a result of the changing electrode | electrolyte interface due to the onset of process fluid flow past the electrodes during operation. At the end of the pre-test, indicated by the black broken lines in **Figure 8-3a**, the potential began decreasing rapidly and continued to do so for *ca*. 2 h after the plant was shut down, but then gradually levelled up until the first operational period. This behaviour was expected because, although the valves which allow flow between the stripper and absorber (SOV152 and SOV132) were shut, preventing flow of process fluid between the stripper to the absorber, solvent continued to flow under gravity past the coupons, which were installed in vertical pipelines. The potential transient seemed to indicate that a steady state potential was not achieved after initial immersion and before the first operational period (period 1) commenced. This is reasonable since the electrolyte would have been diffusing slowly into the pores of the surface film on the pre-treated coupon, and the untreated electrode possibly had a thin oxide layer, based on the OCP of *ca*. -0.05 V, which was also evolving with time. In each subsequent operational period, the potential transient showed the same behaviour with a minor decrease in potential as the flow paths in the pilot plant were opened, though not discernible in **Figure 8-3a**, and a subsequent rapid increase through a maximum followed by a decrease. Unlike the OCP data recorded during the pre-test, the decrease was included in the operational periods since, although the flow paths were closed,

the plant was still considered operational because the manual steam valve could be shut only after the temperature in the stripper decreased to < 60 °C. During non-operational periods after *ca*. 25 h, the potential of the electrodes remained fairly constant, as indicated by the OCP plateau in **Figure 8-3a**, since there was no or little change to the electrode or solution at the interface during these periods. It should also be stated that the minimal, though detectable change in both potential transients at *ca*. 40 h (**Figure 8-3a**) was due to transference of process fluid between the stripper and the absorber for use in a different section of the plant, unrelated to this project.

From **Figure 8-3b**, it can be seen that the OCP of the pre-treated coupon was relatively stable for the first 70 h *i.e*. periods 1 - 2. However, the average OCP subsequently decreased from *ca*. +0.06 V to -0.05 V by 150 h but remained relatively stable until 175 h of immersion (*i.e*. up to period 4). After the last operational period, the OCP decreased further and averaged at *ca*. -0.12 V.

The OCP of the untreated electrode was consistently more negative than the pre-treated coupon, suggesting that the coating was providing useful protection. The initial potential of the untreated electrode decreased more noticeably than the pre-treated electrode from an average of *ca*. -0.03 V to *ca*. -0.13 V within the first 10 h of immersion (**Figure 8-3b**). The average potential of the untreated electrode steadily decreased between 10 h of immersion and *ca*. 125 h of immersion. The change in OCP between 150 and 200 h was consistent with the OCP behaviour exhibited by the pre-treated electrode.

Based on the initial OCPs of *ca*. -0.05 V and *ca*. +0.1 V, respectively of the pre-treated and untreated coupons, and the solution pH of *ca*. 10.2, iron oxide is predicted to be the most thermodynamically favourable phase based on the E - pH diagram (Appendix, Section 12.6, **Figure 12-30**). Although it is likely that an iron oxide film may have formed on the untreated electrode, it was found that the predominant phase on the pre-treated electrode was $FeCO_3$ even at the potentials indicative of oxide phases; this will be discussed in Section 8.3.1.1. The continuous decrease in the potential of the pre-treated electrode with time for the duration of the study was possibly due to continued diffusion of electrolyte through the porous film to the underlying substrate. Most notably, despite the continued decrease in the pre-treated electrode OCP, it remained well above that of the untreated electrode, which indeed is a promising result. This suggests strongly that the coating produced in the 1 M $MDEA_{(aq)}$ solution was able to withstand exposure to $MEA_{(aq)}$ under unfavourable low temperatures for protracted time periods and relatively lean conditions. Although this suggests that the film

remained present, it does not categorically prove that its electrical resistance has been preserved. Similarly, the increasingly negative OCP exhibited by the untreated electrode, thought to be covered in a spontaneously formed oxide film, was possibly due to breakdown of this likely superficial film.

Therefore, the OCP measurements suggested that the coating was effective in providing some degree of protection, though this still required additional corroboration using EIS measurements. On the whole this result was particularly exciting since the process fluid, at a pH of 10.2 was not saturated with $CO_2$, and the temperature was only relatively high (at most 60 °C) for a total of 5 h. Both of these conditions were conducive to $FeCO_3$ dissolution but the film seemingly remained intact.

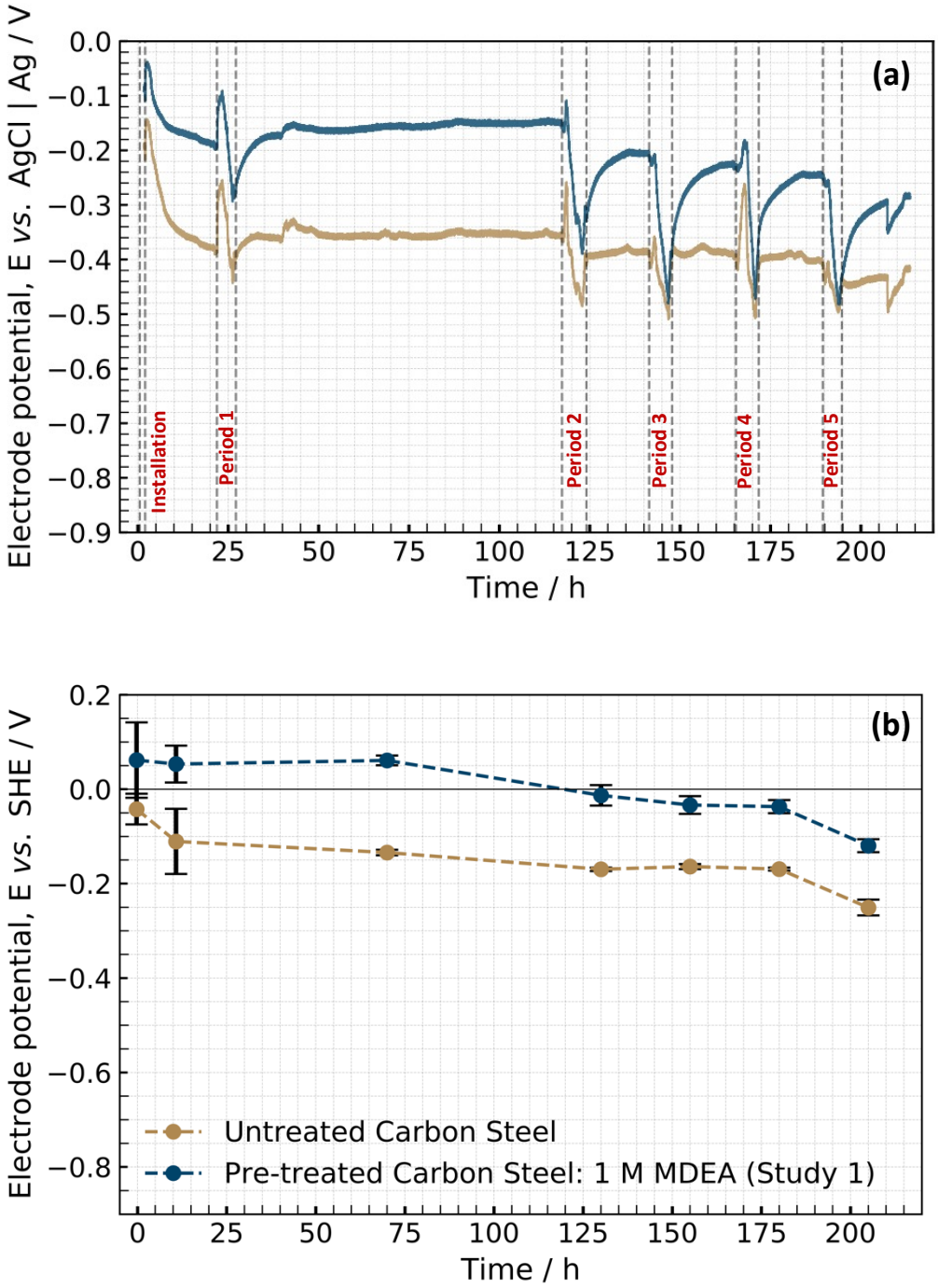



**Figure 8-3: (a)** Open circuit potential transients (*vs*. AgCl | Ag, not temperature corrected) of uncoated and 1 M $MDEA_{(aq)}$ pre-treated carbon steel. **(b)** Average open circuit potentials (*vs*. SHE, temperature corrected), calculated using potentials recorded over non-operational periods; error bars shown in black are barely visible as the OCP deviation was minimal for most averaged open circuit potentials.

### 8.3.1.2 Stability of 3 M $MDEA_{(aq)}$ generated film

The *in-situ,* continuous potential transients of the CS coupon pre-treated in the 3 M $MDEA_{(aq)}$ solution saturated with $CO_2$ at 80 °C, together with those for an untreated CS coupon, are shown in **Figure 8-4a**. The average, temperature-corrected OCPs (*vs*. SHE) are presented in **Figure 8-4b**.

From **Figure 8-4a**, it can be seen that, after insertion of the pre-treated and untreated coupons into the pilot plant and initiating the flow of process fluid around the plant in the pre-test, both potential transients increased and then decreased gradually after the plant was shut down. The potentials of both electrodes gradually declined and did not attain a steady state before the first operational period. Again, this is thought to have been caused by the process fluid slowly diffusing through the pores of the coating generated in the pre-treatment process and possibly due to the slow dissolution through an oxide film, likely to have been formed in air on the untreated coupon. Similar potential responses were observed during each subsequent operational period as those recorded in the 1 M pre-treatment study, where the potential increased rapidly to a maximum and then decreased. This occurred for all operational periods with the maximum recorded potential varying for each period.

**Figure 8-4b**, allows for easy comparison between the untreated and pre-treated coupon OCPs. Initially the OCP of the pre-treated electrode was *ca*. +0.15 V, substantially higher than that measured for the untreated electrode, which exhibited a potential of *ca*. -0.02 V. At those potentials, and at a solution pH of *ca*. 9.6, $Fe_2O_3$ was predicted to be the most thermodynamically stable phase, though $FeCO_3$ was the predominant phase on the pre-treated sample (Section 8.3.2.2.2). Within the first 10 h of immersion, the deviation between the average OCPs of the pre-treated and untreated electrodes was smaller than it was at the beginning of the immersion period, with the average OCP of the un-treated coupon increasing to a more positive value of *ca*. 0 V, and the pre-treated decreasing from *ca*. +0.15 V to *ca*. +0.1 V. It should be noted that the spread of the OCP values for both electrodes was relatively high at ± 0.11 V as indicated by the error bars in **Figure 8-4b**. After operational period 1, the steady state OCPs of both electrodes were notably lower than OCPs measured prior to the operational period, with the average OCP of the pre-treated being *ca*. -0.1 V and the untreated electrode potential being -0.175 V. Both the pre-treated and untreated electrode potentials decreased again after operational period 2, and the difference between the two decreased further. By contrast, there were minimal OCP changes, apparent from the average

OCP (**Figure 8-4b**), as well as potential transients (**Figure 8-4a**), for both the pre-treated and untreated electrodes as a result of operational period 3.

After period 4, the deviation between the average OCPs of the untreated and pre-treated electrodes became narrow with the untreated electrode potential being -0.19 V, *i.e.* positive of the pre-treated electrode, which had an average OCP of -0.2 V, moderately lower than its potential prior to period 4. At the very end of the 5$^{th}$ operational period, the pre-treated electrode potential decreased substantially to -0.6 V, equivalent to that of a coupon, which was uncoated and had not developed an oxide film, indicating that the film integrity was compromised and it most likely became ineffective. By contrast, the OCP of the untreated electrode underwent a small decrease, from -0.2 V to *ca.* -0.23 V after period 5.

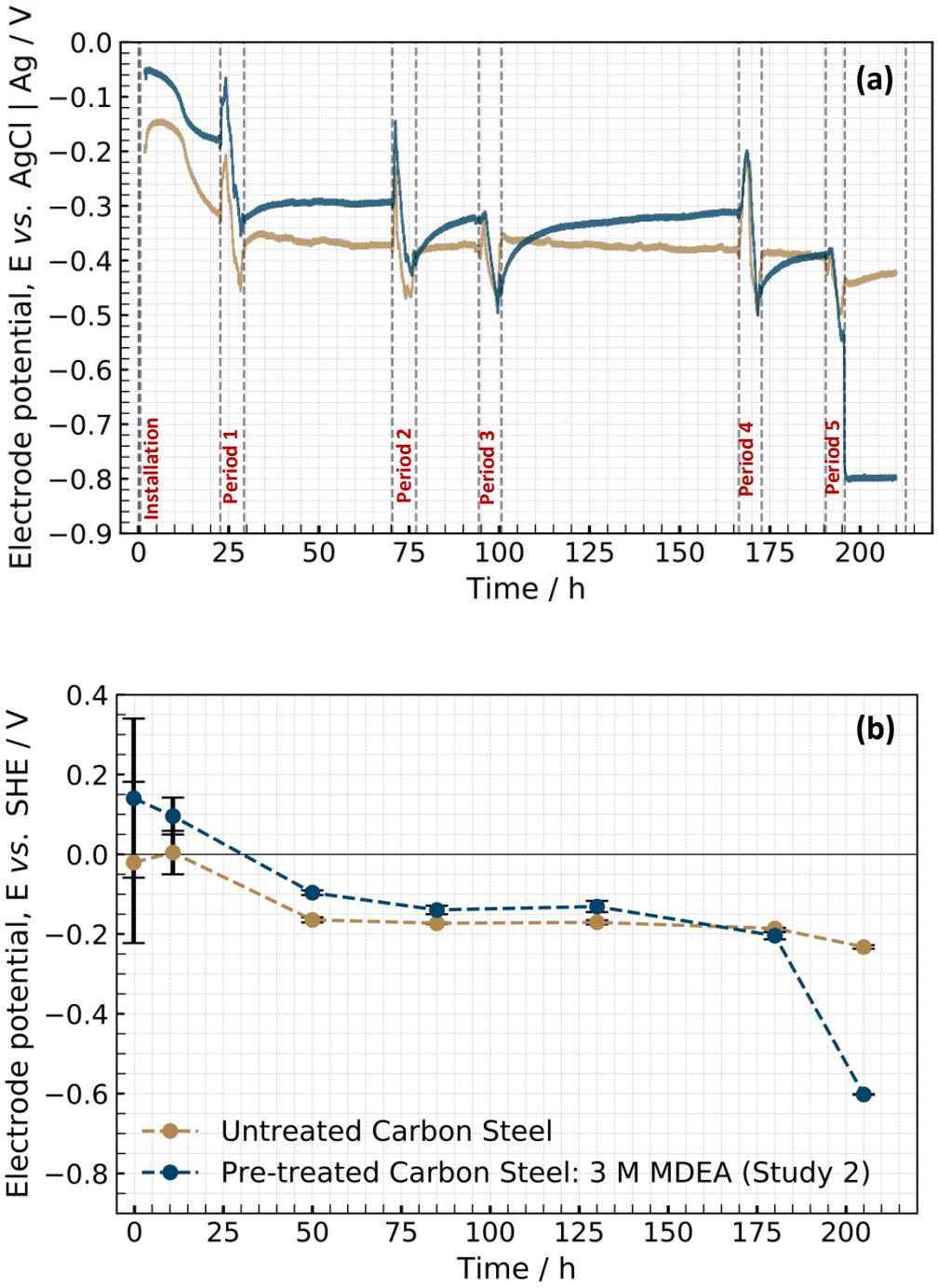



**Figure 8-4: (a)** Open circuit potential transients (*vs*. AgCl | Ag, not temperature corrected) of uncoated and 3 M $MDEA_{(aq)}$ pre-treated carbon steel. **(b)** Average open circuit potential (*vs*. SHE, temperature corrected) calculated using potentials over non-operational periods; error bars shown in black are barely visible as the OCP deviation was minimal for most averaged open circuit potentials.

**Figure 8-5** shows the OCPs of electrodes pre-treated in 1 M and 3 M $MDEA_{(aq)}$ solutions saturated with $CO_2$ at 80 °C whilst installed in the pilot plant. The initial OCP of the electrode pre-treated with the 3 M solution was +0.14 V, which was more positive than that of the electrode pre-treated in the 1 M solution with an OCP of +0.06 V. As mentioned previously, although this OCP suggests the presence of iron oxide, the predominant phase on both coupons was detected *via* XRD to be $FeCO_3$. Although the OCP of the coupon pre-treated in the 3 M $MDEA_{(aq)}$ solution was initially more positive, it decreased quickly and became negative within 40 h of immersion. By contrast, the OCP of the 1 M pre-treated coupon stayed positive until *ca*. 120 h of immersion. The average OCPs of both coupons became increasingly negative with time and both underwent an increased rate of potential change nearing the end of each study, between 175 h and 200 h of immersion. However, the OCP of coupon pre-treated in the 1 M solution remained significantly more positive than that of the 3 M generated film, suggesting that the film produced in the 1 M pre-treatment solution was more durable than that produced in the 3 M solution. This is consistent with the results presented in Chapter 7, where the coating formed in the 1 M solution was considerably more stable than that formed in the more concentrated solutions.

Although the operational protocols were quite similar, the initial process fluid conditions differed moderately between the two studies. The largest differences were in the initial pH and temperature of the process fluid, which, at the beginning of Study 1 (with the coupon pre-treated in the 1 M solution), were *ca*. 10.2 and 23.6 °C, respectively, whereas at the beginning of Study 2 (with the 3 M generated film) those values were *ca*. 9.6. and 19 °C, respectively. Since pH is a good indicator of $CO_2$ saturation, and high concentrations of dissolved $CO_2$ are favourable for $FeCO_3$ stability, the higher initial pH, experienced by the coupon coated in the 1 M solution was more likely to have resulted in film degradation. On the other hand, the initial lower temperature of the process fluid, in which the 3 M pre-treated coupon was immersed, was slightly more conducive to $FeCO_3$ dissolution. Subsequently, the pH of the process fluid of corresponding operational periods were very similar and were within ± 0.26 units of each other (Appendix, Section 12.6, **Figure 12-25** - **Figure 12-28**). On balance, these differences are unlikely to have been the cause of the earlier breakdown of the 3 M coating.

Another important difference, which may have been responsible (in part) for the difference in OCP behaviour exhibited by the two coupons, was the time interval between the 1st and 2nd operational periods, which was 90 h in the case of Study 1 (with the 1 M generated film), but

only 40 h in Study 2 (with the 3 M pre-treated coupon). This means that the 1 M pre-treated coupon was in stagnant solution for a longer period of time. Since the temperature and pH of the solution were not favourable for $FeCO_3$ stability, there may have been some dissolution of the $FeCO_3$ crystals on the coupon pre-treated in the 1 M solution. However, given the density of the film, if there was dissolution, the local $Fe^{2+}$ concentration within the pores would likely have been high, thereby preserving and possibly enhancing the film. The 3 M pre-treated coupon would have been exposed to more continuous fluid flow, which would not be favourable for keeping the film intact. Further, the 3 M generated film was thought to be thicker but less densely packed (Section 8.3.2.2.2) and so would allow for electrolyte ingress. The enhanced protection afforded by a higher density film as opposed to a thicker film was discussed in Chapter 7.

The final difference worth mentioning is that the overall immersion period of the 1 M pre-treated coupon was *ca*. one hour less than that of the 3 M pre-treated coupon, and the latter broke down in the final hour of operation. It is imaginable that the film on the 1 M pre-treated coupon may have also broken down if immersed for an additional hour, but the OCP of the 1 M generated film was consistently more positive than the 3 M generated film from *ca*. 20 h of immersion onward. Despite these differences, it may be deduced that the 1 M generated film was inherently more stable than that formed in the 3 M solution.

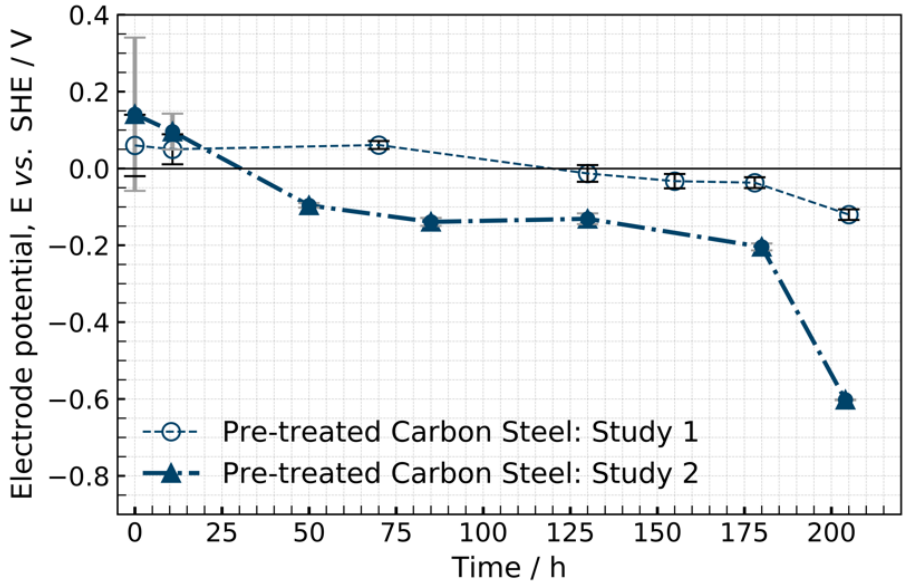



**Figure 8-5:** Average open circuit potential calculated using potentials over non-operational periods of pre-treated coupons in pilot plant. Error bars shown in grey (1 M) and black (3 M) are barely visible as the OCP deviation was minimal for most averaged open circuit potentials.

## 8.3.2 Electrochemical impedance spectroscopy results

Electrochemical impedance spectroscopy was used to monitor the evolution of the carbon steel surface during the pre-treatment process and to determine the resistance provided by the surface films generated. Analyses of EIS data collected at the beginning and end of the pre-treatment process will be presented Section 8.3.2.2. EIS was also used to determine if resistive films were still present on the coupons after removal from the pilot plant. An analysis of the EIS data measured after coupon removal from the pilot plant will be presented subsequently (Section 8.3.2.4).

### 8.3.2.1 Equivalent circuits

Measured EIS data were modelled using equivalent circuits (*EC*) to extract useful data, such as charge transfer resistance, to compare the performances quantitatively of the two pre-treatment conditions. $EC_1$ (**Figure 7-1**), $EC_3$ (**Figure 7-2**) and $EC_4$ (**Figure 8-6**) were used to model the collected EIS data. The *EC* selection and fitting process, along with a description of $EC_1$ and $EC_3$, were given in Chapter 7 (Section 7.1.2.1), and so will not be repeated here.

From visual inspection of the EIS data obtained at the OCP with a CS electrode in 3 M $MDEA_{(aq)}$ solution saturated with $CO_2$ at 80 °C at the end of the pre-treatment process, two distinct (*i.e.* non-convoluted) semicircles were observed, one at a higher frequency > $10^3$ Hz, and one at *ca.* $10^0$ Hz, together with two diffusion features, one between the two semicircles and one after the second semicircle *i.e.* at low frequencies (< $10^{-1}$ Hz). The physical interpretation of two diffusion features is that the film may have consisted of layers of variable packing (and hence tortuosity), so each layer would result in different diffusion rates of species through them. To model these EIS data, both $EC_3$ and $EC_4$ were used. $EC_3$ was first attempted since it modelled the EIS data collected with a CS sample at the end of the pre-treatment in 3 M $MDEA_{(aq)}$ well in Chapter 7 and it was unclear whether a separate diffusion feature would be needed. $EC_4$ was based on $EC_3$ with an additional diffusion element ($W_1$) in the coating RC loop (**Figure 8-6**). $EC_4$ was found to model the EIS data better than $EC_3$, as was expected from inspection of the measured EIS data. The diffusion element as well as the capacitors were modelled using constant phase elements ($Q$) to account for the non-ideal capacitive and diffusion behaviour of the films.

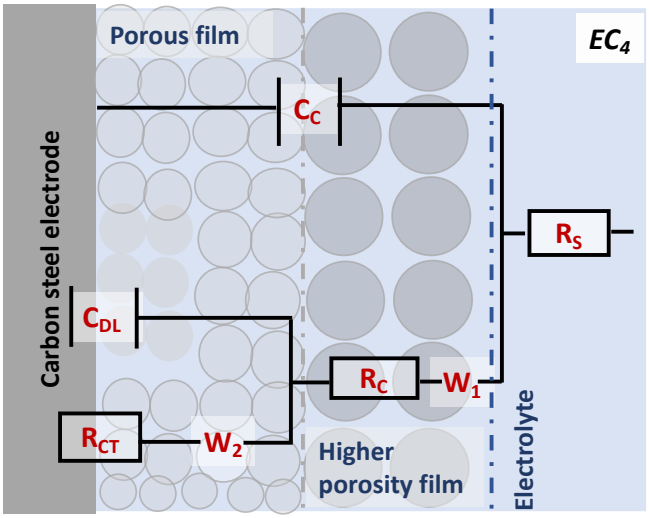



**Figure 8-6**: Equivalent circuit used for fitting the experimental impedance data obtained with CS electrodes pre-treated in 3 M $MDEA_{(aq)}$ solution saturated with $CO_2$.

### 8.3.2.2 Pre-treatment of carbon steel coupons

#### 8.3.2.2.1 1 M $MDEA_{(aq)}$ $CO_2$ 80 °C:

After immersion of the CS coupon (**Figure 8-17**) for *ca*. 5 minutes in the 1 M $MDEA_{(aq)}$ solution saturated with $CO_2$ at 80 °C the OCP stabilised to -0.599 V (**Table 8-1**), from which it was inferred that there was little or no oxide product present on the surface of the electrode. The impedance data obtained during the pre-treatment of the CS coupon in the 1 M solution is shown in **Figure 8-8a** - **d**. The Nyquist plot (**Figure 8-8a** - **b**) of the EIS data recorded at the beginning of the pre-treatment process appeared to consist of one semicircle, suggesting the presence of a single interfacial process. The Bode representation of the phase angle (**Figure 8-8c**) supported this interpretation, which suggested the presence of one time constant at *ca*. 20 Hz, so the data was best represented by $EC_1$ (**Figure 7-1**). Given that the CS coupon was initially bare, the low charge transfer resistance of $4 \times 10^{-2}$ Ω $m^2$ (**Table 8-2**) was reasonable. It should be acknowledged that an inductive feature seemed to be present at high frequencies > $10^4$ Hz and low frequencies of *ca*. $10^{-2}$ Hz. This was present in initial EIS data regardless of electrolyte composition so it was thought to be an experimental artefact associated with the inductance of the connecting leads.

After 116 h (*ca*. five days) of immersion, the coupon attained an OCP of -0.129 V, which suggested the presence of (some) oxide on the electrode surface (Appendix, Section 12.6, **Figure 12-30**). The coupons appeared to be completely covered in a black coating (**Figure 8-10b**). The presence of oxide within the film was demonstrated in Chapter 7 to likely lead to

the ultimate demise of the film; accordingly, these experiments were repeated but $O_2$ ingress, which is thought to be responsible for the presence of oxide, was unavoidable. The prevention of $O_2$ contamination was far more difficult in these experiments and was likely due to the relatively large surface area ($9.85 \times 10^{-4}$ $m^2$) and shape of the coupon. This meant that the top (or upper section) of the coupon was near to the interface of the solution, and the headspace of the flask, so each time measurements were taken, the $O_2$ which would have entered the flask upon opening it would have successfully made its way to the electrode surface. The solution Fe concentration was 257 mg $dm^{-3}$ (0.0047 mol $dm^{-3}$) , and based on a $CO_3^{2-}$ concentration of $2 \times 10^{-3}$ mol $dm^{-3}$, and $K_{sp}$ (Equation **6-2**) of $7 \times 10^{-10}$ $mol^2$ $dm^{-6}$ (Appendix, Section 12.4.3), the solution $FeCO_3$ saturation ratio was calculated to be *ca*. $1 \times 10^4$ (Equation **5-10**), confirming that the solution conditions were exceedingly favourable for $FeCO_3$ precipitation. *Ex-situ* XRD did not detect any oxide based species, but it did detect $FeCO_3$, as well as the underlying substrate (Fe). Oxide ($Fe_3O_4$ and or $Fe_2O_3$) or possibly (hydr-)oxide ($Fe(OH)_3$) phases, if present, were possibly amorphous in nature and hence undetectable with XRD. Imaging with SEM showed a film of only triagonal-capped crystals, characteristic of $FeCO_3$ (Joshi *et al*., 2018), and electron dispersive spectroscopy (EDX) confirmed the chemical composition of Fe: 42.08, O : 42.08, C: 15.83, % by mass, both indicative of $FeCO_3$. Therefore, it was concluded that the electrode surface was not covered in a continuous oxide film but instead possibly had a mixed oxide-carbonate film (**Figure 8-7**) nearer to the underlying substrate, which would be responsible for the OCP of -0.129 V, and possibly a predominantly $FeCO_3$ outer film.

The EIS data measured after *ca*. five days of immersion was noticeably different from the initial EIS data. The Nyquist plot (**Figure 8-8a** - **b**) consisted of at least two overlapping semicircles and a diffusion feature represented by the *ca*. 45 ° tail recorded at frequencies lower than *ca*. 6 Hz. **Figure 8-8c** confirmed the presence of two time constants at *ca*. $2 \times 10^5$ Hz, likely due to the coating, and at *ca*. 360 Hz, thought be due to charge transfer. The coating time constant was measured at frequencies higher than those obtained with the smaller electrodes in Chapter 7, which were recorded at *ca*. $10^3$ - $10^{4.5}$ Hz. Since the film was believed to be a mixed oxide-carbonate coating, it would be less resistive than a pure carbonate film as was described in Chapter 7, Section 7.2.4. The smaller coating resistivity could have resulted in the higher frequency time constant. The charge transfer time constant was captured at a relatively high frequency compared to that obtained after initial immersion (**Figure 8-8c**). This shift could be due to the increased charge transfer resistance but it may

also be indicative of a contribution from the pure $FeCO_3$ outer coating. Although the CS electrode was contaminated with $O_2$, the film did increase the impedance by up to two orders of magnitude at frequencies < *ca*. $10^{5.5}$ Hz (**Figure 8-8c**). From iterative circuit fitting, it was found that $EC_2$ (**Figure 7-2**) best described the measured EIS data, thus confirming that two time constants were present together with a diffusion element. The coating resistance was found to be $1 \times 10^{-2}$ Ω m$^2$ (**Table 8-3**), smaller than that of the initial charge transfer resistance, whilst the charge transfer resistance was $3 \times 10^{-1}$ Ω m$^2$, almost an order of magnitude greater than that measured after initial immersion. As explained in Chapter 7, the coating serves to limit the electroactive surface area and so the charge transfer resistance should be used as the measure of protection provided by the coating rather than the coating resistance. The surface area to volume ratio is significantly higher here at 3.9 m$^{-1}$, than that used for the experiments reported in Chapter 7, which has been demonstrated in the literature to favour more protective film formation (Kinsella, Tan & Bailey, 1998). Accordingly, the impact of the mixed nature of the coating on the resistance to charge transfer may have been lessened by the higher surface area to volume ratio.

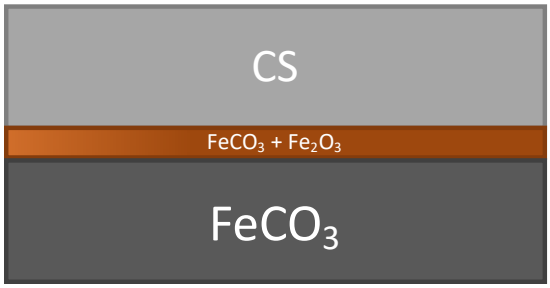



**Figure 8-7**: Schematic of a CS electrode coated with an inner mixed phase layer and outer $FeCO_3$ layer, relevant to open circuit potentials *ca*. ≥ +0.3 V.

#### 8.3.2.2.2 3 M $MDEA_{(aq)}$ $CO_2$ 80 °C:

The impedance data obtained during the pre-treatment of the CS coupon in the 3 M $MDEA_{(aq)}$ solution saturated with $CO_2$ at 80 °C is shown in **Figure 8-8e** - **h**. After initial immersion, the coupon attained an OCP of -0.624 V (**Table 8-1**), indicating that the surface was initially free of oxide product. The Nyquist plot (**Figure 8-8e**) obtained at this OCP was similar to that obtained with the coupon in the 1 M solution, which indicated a single electrode process. However, the diameter (*i.e*. resistance) of the semicircle appeared to be smaller than that obtained in the 1 M solution. The single electrode process was confirmed by the Bode representation of the phase angle (**Figure 8-8f**) with one time constant evident at *ca*. 14 Hz, slightly smaller than that obtained in the 1 M electrolyte. From circuit fitting with $EC_1$

(**Figure 7-1**) the charge transfer resistance was found to be $1 \times 10^{-2}$ Ω m$^2$ (**Table 8-2**); again this is reasonable assuming that the electrolyte could freely access the CS substrate.

Consistent with the 1 M results, after 189 h (*ca*. eight days) of immersion, the OCP was -0.207 V (**Table 8-1**), and the solution Fe concentration was 496 mg dm$^{-3}$ (0.01 mol dm$^{-3}$), which using a $CO_3^{2-}$ concentration of $3 \times 10^{-3}$ mol dm$^{-3}$, and $K_{sp}$ of $9 \times 10^{-10}$ mol$^2$ dm$^{-6}$ (Appendix, Section 12.4.3), gives the solution $FeCO_3$ saturation ratio of $3.3 \times 10^4$ (Equation **5-10**), which far exceeded that needed for $FeCO_3$ precipitation. The coupons appeared to be completely covered in a black coating (**Figure 8-10c**). Similar to the coupon exposed to the 1 M solution, XRD detected only $FeCO_3$ (**Figure 8-9d**) and the underlying Fe substrate, but did not identify any oxide species, again possibly due to their amorphous nature. From the Bode representation of the impedance modulus (**Figure 8-8g**), it can be seen that the electrode impedance was almost two orders of magnitude higher than that of the initially immersed coupon for all frequencies. From visual inspection of the Nyquist plot (**Figure 8-8e** - **f**), at least two semicircles were apparent but did not appear to be overlapped. Instead, a diagonal feature seemed to be present between the two semicircles (**Figure 8-8f**), as well as another diffusion element at frequencies < 0.16 Hz. The presence of two diffusion features is reasonable since the mixed oxide-carbonate layer would contain trigonal-pyramidal capped $FeCO_3$ crystals together with tabular $Fe_2O_3$ and / or octahedral $Fe_3O_4$ (Barbosa *et al*., 2015), and may not pack together as tightly as the crystals in the pure $FeCO_3$ layer. The higher intensity of the $FeCO_3$ predominant peak relative to the Fe predominant peak (**Figure 8-9d**), suggests that the film was relatively thick and likely less densely packed. Furthermore, the two films (inner mixed oxide-carbonate and outer carbonate) were likely less interlaced, therefore, diffusion through the two layers were likely sufficiently fast and were captured in the time scale of the EIS data collection. The Bode representation of the phase angle (**Figure 8-8g**) confirmed the presence of two time constants, which appeared to be captured at widely spaced frequencies, providing further evidence that the semicircles observed in the Nyquist plot (**Figure 8-8e** - **f**) were not convoluted. The time constant recorded at *ca*. $2.5 \times 10^5$ Hz, is thought to be due to the coating, and that measured at *ca*. 5 Hz is the charge transfer time constant. Both $EC_3$ (**Figure 7-2**) and $EC_4$ (**Figure 8-6**) were used to model the EIS data and $EC_4$ was found to better represent the measured data with a weighted $\chi^2$ of 0.02 (**Table 8-3**). From the circuit fitting, the coating resistance was found to be $1 \times 10^{-3}$ Ω m$^2$, an order of magnitude lower than the initial charge transfer resistance, and the charge transfer resistance was $7 \times 10^{-2}$ Ω m$^2$, which is greater than the initial resistance, though still of the same order

of magnitude. It should be mentioned that this charge transfer resistance is lower than the final charge transfer resistance reported in Chapter 7, which were conducted with steel samples of a smaller surface area to volume ratio (0.076 $m^{-1}$).

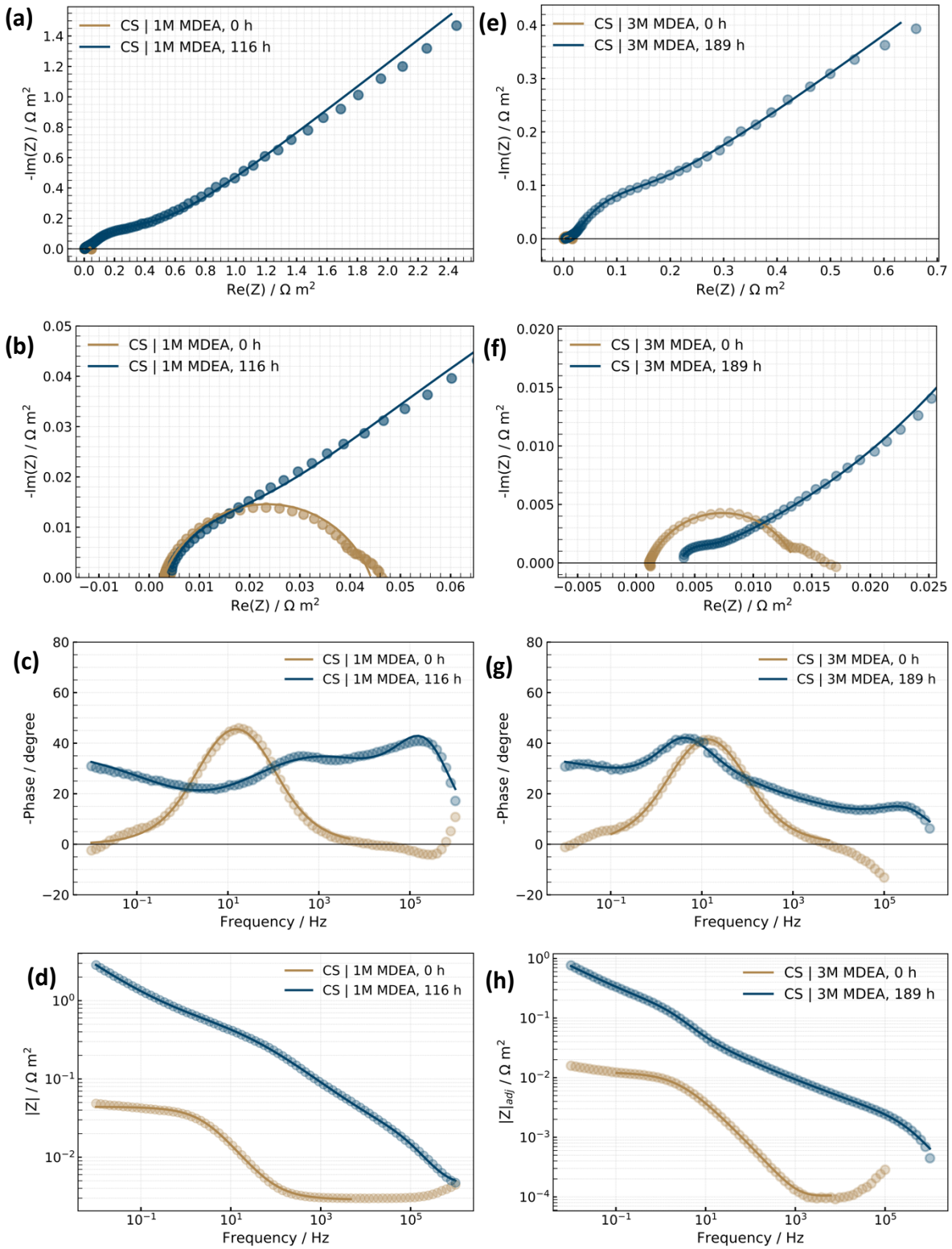



**Figure 8-8:** Experimental (o) and simulated (-) impedance data at OCP during pre-treatment of a CS coupon in 1 M $MDEA_{(aq)}$ solution saturated with $CO_2$ (pH 7.9) 80 °C: **(a - b)** Nyquist representation and Bode representation of the **(c)** phase angle and **(d)** magnitude of the impedance; and in 3 M $MDEA_{(aq)}$ solution saturated with $CO_2$ (pH 8.3) 80 °C: **(e - f)** Nyquist representation and Bode representation of the **(g)** phase angle and **(h)** magnitude of the impedance.

**Table 8-1:** Temperature corrected open circuit potentials of CS coupons at the beginning and end of pre-treatment in $MDEA_{(aq)}$ saturated with $CO_2$ at 80 °C.

| MDEA concentration | OCP *vs*. SHE / V pre-treatment start | OCP *vs*. SHE / V pre-treatment end |
|---|---|---|
| 1 M | -0.599 | -0.129 |
| 3 M | -0.624 | -0.207 |

**Table 8-2:** Normalised $EC_1$ component values for impedance data obtained when CS coupons were initially immersed in $MDEA_{(aq)}$ solutions saturated with $CO_2$ at 80 °C.

| MDEA concentration | $R_{CT}$ / Ω m² | $C_{DL}$ / F m$^{-2}$ | $\frac{\chi^2}{\lvert Z \rvert}$ |
|---|---|---|---|
| 1 M (0 h) | $4 \times 10^{-2}$ | 4 | 0.06 |
| 3 M (0 h) | $1 \times 10^{-2}$ | 16 | 0.005 |

**Table 8-3:** Normalised $EC_3$ and $EC_4$ component values for impedance data obtained at end of pre-treatment of CS coupons in $MDEA_{(aq)}$ solutions saturated with $CO_2$ at 80 °C.

| MDEA concentration | $R_C$ / Ω m² | $Q_C$ / F s$^{\alpha-1}$ m$^{-2}$ | $R_{CT}$ / Ω m² | $Q_{DL}$ / F s$^{\alpha-1}$ m$^{-2}$ | $\frac{\chi^2}{\lvert Z \rvert}$ |
|---|---|---|---|---|---|
| 1 M (116 h) | $1 \times 10^{-2}$ | $2 \times 10^{-3}$ | $3 \times 10^{-1}$ | $1 \times 10^{-1}$ | 0.05 |
| 3 M (189 h) | $1 \times 10^{-3}$ | $2 \times 10^{-4}$ | $7 \times 10^{-2}$ | $1 \times 10^{0}$ | 0.02 |

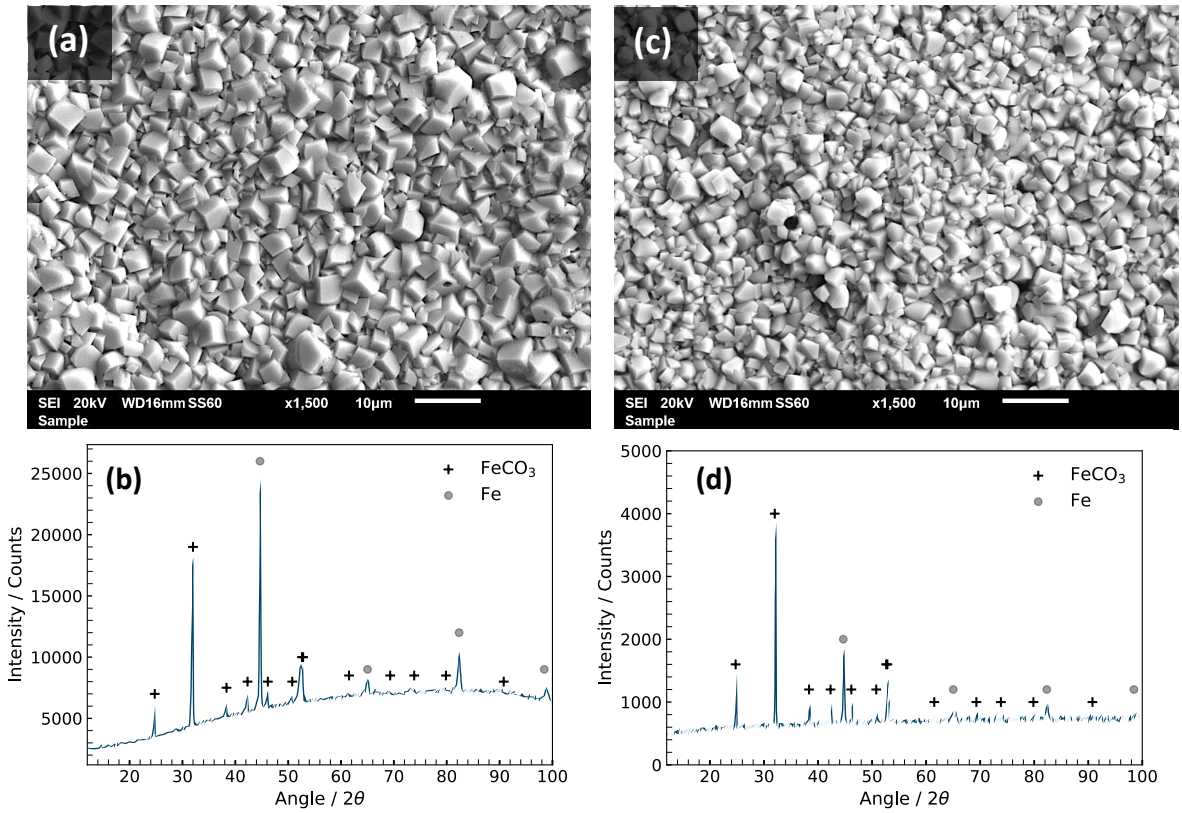



**Figure 8-9**: *Ex-situ* surface characterisation of CS coupon after pre-treatment in $MDEA_{(aq)}$. Pre-treatment solution: 1 M $MDEA_{(aq)}$ - $CO_2$ (pH 7.9) for *ca*. 116 h at 80 °C using **(a)** SEM, 1500x magnification and **(b)** XRD[34]; 3 M $MDEA_{(aq)}$ - $CO_2$ (pH 8.3) for *ca*. 189 h at 80 °C using **(c)** SEM, 1500x magnification and **(d)** XRD.

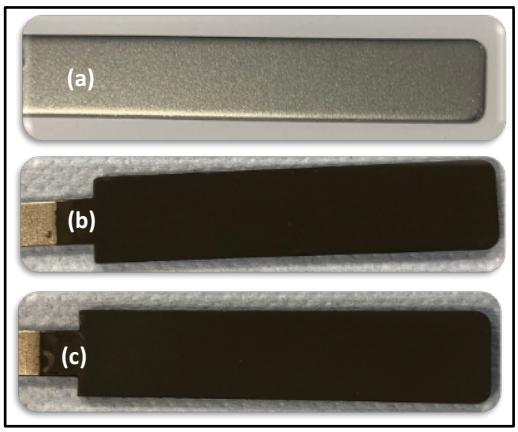



**Figure 8-10**: Photos of **(a)** pristine CS coupon, and CS coupon pre-treated in **(b)** 1 M $MDEA_{(aq)}$ solution saturated with $CO_2$ (pH 7.9) for *ca*. 116 h, and **(c)** 3 M $MDEA_{(aq)}$ solution saturated with $CO_2$ (pH 8.3) for *ca*. 189 h, both at 80 °C.

[34] A sample of the coupon pre-treated in 1 M $MDEA_{(aq)}$ solution saturated with $CO_2$ at 80 °C was cut manually using a hacksaw, resulting in the sample having jagged edges, which probably resulted in the uneven background of the XRD spectra.

### 8.3.2.3 Comparison of pre-treatment

CS coupons were pre-treated in 1 and 3 M $MDEA_{(aq)}$ solutions saturated with $CO_2$ at 80 °C. When both CS coupons were immersed initially, OCPs indicated that coupons were oxide free with the OCP of the coupon in the 3 M solution being -0.624 V, slightly lower than the potential of the coupon in the 1 M solution, which was -0.599 V. This is expected given that the 3 M solution pH was 8.3, slightly greater than for the 1 M solution, as was explained in Chapter 7, Section 7.2.1.

Initial EIS data recorded in both solutions at respective OCPs were modelled best with $EC_1$, indicating that a single interfacial process was operative on both coupons, and given that the coupons were freely accessible to the electrolytes, this process was thought to be Fe dissolution. The Nyquist plot showed that the diameter of the semicircle, which represents the electrode resistance to charge transfer, was larger in the 1 M solution than in the 3 M solution. From circuit fitting, it was confirmed that the initial charge transfer resistance of the coupon in the 1 M solution was *ca*. four times that measured in the 3 M solution, and the interfacial capacitance, indicative of the electroactive surface area of the coupon in the 3 M solution, was *ca*. four times that of the coupon in the 1 M solution. These circuit fitting values agreed with the deductions made from visual comparison of the EIS data collected when the coupons were immersed initially in both solutions. However, it is unexpected since the pH of the 3 M solution (8.3) was higher than that of the 1 M solution (7.9). The only explanation which could be offered is that there was a degree of variability of the coupon surfaces because they were not polished prior to immersion in the solution. Since the coupons were flat, rectangular samples of *ca*. 40 mm in length, and had a uniform glass bead finish, it was thought that manual polishing would result in an even less uniform surface. Furthermore, the steel used to make the pipelines and reactors in industry would likely not be polished, but used as received. The absence of this coupon preparation step was possibly responsible for the unexpected relative resistance of the coupons when immersed initially in the two electrolytes.

At the end of each pre-treatment process, electrically resistive surface films were produced on both coupons, with the film produced in 1 M solution being over four times as resistive and taking *ca*. 63 % less time to form than that in the 3 M solution. The dissolved Fe concentration in the 1 M solution was *ca*. half of that detected in the 3 M solution. This was reasonable since the initial charge transfer resistance in the 1 M solution was higher than that

in the 3 M solution, and the coupon was immersed for 73 h longer in the 3 M solution than the coupon immersed in the 1 M electrolyte. Based on the solution Fe concentrations, the $FeCO_3$ saturation ratio of the 3 M solution was calculated to be $3 \times 10^4$, higher than that estimated for the 1 M solution ($1 \times 10^4$), and far greater than that needed for $FeCO_3$ precipitation in both solutions. Although both solutions were conducive to $FeCO_3$ precipitation, and post surface characterisation using XRD detected only $FeCO_3$, OCPs at the end of the pre-treatment periods were indicative of the presence of (hydr-)oxide phases on both coupons. Therefore, both coupons were subject to exposure to dissolved $O_2$, which was thought to result in a mixed oxide-carbonate film at the electrode surface (**Figure 8-7**).

EIS fitting revealed that two different film structures were present on the CS coupons pre-treated using the two amine solutions. In the case of the 1 M, a more compact film was present and was modelled with $EC_3$ (**Figure 7-2**), which consisted of two time constants and one diffusion feature, whereas the film produced in 3 M electrolyte was best modelled using $EC_4$ (**Figure 8-6**), which was comprised of two RC loops with additional diffusion elements in both loops, indicative of a less compact film with variable crystal packing. The enhanced packing of the coating generated in the 1 M solution was consistent with the Fe concentration detected in the solutions, which was substantially smaller in the 1 M solution due to the improved protection provided the densely packed film.

### 8.3.2.4 Performance of pre-treated carbon steel coupons in the pilot plant

To determine if electrically resistive films were still present on the pre-treated coupons after immersion in the pilot plant for *ca*. 225 hours, and to determine the protection provided by the coating in the pilot plant solution, impedance spectra at the OCP of the retrieved coupons (**Figure 8-11**) were measured in an aliquot of the pilot plant solution and are presented in **Figure 8-12**.

Aliquots of the pilot plant solution were collected at the end of each study from the tap located below the filter (N200) (Chapter 3, **Figure 3-14**). The coupons were then dislodged from tapping points and gently wiped to remove any residual solution from the surface. From visual inspection (**Figure 8-11**) and comparison to images of coupons before immersion in the plant (**Figure 8-10b** - **c**), electrodes appeared still to be coated

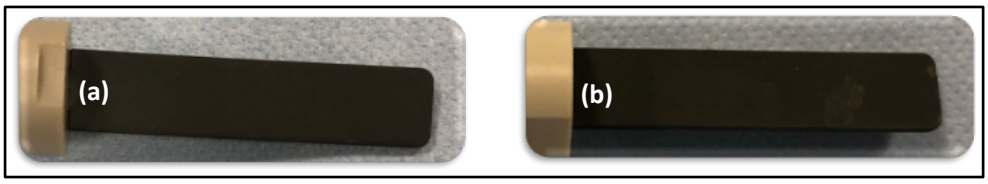



**Figure 8-11:** Pre-treated coupons after removal from pilot plant. **(a)** Pre-treated in 1 M $MDEA_{(aq)}$ and **(b)** Pre-treated in 3 M $MDEA_{(aq)}$.

250 mL of the collected aliquot was heated to 60 °C, the maximum temperature to which it was exposed in the pilot plant. Although the pH of the process fluid was 10 whilst in the plant, it would have been difficult to maintain a solution pH of 10, since $CO_2$ present in the solution would have been released upon heating the solution. Instead, it was decided that the coupon impedance should be collected in $CO_2$ saturated solutions since the coupons were intended to be tested in rich (*i.e*. saturated), hot conditions, representative of the environment experienced by the pipelines leading to the stripper. Each coated coupon was then immersed in the corresponding prepared solution, and the OCP was recorded and the impedance data at the OCP was measured.

#### 8.3.2.4.1 1 M $MDEA_{(aq)}$-$CO_2$ pre-treated coupon:

Upon immersion, the coupon, originally pre-treated in the 1 M solution, attained an OCP of +0.109 V (**Table 8-4**), suggesting that the coating was still present. This potential was more positive than the final average OCP of -0.12 V recorded in the pilot plant (**Figure 8-3b**). It is reasonable that the OCP of the electrode deviated from that measured in the pilot plant

because the solution temperature and saturation were different in the laboratory. Also, it is probable that the coupons re-oxidised between removal from the pilot plant and testing in the laboratory.

The post-pilot plant EIS data (pink) of the coupon pre-treated in the 1 M $MDEA_{(aq)}$ solution saturated with $CO_2$ is shown in **Figure 8-12a** - **d**; the EIS data measured at the beginning (brown) and end (blue) of the pre-treatment process were also included in the EIS plots. The pink Nyquist plots (**Figure 8-12a** - **b**) appeared to consist of two convoluted semicircles at high and intermediate frequencies and a diagonal line at *ca*. 45 °, at lower frequencies. The presence of two time constants was confirmed by the Bode representation of the phase angle (**Figure 8-12c**), where the higher frequency time constant, likely due to the coating, was measured at *ca*. $10^5$ Hz and, what is thought to be the charge transfer time constant, at *ca*. $10^3$ Hz, both of which are similar to the pre-treated coupons before installation in the pilot plant. The Bode representation of the impedance magnitude (**Figure 8-12d**) was notably greater than that measured on the uncoated coupon at all perturbation frequencies, demonstrating that the surface film endured exposure to the pilot plant solution and continued to provide protection to the underlying substrate. However, it was moderately smaller than that measured at the end of the pre-treatment process, indicating that some film degradation had occurred.

The measured EIS data was modelled best with $EC_3$ (**Figure 7-2**), the same circuit used to describe the EIS data measured at the end of the pre-treatment period. This indicated that there was no substantial change to the surface processes. The coating and charge transfer resistances (**Table 8-5**) were found to be 30 and 23 % smaller, respectively, after installation in the pilot plant. All three surface images (**Figure 8-13a** - **c**) of the coupon after the final EIS measurement indicate that a packed crystalline coating, confirmed by XRD (**Figure 8-14a**) to be $FeCO_3$, was still present on the surface. However, small film defects (*ca*. 10 μm) were observable (**Figure 8-13a**), as well as darkened spots on individual crystals (**Figure 8-13b**), which are thought to indicate the onset of crystal dissolution. Many miniature specs blanketed regions of crystals (**Figure 8-13c**), and were thought to be nascent $FeCO_3$ crystals, suggesting dissolution and re-precipitation of the coating and possibly an unstable film.

#### 8.3.2.4.2 3 M $MDEA_{(aq)}$ – $CO_2$ pre-treated coupon :

When the coupon pre-treated in 3 M $MDEA_{(aq)}$ solution saturated with $CO_2$ was immersed in the prepared pilot plant sample solution, the OCP was 0 V (**Table 8-4**). This was unexpected

since the OCP of this electrode decreased to -0.6 V in the pilot plant (**Figure 8-4b**), indicating that there was sufficient film dissolution to allow the electrolyte to access the underlying CS substrate easily. When the coupon was removed from the pilot plant, it is possible that the exposed underlying surface was oxidised in air, likely forming an oxide coating, thought to be superficial in nature. The post-pilot plant EIS data measured at the OCP (pink) is presented in (**Figure 8-12e** - **h**); the EIS data measured at the beginning (brown) and end (blue) of the pre-treatment process were also included in the EIS plots. The pink Nyquist plots (**Figure 8-12e** - **f**) appeared to consist of one semicircle suggesting the presence of a process with one time constant and a *ca*. 45 ° line, indicating a diffusion process. It was difficult to ascertain definitive features from visual inspection of **Figure 8-12g**. From visual inspection, there may be a time constant measured at frequencies between $10^4$ and $10^5$ Hz, which would be due to the coating. Another time constant, likely related to charge transfer, was recorded at *ca*. $10^{-1}$ Hz, but it was difficult to deduce whether the perceived inflection at $10^{-1}$ Hz was due to a RC process or due to a finite length diffusion process[35] (**Figure 8-12g**). Regardless of the surface features, the Bode representation of the ohmic resistance corrected impedance modulus (**Figure 8-12h**) of the pre-treated electrode was greater than that of the uncoated coupon at all measured frequencies, indicating that the coating continued to provide protection, contradicting the final OCP measured in the pilot plant (**Figure 8-4b**). However, the magnitude of the impedance was smaller than that of the coupon at the end of the pre-treatment process. Since the surface processes present were not obvious from visual inspection of the EIS data, $EC_1$, $EC_3$ and $EC_4$ were used to model the data. $EC_4$ gave the best fit, which was reasonable since this circuit was also used to model the EIS data measured at the end of the pre-treatment process. From the circuit fitting, it was found that the coating resistance minimally increased from $1 \times 10^{-3}$ Ω m$^2$ (**Table 8-3**) to $2 \times 10^{-3}$ Ω m$^2$(**Table 8-5**). This is unexpected and contrary to the data obtained from the Bode representation of the phase angle (**Figure 8-12g**). However, given that these resistances are exceedingly low, an order of magnitude lower than the initial charge transfer resistance, it is reasonable to consider these as equivalent. Further, the charge transfer resistance is the relevant metric for comparison given that the mechanism of protection of the coating is to

[35] Finite length diffusion processes are explained in Chapter 2, 0 and may be indicative of diffusion of electroactive species through a porous film (Orazem & Tribollet, 2008).

physically decrease the electroactive area, rather than to act as an electrical insulator. The charge transfer resistance was found to be $2 \times 10^{-2}$ Ω $m^2$ (**Table 8-5**), much lower than that of the coupon at the end of the pre-treatment process. This is consistent with the observations made from surface imaging (**Figure 8-13d** - **f**), which showed that a film of densely packed crystals was present in some areas (**Figure 8-13d**), confirmed by XRD to be $FeCO_3$ (**Figure 8-14b**), but more importantly, large areas (*ca*. 15 μm) were observable where the underlying substrate was clearly unprotected (**Figure 8-13e**) from the electrolyte, and amorphous material, possibly $Fe_2O_3$ or even $Fe(OH)_3$, was also visible in other sections (**Figure 8-13f**). This interpretation of the surface images agrees with the notable decrease in OCP in the pilot plant to -0.6 V and subsequent oxidation in air before the final EIS test.

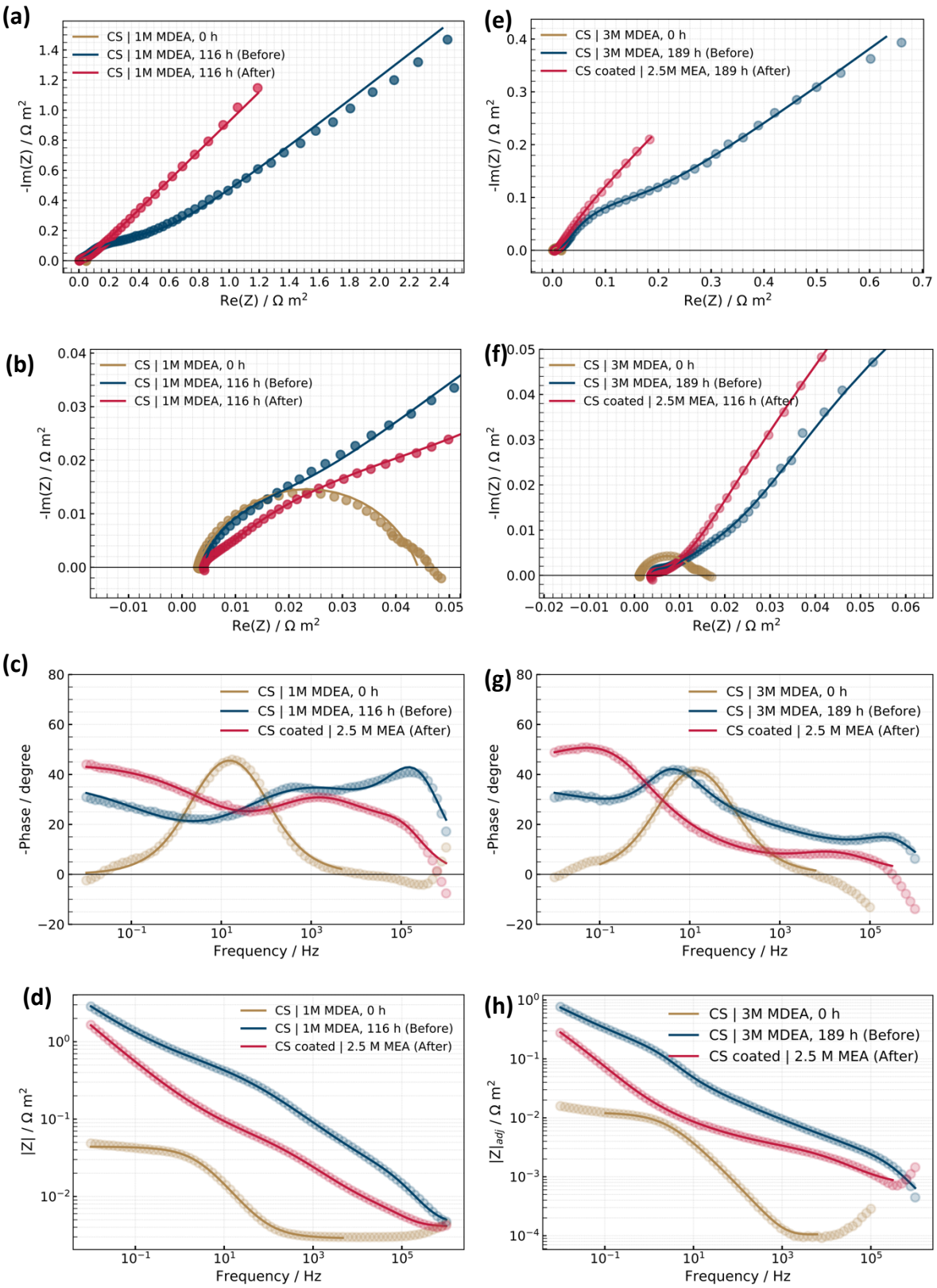



**Figure 8-12:** Experimental (o) and simulated (-) impedance data at OCP obtained with CS coupons, after removal from the pilot plant, **(a - b, e - f)** Nyquist representation and Bode representation of the **(c, g)** phase angle and **(d, h)** magnitude of the impedance, in sample of pilot plant solution, 2.5 M $MEA_{(aq)}$, saturated with $CO_2$ (pH 7.7) at 60 °C.

**Table 8-4:** Temperature corrected open circuit potential of pre-treated coupons in 2.5 M $MEA_{(aq)}$, saturated with $CO_2$ at 60 °C (pilot plant solution sample, pH *ca*. 7.7) after removal of coupons from the pilot plant.

| **Pre-treatment solution** | **OCP *vs*. $SHE_{25\,°C}$** |
|---|---|
| 1 M $MDEA_{(aq)}$ – $CO_2$ , 80 °C | +0.089 V |
| 3 M $MDEA_{(aq)}$ – $CO_2$ , 80 °C | -0.020 V |

**Table 8-5:** Normalised $EC_3$ and $EC_4$ component values used to model impedance data obtained with pre-treated CS coupons after removal from the pilot plant and immersed in sample of pilot plant solution 2.5 M $MEA_{(aq)}$, saturated with $CO_2$ (pH *ca*. 7.7) at 60 °C.

| **Pre-treatment solution** | $R_C$ / Ω m² | $Q_C$ / F $s^{\alpha-1}$ $m^{-2}$ | $R_{CT}$ / Ω m² | $Q_{DL}$ / F $s^{\alpha-1}$ $m^{-2}$ | $\frac{\chi^2}{\lvert Z \rvert}$ |
|---|---|---|---|---|---|
| **1 M $MDEA_{(aq)}$** | $3 \times 10^{-3}$ | $2 \times 10^{-3}$ | $7 \times 10^{-2}$ | $1 \times 10^{-1}$ | 0.01 |
| **3 M $MDEA_{(aq)}$** | $2 \times 10^{-3}$ | $3 \times 10^{-1}$ | $2 \times 10^{-2}$ | $3 \times 10^{1}$ | 0.04 |

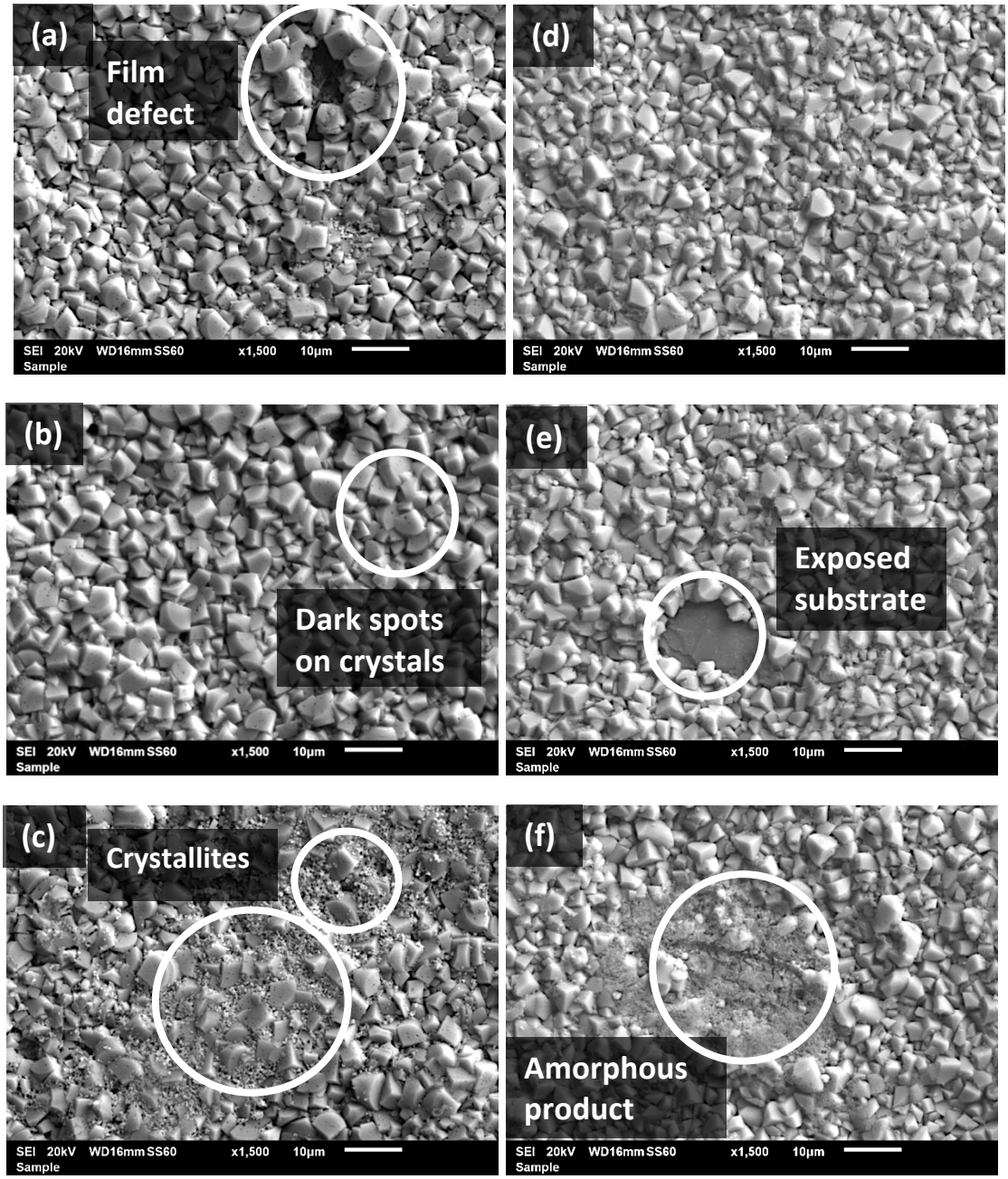



**Figure 8-13:** *Ex-situ* SEM images (at 1500x magnification) of coupons pre-treated in **(a - c)** 1 M $MDEA_{(aq)}$ and **(d - f)** 3 M $MDEA_{(aq)}$ solutions, after removal from the pilot plant and laboratory EIS measurements in 2.5 M $MEA_{(aq)}$, saturated with $CO_2$ at 60 °C.

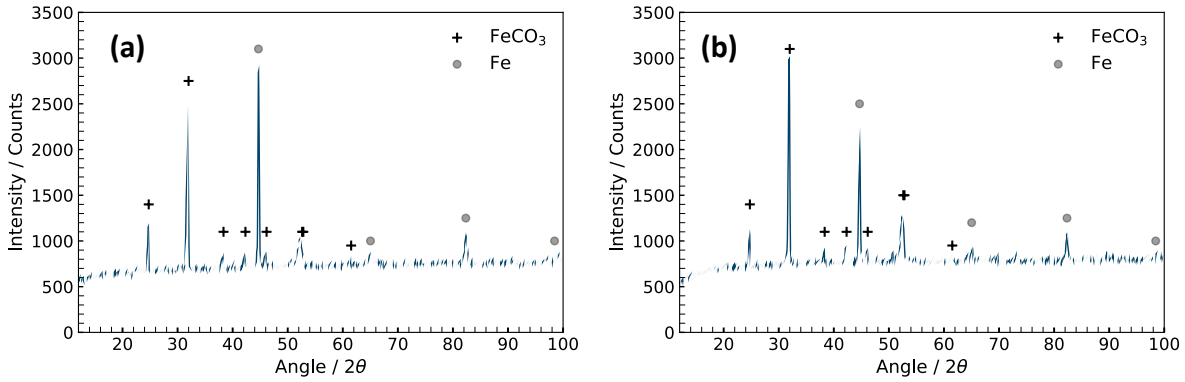



**Figure 8-14:** *Ex-situ* surface characterisation with XRD of coupons pre-treated in **(a)**1 M $MDEA_{(aq)}$ and **(b)** 3 M $MDEA_{(aq)}$ solutions, after removal from the pilot plant and laboratory EIS measurements in 2.5 M $MEA_{(aq)}$, saturated with $CO_2$ at 60 °C.

### 8.3.2.5 Untreated coupon

To compare the performance of the pre-treated coupons to the untreated coupons, both untreated coupons were retrieved form the pilot plant (**Figure 8-15a**) and the OCP and EIS at OCP were measured in the prepared aliquots of pilot plant solution (**Figure 8-16**). The untreated samples, used for each of the two pilot plant studies were nearly identical in appearance and exhibited the same impedance behaviour, so data corresponding to only one of the untreated samples is presented here.

There was no observable change of the electrode appearance (**Figure 8-15 a**) after removal from the pilot plant. When the electrode was immersed in the prepared solution, an OCP of -0.1 V was attained. This was only slightly more positive than the OCP of the electrode in the pilot plant, which was *ca*. -0.2 V (**Figure 8-2b**), and suggested the presence of $Fe_2O_3$ on the electrode surface.

Surprisingly, the measured EIS data demonstrated that the electrode impedance was relatively high; the Nyquist plot (**Figure 8-16a**) seemed to consist of one large semicircle, suggesting one electrode process. Only one time constant could be ascertained at *ca*. $10^0$ Hz from the Bode representation of the phase angle (**Figure 8-16c**), corroborating the presence of a single electrode process. Furthermore, from iterative circuit fitting it was found that the EIS data was best modelled with $EC_1$ with a resistance to charge transfer of $6 \times 10^0$ Ω $m^2$ (**Table 8-6**). Surface images (**Figure 8-19a - b**) were identical to that of a pristine coupon sample, included in the Appendix (Section 12.6, **Figure 12-29**), also confirming that there was no precipitation of protective product on the coupon surface during immersion in the pilot plant.

This EIS response of the untreated coupon previously installed in the pilot plant was unexpected, so after measuring the OCP and EIS data of the uncoated pilot plant-tested electrode, the electrode was removed from the solution, and a 'new' CS coupon, from the same batch of coupons as that installed in the pilot plant, was tested in the same solution. The immediate OCP of the 'new' CS coupon in the solution was +0.2 V but it steadily decreased to -0.18 V, then rapidly decreased to, and stabilised at -0.566 V (**Figure 8-17**). During this change in potential, small darkened spots, thought to be pits, formed on one face of the coupon, as shown in **Figure 8-15b**. Subsequent imaging with SEM were also difficult to interpret and did not necessarily show the presence of large pits, but a highly roughened surface (**Figure 8-19 d** - **e**). Regardless, the development of pits on CS was unexpected since corrosion of this type was not observed previously in any experiments conducted using carbon steel in $MEA_{(aq)}$ solutions. It was also verified that the reference electrode, which contains KCl, was not damaged and so no chloride ions were inadvertently released into the solution.

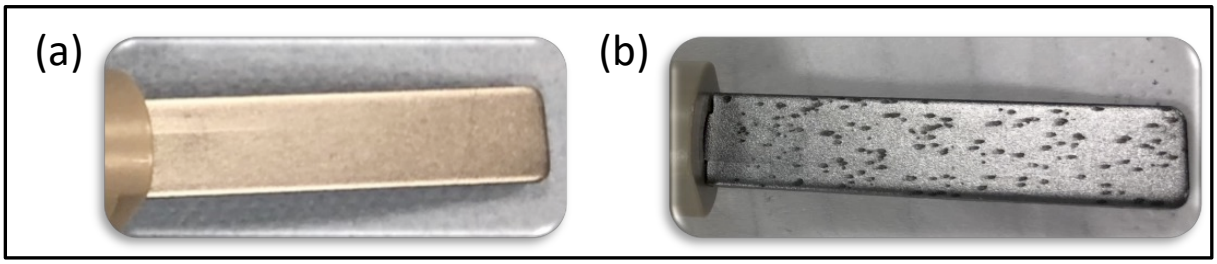



**Figure 8-15:** Untreated CS coupons **(a)** previously installed in pilot plant and **(b)** not exposed to pilot plant, both after EIS measurement in pilot plant solution sample 2.5 M $MEA_{(aq)}$, saturated with $CO_2$ (pH *ca*. 7.7) at 60 °C.

**Table 8-6:** Normalised $EC_1$ component values for impedance data obtained when a CS electrode was immersed in 2.5 M $MEA_{(aq)}$ saturated with $CO_2$ at 60 °C.

| CS coupon | $R_{CT}$ / Ω m² | $C_{DL}$ / F m⁻² | $\frac{\chi^2}{\lvert Z \rvert}$ |
|---|---|---|---|
| **Uncoated** | $6 \times 10^{0}$ | 4 | 0.06 |
| **New** | $2 \times 10^{-1}$ | 2 | 0.12 |

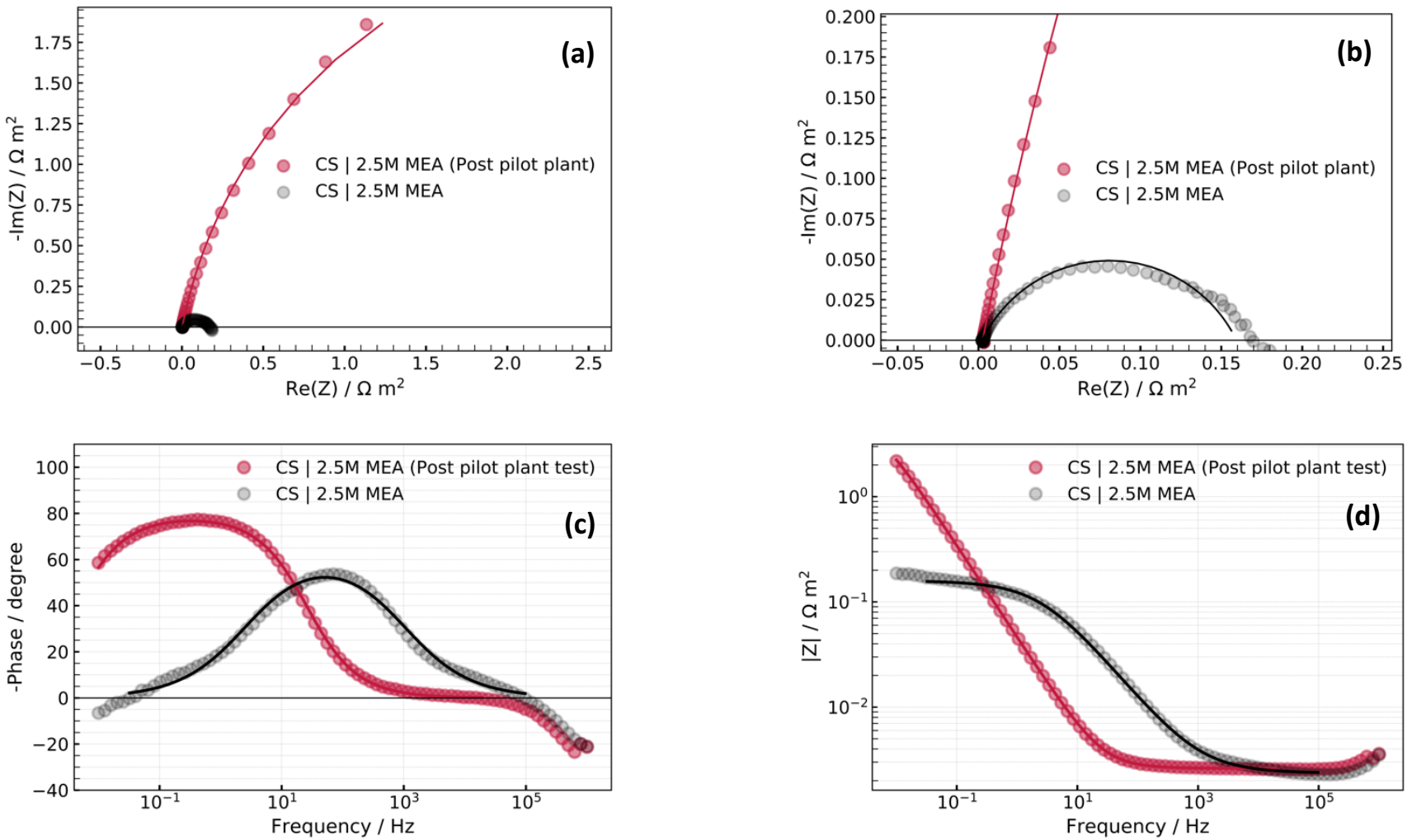



**Figure 8-16:** Experimental (o) and simulated (-) impedance data obtained with uncoated CS coupon after removal from pilot plant (pink) and with new CS coupon (black) in a sample of the pilot plant solution, 2.5 M $MEA_{(aq)}$, saturated with $CO_2$ (pH *ca*. 7.7) at 60 °C. **(a** - **b)** Nyquist representation and Bode representation of the **(c)** phase angle and **(d)** magnitude of impedance.

To further investigate the unexpected EIS behaviour exhibited by the untreated coupon previously installed in the pilot plant, and the pits developed on the 'new' CS coupon after immersion in the aliquot of pilot plant solution, the OCP behaviour of the coupon was examined more closely. The initial potential transient recorded when the 'new' coupon was immersed initially in the prepared aliquot of pilot plant solution was consistent with that observed when CS coupons were immersed initially in pre-treatment solutions (**Figure 8-17**). However, the time taken to attain a stable OCP varied. The OCP transients, which started at -0.2 V or more positive, suggested that the coupons may have been covered with thin oxide layers of the order of nanometres or localised oxide areas, which would not have been observable with low resolution surface imaging (**Figure 8-19**), nor detectable with XRD (**Figure 8-19c**). However, the oxide layers were broken down after immersion in the high temperature solutions; the oxide film on the coupons exposed to 80 °C broke down within 5 – 10 minutes, much faster than the coupon immersed in the 60 °C solution, which took just under 40 minutes to break down (**Figure 8-17**).

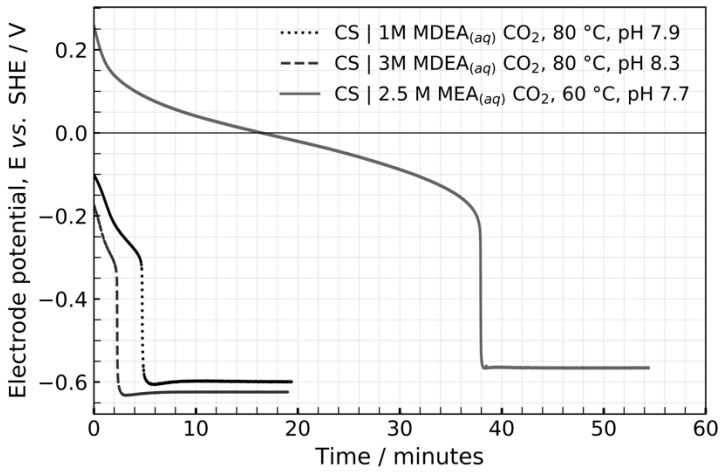



**Figure 8-17:** Open circuit potential transients of CS coupon immediately after immersion in aqueous amine solution saturated with $CO_2$.

It is probable that the surface of the 'new' CS coupon, was partially covered in an iron oxide ($Fe_2O_3$) film. Immersion in the aqueous amine solution may have resulted in oxidative dissolution of any uncovered Fe accelerated by reduction of neighbouring $Fe_2O_3$ and hence development of pits (**Figure 8-18**) as was observed in **Figure 8-15b**.

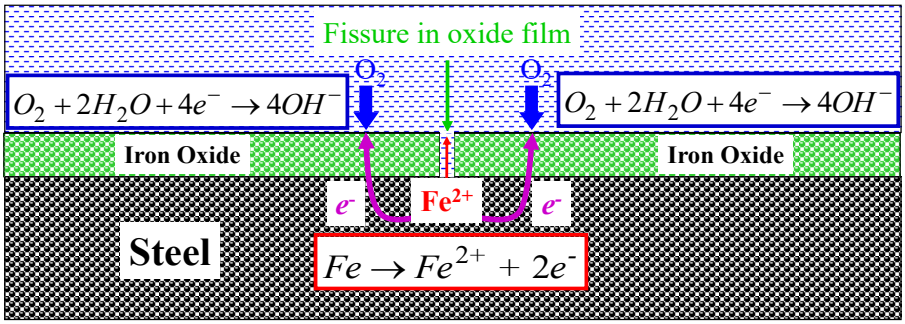



**Figure 8-18:** Schematic of formation of pits through breakdown of an iron oxide film, solution ingress and reductive dissolution of the oxide film.

The impedance of the 'new' CS coupon at -0.566 V confirmed that the bare coupon was not resistive to Fe dissolution. The black Nyquist plot (**Figure 8-16a** - **b**) consisted of one semicircle, suggesting the presence of one electrode process, and was corroborated by the Bode representation of the phase angle (**Figure 8-16c**) with only one process operative with a time constant at *ca*. $10^2$ Hz. Both sets of EIS data were modelled using $EC_1$, confirming that Fe dissolution was the only process occurring at the surface of the electrode. From **Figure 8-16d**, the overall resistance of the 'new' CS electrode, measured at low frequencies ($10^{-2}$ Hz) was *ca*. one order of magnitude less than that of the uncoated electrode, which was installed in the pilot plant. The circuit fitting values given in **Table 8-6** confirmed that the charge transfer resistance of the 'new' electrode was substantially lower than that of the uncoated electrode installed previously in the pilot plant. The interfacial capacitance of the surface, which is a measure of the electroactive area, was however 50 % less than that of the uncoated electrode.

The uncoated CS coupon installed in the pilot plant was exposed initially to low temperatures of *ca*. 20 °C for at least 24 h and subjected to temperatures > 50 °C for relatively short periods of time of *ca*. 3 h, and the pH of the pilot plant solution was *ca*. 10. Under these mild temperatures, the superficial oxide coating remained intact and provided protection to the underlying substrate. However, under normal operating conditions the carbon steel pipelines between the pre-heater and the stripper would be exposed to much higher temperatures of 80 - 120 °C and the $MEA_{(aq)}$ solvent would be saturated with $CO_2$ (pH *ca*. 7.5 – 8), depending on the amine concentration. The superficial oxide layer likely would dissolve, as demonstrated by the lab based experiments, leaving the bare carbon steel unprotected.

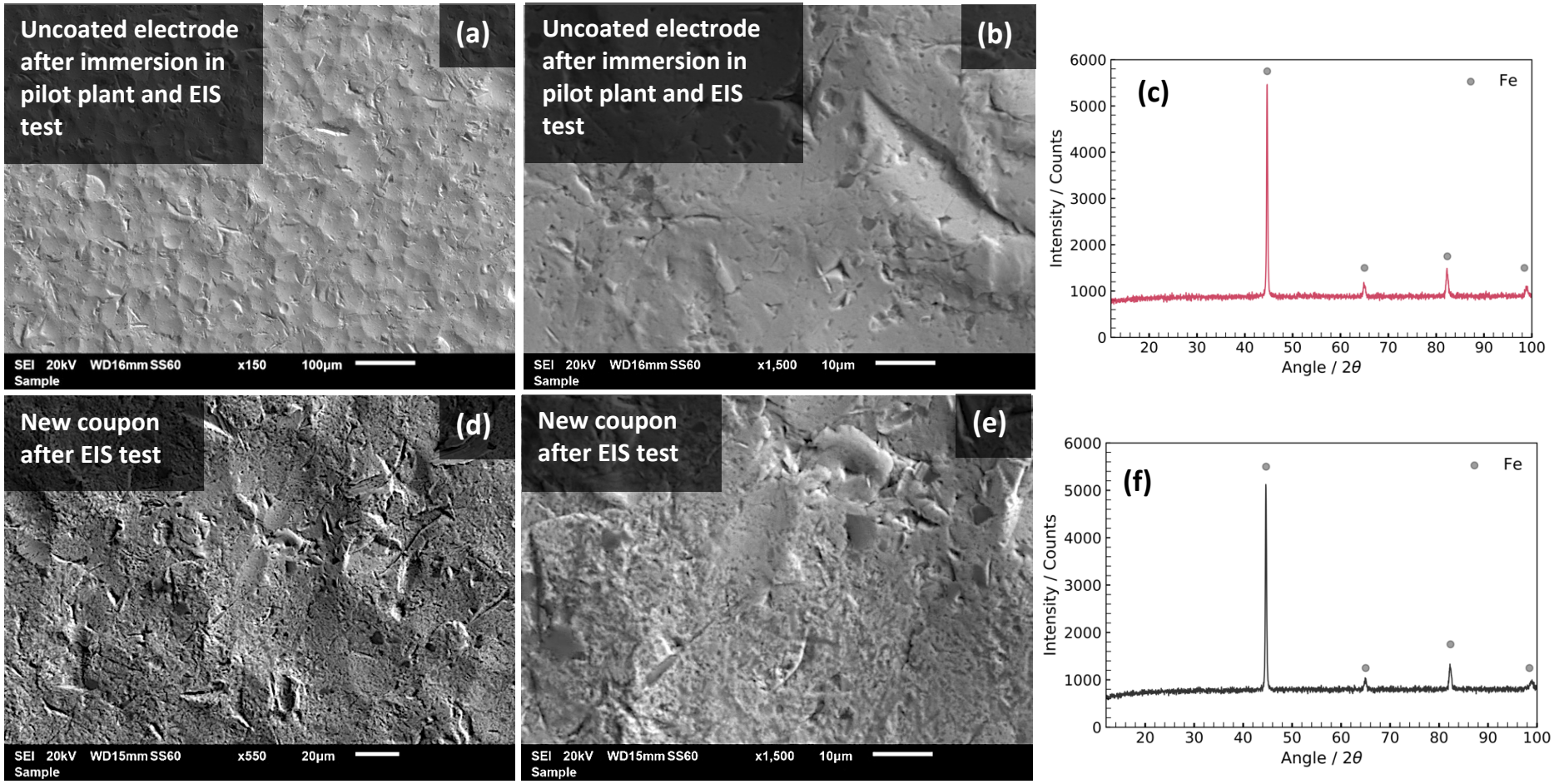



**Figure 8-19:** *Ex-situ* surface characterisation using SEM imaging of uncoated coupons **(a** - **b)** after removal from the pilot plant, and **(d – e)** not installed in the pilot plant, and XRD **(c)** after removal from the pilot plant and **(f)** not installed in the pilot plant, all after EIS measurement in sample of the pilot plant solution, 2.5 M $MEA_{(aq)}$, saturated with $CO_2$ (pH *ca*. 7.7) at 60 °C.

## 8.4 Conclusions

Pre-treatment of carbon steel, C1018, as a corrosion mitigation strategy, was assessed by conducting two studies in the Carbon Capture Pilot plant in the Department of Chemical Engineering, Imperial College London. The coupons were pre-treated at 80 °C and in $CO_2$ saturated solutions, conditions representative of pipelines between the heat exchanger and inlet of the stripper since these are conducive to $FeCO_3$ formation.

However, the tapping points in the plant were, located between the outlet of the heat exchanger and the inlet of the absorber. Ordinarily, unsaturated, cool (*i.e.* < 40 °C) process fluid would flow through these pipelines. To work around this, the plant was run in manual mode whereby the stripper was not heated to sufficiently high temperatures to allow for $CO_2$ desorption. The cooling water supply to the heat exchanger was also left off to ensure that the solution to which the coupons were exposed were as hot and saturated as possible. The pilot plant could be operated only on an intermittent basis when the operator was on site. With these limitations the performance of coatings were not evaluated under normal operational conditions, but instead under conditions typical of plant start-ups. Due to the limited number of tapping points pre-treated coupons were tested separately but the same operating protocols were followed for corresponding operational periods with minor inconsistencies between the two studies.

Protective films were formed on coupons pre-treated with 1 and 3 M $MDEA_{(aq)}$ solutions saturated with $CO_2$ at 80 °C. Open circuit potential measurements revealed that both coupons had been subject to exposure to dissolved $O_2$, which was difficult to avoid given the large electrode surface area to volume ratio of 3.9 $m^{-1}$. Contamination with $O_2$ likely led to the development of interspersed oxide based phase at the electrode | coating interface. Since the $FeCO_3$ saturation ratio of both the 1 M and 3 M electrolytes were exceedingly high, at $1.0 \times 10^4$ and $3 \times 10^4$ respectively, continued development of $FeCO_3$, which was confirmed by XRD, was not disrupted by $O_2$ contamination. The film formation rate was 63 % faster in the 1 M electrolyte than that in the 3 M electrolyte. Although the film formation rate was higher in the 1 M solution, the film formed in the 3 M solution was apparently thicker, but more importantly, was only 25 % as resistive as that formed in the 1 M electrolyte. The EIS data also demonstrated two different coating structures were present on the CS coupons pre-treated using the two amine solutions. The more compact coating, generated in 1 M $MDEA_{(aq)}$ solution, resulted in the presence of two processes with their respective times constants, and

one diffusion feature, whereas the less packed film formed in 3 M electrolyte resulted in the presence of two time constants and two diffusion features.

For each pilot plant study, a pre-treated CS coupon and an untreated CS coupon were installed in available tapping points for *ca*. 225 hours and the open circuit potentials, found previously to be a good indicator of film effectiveness, were measured continuously. The coupons were exposed to temperatures of up to 60 °C for a total of five hours and the solution pH remained at 10 ± 0.5 units. From the OCP data, the 1 M generated coating withstood the process conditions with an initial OCP of +0.06 V that decreased gradually to -0.12 V. The uncoated electrode potential followed a similar trend but exhibited a consistently more negative potential than the coated electrode, starting at -0.03 V and decreasing to -0.25 V. By contrast, the 3 M pre-treated coupon started at an OCP of +0.15 V, but at the end of the last operational period, the OCP decreased to -0.602 V, becoming more negative than the uncoated coupon, indicating that the film had broken down.

After removal from the pilot plant, the impedance of both pre-treated electrodes were tested in collected samples of pilot plant solution, heated to the maximum temperature (60 °C) to which each was exposed whilst in the plant, and saturated with $CO_2$. The EIS data indicated that both pre-treated coupons still maintained film coatings after removal from the pilot plant. This was consistent with the OCP data measured in the pilot plant of the coupon pre-treated in the 1 M solution. The electrical resistance after removal form the pilot plant was smaller than that before installation in the plant, and some minor defects were observed on the surface. This was promising since the conditions present in the pilot plant were likely to promote $FeCO_3$ dissolution. Based on the OCP measurements in the pilot plant of the coupon pre-treated in the 3 M solution, it is likely that the EIS data, which indicated a film was still intact, was due to oxidation of the exposed substrate and the film rather than the presence of the original film generated in the 3 M pre-treatment solution. This was substantiated with the SEM images, which showed relatively large areas (> 10 μm) of exposed substrate.

Lastly, the coupons used for this study were used as received and not polished. This resulted in some variability between coupons and would have affected the results. However, the EIS trends exhibited by pre-treated coatings were consistent with those presented in Chapter 7. Based on initial OCP measurements immediately after immersion in different aqueous solutions, uncoated coupons were seemingly coated with a thin oxide layer. This layer broke down when exposed to sufficiently high solution temperatures with the oxide film degradation occurring within 5 minutes when submerged in 80 °C solution, but around 40

minutes when exposed to 60 °C solution. The uncoated electrodes immersed in the pilot plant were exposed predominantly to lower temperatures of *ca*. 20 °C, which seemingly preserved the oxide coating. However, this would not have occurred if the coupons were exposed to typical operating temperatures.

Since the superior $FeCO_3$ film induced by 1 M $MDEA_{(aq)}$ solution saturated with $CO_2$ did in fact undergo some degradation from a relatively short exposure period to $MEA_{(aq)}$, and considering the immense damage which could ensue if there were non-uniform film disintegration, pre-treatment with MDEA cannot yet be recommended as a reliable corrosion mitigation strategy.

# 9 Conclusions

The aim of this project was to determine whether pre-treated carbon steel (C1018) could be used in place of stainless steel (SS 316 L) in the high temperature, $CO_2$ rich areas of the post combustion $CO_2$ capture plant. The proposed strategy involved pre-treating carbon steel through intermittent exposure to aqueous methyldiethanolamine ($MDEA_{(aq)}$) as the $CO_2$ capture solvent to induce the formation of an $FeCO_3$ film. The hypothesis was that this film would protect the underlying carbon steel substrate from corrosive attack by the primary $CO_2$ capture solvent aqueous monoethanolamine ($MEA_{(aq)}$). Elucidation of the divergent behaviour exhibited by carbon steel in $MEA_{(aq)}$ and $MDEA_{(aq)}$ solutions saturated with $CO_2$ was also an aim of this project.

Thermodynamic data available in the literature was used to calculate equilibrium chemical speciation of the $CO_2$ capture solvents. All thermodynamically feasible electrochemical reaction equilibrium equations for an iron-$CO_2$-$H_2O$ system were computed to generate potential-pH diagrams, providing thermodynamic predictions of the behaviour of such systems and aiding interpretation of experimental results. A range of electrochemical techniques and *ex-situ* surface characterisation analyses were conducted to investigate this system.

In Chapter 5, cyclic voltammetry experiments were used to compare the different electrochemical behaviour exhibited by iron, as a surrogate for carbon steel, in both amine solutions saturated with $CO_2$. Voltammograms measured in $MEA_{(aq)}$ solutions saturated with $CO_2$ consisted of three anodic reactions between -0.5 to -0.45 V, -0.4 to -0.2 V, and -0.1 to +0.1 V (*vs*. SHE), interpreted to be due to $Fe(OH)_2$, $FeCO_3$ and $Fe_2O_3$ formation, respectively. Voltammograms closely resembled those published in the literature for iron in alkaline carbonate solutions without amines present. Furthermore, voltammograms obtained with a Pt

electrode in $MEA_{(aq)}$ solutions confirmed the MEA species ($MEACOO^-$, $MEAH^+$) to be electro-inactive. In $MDEA_{(aq)}$ solutions, $FeCO_3$ formation was the most discernible oxidation reaction, especially at higher concentrations (5 M) within a potential range of -0.4 to -0.2 V. $Fe(OH)_2$ appeared to occur only if $H_2$ evolution was first instigated, causing localised pH increases. Minimal oxidation of $FeCO_3$ to $Fe_2O_3$ was apparent, suggesting that the $FeCO_3$ formed in $MDEA_{(aq)}$ solutions was less prone to oxidation. Cyclic voltammetry experiments therefore allowed verification that the amines were not electro-active and demonstrated that $FeCO_3$ oxidation was less likely in $MDEA_{(aq)}$ solutions. The first objective of this thesis, which was to establish the effect of amines on the electrochemical behaviour of carbon steel in $CO_2$ capture plants, was thus achieved.

In Chapter 6, the $FeCO_3$ formation reaction on rotating iron disc electrodes in aqueous amine solutions saturated with $CO_2$ was investigated using chronoamperometry and *ex-situ* surface characterisation including SEM-EDX and XRD. Firstly, the potential corresponding to $FeCO_3$ formation (*ca.* -0.4 V) in each solution was determined through cyclic voltammetry, and then applied to a rotating Fe disc electrode to determine the time dependence of the reaction kinetics at 80 °C. Current density transients implied the formation of a resistive surface film, causing current densities to decay to near zero currents, except for that measured in the 5 M $MEA_{(aq)}$ solution. The calculated $FeCO_3$ saturation ratios in the bulk, determined from the current density transients, were $\gg$ 1 in all solutions, suggesting conditions were conducive to film formation. Product formation was confirmed, by *ex-situ* surface imaging, to have occurred on all electrodes in $MDEA_{(aq)}$ solutions and in the 1 M $MEA_{(aq)}$ solution. Although the bulk $FeCO_3$ saturation ratio was estimated to be the highest in the 5 M $MEA_{(aq)}$ solution (> 500), no trace of $FeCO_3$ was observed on the electrode tested in this solution. A simple diffusion-reaction model involving $Fe^{2+}$, $HCO_3^-$ and $H^+$ ions was constructed to estimate local concentrations of each species and was based on the Nernst-Planck equation incorporating convective transport and $FeCO_3$ formation kinetics. The flux of $Fe^{2+}$ ions away from the electrode was determined from the current density transient recorded in the 5 M $MEA_{(aq)}$ solution.

The $FeCO_3$ formation reaction was modelled using the reaction shown below, with $HCO_3^-$ ions as the source of $CO_3^{2-}$ ions, resulting in the release of $H^+$ ions. This reaction was modelled instead of the direct reaction between $Fe^{2+}$ and $CO_3^{2-}$ since at mildly alkaline conditions of amine solutions saturated with $CO_2$ (pHs of 7.7 – 8.6), dissolved '$CO_2$' exists predominantly as $HCO_3^-$; $Fe^{2+}$ and $CO_3^{2-}$ ions do not co-exist as predominant species at any

pH. The $FeCO_3$ saturation ratio at the electrode surface was then determined from the accumulated $Fe^{2+}$ concentration predicted from the model, and the $CO_3^{2-}$ concentration, calculated based on the solution pH and $HCO_3^-$ concentration estimated by the model.

$$FeCO_{3(c)} + H^+_{(aq)} + 2e^- \rightleftharpoons Fe_{(s)} + HCO^-_{3\,(aq)}$$

The model estimated that the local pH would have decreased by over 4 units within 1000 seconds, which would correspond to a saturation ratio of 0.01, creating conditions unfavourable for $FeCO_3$ precipitation. The substantial pH and saturation ratio changes were overestimated since the chemical equilibrium between $HCO_3^-$ and $CO_3^{2-}$, or any other homogenous reactions except for $FeCO_3$ formation, was not successfully incorporated into the model. Based on the experimental confirmation that $FeCO_3$ formed in all $MDEA_{(aq)}$ solutions, it is proposed that $MDEA_{(aq)}$ solutions were effective buffers and so would prevent substantial local pH changes, and, in part, explain the enhanced $FeCO_3$ stability in $MDEA_{(aq)}$ solutions. Since the $pK_a$ of $MDEA_{(aq)}$ is *ca*. 7.7, and its solution pH when saturated with $CO_2$ is either equal to or above this, it optimally consumes the $H^+$ ions released. Furthermore, the higher solution pH than $MEA_{(aq)}$ solutions, at a given concentration, also indicates a higher $CO_3^{2-}$ concentration, which will also act to impede pH change by forming $HCO_3^-$. Accordingly, a buffering mechanism is thought to contribute to the formation of stable $FeCO_3$ surface films in $MDEA_{(aq)}$ solutions saturated with $CO_2$. The second objective of this thesis, which was to hypothesise a mechanism for $FeCO_3$ formation and dissolution in $CO_2$ saturated $MEA_{(aq)}$ and $MDEA_{(aq)}$ solutions, was thus achieved.

Although pre-treatment of carbon steel in $MDEA_{(aq)}$ solutions to form $FeCO_3$ films has been proposed in the literature as a corrosion mitigation strategy for PCCC plants, the protection of the $FeCO_3$ film had not been confirmed previously in amine solutions. Electrochemical impedance spectroscopy was used to determine if $FeCO_3$ films on carbon steel in $MDEA_{(aq)}$ solutions provided protection to the underlying substrate, and to determine the time and concentration for optimal film formation. Based on extracted resistance values from circuit fitting of measured impedance spectra, it was demonstrated that $FeCO_3$ films did in fact provide protection with the resistance to charge transfer increasing by two orders of magnitude after 72 hours of exposure to dilute (1 M) $MDEA_{(aq)}$ $CO_2$ saturated solutions. Film formation times were found to increase as MDEA concentration increased, with a pre-treatment period of 72 hours needed in the 1 M, 96 hours in the 3 M, and 156 hours in the 5 M solution for an electrode surface area to electrolyte volume ratio of 0.076 $m^{-1}$. The film

formed in the 1 M $MDEA_{(aq)}$ pre-treatment solution was also found to consist of *ca*. 1 μm crystals that were packed tightly together. The compact crystalline layer was thought to result in the high resistivity, with a charge transfer resistance of up to 3.5 times that formed in the other $MDEA_{(aq)}$ solutions. It is also highlighted that film density is more crucial than film thickness, as deduced from XRD data where thicker, but less protective films formed in the more concentrated 3 and 5 M solutions. Since the resistance to charge transfer was reported to be demonstrably greater than the film resistance, by at least an order of magnitude, it is proposed that the film provided a physical diffusion barrier, decreasing the electroactive area, rather than acting as an electrical insulator. Stability tests were also conducted in which each pre-treated film was transferred directly from the $MDEA_{(aq)}$ solution to a 5 M $MEA_{(aq)}$ solution. It was determined that the films formed in the concentrated $MDEA_{(aq)}$ solutions (3 and 5 M) were minimally or no longer protective after one week of exposure to the $MEA_{(aq)}$ solution relative to an untreated electrode. By contrast, the film formed in the 1 M solution was demonstrated to be stable and provided protection to the underlying substrate, with the charge transfer resistance calculated to be an order of magnitude higher than that of the untreated carbon steel. Although the film resistance decreased after initial transfer to an $MEA_{(aq)}$ solution, it stabilised showing little change between one day and one week of immersion in the $MEA_{(aq)}$ solution. Therefore, 1 M $MDEA_{(aq)}$ solution saturated with $CO_2$ is proposed to be the optimal pre-treatment solution from the solutions tested to generate a resistive $FeCO_3$ film that was stable in $MEA_{(aq)}$ solution saturated with $CO_2$; hence the third objective was achieved.

The impact of $O_2$ was demonstrated to be detrimental to the development of a dense protective $FeCO_3$ film and an $O_2$ contaminated film was found to be unstable in the $MEA_{(aq)}$ solution. Adventitious ingress of $O_2$ was proposed to have resulted in the formation of trace amounts of iron oxide that were undetectable by XRD, but were ascertained by OCP values increasing from *ca*. -0.5 to -0.1 V, at which $Fe_2O_3$ is the most thermodynamically stable phase. The EIS data indicated that the modulus of the impedance at low frequencies increased by an order of magnitude, when the oxide-carbonate film formed but when the specimen was transferred to the $MEA_{(aq)}$ solution, the OCP immediately decreased to that representative of an uncoated electrode (*ca*. -0.6 V) and, more importantly, the resistance decreased to below that of an uncoated sample. Surface images provided evidence for accelerated attack, revealing a highly roughened substrate, possibly with pits. It is proposed that the presence of adventitious $O_2$ resulted in the formation of porous iron oxide at the electrode surface, which

may have been responsible for the non-uniform oxidative dissolution of the underlying substrate.

To test the performance of the pre-treated coupons, these, together with untreated carbon steel coupons were installed in the $CO_2$ capture pilot plant in the Department of Chemical Engineering, Imperial College London, which uses 2.5 M $MEA_{(aq)}$ as the solvent. Electrode holders were designed and fabricated in-house to enable continuous *in-situ* OCP measurements of pre-treated and untreated electrodes. The use of this pre-treatment strategy was intended for hot (80 °C), $CO_2$ rich sections of the plant, specifically between the heat exchanger and the inlet of the stripper. Unfortunately, there were no tapping points available in that section of the pilot plant. Instead, installation points were available between the heat exchanger and the inlet of the absorber. In an attempt to test the electrodes under the intended conditions, the pilot plant was operated manually, such that the temperature in the stripper was kept below 120 °C, to decrease $CO_2$ stripping, and the cooling water sources to any heat exchangers were not turned on. This allowed the electrodes to be exposed intermittently to temperatures up to 60 °C and pH *ca*. 10; the required conditions being 80 °C and pH 7.7. Furthermore, the plant could only be operated for short periods of time so the total immersion period was *ca*. 225 hours, but cumulative operational hours *ca*. 10. Coupons pre-treated in 1 and 3 M $MDEA_{(aq)}$ solutions prepared in the lab, were unavoidably $O_2$ contaminated because of the large surface area to volume ratio (3.9 $m^{-1}$) and vertical orientation of the coupon in the vessel even though the solutions were deaerated with $N_2$ followed by $CO_2$ prior to starting pre-treatment and $CO_2$ was continuously bubbled through the solution for the duration of the pre-treatment process. Large coupon surface area to solution volume ratio was reported in the literature to enhance $FeCO_3$ formation, due to the expected high $Fe^{2+}$ concentrations resulting from initial dissolution of Fe. Indeed, this was found to be so, from the substantial saturation ratios of *ca*. $10^4$ based on measured $Fe^{II}$ concentration in solution, and hence $FeCO_3$ was still formed even though the surface was $O_2$ contaminated. The film generated in the 1 M $MDEA_{(aq)}$ solution was found to be four times as resistive as that formed in the 3 M $MDEA_{(aq)}$ solution. The OCP of the coupon with the film generated in the 1 M solution was far less negative than that expected for an uncoated coupon (*ca*. -0.6 V), whilst near the end of the pilot plant study, the OCP of the coupon pre-treated in the 3 M solution decreased to -0.6 V, suggesting that the film had broken down. Subsequent EIS measurements demonstrated that the coating produced in the 1 M solution remained intact but the resistance to charge transfer decreased by 23 %, though surface images showed little film degradation. The resistance

provided by the film produced in 3 M solution was found to decrease by 29 % after removal from the pilot plant and surface imaging revealed that the film, though still mostly intact, was detached over areas > 10 μm. This was sufficient to allow exposure of the underlying substrate to the electrolyte, and hence enable oxidative dissolution of Fe and reductive dissolution of $FeCO_3$.

Based on the observed film disintegration after relatively short exposure periods to the $MEA_{(aq)}$ solution in the pilot plant study, and considering the possibility of the feed gas containing residual $O_2$, use of pre-treatment as a corrosion mitigation strategy cannot yet be recommended. However, it is worth noting that if non-$O_2$ contaminated films were to be produced, then the film stabilities, specifically those generated from 1 M solutions, would likely be higher as was demonstrated in the lab-scale experiments. Furthermore, the pre-treated coupons were exposed to low temperature, $CO_2$ lean conditions, both of which are not conducive to $FeCO_3$ stability. The results reported from the pilot plant study therefore likely underestimated the performance of the pre-treated electrodes.

# 10 Future work proposal

Although methyldiethanolamine has been used for natural gas sweetening, the low pressures (1 atm) used within the post combustion $CO_2$ capture plant, as well as the required high production rates for PCCC need to be considered to determine if the use of methyldiethanolamine, as an intermittent $CO_2$ capture solvent for post combustion $CO_2$ capture, is feasible.

A spectro-electrochemical flow cell was designed to conduct surface and solution characterisation using Raman spectroscopy along with electrochemical measurements. However, this cell could not be used since the Raman spectrophotometer was no longer available. Using this cell, the onset of $FeCO_3$ precipitation and subsequent dissolution due to local solution pH decrease during potentiostatic experiments could be confirmed. The formation of a ferrous-monoethanolamine carbamate complex has been proposed in the literature (Shimizu, Hirano & Tomoe, 2016), to decrease the available $Fe^{II}$ concentration in solution for $FeCO_3$ formation, thus explaining the preferential formation and stability of $FeCO_3$ in methyldiethanolamine, which does not form carbamate upon $CO_2$ capture. Detection of such a complex, if present, was unsuccessful in this work because of the rapid oxidation of $Fe^{II}$ upon sampling for analysis using UV-Vis spectroscopy, even when bubbling high purity $N_2$ through the UV-Vis cuvette. Although the buffering effect of methyldiethanolamine has been proposed in this thesis to be responsible (in part) for the superior stability of $FeCO_3$ in these solutions, the complex formation hypothesis may also be true. *In-situ* UV-Vis spectroscopy will need to be used to accomplish this.

Lastly, the diffusion reaction model presented in Chapter 6 should be extended to incorporate homogeneous reactions, specifically $CO_2$ - $H_2O$ equilibrium, and amine protonation reactions to produce more accurate local concentration profiles due to $FeCO_3$ formation.

# 11 References


1. Administration, U.S.E.I. (2021) *Carbon dioxide produced when different fuels are burned*. [Online]. June 2021. Carbon dioxide produced when different fuels are burned. Available from: https://www.eia.gov/tools/faqs/faq.php?id=73&t=11.
2. Amirudin, A. & Thierry, D. (1995) Application of electrochemical impedance spectroscopy to study the degradation of polymer-coated metals. *Progress in Organic Coatings*. [Online] 26 (1), 1–28. Available from: doi:10.1016/0300-9440(95)00581-1.
3. Amjad, M., Sumrra, S.H., Akram, M.S. & Chohan, Z.H. (2016) Metal-based ethanolamine-derived compounds: a note on their synthesis, characterization and bioactivity. *Journal of Enzyme Inhibition and Medicinal Chemistry*. [Online] 31 (sup4), 1–10. Available from: doi:10.1080/14756366.2016.1220375.
4. Amundsen, T.G., Øi, L.E. & Eimer, D.A. (2009) Density and Viscosity of Monoethanolamine + Water + Carbon Dioxide from (25 to 80) °C. *Journal of Chemical & Engineering Data*. [Online] 54 (11), 3096–3100. Available from: doi:10.1021/je900188m.
5. Azoulay, I., Rémazeilles, C. & Refait, Ph. (2012) Determination of standard Gibbs free energy of formation of chukanovite and Pourbaix diagrams of iron in carbonated media. *Corrosion Science*. [Online] 58, 229–236. Available from: doi:10.1016/j.corsci.2012.01.033.
6. Barbosa, P.F., Lagoeiro, L., Scholz, R., Graça, L.M., et al. (2015) Magnetite-hematite transformation: correlation between natural and synthetic features. *Mineralogy and Petrology*. [Online] 109 (3), 329–337. Available from: doi:10.1007/s00710-014-0340-8.
7. Bard, A.J. & Faulkner, L.R. (2001) *Electrochemical Methods: Fundamentals and Applications*. 2nd edition. University of Texas, John Wiley & Sons, Inc.
8. Bard, A.J., Parsons, R., Jordan, J. & Parsons, R. (1985) *Standard Potentials in Aqueous Solution*. Monographs in electroanalytical chemistry and electrochemistry. [Online]. New York : Marcel Dekker. Available from: doi:10.1201/9780203738764-1.

9. Barker, R., Shaaili, I.A., Motte, R.A.D., Burkle, D., et al. (2019) Iron carbonate formation kinetics onto corroding and pre-filmed carbon steel surfaces in carbon dioxide corrosion environments. *Applied Surface Science*. [Online] 469, 135–145. Available from: doi:10.1016/j.apsusc.2018.10.238.
10. Bénézeth, P., Dandurand, J.L. & Harrichoury, J.C. (2009) Solubility product of siderite (FeCO3) as a function of temperature (25–250 °C). *Chemical Geology*. [Online] 265 (1–2), 3–12. Available from: doi:10.1016/j.chemgeo.2009.03.015.
11. Bockris, J.O. (2000) *Modern electrochemistry. 2B, Electrodics in chemistry, engineering, biology, and environmental science*. 2nd edition. New York, Plenum Publishing Corporation.
12. Bockris, J.O. & Drazic, D. (1962) The kinetics of deposition and dissolution of iron: Effect of alloying impurities. *Electrochimica Acta*. [Online] 7 (3), 293–313. Available from: doi:10.1016/0013-4686(62)87007-8.
13. Bockris, J.O., Drazic, D. & Despic, A.R. (1961) The electrode kinetics of the deposition and dissolution of iron. *Electrochimica Acta*. [Online] 4 (2–4), 325–361. Available from: doi:10.1016/0013-4686(61)80026-1.
14. Bockris, J.O., Reddy, A.K.N. & Gamboa-Aldeco, M. (2002) *Modern Electrochemistry 2A, Fundamentals of Electrodics*. [Online] Available from: doi:10.1007/b113922.
15. Brandes, E.A. & Brook, G.B. (1998) *Smithells Metals Reference Book*. Elsevier Science & Technology.
16. Braun, R.D. (1991) Solubility of iron(II) carbonate at temperatures between 30 and 80°. *Talanta*. [Online] 38 (2), 205–211. Available from: doi:10.1016/0039-9140(91)80131-i.
17. Bui, M., Adjiman, C.S., Bardow, A., Anthony, E.J., et al. (2018) Carbon capture and storage (CCS): the way forward. *Energy & Environmental Science*. [Online] 11 (5), 1062–1176. Available from: doi:10.1039/c7ee02342a.
18. Burkle, D., Motte, R.D., Taleb, W., Kleppe, A., et al. (2017) In situ SR-XRD study of FeCO3 precipitation kinetics onto carbon steel in CO2-containing environments: The influence of brine pH. *Electrochimica Acta*. [Online] 255, 127–144. Available from: doi:10.1016/j.electacta.2017.09.138.
19. Burkle, D.P. (2017) *Understanding the Formation of Protective FeCO3 on to Carbon Steel Pipelines during CO2 Corrosion*.

20. Campbell, K.L.S., Yu, L.C.Y. & Williams, D.R. (2017a) Siderite corrosion protection for carbon steel infrastructure in post-combustion capture plants. *International Journal of Greenhouse Gas Control*. [Online] 58, 232–245. Available from: doi:10.1016/j.ijggc.2017.01.018.
21. Campbell, K.L.S., Yu, L.C.Y. & Williams, D.R. (2017b) Using Pre-treated Carbon Steel for Post-combustion Carbon Capture Infrastructure. *Energy Procedia*. [Online] 114, 1991–1997. Available from: doi:10.1016/j.egypro.2017.03.1333.
22. Campbell, K.L.S., Zhao, Y., Hall, J.J. & Williams, D.R. (2016) The effect of CO2-loaded amine solvents on the corrosion of a carbon steel stripper. *International Journal of Greenhouse Gas Control*. [Online] 47, 376–385. Available from: doi:10.1016/j.ijggc.2016.02.011.
23. Castro, E.B., Valentini, C.R., Moina, C.A., Vilche, J.R., et al. (1986) The influence of ionic composition on the electrodissolution and passivation of iron electrodes in potassium carbonate-bicarbonate solutions in the 8.4–10.5 pH range at 25°C. *Corrosion Science*. [Online] 26 (10), 781–793. Available from: doi:10.1016/0010-938x(86)90063-6.
24. Castro, E.B. & Vilche, J.R. (1991) Electrooxidation/electroreduction processes at composite iron hydroxide layers in carbonate-bicarbonate buffers. *Journal of Applied Electrochemistry*. [Online] 21 (6), 543–551. Available from: doi:10.1007/bf01018608.
25. Castro, E.B., Vilche, J.R. & Arvia, A.J. (1991) Iron dissolution and passivation in K2CO3-KHCO3 solutions. rotating ring disc electrode and XPS studies. *Corrosion Science*. [Online] 32 (1), 37–50. Available from: doi:10.1016/0010-938x(91)90062-t.
26. Chokshi, K., Sun, W. & Nešić, S. (2005) Iron carbonate scale growth and the effect on inhibition in CO2 corrosion of mild steel. In: *Corrosion 2005*. 2005 Texas, NACE Corrosion. p.
27. Crolet, J.L., Thevenot, N. & Nešić, S. (1998) Role of Conductive Corrosion Products in the Protectiveness of Corrosion Layers. *Corrosion*. [Online] 54 (3), 194–203. Available from: doi:10.5006/1.3284844.
28. Davies, D.H. & Burstein, G.T. (1980) The Effects of Bicarbonate on the Corrosion and Passivation of Iron. *Corrosion*. [Online] 36 (8), 416–422. Available from: doi:10.5006/0010-9312-36.8.416.

29. deWaard, C. & Milliams, D.E. (1975) Carbonic Acid Corrosion of Steel. *Corrosion*. [Online] 31 (5), 177–181. Available from: doi:10.5006/0010-9312-31.5.177.
30. Dražić, D.M. (1989) Modern Aspects of Electrochemistry. In: B. E. Conway, J. O'M. Bockris, & R. E. White (eds.). *Iron and its electrochemistry in an active state*. [Online]. New York, Plenum Press. p. Available from: doi:10.1007/978-1-4684-8667–4.
31. Dražić, D.M. & Hao, C.S. (1982) The anodic dissolution process on active iron in alkaline solutions. *Electrochimica Acta*. [Online] 27 (10), 1409–1415. Available from: doi:10.1016/0013-4686(82)80031-5.
32. Dugstad, A. (1998) *Mechanism of protective film formation during CO2 corrosion of carbon steel*. In: [Online]. 1998 San Diego, CA. p. Available from: https://onepetro.org/NACECORR/proceedings-abstract/CORR98/All-CORR98/NACE-98031/127616.
33. DuPart, M.S., Bacon, T.R. & Edwards, D.J. (1993a) Understanding corrosion in alkanolamine gas treating plants: Part 1. *Hydrocarbon Processing*. 72 (4).
34. DuPart, M.S., Bacon, T.R. & Edwards, D.J. (1993b) Understanding corrosion in alkanolamine gas treating plants: Part 2. *Hydrocarbon Processing*. 72 (5).
35. Farelas, F., Brown, B. & Nešić, S. (2013) Iron Carbide and its Influence on the Formation of Protective Iron Carbonate in CO2 Corrosion of Mild Steel. In: *CORROSION 2013*. [Online]. 2013 Orlando, FL. p. Available from: https://onepetro.org/NACECORR/proceedings-abstract/CORR13/All-CORR13/NACE-2013-2291/121443.
36. Farelas, F., Galicia, M., Brown, B., Nešić, S., et al. (2010) Evolution of dissolution processes at the interface of carbon steel corroding in a CO2 environment studied by EIS. *Corrosion Science*. [Online] 52 (2), 509–517. Available from: doi:10.1016/j.corsci.2009.10.007.
37. Fernandes, D., Conway, W., Wang, X., Burns, R., et al. (2012) Protonation constants and thermodynamic properties of amines for post combustion capture of CO2. *The Journal of Chemical Thermodynamics*. [Online] 51, 97–102. Available from: doi:10.1016/j.jct.2012.02.031.
38. Fisher, A.C. (1996) *Electrode dynamics*. Oxford chemistry primers 34. New York, Oxford University Press.

39. Fontana, M.G. (1986) *Corrosion engineering*. McGraw-Hill series in materials science and engineering. 3rd edition. New York, McGraw-Hill.
40. Fosbøl, P.L., Thomsen, K. & Stenby, E.H. (2013) Review and recommended thermodynamic properties of FeCO3. *Corrosion Engineering, Science and Technology*. [Online] 45 (2), 115–135. Available from: doi:10.1179/174327808x286437.
41. Gao, M., Pang, X. & Gao, K. (2011) The growth mechanism of CO2 corrosion product films. *Corrosion Science*. [Online] 53 (2), 557–568. Available from: doi:10.1016/j.corsci.2010.09.060.
42. Garside, J. (1985) Industrial crystallization from solution. *Chemical Engineering Science*. [Online] 40 (1), 3–26. Available from: doi:10.1016/0009-2509(85)85043-0.
43. Gray, L.G., Anderson, S., Danysh, B.G. & Tremaine, M.J. (1990) Effect of pH and temperature on the mechanism of carbon steel corrosion by aqueous carbon dioxide. In: *CORROSION 90*. 1990 Las Vegas, NV. p.
44. Green, D.W. & Perry, R.H. (2008) Perry's Chemical Engineers' Handbook. In: *Physical and Chemical Data*. 8th edition. [Online]. McGraw-Hill Companies, Inc. pp. 2–130. Available from: doi:10.1036/0071422943.
45. Greenberg, J. & Tomson, M. (1992) Precipitation and dissolution kinetics and equilibria of aqueous ferrous carbonate vs temperature. *Applied Geochemistry*. [Online] 7 (2), 185–190. Available from: doi:10.1016/0883-2927(92)90036-3.
46. Gunasekaran, P., Veawab, A. & Aroonwilas, A. (2013) Corrosivity of Single and Blended Amines in CO2 Capture Process. *Energy Procedia*. [Online] 37, 2094–2099. Available from: doi:10.1016/j.egypro.2013.06.088.
47. Hamborg, E.S. & Versteeg, G.F. (2009) Dissociation Constants and Thermodynamic Properties of Amines and Alkanolamines from (293 to 353) K. *Journal of Chemical & Engineering Data*. [Online] 54 (4), 1318–1328. Available from: doi:10.1021/je800897v.
48. Han, J., Brown, B.N. & Nešić, S. (2010) Investigation of the Galvanic Mechanism for Localized Carbon Dioxide Corrosion Propagation Using the Artificial Pit Technique. *Corrosion*. [Online] 66 (9), 095003-095003–095012. Available from: doi:10.5006/1.3490308.
49. Han, J., Young, D., Colijn, H., Tripathi, A., et al. (2009) Chemistry and Structure of the Passive Film on Mild Steel in CO2 Corrosion Environments. *Industrial &*

*Engineering Chemistry Research*. [Online] 48 (13), 6296–6302. Available from: doi:10.1021/ie801819y.

50. Helgeson, H.C. (1969) Thermodynamics of hydrothermal systems at elevated temperatures and pressures. *American Journal of Science*. [Online] 267 (7), 729–804. Available from: doi:10.2475/ajs.267.7.729.
51. Hirschorn, B., Orazem, M.E., Tribollet, B., Vivier, V., et al. (2010) Determination of effective capacitance and film thickness from constant-phase-element parameters. *Electrochimica Acta*. [Online] 55 (21), 6218–6227. Available from: doi:10.1016/j.electacta.2009.10.065.
52. Hunnik, E.V., Hendriksen, E. & Pots, B.F. (1996) The formation of protective FeCO3 corrosion product layers in CO2 corrosion. In: *CORROSION 96*. [Online]. 1996 Denver, CO. p. Available from: https://onepetro.org/NACECORR/proceedings-abstract/CORR96/All-CORR96/NACE-96006/113083.
53. Ieamsupapong, S., Brown, B., Singer, M. & Nešić, S. (2017) Effect of solution pH on corrosion product layer formation in a controlled water chemistry system. In: *CORROSION 2017*. 2017 New Orleans, LA. p.
54. Ingham, B., Ko, M., Kear, G., Kappen, P., et al. (2010) In situ synchrotron X-ray diffraction study of surface scale formation during CO2 corrosion of carbon steel at temperatures up to 90°C. *Corrosion Science*. [Online] 52 (9), 3052–3061. Available from: doi:10.1016/j.corsci.2010.05.025.
55. Ingham, B., Ko, M., Laycock, N., Burnell, J., et al. (2012) In situ synchrotron X-ray diffraction study of scale formation during CO2 corrosion of carbon steel in sodium and magnesium chloride solutions. *Corrosion Science*. [Online] 56, 96–104. Available from: doi:10.1016/j.corsci.2011.11.017.
56. Ingham, B., Ko, M., Laycock, N., Kirby, N.M., et al. (2015) First stages of siderite crystallisation during CO 2 corrosion of steel evaluated using in situ synchrotron small- and wide-angle X-ray scattering. *Faraday Discussions*. [Online] 180, 171–190. Available from: doi:10.1039/c4fd00218k.
57. Ingham, B., Ko, M., Shaw, P., Sk, M.H., et al. (2018) Effects of Oxygen on Scale Formation in CO 2 Corrosion of Steel in Hot Brine: In Situ Synchrotron X-ray Diffraction Study of Anodic Products. *Journal of The Electrochemical Society*. [Online] 165 (11), C756–C761. Available from: doi:10.1149/2.0461811jes.

58. Islam, M.M., Pojtanabuntoeng, T., Gubner, R. & Kinsella, B. (2021) Electrochemical investigation into the dynamic mechanism of CO2 corrosion product film formation on the carbon steel under the water-condensation condition. *Electrochimica Acta*. [Online] 390, 138880. Available from: doi:10.1016/j.electacta.2021.138880.
59. Johnson, M.L. & Tomson, M.B. (1991) Ferrous carbonate precipitation kinetics and its impact on CO2 corrosion. In: *CORROSION 91*. 1991 Houston, TX. p.
60. Jones, D.A. (1996) *Principles and prevention of corrosion*. 2nd edition. Upper Saddle River, NJ, Prentice Hall.
61. Joshi, G.R., Cooper, K., Zhong, X., Cook, A.B., et al. (2018) Temporal evolution of sweet oilfield corrosion scale: Phases, morphologies, habits, and protection. *Corrosion Science*. [Online] 142, 110–118. Available from: doi:10.1016/j.corsci.2018.07.009.
62. Kahyarian, A., Brown, B. & Nešić, S. (2017) Electrochemistry of CO2 corrosion of mild steel: Effect of CO2 on iron dissolution reaction. *Corrosion Science*. [Online] 129, 146–151. Available from: doi:10.1016/j.corsci.2017.10.005.
63. Kahyarian, A. & Nešić, S. (2019) A New Narrative for CO 2 Corrosion of Mild Steel. *Journal of The Electrochemical Society*. [Online] 166 (11), C3048–C3063. Available from: doi:10.1149/2.0071911jes.
64. Kamps, Á.P.-S. & Maurer, G. (1996) Dissociation Constant of N-Methyldiethanolamine in Aqueous Solution at Temperatures from 278 K to 368 K. *Journal of Chemical & Engineering Data*. [Online] 41 (6), 1505–1513. Available from: doi:https://doi.org/10.1021/je960141+.
65. Kandegedara, A. & Rorabacher, D.B. (1999) Noncomplexing Tertiary Amines as "Better" Buffers Covering the Range of pH 3–11. Temperature Dependence of Their Acid Dissociation Constants. *Analytical Chemistry*. [Online] 71 (15), 3140–3144. Available from: doi:10.1021/ac9902594.
66. Karpinski, P.H. & Bałdyga, J. (2019) Handbook of Industrial Crystallization. In: *Chapter 8 - Precipitation Proceses*. [Online]. Cambridge, Cambridge University Press. pp. 216–217. Available from: doi:10.1017/9781139026949.
67. Khorrami, M.R., Raeissi, K., Shahban, H., Torkan, M.A., et al. (2008) Corrosion Behavior of Carbon Steel in Carbon Dioxide-Loaded Activated Methyl Diethanol Amine Solution. *Corrosion*. [Online] 64 (2), 124–130. Available from: doi:10.5006/1.3280680.

68. Kim, C.-H., Pyun, S.-I. & Kim, J.-H. (2003) An investigation of the capacitance dispersion on the fractal carbon electrode with edge and basal orientations. *Electrochimica Acta*. [Online] 48 (23), 3455–3463. Available from: doi:10.1016/s0013-4686(03)00464-x.
69. Kinsella, B., Tan, Y.J. & Bailey, S. (1998) Electrochemical Impedance Spectroscopy and Surface Characterization Techniques to Study Carbon Dioxide Corrosion Product Scales. *Corrosion*. [Online] 54 (10), 835–842. Available from: doi:10.5006/1.3284803.
70. Kittel, J., Fleury, E., Vuillemin, B., Gonzalez, S., et al. (2012) Corrosion in alkanolamine used for acid gas removal: From natural gas processing to CO2 capture. *Materials and Corrosion*. [Online] 63 (3), 223–230. Available from: doi:10.1002/maco.201005847.
71. Kittel, J. & Gonzalez, S. (2014) Corrosion in CO2 Post-Combustion Capture with Alkanolamines – A Review. *Oil & Gas Science and Technology – Revue d'IFP Energies nouvelles*. [Online] 69 (5), 915–929. Available from: doi:10.2516/ogst/2013161.
72. Kittel, J., Idem, R., Gelowitz, D., Tontiwachwuthikul, P., et al. (2009) Corrosion in MEA units for CO2 capture: Pilot plant studies. *Energy Procedia*. [Online] 1 (1), 791–797. Available from: doi:10.1016/j.egypro.2009.01.105.
73. Kohl, A.L. & Nielsen, R.B. (1997a) *Gas Purification*. 5th edition. [Online]. Elsevier. Available from: doi:10.1016/b978-088415220-0/50003-3.
74. Kohl, A.L. & Nielsen, R.B. (1997b) *Gas Purification*. 5th edition. [Online]. Available from: doi:10.1016/b978-088415220-0/50002-1.
75. Labiyi, F. (2016) *Electrochemical Kinetics and Mechanisms of Iron Oxidation in CO2-containing Aqueous Monoethanolamine*.
76. Lee, A.Y., Erdemir, D. & Myerson, A.S. (2019) Handbook of Industrial Crystallization. In: *Chapter 2- Crystals and crystal growth*. [Online]. pp. 32–75. Available from: doi:10.1017/9781139026949.002.
77. Li, S., Zeng, Z., Harris, M.A., Sánchez, L.J., et al. (2019) CO2 Corrosion of Low Carbon Steel Under the Joint Effects of Time-Temperature-Salt Concentration. *Frontiers in Materials*. [Online] 6, 10. Available from: doi:10.3389/fmats.2019.00010.

78. Liu, C., Gao, J., Liu, T., Zhang, L., et al. (2019) Dielectric properties and microwave heating characteristics of Huimin siderite ore. *Journal of Microwave Power and Electromagnetic Energy*. [Online] 53 (2), 1–14. Available from: doi:10.1080/08327823.2019.1607492.
79. Ltd., M.I. (2021) *World Stainless Steel Prices*. [Online]. March 2021. Available from: https://www.meps.co.uk/gb/en/products/world-stainless-steel-prices [Accessed: August 2021].
80. Lukács, Z. (1999) Evaluation of model and dispersion parameters and their effects on the formation of constant-phase elements in equivalent circuits. *Journal of Electroanalytical Chemistry*. [Online] 464 (1), 68–75. Available from: doi:10.1016/s0022-0728(98)00471-9.
81. Lukács, Z. (1997) The numerical evaluation of the distortion of EIS data due to the distribution of parameters. *Journal of Electroanalytical Chemistry*. [Online] 432 (1–2), 79–83. Available from: doi:10.1016/s0022-0728(97)00217-9.
82. Malmberg, C.G. & Maryott, A.A. (1956) Dielectric constant of water from 0 to 100 °C. *Journal of Research of the National Bureau of Standards*. [Online] 56 (1), 1. Available from: doi:10.6028/jres.056.001.
83. Marion, G.M., Catling, D.C. & Kargel, J.S. (2003) Modeling aqueous ferrous iron chemistry at low temperatures with application to Mars. *Geochimica et Cosmochimica Acta*. [Online] 67 (22), 4251–4266. Available from: doi:10.1016/s0016-7037(03)00372-7.
84. Mercier-Bion, F., Li, J., Lotz, H., Tortech, L., et al. (2018) Electrical properties of iron corrosion layers formed in anoxic environments at the nanometer scale. *Corrosion Science*. [Online] 137, 98–110. Available from: doi:10.1016/j.corsci.2018.03.028.
85. Motte, R.D., Basilico, E., Mingant, R., Kittel, J., et al. (2020) A study by electrochemical impedance spectroscopy and surface analysis of corrosion product layers formed during CO2 corrosion of low alloy steel. *Corrosion Science*. [Online] 172, 108666. Available from: doi:10.1016/j.corsci.2020.108666.
86. Nazari, M.H., Allahkaram, S.R. & Kermani, M.B. (2010) The effects of temperature and pH on the characteristics of corrosion product in CO2 corrosion of grade X70 steel. *Materials & Design*. [Online] 31 (7), 3559–3563. Available from: doi:10.1016/j.matdes.2010.01.038.

87. Nešić, S. & Lee, K.-L.J. (2003) A Mechanistic Model for Carbon Dioxide Corrosion of Mild Steel in the Presence of Protective Iron Carbonate Films—Part 3: Film Growth Model. *Corrosion*. [Online] 59 (7), 616–628. Available from: doi:10.5006/1.3277592.
88. Newman, J. & Thomas-Alyea, K.E. (2012) *Electrochemical Systems*. The ECS Series of Texts and Monographs. 3rd edition. John Wiley & Sons, Incorporated.
89. Nordstrom, D.K., Plummer, L.N., Langmuir, D., Busenberg, E., et al. (1990) Chemical Modeling of Aqueous Systems II. *ACS Symposium Series*. [Online] 398–413. Available from: doi:10.1021/bk-1990-0416.ch031.
90. Nordsveen, M., Nešić, S., Nyborg, R. & Stangeland, A. (2003) A Mechanistic Model for Carbon Dioxide Corrosion of Mild Steel in the Presence of Protective Iron Carbonate Films—Part 1: Theory and Verification. *Corrosion*. [Online] 59 (5), 443–456. Available from: doi:10.5006/1.3277576.
91. Orazem, M.E., Pébère, N. & Tribollet, B. (2006) Enhanced Graphical Representation of Electrochemical Impedance Data. *Journal of The Electrochemical Society*. [Online] 153 (4), B129. Available from: doi:10.1149/1.2168377.
92. Orazem, M.E. & Tribollet, B. (2008) *Electrochemical Impedance Spectroscopy*. Electrochemical Society series. [Online]. Hoboken, N.J.: Wiley-Interscience. Available from: doi:10.1002/9780470381588.
93. Pessu, Mr.F., Barker, R. & Neville, A. (2015) The influence of pH on localized corrosion behaviour of X65 (UNS K03014) carbon steel in CO2-saturated brines. *CORROSION*. [Online] 71 (12), 1452–1466. Available from: doi:10.5006/1770.
94. Preis, W. & Gamsjäger, H. (2002) Critical evaluation of solubility data: enthalpy of formation of siderite. *Physical Chemistry Chemical Physics*. [Online] 4 (16), 4014–4019. Available from: doi:10.1039/b203626f.
95. Reffass, M., Sabot, R., Savall, C., Jeannin, M., et al. (2006) Localised corrosion of carbon steel in NaHCO3/NaCl electrolytes: role of Fe(II)-containing compounds. *Corrosion Science*. [Online] 48 (3), 709–726. Available from: doi:10.1016/j.corsci.2005.02.016.
96. Rho, S.-W., Yoo, K.-P., Lee, J.S., Nam, S.C., et al. (1997) Solubility of CO2 in Aqueous Methyldiethanolamine Solutions. *Journal of Chemical & Engineering Data*. [Online] 42 (6), 1161–1164. Available from: doi:10.1021/je970097d.

97. Rodríguez-Amaro, R. & Ruiz, J.J. (2001) *Handbook of Surfaces and Interfaces of Materials*. [Online] (J. Electrocutai. Chem.1861985), 649–684. Available from: doi:10.1016/b978-012513910-6/50019-0.

98. Rosenholtz, J.L. & Smit, D.T. (1936) The dielectric constant of mineral powder. *The American mineralogist*. 21 (2), 115–120.

99. Sadeek, S., Williams, D.R. & Campbell, K.L.S. (2017) Use of green inhibitors and pre-treated carbon steel for reduced corrosion. In: *EUROCORR 2017 in combination with the 20th International Corrosion Congress and the Process Safety Congress 2017: Corrosion Control for safer living part 3*. 3 August 2017 Prague, Czech Republic. p.

100. Sadeek, S.A., Williams, D.R. & Campbell, K.L.S. (2018) Using sodium thiosulphate for carbon steel corrosion protection against monoethanolamine and 2-amino-2-methyl-1-propanol. *International Journal of Greenhouse Gas Control*. [Online] 78, 125–134. Available from: doi:10.1016/j.ijggc.2018.08.004.

101. Saunders, J.A. & Swann, C.T. (1992) Nature and origin of authigenic rhodochrosite and siderite from the Paleozoic aquifer, northeast Mississippi, U.S.A. *Applied Geochemistry*. [Online] 7 (4), 375–387. Available from: doi:10.1016/0883-2927(92)90027-z.

102. Schiller, C.A. & Strunz, W. (2001) The evaluation of experimental dielectric data of barrier coatings by means of different models. *Electrochimica Acta*. [Online] 46 (24–25), 3619–3625. Available from: doi:10.1016/s0013-4686(01)00644-2.

103. Schmitt, G. & Rothmann, B. (1977) Untersuchungen zum Korrosionsmechanismus von unlegiertem Stahl in sauerstofffreien Kohlensäurelösungen. Teil I. Kinetik der Wasserstoffabscheidung. *Materials and Corrosion*. [Online] 28 (12), 816–822. Available from: doi:10.1002/maco.19770281203.

104. Shimizu, M., Hirano, S. & Tomoe, Y. (2016) Corrosivity Difference among Alkanolamine Solutions Saturated with CO2. *Zairyo-to-Kankyo*. [Online] 65 (9), 365–368. Available from: doi:10.3323/jcorr.65.365.

105. Silva, C.A.R., Liu, X. & Millero, F.J. (2002) Solubility of Siderite (FeCO3) in NaCl Solutions. *Journal of Solution Chemistry*. [Online] 31 (2), 97–108. Available from: doi:10.1023/a:1015275618138.

106. Sk, M.H., Abdullah, A.M., Ko, M., Ingham, B., et al. (2017) Local supersaturation and the growth of protective scales during CO2 corrosion of steel: Effect of pH and solution flow. *Corrosion Science*. [Online] 126, 26–36. Available from: doi:10.1016/j.corsci.2017.05.026.

107. Soosaiprakasam, I.R. & Veawab, A. (2008) Corrosion and polarization behavior of carbon steel in MEA-based CO2 capture process. *International Journal of Greenhouse Gas Control*. [Online] 2 (4), 553–562. Available from: doi:10.1016/j.ijggc.2008.02.009.

108. Strategy, D. for B., Energy and Industrial (2021) *2020 UK greenhouse gas emissions, provisional figures*. [Online]. Available from: https://assets.publishing.service.gov.uk/government/uploads/system/uploads/attachment_data/file/972583/2020_Provisional_emissions_statistics_report.pdf.

109. Stumm, W. & Morgan, J.J. (1995) *Aquatic chemistry: chemical equilibria and rates in natural waters*. Environmental science and technology. 3rd edition. [Online]. Wiley. Available from: doi:10.5860/choice.33-6312.

110. Sun, W. & Nešić, S. (2008) Kinetics of Corrosion Layer Formation: Part 1—Iron Carbonate Layers in Carbon Dioxide Corrosion. *Corrosion*. [Online] 64 (4), 334–346. Available from: doi:10.5006/1.3278477.

111. Sun, W., Nešić, S. & Woollam, R.C. (2009) The effect of temperature and ionic strength on iron carbonate (FeCO3) solubility limit. *Corrosion Science*. [Online] 51 (6), 1273–1276. Available from: doi:10.1016/j.corsci.2009.03.009.

112. Sun, Y., Remias, J.E., Neathery, J.K. & Liu, K. (2011) Electrochemical study of corrosion behaviour of carbon steel A106 and stainless steel 304 in aqueous monoethanolamine. *Corrosion Engineering, Science and Technology*. [Online] 46 (6), 724–731. Available from: doi:10.1179/1743278210y.0000000001.

113. Tanupabrungsun, T., Brown, B. & Nešić, S. (2013) Effect of pH on CO2 corrosion of mild steel at elevated temperatures. In: *CORROSION 2013*. 2013 Orlando, Fl. p.

114. Teng, T.T., Maham, Y., Hepler, L.G. & Mather, A.E. (1994) Viscosity of Aqueous Solutions of N-Methyldiethanolamine and of Diethanolamine. *Journal of Chemical & Engineering Data*. [Online] 39 (2), 290–293. Available from: doi:10.1021/je00014a021.

115. Tomoe, Y., Shimizu, M. & Kaneta, H. (1996) Active dissolution and natural passivation of carbon steel incarbon dioxide-saturated alkanolamine solutions. In: *Active dissolution and natural passivation of carbon steel incarbon dioxide-saturated alkanolamine solutions*. Journal of the Japanese Association for Petroleum Technology. 1996 pp. 1–12.

116. Urbansky, E.T. & Schock, M.R. (2000) Understanding, Deriving, and Computing Buffer Capacity. *Journal of Chemical Education*. [Online] 77 (12), 1640. Available from: doi:10.1021/ed077p1640.

117. Valentini, C.R., Moina, C.A., Vilche, J.R. & Arvia, A.J. (1985) The electrochemical behaviour of iron in stagnant and stirred potassium carbonate-bicarbonate solutions in the 0–75°C temperature range. *Corrosion Science*. [Online] 25 (11), 985–993. Available from: doi:10.1016/0010-938x(85)90067-8.

118. Veawab, A. & Aroonwilas, A. (2002) Identification of oxidizing agents in aqueous amine–CO2 systems using a mechanistic corrosion model. *Corrosion Science*. [Online] 44 (5), 967–987. Available from: doi:10.1016/s0010-938x(01)00125-1.

119. Veawab, A., Tontiwachwuthikul, P. & Bhole, S.D. (1997) Studies of Corrosion and Corrosion Control in a CO2–2-Amino-2-methyl-1-propanol (AMP) Environment. *Industrial & Engineering Chemistry Research*. [Online] 36 (1), 264–269. Available from: doi:10.1021/ie9504563.

120. Veawab, A., Tontiwachwuthikul, P. & Chakma, A. (1999) Corrosion Behavior of Carbon Steel in the CO2 Absorption Process Using Aqueous Amine Solutions. *Industrial & Engineering Chemistry Research*. [Online] 38 (10), 3917–3924. Available from: doi:10.1021/ie9901630.

121. Vella, L. & Emerson, D. (2012) Electrical Properties of Magnetite- and Hematite-Rich Rocks and Ores. *ASEG Extended Abstracts*. [Online] 2012 (1), 1–4. Available from: doi:10.1071/aseg2012ab232.

122. Videm, K., A.Dugstad & L.Lunde (1994) Parametric study of CO2 corrosion of carbon steel. In: *CORROSION 94*. 1994 p.

123. Więckowski, A., Ghali, E., Szklarczyk, M. & Sobkowski, J. (1983) The behaviour of iron electrode in CO2– saturated neutral electrolyte—I. Electrochemical study. *Electrochimica Acta*. [Online] 28 (11), 1619–1626. Available from: doi:10.1016/0013-4686(83)85226-8.

124. Xiang, Y., Choi, Y.-S., Yang, Y. & Nešić, S. (2015) Corrosion of Carbon Steel in MDEA-Based CO2 Capture Plant under Regenerator Condition: Effect of O2 and HSS. *Corrosion*. [Online] 71 (1), 30–37. Available from: doi:10.5006/1354.

125. Xiang, Y., Yan, M., Choi, Y.-S., Young, D., et al. (2014) Time-dependent electrochemical behavior of carbon steel in MEA-based CO2 capture process. *International Journal of Greenhouse Gas Control*. [Online] 30, 125–132. Available from: doi:10.1016/j.ijggc.2014.09.003.

126. Yu, L.C.Y., Campbell, K.L.S. & Williams, D.R. (2016) Using carbon steel in the stripper and reboiler for post-Combustion CO2 capture with aqueous amine blends. *International Journal of Greenhouse Gas Control*. [Online] 51, 380–393. Available from: doi:10.1016/j.ijggc.2016.04.031.

127. Yu, L.C.Y., Sadeek, S., Williams, D.R. & Campbell, K.L.S. (2017) Investigating the Corrosion Due to High Capacity and Uptake Promoter Amine Blends on Carbon Steel. *Energy Procedia*. [Online] 114, 1998–2008. Available from: doi:10.1016/j.egypro.2017.03.1334.

128. Zhang, Y. & Chen, C.-C. (2011) Thermodynamic Modeling for CO2 Absorption in Aqueous MDEA Solution with Electrolyte NRTL Model. *Industrial & Engineering Chemistry Research*. [Online] 50 (1), 163–175. Available from: doi:10.1021/ie1006855.

129. Zheng, L., Landon, J., Matin, N.S. & Liu, K. (2016a) FeCO3 Coating Process toward the Corrosion Protection of Carbon Steel in a Postcombustion CO2 Capture System. *Industrial & Engineering Chemistry Research*. [Online] 55 (14), 3939–3948. Available from: doi:10.1021/acs.iecr.5b04145.

130. Zheng, L., Matin, N.S., Landon, J., Thomas, G.A., et al. (2016b) CO2 loading-dependent corrosion of carbon steel and formation of corrosion products in anoxic 30wt.% monoethanolamine-based solutions. *Corrosion Science*. [Online] 102, 44–54. Available from: doi:10.1016/j.corsci.2015.09.015.

# 12 Appendices

## 12.1 Chapter 2 appendix

### 12.1.1 Thermodynamic data

**Table 12-1:**Thermodynamic data used in the construction of E-pH diagrams (Bard *et al*., 1985).

| **Species** | **Phase** | **$\Delta G°_{f,298\ K}$ (J mol$^{-1}$)** |
|---|---|---|
| Fe | c | - |
| $Fe_2O_3$ | c | -742,200 |
| $Fe_3O_4$ | c | -1,015,359 |
| $Fe(OH)_2$ | c | -492,017 |
| $Fe(OH)_3$ | c | -696,600 |
| $Fe^{2+}$ | aq | -78,870 |
| $Fe^{3+}$ | aq | -4,600 |
| $CO_2$ | g | -394,383 |
| $CO_2$ | aq | -386,200 |
| $H_2CO_3$ | aq | -607,630 |
| $HCO_3^-$ | aq | -587,060 |
| $CO_3^{2-}$ | aq | -527,900 |
| $FeCO_3$ | c | --666,715 |
| $Fe_2CO_3(OH)_2$ | c | -1,171,500 |

**Table 12-2:** Chemical reactions and corresponding equilibrium equations for the $CO_2$-$H_2O$ system.

| Description | Reaction | Equilibrium |
|---|---|---|
| $CO_2$ dissolution | $CO_{2(g)} \rightleftharpoons CO_{2(aq)}$ | $H = \frac{C_{CO_{2(aq)}}}{P_{CO_{2(g)}}}$ |
| Bicarbonate formation | $CO_{2(aq)} + H_2O \rightleftharpoons HCO_3^- + H^+$ | $K_1 = \frac{C_{HCO_3^-(aq)} C_{H^+(aq)}}{C_{CO_{2(aq)}}}$ |
| Bicarbonate dissociation | $HCO_3^- \rightleftharpoons CO_3^{2-} + H^+$ | $K_2 = \frac{C_{CO_3^{2-}(aq)} C_{H^+(aq)}}{C_{HCO_3^-(aq)}}$ |

**Table 12-3:** Reactions considered in the construction of the E-pH diagram for the Fe-HO system with corresponding equations for reversible or equilibrium potentials or pH.

| Reaction | E-pH |
|---|---|
| $Fe \rightleftharpoons Fe^{2+} + 2e^-$ | $E_{r,Fe/Fe^{2+}} = E°_{Fe/Fe^{2+}} + \frac{RT}{2F} \ln [Fe^{2+}]$ |
| $Fe + 2\,H_2O \rightleftharpoons Fe(OH)_2 + 2H^+ + 2e^-$ | $E_{r,Fe/\,Fe(OH)_2} = E°_{Fe/\,Fe(OH)_2} - \frac{RT}{2F} pH$ |
| $Fe^{2+} \rightleftharpoons Fe^{3+} + e^-$ | $E_{r,Fe/Fe^{3+}} = E°_{Fe/Fe^{3+}} + \frac{RT}{F} \ln \left\{\frac{[Fe^{3+}]}{[Fe^{2+}]}\right\}$ |
| $Fe^{2+} + 2H_2O \rightleftharpoons Fe(OH)_2 + 2H^+$ | $pH = -\frac{1}{2} \log K_{Fe^{2+}/Fe(OH)_2} - \frac{1}{2} \log [Fe^{2+}]$ |
| $3Fe^{2+} + 4H_2O \rightleftharpoons Fe_3O_4 + 8H^+ + 2e^-$ | $E_{r,\,Fe_3O_4/Fe^{2+}} = E°_{\,Fe_3O_4/Fe^{2+}} - \frac{3RT}{2F} \ln[Fe^{2+}] - \frac{4RT}{F} pH$ |
| $2Fe^{2+} + 3H_2O \rightleftharpoons Fe_2O_3 + 6H^+ + 2e^-$ | $E_{r,Fe_2O_3/Fe^{2+}} = E°_{rev,Fe_2O_3/Fe^{2+}} - \frac{RT}{F} \ln[Fe^{2+}] - \frac{3RT}{F} pH$ |
| $2Fe^{3+} + 3H_2O \rightleftharpoons Fe_2O_3 + 6H^+$ | $pH = -\frac{1}{6} \log K_{Fe^{3+}/Fe_2O_3} - \frac{1}{6} \log [Fe^{3+}]$ |
| $3Fe(OH)_2 \rightleftharpoons Fe_3O_4 + 2H_2O + 2H^+ + 2e^-$ | $E_{r,\,Fe_3O_4/Fe(OH)_2} = E°_{Fe_3O_4/Fe(OH)_2} - \frac{3RT}{F} pH$ |
| $2Fe_3O_4 + H_2O \rightleftharpoons 3Fe_2O_3 + 2H^+ + 2e^-$ | $E_{r,\,Fe_3O_4/Fe_2O_3} = E°_{Fe_3O_4/Fe_2O_3} - \frac{RT}{F} pH$ |

**Table 12-4:** Additional reactions considered in the construction of the E-pH diagram for the Fe–$H_2O$–$CO_2$ system, with corresponding equations for reversible or equilibrium potentials or pH.

| Reaction | E-pH |
|---|---|
| $Fe + CO_{2(aq)} + H_2O \rightleftharpoons FeCO_3 + 2H^+ + 2e^-$ | $E_{r,FeCO_3/Fe} = E°_{FeCO_3/Fe} - \frac{RT}{2F}\ln\left[CO_{2(aq)}\right] - \frac{RT}{F}pH$ |
| $Fe^{2+} + CO_{2(aq)} + H_2O \rightleftharpoons FeCO_3 + 2H^+$ | $pH = -\frac{1}{2}logK_{Fe^{2+}/FeCO_3} - \frac{1}{2}log[Fe^{2+}] - \frac{1}{2}log\,[\,CO_{2(aq)}]$ |
| $Fe + HCO_3^- \rightleftharpoons FeCO_3 + H^+ + 2e^- + 2H_2O$ | $E_{r,FeCO_3/Fe} = E°_{FeCO_3/Fe} - \frac{RT}{2F}\ln[HCO_3^-] - \frac{RT}{2F}pH$ |
| $Fe^{2+} + HCO_3^- + H_2O \rightleftharpoons FeCO_3 + H^+$ | $pH = -logK_{\frac{Fe^{2+}}{FeCO_3}} - log[Fe^{2+}] - \frac{1}{2}log\,[HCO_3^-]$ |
| $Fe(OH)_2 + HCO_3^- + H^+ \rightleftharpoons FeCO_3 + H_2O$ | $pH = logK_{Fe(OH)_2/FeCO_3} + log\,[HCO_3^-]$ |
| $3FeCO_3 + 4H_2O \rightleftharpoons Fe_3O_4 + 3HCO_3^- + 5H^+ + 2e^-$ | $E_{r,Fe_3O_4/FeCO_3} = E°_{Fe_3O_4/FeCO_3} - \frac{RT}{2F}\ln[HCO_3^-] - \frac{RT}{2F}pH$ |
| $Fe + CO_3^{2-} \rightleftharpoons FeCO_3 + 2e^-$ | $E_{r,FeCO_3/Fe} = E°_{FeCO_3/Fe} - \frac{RT}{2F}\ln[CO_3^{2-}]$ |
| $Fe(OH)_2 + CO_3^{2-} + 2H^+ \rightleftharpoons FeCO_3 + 2H_2O$ | $pH = \frac{1}{2}logK_{Fe(OH)_2/FeCO_3} + \frac{1}{2}log\,[CO_3^{2-}]$ |
| $FeCO_3 + 4H_2O \rightleftharpoons Fe_3O_4 + 8H^+ + 3CO_3^{2-} + 2e^-$ | $E_{r,Fe_3O_4/FeCO_3} = E°_{,Fe_3O_4/FeCO_3} + \frac{3RT}{2F}\ln[CO_3^{2-}] - \frac{4RT}{F}pH$ |

## 12.1.2 Copyright permissions

**Table 12-5:** Copyright permissions[36]

| Element | Source of work | Copyright holder | Granted |
|---|---|---|---|
| **Figure 2-14** | Valentini, C.R., Moina, C.A., Vilche, J.R. & Arvia, A.J. (1985) The electrochemical behaviour of iron in stagnant and stirred potassium carbonate-bicarbonate solutions in the 0–75°C temperature range. *Corrosion Science*. [Online] 25 (11), 985–993. | Elsevier | Yes |
| **Figure 2-15** | Han, J., Brown, B.N. & Nešić, S. (2010) Investigation of the Galvanic Mechanism for Localized Carbon Dioxide Corrosion Propagation Using the Artificial Pit Technique. *Corrosion*. [Online] 66 (9), 095003-095003–095012. | AMPP Global Center Inc | Yes |
| **Figure 2-16** | Joshi, G.R., Cooper, K., Zhong, X., Cook, A.B., et al. (2018a) Temporal evolution of sweet oilfield corrosion scale: Phases, morphologies, habits, and protection. *Corrosion Science*. [Online] 142, 110–118. | Elsevier | Open access |
| **Figure 2-18** | Sk, M.H., Abdullah, A.M., Ko, M., Ingham, B., et al. (2017) Local supersaturation and the growth of protective scales during CO2 corrosion of steel: Effect of pH and solution flow. *Corrosion Science*. [Online] 126, 26–36. | Elsevier | Yes |
| **Figure 2-31** | Soosaiprakasam, I.R. & Veawab, A. (2008) Corrosion and polarization behavior of carbon steel in MEA-based CO2 capture process. *International Journal of Greenhouse Gas Control*. [Online] 2 (4), 553–562. | Elsevier | Yes |
| **Figure 2-32** | Sun, Y., Remias, J.E., Neathery, J.K. & Liu, K. (2011) Electrochemical study of corrosion behaviour of carbon steel A106 and stainless steel 304 in aqueous monoethanolamine. *Corrosion Engineering, Science and Technology*. [Online] 46 (6), 724–731. | Taylor & Francis | N/A |

[36] Taylor & Francis has offered reuse of its content for a thesis or dissertation.

# 12.2 Chapter 4 appendix

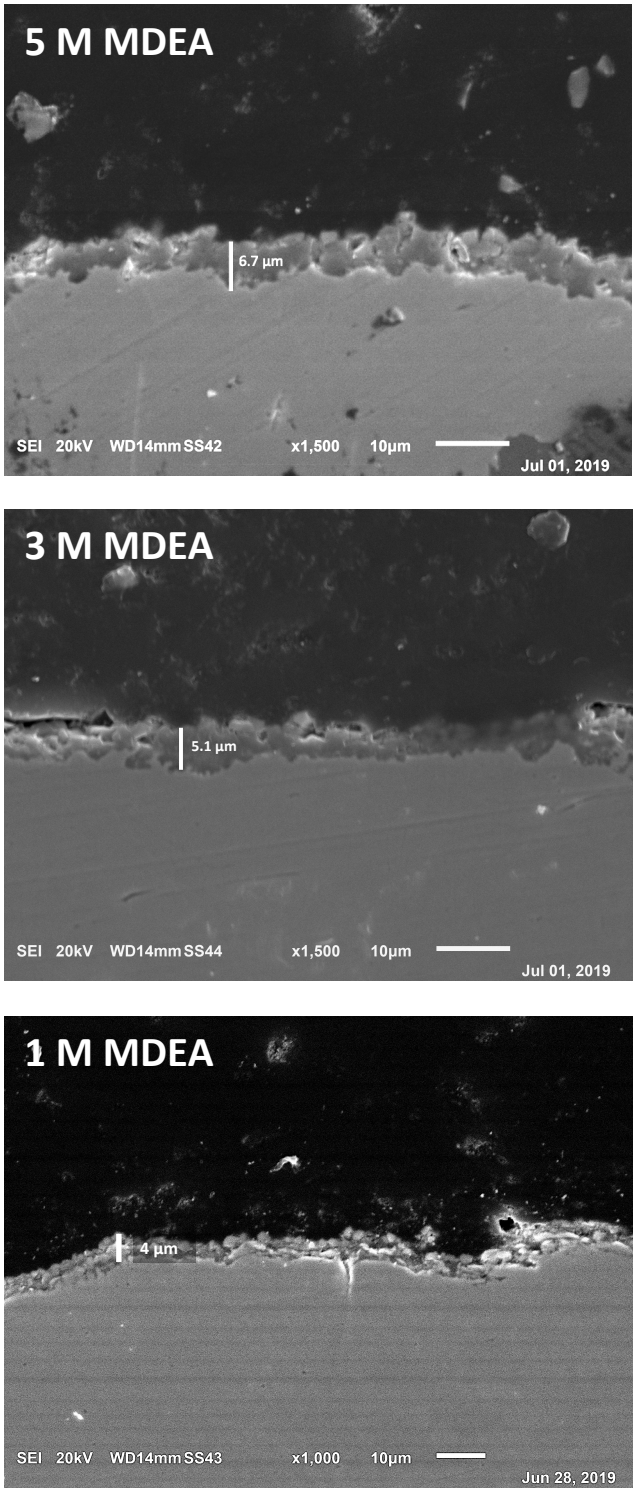



**Figure 12-1:** Images of cross-section of coupons after immersion in $MDEA_{(aq)}$ solutions saturated with $CO_2$ at 80 °C.

## 12.3 Chapter 5 appendix

### 12.3.1 Cyclic voltammograms of iron and carbon steel in $MEA_{(aq)}$ solution saturated with $CO_2$

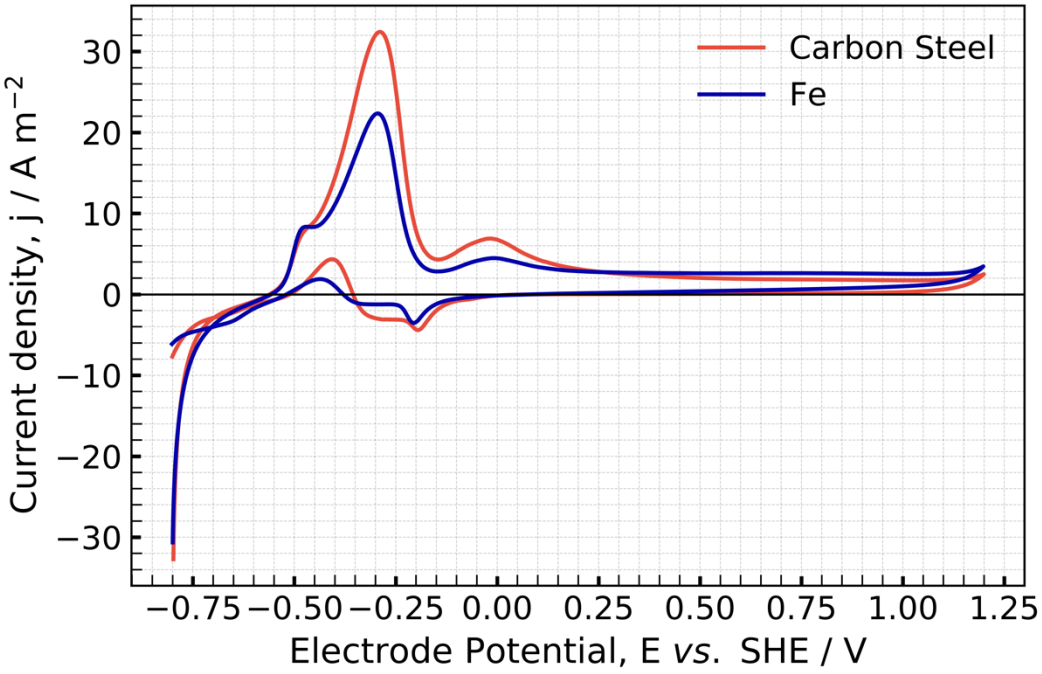



**Figure 12-2:** Cyclic voltammograms recorded on stationary Fe and carbon steel disc electrodes in 5 M $MEA_{(aq)}$ solution saturated with $CO_2$ at 25 °C.

## 12.3.2 Effect of potential scan rate on PII current density

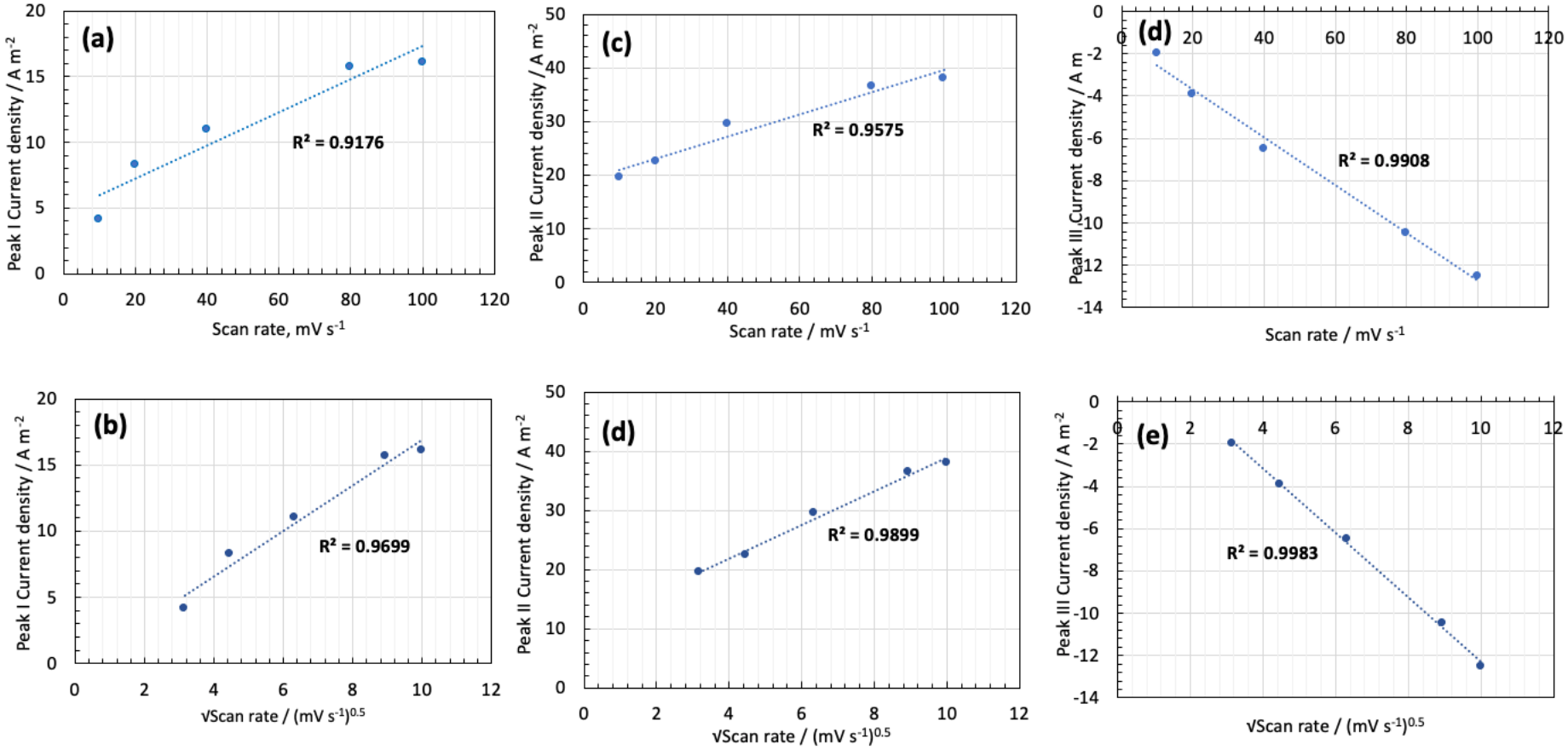



**Figure 12-3:** Effect of potential scan rate on the magnitude of **(a** - **b)** PI, **(c** - **d)** PII, and **(d** - **e)** PIII on iron in 5 M $MEA_{(aq)}$ solution saturated with $CO_2$ (pH 7.9) at 25 °C.

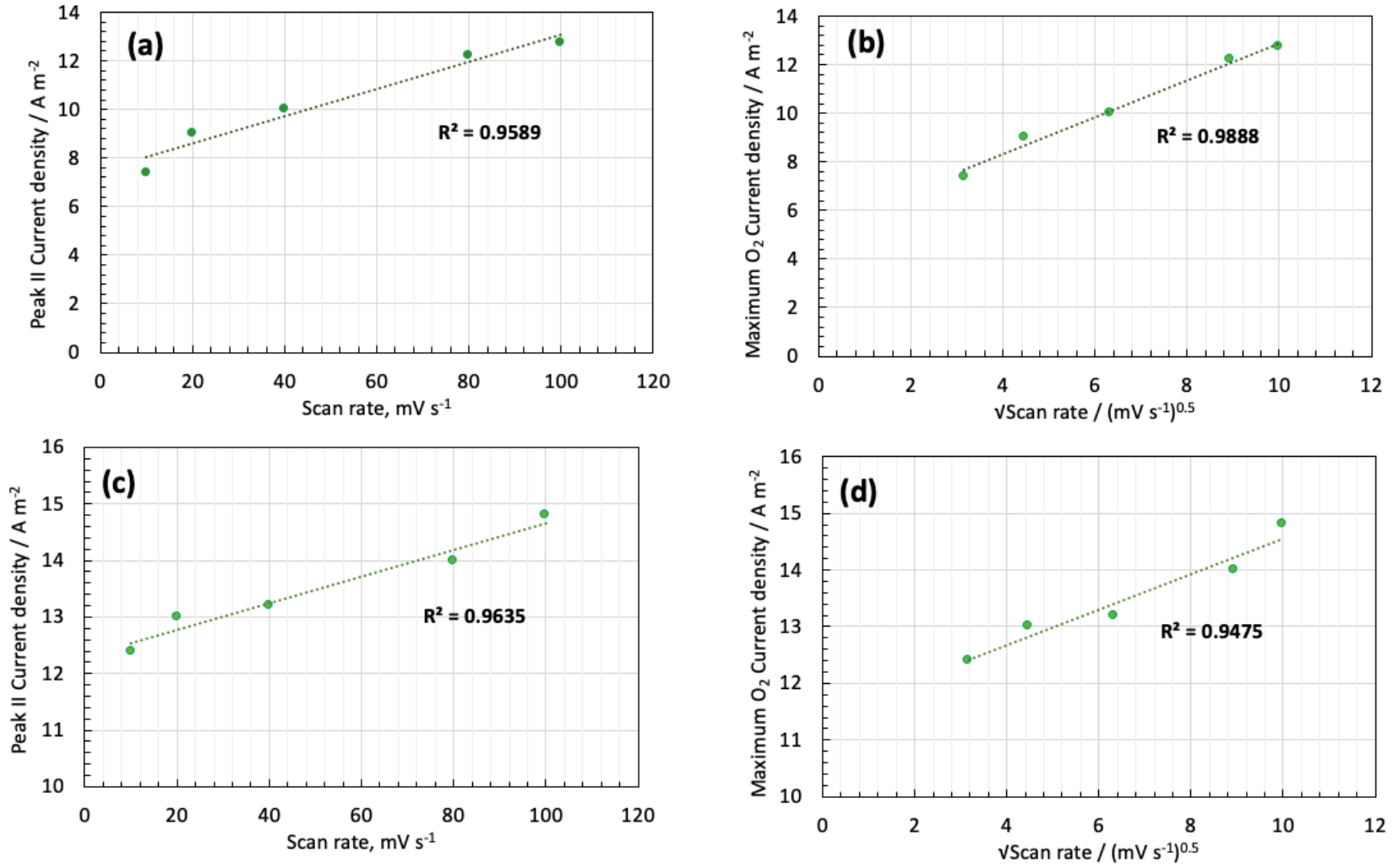



**Figure 12-4:** Effect of potential scan rate on the magnitude of **(a - b)** PII, **(c - d)** $O_2$ evolution current on iron in 5 M $MDEA_{(aq)}$ solution saturated with $CO_2$ (pH 8.6) at 25 °C.

### 12.3.3 Dynamic viscosity

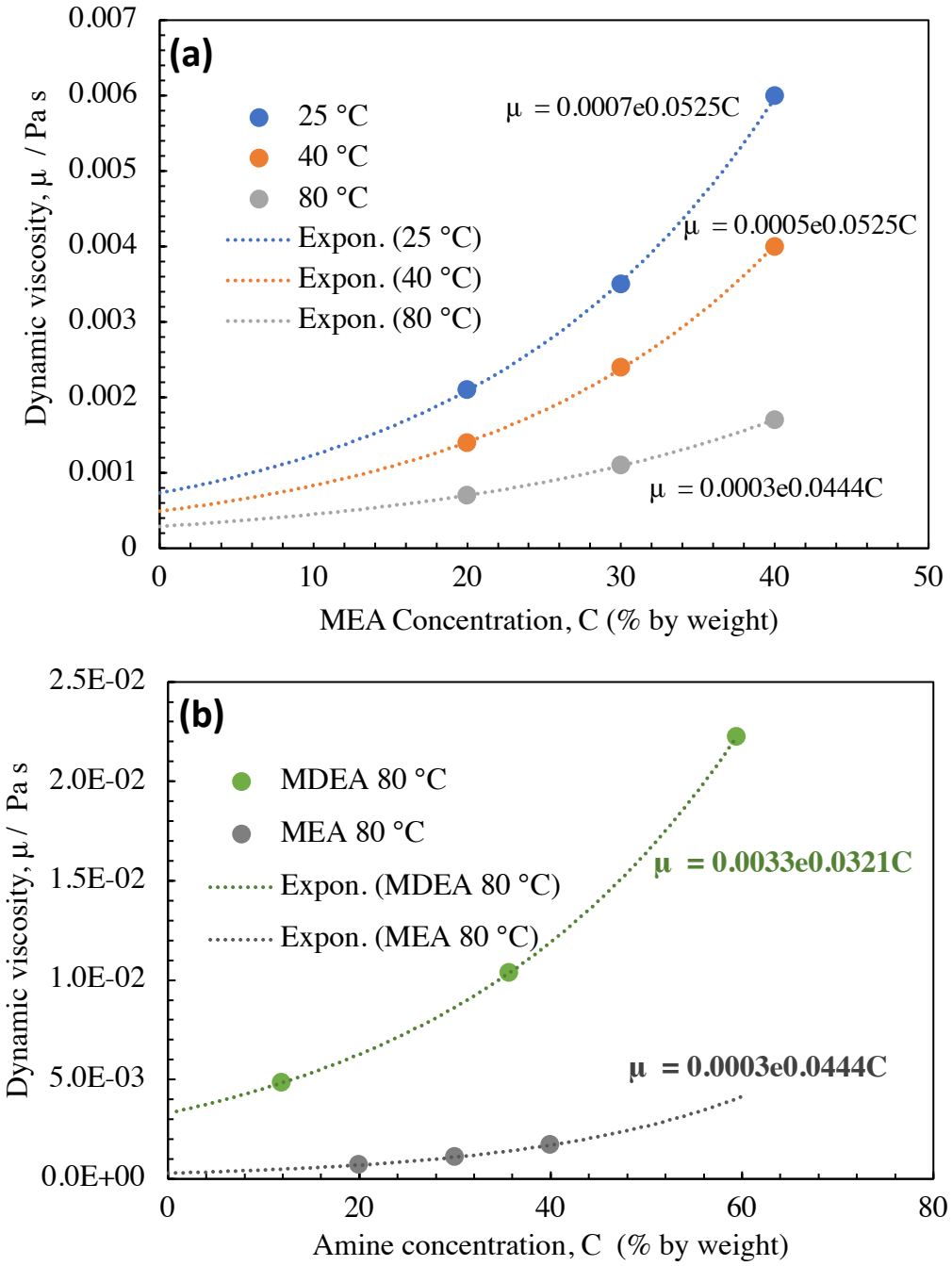



**Figure 12-5:** Dynamic viscosity as a function of **(a)** MEA concentration (saturated with $CO_2$) and temperature and **(b)** MDEA and MEA concentration at 80 °C. These were derived from data taken from (Amundsen, Øi & Eimer, 2009) for MEA and MDEA (Teng *et al.*, 1994).

### 12.3.4 Cyclic voltammograms on Fe in $MEA_{(aq)}$ $CO_2$ as a function of temperature

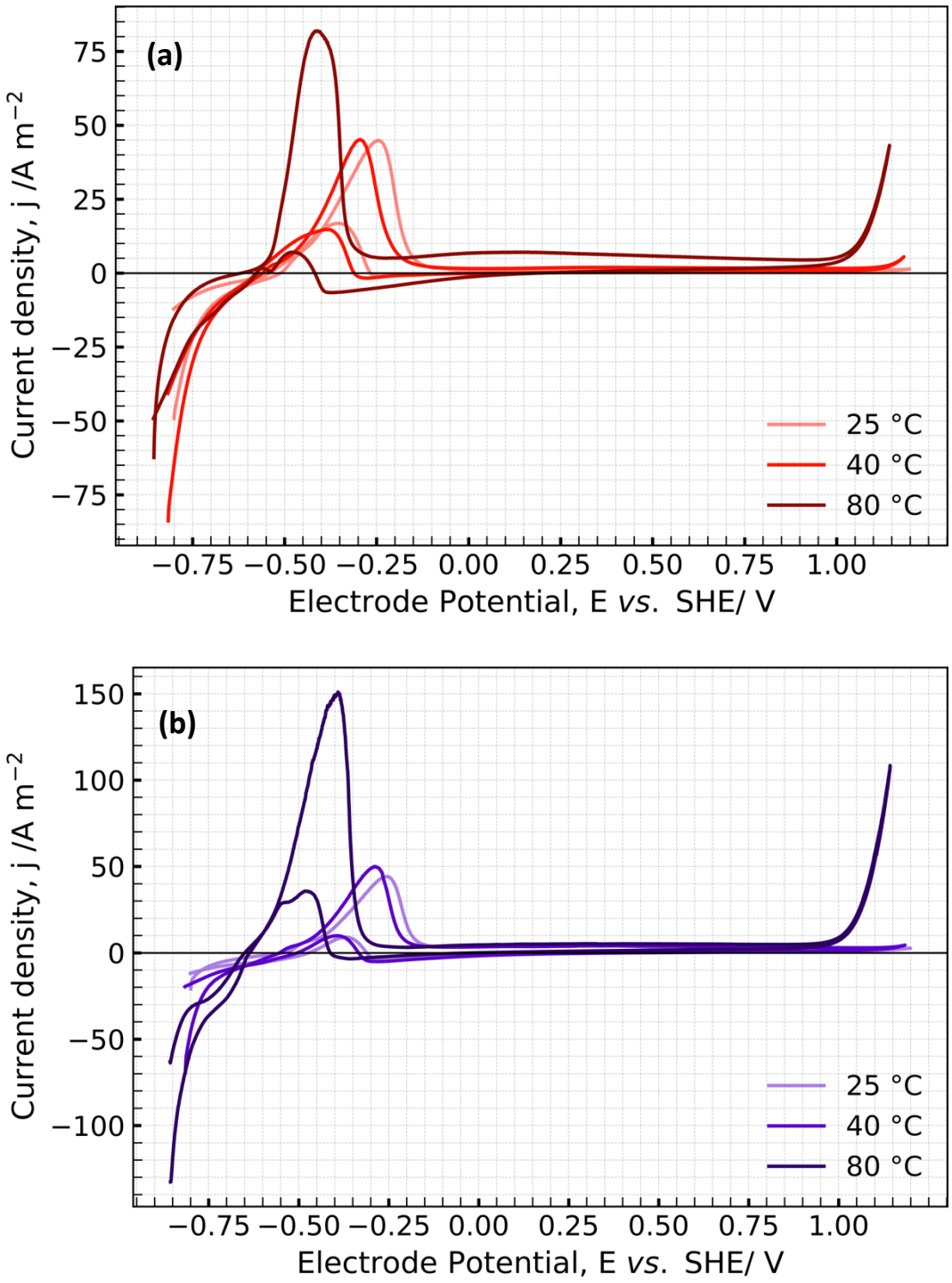



**Figure 12-6:** Cyclic voltammograms recorded on rotating Fe disc electrodes in **(a)** 1 M $MEA_{(aq)}$ and **(b)** 3 M $MEA_{(aq)}$ solutions saturated with $CO_2$ at 25 – 80 °C.

### 12.3.5 Cyclic voltammograms on Fe in $MDEA_{(aq)}$ $CO_2$ as a function of temperature

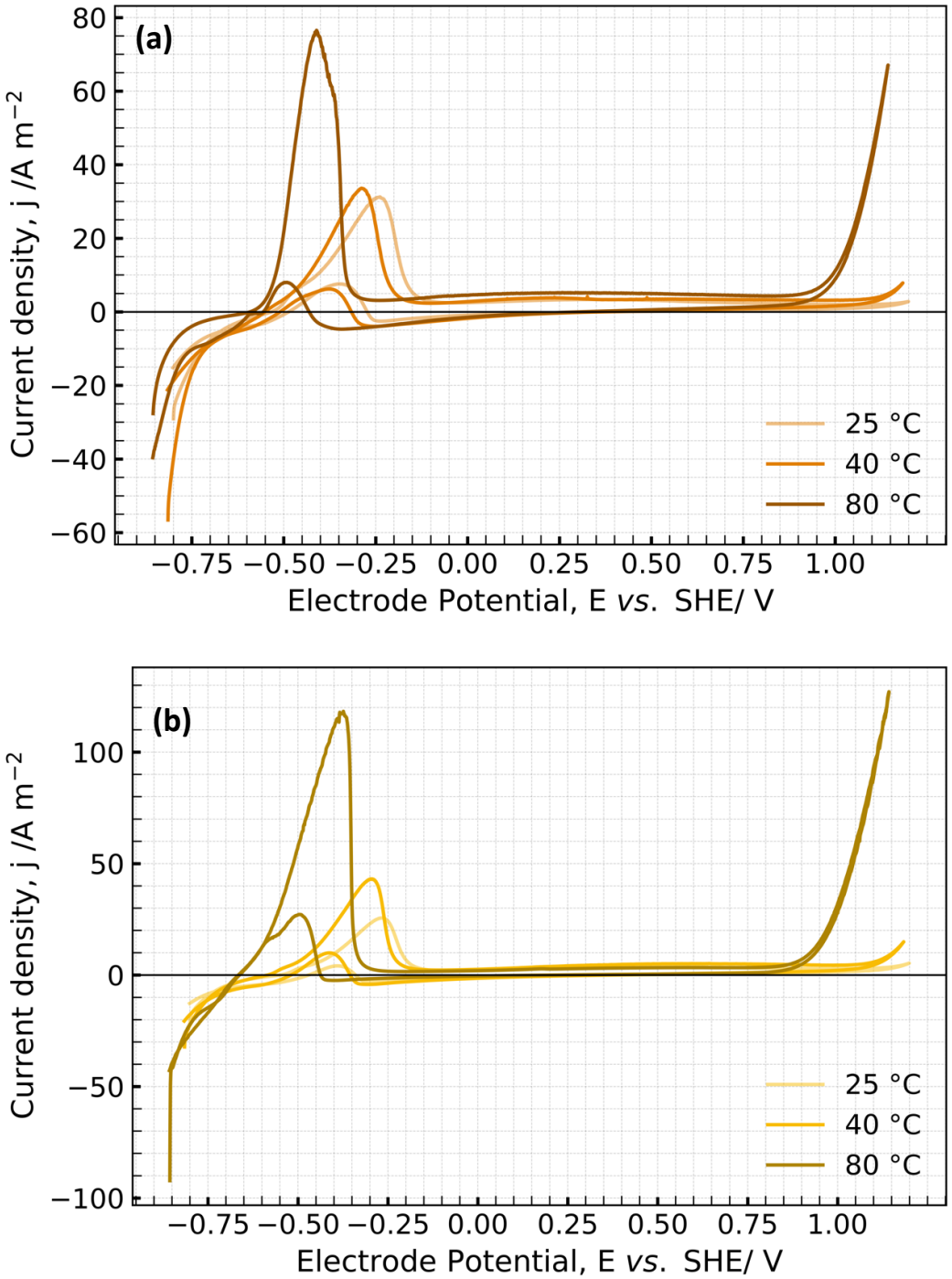



**Figure 12-7:** Cyclic voltammograms recorded on rotating Fe disc electrodes in **(a)** 1 M $MDEA_{(aq)}$ and **(b)** 3 M $MDEA_{(aq)}$ solution saturated with $CO_2$ at 25 – 80 °C.

## 12.3.6 Monolayer calculation

To estimate the maximum[37] number of $FeCO_3$ monolayers formed during the positive-going scan, it was assumed that the total charge passed at PII was due to $FeCO_3$ formation *via* Reaction **12-1** (Faradaic efficiency of unity).

The total charge passed ($Q$, C) was converted to moles of $FeCO_3$ ($m_{FeCO3}$) formed using Equation **12-2**. The total charge was estimated by first selecting the relevant section of the voltammogram, for example **Figure 12-8a**, then determining the time elapsed within the relevant potential scan window; in **Figure 12-8a** the time elapsed was approximately 20 seconds (**Figure 12-8b**). The time and current are then used to determine total charge as shown in Equation **12-2**. The total charge density passed in the voltammogram shown in **Figure 12-8a** was found to be 224 C $m^{-2}$, for an electrode surface area ($A_{electrode}$) of 3.1 × $10^{-5}$ $m^2$ (diameter = 6.3 mm) this is equivalent to 7 × $10^{-3}$ C, which is equivalent to 3.6 × $10^{-8}$ moles.

$$Fe_{(s)} + HCO_{3\,(aq)}^{-} \rightarrow FeCO_{3(c)} + H^{+}_{(aq)} + 2e^{-} \qquad \textbf{12-1}$$

$$m_{FeCO_3} = \frac{Q}{2\,F} = \frac{\sum I \Delta t}{2\,F} \qquad \textbf{12-2}$$

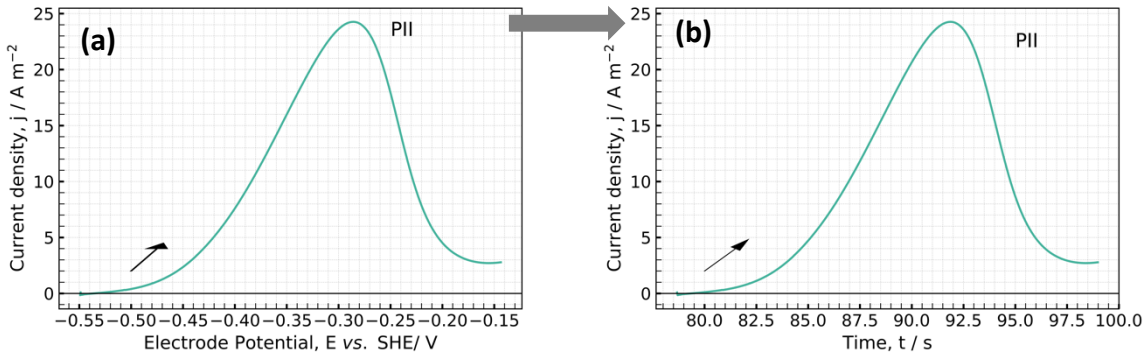



**Figure 12-8**: PII extracted from the voltammogram presented in Chapter 5 **Figure 5-4** with **(a)** current as a function time and **(b)** current as a function of total time elapsed from start of experiment.

The moles of $FeCO_3$ can be converted to the volume of product ($V_{FeCO3}$) formed using the molecular weight ($M_{FeCO3}$, g $mol^{-1}$) and density ($\varrho_{FeCO3}$, g $m^{-3}$) of the product using Equation

[37] This calculation assumes that $FeCO_3$ was formed *via* surface transformation and a faradaic efficiency of unit and the electrode surface roughness was unaccounted for. It is therefore the uppermost quantity of $FeCO_3$ which could have formed and is most probably an overestimate.

**12-3**. This can then be converted to thickness of product layer ($L_{FeCO3}$, m) from Equation **12-4**, and then to monolayers of product using the atomic diameter (estimated from Equation **12-5**) of the product (Equation **12-6**).

$$V_{FeCO_3} = \frac{m_{FeCO_3} M_{FeCO_3}}{\rho_{FeCO_3}} = \frac{3.6 \times 10^{-8}\text{mol} \times 115.85\ \text{g mol}^{-1}}{3.9 \times 10^{6}\text{g m}^{-3}} \quad \textbf{12-3}$$

$$L_{FeCO_3} = \frac{V_{FeCO_3}}{A_{electrode}} = \frac{1.08 \times 10^{-12}\text{m}^3}{3.1 \times 10^{-5}\text{m}^2} = 3.45 \times 10^{-8}\ \text{m} \quad \textbf{12-4}$$

$$Fe_{diameter} = 1.26 \times 10^{-10}\text{m} \times 2$$

$$CO_{3\ diameter} = 1.78 \times 10^{-10}\text{m} \times 2 \quad \textbf{12-5}$$

$$FeCO_{3\ diameter} = 6.08 \times 10^{-10}\text{m}$$

$$\text{monolayers}_{FeCO_3} = \frac{L_{FeCO_3}}{FeCO_{3\ diameter}} = \frac{3.45 \times 10^{-8}\text{m}}{6.08 \times 10^{-10}\text{m}} = 56 \quad \textbf{12-6}$$

The maximum[38] local pH change due to $FeCO_3$ formation *via* Reaction **12-1** was estimated by assuming 1 mole of $H^+$ formed per mole of $FeCO_3$ (*i.e.* $3.6 \times 10^{-8}$ moles). The moles of $H^+$ were added to the moles of $H^+$ already present in solution based on the bulk pH of 7.9. The total moles of $H^+$ at the electrode surface was then converted to the local concentration using the volume of the diffusion layer ($V_{diffusion\ layer}$) estimated from Equation **12-7**. The diffusion layer thickness ($\delta$, m) was estimated from Equation **12-8** (Bard & Faulkner, 2001), the diffusion coefficient of $H^+$ ($D_{H+} = 9.3 \times 10^{-9}$ m$^2$ s$^{-1}$ ) was taken from (Newman & Thomas-Alyea, 2012), and the time ($t$, s) was taken as the average time between the beginning and ending of the $FeCO_3$ formation reaction (10 s). The local concentration of $H^+$ was then converted to the local pH using Equation **12-9**.

$$V_{diffusion\ layer} = A_{electrode}\ \delta \quad \textbf{12-7}$$

$$\delta = 2\sqrt{Dt} \quad \textbf{12-8}$$

$$pH = -\log[H^+] = 1.72 \quad \textbf{12-9}$$

The $HCO_3^-$ concentration (mol L$^{-1}$) could then be determined at the local pH from the equilibrium constant ($K_{eq}$) for Reaction **12-10**. $K_e$ was calculated using Equations **12-11** - **12-12**; Gibbs energy of formation data used is included in **Table 12-1**, *i* represents product

[38] This calculation does not account for diffusion of $H^+$ away from the electrode surface and is therefore an overestimate of the local pH decrease.

species and *j*, reactant species. Equation **12-13** was then used where the partial pressure of $CO_2$ ($pCO_2$, atm) was equated to 1 atm since $CO_2$ was continuously bubbling through an open vessel.

$$CO_{2(g)} + H_2O_{(l)} \rightarrow HCO_{3\,(aq)}^{-} + H^{+}{}_{(aq)} \qquad \textbf{12-10}$$

$$\Delta G^{o}{}_{rxn} = \sum_{i,products} \nu_i \, \Delta G_i^o - \sum_{j,reactants} \nu_j \, \Delta G_j^o = 44\,501 \text{ J mol}^{-1} \qquad \textbf{12-11}$$

$$\Delta G_{rxn} = -RT \ln K_{eq} \qquad \textbf{12-12}$$

$$[HCO_3^-] = \frac{pCO_2 K_{eq}}{10^{-pH}} = \frac{1 \times 1.60 \times 10^{-8}}{10^{-1.72}} = 8 \times 10^{-7} \text{mol L}^{-1} \qquad \textbf{12-13}$$

# 12.4 Chapter 6 appendix

## 12.4.1 Surface images

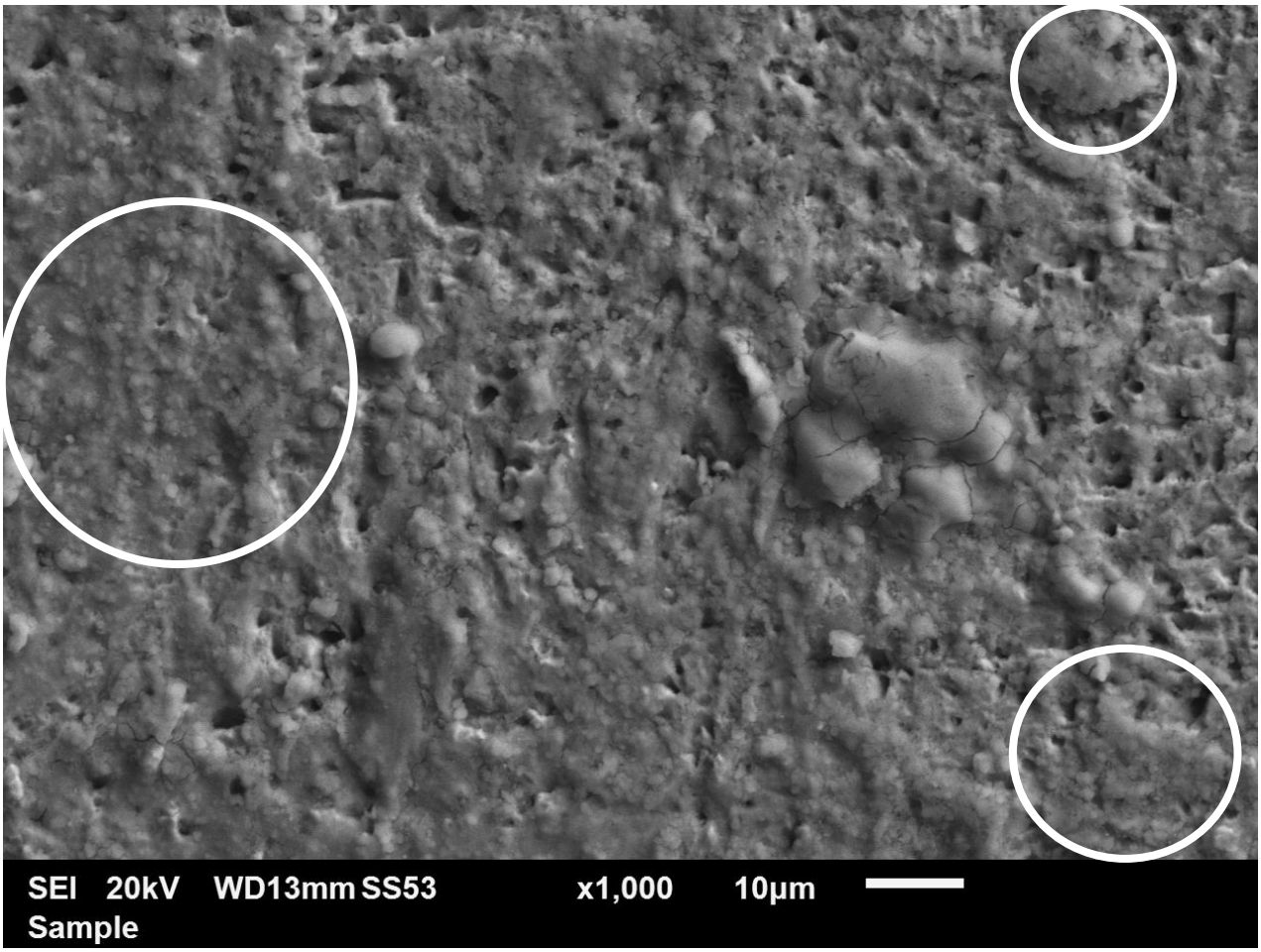
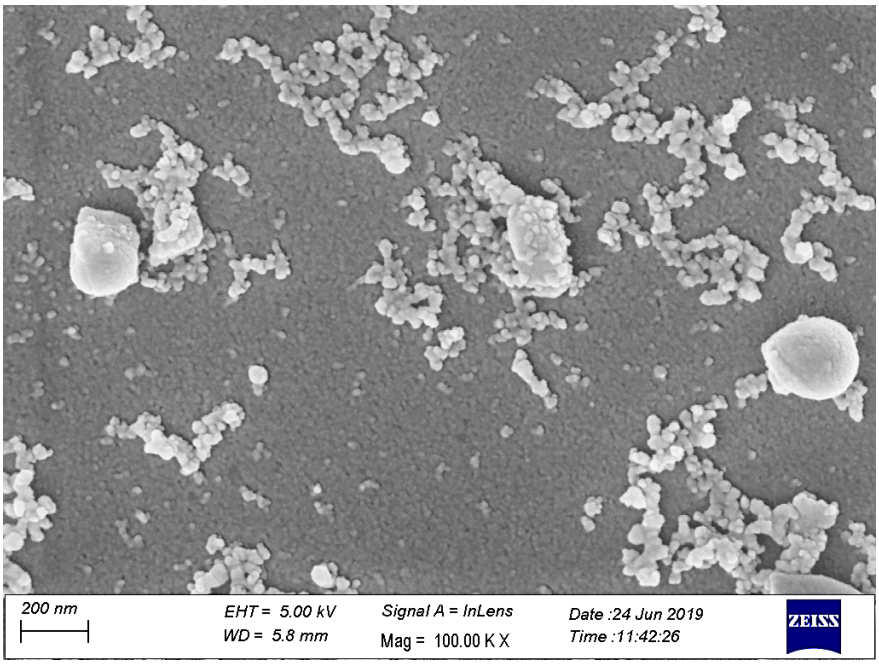



**Figure 12-9:** *Ex-situ* surface image taken with a scanning electron microscope (1000x) of an Fe disc electrode surface after completion of chronoamperometry experiment in 3 M $MEA_{(aq)}$ solution saturated with $CO_2$ at 80 °C. Areas where $FeCO_3$ crystals may be present are highlighted.



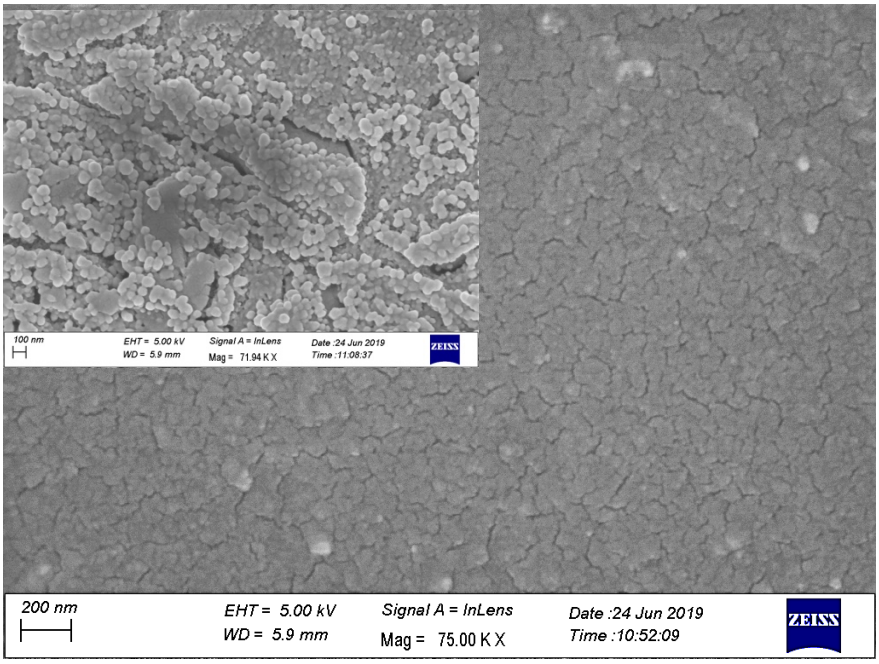




**Figure 12-10:** *Ex-situ* surface characterisation using scanning electron microscope of Fe electrode after completion of potentiostatic experiment (at $FeCO_3$ formation potential) in 5 M $MDEA_{(aq)}$ solution saturated with $CO_2$ at 80 °C, 1000 RPM.

## 12.4.2 Diffusion coefficients

**Table 12-6:** Diffusion coefficients of $Fe^{2+}$, $HCO_3^-$ and $H^+$ at 25 °C, in water (Newman & Thomas-Alyea, 2012).

| Species | Diffusion coefficient ($m^2 s^{-1}$) |
|---|---|
| $Fe^{2+}$ | $0.72 \times 10^{-9}$ |
| $HCO_3^-$ | $1.105 \times 10^{-9}$ |
| $H^+$ | $9.312 \times 10^{-9}$ |

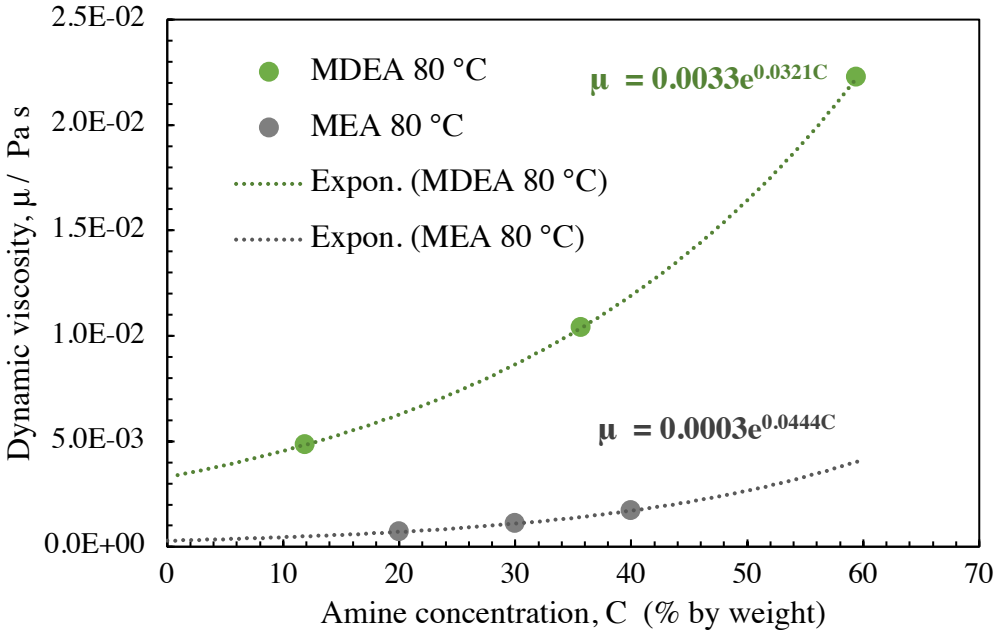



**Figure 12-11:** Dynamic viscosity as a function of amine concentration at 80 °C used to correct diffusion coefficients shown in Table **12 -6** . These were derived from data taken from (Amundsen, Øi & Eimer, 2009) for MEA and (Teng *et al*., 1994) for MDEA.

### 12.4.3 $FeCO_3$ saturation ratio

The $FeCO_3$ saturation ratio is a function of the concentration of $Fe^{2+}$ , $CO_3^{2-}$ and the solubility limit ($K_{sp}$) as described by Equation **12-14**.

$$S_{FeCO_3} = \frac{[Fe^{2+}][CO_3^{2-}]}{K_{sp}} \quad \textbf{12-14}$$

- $Fe^{2+}$ concentration:

  **1)** Bulk concentration - calculating the moles of $Fe^{2+}$ ($m_{Fe2+}$) from the total charge passed ($Q$) in the chronoamperometry experiments using Faraday's law of electrolysis (Equation **12-15**) (assuming 2 electrons transferred per mole of $Fe^{2+}$ produced), and converting to concentration ($C_{Fe2+}$) (Equation **12-16**) using the total electrolyte volume ($V$) *i.e.* assuming all the moles of $Fe^{2+}$ produced were transported to the bulk. The effects of diffusion and $FeCO_3$ formation were not considered in this calculation. The $Fe^{2+}$ concentration calculated following this method was used to estimate the $FeCO_3$ saturation ratio ($S_{FeCO3}$) in the bulk. An example of this calculation at the end of the chronoamperometry experiment in 5 M $MEA_{(aq)}$ -$CO_2$ 80 °C is shown below (Equation **12-17**).

$$m_{Fe^{2+}} = \frac{Q}{2\,F} \quad \textbf{12-15}$$

$$C_{Fe^{2+}} = \frac{m_{Fe^{2+}}}{V} \quad \textbf{12-16}$$

$$C_{Fe^{2+}|5M\ MEA,\ final\ time} = \frac{10.6645\ C}{2\ (96485\ C\ mol^{-1})} \times \frac{1}{160\ mL} \times \frac{1000\ mL}{1\ dm^{-3}} \quad \textbf{12-17}$$

$$C_{Fe^{2+}|5M\ MEA,\ final\ time} = 3.45 \times 10^{-4}\ mol\ dm^{-3} \quad \textbf{12-18}$$

  **2)** Local concentration: formulating the current as a function of time using a best fit line through the current transient, and setting the flux of $Fe^{2+}$ at the electrode surface based on the linear function, then using MATLAB to predict the $Fe^{2+}$ based on this flux, the diffusion of $Fe^{2+}$ due to both the concentration gradient and convective diffusion from the rotating disc electrode, as well as the $FeCO_3$ reaction. The former is described here and the code used for the latter is given in Section 12.4.8.

- For the bulk calculations, the $CO_3^{2-}$ concentration estimation is described in 12.4.4. The local $CO_3^{2-}$ concentration was calculated based on the $HCO_3^-$ and pH predicted from the diffusion reaction model.
- $K_{sp}$ is a function of the temperature and ionic strength and is described in 12.4.5.

A summary of the $K_{sp,}$ used in both the bulk and local saturation ratio calculation, the $CO_3^{2-}$ and $Fe^{2+}$ concentration used in the bulk saturation ratio calculation are included in **Table 12-7**.

**Table 12-7:** $K_{sp}$ , $CO_3^{2-}$ and $Fe^{2+}$ used in $S_{FeCO3}$ calculation. $K_{sp}$ used in bulk and local $S_{FeCO3}$ calculation. $CO_3^{2-}$ concentration used in bulk $S_{FeCO3}$ calculation. $Fe^{2+}$ concentration used for the final time bulk $S_{FeCO3}$ calculation.

| **Amine** | **MEA** | | | **MDEA** | | |
|---|---|---|---|---|---|---|
| **Amine concentration (M)** | **1** | **3** | **5** | **1** | **3** | **5** |
| **$K_{sp}$ $\times 10^{-10}$ (mol$^2$ dm$^{-6}$)** | 1.30 | 5.49 | 9.48 | 7.22 | 9.14 | 10.2 |
| **$CO_3^{2-}$ concentration $\times$ $10^{-3}$ (mol dm$^{-3}$)** | 1.00 | 1.30 | 1.50 | 1.50 | 3.40 | 5.29 |
| **$Fe^{2+}$ concentration $\times$ $10^{-5}$ (mol dm$^{-3}$)** | 1.08 | 15.96 | 34.54 | 2.19 | 2.93 | 0.93 |

## 12.4.4 Dissolved $CO_2$ concentration

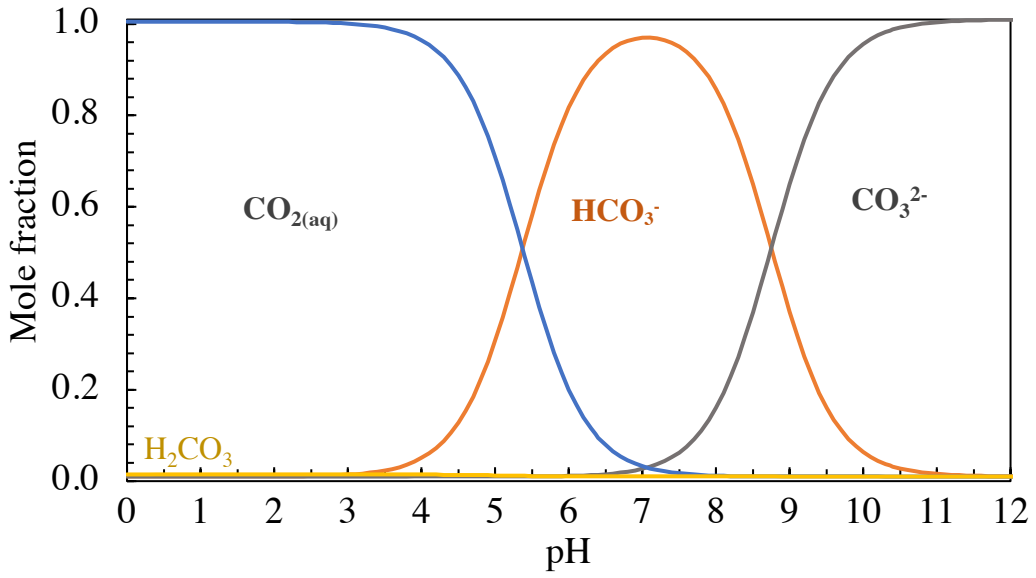



**Figure 12-12:** $CO_2$-$H_2O$ speciation calculated using equilibrium concentrations predicted with Gibbs energy of formation data in (Bard *et al.*, 1985).

$$C_{CO_{2(aq)}} + C_{H_2CO_3} + C_{HCO_3^-} + C_{CO_3^{-2}} = C_{\text{dissolved } CO_2} \quad \textbf{12-19}$$

$$C_{\text{dissolved } CO_2} \approx \mathbf{x}_i \frac{\rho_{H_2O}}{M_{H_2O}} = e^{-8.358} \times \frac{997 \text{ kgm}^{-3}}{18 \text{ kg kmol}^{-1}} = 0.0129 \text{ M} \quad \textbf{12-20}$$

where $\boldsymbol{x_i}$ is computed based on Equation **12-21** (Green & Perry, 2008)

$$\ln \mathbf{x}_i = -159.854 + \frac{8741.68}{T} + 21.6694 \ln T + -1.10261 \text{x} 10^{-3} T$$

$$\ln \mathbf{x}_i = -159.854 + \frac{8741.68}{(273.15 + 80)} + 21.6694 \ln(273.15 + 80) + -1.10261 \text{x} 10^{-3}(273.15 + 80) = -8.358 \quad \textbf{12-21}$$

At *ca*. pH ≥ 7.3, $HCO_3^-$ and $CO_3^{2-}$ are the predominant species so the total dissolved $CO_2$ was assumed to be the sum of $HCO_3^-$ and $CO_3^{2-}$ concentrations. If the dissolved $CO_2$ was less than the concentration of dissolved $CO_2$ at 80 °C, both concentrations were recalculated using the mole fraction and total dissolved $CO_2$. It was assumed that the additional $CO_2$ absorbed by MEA existed as MEA carbamate and so the concentration of $HCO_3^-$ and $CO_3^{2-}$ were dependent only on the pH of the $CO_2$ saturated amine solution and was independent of the $CO_2$ loading of the $MEA_{(aq)}$ solution. The additional $CO_2$ absorbed by MDEA was assumed to exist only as $HCO_3^-$ and hence the $CO_3^{2-}$ concentration was thought to be unaffected by the $CO_2$ loading of the $MDEA_{(aq)}$ solution. Therefore, the $CO_3^{2-}$ concentration in the $MDEA_{(aq)}$ solutions used to determine the saturation ratio ($S_{FeCO3}$) (*via* Equation **12-14**) is an underestimate.

$$\text{at pH} = 7.9 \text{ and T} = 80 \text{ °C}, \quad C_{HCO_3^-} = 20.79 \text{ M}, \quad C_{CO_3^{2-}} = 2.93 \text{ M}$$

$$C_{CO_3^{2-}} = \left(\frac{2.93}{20.79 + 2.93}\right) \times C_{\text{dissolved } CO_2} = 0.12 \times 0.0129 = 0.00159 \text{ M}$$

$$C_{HCO_3^-} = (1 - 0.12) \times 0.0129 = 0.01135 \text{ M}$$

**Table 12-8**: $CO_3^{2-}$ mole fractions used to calculate $CO_3^{2-}$ dissolved concentrations in MEA–$CO_2$ solutions at 80 °C

| **Concentration (M)** | 1 | 3 | 5 |
|---|---|---|---|
| **pH** | 7.7 | 7.8 | 7.9 |
| **$CO_3^{2-}$ mole fraction** | 0.08 | 0.10 | 0.12 |

**Table 12-9:** $CO_3^{2-}$ mole fractions used to calculate $CO_3^{2-}$ dissolved concentrations in MDEA–$CO_2$ solutions at 80 °C

| **Concentration (M)** | 1 | 3 | 5 |
|---|---|---|---|
| **pH** | 7.9 | 8.3 | 8.6 |
| **$CO_3^{2-}$ mole fraction** | 0.12 | 0.26 | 0.41 |

## 12.4.5 Solubility limit

The solubility limit or $K_{sp}$ of $FeCO_3$ is a function of the temperature and ionic strength as shown by Equation **12-22** (Sun, Nešić & Woollam, 2009).

$$\log K_{sp} = -59.3498 - 0.041377\,T - \frac{2.1963}{T} + 24.5724\log(T) + 2.518\,I^{0.5} - 0.657\,I \qquad \textbf{12-22}$$

### 12.4.5.1 Ionic strength

To calculate the ionic strength ($I$) of the solution, the concentration ($C_i$) of the dissolved species and corresponding species charge ($z_i$) would be needed.

$$I = \frac{1}{2}\sum C_i\,z_i^2 \qquad \textbf{12-23}$$

**Monoethanolamine**

Using the equilibrium equations for reactions **12-24** - **12-29**, along with an amine mass balance (Equation **12-30**) and $pCO_2$ = 1 atm, the equilibrium concentrations of the 8 species (*i.e.* not including $H^+$) included in Equation **12-24** - **12-29** were determined. Equilibrium constants were determined using Gibbs energy of formation data. The partial pressure of $CO_2$ was set to 1 atm since $CO_2$ was continuously bubbling through an open vessel containing the amine solution. The equations were solved simultaneously using the *solve* function in MATLAB. Dissolved $CO_2$ concentrations were not limited in the calculation but then corrected using the mole fraction of total dissolved $CO_2$.The additional $CO_2$ absorbed by MEA was assumed to exist as carbamate ($MEACOO^-$). The total dissolved $CO_2$, not including that captured by MEA producing $MEACOO^-$, was corrected based on a maximum total dissolved concentration 0.0129 mol $dm^{-3}$. The total amine concentration was set to 1, 3 or 5 M. The concentrations at the solution pH were used in the ionic strength calculation. An example of the script is given in Section 12.4.11.

$$CO_{2(g)} \overset{K_1}{\leftrightarrow} CO_{2(aq)} \quad \textbf{12-24}$$

$$CO_{2_{(aq)}} + H_2O \overset{K_2}{\leftrightarrow} H_2CO_3 \quad \textbf{12-25}$$

$$CO_{2_{(aq)}} + H_2O \overset{K_3}{\leftrightarrow} HCO_3^- + H^+ \quad \textbf{12-26}$$

$$HCO_3^- \overset{K_4}{\leftrightarrow} CO_3^{2-} + H^+ \quad \textbf{12-27}$$

$$MEA + HCO_3^- \overset{K_5}{\leftrightarrow} MEACOO^- + H_2O \quad \textbf{12-28}$$

$$MEA + H^+ \overset{K_6}{\leftrightarrow} MEAH^+ \quad \textbf{12-29}$$

$$\text{Total amine concentration} = [MEA] + [MEAH^+] + [MEACOO^-] \quad \textbf{12-30}$$

$$pCO_2 = 1 \text{ atm} \quad \textbf{12-31}$$

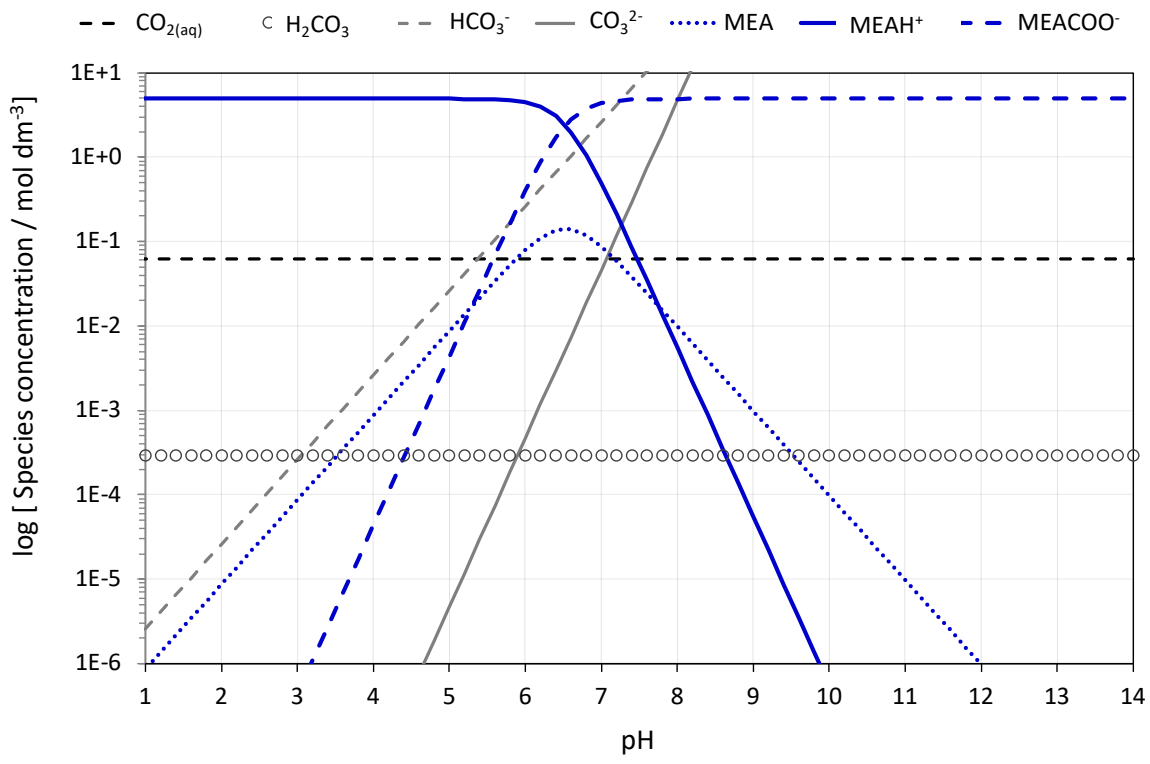



**Figure 12-13:** Equilibrium concentrations of dissolved species in MEA–$CO_2$–$H_2O$ at 80 °C.

**Table 12-10:** Ionic strength of MEA–$CO_2$ solutions at 80 °C based on equilibrium concentrations calculated using Gibbs energy of formation data (Bard *et al*., 1985).

| **Concentration (M)** | 1 | 3 | 5 |
|---|---|---|---|
| **Ionic strength (M)** | 0.52 | 1.50 | 2.48 |

**Methyldiethanolamine**

The equilibrium concentration of dissolved species in $MDEA_{(aq)}$ solutions saturated with $CO_2$ at 80 °C were calculated following the same method as that described for MEA. An equilibrium equation for reaction **12-32** and an amine mass balance (Equation **12-33**) were solved simultaneously along with **12-24** - **12-36** and **12-31** to determine the solution speciation. Since MDEA $CO_2$ capture involves formation of $HCO_3^-$ and does not involve carbamates, the total dissolved $CO_2$ used to correct the $CO_3^{2-}$ and $HCO_3^-$ was calculated using $CO_2$ loading per mole of amine ratios listed in **Table 12-11**. The ionic strengths shown in **Table 12-11** were calculated using the dissolved species concentrations from **Figure 12-14** at the solution pH, with the dissolved $CO_2$ species concentrations being corrected based on a maximum total dissolved concentration determined from the $CO_2$ loading per mole of amine ratio.

$$MDEA + H^+ \overset{K_{MDEA,6}}{\longleftrightarrow} MDEAH^+ \qquad \textbf{12-32}$$

$$\text{Total amine concentration} = [MDEA] + [MDEAH^+] \qquad \textbf{12-33}$$

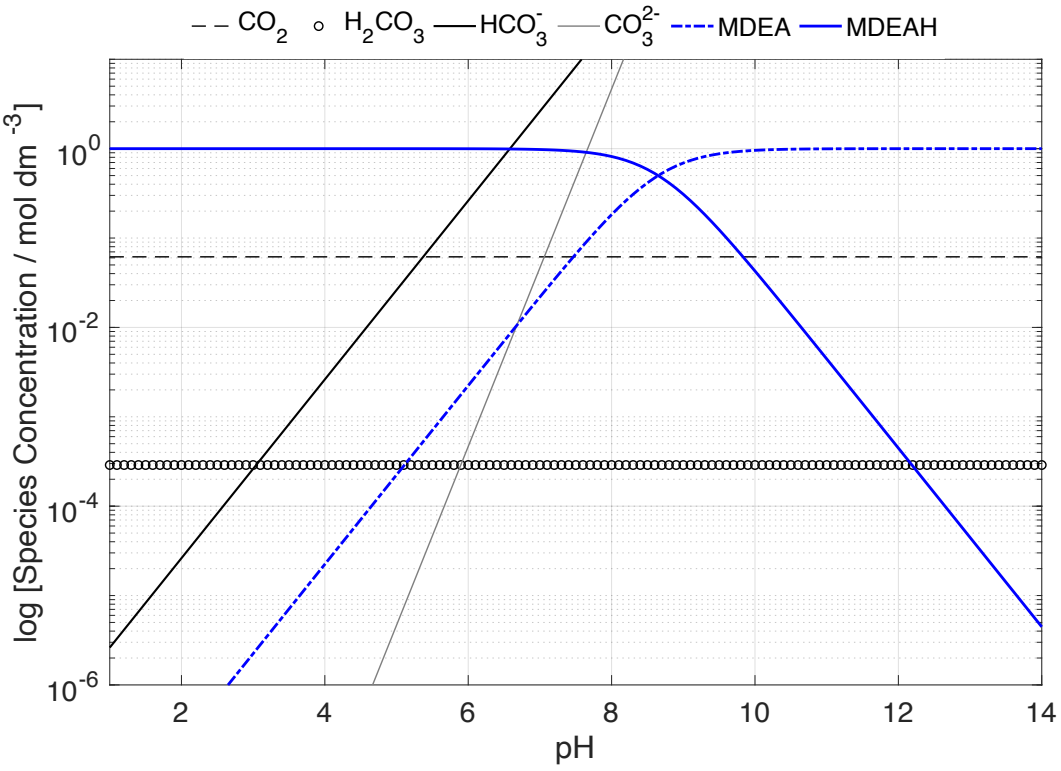



**Figure 12-14:** Equilibrium concentrations of dissolved species in MDEA–$CO_2$–$H_2O$ at 80 °C.

**Table 12-11:** Ionic strength of MDEA–$CO_2$ solutions at 80 °C based on equilibrium concentrations calculated using Gibbs energy of formation data (Bard *et al*., 1985) and $CO_2$ loading data ($\alpha$) estimated from (Rho *et al*., 1997).

| **Concentration (M)** | 1 | 3 | 5 |
|---|---|---|---|
| $\boldsymbol{\alpha}$ **(mol$_{CO2}$ mol$_{amine}^{-1}$)** | 1 | 0.5 | 0.25 |
| **Ionic strength (M)** | 1.88 | 2.38 | 2.72 |

## 12.4.6 Acid dissociation constants

The acid dissociation constant or equilibrium constant for reaction **12-34** is given by Equation **12-35**, assuming the activity coefficients are equal to unity. The $pK_a$ was calculated for reaction **12-34** using **12-36** with a= -819.7, b = 10.9756, c = 0, d = -79.474 taken from (Kamps & Maurer, 1996) and is valid for a temperature range of 273 to 368 K. At 353.15 K (80 °C), the $pK_a$ was calculated to be 7.65.

$$HA \leftrightarrow A^- + H^+ \qquad \textbf{12-34}$$

$$K_a = \frac{[A^-][H^+]}{[HA]}, \qquad pK_a = -\log K_a \qquad \textbf{12-35}$$

$$\ln K_a = \frac{a}{T_k} + b \ln T_k + cT + d \qquad \textbf{12-36}$$

A linear fit of reported dissociation constants of the reaction **12-29**. for temperatures between 293 and 353.14 K in (Hamborg & Versteeg, 2009) (**Figure 12-15**) was used to calculate the $pK_a$ of reaction **12-35**. At 80 °C (353.15 K), the $pK_a$ was calculated to be 8.05.

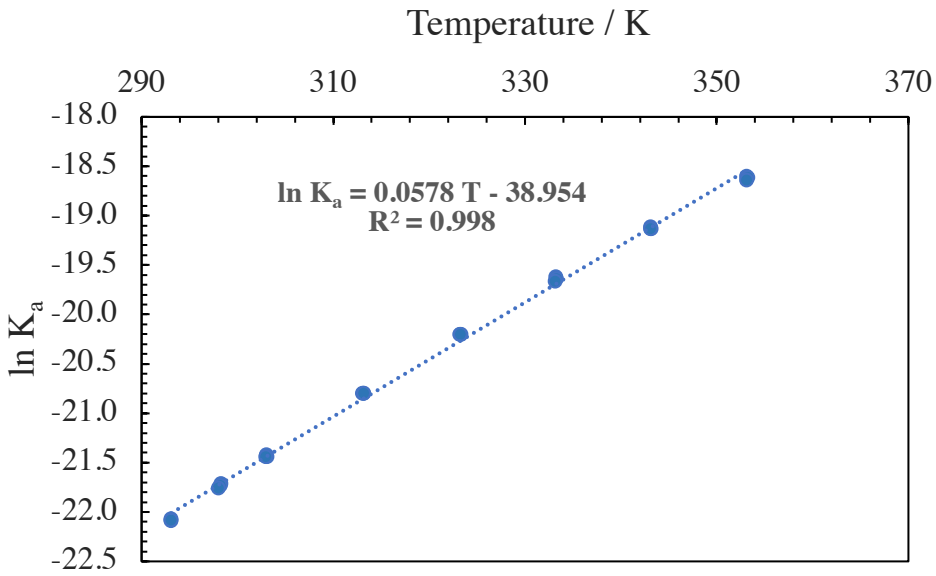



**Figure 12-15 :** Linear fit of ln $K_a$ data as a function of time reported in (Hamborg & Versteeg, 2009).

## 12.4.7 In-situ spectro-electrochemistry cell

Chronoamperometry and voltammetry experiments with *in-situ* Raman spectroscopy (Renishaw Raman spectrometer fitted with laser 532 nm wavelength laser) were planned. These experiments would have allowed for detection and identification of dissolved and solid (amorphous or crystalline) species. These experiments however could not be executed due to COVID-19. The spectro-electrochemical flow cell was designed based on a reactor found in the literature (Timm *et al*., 2017) and is shown in **Figure 12-16**. A schematic of the planned set up is shown in **Figure 12-17**.

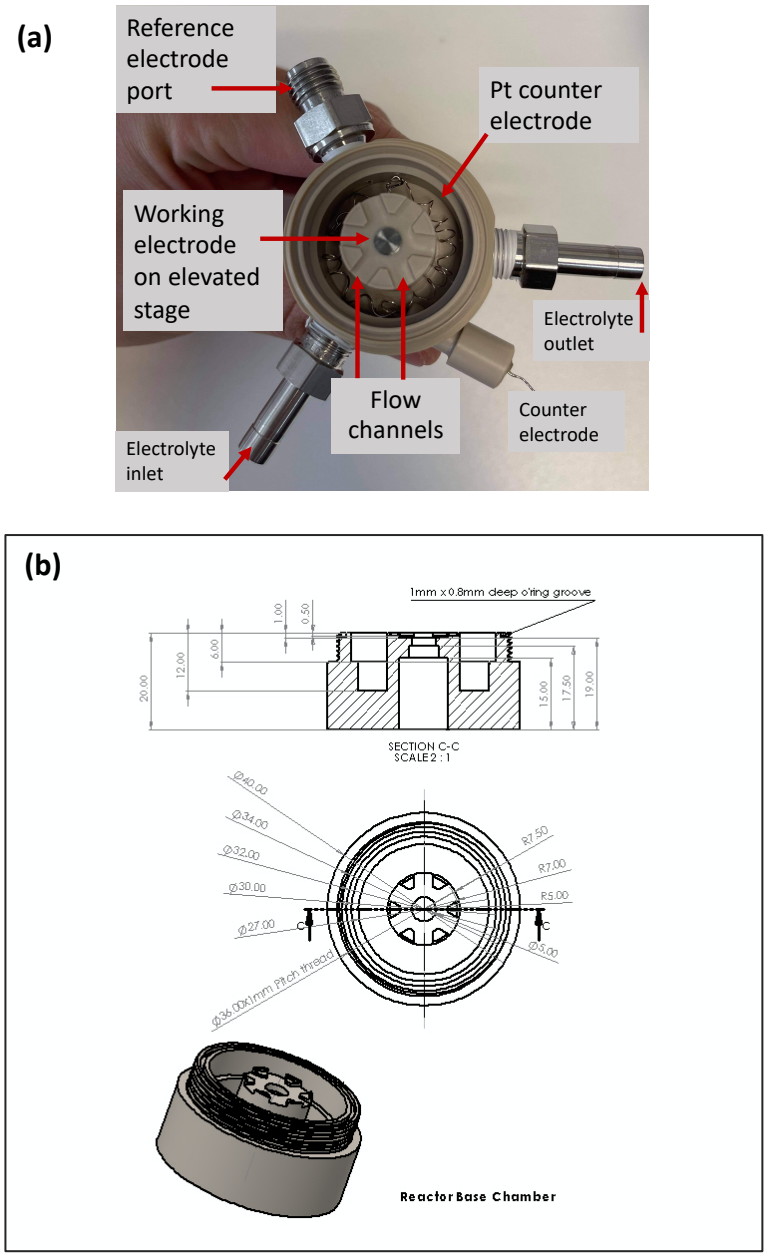



**Figure 12-16**: **(a)** Photo of fabricated spectro-electrochemical flow cell, **(b)** cell dimensions.

An aqueous amine reservoir would have been required for these experiments which would have allowed continuous bubbling of $CO_2$ to 1) maintain anoxic conditions and 2) ensure that the solution was saturated with $CO_2$ without requiring direct $CO_2$ injection into the spectro-electrochemical cell which would have likely resulted in noisy electrochemical measurements or obscure spectroscopy measurements. The aqueous amine $CO_2$ solution would be pumped into the cell which housed the working electrode. A fixed potential (for chronoamperometry) or a potential scan would have been applied to the working electrode and simultaneously, the Raman measurement would have been initiated. The experimental set up would have allowed collection of spent electrolyte to be sampled and analysed using ICP to detect $Fe^{2+}$ concentration in solution.

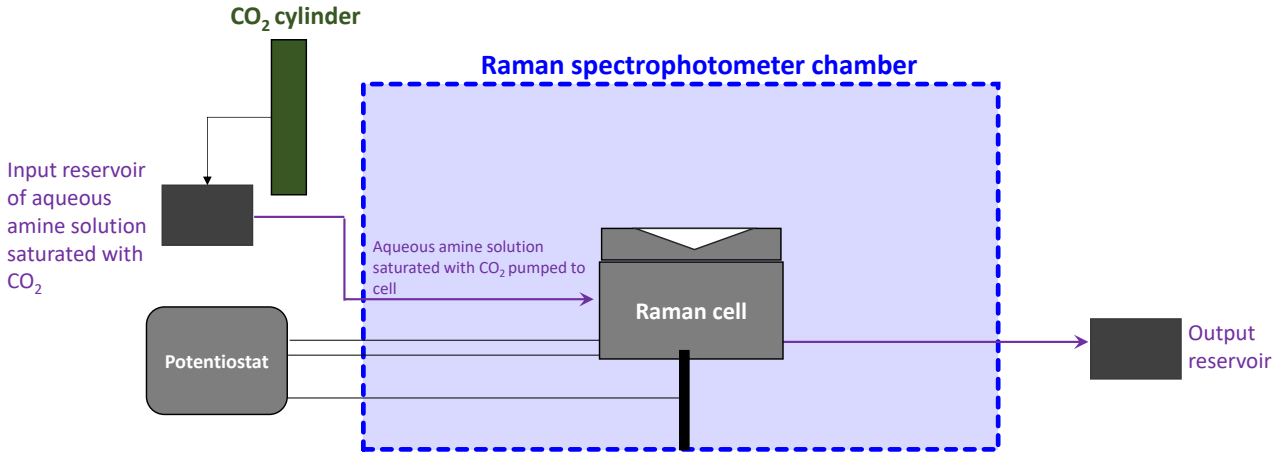



**Figure 12-17**: Schematic of proposed spectro-electrochemical experimental setup

## 12.4.8 MATLAB Scripts

**Equilibrium-concentrations**

### Thermodynamic data

```
%Standard Thermodynamic data (J.mol-1) of the form delG_species_state; source
%A.J.Bard, R.Parsons and J.Jordan (eds), 'Standard potentials in aqueous
%solution, Marcel Dekker, New York, 1985.

delG_H2O_l = -237178;
delG_O2_g = 16300;
delG_H_aq = 0;
delG_OH_aq = -157293;
delG_H2_g = 0;
delG_Fe_c = 0;
delG_Fe2_aq = -91500;
delG_CO3_aq = -527900;
delG_HCO3_aq = -587060;
delG_H2CO3_aq = -607630;
delG_CO2_aq = -386200;
delG_CO2_g = -394383;

%Thermodynamic Modeling for CO2 Absorption in Aqueous MDEA Solution with
%Electrolyte NRTL Model, Industrial & Engineering Chemistry Research 2011 50 (1), 163-175
delG_MDEA_aq = -169000;
delG_MDEAH_aq = -259890;
```

### Constants & conditions

```
%Constants
R=8.31434;% J.mol-1.K-1
Tc= 80;% °C
Tk=Tc+273.15;% K

%Compositional Variables
pco2=1;% atm
ph2=1;% atm
po2=1;% atm

total_amine_conc=1;% mol.L-1
```

```
o2=10^(-2.86)*po2;
```

**Chemical equations Speciation of CO2 in H2O at 298 K, pCO2 1 atm and activity limited to unity. Calculations were based on Gibbs free energy data published in (Bard *et al.*, 1985) .**

$$CO_{2\,(g)} \leftrightarrow CO_{2(aq)} \quad \ldots\ldots\ldots\ldots\ldots\ldots (1)$$

$$CO_{2\,(aq)} + H_2O \leftrightarrow H_2CO_{3(aq)} \quad \ldots\ldots\ldots\ldots\ldots\ldots (5)$$

$$CO_2 + H_2O \leftrightarrow HCO_3^- + H^+ \quad \ldots\ldots\ldots\ldots\ldots\ldots (2)$$

$$MDEA + H^+ \leftrightarrow MDEAH^+ \quad \ldots\ldots\ldots\ldots\ldots\ldots (3)$$

$$HCO_3^- \leftrightarrow CO_3^{2-} + H^+ \quad \ldots\ldots\ldots\ldots\ldots\ldots (4)$$

## Gibbs free energy for reactions 1 - 4

Reference for Keq_r3 Protonation constants and thermodynamic properties of amines for post combustion capture of CO2, J. Chem. Thermodynamics 51 (2012) 97–102

```
delG_r1= delG_CO2_aq - delG_CO2_g;
Keq_r1 = exp (-delG_r1/(R*Tk));

delG_r2= delG_HCO3_aq - delG_CO2_aq - delG_H2O_l;
Keq_r2 = exp (-delG_r2/(R*Tk));

delG_r3 = delG_MDEAH_aq - delG_MDEA_aq - delG_H_aq;
Keq_r3 = 10^8.65; % Kprot taken from
%Keq_r3 = exp(-delG_r3/(R*Tk));

delG_r4= delG_CO3_aq - delG_HCO3_aq;
Keq_r4 = exp(-delG_r4/(R*Tk))



delG_r5= delG_H2CO3_aq - delG_CO2_aq - delG_H2O_l;
Keq_r5 = exp (-delG_r5/(R*T));
```

## System of equations

```
syms h co2 hco3 co3 mdea mdeah pH
solh = h == 10^(-pH);
solco2 = co2 == pco2*Keq_r1;
solh2co3 =  h2co3==co2*Keq_r5;
solhco3 = hco3==Keq_r2*co2/h;
solco3 = co3 == Keq_r4*hco3/h;
solmdeah= mdeah == Keq_r3*mdea*h;
```

```
solmdea= mdea== total_amine_conc-mdeah;


S = solve(solh, solco2,solh2co3, solhco3, solco3, solmdeah, solmdea, [h, co2,h2co3, hco3, co3, mdeah,
mdea]);
Solution_pH = [1:0.1:14];
H = subs(S.h, pH, Solution_pH);
CO2 = subs(S.co2, pH, Solution_pH);
H2CO3 = subs(S.h2co3, pH, Solution_pH);
HCO3 = subs(S.hco3, pH, Solution_pH);
CO3 = subs(S.co3, pH, Solution_pH);
MDEA = subs(S.mdea, pH, Solution_pH);
MDEAH = subs(S.mdeah, pH, Solution_pH);
```

**Diffusion-reaction model**

Defining system of partial differential equations

```
function [c,b,s] = eqn80_DR5MEA_3(x,t,u,DuDx)
%set of partial differential equations which decribes the concentration of
%Fe2+ and HCO3- in the diffusion lay

%species 1: Fe2+
%species 2: HCO3-
%species 3: H+
%species 4: FeCO3
DFe =7.35e-10; % m2/s
DHCO3 = 1.13e-09;% m2/s
DH=9.51e-09; %m2 /s
DFECO3= DFe; %m2 /s

G_Fe2 =-78870; % J mol-1
G_HCO3= -587060; % J mol-1
G_FeCO3 = -666715; % J mol-1
G_H= 0;
Grxn = G_FeCO3 + G_H - G_HCO3 - G_Fe2; % J mol-1

Tc= 80; % ∞C
Tk= Tc+273.15; %K
R= 8.314; % J.mol-1.K-1
Ke_feco3 = exp(-Grxn/ (R*Tk));

omega=104.7; %rad/s

visc=1.07E-06; %kinematic viscosity, m2s-1
v=0.50123*(omega^(3/2))*(visc^(-1/2));
L=1.61*(DFe^(1/3))*(omega^(-1/2))*(visc^(1/6));

kr = exp(21.3 - (64851.4/(R*Tk))); %m4.kmol-1.s-1
A_V= 1/L;  %m-1
```

```
kfeco3 = kr*A_V/1000; % m3.mol-1.s-1
c = [0;1; 1; 1];
b1=DFe*DuDx(1) - v.*x.^2.*u(1);
b2= DHCO3*DuDx(2)- v.*x.^2.*u(2);
b3= DH*DuDx(3)-v.*x.^2.*u(3);
b4 =DFECO3*DuDx(4)-v.*x.^2.*u(4);
b= [b1;b2;b3;b4];

s=[-kfeco3*u(1)*u(2)+ (kfeco3*u(3)*u(4)/Ke_feco3);
    -(kfeco3*u(1)*u(2))+( kfeco3*u(3)*u(4)/Ke_feco3);
   (kfeco3*u(1)*u(2)- kfeco3*u(3)*u(4)/Ke_feco3);
   (kfeco3*u(1)*u(2)- kfeco3*u(3)*u(4)/Ke_feco3)];

end
```

Defining boundary conditions

```
function [pl,ql,pr,qr] = bc80_DR5MEA_3(xl,ul,xr,ur,t)

j_Fe = 104-(0.024.*t);% Am^-2  best fit line through current transient data
%2.82e-09; % m2/s
DFe =7.35e-10; % m2/s
DHCO3 = 1.13e-09;% m2/s
DH=9.51e-09; %m2 /s
DFECO3= DFe; %m2 /s

F =96485;% C mol^-1


N_Fe = j_Fe/(2*F); % A.m-2.A-1.s-1.mol =molm-2s-1

pl= [N_Fe; 0; 0;0];
ql=[DFe; 1;1;1];
pr= [ur(1)-1e-6; ur(2)-11.35; ur(3)-1.2589e-05; ur(4)];
qr=[0;0;0;0];
 end
```

Defining initial conditions

```
function uo = init80_DR5MEA_3(h)

uo=[1e-6; 11.35; 1.2589e-05;0];

end
```

Solving system of PDEs and subsequently estimating saturation ratio from concentrations of dissolved species

```
clear;clc;clf; close all
%% Diffusion model
m= 0;
%Define the solution mesh
DFe =7.35e-10; % m
omega=104.7; %rad/s
visc=1.07E-06; %kinematic viscosity, m2s-1
v=0.50123*(omega^(3/2))*(visc^(-1/2));
L=1.61*(DFe^(1/3))*(omega^(-1/2))*(visc^(1/6));

T_s=1000;
r =50; %number of rows
t = linspace(0,T_s,r);
x = linspace(0,L,r);

%Solve the PDE
sol = pdepe(m, @eqn80_DR5MEA_3, @init80_DR5MEA_3, @bc80_DR5MEA_3, x, t);
uFe =0.001* sol(:,:,1);
uHCO3 = 0.001*sol(:,:,2);
uH= 0.001*sol(:,:,3);
uFeCO3 = 0.001*sol(:,:,4);
s_pH= -log10(uH);
% % uFe
UFe_t = transpose(uFe);
UHCO3_t = transpose(uHCO3);
UH_t=transpose(uH);
```

```
UFeCO3_t = transpose(uFeCO3);

I=4.95/2;
Tc= 80; % ∞C
Tk= Tc+273.15; %K
Tf= Tc* (9/5) + 32;% ∞F
patm= 1; %atm
ppsi= patm * 18.695948775; %psi
pCO2=1; %atm
LogKsp=-59.3498 + (-0.041377*Tk)+(-2.1963/Tk)+(24.5724*log10(Tk))+(2.518*I^0.5)+(-0.657*I);

Ksp=(10.^LogKsp);
Kebi=10^-(10.61-(4.97e-03*Tf)+(1.331e-05*Tf^2)-(2.624e-05*ppsi)-(1.186*I^0.5)+(0.3466*I));

co3=Kebi*(uHCO3./uH);

%Supersaturation calculation
SfeCO3_80 = (uFe .*co3)./Ksp;
```

# 12.5 Chapter 7 appendix

## 12.5.1 Kramer-Kronig

**Table 12-12:** Validation of EIS data collected during film formation using Kramer-Kronig relations

| Solution | Re (Z) | Im (Z) | Δ\|Z\| | Δ Phase |
|---|---|---|---|---|
| 1 M MDEA, $t_o$ | 0.02 | 0.07 | 0.02 | 0.05 |
| 1 M MDEA, $t_f$ | 0.03 | 0.09 | 0.04 | 0.07 |
| 3 M MDEA, $t_o$ | 0.03 | 0.13 | 0.04 | 0.09 |
| 3 M MDEA, $t_f$ | 0.03 | 0.11 | 0.05 | 0.09 |
| 5 M MDEA, $t_o$ | 0.01 | 0.14 | 0.01 | 0.15 |
| 5 M MDEA, $t_f$ | 0.03 | 0.15 | 0.06 | 0.12 |

**Table 12-13**: Validation of EIS data collected during film dissolution using Kramer-Kronig relations

| Pre-treatment | Re (Z) | Im (Z) | Δ\|Z\| | Δ Phase |
|---|---|---|---|---|
| 1 M MDEA 0 h | 0.07 | 0.12 | 0.05 | 0.15 |
| 1 M MDEA 1 day | 0.02 | 0.04 | 0.02 | 0.04 |
| 1 M MDEA 1 week | 0.02 | 0.05 | 0.02 | 0.03 |
| 3 M MDEA 0 h | 0.03 | 0.04 | 0.03 | 0.03 |
| 3 M MDEA 1 day | 0.03 | 0.15 | 0.08 | 0.10 |
| 3 M MDEA 1 week | 0.04 | 0.19 | 0.11 | 0.12 |
| 5 M MDEA 0 h | 0.03 | 0.14 | 0.09 | 0.11 |
| 5 M MDEA 1 day | 0.06 | 0.17 | 0.12 | 0.09 |
| 5 M MDEA 1 week | 0.05 | 0.21 | 0.14 | 0.16 |
| Un-treated 0 h | 0.01 | 0.07 | 0.01 | 0.07 |
| Un-treated 1 day | 0.02 | 0.11 | 0.02 | 0.12 |
| Un-treated 1 week | 0.02 | 0.12 | 0.02 | 0.10 |

## 12.5.2 Repeated experiments

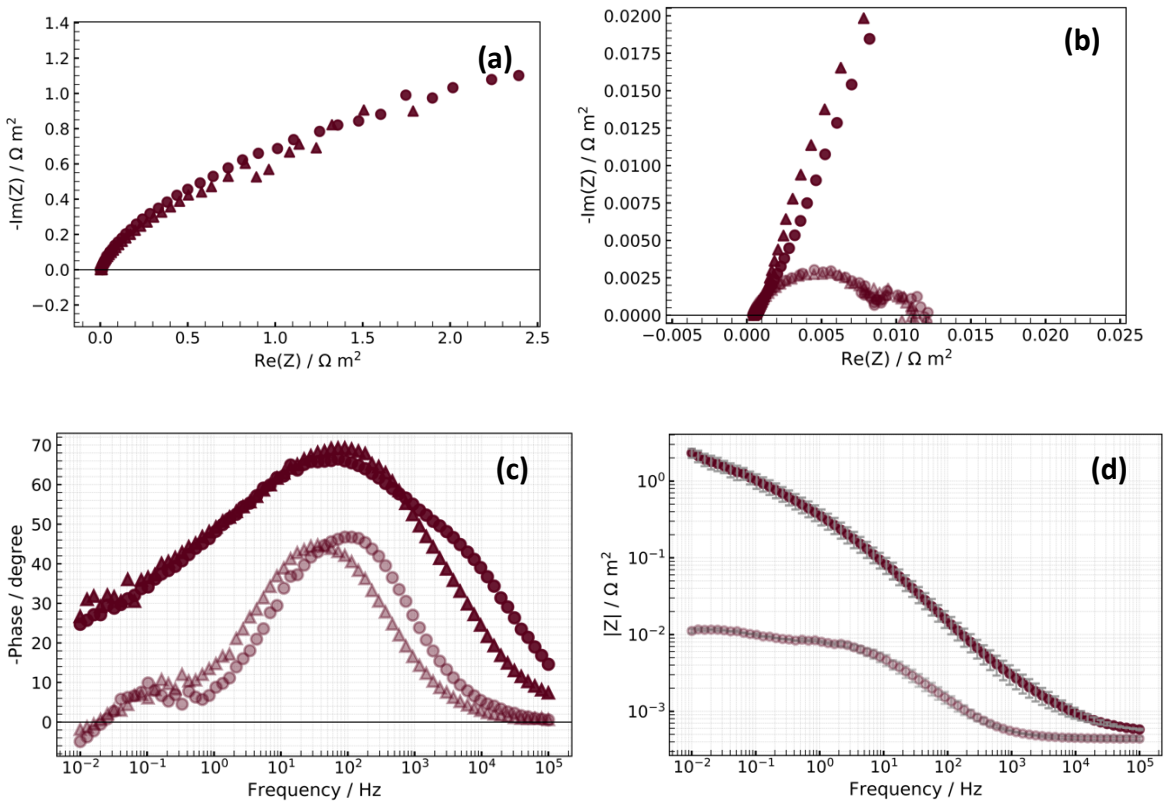



**Figure 12-18:** Experimental EIS data obtained for repeats of film formation on CS electrode immersed in 1 M $MDEA_{(aq)}$ saturated with $CO_2$ (pH 7.9) 80 °C. Pink corresponds to EIS data recorded after initial immersion of CS electrode in solution and dark red corresponds to EIS data recorded at the end of film formation: **(a – b)** Nyquist representation and **(c – d)** Bode representation of EIS data.

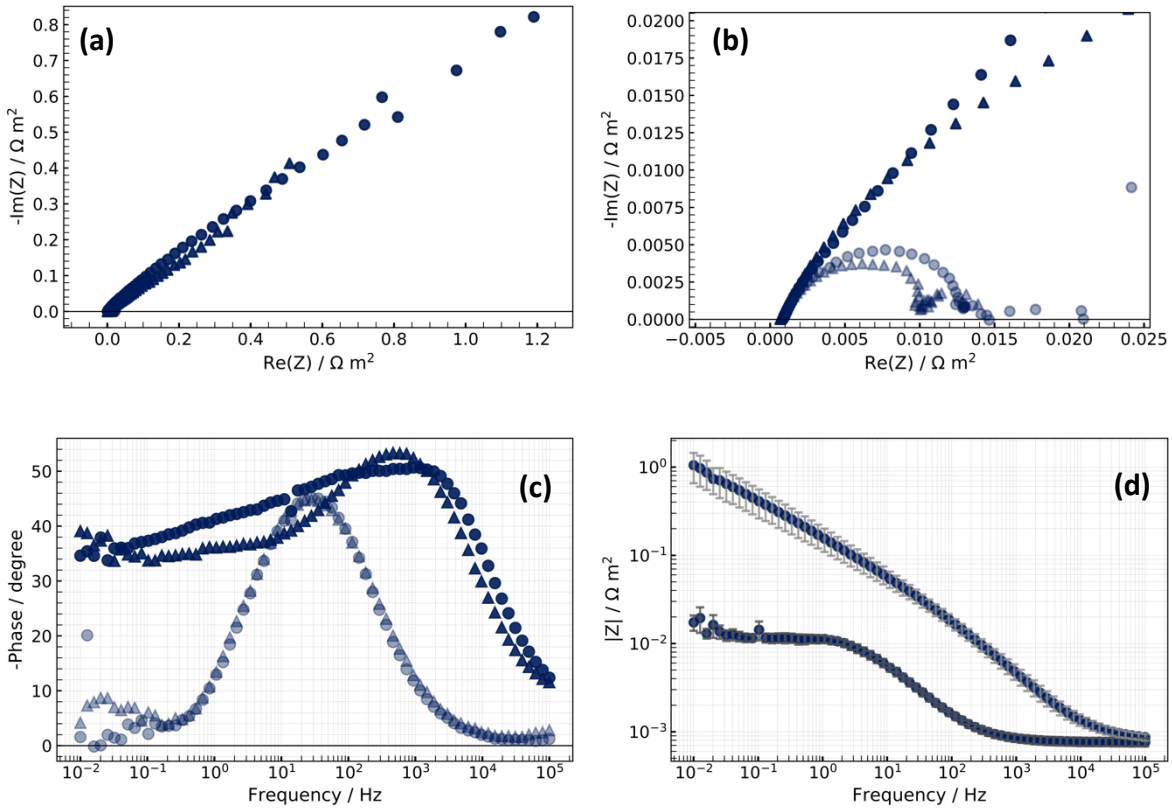



**Figure 12-19**: Experimental EIS data obtained for repeats of film formation on CS electrode immersed in 3 M $MDEA_{(aq)}$ saturated with $CO_2$ (pH 8.3) 80 °C. Light blue corresponds to EIS data recorded after initial immersion of CS electrode in solution and dark blue corresponds to EIS data recorded at the end of film formation: **(a – b)** Nyquist representation and **(c – d)** Bode representation of EIS data.

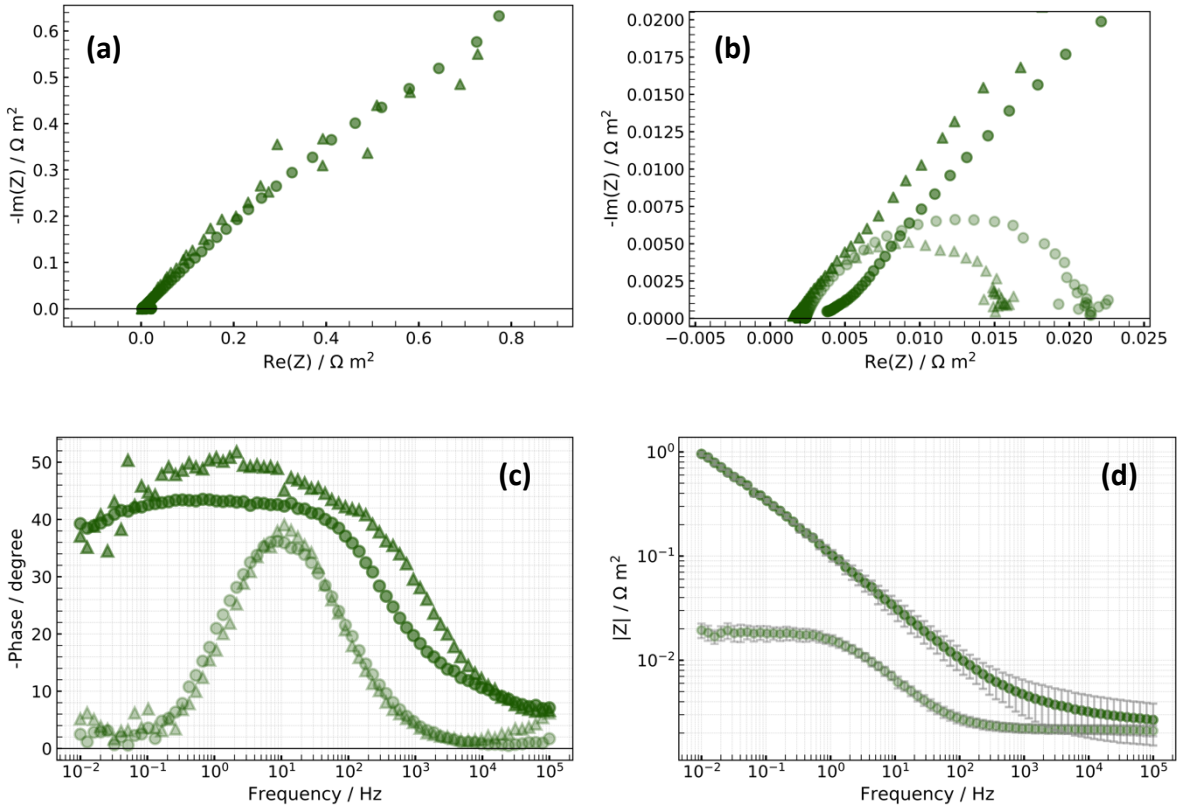



**Figure 12-20:** Experimental EIS data obtained for repeats of film formation on CS electrode immersed in 5 M $MDEA_{(aq)}$ saturated with $CO_2$ (pH 8.6) 80 °C. Light green corresponds to EIS data recorded after initial immersion of CS electrode in solution and dark green corresponds to EIS data recorded at the end of film formation: **(a – b)** Nyquist representation and **(c – d)** Bode representation of EIS data.

## 12.5.3 Circuit fitting values

**Table 12-14:** Circuit fitting values

| **Component** | **CS \| 1 M MDEA$_{(aq)}$ - $CO_2$ 80 °C, 0 h** | **CS \| 3 M MDEA$_{(aq)}$ - $CO_2$ 80 °C, 0 h** | **CS \| 5 M MDEA$_{(aq)}$ - $CO_2$ 80 °C, 0 h** |
|---|---|---|---|
| $R_S$ / Ω | 20.63 | 43.24 | 120 |
| $Q_{DL}$ / F $s^{\alpha-1}m^{-2}$ | 7.29E+00 | 5.73E+00 | 6.07E+00 |
| $\alpha_{DL}$ | 0.74 | 0.77 | 0.74 |
| $R_{CT}$ / Ω $m^2$ | 9.34E-03 | 1.19E-02 | 2.04E-02 |

| **Component** | **CS \| 1 M MDEA$_{(aq)}$ - $CO_2$ 80 °C, 72 h** | **CS \| 3 M MDEA$_{(aq)}$ - $CO_2$ 80 °C, 96 h** | **CS \| 5 M MDEA$_{(aq)}$ - $CO_2$ 80 °C, 156 h** |
|---|---|---|---|
| $R_S$ / Ω | 25.4 | 41.18 | 194 |
| $Q_C$ / F $s^{\alpha-1}m^{-2}$ | 4.24E-01 | 3.71E-01 | 2.05E+00 |
| $\alpha_C$ | 0.7257 | 0.7083 | 0.557 |
| $R_C$ / Ω $m^2$ | 2.00E-02 | 2.93E-02 | 1.31E-02 |
| $Q_{DL}$ / F $s^{\alpha-1}m^{-2}$ | 1.19E-02 | 7.55E-01 | 2.74E-01 |
| $\alpha_{DL}$ | 1 | 0.5751 | 0.708 |
| $R_{CT}$ / Ω $m^2$ | 6.73E-01 | 2.94E-01 | 2.15E-01 |
| $Q_{diff}$ / F $s^{\alpha-1}m^{-2}$ | 1.02E+00 | 1.80E+00 | 1.78E+00 |
| $\alpha_{diff}$ | 0.304 | 0.396 | 0.406 |

| **Component** | **CS coated (1 M) \| 5 MEA$_{(aq)}$ -$CO_2$ , 0 h** | **CS coated (3 M) \| 5 MEA$_{(aq)}$ -$CO_2$ , 0 h** | **CS coated (5 M) \| 5 MEA$_{(aq)}$ -$CO_2$ , 0 h** |
|---|---|---|---|
| $R_S$ / Ω | 14.85 | 15.2 | 10.76 |
| $Q_C$ / F $s^{\alpha-1}m^{-2}$ | 6.28E-01 | 1.42E+00 | 5.68E+00 |
| $\alpha_C$ | 0.838 | 0.6454 | 0.5691 |

| | | | |
|---|---|---|---|
| $R_C$ / Ω m$^2$ | 3.91E-03 | 4.96E-03 | 2.86E-03 |
| Qdl F s$^{\alpha-1}$m$^{-2}$ | 1.87E+00 | 4.52E-02 | 7.93E+00 |
| $\alpha_{DL}$ | 0.501 | 0.959 | 0.7073 |
| $R_{CT}$ / Ω m$^2$ | 2.07E-01 | 1.61E-01 | 8.25E-02 |
| $Q_{diff}$ / F s$^{\alpha-1}$m$^{-2}$ | N/A | 8.05E+00 | 2.27E+00 |
| $\alpha_{diff}$ | N/A | 0.3845 | 0.3361 |

| **Component** | **CS coated (1 M) \| 5 MEA$_{(aq)}$ -CO$_2$ , 1 day** | **CS coated (3 M) \| 5 MEA$_{(aq)}$ -CO$_2$ , 1 day** | **CS coated (5 M) - 5 M \| 5 MEA$_{(aq)}$ -CO$_2$ , 1 day** |
|---|---|---|---|
| $R_S$ / Ω | 12.09 | 14.6 | 10.69 |
| $Q_C$ / F s$^{\alpha-1}$m$^{-2}$ | 1.55E+00 | 5.20E+00 | 5.32E+00 |
| $\alpha_C$ | 0.7345 | 0.5405 | 0.5633 |
| $R_C$ / Ω m$^2$ | 2E-03 | 2.42E-03 | 3.95E-03 |
| $Q_{DL}$ / F s$^{\alpha-1}$m$^{-2}$ | 3.39E-01 | 1.89E+00 | 9.14E+00 |
| $\alpha_{DL}$ | 0.8977 | 0.8061 | 0.7411 |
| $R_{CT}$ / Ω m$^2$ | 3.87E-01 | 1.17E-01 | 1.08E-01 |
| $Q_{diff}$ / F s$^{\alpha-1}$m$^{-2}$ | N/A | 1.07E+00 | 1.02E-01 |
| $\alpha_{diff}$ | N/A | 0.1989 | 0.5 |

| **Component** | **CS coated (1 M) \| 5 MEA$_{(aq)}$ -CO$_2$ , 1 week** | **CS coated (3 M) - 3 M \| 5 MEA$_{(aq)}$ -CO$_2$ , 1 week** | **CS coated (5 M) \| 5 MEA$_{(aq)}$ -CO$_2$ , 1 week** |
|---|---|---|---|
| $R_S$ / Ω | 12.69 | 15.02 | 13.76 |
| $Q_C$ / F s$^{\alpha-1}$m$^{-2}$ | 3.58E+00 | 4.45E+01 | 7.32E+00 |
| $\alpha_C$ | 0.6571 | 0.7381 | 0.5169 |
| $R_C$ / Ω m$^2$ | 2.17E-03 | 6.59E-04 | 1.95E-03 |
| $Q_{DL}$ / F s$^{\alpha-1}$m$^{-2}$ | 6.70E-01 | 5.82E+00 | 2.50E+01 |

| | | | |
|---|---|---|---|
| $\alpha_{DL}$ | 0.8981 | 0.9457 | 0.8164 |
| $R_{CT}$ / Ω m$^2$ | 3.91E-01 | 4.07E-02 | 5.87E-02 |
| $Q_{diff}$ / F s$^{\alpha-1}$m$^{-2}$ | N/A | 1.08E+01 | 1.53E-02 |
| $\alpha_{diff}$ | N/A | 0.2282 | 0.3 |

| **Component** | **CS \| 5 MEA$_{(aq)}$ -CO$_2$ , 0 h** | **CS \| 5 MEA$_{(aq)}$ -CO$_2$ , 1 day** | **CS\| 5 MEA$_{(aq)}$ -CO$_2$ , 1 week** |
|---|---|---|---|
| $R_S$ / Ω | 26.58 | 23.71 | 31.03 |
| $Q_{DL}$ / F s$^{\alpha-1}$m$^{-2}$ | 4.98E+00 | 1.92E+01 | 3.11E+01 |
| $\alpha_{DL}$ | 0.7585 | 0.7691 | 0.7984 |
| $R_{CT}$ / Ω m$^2$ | 2.79E-02 | 3.80E-02 | 3.73E-02 |

## 12.5.4 Surface characterisation

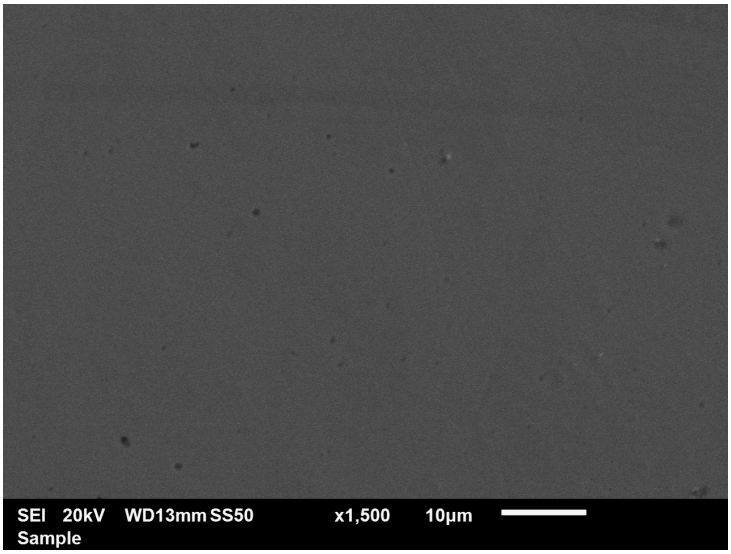
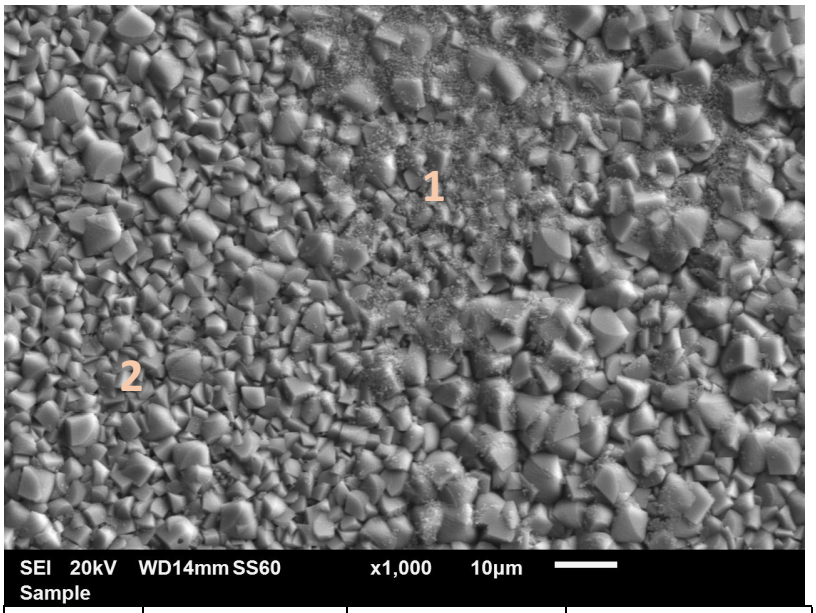
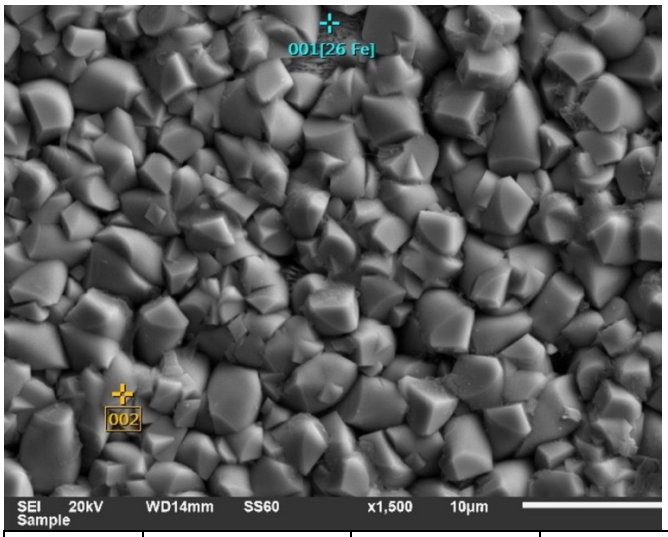



**Figure 12-21:** SEM image of a polished CS electrode



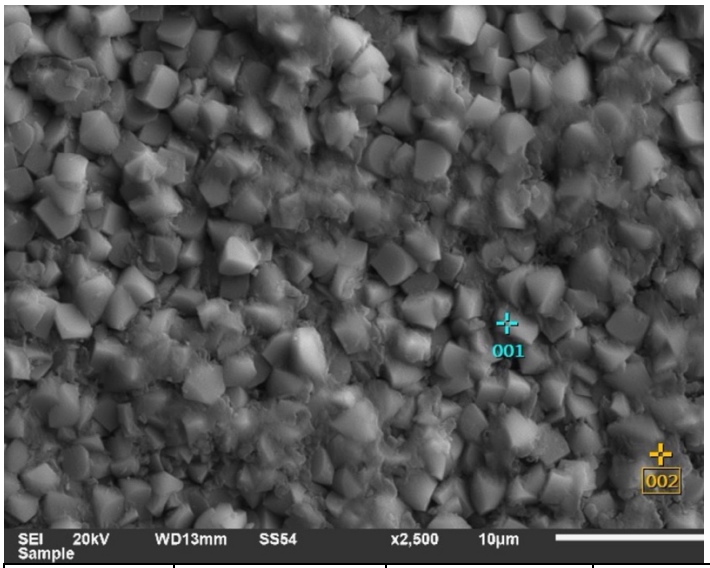

| Position | Fe (mass %) | C (mass %) | O (mass %) |
|---|---|---|---|
| 1 | 59.82 | 10.24 | 29.94 |
| 2 | 62.52 | 11.6 | 25.88 |

**Figure 12-22:** *Ex-situ* SEM images of CS electrode after immersion in 1 M $MDEA_{(aq)}$ saturated with $CO_2$ (pH 7.9) at 80 °C for *ca*. 72 hours and tabulated compositional analysis from point EDX.




| Position | Fe (mass %) | C (mass %) | O (mass %) | Other (mass %) |
|---|---|---|---|---|
| 1 | 94.69 | | 2.9 | Mn: 2.4 |
| 2 | 45.31 | 14.26 | 40.44 | |

**Figure 12-23:** *Ex-situ* SEM images of the CS electrode after immersion in 3 M $MDEA_{(aq)}$ saturated with $CO_2$ (pH 8.2) at 80 °C for *ca*. 96 and tabulated compositional analysis from point EDX




| Position | Fe (mass %) | C (mass %) | O (mass %) |
|---|---|---|---|
| 1 | 43.36 | 16.85 | 39.79 |
| 2 | 51.65 | 30.01 | 18.34 |

**Figure 12-24**: *Ex-situ* SEM image (1500x) of the CS electrode after immersion in 5 M $MDEA_{(aq)}$ saturated with $CO_2$ (pH 8.6) at 80 °C for *ca*. 156 hours tabulated compositional analysis from point EDX.

# 12.6 Chapter 8 appendix

## 12.6.1 Process conditions

**Figure 12-25**- **Figure 12-28** show a comparison of the pH, recorded using AT100 (located at the absorber exit), temperature, monitored using T210 (located in close proximity to the coated electrodes), and the electrolyte flow rate, collected using FT103 (located before filter N200), for each operational period of the two studies. Test 1 corresponds to study 1, which involved the coupon pre-treated in 1 M $MDEA_{(aq)}$ solution saturated with $CO_2$ at 80 °C. Test 2 corresponds to study 2, which involved the coupon pre-treated in 3 M $MDEA_{(aq)}$ solution saturated with $CO_2$ at 80 °C.

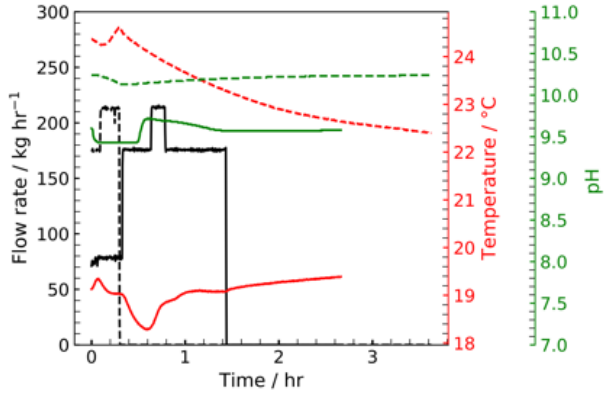



**Figure 12-25:** Mass flow rate (black), temperature (red) and pH (green), of process fluid to which coupons were exposed after initial installation during pre-test in pilot plant.

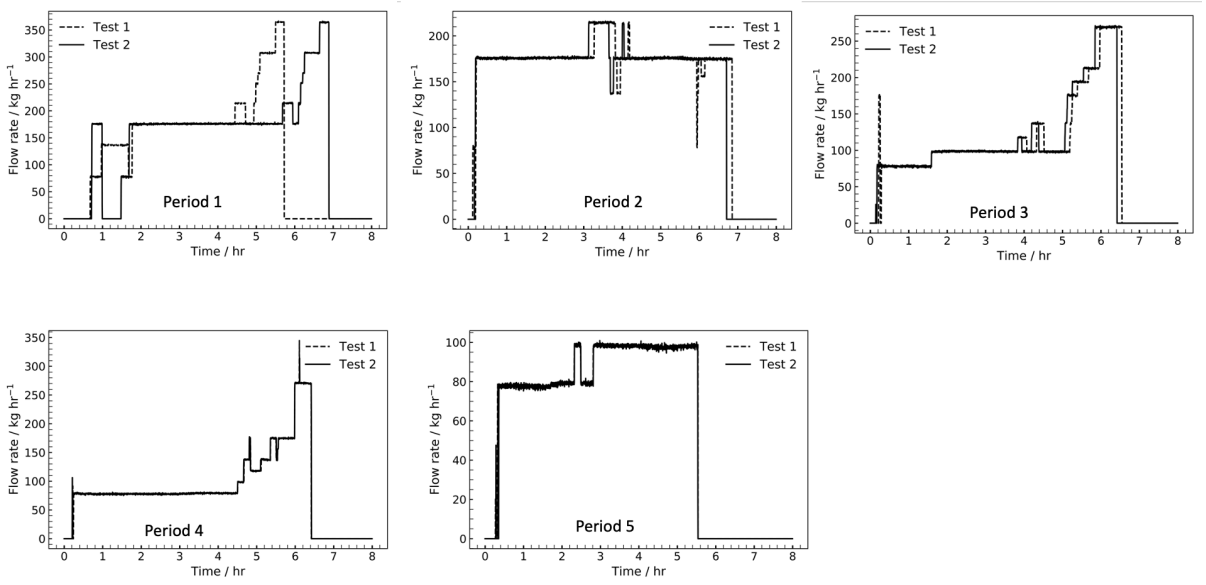


**Figure 12-26:** Mass flow rate (measured using FT103) of process fluid through pipelines in which coupons are installed for each operational period of both pilot plant studies.

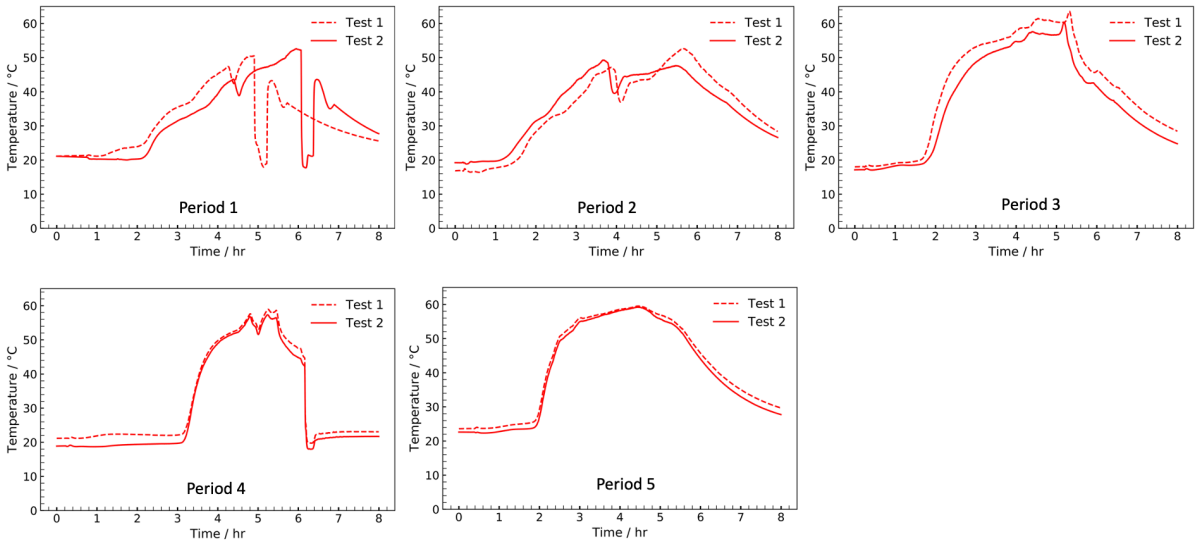



**Figure 12-27:** Process fluid temerpature (measured using TT210) to which coupons were exposed during each operational period of both pilot plant studies.

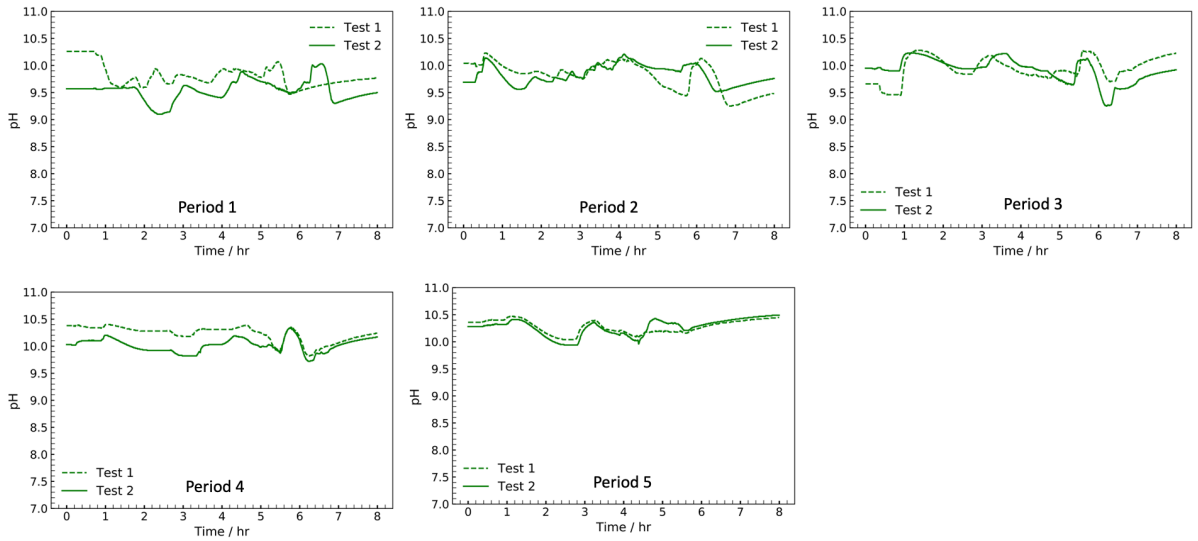



**Figure 12-28**: Process fluid pH (measured using AT100) indicative of conditions which coupons were likely exposed to during each operational period of both pilot plant studies.

## 12.6.2 Surface images

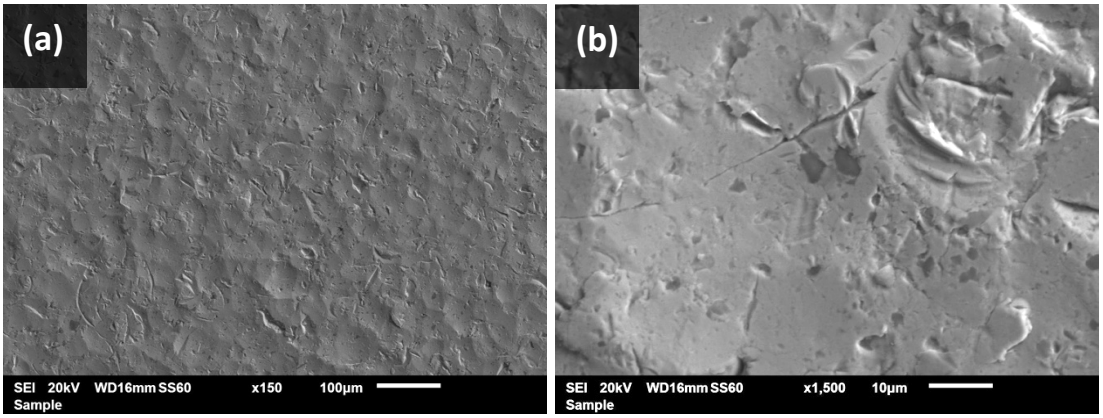



**Figure 12-29:** SEM images of pristine carbon steel coupon at **(a)** 150x and **(b)** 1500x magnifications.

## 12.6.3 Potential-pH

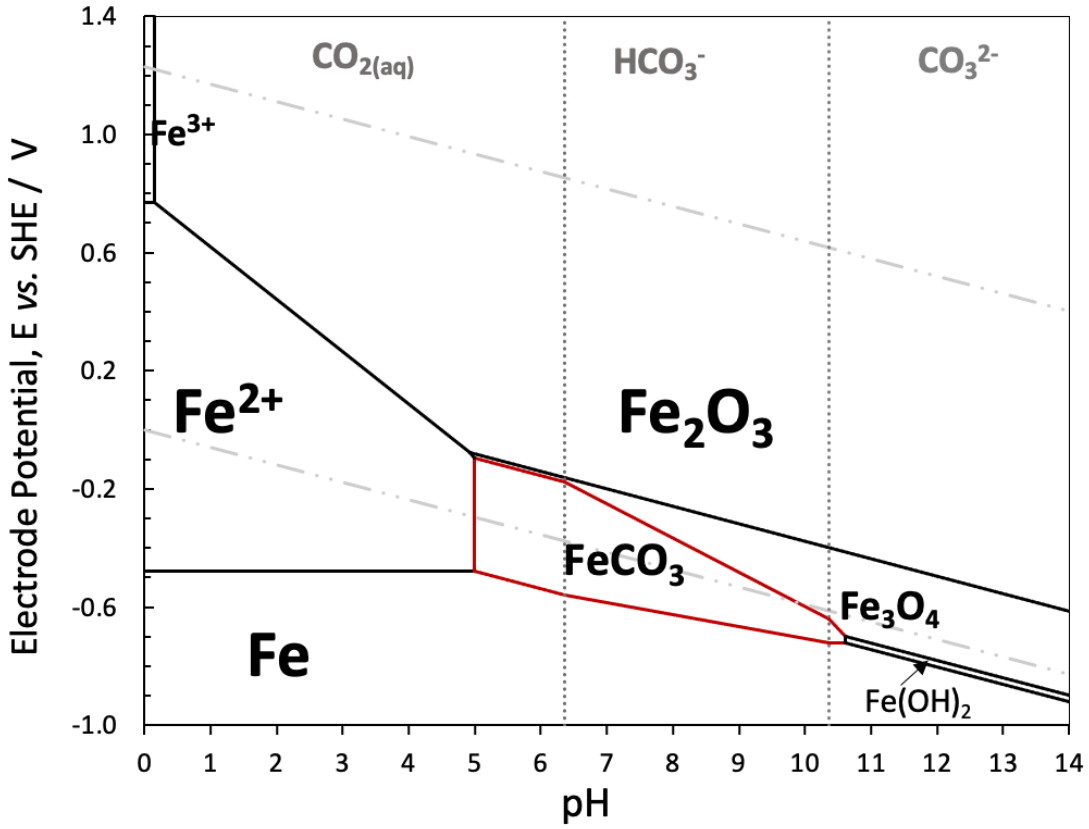



**Figure 12-30:** Potential-pH diagram for Fe-$CO_2$-$H_2O$ system at 25 °C, dissolved Fe activity 257 mg $dm^{-3}$ (0.0047 mol $dm^{-3}$), $pCO_2$ = 0.1 MPa with dissolved activities of $C^{IV}$ species limited to unity at high pH.

### 12.6.4 Kramer-Kronig and EIS circuit fitting

**Table 12-15**: Validation of EIS data collected during film formation using Kramer-Kronig relations

| Electrode \| Solution | Δ Re (Z) | Δ Im (Z) | Δ\|Z\| | Δ Phase |
|---|---|---|---|---|
| CS \|1 M MDEA, 0 h | 0.016 | 0.071 | 0.023 | 0.053 |
| CS \| 1 M MDEA, 116 h | 0.026 | 0.094 | 0.033 | 0.084 |
| CS \| 3 M MDEA, 0 h | 0.018 | 0.105 | 0.020 | 0.093 |
| CS \| 3 M MDEA, 189 h | 0.026 | 0.096 | 0.038 | 0.080 |
| CS pre-treated with 1 M MDEA 116 h \| 2.5 M MEA | 0.017 | 0.115 | 0.015 | 0.121 |
| CS pre-treated with 3 M MDEA 189 h \| 2.5 M MEA | 0.042 | 0.15 | 0.088 | 0.11 |
| CS (previously installed in pilot plant ) \| 2.5 M MEA | 0.169 | 0.51 | 0.282 | 0.375 |
| New CS \| 2.5 M MEA | 0.017 | 0.115 | 0.015 | 0.12 |

**Table 12-16**: Circuit fitting values

| **Component** | **CS \| 1 M MDEA$_{(aq)}$ -CO$_2$ 80 °C, 0 h** | **CS \| 3 M MDEA$_{(aq)}$ -CO$_2$ 80 °C, 0 h** |
|---|---|---|
| $R_S$ / Ω | 2.964 | 1.125 |
| $Q_{DL}$ / F s$^{\alpha-1}$m$^{-2}$ | 2.56E+00 | 9.61E+00 |
| $\alpha_{DL}$ | 0.7929 | 0.7617 |
| $R_{CT}$ / Ω m$^2$ | 4.05E-02 | 1.25E-02 |

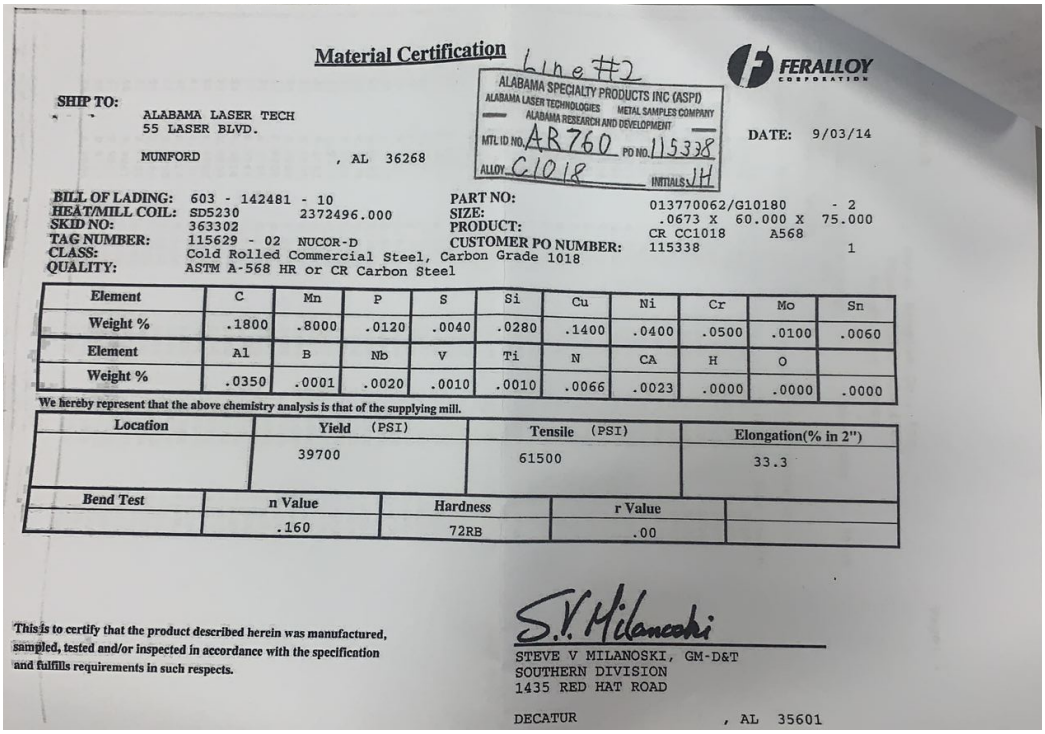
| **Component** | **CS \| 1 M MDEA$_{(aq)}$ -CO$_2$ 80 °C, 116 h** | **CS pre-treated 1 M MDEA$_{(aq)}$ -CO$_2$ 80 °C, 116 h \| 2.5 M MEA$_{(aq)}$-CO$_2$ 60 °C** |
|---|---|---|
| $R_S$ / Ω | 1.69 | 4.17 |
| $Q_C$ / F s$^{\alpha-1}$m$^{-2}$ | 1.76E-03 | 4.80E-04 |
| $\alpha_C$ | 0.8821 | 1 |
| $R_C$ / Ω m$^2$ | 1.40E-02 | 3.06E-03 |
| $Q_{DL}$ / F s$^{\alpha-1}$m$^{-2}$ | 1.14E-01 | 3.42E-01 |
| $\alpha_{DL}$ | 0.600 | 0.55 |
| $R_{CT}$ / Ω m$^2$ | 2.75E-01 | 6.69E-02 |
| $Q_{diff}$ / F s$^{\alpha-1}$m$^{-2}$ | 1.08E+00 | 2.13E+00 |
| $\alpha_{diff}$ | 0.375 | 0.486 |

| **Component** | **CS \| 3 M MDEA$_{(aq)}$ -CO$_2$ 80 °C, 189 h** | **CS pre-treated 3 M MDEA$_{(aq)}$ -CO$_2$ 80 °C, 189 h\| 2.5 M MEA$_{(aq)}$-CO$_2$ 60 °C** |
|---|---|---|
| $R_S$ / Ω | 1.125* | 3.85 |
| $Q_C$ / F s$^{\alpha-1}$m$^{-2}$ | 2.04E-04 | 2.66E-01 |
| $\alpha_C$ | 1 | 0.65 |
| $R_C$ / Ω m$^2$ | 1.15E-03 | 3.06E-03 |
| $Q_{diff1}$ / F s$^{\alpha-1}$m$^{-2}$ | 7.45E+00 | 3.48E+01 |
| $\alpha_{diff1}$ | 0.315 | 0.3821 |

| | | |
|---|---|---|
| $Q_{DL}$ / F $s^{\alpha-1}m^{-2}$ | 1E+00 | 2.69E+01 |
| $\alpha_{DL}$ | 1 | 1 |
| $R_{CT}$ / Ω $m^2$ | 6.97E-02 | 2.02E-02 |
| $Q_{diff2}$ / F $s^{\alpha-1}m^{-2}$ | 9.35E+00 | 1.56E+01 |
| $\alpha_{diff2}$ | 0.456 | 0.4945 |

| **Component** | **CS uncoated (after removing from pilot plant)\| 2.5 M $MEA_{(aq)}$-$CO_2$ 60 °C** | **New CS \|2.5 M $MEA_{(aq)}$-$CO_2$ 60 °C** |
|---|---|---|
| $R_S$ / Ω | 2.652 | 2.389 |
| $Q_{DL}$ / F $s^{\alpha-1}m^{-2}$ | 4.79E+00 | 8.54E-01 |
| $\alpha_{DL}$ | 0.879 | 0.7126 |
| $R_{CT}$ / Ω $m^2$ | 5.74E+00 | 1.57E-01 |

## 12.6.5 Material composition



**Material Certification** Line #2

FERALLOY CORPORATION

ALABAMA SPECIALTY PRODUCTS INC (ASPI)
ALABAMA LASER TECHNOLOGIES METAL SAMPLES COMPANY
ALABAMA RESEARCH AND DEVELOPMENT
MTL ID NO. AR760 PO NO. 115338
ALLOY C1018 INITIALS JH

**SHIP TO:**
ALABAMA LASER TECH
55 LASER BLVD.
MUNFORD , AL 36268

**DATE:** 9/03/14

**BILL OF LADING:** 603 - 142481 - 10
**HEAT/MILL COIL:** SD5230 2372496.000
**SKID NO:** 363302
**TAG NUMBER:** 115629 - 02 NUCOR-D
**CLASS:** Cold Rolled Commercial Steel, Carbon Grade 1018
**QUALITY:** ASTM A-568 HR or CR Carbon Steel

**PART NO:** 013770062/G10180 - 2
**SIZE:** .0673 X 60.000 X 75.000
**PRODUCT:** CR CC1018 A568
**CUSTOMER PO NUMBER:** 115338 1

| Element | C | Mn | P | S | Si | Cu | Ni | Cr | Mo | Sn |
|---|---|---|---|---|---|---|---|---|---|---|
| Weight % | .1800 | .8000 | .0120 | .0040 | .0280 | .1400 | .0400 | .0500 | .0100 | .0060 |
| Element | Al | B | Nb | V | Ti | N | CA | H | O | |
| Weight % | .0350 | .0001 | .0020 | .0010 | .0010 | .0066 | .0023 | .0000 | .0000 | .0000 |

We hereby represent that the above chemistry analysis is that of the supplying mill.

| Location | Yield (PSI) | Tensile (PSI) | Elongation(% in 2") |
|---|---|---|---|
| | 39700 | 61500 | 33.3 |

| Bend Test | n Value | Hardness | r Value | |
|---|---|---|---|---|
| | .160 | 72RB | .00 | |

This is to certify that the product described herein was manufactured, sampled, tested and/or inspected in accordance with the specification and fulfills requirements in such respects.

S.V. Milanoski

STEVE V MILANOSKI, GM-D&T
SOUTHERN DIVISION
1435 RED HAT ROAD
DECATUR , AL 35601

**Figure 12-31:** Material certification for carbon steel (C1018) used in experiments in this thesis. C1018 was sourced from Alabama Specialty Metals, USA.